Numerical Modelling Applications in Mining and Geomechanics

Applications de la modélisation numérique aux travaux miniers et à la géomécanique

Edited by / Édité par
HANI SABRI MITRI
Department of Mining and Metallurgical Engineering
McGill University, Montreal, Quebec, Canada

McGILL UNIVERSITY

PROCEEDINGS OF THE FIRST CANADIAN SYMPOSIUM ON NUMERICAL MODELLING APPLICATIONS IN MINING AND GEOMECHANICS/MONTREAL/QUEBEC/27-30 MARCH 1993

COMPTES RENDUS DU PREMIER SYMPOSIUM CANADIEN SUR LES APPLICATIONS DE LA MODÉLISATION NUMÉRIQUE AUX TRAVAUX MINIERS ET A LA GÉOMÉCANIQUE/MONTRÉAL/QUÉBEC/27-30 MARS 1993

Numerical Modelling Applications in Mining and Geomechanics

Applications de la modélisation numérique aux travaux miniers et à la géomécanique

Edited by / Édité par
HANI SABRI MITRI
Department of Mining and Metallurgical Engineering
McGill University, Montreal, Quebec, Canada

McGILL UNIVERSITY

Organization of the symposium / Organisation du symposium

Technical Advisory Board / Comité consultatif

Michel Aubertin, Ecole Polytechnique, Montreal, Quebec
Euler DeSouza, Queen's University, Kingston, Ontario
John Franklin, University of Waterloo, Kitchener, Ontario
Nick Kripakov, United States Bureau of Mines, Denver, Colorado
Rimas Pakalnis, University of British Columbia

Local Organizing Committee / Comité organisateur

Michel Bilodeau
Frank Boudreault
Laeeque Daneshmend
Ferri Hassani
John Mossop
Laura Mottola
Purnima Mujumdar
Norma Procyshyn
Marina Rosati
Malcolm Scoble
Michel Vachon

Preface

When awarded the honour to chair the First Canadian Symposium on Numerical Modelling Applications in Mining and Geomechanics, I was excited to organize a meeting that is held for the first time in Canada. However, as time passed, my excitement gradually subsided and nervousness began to grow. Deadlines came one after another and nothing seemed to be under control. I must admit that if it had not been for the dedication of Marina Rosati and for the help of the Organizing Committee, this symposium would not have reached maturity.

This is the first of a series of symposia to be hosted and organized by McGill University. The series aims to provide a forum for researchers, engineers and analysts to share, discuss and exchange new ideas and innovations in the application of numerical methods to problems in mining and geomechanics. It is hoped that the symposium will promote further research and enhance collaborative projects in future. I personally hope that each of us will return home with a new thought.

Over forty-five abstracts were submitted for consideration, from which thirty papers from Canada, U.S.A. and France have been selected. These consist of two Keynote Addresses and twenty-eight papers divided into the following themes:

1. Underground Mining
2. Soft Rock
3. Coal Mining
4. Subsidence
5. Open Pit Mining
6. Hard Rock
7. Ground Support
8. Miscellaneous Applications

I would like to express my sincere thanks to the members of the Technical Advisory Board and Technical Session Leaders for their help in making the symposium a success.

Now that this Preface is written and another deadline has just been met, things finally seem to be under control.

Welcome to Montreal!

Hani Sabri Mitri
Symposium Chairman

Préface

Quand on me conféra l'honneur de présider le premier symposium canadien sur les applications de la modélisation numérique aux travaux miniers et à la géomécanique, j'étais très enthousiaste à l'idée d'organiser une rencontre qui se tiendrait pour la première fois au Canada. Cependant, comme le temps passait, mon enthousiasme fit graduellement place à une nervosité grandissante. Les délais venaient à échéance l'un après l'autre et tout me semblait hors de contrôle. Je dois admettre que sans le dévouement de Marina Rosati et l'aide apportée par le Comité organisateur, ce symposium n'aurait pu voir le jour.

Ce symposium est le premier d'une série dont McGill sera l'hôte et l'organisateur. La série vise à constituer un forum pour les chercheurs, ingénieurs et analystes afin d'apporter, échanger et discuter des nouvelles idées et des innovations dans l'application des méthodes numériques aux problèmes rencontrés dans les travaux miniers et la géomécanique. Nous espérons que ce symposium saura promouvoir la recherche et accroître la collaboration dans l'avenir. J'espère personnellement que chacun de vous retournera chez lui avec de nouvelles idées.

Plus de quarante-cinq résumés ont été soumis pour examen, parmi lesquels trente écrits provenant du Canada, des États-Unis et de la France furent choisis. Ils consistent en deux lectures et vingt-huit abrégés répartis selon les sujets suivants:

- Mines souterraines
- Roche tendre
- Mines de charbon
- Affaissement
- Mines à ciel ouvert
- Roche dure
- Soutènement
- Autres

J'aimerais exprimer mes sincères remerciements aux membres du Comité consultatif et aux chefs de session pour leur aide afin de faire de ce symposium un succès.

Maintenant que cette préface est rédigée et que tous les délais ont été respectés, les choses semblent finalement sous contrôle.

Bienvenue à Montréal!

Hani Sabri Mitri
Président du symposium

Table of contents / Table des matières

Keynote Address

Trends in design of work in rock

By

John A. Franklin

TRENDS IN DESIGN OF WORKS IN ROCK

John A. Franklin
Research Professor
Department of Earth Sciences
University of Waterloo
Waterloo, Ontario, Canada

A HISTORICAL PERSPECTIVE

Perhaps my main if not only qualification to give this introductory talk is that being of somewhat mature age, I can look back on the evolution of design methods in rock mechanics since the first 1966 ISRM Congress in Lisbon, which I was privileged to attend as a student.

Many of the techniques prevalent at that time have all but disappeared, a reminder of the transient nature of much of our research. This includes the photoelastic models which gave colourful and attractive if somewhat idealized stress distribution. Great contortions were required to investigate problems other than simple elasticity. In an attempt to "go viscous" a fellow student (now a professor of mining) built his photoelastic model out of Jello. It was stored in the office next to mine. No-one actually ate the model, which grew mouldy and opaque in just a few days. Equally cumbersome were the very large physical models of dam foundations and mine workings, which took weeks to build out of plaster, sand and sawdust. At the time these provided a steady income for a few well-known geomechanics laboratories in Europe, but like the electric analogues made from conducting paper or complex networks of resistors, the few that remain are now museum pieces gathering dust.

Back in the 1960's and early 70's, we were very proud of our new Imperial College IBM computer with its capacity of 640K. It occupied a whole room of the Engineering Building. Our programs and data were card-punched and verified by an army of keyboard operators. If we took care to limit ourselves to small problems, we could experiment with the finite element analyses that were emerging from Professor Zienkiewicz and colleagues in the University of Wales. It was about then that people started to realize that rock contained joints. The limitations of elastic analyses soon became apparent.

Since that time we have seen rapid emergence of programs with increasing degrees of sophistication and power, boundary-discretization methods, distinct element discontinuum models, and the key block approach of Goodman and students at Berkeley. Advanced computer graphics methods have made problems easier to visualize as well as to solve.

Perhaps even more influential has been the steady fall in the price of hardware, a corresponding increase in computer literacy, and the emergence and growth of a software industry to supply this new market. As President of the ISRM Commission on Education, I have had the chance to make a small contribution to this technology by putting together a collection of educational software, available at modest cost from the Secretariat in Lisbon. The collection includes a selection of finite element, boundary element, limiting equilibrium and other popular forms of program, making the latest software innovations more readily accessible to geomechanics teachers in developing nations as well as in the more technologically advanced communities worldwide.

WHERE ARE WE NOW?

The dollar value of geomechanics investigations follows a skewed distribution with many small-budget projects and progressively fewer larger ones. By far the majority of these investigations are at the inexpensive end of the spectrum where there is little time for analytical work or elaborate testing. Most of the effort on these smaller projects goes into site investigation, and decisions are based mostly on judgement and the characteristics of the ground as best they can be determined.

Just ten years ago, we could have said with some confidence that geomechanics analyses were applicable to just a few of the high-budget projects like planning a new mine, designing a dam foundation or stabilizing a cavern. However, with the popularization of microcomputer technology, there has been a dramatic shift towards the use of computer modelling in routine medium and even low-budget investigations. This trend will no doubt continue, not so much because of cost considerations (if never was very expensive to hire an analyst), but as a result of two other factors:

- with a computer at the mine or construction site there is now minimal delay between questions and answers. The engineer no longer has to wait for a report from a consultant;
- with control of analysis now in the hands of the user, the algorithms can be edited day-by-day until they ask the right questions and give answers that are really useful.

Computer simulation is now feasible not just at the early planning stages when there is ample time for experimentation, but increasingly during the actual operations of mining and construction, when adjustments to excavation and support must be made with very little delay in response to changing ground conditions.
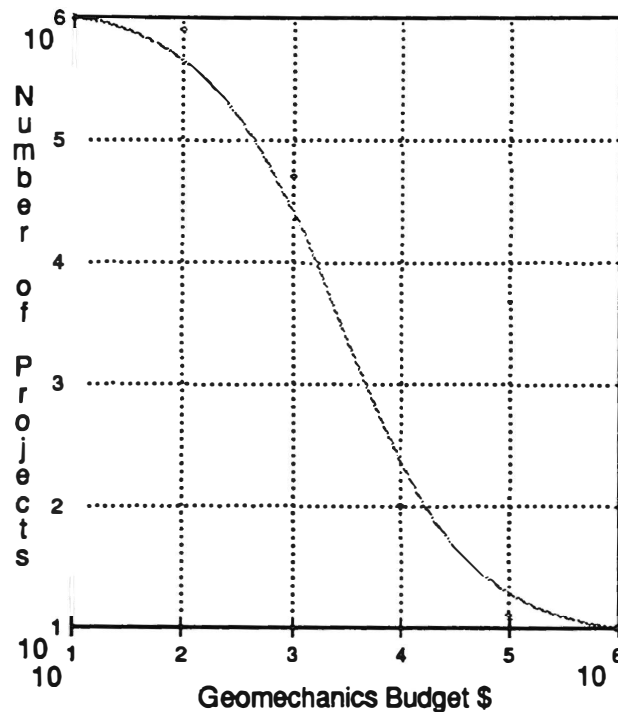
In spite of all the advances however, there remain some quite astounding gaps between the questions of real interest and the answers the analyst can provide. Take the design of stopes and tunnels, for example. Why are nearly all our design methods dimensionless and time-independent, when we know that a small excavation is more stable than a large one, and remains stable for longer? The standard method of tunnelling through bad ground is to slash to full dimensions only after stabilizing a small heading. Similarly, the miner selects large open stopes in massive rock, but cut-and-fill or even caving methods in broken and weak rock. The fundamental rule is that the worse the rock, the smaller the openings that can be tolerated , and the greater the reliance on backfill or broken ore to support the remainder of the stope (Franklin and Palassi, 1993). Most continuum mechanics methods tell us about stresses, not stand-times or stable dimensions. They don't ask the right questions, let alone answer them.

WHERE ARE WE HEADING?

It seems that the gap is narrowing between the questions of real interest to the engineer, and the answers provided. The analyst and engineer are rapidly becoming one and the same person. However, the scope of analysis should be greatly expanded. Design is a decision making process, and includes not only stress analysis but the choice between blasting and boring, design of blast patterns, prediction of rates of TBM advance, and selection and design of optimum support systems. Many of the questions are inaccessible to continuum mechanics solutions and can best be addressed by empirical methods where ground quality is correlated directly with ground behaviour. These methods have long been regarded as the "poor relation" of classical mechanics, yet are no less amenable to a scientific approach.

The complex and interactive nature of rock engineering design is an ideal application for expert systems, which lend themselves to storage and management of a large body of experience on rock behaviour under a variety of conditions, together with a diverse bag of empirical, analytical and numerical tools. As the knowledge of more and more human experts is incorporated in the program, the level of expertise rises and soon can exceed that of any specific expert. The program can pinpoint inconsistencies between one expert and another. It becomes an excellent teaching tool, as well as a practical one to apply. This is one of the most rapidly growing fields and an attractive new direction for the rock engineer.

In conclusion, our aim should be to develop analytical methods of real practical value for everyday types of project. This can be achieved in a number of ways:

- greater focus on the information requirements of medium to small sized investigations;
- greater diversity in the scope of questions addressed;
- improved transfer of technology including the development of more user-friendly software;
- increased focus on the development of scientifically-based empirical design tools;
- incorporation of empirical, analytical and hybrid design methods into expert systems.

This is an exciting time in the field of geomechanics analysis. A glance through the papers in this symposium and in a growing number of specialist journals shows the broad scope of problems being addressed today. I thank you for the opportunity of introducing the symposium and look forward to the presentations and a challenging exchange of ideas.

REFERENCES

Franklin, J.A. and Palassi, M., 1993. Maximum span and stand-time of shallow excavations. Proc. Int. Cong. Mine Design, Queen's University, Kingston, Ontario, August 1993.

Session 1

Underground Mining

Mines souterraines

Three dimensional stress analysis techniques applied to mine design at Golden Giant Mine

D.R. Grant, Y. Potvin

Noranda Technology Centre, Pointe Claire, Quebec

P. Rocque

Hemlo Gold Mines Inc., Golden Giant Mine, Marathon, Ontario

ABSTRACT

The Golden Giant Block 4 orebody is tabular striking generally east-west and dipping to the north at 70 degrees. The Block 4 ore zone is located at a depth of 1000 metres below surface and its thickness ranges between 15 meters at the east end to 40 meters at the west end. Mining in a highly stressed environment required preliminary design work to ensure overall stability of the stopes. Potential effects of mining induced stress on adjacent openings were explored using a three dimensional boundary element program. The purpose of this numerical modelling study is to qualitatively compare the influence of different mining sequences on the redistribution of stresses. For the two mining scenarios analyzed, it was found that one option allowed mining in a moderately stressed environment which, given present experience, should be regarded as the most favourable mining alternative.

RESUME

Le gisement de la mine Golden Giant incluant la zone du bloc 4, est de forme tabulaire avec une orientation est-ouest et un pendage d'environ 70 degrées. Le bloc 4 qui a une épaisseur variant de 15mètres à 40 mètres, est situé à une profondeur de 1000 mètres. Etant donné les conditions de contraintes élevées, un travail de conception préliminaire a été requis afin de d'assurer la stabilité des chantiers. Les effets potentiels sur les chantiers adjacents reliés aux contraintes induites élevées ont été étudié à l'aide d'un logiciel d'éléments frontières tridimensionnel. Les simulations numériques de contraintes avaient pour but de comparer qualitativement l'influence de différentes séquences de minage sur la redistribution des contraintes. Des deux scenarios analysés, une option permet l'exploitation dans des conditions de contraintes modérément élevées, ce qui la confirme comme étant l'alternative la plus avantageuse.

INTRODUCTION

A complete geomechanical mine design involves three main phases of investigation. The first phase is the collection of all available geomechanics input data including rock mass strength data (intact properties and structural mapping data) and the virgin state of in situ stress environment. Obtaining quality input data is critical and determines how good the initial design will be. With the geomechanics input data and the orebody geometry organized the next phase of the design process can proceed. The second phase is to determine the method of extraction (appropriate mining method) and the potential effects of mining on the adjacent rock mass. Determining the structural stability of stope surfaces can be estimated using the stability graph method, while pillar dimensions and stope sequencing options can be analyzed using three dimensional stress modelling techniques. Location of development (ore passes, footwall drifts, etc.) and degree of support should be addressed at this time. This initial design is then compared with production constraints to insure an operating balance. The initial mine design is then implemented and the monitoring phase of design starts. The final phase closes the design loop by monitoring the response of the rock mass to mining using visual observations or various levels of instrumentation programs. Using monitoring data and changes in mining geometry, the initial design can be enhanced by calibrating the design tools used to the specific site rock mass conditions at the mine.

Three dimensional boundary element stress analysis is one of the tools used to predict induced stress levels in the rock mass adjacent to mining excavations. Each of these design tools has to be calibrated and incorporated into the design process. This paper will present a mining case history to discuss the application of three dimensional boundary element modelling as a tool to compare two proposed stope sequences for the mining of Block 4 at the Golden Giant Mine.

CANMET's BEAP (Boundary Element Analysis Program) program was used for the Golden Giant Mines block 4 dimensional boundary element modelling study. The program is a three dimensional boundary element program developed by J.A.C. Diering as a PhD thesis, at Pretoria University (1987). Its development was sponsored by CANMET, INCO (Thompson Division) and GEMCOM (Pty.) Limited.

BEAP OPERATING DETAILS

Several publications have described the technical details of the BEAP program and the special boundary element used in the program (Diering, 1987;Diering and Stacey, 1987;Diering and Yu, 1988). From a user's perspective, BEAP is powerful and flexible. BEAP problems sizes in this study ranged between 20,000 and 25,000 degrees of freedom and demonstrate the ability of the program to model mine wide geometries. Noranda

Technology runs BEAP on both DOS based PC and SUN SPARC workstations.

The pre-processing (mesh generation) is accomplished by using Noranda's three dimensional AutoCAD mine modelling system A-MINE and CANMET's pre-processor. This permits the user to design, optimize, and edit the boundary element mesh while accessing the mines stope geometry information in the same system. Post-processing (results presentation) is also done with third party software and Noranda's A-MINE system. The typical method of presenting BEAP output is on two dimensional planes representing longitudinal sections, cross sections and level plans in the mine. Because other geomechanics information is available within the A-MINE system it is possible to overlay underground development geometries, geological contacts and structures and microseismic events into a composite output format.

CALIBRATION OF BEAP AT GOLDEN GIANT

The mining extraction at the end of 1990 and the end of 1991 were taken as rough calibration points for the 1995, 1996 and 1997 BEAP simulations. Underground site visits were made to the Hemlo Mining Camp to observe ground conditions and talk to the ground control personnel.

In areas where ore zone thicknesses range between 5 and 15 metres it was generally observed that vibrating wire stress cells worked well for an increase of up to 25 to 30 MPa (in the elastic range of the rock mass). The stress cells are generally measuring stress change perpendicular to the orebody. This is believed to be close to the maximum principal stress direction (Golder 1987). The measured premining stress levels (using overcoring techniques) at this depth are about 30 to 40 MPa for sigma 1 and about to for sigma 3.

The visual observations associated with these changes in stress are typically, rock bolts heads shearing off, onion skin fracturing seen in drift corners, blast holes closing and/or shearing, and increased water inflow through the fractured rock mass. In some cases ground falls would follow the above precursor activity.

In areas where the ore zone thicknesses range between 25 and 40 metres it was observed that secondary pillars can be successfully mined in the 70 to 90 MPa range as predicted by the BEAP modelling. It was noticed that the behaviour of the rock mass to be very time dependent. Minimizing mining cycle time and maintaining confinement on the secondary pillars has a significant affect on the state of rock mass deterioration.

The 1990 BEAP simulation produced a good correlation with the instrumentation and visual observations. Using consistent input parameters for all the BEAP simulations a crude

threshold stress level of seventy MPa is used as criterion to highlight potential problem areas. During the 1991 BEAP simulation it is believed that in areas of greater orebody thickness the rock mass yields more passively as model predicted stresses increase above the seventy MPa level.

SEQUENCING OF BLOCK 4

The Hemlo orebody is tabular striking east-west with 16 degree northeasterly bend at the east end of the deposit. The dip ranges between 50 and 70 degrees to the north. The thickness of the ore varies from five metres (east end) to forty metres (west end). The Golden Giant Mine Block 4 mining thickness ranges between 15 and 40 metres. The local geology consists of foliated metasediments and metavolcanics of various mineralogical composition. A thirty metre diabase dyke striking north-south and dipping steeply east is located in the centre of the Hemlo mining camp.

The mining plan for Block 4 has been under review by Golden Giant mine engineering staff. Figure 1 shows the Golden Giant Mines Block 4 located down dip of the block 3 pyramid and on the east abutment of the Williams Mine. Two mining sequences have been proposed for the extraction of the Block 4 mining block.

The intent of the study was to use numerical modelling to identify potential stress problems in Block 4 and focus on the following points:

- document the current stability of the rock mass in the Hemlo camp with respect to the estimated level of induced stress,
- identify the regions of high stress associated with block 4 mining,
- suggest potential geomechanical mining problems that may occur due to these levels of induced stress, and;
- make some general comments on methods and strategies to mine in these expected conditions.

Two separate mining scenarios for Block 4 have been proposed. Figures 2 and 3 show isometric views of the proposed mine plans at years 1995 and 1996. These figures are AutoCAD drawings showing the actual boundary element meshes used in each BEAP simulation. In the vicinity of block 4 each element face represents a stope height of 25 metres. Plan one is a top-down mining approach that would start mining in the top upper west corner underneath the block 3, west of dyke stopes and against the Williams mine's eastern abutment. The general shape of the mining advance would be an inverted pyramid similar to the mine plan proposed for block 3 west. The mining advances down dip with an eastward retreat while encasing the diabase "Lac" dyke. Plan two is a bottom-up mining approach that requires establishing a starting mining elevation (initial mucking
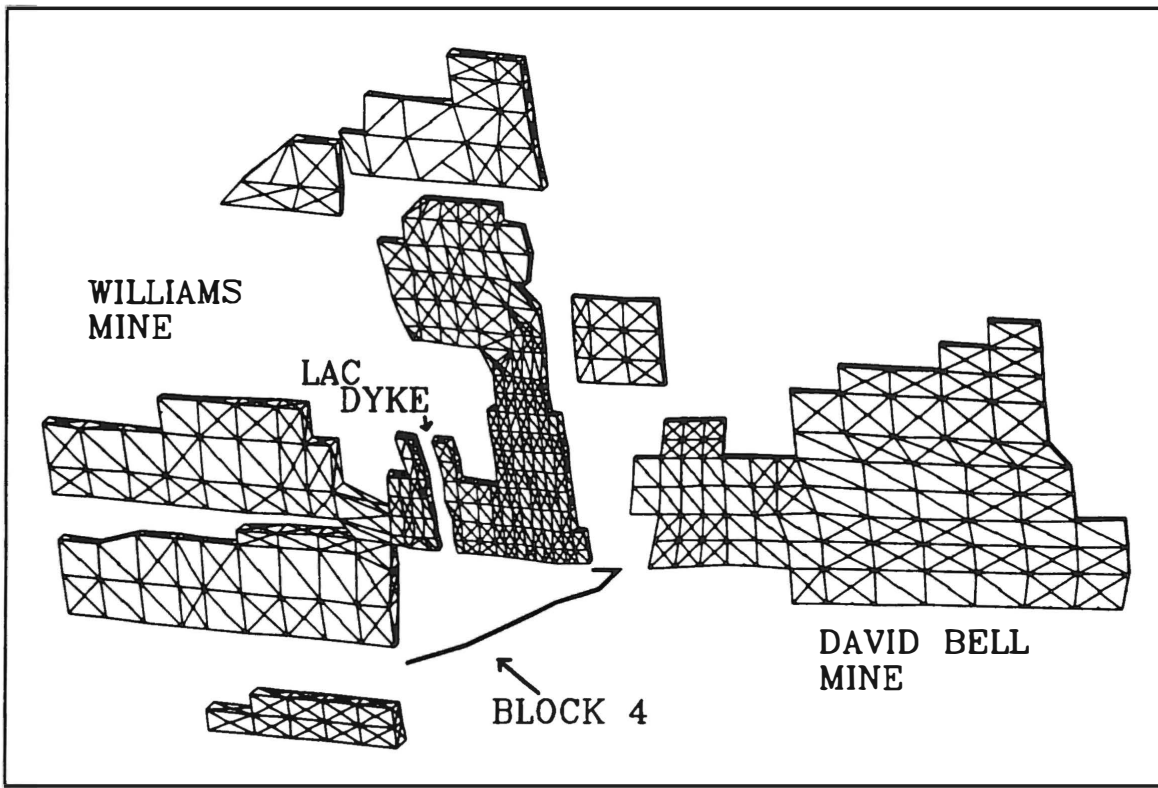
Figure 1. The BEAP boundary element mesh showing the planned extent of mining
throughout the Hemlo camp at the end of 1994. The location of the block 4
is indicated below the block 3 pyramid and on the east abutment of the Williams
Mine.

horizon) and mining up dip with primary and secondary stopes retreating up and eastward.
Plan two tries to incorporate the general strategy that the Williams mine has successfully
employed to date.

MODELLING RESULTS FOR THE TWO MINING SCENARIOS

1995: Plan 1 and Plan 2 Results and Interpretation

A plane of benchmarks for stress calculation was created in the longitudinal section of the
orebody with a spacing of 2.5 metres. Longitudinal sections are generally used to
maximize the presentation of the data for sub vertical orebodies and were used for each of
the simulations. Stress benchmark planes càn be calculated and presented for any two

dimensional section in the three dimensional model. This can be useful for predicting the extent of induced stresses in footwall development areas.

From the 1995 results of mining plans 1 and 2, it appears that mining plan 1 starts mining in the high stressed corner Block 3/Williams abutment (90 to 100 MPa model predicted stresses). Mining plan 2 starts mining primary stopes at a lower elevation in relatively lower levels of modelled predicted stresses (50 to 70 MPa).
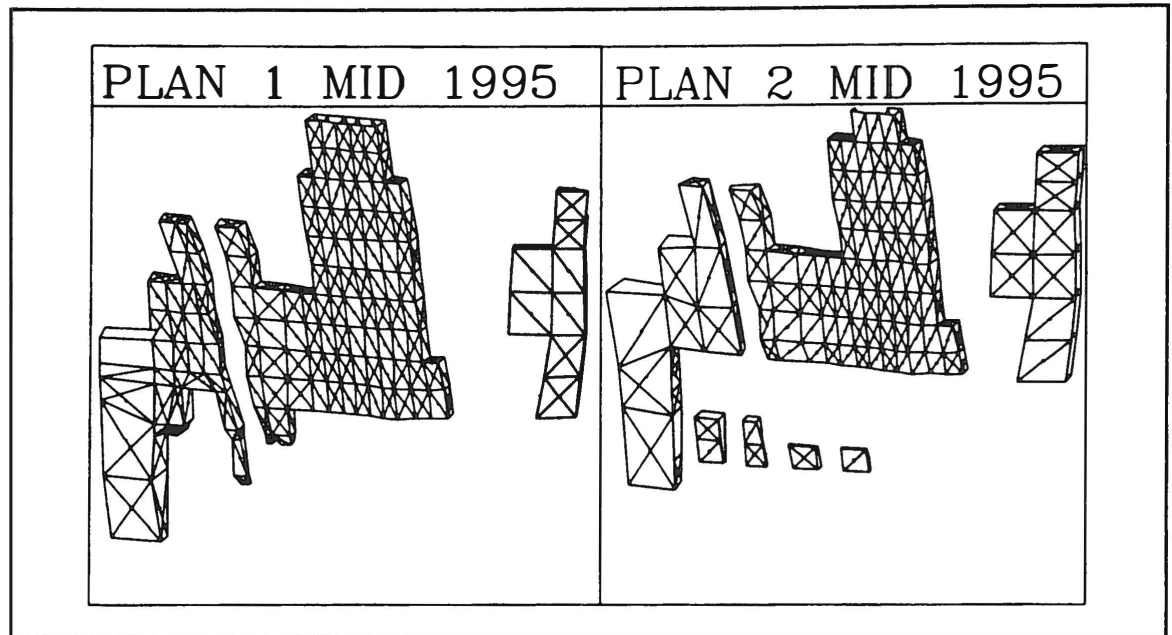
Figure 2. A window showing part of the BEAP boundary element meshes of the two proposed mining plans for the Golden Giant Mine Block 4 at the middle of 1995. View looking north.

1996: Plan 1 and Plan 2 Results and Interpretation

Figures 4 and 5 show maximum principal stress distributions (longitudinal sections) in Block 4 (predicted by BEAP) for Plan 1 and Plan 2 at the end of 1996. Plan 1 continues to show very high stress levels (in excess of 100 MPa) in the abutment area which is generally the next production stope.

The 1996 Plan 2 shows that secondary stopes are highly stressed. The two secondary pillars have model predicted stresses in greater than 100 MPa.
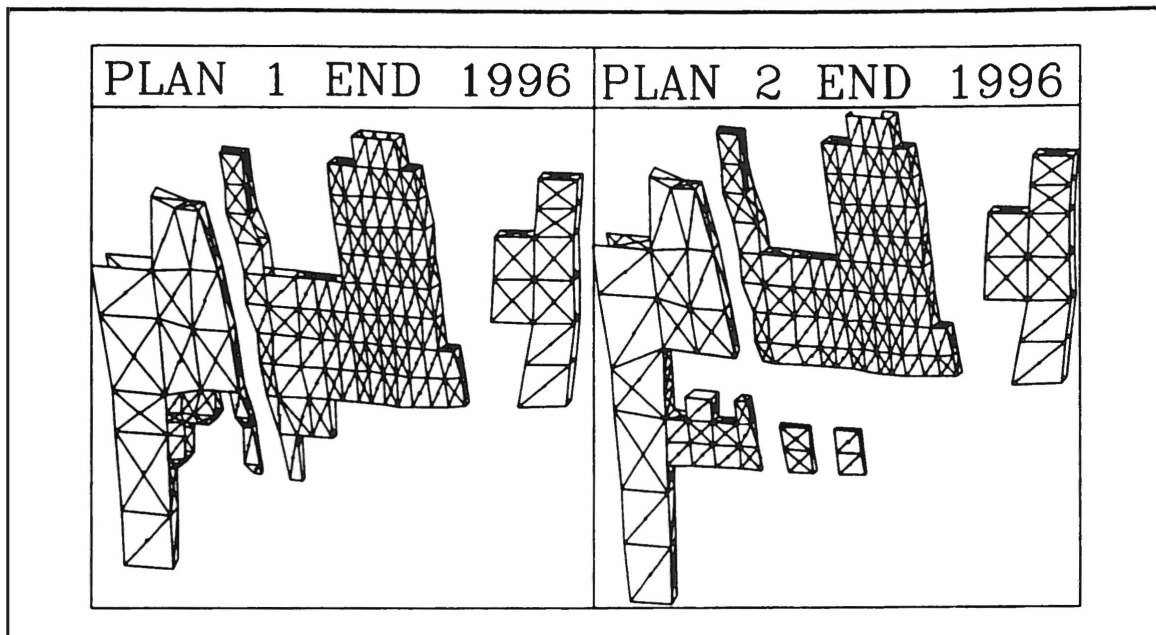
Figure 3. A window showing part of the BEAP boundary element meshes of the two proposed mining plans for the Golden Giant Mine Block 4 at the end of 1996. View looking north.

The dyke is also overstressed in both plan 1 and plan 2. Experience to date indicates that when the Lac dyke is mined on both sides for heights of 100 metres yielding and stress shedding occurs. At present it is beyond the capability of BEAP to model stress shedding.

The mining consequences of the high stresses predicted would likely be:

- the need for special artificial support and support rehabilitation,
- transverse cracking in secondary pillars, and abutment stopes,
- problems with brow control,

In both mining plans reduction of the stope cycle time will be critical to minimize stress related mining problems.

1997: Plan 1 and Plan 2 Results and Interpretation

It is very apparent that by 1997, high stress conditions are going to be evident in most working faces in mining Block 4 west for both plan 1 and plan 2. The BEAP program
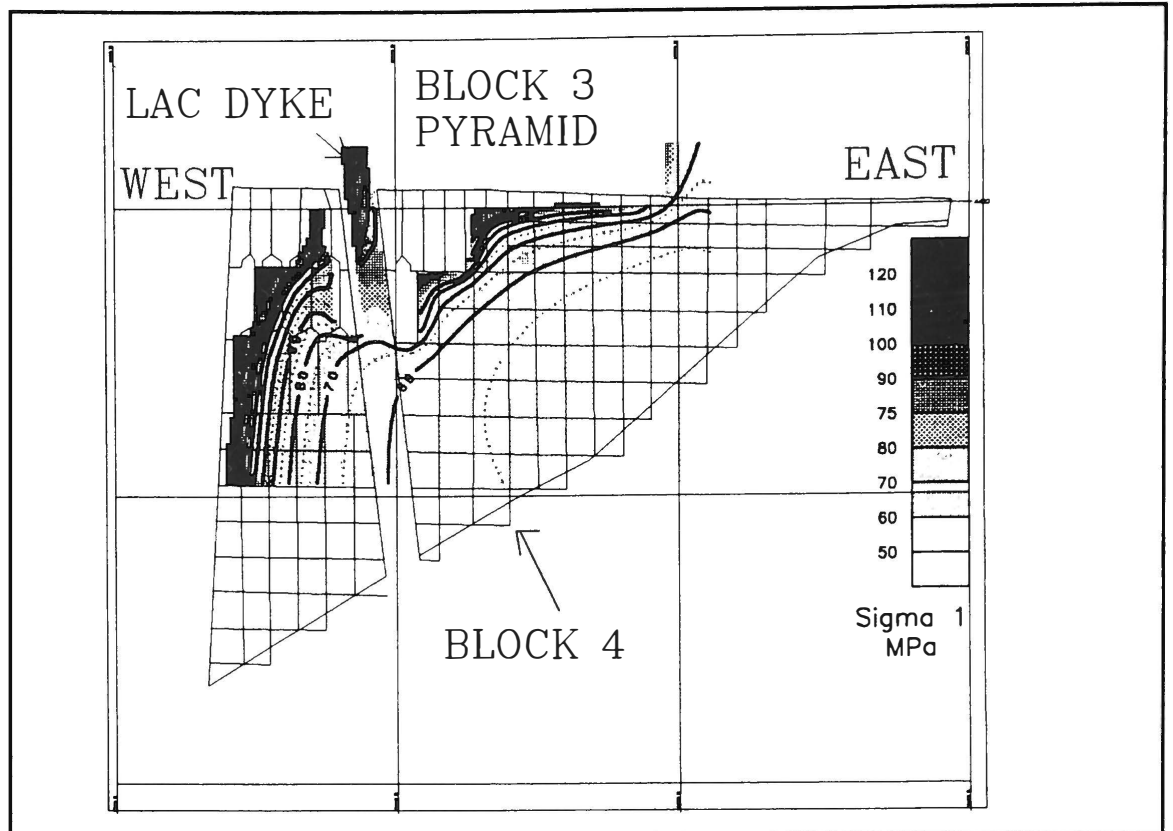
Figure 4. Shows a longitudinal plane, looking north, of results (Maximum principal stress)
predicted by BEAP for mining plan 1 at the end of 1996.

cannot accurately estimate stress problems when a sizable quantity of failed ground exists.
The model assumes that these regions can carry an infinite load, while in reality they may
only be carrying a nominal load.

Preferred Mining Plan

In order to select the preferred mining plan, numerous production and rock mechanics
factors were evaluated individually. The production factors included stope cycle time,
flexibility, ease of mucking, minimizing development outside of the ore, and cost of
backfill. The main rock mechanics factors that where considered include structural stability
of stope surfaces, backfill stability, and stress effects on temporary pillars.
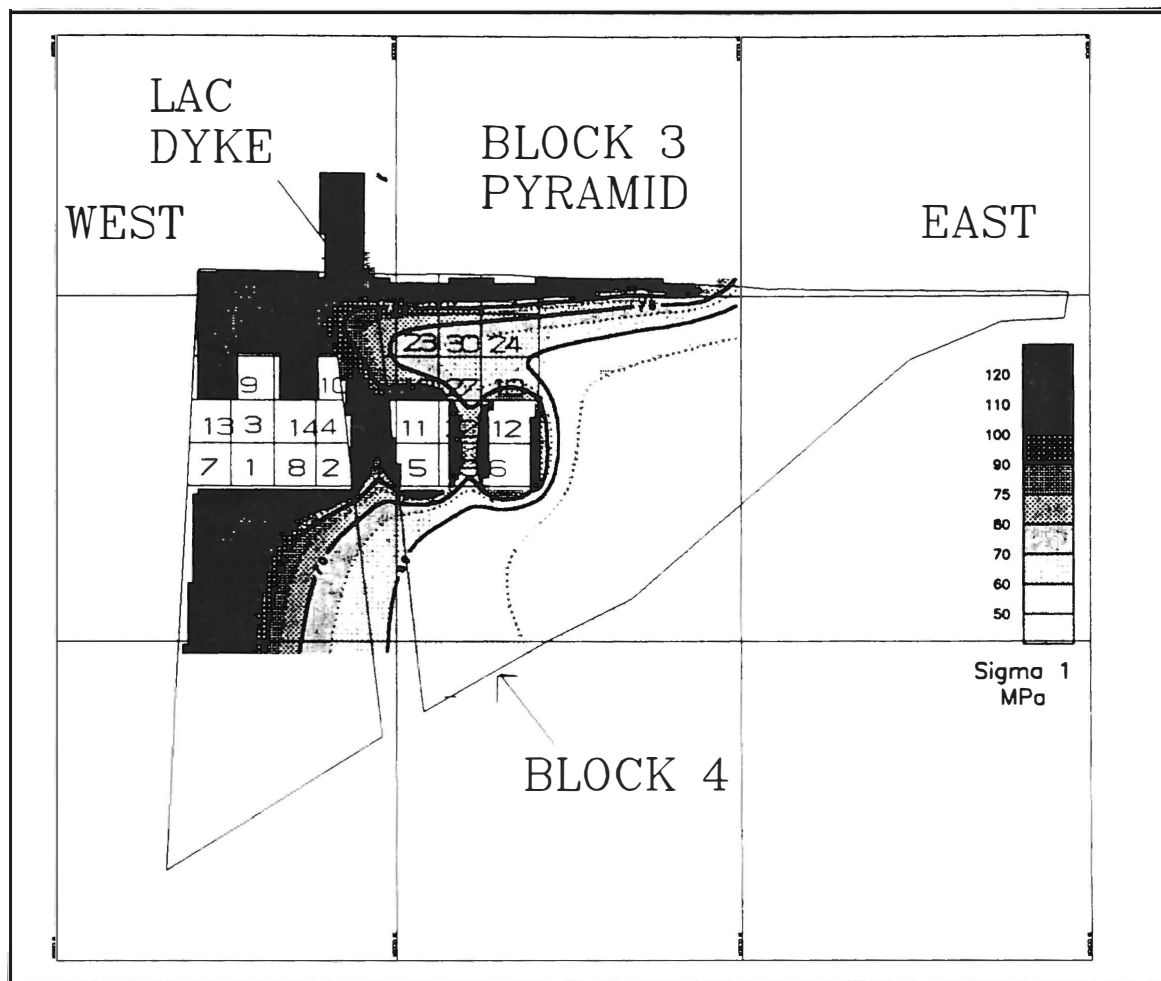
Figure 5. Shows a longitudinal plane, looking north, of results (Maximum principal stress) predicted by BEAP for mining plan 2 at the end of 1996.

Mining plan 2 allows mores stopes to be extracted at lower stress levels and is therefore favoured from an induced stress level perspective. Mining plan 1 would require the uncertainty of constantly mining under and against large backfill backs and walls. Mining plan 2 is stope pillar mining method and increases the flexibility of production. This is an advantage but close control is required on height of high primary stoping before backfilling is necessary.

Table 1 shows the number of stopes, from each mining plan, that would be exposed to a range of model predicted stresses. A more accurate comparison would be to quantify the

number of ounces at varying stress levels. As a result of this study mining plan 2 was selected to create a balance between rock mechanics and production concerns.

TABLE 1 Average Maximum Principal Stress in Active Production Stopes

Average Maximum Principal Stress	Number of Stopes Mining Plan 1	Number of Stopes Mining 2
40 to 50 MPa	0	1
50 to 60 MPa	1	5
60 to 70 MPa	3	4
70 to 80 MPa	0	4
80 to 90 MPa	2	4
90 to 100 MPa	1	2
plus 100 MPa	16	14

LIMITATIONS OF BEAP

It is necessary to explain the practical limitations of using a numerical model to estimate the induced stresses for mining applications. The intention of this numerical modelling study was to qualitatively test the influence of a design parameter (ie. the comparison of alternative mine plans discussed in this paper). Before exerting large amounts of effort to build and run three dimensional mine models the model was 'calibrated' to observed rock mass conditions. Calibration is a loose term because of the many limiting factors involved in any numerical simulation.

The following factors are the most significant sources of inaccuracy and their potential effect on the modelling results is discussed below:

Excavation Geometries
BEAP is a completely three dimensional numerical model and can account for significant geometrical changes in a stope and pillar geometry. However, it is presumed that all intact ground modelled has infinite load carrying capacity which is a poor assumption especially in the later stages of Block 4 mining. The above BEAP simulations modelled only the stopes and ignored the influence of drifts. This is a reasonable assumption.

Material Properties

The input for the material properties of the rock mass used by BEAP is simplified. Only one value for an elastic modulus and poisson's ratio was used for the orebody, hangingwall and footwall. The significance of the geological structure likely has dominant effect on local and regional stress redistributions.

Importance of In Situ Stress Levels for these Simulations

Almost all of the comparisons made in the above paper have very similar premining stress conditions. Most of the areas are between 4300 and 4600 (700 to 1000 metres below surface; estimated premining sigma one of approximately 40 MPa). While our level of confidence in the actual premining stress field at this depth is high, almost all of the regions discussed are subject to approximately the same stress regime. This diminishes to a degree the necessity for precise measurements of the maximum principal stress.

CONCLUSIONS

This BEAP numerical modelling study was performed to qualitatively compare two mining strategies for the Block 4 mining area and tied to find a balance between rock mechanics and production constraints.

Additional instrumentation would be very useful to continue the calibration process. Stress cells and extensometers installed in key areas followed up with borehole camera observation holes would add confidence to numerical modelling interpretation.

Information about the geomechanical parameters in various mining zones should to be collected because different rock zones may react differently to the same level of model predicted stress. A continuous logging of observed ground conditions, as the mining progresses, would add confidence to the database of mining related stress problems.

ACKNOWLEDGEMENTS

The authors would like to thank Golden Giant Mine for permission to present and discuss the above results.

REFERENCES

Diering, J.A.C., 1987, "Advanced Elastic analysis of complex mine excavations Using Three-Dimensional Boundary Element Techniques," PhD Thesis, Pretoria University, South Africa, 201 pp.

Diering, J.A.C., and Stacey, T.R., 1987, "Three Dimensional Stress Analysis: A Practical Planning Tool for Mining Problems,". Proc 20th Int Symp APCOM, Johannesburg,SAIMM, (1987) 22-42.

Diering, J.A.C., and Yu, Y.S., 1988, "Three Dimensional Stress Analysis: A Formulation for Mining Problems," Computers and Geotechnics, Vol. 5, 151-170.

Grant, D.R., Hudyma, M.R., and Ecobichon, D.,1990, "Geomechanics Investigation of Mining Block 3 West at Hemlo Gold Mines," Internal Noranda Technology Report, 39 pp.

Grant, D.R., Hudyma, M.R., Diering, J.A.C., 1991," Three Dimensional Stress Analysis Using BEAP. 2nd Canadian Conference on Computer Applications in the Mineral Industry, Vancouver, Canada.

Grant, D.R., and Potvin, Y., 1992 "Proposed Mine Plan for Golden Giant Mines Block 4," Internal Noranda Technology Report, 56 pp.

Grant, D.R., 1992 "Comparison of Rock Mass Conditions and Three Dimensional Stress Modelling at the Williams Mine Block 4," Internal Noranda Technology Report, 24 pp.

Sill Pillar Excavation of a Cut and Fill Operation

R. Pakalnis
University of British Columbia

K. Cook
Detour Lake Mine, Placer Dome Ltd.

S. Vongpaisal
CANMET

ABSTRACT

Synonymous with cut and fill mining is the establishment of mine levels in order to maximize the number of production faces. The Detour Lake Mine is a 2200 tonne per day mechanized cut and fill operation mining to present depths of 660m below surface. Mine levels are at approximately 100m intervals with intervening sills between 15m to 20m in vertical thickness and ore widths(FW to HW) in excess of 35m. Sill pillars were established in 1987 with the objective of extraction once mining has progressed to a sill level. The extraction of the 260m sill has recently been successfully completed. This paper describes the methodology of sill pillar design with the objective of removal. Three dimensional numerical codes were employed to establish induced stress levels. Empirical codes enabled pillar strengths and sill/span dimensions to be established. The intervening sill was excavated to an average sill thickness of 3 to 4m over stope widths of 25m along a 150m strike length. The numerical/empirical model had to incorporate the effect of 100m of backfill above the sill and approximately 200m of mining below. A successful tool was developed in the extraction of subsequent intervening sills.

INTRODUCTION

The Detour Lake Mine(DLM) is a 2200 tonne per day gold mine located 300km northeast of Timmins, Ontario. Underground production commenced in 1987 employing mechanized cut and fill, longhole and captive cut and fill techniques. Mining by cut and fill methods extends to 560m below surface. The orebody is variable in width ranging from 5m to 40m. The inclination of the orebody varies from a low of 45° to an average of 60°. The orebody plunges to the west at 45° and has an average strike length of 20m. There are three interrelated gold bearing zones, namely Main, Quartz and Talc Zone. The Main and Quartz zone are comprised of mafics whereas the Talc zone is comprised of weaker talc and chloritic materials.

In 1989, the mine entered into a research agreement with the Canada Centre for Mineral and Energy Technology(CANMET) to develop stability guidelines for wide cut and fill stopes. The cut and fill mining method requires the establishment of multiple working levels in order to ensure that sufficient mining areas exist, Figure 1. This necessitates that sill pillars be developed separating intervening levels. A major focus of this study was to maximize extraction through the removal of sills. Mechanized cut and fill levels at DLM have been established at the 260m, 360m, 460m and the 560m Levels below surface. Sill pillars are left beneath each of the stopes on the above levels and a crown pillar is maintained between the 260 stope and the pit. Individual lifts are 5m in vertical height with footwall to hanging wall widths ranging from 6m for the poorer quality materials(Talc Zone) to over 30m(Main Zone) for the more competent andesites. DLM has been able to maximize spans by developing empirical relationships based upon historic and mine specific observations relating rock mass quality to the exposed span(Pakalnis, 1992). This has resulted in cut and fill spans that are amongst the largest in North America. This approach has been extended to the design and subsequent extraction of the intervening sills. The 260 sill pillar was the first to be mined and extraction commenced in February/92 and was completed in December/92. The 260 sill pillar is defined as the pillar between the 260m Level and the back of the 18th lift of the 360 stope immediately below, Figure 1. The vertical thickness of the sill at the time of extraction ranged from 13m to 15m.

SILL DIMENSIONS

The strength of a pillar is determined by many factors, the most critical being:

- Pillar Geometry
- Rock Mass Quality
- Uniaxial Compressive Strength

Hoek(1980) has shown a relationship to exist between the width to height ratio of a pillar and the ratio of average pillar strength to compressive intact strength for varying rock mass quality, Figure 2. Laboratory testing of the rock samples at DLM yielded an average uniaxial compressive strength of 165MPa for the Main Zone. The rock mass rating for the Main Zone

18

is generally between 75% and 85%(CSIR-Bieniawski, 1984). The pillar height and width were recorded as shown in Figure 2. This resulted in final pillar shapes and strengths as shown in Table 1. Three dimensional boundary element codes were employed, BEAP3D(CANMET, 1991) and MAP3D(Wiles,1991), to estimate sill pillar stress levels. Three dimensional codes were employed due to the shallow plunge of the orebody which would make plane strain assumptions overly conservative. The modelled geometry for the ultimate sill pillar geometry is shown in Figure 3a and the induced stress levels in Table 2. Table 3 summarizes the induced stress results for the mine geometry at the time of 260 sill excavation, Figure 3b. The stress levels were found to be well under the rock mass strengths estimated in Table 1. This enabled a mine schedule and plan to be developed based upon leaving an intervening stable pillar for purposes of mining by entry methods and subsequently converting to a non-entry method for sill removal.

The sill pillar factor of safety, defined as the average pillar strength divided by the average pillar stress was found to be greater than 1.5 for each pillar configuration when the stopes reached their final elevation. The model and empirical formulations employed were commensurate with the level of accuracy required since the rock mass strength was much larger than the induced stress levels and further analysis and refinement was not warranted since reducing the sill pillar thickness to below 15m would not have allowed for efficient extraction by subsequent methods.

SITE DESCRIPTION

The first lifts on the 260, 360 and 460m levels were filled with a 10:1 cemented fill and the floor reinforced with rebar and a weld mesh screen. This was to ensure that maximum recovery would be possible when it came time to mine the intervening pillar. This was initiated in 1987. A layer of 10cm x 10cm(4" x 4") weldmesh was laid on the floor with 20mm diameter rebar(5/8") placed vertically upright and bent at the base. The base was supported by wooden blocks/crosses. The weldmesh was placed on top of the rebar/blocks. The tops of the rebar were tied together in order to be supported vertically. The rebar was 1.8m(6') long and placed on a 1.8m x 1.8m(6' x 6') pattern. The weldmesh was anchored to the walls by 1.8m(6') rebar approximately 1m from the base of the wall. The first lift was backfilled to within 1m of the back with a 10:1 sand to cement(by volume) backfill. Subsequent lifts did not employ cement. High perc esker sand material was employed as backfill at DLM having percolation rates in excess of 0.8m/hr.

The 260 sill was cored in December/90 from access approximately 5m above the top of the 260 sill. The purpose of the coring was to determine the effectiveness of the cemented fill mat that was placed in 1987 and to access the pillar for purposes of installing a stressmeter in order to monitor induced stresses during sill excavation. The coring of three test holes had shown minimal cement, however, isolated pockets were present. It was concluded that much of the cement had washed out with the water during backfilling and consequently a minimal amount was available for support. Figure 3 is a plan of the 18th lift of the 360 stope. The mine grid is shown along with the production rings(R10-R110). Generally the sill thickness

ranges from 12 to 15m prior to excavation. Figure 4 shows production ring section #102. Table 4 summarizes the rock mass rating for the 260m sill as observed prior to excavation.

DESIGN APPROACH

The stress levels in the 260 sill have been estimated at 36MPa, Table 3. The intervening 260 sill dimensions have been approximated for modelling purposes as being 15m in vertical dimension and 20m in footwall to hanging wall dimension. The overall pillar strength was estimated at 66MPa, Table 1. The above was based upon a rock mass rating of 73%, Table 4. The correction of "-10%" applies for span support(Pakalnis, 1992) and therefore the uncorrected RMR was employed for purposes of analysis since the presence of flat structures have not been calibrated to a strength reduction. The stress monitoring to date has shown that the stresses are still increasing within the pillar, Figure 5, with stressmeter(SM 260-2) located above the central portion of the stope exhibiting the greatest magnitudes as expected. This suggests that the pillar is competent and has not undergone deterioration and/or failure. This trend continued until the final pillar blast in September/92. The stress increases are not exceptionally large relative to the overall pillar strength. The options that are possible for excavation of the 260 sill were as follows:

1) Rely on the cement mat that was placed immediately above the pillar. The amount of actual cemented areas is questionable as shown by drilling. Isolated areas along the sill are cemented but it can not be relied on for stability along the entire sill length.

2) Cave the cement mat and rely on an AVOCA type method. This would ensure controlled conditions, however, the problem of recovery and dilution due to the sand fill mixing with the ore must be accounted for in the overall costs. The cement mat which is comprised of mesh/rebar and isolated pockets of cement will be more difficult to cave. Also the 260-T70 access culvert drift shows that artesian conditions exist within the sill(Stressmeter 260-2). This indicates that water is present in the sill to at least a 5m height. This will cause further problems in terms of sand/ore recovery.

3) Leave an ore remnant to act as a barrier between the 260 and 360 stopes. The width of the Main Zone is generally between 5m to 20m with most of the area under 15m in span.

REMNANT DESIGN

The rock mass rating in the vicinity of the 260 sill is 73%. Flat structures have been observed at the level and therefore the design rock mass rating for span estimation has been reduced to 63%. Sill pillar thicknesses have been estimated from a study by Carter/CANMET(1990) where the optimum crown dimensions have been determined empirically based upon a database in excess of 200 individual crown pillar case records. The approach to sill pillar design is shown in Figure 6. A rock mass rating of 63% would dictate a sill thickness to span ratio of 0.5 whereas a rock mass rating of 73% would dictate that a sill thickness be equal to

0.2 x span. This indicates that a 10m span would necessitate a remnant between 2m and 5m thick. The slot raise driven in the vicinity of the 3m remnant(east), Figure 3 was completed in February/92 and no flat structures were indicated at that time. The design thickness selected was based upon a thickness /span ratio of 0.3. This allows for blast damage and would dictate that spans under 10m would require sill thicknesses of 3m and those in excess would employ a minimum 4m skin. This is based upon the maximum failure geometry recorded at DLM being under 3m in vertical height, Figure 4. The span dimensions are shown in Table 5 for the individual production rings. Three spans are identified as follows:

- blast limit span refers to the span at the base of the sill remnant
- blast span refers to the sill excavation at the brow
- stope span refers to the 300 #18 Lift outline
                                (refer Figure 4)

The design pillar thicknesses are shown in Table 5. Generally the 0.3 x span criteria was employed coupled with a minimum sill thickness of 4m for spans exceeding 10m. It was recognized that where the sill thickness was under the 0.3 criteria that failure would possibly result but caving should not extend to the overlying fill.

SILL PILLAR EXTRACTION

Blasting commenced on May 23/92 with the extraction of the slot in the western portion of the orebody. It was decided to mine the narrower part of the sill(west) and to retreat to the #6 attack, Figure 3. Table 6 summarizes the excavation history. Ground Movement Monitors(GMM) were placed at locations shown in Figure 3. All production drilling was completed prior to the commencement of blasting. Production rings were on a 1.5m(5ft) row spacing. Haulage was by remote control 5yd scoop. Super Swellex bolts(3.7m) were installed for brow support at Ring locations #30,#50,#103 and #104. The bolts were spaced at a 1.5m spacing along each row. The bolts served to support the retreating brow and coincide with the blast sequence shown in Table 6. Blasting of the western part of the Main Zone was completed with no visible failure of the remnant sill. Damp areas were noticed upon extraction, however, actual flows were not observed. GMM's recorded noticeable movement(greater than 1mm/24 period) upon the extraction of Ring #43-50. The presence of partially opened flat jointing was noticed between rings #51-70 yielding a rock mass rating of 53%. The increased back deterioration dictated that rings #51-65 be blasted in a single blast. The mining of the eastern part of the sill was accelerated in order to minimize the potential for joints to open over time. Approximately 50m of strike length was detonated in a single blast(multiple delays). The spans in this area are generally over 15m and therefore a larger potential for instability existed. Mining has been completed with no failure noticed in the remnant sill. Rings #66-70 were not blasted due to poor back conditions.

TABLE 1

DLM SILL PILLAR STRENGTHS – ULTIMATE GEOMETERY				
LOCATION	PILLAR WIDTH	PILLAR HEIGHT	Wp/h	PILLAR STRENGTH
CROWN	24 to 26m	20m	1.3	116MPa(0.7X165)
260 SILL	14 to 15m	20m	0.75	66MPa(0.4X165)
360 SILL	53m*	25m	2.1	149MPa(0.9X165)
360 SILL	20m(ULTIMATE)	25m	0.8	66MPa(0.4X165)
460 SILL	20m	25m	0.8	66MPa(0.4X165)
560 SILL	15m	10m	1.5	132MPa(0.8X165)

* PILLAR WIDTH PRIOR TO 260 EXTRACTION

TABLE 2

DLM INDUCED SILL PILLAR STRESSES – ULTIMATE(MAP3D)		
LOCATION	PILLAR THICKNESS(WIDTH)	PILLAR STRESS
CROWN	26m	16MPa
260 SILL	15m	37MPa
360 SILL	20m	45MPa
460 SILL	20m	50MPa
560 SILL	15m	80MPa

TABLE 3

DLM INDUCED SILL PILLAR STRESSES – 1992		
LOCATION	PILLAR THICKNESS(WIDTH)	PILLAR STRESS
CROWN	24 to 26m	15MPa
260 SILL	14 to 15m	36MPa
360 SILL	53m	34MPa

TABLE 4

ROCK MASS CLASSIFICATION – 260 SILL PILLAR			
No.	PARAMETER	DESCRIPTION	RATING (%)
1	STRENGTH	165MPa(R4)	13
2	RQD	90%	18
3	SPACING	200-400 mm	15
4	CONDITION	SLIGHTLY SMOOTH/TIGHT	17
5	WATER	DRY	10

SUB-TOTAL	73%
FLAT STRUCTURES PRESENT -10% CORRECTION	-10%

TOTAL	63%

TABLE 5

RING #	260 SILL PILLAR SECTION SPANS/THICKNESSES			
	SPAN(FW/HW)			THICKNESS
	BLAST LIMIT (m)	BLAST (m)	STOPE (m)	SILL PILLAR (m)
14	6	9	21	3
18	7	11	22	3
22	7	12	21	3
26	7	11	20	3
30	7	11	20	3
34	9	13	22	3
38	9	13	25	3
42	14	14	26	5
51	17	16	19	5
53	17	15	18	5
55	16	14	20	5
57	15	13	18	5
59	15	13	18	5
61	14	13	19	5
63	13	12	18	5
65	13	12	21	5
66-70	RINGS NOT BLASTED		36	15
71	14	14	28	5
73	15	16	27	5
75	16	17	25	5
77	15	16	24	5
79	14	15	19	5
81	13	15	19	5
83	12	13	18	5
85	12	12	16	5
87	12	14	17	5
88	25	17	17	7
89	26	18	19	7
91	24	18	20	6
93	23	17	19	6
95	22	16	19	6
97	21	15	19	4
99	20	15	19	4
101	19	14	20	4
102	18	13	18	4
103	17	13	16	4
105	17	14	16	4
107	17	14	17	4
109	15	11	15	4
111	14	7	11	4

TABLE 6

260 SILL PILLAR EXCAVATION HISTORY	
RINGS BLASTED	DATE('92)
BLASTED WEST OF SLOT RAISE + RINGS 13-15	MAY 23, MAY 25
RINGS 16-18	MAY 27
RINGS 19-22	MAY 28
RINGS 23-28	JUNE 1
RINGS 29-42	JUNE 11
RINGS 43-50	JUNE 24
RINGS 51-65	JULY 7
RINGS 66-70	NOT BLASTED
BLASTED EAST OF SLOT RAISE + RINGS 112-110	AUGUST 20
RINGS 109-105	AUGUST 27
RINGS 104-71	SEPTEMBER 14/ FINAL BLAST
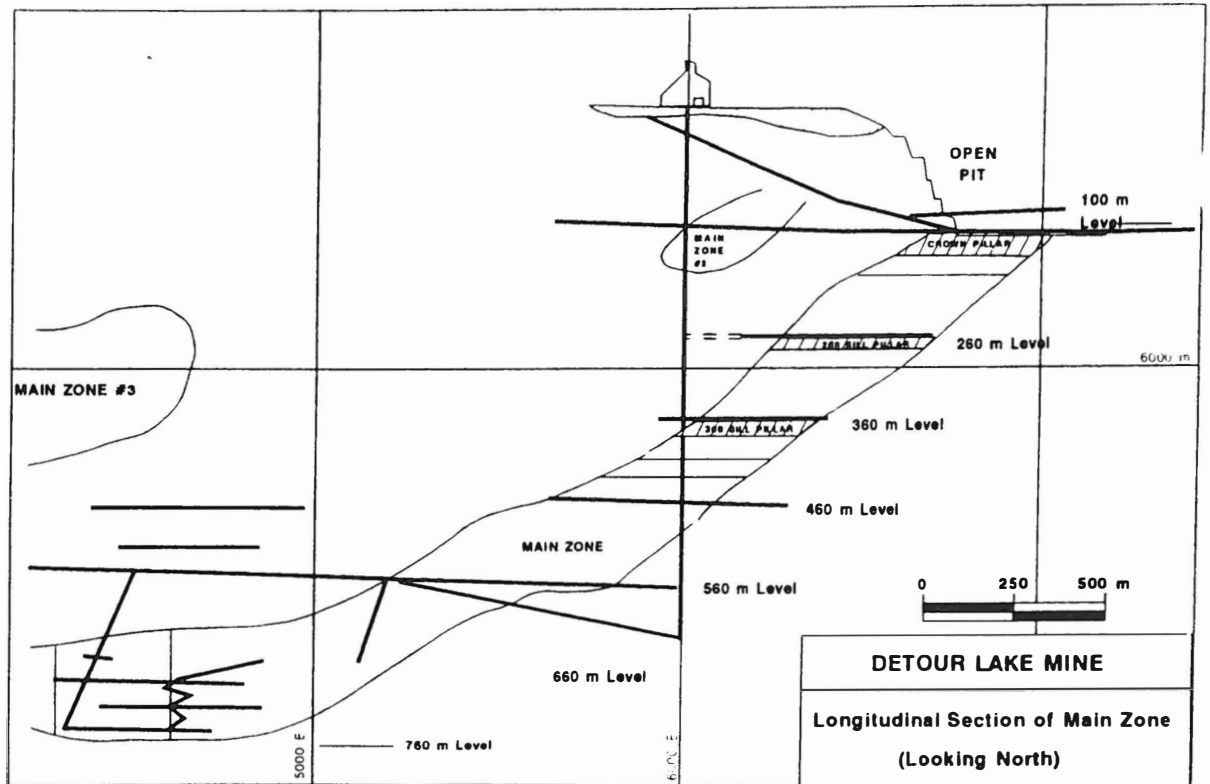
Figure 1: Longitudinal Section of Detour Lake Mine
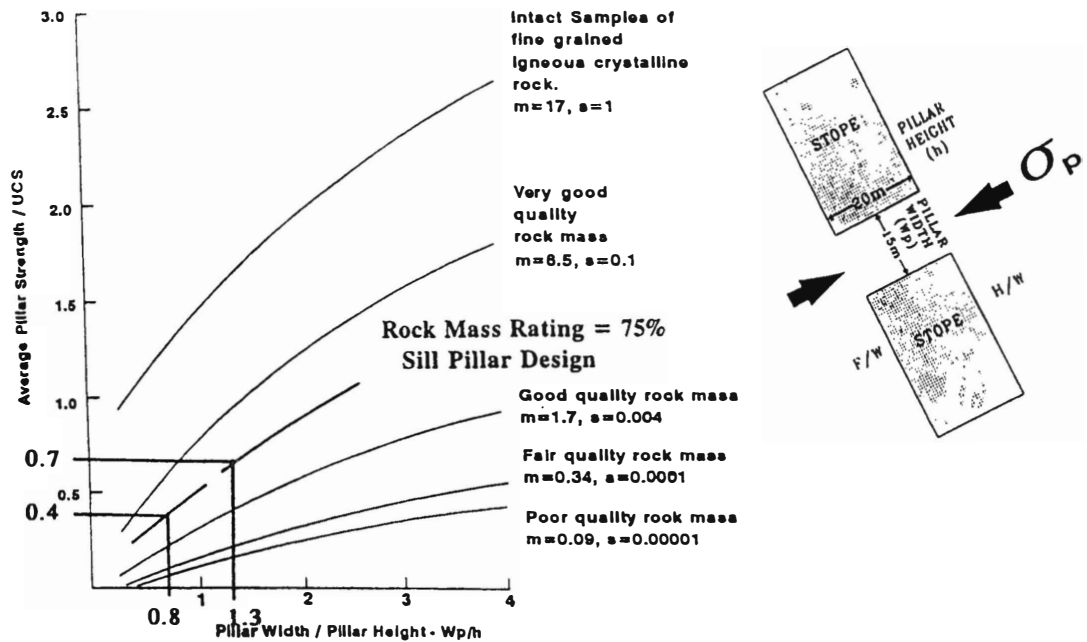
Figure 2: Rock Mass Strength (Hoek, 1980)
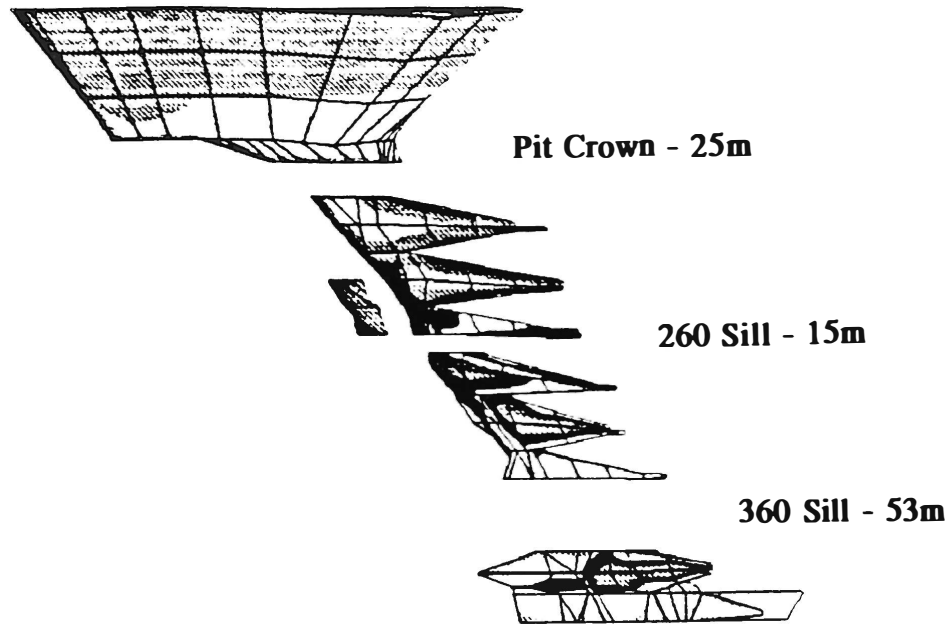
Figure 3a: Modelled Geometery - 260 Sill Extraction
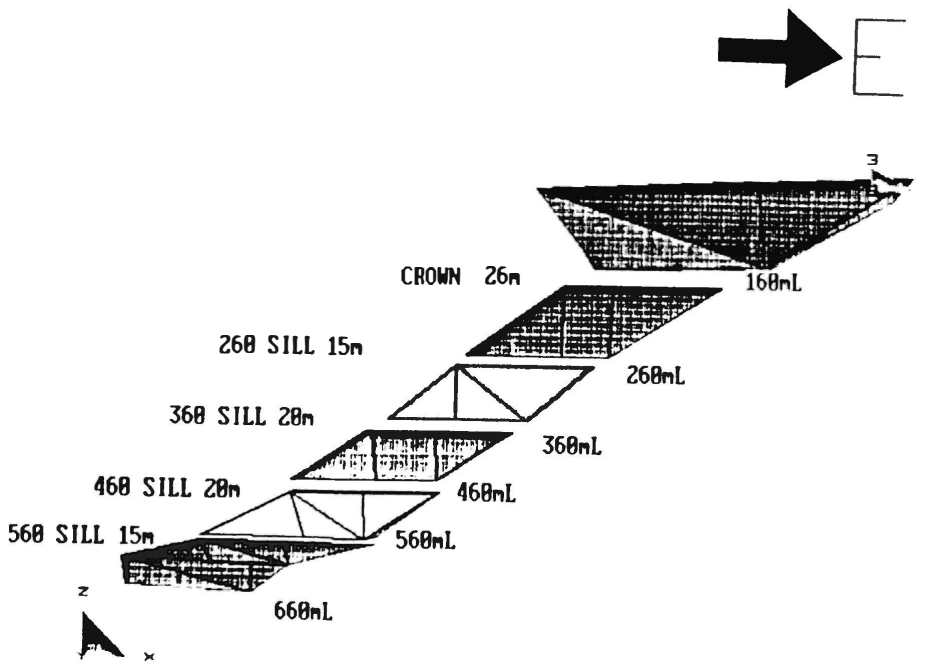
Figure 3b: Modelled Geometry - Ultimate Stope/Pillar Design
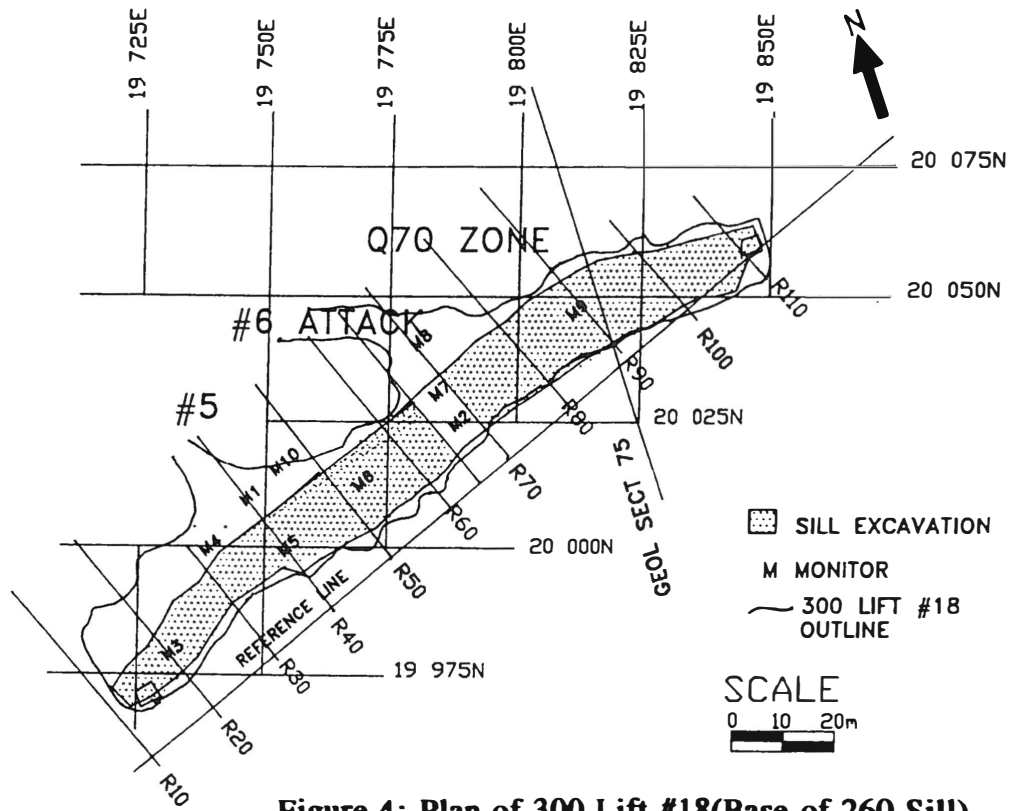
Figure 4: Plan of 300 Lift #18(Base of 260 Sill)
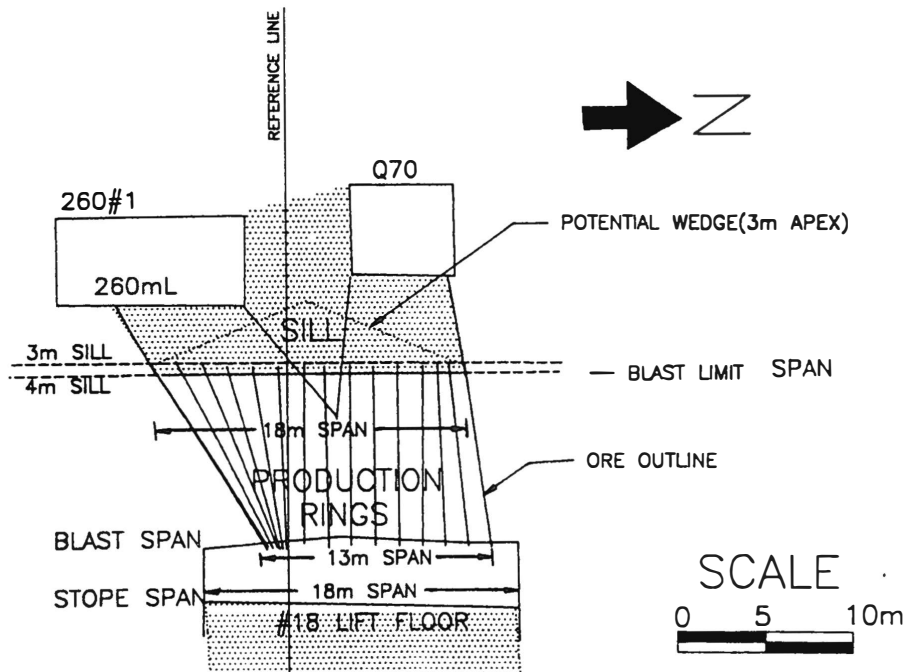
Figure 5: Production Ring Section #102

26
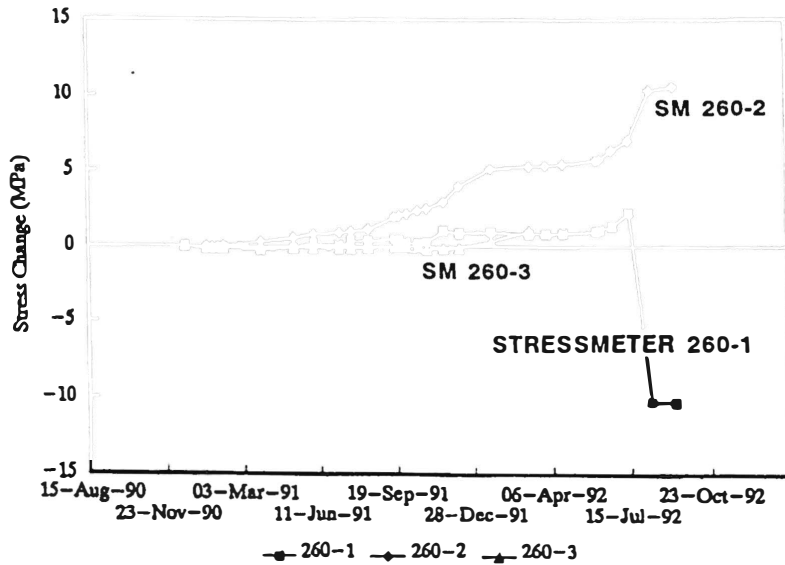
Figure 6: 260 Sill Pillar Stress Monitoring
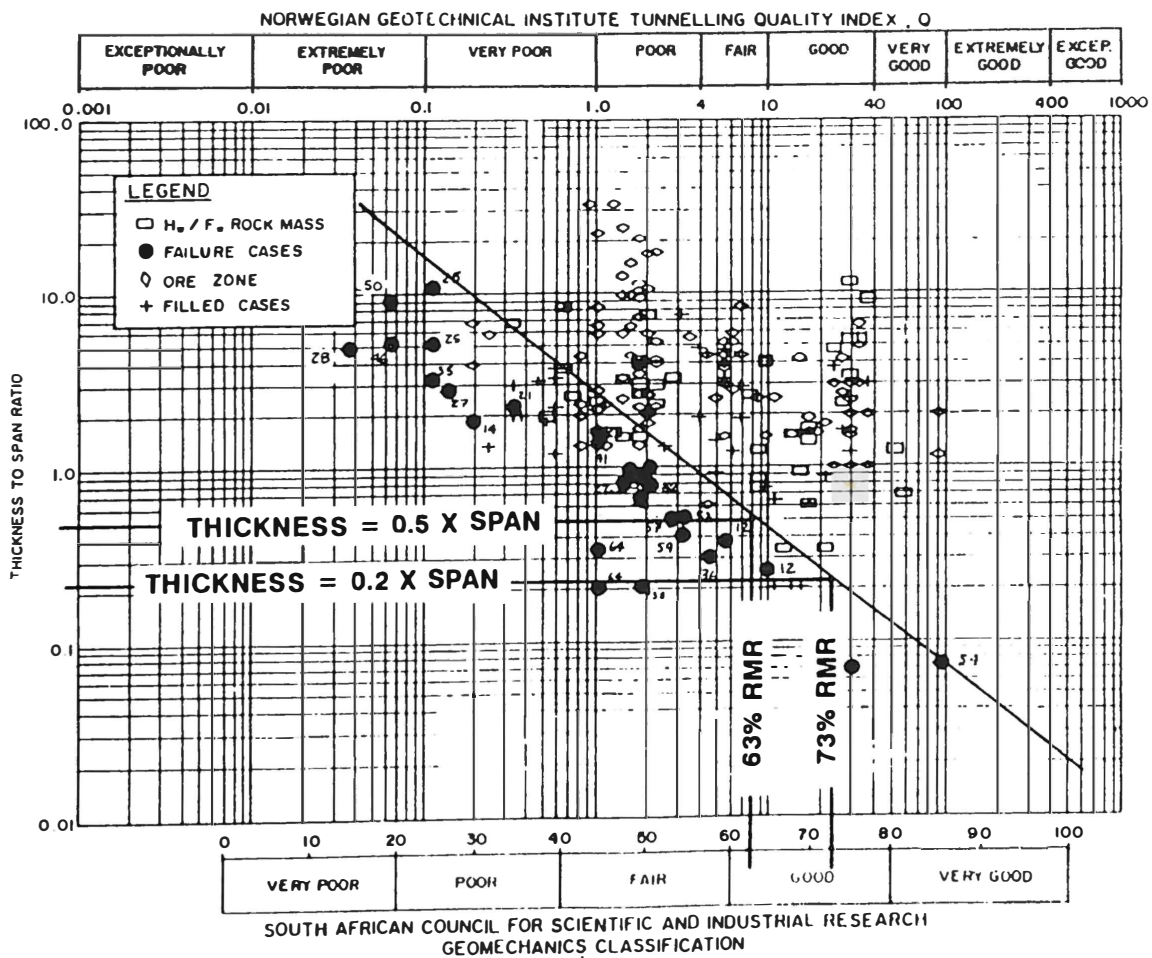
Figure 7: Crown Pillar Thickness Estimation(Carter, 1990)

27

CONCLUSIONS·

The remnant extraction was concluded to be a success. The sill design approach included analytical, empirical and observational approaches to design. Monitoring of the back, coupled with a local support program enabled the mining of sill spans in excess of 20m employing remnants of 4m thicknesses. This is a thickness to span ratio of 0.2. The methods of extraction and design employed for the 260 sill will be employed for subsequent sills at DLM. The design method is one where flexibility is maintained. Failure of the immediate back would require a barricade to be built and re-slotting and/or converting to an AVOCA method of extraction. The method of remnant extraction that was employed enabled maximum extraction, minimal dilution under controlled conditions. The approach to pillar design/excavation is one of implement and modify as practice dictates. This has proven successful since inception of design in 1987 to present day(1993). Empirical tools were employed augmented with numerical codes to estimate stresses and pillar strengths. The resultant design being calibrated by observational, instrumentation, analytical and empirical approaches.

ACKNOWLEDGEMENTS

LIST OF REFERENCES

Bieniawski, Z.T.(1984) Rock Mechanics Design in Mining and Tunnelling, A.A. Balkema, Rotterdam.

CANMET(1991) BEAP3D - Three Dimensional Boundary Element Application Package, CANMET Project No. 23440-9-9139.

Carter, T.G., Wong, J.S., Yuen, C.(1990) Crown Pillar Stability Back-Analysis, CANMET Dept. of Energy, Mines, and Resources, Canada, DSS File No. 098Q23440-8-9074.

Hoek, E., Brown, E.T.(1980) Underground Excavations in Rock, Institution of Mining and Metallurgy, London.

Pakalnis, R., Vongpaisal, S., Lang., B., Cook, K.(1993) Ground Stability Guidelines for Cut & Fill Mining of Wide Ore Bodies, Dept. of Energy, Mines, and Resources, Canada, DSS File No. 14SQ.23440-49-9145

Wiles, T.(1991) Map3D Mining Analysis Program. Mine Modelling Ltd., Sudbury, Canada.

MINE DESIGN VALIDATION UTILIZING 3-D FINITE ELEMENT MODEL
LA MINE DOYON

W. Quesnel
Lac Minerals

P. Chau
Bharti Engineering Associates

ABSTRACT

Numerical modelling techniques have been applied to the mine design of the lower block of the main zone at Doyon Mine. An experimental stope at the upper level was excavated and monitored with extensometers in the hangingwall. Two-dimensional finite difference model FLAC was initially used for calibration runs of the test stope. Subsequent runs were carried out using the three-dimensional finite element model VISAGE to look at the optimum stope length for the footwall lens. Different mining and backfill sequences for the hangingwall lens were also examined using the 3-D VISAGE model.

INTRODUCTION

Doyon mine is located 40 Km east of Rouyn-Noranda in Western Quebec. It is jointly owned by Lac Minerals and Cambior with each holding a 50% interest (CIM, 1990). Lac Minerals operates the mine under the direction of a management committee (CIM, 1990). Production began in 1980 from the Main zone open pit. An exploration ramp was driven in 1983 from the Main pit at the fourth level. Encouraging results led to the sinkage of a 655 m deep shaft in the footwall of the Main zone. Following the completion of the shaft in 1986, both underground and surface mining began in the West zone. The Main zone underground operations commenced in 1987 and the focus of this paper concentrates on the mining of the lower block of the Main zone.

BACKGROUND INFORMATION

Fig. 1 shows the typical geological section of the Main zone (Whiteway, 1991). Gold is found in the felsic volcanic ore rock with average grade of 5.4 grams/tonne. The hangingwall rocks are composed of weak sericitic schists while the footwall rocks are mainly mafic tuff and blocky tuff. The lower block orebody of the Main zone is striking East-West and is generally dipping from 50 degrees to 70 degrees to the South. The ore width varies from 3 m to 20 m, averaging 7.5 m in the footwall lens and 15 m in the hangingwall lens.

The upper block of the main zone was mined using the blasthole stoping method with some variations. Five primary levels developed from the shaft, spaced 120 m vertically, provide access to the underground workings. Sublevels of 15 m spacing are adopted in the upper block and most of the development is located in the footwall. The close spacing of the sublevels leads to high levels of development, which translate into high mining costs.

It was recognized by the mine that a critical review of the mine design was a high priority and the optimum mining approach for the extraction of the lower block of the Main zone should be examined. The main interest of the mine was to look at the possibility of cutting down the development cost by increasing the sublevel spacing from its original 15 m to 30 m. The new stope height would become 30 m and the mine wished to identify any potential ground problems for the new mining approach. This paper summarizes the work that has been completed to review the optimum mining approach of the lower block. The footwall lens and the hangingwall lens were examined individually because of the different geometries.

UPPER LEVEL TEST STOPE

A test stope was excavated at the upper level (4-0L) to provide data for model calibrations. Figure 2 shows the layout of the test stope and the locations of monitoring devices. The 4-0 L test stope is located 200 m below the surface and is dipping approximately 45 degrees to the South. The dimensions of the test stope are roughly 8 m wide, 25 m high and 40 m long. The hangingwall of the test stope was reinforced with 15 m to 20 m long cablebolts at a 2 m x 3 m pattern using double 5/8" diameter cables. Monitoring devices consisted of five extensometers numbered as A, B, C, D and E, each with five anchors, which were installed in the hangingwall at 8 m spacings along the strike to monitor the hangingwall movement. The test stope was opened up progressively along the strike and no backfill was used. Fig. 3 shows the amount of hangingwall movement recorded by Extensometer C after the test stope was completely mined. It was found that the immediate hangingwall measured movement was roughly about 2 to 3 cm. In general, the 4-0L stope was quite stable.

Calibration runs were carried out using the 2D finite difference code FLAC in an attempt to reproduce the same movement patterns recorded by the extensometers. Several sets of input data have been tried and results of those computer runs have been examined and compared. The most representative set of input data which has been found is listed in Table 1. Fig. 4 shows the modelled rockmass responses upon mining of the test stope with cable reinforcements. Modelling

results indicate that mining of the reinforced test stope would induce approximately 15 m wide relaxation zones in the hangingwall and the immediate hangingwall movement would be restricted to within 4 to 5 cm. Judging from the close agreement of the monitored and predicted hanging wall movements, it can be concluded that the input data used for modelling are quite reasonable.

MODELLING OF THE LOWER BLOCK FOOTWALL LENS

The footwall lens in the lower block is relatively narrow compared to the width of the hangingwall lens. Typical width of the footwall lens is approximately 7.5 m. The proposed mining plan called for mining of the footwall lens with open stoping method with no backfill or delayed backfill. Typical stope height would be 30 m. Mining would commence from the centre of the stope and spread out in two directions with 5 m panel sequences.

The 3-D finite element model VISAGE had been used to simulate the effects of mining of the footwall lens. VISAGE is a state-of-the-art 3-D nonlinear finite element program specially designed for mining and geotechnical applications. VISAGE can model the behaviour of linear and nonlinear materials as well as continuum and discontinuum media under static, dynamic or seepage loading conditions. Fig. 5 shows the simulated sequence of the footwall lens. A total of eight runs had been carried out to simulate the mining responses with increasing span length from 5 m to 40 m to determine how many panels could be mined without causing any significant ground failures. The widths of relaxation zones were also monitored for all those eight mining steps to identify the extent of failures and thereby to provide information assessing the support requirements.

Modelling results of the eight mining steps are summarised in Table 2 and typical results of mining of the 20 m long stope are plotted in Fig. 6. The major findings of these runs are summarised as follows :

1. The 30 m high, 7.5 m wide open stope of the footwall lens can be mined up to 15 m in length without causing any significant ground problems. Problems will start to occur when the span of the open stope is opened to 20 m.

2. Width of the hangingwall relaxation zones will increase from 7.5 m to 13 m when the span of the open stope increases from 20 m to 40 m.

3. The predicted hangingwall movement will be restricted to 3 cm when the stope span is kept to 15 m.

4. However, the hangingwall movement will increase significantly from 4 cm to 12 cm when the stope span increases from 20 m to 40 m.

Based on the above findings, it was recommended that the stope span of the footwall lens be kept to within 15 m should cablebolts not be used, and backfill be placed before proceeding to the next stope.

MODELLING OF THE LOWER BLOCK HANGINGWALL LENS

The shape of the hangingwall lens is quite irregular at the lower block. The width of the hangingwall lens averages about 15 m and varies from 5 m to 20 m. Mining plans called for mining of the hangingwall lens using the open stoping method with two proposed sequences. Primary stopes of 6m and secondary stopes of 12 m were proposed. These two sequences are described as follows :

1.   One-lift mining - First primary stope of 6 m width will initially be mined and backfilled with cemented rockfill. Secondary stope of 12 m width will then be opened and filled with weakly cemented or straight rockfill before moving on to the next primary stope. Mining will repeat with 1-2-3-4 pattern and progress along strike on the same level. Typical stope height will also be 30 m. (see Fig. 7(a) for details).

2.   Two-lift mining - Two primary stopes, No. 1 and No. 5 stopes, of the first lift, will be mined initially. Mining of the same primary stopes (No. 1 and No. 5 stopes) will move to the second lift once the first lift stopes are filled with cemented rockfill. The No. 3 primary stope will be mined and filled at the first lift before moving onto the second lift. Once all the second lift primary stopes have been filled, mining of the secondary stopes commences. (see Fig. 7(b) for details)

Modelling results of the two proposed sequences are summarised in Table 3. Results given by Table 3 can be analyzed as follows :

(A)   One-Lift Sequence

1.   Mining of the first primary stope will experience no ground problems whatsoever.

2.   Ground problems start to occur as soon as the first secondary stope is mined out and ground problems will continue as mining progresses.

3.   Typical width of relaxation zones will be restricted to 10 m and the hangingwall movement will be kept below 6 cm.

(B)   Two-Lift Sequence

1.   Mining of the primary stopes will not induce any significant movements or ground problems.

2.   The hangingwall movement will be restricted to 2 cm during primary stope mining.

3.   Mining of the secondary stopes could induce sloughage problems and typical width of relaxation zones will be 12 m. The anticipated hangingwall movement of the secondary stope will be within 6 cm.

Comparing the results of the two proposed sequences, it was indicated that the primary stopes would experience less ground problems if the two-lift sequence was used. The two-lift mining sequence, therefore, was considered to be a better option even though overbreak could still be a problem during the secondary stope recovery. However, anticipated sloughage can be controlled with cablebolt support of the hangingwall.

TABLE 2 - RESULTS OF MINING OF THE FOOTWALL LENS

Stope Length (m)	Hangingwall Movement (cm)	Width of Relaxation Zone (m)
5	0.8	
10	2.0	
15	3.0	
20	4.0	7.5
25	5.0	12.0
30	8.0	12.0
35	9.0	13.0
40	12.0	13.0

TABLE 3 - RESULTS OF MINING OF THE HANGINGWALL LENS

1) One-Lift Mining

Mining Stage	Hangingwall Movement (cm)	Width of Relaxation Zone (m)
6 m Primary Stope	0.8	
12 m Secondary Stope	3.6	10
6 m Primary Stope	3.9	8
12 m Secondary Stope	5.5	10
6 m Primary Stope	4.7	5

2) Two Lift Mining

Mining Stage	Hangingwall Movement (cm)	Width of Relaxation Zone (m)
First lift primary stopes (No. 1,5)	0.9	
Second lift primary stopes (No. 1,5)	0.7	
First lift primary stope (No. 3)	1.4	
Second lift primary stope (No. 3)	1.1	
First lift first secondary stope (No. 2)	5.0	12.0
First lift second secondary stope (No. 4)	6.0	12.0
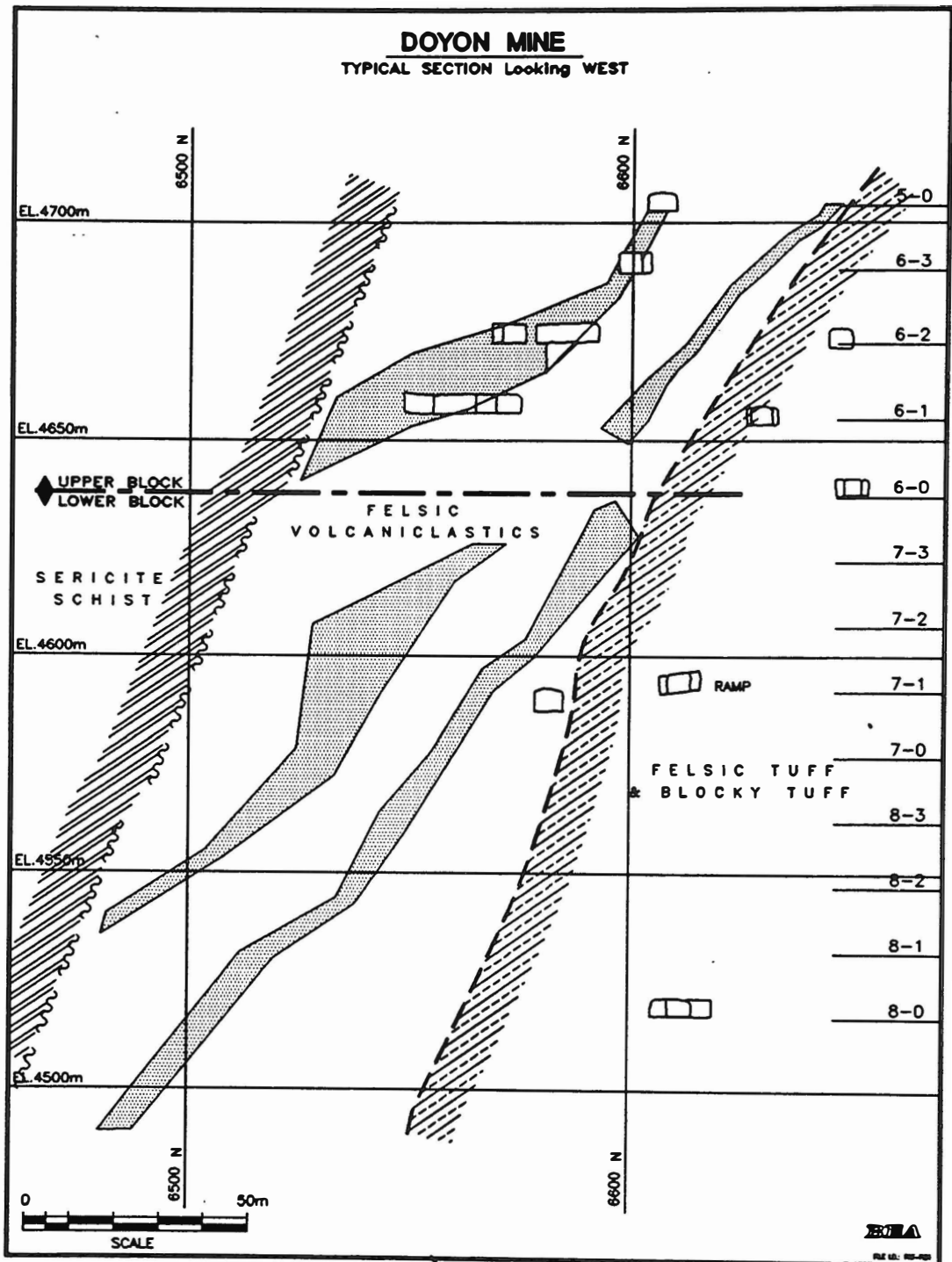
FIG. 1 TYPICAL GEOLOGICAL SECTION OF THE MAIN ZONE
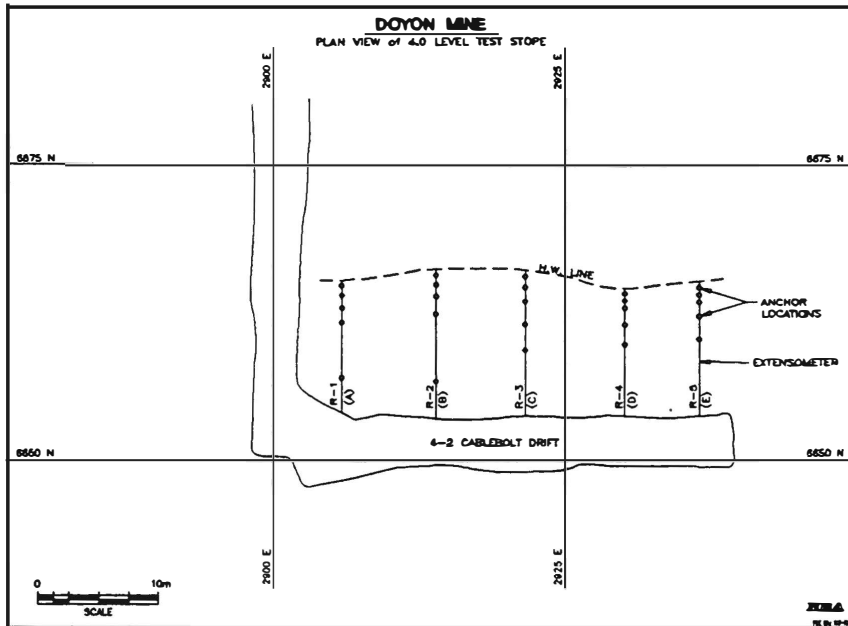
(A) PLAN VIEW
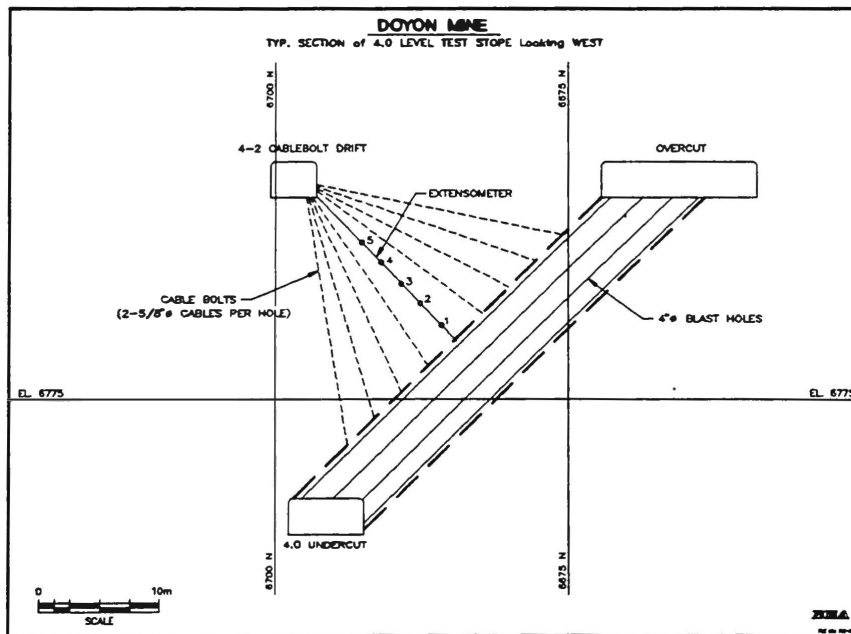
(B) SECTION LOOKING WEST

FIG. 2 LAYOUT OF THE 4-0L TEST STOPE
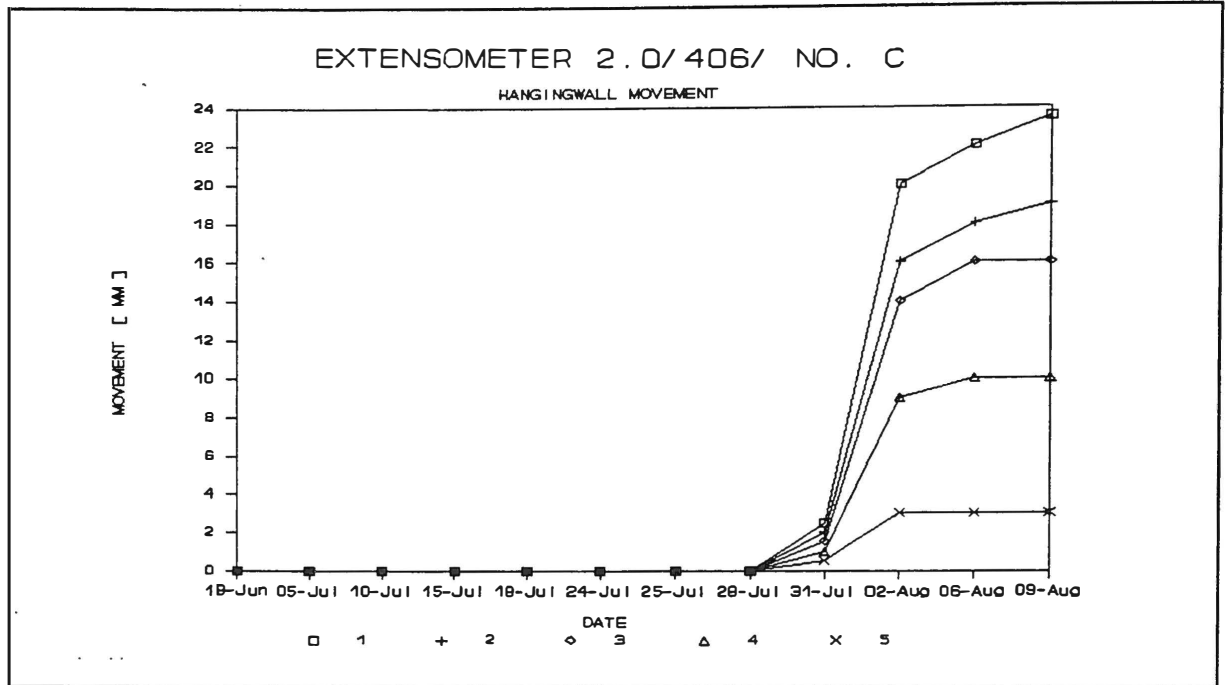
FIG. 3 HANGINGWALL MOVEMENT RECORDED BY EXTENSOMETER NO. C
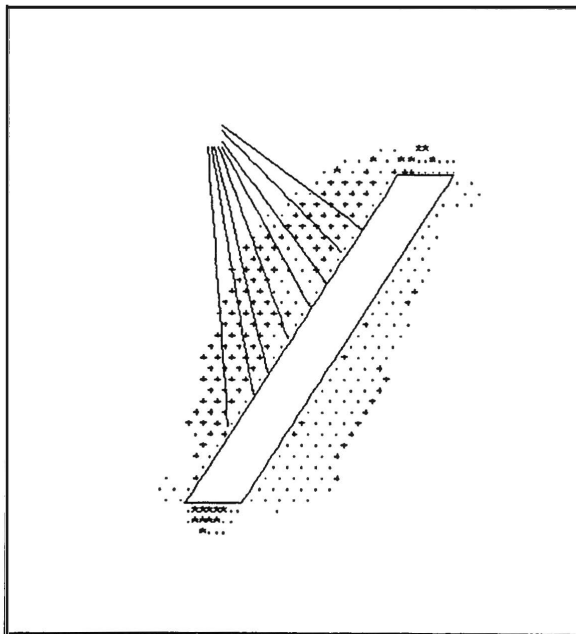
(A) RELAXATION PLOT
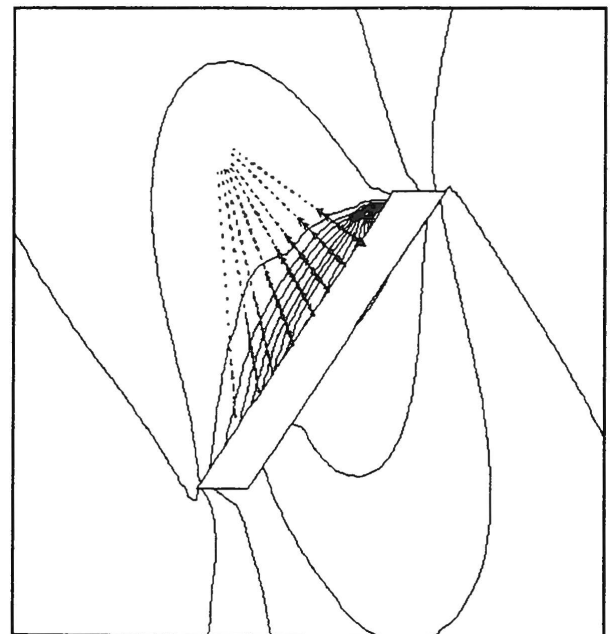
(B) DISPLACEMENT CONTOUR PLOT

FIG. 4 MODELLING RESULTS OF THE 4-0L TEST STOPE

MINING DIRECTION

RELAXATION PLOT

L = 15 m

1

RELAXATION PLOT

L = 20 m

2

RELAXATION PLOT

L = 25 m

3

RELAXATION PLOT

L = 30 m

4

FIG. 7 (A) ONE-LIFT MINING OPTION

FIG. 7 (B) TWO-LIFT MINING OPTION
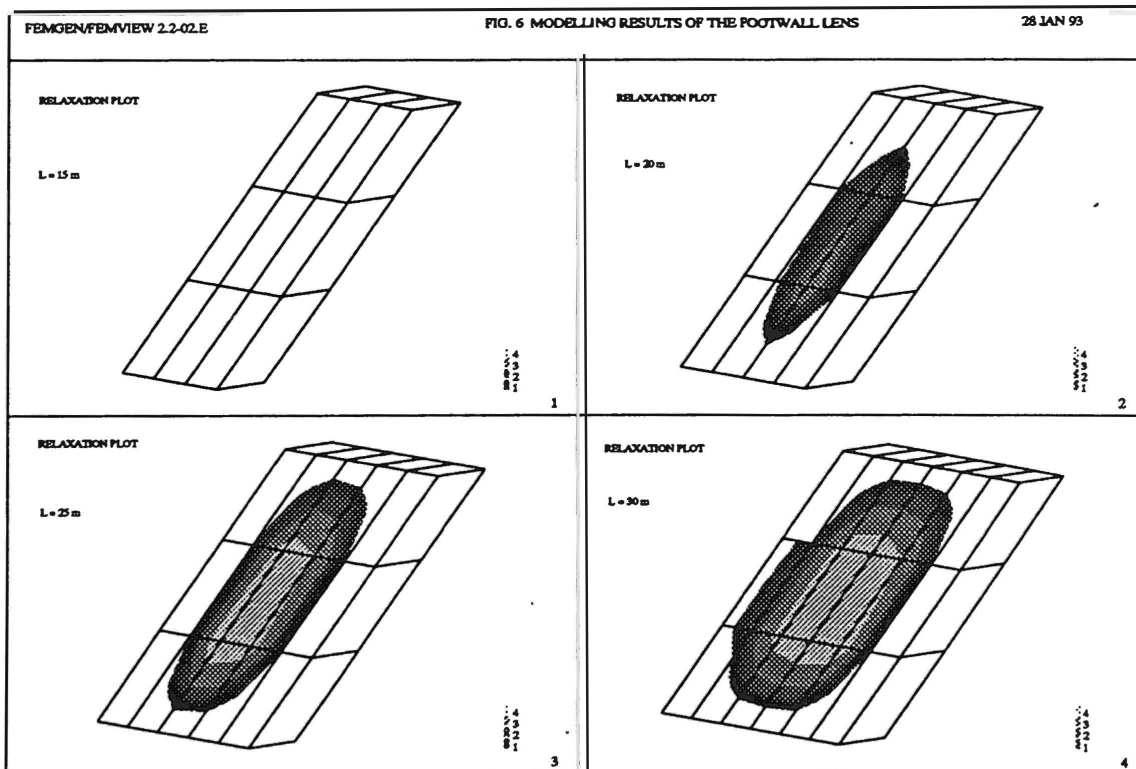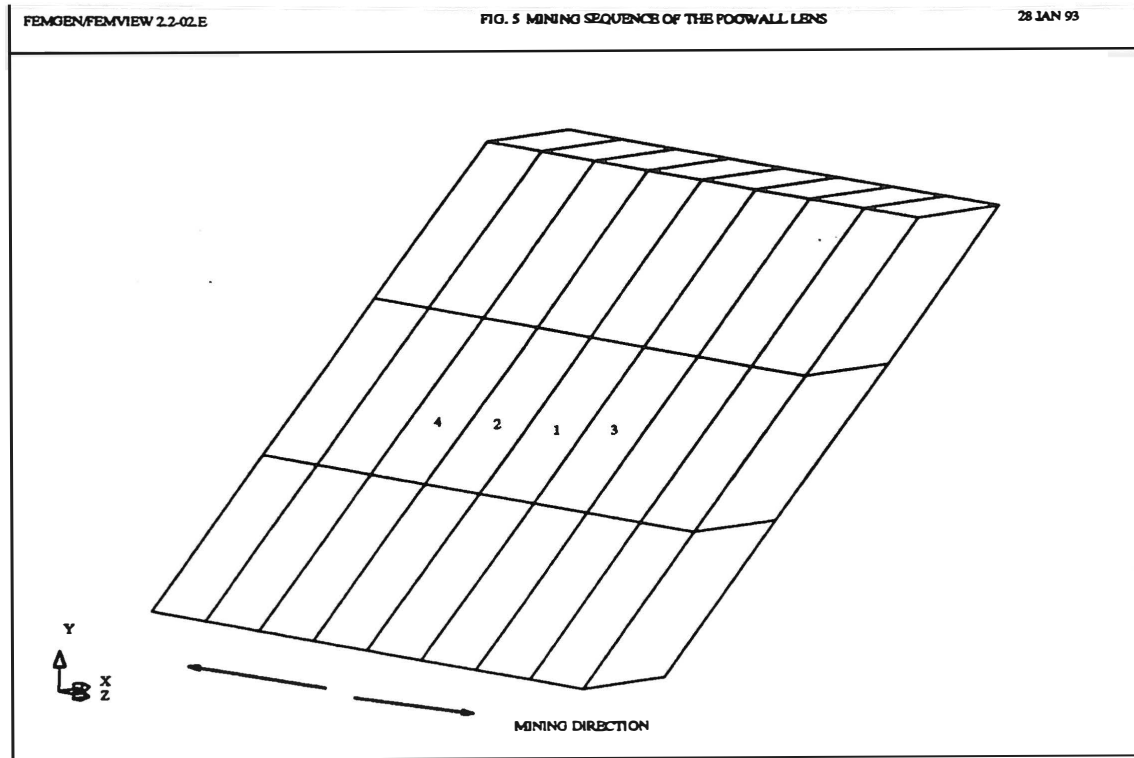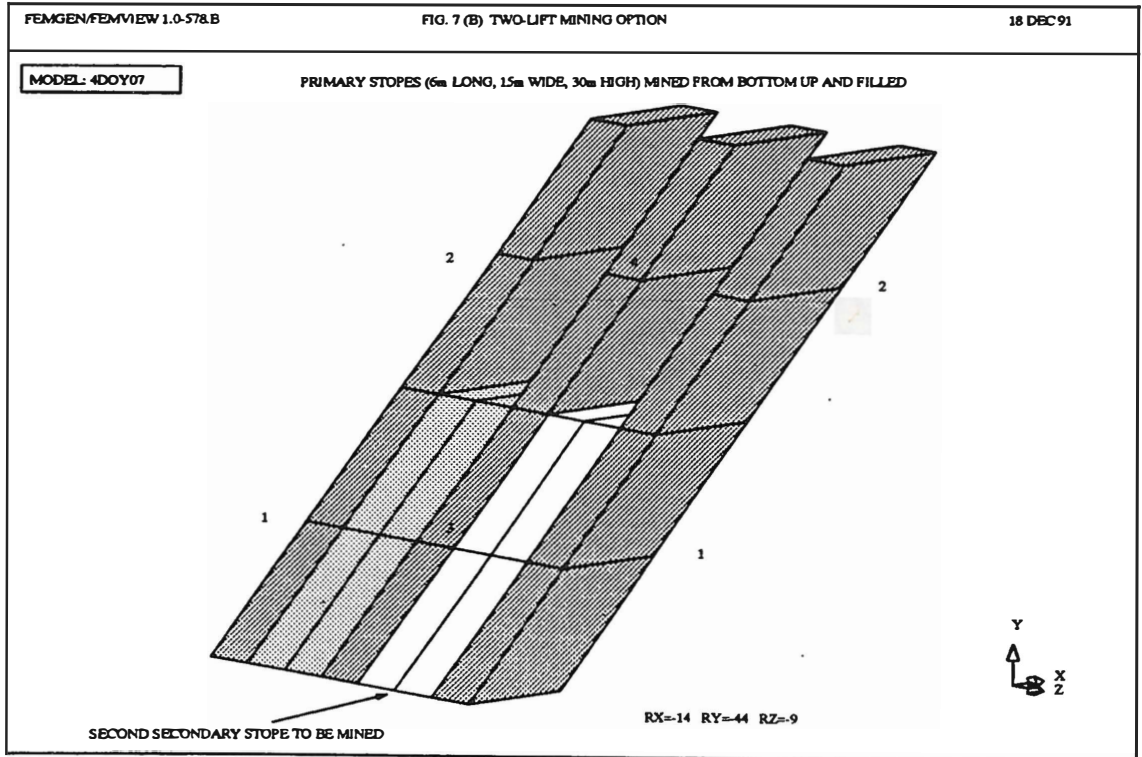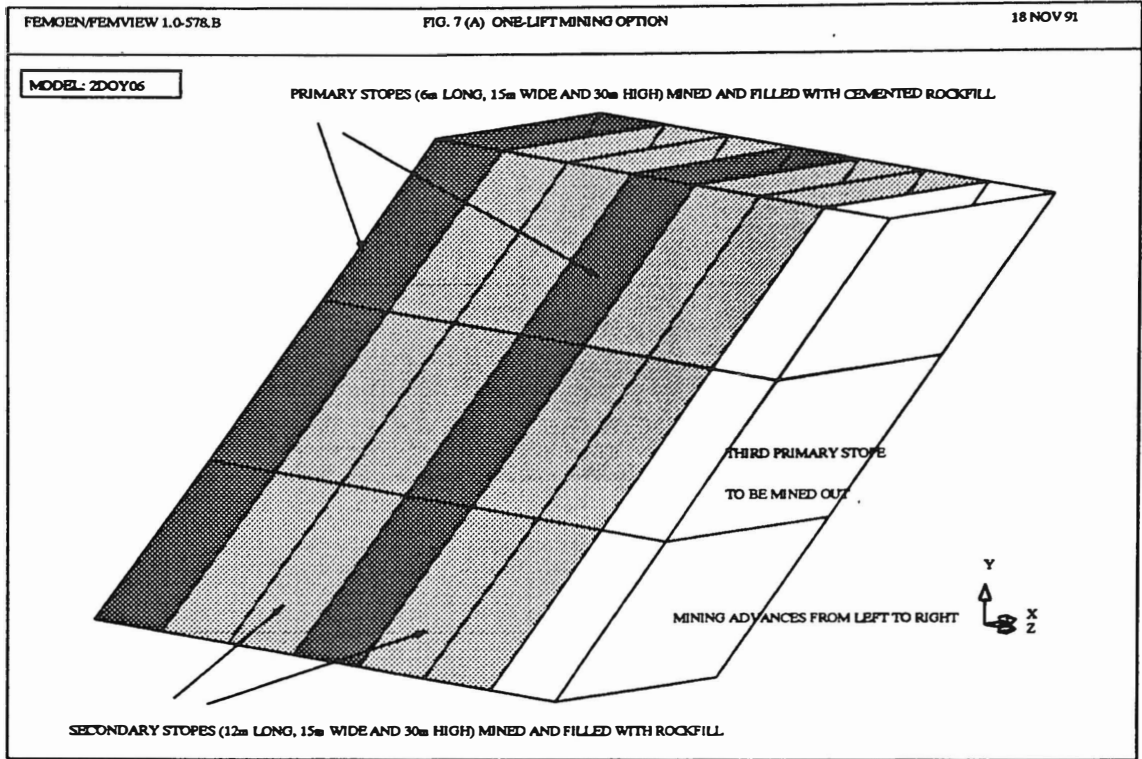
CONCLUSIONS

Based on the results of the modelling runs, it can be concluded that it would be feasible to increase the stope height to 30 m for mining of the lower block of the main zone using the open stoping method. Therefore, sublevel spacing could be increased to 30 m in order to reduce the cost of development. The optimum stope length for the footwall lens would be between 15 m and 22 m. The stope length of the footwall lens should be kept within 15 m if there is no cable reinforcements. Mining of the hangingwall lens with 6 m primary stopes and 12 m secondary stopes would not experience serious ground problems. Mining of the hangingwall lens should be carried out with two-lift sequence, which would eliminate or minimize ground problems during primary stope recovery. A systematic cablebolting of the hangingwall, especially in the secondary stopes, should be further evaluated.

REFERENCES

1.   P. Chau, Jan. 1992, "Lac Minerals Ltd., Doyon Mine, Geotechnical Assessment", Bharti Engineering internal report, Report No. 91-2182C-3.

2.   CIM Bulletin, Nov. 1990, "The Cambior Story : The Doyon Mine", CIM Bulletin, Volume 83, No. 943, p.50-53

3.   G. Ferguson, Jan. 1992, "La Mine Doyon, Mine Design, Lower Block - Main Zone", Bharti Engineering internal report, Report No. 91-2182C-2.

4.   P. Whiteway, Aug. 1991, "Tough Sledding", Canadian Mining Journal, June/July/August issue, p.41-45.

ACKNOWLEDGEMENT

TABLE 1 - INPUT DATA FOR COMPUTER MODELLING

Rockmass			In Situ Field Stresses
Modulus of Elasticity	E	10 GPa	σ_1 (perpendicular to strike) = 2.24 σ_v
Poisson's Ratio	υ	0.2	σ_3 (parallel to strike) 1.5 σ_v
Cohesive Strength	C	3.0 MPa	
Friction Angle	ϕ	35.0 degrees	Where σ_v vertical stresses
Density		2700 kg/m³	overburden weight

MODELLING DISCONTINUOUS ROCKMASSES IN THREE DIMENSIONS USING MAP3D

Terry D. Wiles
Mine Modelling Ltd.

D. Nicholls
Inco Manitoba Ltd.

ABSTRACT

In this paper, several examples of the use of MAP3D (three-dimensional stress analysis program), to simulate discontinuous rockmass response are presented. This simulation capability has been achieved by incorporation of displacement discontinuities into the indirect boundary element procedure used in MAP3D. Fault slip and crack opening can both be accommodated.

To build the mining geometries, one need only specify the features of interest, i.e. the mining blocks and the faults. The intersection between these entities, detection of overlap areas and discretization into boundary elements, is automatically conducted by MAP3D as part of the analysis.

Application to real mining problems illustrate that the incorporation of fault slip can have an overwhelming influence on the rockmass response. Stresses and displacements are redistributed, thus enhancing stability at some locations, but increasing stress concentrations at others.

INTRODUCTION

Linear elastic, three-dimensional numerical modelling is now conducted on a routine basis at many mining camps. This is a result of the recognition of the importance of three-dimensional effects, recent progress in ease of use of 3-D numerical models, and the enormous increase of the computation power of affordable personal computers.

The influence of discontinuities such as faults and joints is normally not considered, even though both finite element (Goodman fault element, Goodman, 1976) and distinct element (UDEC and 3DEC, Cundall, 1971) codes with this capability have been available for some time. While the importance of fault slip is well understood, simulation of discontinuous rockmasses is at present undertaken only for special modelling projects normally involving consultants or expert research staff. This situation exists because of the difficulty in setting up and using these models, and the long run times required for such simulations.

Although the displacement discontinuity technique (NFOLD, MINTAB, DZTAB, EXAMINETAB, see Starfield and Fairhurst, 1968) has been used extensively for the simulation of tabular mining problems, very few models have incorporated this facility into a three-dimensional boundary element analysis program. MAP3D (Wiles, 1993) does have this capability. Combined with the ability to automatically build intersections between bisecting faults and excavations, this overcomes the complication of setting up and using these models, while maintaining ease of use and short run times.

DISPLACEMENT DISCONTINUITIES IN THE BOUNDARY ELEMENT METHOD

The MAP3D model formulation is based on the indirect boundary element method. For the case of a homogeneous, elastic medium, an indirect boundary element procedure known as the fictitious force method (Banerjee and Butterfield, 1981) can be stated as follows

$$\sigma^s = T \cdot \sigma^f + C \cdot P \tag{1}$$

where σ^s represents a vector of normal and shear stresses acting on the boundary elements at the surfaces of the excavations, σ^f represents the far field stress state, T represents the stress transformation matrix from the axes of the far field stress state to the axes at each boundary element, P represents the normal and shear (fictitious) forces applied at each boundary element, and C represents a matrix of influence coefficients relating the applied normal and shear forces P to the stress change at each boundary element.

In order to incorporate displacement discontinuities into the solution process, one need only superimpose their effects on the existing geometry. This requires that the influence of each displacement discontinuity (Wiles and Curran, 1982) be determined, at every other boundary element, thus adding additional rows and columns to the C matrix. The additional unknowns added to the vector P represent the amount of ride (fault slip) and closure (or crack opening) on the displacement discontinuity surfaces.

In a normal boundary element analysis procedure, the stresses σ^s and σ^f are specified, the matrices T and C are calculated from the geometry, and then the unknown vector P is solved for using the above equations. To incorporate the influence of the displacement discontinuities, it is

necessary to evaluate the normal and shear stresses acting on each displacement discontinuity surface during the solution process. If the shear stress is less than the shear strength (determined for example using a Mohr-Coulomb failure criterion), then the amount of fault slip is zero. Alternatively, if the shear stress exceeds the shear strength, then the shear stress is set equal to the strength

$$\tau = S_o + \sigma_n \cdot \tan\phi \tag{2}$$

where σ_n represents the normal stress, and S_o and ϕ represent respectively the cohesion and friction angle. The amount of fault slip is solved for as part of the matrix solution along with the other components of vector **P**.

More complex fault response can be easily incorporated by using additional expressions relating the normal and shear stresses to the closure and ride. This can include the simulation of gouge material, non-linear normal stiffness, dilation, peak and residual strengths etc. While these effects are well known (Goodman, 1976, Bandis et al, 1983, Saeb and Amadei, 1992), they are also very difficult to accurately quantify.

SUPERIMPOSING FAULTS ON EXCAVATION GEOMETRIES

In the mining example illustrated in figure 1, an inclined fault intersects a simple rectangular shaped stope. This example is presented to illustrate the far reaching influence that the presence of a fault can have on the rockmass response around an excavation.

Figure 1 - Inclined Fault

To build this geometry in MAP3D, one need only specify two features, the stope and the fault. The intersection between these entities, detection of overlap areas and discretization into boundary elements, is automatically conducted by MAP3D as part of the analysis. This figure illustrates the final boundary element mesh, ready for analysis.
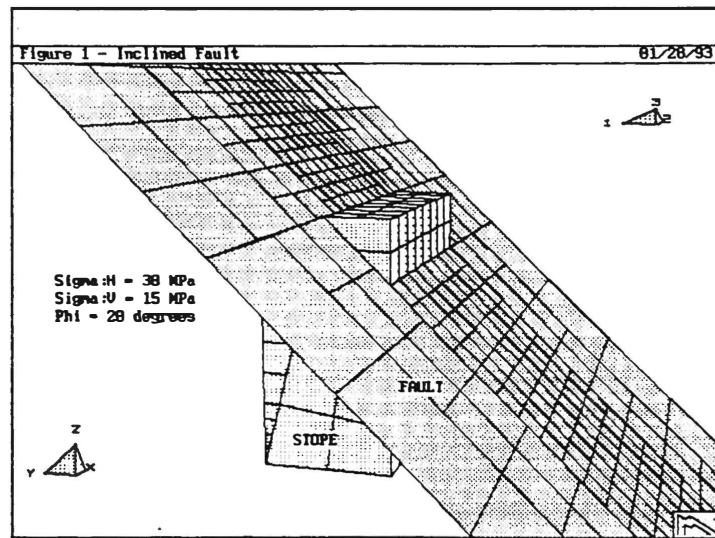
In this problem, the far field stress state has been specified as 30MPa in both horizontal directions, and 15MPa in the vertical direction. The elastic properties of the host rockmass are Young's modulus of 60GPa and Poisson's ratio of 0.25. The stope is 2m wide, 4m high and 4m long (along strike). The fault dips at 45° and strikes parallel to the stope. The fault has a friction angle of 20° with no cohesion. At the far field

stress state, the fault has a strength of 8.2MPa and an active shear stress of 7.5MPa, giving a safety factor of 1.1, a stable condition.

In the adjacent figures, analysis results are presented on a transverse section taken at the mid-point of the stope. Owing to slip on the fault, it can be observed that (figure 2) the major principal stress is distributed non-uniformly around the stope. The presence of the fault has significantly reduced the stress concentration directly over the top of the stope, and redistributed the stresses adjacent to the fault slip area.

Figure 3 illustrates that the minor principal stresses are even more intensely redistributed, showing a reduction in the stress concentration over the upper right hand corner of the stope, and the development of some tensile stresses.

The displacements (figure 4) show reduced closure of the stope in the area above and to the right of the fault.

During the analysis, the fault slips a maximum of 0.14mm at the side of the stope. This occurs over a length of almost 2m. In the area directly above the stope, the fault slips a maximum of 0.6mm. This slip occurs over a length of more

Figure 2 - Major Principal Stresses

Figure 3 - Minor Principal Stresses

Figure 4 - Displacements
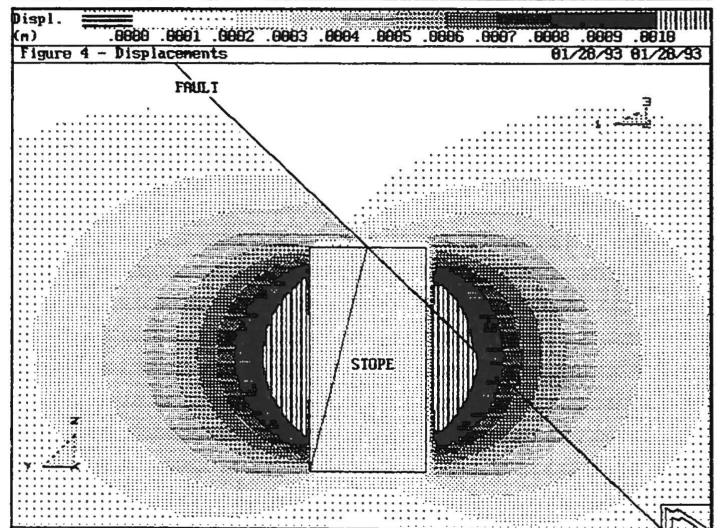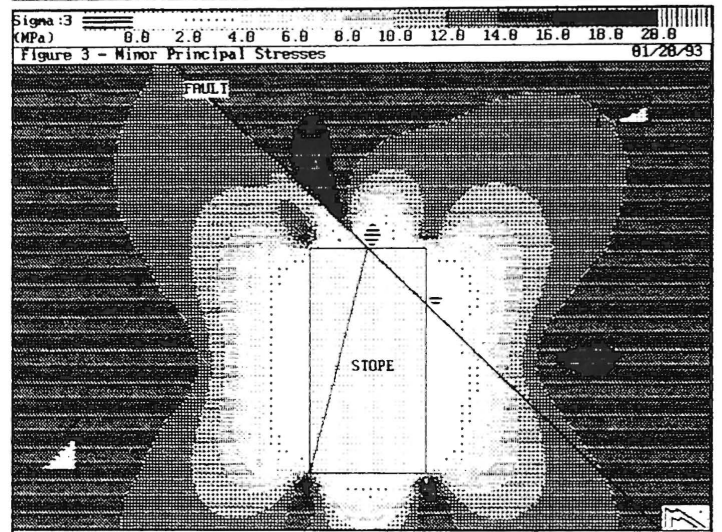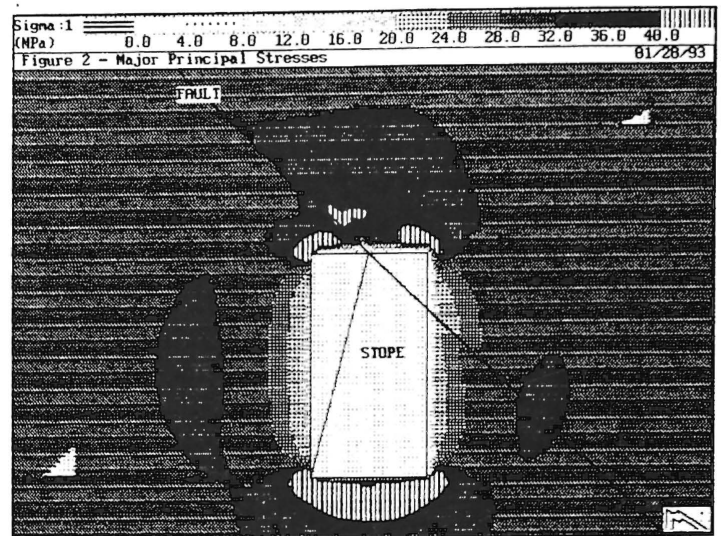
than 5m. As the stope is only 2m wide, this represents a relatively far reaching influence.

HANGINGWALL AND FOOTWALL FAULTS PASSING NEAR MINING BLOCKS

At the INCO Thompson Birchtree Mine, there are well defined fault zones in both the hangingwall and footwall of the orebody. The location of these relative to the mining blocks is illustrated in figure 5 which shows a three-dimensional perspective view looking down in a south-east direction.

The rockmass at this mine is well jointed and very weak. A far field stress state of 38MPa acting in the hangingwall- footwall direction (east-west), 25MPa acting along the strike of the orebody, and 16MPa vertical, has been used. The Young's modulus of the rockmass is 13.5GPa, with a Poisson's ratio of 0.25. Both faults have been assigned a Young's modulus of 5GPa with a gouge thickness of 1m, and a friction angle of 20° with no cohesion.

Figures 6 and 7 show the major principal stresses around the 21800 block in Birchtree Mine respectively without and with the faults. The view shows a transverse section, positioned such that the observer is looking directly along the strike of
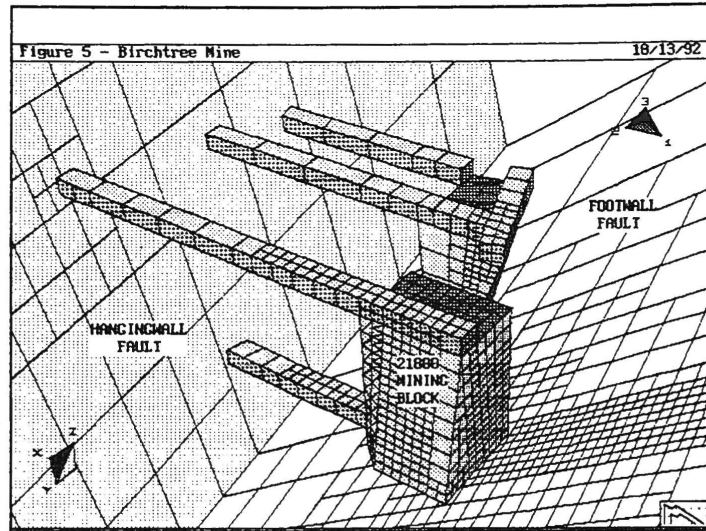
Figure 5 - Birchtree Mine

Figure 6 - Major Principal Stresses - Without Faults
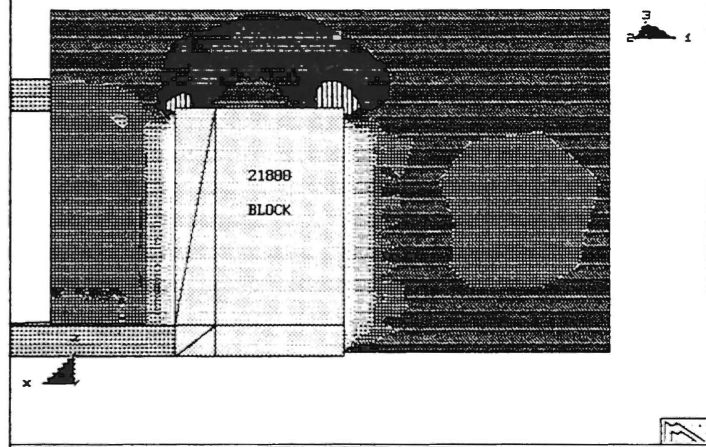
Figure 7 - Major Principal Stresses - With Faults
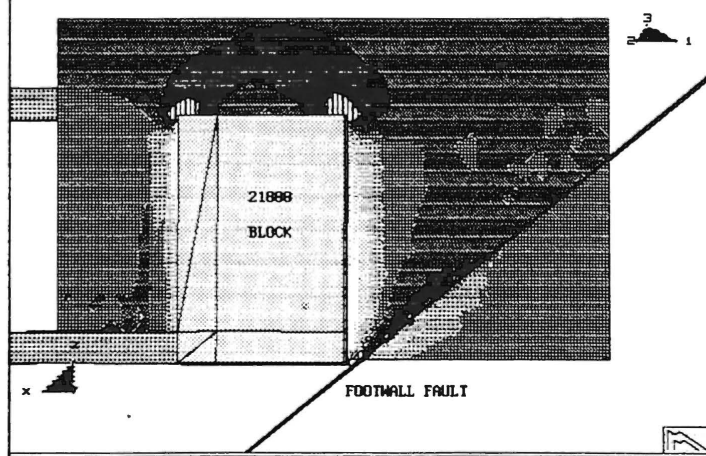
the footwall fault. In these figures it can be observed that the presence of the faults does not significantly influence the magnitude of the major principal stresses, except in the immediate vicinity of the fault.

However, the minor principal stresses (figures 8 and 9) are significantly reduced both over the back of the mining block, and at the lower portion of the footwall side of the block. In the zone for the first 5m above the back of the block, the confinement goes from 2 to 4MPa without the faults, to less than 2MPa, with both faults. Along the lower footwall side of the mining block, the tension zone more than doubles in size, from 1.6m to nearly 4m thickness.

The displacements are illustrated in figures 10 and 11. These figures show that due to the presence of the faults, the total closure across the mining blocks increases from 0.077m to 0.1m (30% increase). The footwall fault shears a maximum of 0.06m near the lower footwall side of the mining block.

Although in this case the stress changes predicted by the model appear to be insignificant between the case with and without the discontinuity, in a rockmass as weak and unstable as this, small changes can cause real problems. In this orebody, instability is usually

Sigma :3
(MPa)   0.0 2.0 4.0 6.0 8.0 10.0 12.0 14.0 16.0 18.0 20.0
Figure 8 - Minor Principal Stresses - Without Faults   01/21/93

Sigma :3
(MPa)   0.0 2.0 4.0 6.0 8.0 10.0 12.0 14.0 16.0 18.0 20.0
Figure 9 - Minor Principal Stresses - With Faults   10/13/92

FOOTWALL FAULT

Displ.
(m)   .000 .020 .040 .060 .080 .100 .120 .140 .160 .180 .200
Figure 10 - Displacements - Without Faults   01/21/93

45
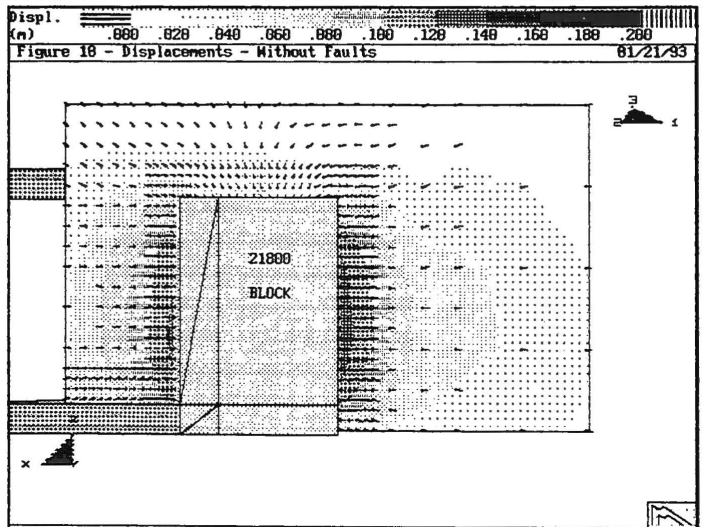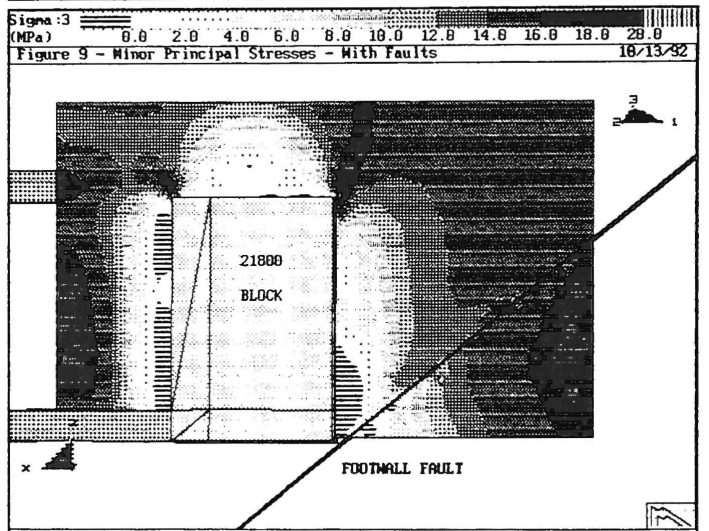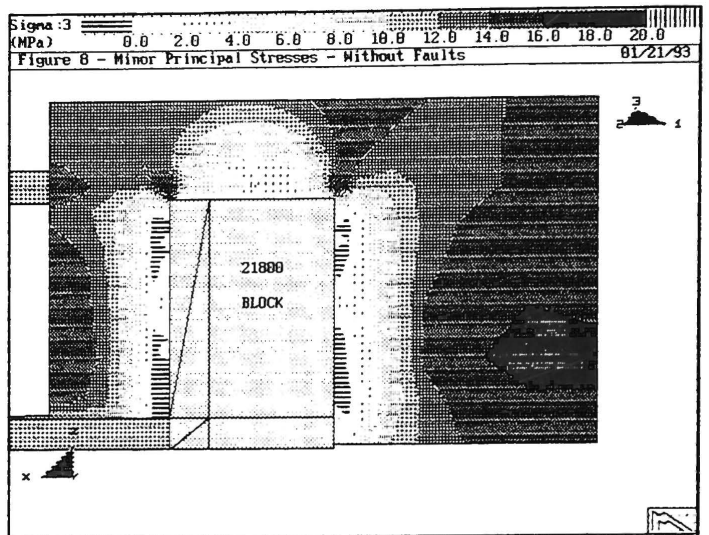
associated with low confinement zones. The zone of low stress over the back of the mining block represents a large volume of material.

This is further emphasized by considering the minor principal stresses on a longitudinal section taken through the same mining block. Figures 12 and 13 show that the confinement in the pillar between the two mining blocks has increased due to the presence of the faults. The increase in the confinement in this pillar is sufficient to bring the safety factor from below one, to well above one through most of the pillar.

The tension zones have also moved. Note the formation of a tension zone adjacent to the access drift at the top of the 21800 block. Also, the tension zone at the upper right side (north) of this block has moved to the bottom of this face.

We believe at this time that the footwall discontinuity is stable and have not seen, by visual observation, any movement along the exposed sections of this fault. Strain measuring devices will be installed across the fault to determine if there is movement that cannot be detected visually. The results from these will be used to further calibrate the model.

Figure 11 - Displacements - With Faults

Figure 12 - Minor Principal Stresses - Without Faults

Figure 13 - Minor Principal Stresses - With Faults
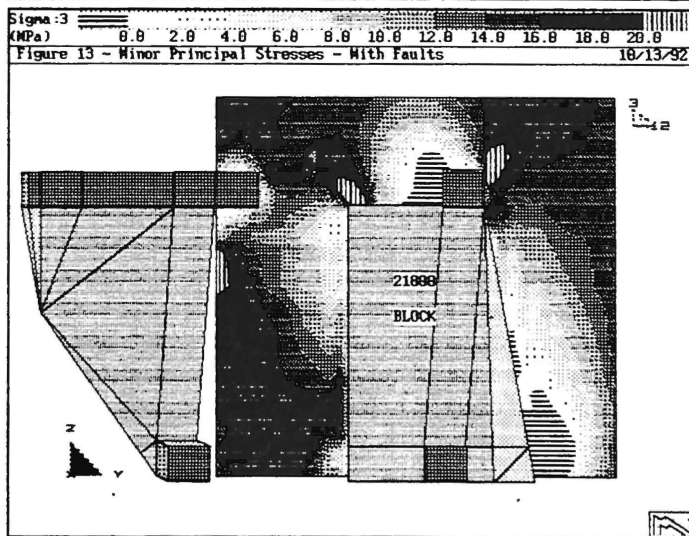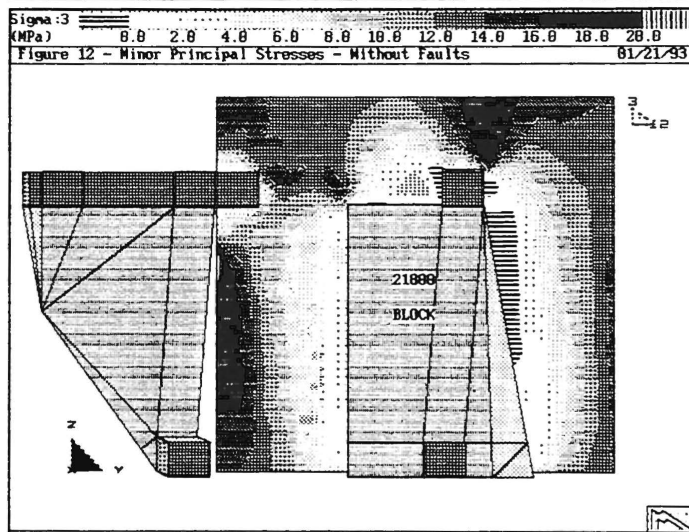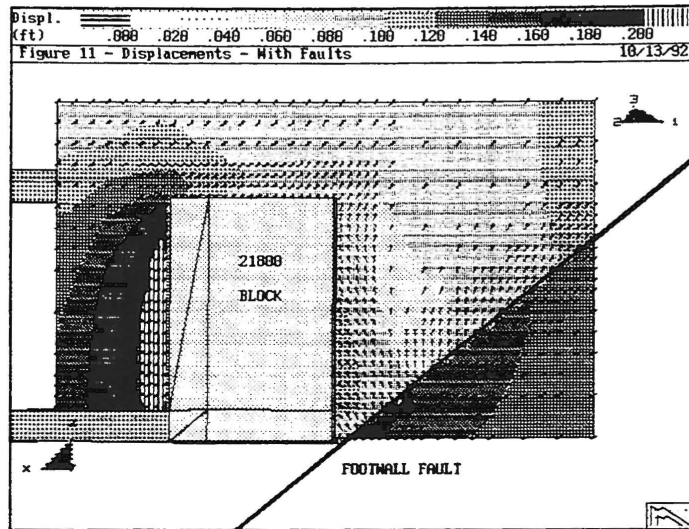
HANGINGWALL PILLAR FORMED BY A WEAK FAULT

This final example illustrates a near surface mining problem where a weak fault is located 3m into the hangingwall of the mine. The shape of the stope has been simplified to a rudimentary rectangular shape with dimensions of 30m along strike, 30m high and 12m thick, as shown in figure 14.

For this analysis, the far field stresses have been assumed to vary linearly with depth giving, at the mid-height of the mining block (35m depth), a maximum horizontal far field stress of 14MPa oriented parallel to the strike of the fault. The other horizontal stress and the vertical stress are equal to 3.2MPa. The rockmass is assumed to have a Young's modulus of 25GPa and a Poisson's ratio of 0.25. The fault has been given 1m of gouge with a modulus 5GPa, and a friction angle of 9°.

Simple calculations illustrate that owing to the low frictional strength of the fault, it is necessary that the maximum horizontal far field stress be oriented less than 3° from the strike of the fault or else the fault will be over-stressed and unstable.

The predicted major and minor principal stresses are illustrated on a transverse section taken at the mid-
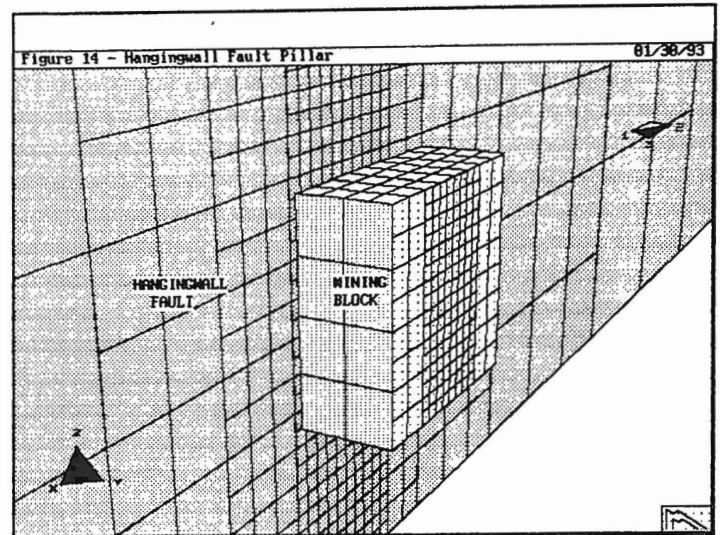
Figure 14 - Hangingwall Fault Pillar
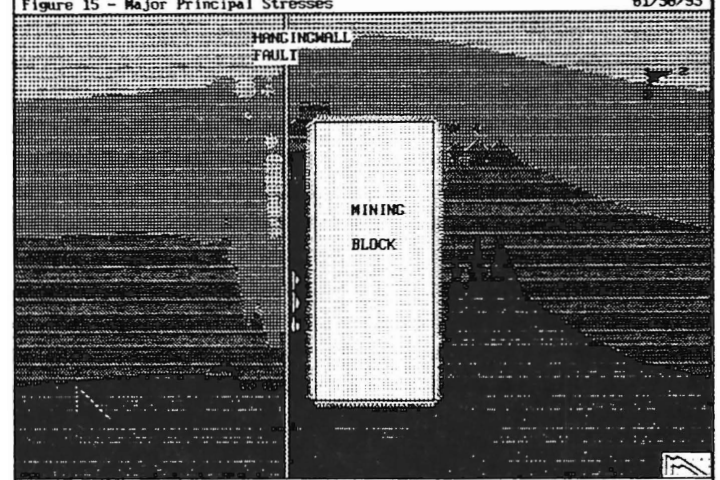
Figure 15 - Major Principal Stresses

Figure 16 - Minor Principal Stresses

47
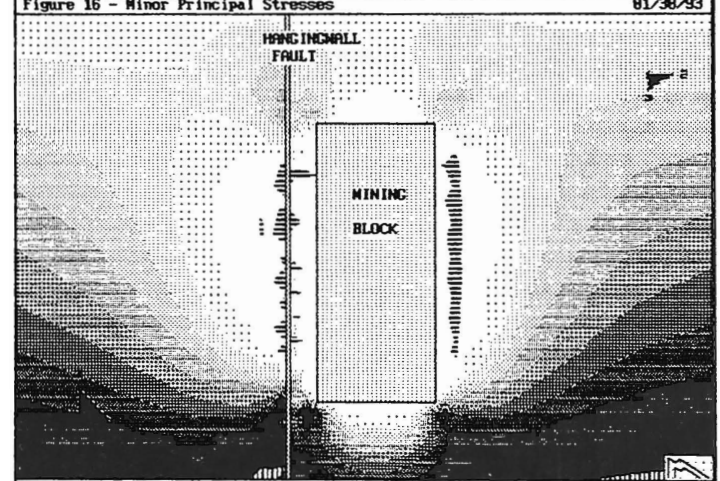
point of the mining block. In figure 15, it can be observed that the major principal stress is concentrated in the ground between the fault and the hangingwall side of the mining block. At this same location, the minor principal stress is zero or tensile (figure 16). Under these conditions it is unlikely that the ground will remain stable.

It appears that the fault causes the 2m of ground between the fault and hangingwall side of the mining block to act as a pillar. This is because the normal arching of stresses around the hangingwall side of the mining block are partially cut-off by the fault, and directed through the pillar instead of out into the hangingwall.

In figure 17, the rockmass displacements are shown on a plan taken at the mid-height of the mining block. It is clearly illustrated here that the fault slips for at least one strike length of the mining block on either side of the stope. On a mining scale this would represent a very large distance.
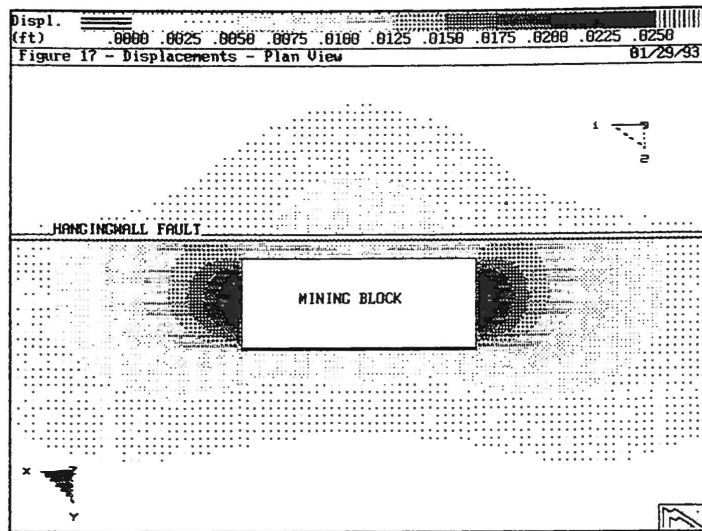
SUMMARY AND CONCLUSIONS

The examples presented in this paper demonstrate that discontinuous rockmasses can be modelled in 3-dimensions using the MAP3D analysis program.

Three different mining geometries have been presented. Each of these tests a different mode of fault slip. In all three cases, slip on the fault has resulted in significant redistribution of stresses. The first example illustrates a fault intersecting a stope. Fault slip occurred as far as 2.5 times the stope width away.

The second example illustrates a mining case where the footwall fault passes just below the mining block. Slip of 0.06m on this fault results in the movement of tension zones to different locations around the mining block. The confinement in the pillar between the mining blocks is elevated thus increasing its stability.

In the third example, a weak fault in the hangingwall of the mine results in a loss of arching into the hangingwall rocks, thus loading up the

pillar formed by the hangingwall side of the mining block and the fault. This coupled by the loss of confinement in this pillar would likely lead to instability in this pillar. Slip of nearly 0.003m occurs adjacent to the mining block. The fault moves at a maximum distance of one strike length away from the mining block. For a large mine this could represent a very large distance.

Since the discontinuities are incorporated into the boundary element analysis procedure, only the boundaries are discretized, thus complex problems can be simulated with relative ease. The advantages of the boundary element method, over domain methods such as the finite element or finite difference techniques, is maintained.

Model construction is very easy since MAP3D automatically builds intersections between mining blocks and faults. The detection of overlapping areas and discretization into boundary elements, is automatically conducted by MAP3D as part of the analysis.

With this capability, users can now readily consider the effect of fault slip on their mine designs. The authors feel that this is a very important step, as the accuracy and reliability of mine designs will be enhanced.

REFERENCES

Bandis, S., A. Lumsden and N. Barton, 1983, Fundamentals of Rock Joint Deformation, Int. J. Rock Mech. Min. & Geo. Abstr., V. 20, pp. 249-268.

Banerjee, P.K. and R. Butterfield, 1981, Boundary element analysis methods in engineering science, McGraw-Hill Book Comp Limited, New York.

Cundall, P.A., 1971, A Computer Model for Simulating Progressive, Large Scale Movements in Blocky Rock Systems, ISRM Symp., Nancy, France.

Goodman, R.E., 1976, Methods in Geological Engineering in Discontinuous Rocks, West Publishing Comp., New York.

Saeb, S. and B. Amadei, 1992, Modelling Rock Joints under Shear and Normal Loading, Int. J. Rock Mech. Min. & Geo. Abstr., V. 29, N. 3, pp. 267-278.

Starfield, A.M. and C. Fairhurst, 1968, How High-Speed Computers Advance Design of Practical Mine Pillar Systems, Energy Min. J., pp. 78-84.

Wiles T.D., and J.H. Curran, 1982, The use of 3-D Displacement Discontinuity Elements for Modelling, Proc. 4th Int. Conf. Num. Methods in Geomech., Edmonton, Alberta, pp. 103-112.

Wiles T.D., 1993, MAP3D user manual, Mine Modelling Limited, Copper Cliff, Ontario, Canada.

Session 2

Soft Rock

Roche tendre

NUMERICAL INTEGRATION SCHEMES FOR MODELS DESCRIBING THE VISCOPLASTIC BEHAVIOR OF SOFT ROCKS WITH STATE VARIABLES

Michel AUBERTIN
École Polytechnique, Montréal, Québec, Canada H3C 3A7

ABSTRACT

The inelastic behavior of soft rocks, such as rocksalt and potash, is rate- and history-dependent. In order to account for such complex phenomena, sophisticated viscoplastic models have been formulated in recent years, many of which using the concept of evolutionary state variables. These models can however induce some difficulties in integrating the constitutive differential equations. In this paper, various integration schemes are presented and discussed in relation with the implementation of state variable models into finite element codes.

RÉSUMÉ

Le comportement inélastique de roches tendres, comme le sel gemme et la potasse, dépend du temps et des effets de l'histoire mécanique. Afin de rendre compte de ces phénomènes complexes, divers modèles viscoplastiques relativement sophistiqués ont été proposés au cours des dernières années. Parmi ceux-ci, plusieurs utilisent des variables d'état évolutives. Ces modèles peuvent toutefois engendrer des difficultés pour l'intégration des équations différentielles constitutives. Dans cet article, l'auteur présente et discute divers algorithmes d'intégration numérique, en relation avec l'introduction des modèles avec variables d'état dans des codes d'éléments finis.

1 INTRODUCTION

For over thirty years, there has been a continued interest in the mechanical behavior of soft and rather ductile rocks, such as rocksalt and potash, in relation with the excavation of underground openings for mining activities, or for public works such as the storage of petroleum products and industrial wastes. The behavior of these rocks, which is mostly inelastic, largely depends on the mechanical history components, including the loading path, the strain and strain rate trajectories, and the elapsed time. In traditional models of elasticity and/or plasticity used in geomechanics, these effects are largely or entirely neglected. So-called creep laws based on empirical formulations are also generally inadequate for complex loading conditions, because they fail to consider properly the hereditary nature of the inelastic flow. Accordingly, more realistic and sophisticated models have been proposed in recent years. Many of these models are presented in the context of viscoplasticity proposed by Perzyna (1963) and extended for geomaterials by Zienkiewicz and Cormeau (1974). Going one step further, others have used unified inelastic models with evolutionary state variables, which can be considered as extensions of the classical theories of plasticity for mixed hardening materials, and which are very attractive for their strong physical basis.

When designing underground excavations in these soft rocks, the complexity is such that most mechanical calculations are carried out by computer codes, generally using the finite element method (FEM). This requires a numerical procedure to solve the differential equations of the constitutive model, i.e. the kinetic law, which expresses the stress-strain rate relationship, and the evolution laws which define hardening and/or softening through state variables. Unfortunately, many of the recently developed inelastic models can generate some difficulties in that respect.

In this paper, the author presents and discusses some of the integration schemes that can be used to solve this problem of great importance for the accuracy of the calculated solutions. It should be mentioned that only the local integration procedures are discussed here. The question of global equilibrium of the structure is not presented because of space limitations; the reader should consult specialized publications for that matter (e.g., Owen and Hinton, 1980; Zienkiewicz and Taylor, 1989).

2 INELASTIC MODELS WITH STATE VARIABLES

The success of mathematical modeling of a deformation process is highly dependent upon the accuracy with which the mechanical constitutive equations represent the flow behavior of the deforming material (Eggert and Dawson 1987). Accordingly, the development of mathematical models, which describe and predict the inelastic behavior of engineering materials is proceeding with an ever increasing momentum. An important factor to this impetus is the growing recognition of the serious limitations of the classical partioned approach of treating inelastic behavior as the linear summation of rate-independent (plastic)

and rate-dependent (creep) components. When the loading conditions are fairly uniform and the material remains within a small range of stress (or strain rate) and temperature during a process, such relatively simple material descriptions may be adequate, but they are not for complex loading cases. Apart from neglecting the known interaction between plasticity and creep, such models are inadequate because the viscous component is generally formulated from empirical creep laws using invalid hardening variables, such as time or equivalent (isotropic) strain, which cannot account for complex mechanical histories (Aubertin et al., 1992).

As an alternative, a state variable approach to the inelastic behavior of these rocks has been developed. The basic assumption embodied in the state variable models discussed here is the unified treatment of inelastic strain, i.e. no distinction is given to viscous (creep) and plastic straining. In addition, both elastic and inelastic strains are considered to be present when the yield condition is exceeded. One can then write, for the total strain rate tensor:

$$\tag{1}$$

where superscript e and i identify the elastic and inelastic components respectively. In unified models, the yield condition is usually expressed in the stress space. Some unified models however do not consider any yielding criteria so that there is no purely elastic domain; in this case, inelastic flow is assumed to occur at all non-zero values of stress, although at low stress the rate of inelastic flow may be negligible (Lush et al., 1989).

The expression unified is thus taken to mean that all aspects of inelastic behavior, such as plastic, creep and relaxation under transient and stationary flow conditions, are included in the kinetic law for $\dot{\epsilon}_{ij}^{i}$, and are consequently particular response characteristics for different loading histories (Chan et al., 1985).

Unified models have been initially developed for metals (see reviews by: Allen and Beek, 1985; Chaboche, 1989; Marchand and Moosbrugger, 1991), and extended more recently to other ductile crystalline materials, such as ice (Pohé and Bruhns, 1992) and rocksalt (Aubertin et al., 1992). These state variable models are phenomenological in nature, although in many cases, the evolutionary variables represent, in an average sense, specific conditions which exist at the microstructural level. In fact, these variables should together contain the relevant effects of the mechanical history. With unified models, it is considered that the present state of the material depends only on the present values of the observable (external) variables and of a set of suitably chosen state (internal or hidden) variables which represent the effect of the mechanical history, so that the inelastic strain rate tensor $\dot{\epsilon}_{ij}^{i}$ is always delivered in an explicit fashion (Chandra and Mukherjee, 1984; Chaboche, 1989). Such models have been known to extend the range of validity of material description beyond that of simpler relationships (Eggert and Dawson, 1987).

According to the unified approach, the inelastic constitutive model is composed of a kinetic law, describing the flow at constant structure, and of a series of evolution laws for each state variables. One can then write for the inelastic strain rate tensor (Aubertin et al., 1991a):

$$\dot{\epsilon}_{ij}^{i} = \dot{\epsilon}_{ij}^{i} \left[\sigma_{ij}, \ T, \ Y_{ij,k} \right] \tag{2}$$

$$\dot{Y}_{ij,k} = \dot{Y}_{ij,k} \left[\sigma_{ij}, \ T, \ Y_{ij,k} \right] \tag{3}$$

with $k = 1, 2, 3, \ldots n,$

where σ_{ij} is the stress tensor, T is the temperature and $Y_{ij,k}$ is a set of n evolutionary state variables, together representing the modification of the structural state of the material through local averages of dislocation density and arrangements, and of continuum damage. As such, the state variables are usually represented by scalars (Y), vectors (Y_i) or second-order tensors (Y_{ij}).

3 NUMERICAL IMPLEMENTATION

3.1 Local integration

When using a FE code for structural analysis, the resolution of non-linear algebric systems requires linear iterations at the structural (global) level for equilibrium equations, and the numerical integration of the constitutive equations at the local level (Boulon et al., 1991). For rate-dependent problems with a state variable model, the critical aspect of the local solution of constitutive equations is more acute because it requires the additional computational effort of integrating the evolution equations for these variables. Methods for the numerical solution of such systems of first-order ordinary differential equations, which form an initial value problem, have received much attention in recent years. Various methods (also called algorithms or schemes) provide rules for the computation of an approximation of the relevant variables at the time-step t_{n+1} ($= t_n + \Delta t_n$) in terms of the solution at time t_n, and of earlier steps in some cases (e.g., Hugues and Taylor, 1978; Argyris et al., 1978; Kumar et al., 1980; Owen and Hinton, 1980; Chandra and Mukherjee, 1984, Haisler and Imbrie, 1985; Hornberger et al., 1987; Chaboche, 1987; Chang et al., 1988; Zienkiewicz and Taylor, 1989; Lush et al. 1989).

3.2 Stiff equations

It has long been known that, when integrated, the differential equations of unified models have stiff regimes that present some numerical difficulties in time-dependent analysis (Boyle and Spence, 1983; Cordts and Kollman, 1985; Chang et al., 1985). A characteristic of

mathematically stiff equations is that ordinary numerical schemes of integrating such equations can be inefficient and produce uncontrolled errors that can result in untrustworthy results and/or non-convergence of the FE solution.

The stiffness of the equations originates from the non-linear relationships of the kinetic law and of the evolution laws. It is a well known phenomenon in numerical methods when one has to deal with a system of two or more first-order (or higher-order) equations, and which arises in any problem in which the dependent variables (here $\dot{\epsilon}_{ij}^{i}$ and $Y_{ij,k}$) can be expressed in terms of more than one very different scales in the independent variables (Derrick and Grossman, 1987). In this case, the numerical method can produce solutions that rapidly deviates from the exact solution, as each step can introduce an ever increasing error. For FE structural analysis, stiff behavior usually occurs with the onset of a significant amount of inelastic strains. A more formal discussion on stiffness of a set of differential equations has been presented by Hugues and Taylor (1978).

The accurate integration of these stiff equations can be accomplished by various means, including the use of very small time steps and of high-order or multi-point integration schemes, as discuss in the following.

3.3 Numerical schemes

The local time integration of the highly non-linear differential equations of inelastic flow is essentially done through a linearization procedure, and by using the elastic solution on a step-by-step basis. Usually, the elastic solution is used at zero time to obtain the initial values of stresses, strains and displacements (Chandra and Mukherjee, 1984).

The time integration scheme can be described as follow for the popular rate approach of discretization (Chaboche, 1987). From the knowledge of stresses, state variables and temperature at time t_n, one computes the inelastic strain rates, the displacement rates (from the stiffness matrix) and, from the total and elastic strain rates, the stress rate at time t_n. Then, the unknown at time t_{n+1} are obtained with an appropriate scheme. For instance, if one uses the well-known explicit Euler's scheme, one can write:

$$(\epsilon_{ij}^{i})_{n+1} = (\epsilon_{ij}^{i})_n + \Delta t_n \, (\dot{\epsilon}_{ij}^{i})_n \tag{4}$$

Similar equations can also be written for each state variables at time t_{n+1}, considering the value of its time derivative at time t_n; the same can also be said for the calculation of displacements and stresses.

Instead of the rate approach, one can choose an integrated discretization approach, where the rate equations are replaced by their incremental form (Chaboche, 1987). In this case, the following procedure can be implemented. From the knowledge of the inelastic strain and

temperature at time t_n, one can evaluate the inelastic strain increments, the incremental elasticity matrix and the displacements at time t_n, which allow the determination of the stresses at the same instant. Then, the values of the inelastic strain rate and of the state variables time derivatives are obtained at time t_n. The unknowns at time t_{n+1} can now be defined by the same first-order scheme used in the rate approach (equation 4). The advantage of the integrated procedure is that there is no need for the incrementation of the stresses and displacements. It is thus often preferred in FE calculations with state variable models (Chaboche, 1987).

Instead of the simple Euler method, more sophisticated integration schemes can be used for the determination of the required unknowns ϵ_{ij}^i and $Y_{ij,k}$; in the following, the simple canonic form is used:

$$X_n = \left\{ \dot{\epsilon}_{ij}^i \, , \, Y_{ij,k} \right\}_n \tag{5}$$

$$\dot{X}_n = \dot{X} \, [t_n \, , \, X_n] \tag{6}$$

$$X_{n+1} = X_n + \Delta X_n \tag{7}$$

$$\Delta X_n = \int_{t_n}^{t_{n+1}} \dot{X} \, dt = \int_{X_n}^{X_{n+1}} dX \tag{8}$$

where X represents the variables necessary for the solution of the problem by the integrated approach.

The time integration procedures for defining X_{n+1}, presented in the following, are used to solve ordinary differential equations of the form of equations 5 to 8. Table 1 presents the usual approximation formula for some of the best known integration methods; other methods have also been reported in the above mentioned references. The methods in Table 1 can be divided into explicit and implicit procedures.

3.3.1 Explicit schemes: With these schemes, the solution at time t_{n+1} is completely determined from conditions existing at time t_n, or earlier. They include:

a) The first-order (forward) Euler: It is by far the simplest, easiest to implement, and best known of all schemes, and it has been used frequently to compute rate-dependent problems under various conditions (e.g., Zienkiewicz and Cormeau, 1974; Aubertin et al., 1991b). When the forward Euler scheme is used for solving stiff equations, small

step size must be used in order to obtain accuracy. The size of the time-step is restricted by numerical stability requirements (e.g., numerical examples given by Boyle and Spence, 1983, and by Derrick and Grossman, 1987), which may lead to a very large number of solution increments in FE analysis (Lush et al., 1989). As a rule of thumb, it seems that the Euler scheme remains stable when the size of the strain increment is kept below 10^{-4} for various state variable models (Chan et al., 1985).

b) The modified Euler: This scheme also called Euler-Cauchy, is considered explicit because only one evaluation is made for X_{n+1}, contrary to implicit schemes presented in the following section. It is considered more stable than the Euler (and the second-order Euler presented next), but it does not allow the prediction of the associated time-step as discussed later.

c) The second-order Euler: This scheme necessitate the evaluation of $\delta\dot{X}/\delta X$, which implies the solution of the first-order equation relating the stiffness matrix and displacement rates to the external and internal forces.

d) The Runge-Kutta (fourth-order, with Simpson's rule): This is also a very well known numerical scheme (e.g., Dhatt and Touzot 1981; Derrick and Grossman, 1987; Zienkiewicz and Taylor, 1989). It has been considered by some to have the more desirable properties (Boyle and Spence, 1983). It implies the calculation of X at various intervals of the time-step Δt_n. Although offering good stability and convergence, it can be costly because it requires multiple evaluations of the constitutive law for each time-step (Meric and Cailletaud, 1991).

e) The Adams-Bashforth (mth-order): Here, the solution is obtained from that of the previous m increments. Only one evaluation of X is necessary for each time step, contrary to the Runge-Kutta scheme (Merric and Cailletaud, 1991). The β_i coefficients are defined from the proper expansion terms. When m equals 2, it reduces to the two-step Adams method (e.g., Kumar et al., 1980).

3.3.2 Implicit (and semi-implicit) schemes: These schemes include all the other methods presented in Table 1. They all imply the evaluation of the unknown rate parameter $\dot{X}$ at the end of each time step. This requires an iterative procedure such as the substitution method the Newton-Raphson method, the (Broyden-Fletcher-Goldfarb-Shanno) BFGS method, or the (Daviden-Fletcher-Powell) DFP method (Owen and Hinton, 1980; Dhatt and Touzot, 1981; Zienkiewicz and Taylor 1989). With an FE code, the Newton-Raphson method often seems to be more efficient for most 2D problems (<600 elements), while the BFGS technique becomes more efficient for true 3D meshes, especially for high number of load increments (Aazizou, 1990). One should be reminded here that the Newton-Raphson procedure can become inconvenient because the Jacobian (stiffness) matrix has to be formed

and solved for each time step. This can be particularly difficult for non-associated flow rules where the matrix can become non-symmetric.

The implicit schemes include:

a) The θ-method: This is probably the most popular of the implicit methods (Owen and Hinton, 1980; Zienkiewicz and Taylor, 1989; Sham and Chow, 1989) and it has often been used with viscoplastic models for geomaterials (e.g., Desai and Zhang, 1987; Rizkalla and Mitri, 1991). Also known as the α-method by some authors (where $\alpha = 1-\theta$; e.g., Lemaitre and Chaboche, 1988) or as the generalized mid-point rule (Hornberger et al., 1987), the θ-method reduces to the explicit first-order Euler scheme when $\theta = 0$, and to the fully implicit Euler backward rule when $\theta = 1$; when $\theta = 0.5$, it becomes an implicit trapezoidal scheme (also known as the Crank-Nicholson scheme for linear equations). The θ-method is unconditionally stable for $\theta \geq 0.5$, so that there is no imposed limitations on the time step size. A θ value of 0.5 usually gives the minimum CPU time, and it is often considered the optimum choice for most loading cases (Hornberger et al., 1987; Desai and Zhang, 1987; Meric and Cailletaud, 1991).

b) The Adams-Moulton method (order m + 1): With this scheme, the solution is defined from the known (past) values of $\dot{X}$ and by its value at time t_{n+1}. As with the Adams-Bashforth method, the coefficient γ_i are defined from the proper series expansion.

c) The predictor-corrector methods: Here, the predictor (often taken of order 1) and the corrector can be of different order.   The iterations on the corrector stop when convergence is attained or when a preset number is reached.

Before going further, it should be mentioned here that many implicit algorithms can be rendered explicit by approximating the unknown quantities at the end of the time steps in terms of those at the beginning using a truncated series (Sham et Chow, 1989). For instance, the implicit trapezoidal method can become explicit by using a Taylor series expansion, so that:

$$\dot{X}_{n+1} = \dot{X}_n + \Delta t_n \left(\frac{\delta \dot{X}}{\delta t} \right)_n \tag{9}$$

3.3.3 Step linkage: The various integration schemes presented in Table 1 could also be divided into independent step methods and linked step methods (Meric and Cailletaud, 1991). In the former group, which comprises the three Euler explicit schemes, the Runge-Kutta method and the θ-method, the X value at time t_{n+1} is calculated from the value obtained at time t_n, independently of the values obtained at t_{n-1} or earlier. In the latter group, which includes the two Adams methods and the predictor-corrector methods, one considers for each time step the solutions previously obtained. Although the linked step methods are very

efficient to integrate constitutive laws, the need for keeping the results obtained at previous time increments can become cumbersome for big problems with such schemes.

3.4 Time-stepping control

In order to follow with an acceptable accuracy the solution of the highly non-linear differential equations of unified inelastic models, it is common to add a time-step control procedure to the integration scheme (Chaboche, 1987; Sham and Chow, 1989). In fact, it could be said that the efficiency of an integration method largely depends on the time-step control strategy (Hornberger et al., 1987). The size of the time-step Δt depends on the non-linearity, so that Δt can be very large when the solution is nearly linear (such as when a stationary condition is approached), but it must be reduced when non-linearity is pronounced.

Several kinds of control can be defined, depending on the number of comparative terms used in the series expansion of the solution of the X variables (Chandra and Mukherjee, 1984). Usually, time-step control is based on comparison of a suitably defined (calculated) error er with prescribed error limits er_{min} and er_{max}. If tolerance is violated, the time-step must be reduced and the solution repeated. As an example, let us consider the Taylor expansion of the inelastic strain at time t_{n+1} (Chaboche, 1987):

$$(\epsilon_{ij}^i)_{n+1} = (\epsilon_{ij}^i)_n + \Delta t_n \, (\dot{\epsilon}_{ij}^i)_n + 0.5 \, (\ddot{\epsilon}_{ij}^i)_n \, \Delta t_n^2 + (\dddot{\epsilon}_{ij}^i)_n \, \Delta t_n^3/6 \qquad (10)$$

One of the most popular time-step control method is the comparison of the truncation error and the present solution (Kumar et al., 1980). Here, the truncation error is approximated by the term in the Taylor's expansion just above the term used in the actual incrementation. For instance, when calculating $(\epsilon_{ij}^i)_{n+1}$, the first-order Euler forward scheme introduces the following error:

$$er \simeq 0.5 \mid \ddot{\epsilon}_{ij}^i \mid_n \Delta t_n^2 \qquad (11)$$

The time-step can then be defined by comparison to a previously defined expected relative error, such as:

$$er < \eta \, J_{2I} \qquad (12)$$

with: $\qquad J_{2I}$: second invariant of the inelastic strain tensor.

$$J_{2I} = \left[\frac{2}{3} \, (\epsilon_{ij}^i)_n \, (\epsilon_{ij}^i)_n \right]^{1/2} \qquad (13)$$

This leads to:

$$\Delta t_n = \left[\frac{2 \ \eta \ J_{2I}}{|\ddot{\epsilon}_{ij}^i \ |_n} \right]^{1/2} \tag{14}$$

At the beginning of the inelastic flow, the use of equation 14 can give rise to extremely small time-steps; in this case, the relative error is often evaluated by using the total strain instead, as initially proposed by Zienkiewicz and Cormeau (1974):

$$\Delta t_n < \left[\frac{2\eta \ J_{2D}}{|\ddot{\epsilon}_{ij}^i|_n} \right]^{1/2} \tag{15}$$

where J_{2D} is the second invariant of the total strain tensor. However, because it presents some degree of arbitrariness and numerical difficulties in non-monotonous loading, the use of total strain can be a problem. In order to overcome these difficulties, one can use a time-step control based on the comparison between truncation error and the present increment (Chaboche, 1987). With the Euler scheme, one can then write:

$$0.5 \ (\ddot{\epsilon}_{ij}^i)_n \ \Delta t_n^2 < \eta \ (\Delta \epsilon_{ij}^i)_n = \eta \ (\dot{\epsilon}_{ij}^i)_n \ \Delta t_n \tag{16}$$

which leads to:

$$\Delta t_n < 2\eta \ \left| \frac{\dot{\epsilon}_{ij}^i}{\ddot{\epsilon}_{ij}^i} \right|_n \tag{17}$$

Another alternative to time-marching control is the use of the second invariant of the strain tensor and of the strain rate mode:

$$\Delta t_n < \eta \ \frac{J_{2D}}{|\dot{\epsilon}_{ij}^i|_n} \tag{18}$$

The value of η must then be defined; a value of 0.01 is often considered to be an optimal choice.

When approaching stationary conditions, one should consider increasing the time step; this could be done by using the following:

$$\Delta t_{n+1} = \propto \Delta t_n \tag{19}$$

with $\alpha \geq 1$; an α value of 1.2 is often used (Desai and Zhang, 1987; Aubertin et al., 1991b), although values of 1.5 to 2 have also been proposed (Owen and Hinton 1980; Boyle and

Spence 1983; Chaboche, 1987). If the solution becomes more non-linear, deviating from stationary conditions, the above procedure must be used with $\alpha < 1$, in order to reduce the time step.

The final choosen time-step is the minimum of all the possible Δt_n, with the following limitations:

$$\Delta t_{min} < \Delta t_n < \Delta t_{max} \qquad (20)$$

where Δt_{min} and Δt_{max} are fixed by the user.

For each iteration, there is also a solution with a global calculation at time t_{n+1}. A condition for iteration to stop must be implemented for each point of the structure; for instance, one can use (Lemaitre and Chaboche 1988):

$$|X_{n+1} - X_n| \le \mu |X_n| \qquad (21)$$

A value of $\mu = 0.01$ seems to offer a good cost-precision compromise. It should be noted however that with subincrementing techniques, the local time-step chosen to integrate the constitutive equations at the material point can be different from the global time-step choosen for the solution of the structural (global) equilibrium equations (Chang et al., 1988).

4 DISCUSSION

Because various constitutive models may behave very differently using the same integration scheme, it seems that there are yet no general rules for selecting an integration algorithm, as its efficiency and accuracy largely depend on the problem being solved (Haisler and Imbrie, 1985; Hornberger et al., 1987).

Implicit algorithms are iterative in nature and are often unconditionally stable, thus allowing large time steps to be employed. On the other hand, iterative steps are not necessary in explicit methods, which are usually easier to implement; however, they are often only conditionally stable.

In the past, many have discarded one-step time integration methods, such as the explicit forward Euler scheme, due to potential numerical instabilities (e.g., Boyle and Spence 1983; Cordts and Kollman, 1985). This conclusion however has recently been questioned by some authors (Chang et al., 1985, 1988; Haisler and Imbrie, 1985). In fact, many have found that, for various inelastic models, low-order explicit schemes used in conjunction with a subincrementation strategy with adaptive (or automatic) time-stepping and an error check, can be very effective and accurate. For FE analysis, they can then become very advantageous when compared to higher-order explicit schemes (such as the Runge-Kutta

methods; e.g., Kumar et al., 1980), or even to implicit schemes (e.g., Chandra and Mukherjee, 1984; Sham and Chow, 1989; Meric and Cailletaud, 1991). For instance, it has often been observed that although the number of time-steps is larger with low-order explicit schemes, the CPU time for each step is much more important (up to 5 times more) with more sophisticated implicit schemes. This is due to the evaluation and reduction of the (tangent) stiffness matrix at each time-step and to the iteration associated to implicit schemes. Also, it has been noted that the use of smaller time step in low-order explicit schemes does not influence that much the computation time for integrating the constitutive equations (Haisler and Imbrie, 1985).

Among the non-explicit schemes, the semi-implicit integration techniques appear to be more precise for small time increments, and very efficient when associated with a substepping technique in 2D problems and in small 3D problems. On the other hand, fully implicit methods seem to give the best results for 3D problems and in the case of large increments, when a consistent stiffness matrix is used on the global level (Aazizou et al., 1991). In theses cases however, the choice of an appropriate iteration method is also very important.

5 CONCLUSION

In this article, various numerical integration schemes have been presented and discussed in relation with the solution of viscoplastic problems encountered when dealing with soft and rather ductile rocks, such as rocksalt and potash. It is first established that one should use evolutionary state variable models to describe these materials, so that rate and hereditary effects can be properly considered. Because such models have mathematically stiff equations, they require an efficient integration method. At the present time, it is difficult to give precise quantitative rules for selecting the most appropriate scheme. Nevertheless, from the discussion presented, it is inferred that simple low-order explicit schemes can be very advantageous when combined to a carefully controlled time-stepping strategy.

ACKNOWLEDGEMENTS

REFERENCES

Aazizou, K. 1990. Calcul par éléments finis en plasticité et viscoplasticité. Thèse, Docteur en Sciences et Génie des Matériaux. Ecole Nationale Supérieure des Mines de Paris, 161 pages.

Aazizou, K., Burlet, H. and Cailletaud, G. 1991. Comparison of various plasticity/viscoplasticity models. Constitutive Laws for Engineering Materials, (Proc. 3rd Int. Conf.), Desai, C.S. et al. (editors), ASME Press, 651-654.

Allen, D.H. and Beek, J.M. 1985. On the use of internal state variables in thermoviscoplastic constitutive equations, Nonlinear Constitutive Relations for High Temperature Application, NASA, 83-101.

Argyris, J.H., Vaz, L.E. and William, K.J. 1978. Improved solution methods for inelastic rate processes. Computer Methods in Applied Mechanics and Engineering, 16, 231-277.

Aubertin, M., Gill, D.E. and Ladanyi, B. 1991a. A unified viscoplastic model for the inelastic flow of alkali halides. Mechanics of Materials, 11, 63-82.

Aubertin, M. Gill, D.E. and Ladanyi, B. 1991b. SUVIC: A unified model for the inelastic flow of crystalline materials including soft rocks and ceramics. Computational Methods and Experimental Measurements V. Elsevier Applied Sci., 705-716.

Aubertin, M., Gill, D.E. and Ladanyi, B. 1992. Modeling the transient inelastic flow of rocksalt. Proc. Seventh Symp. on Salt, (Kyoto), Elsevier Science Pub., 1, 93-104.

Boulon, M., Darve, F., Gamali, H.E. and Touret, J.P. 1991. Use of incrementally non linear constitutive equations by the finite element method. Computer Methods and Advances in Geomechanics, Beer, Booker & Carter (eds.), Balkema, 581-586.

Boyle, J.T. and Spence J. 1983. Stress Analysis for Creep. Butterworths, London.

Chaboche, J.L. 1987. A review of computational methods for cyclic plasticity and viscoplasticity, Computational Plasticity - Models, Software and Applications, Pineridge Press, II, 379-411.

Chaboche, J.L. 1989. Constitutive equations for cyclic plasticity and cyclic viscoplasticity, Int. J. Plasticity, 5, 247-302.

Chan, K.S., Bodner, S.R., Walker, K.P. and Lindholm, U.S. 1985. A survey of unified constitutive theories. Nonlinear Constitutive Relations for High Temperature Applications, NASA, 1-23.

Chandra, A. and Mukherjee, S. 1984. A finite element analysis of metal forming processes with thermomechanical coupling, Int. J. Mech. Sci., 26, 661-676.

Chang, T.Y., Chang, J.P. and Thompson, R.L. 1985. On numerical integration and computer implementation of viscoplastic models. Nonlinear Constitutive Relations for High Temperature Application, NASA, 187-200.

Chang, T.Y., Chen, J.Y. and Chu, S.C. 1988. Viscoplasticity finite element analysis by automatic subincremending technique. J. Engng Mech., ASCE, 114(1), 76-80.

Cordts, D. and Kollman, F.G. 1985. A new implicit time integration scheme for inelastic constitutive equations with internal state variables. Proc. NUMETA'85 Conf., A.A. Balkema, 1, 411-416.

Derrick, W.R. and Grossman, S.I. 1987. Numerical Methods, A First Course in Differential Equations with Applications, Third Edition, West Publishing Co. (St-Paul).

Desai, C.S. and Zhang, D. 1987. Viscoplastic model for geologic materials with generalized flow rule. Int. J. Num. and Anal. Meth. in Geomech., 11, 603-620.

Dhatt, G. and Touzot, G. 1981. Une présentation de la méthode des éléments finis. Maloine S.A. Editeur.

Eggert, G.M. and Dawson, P.R. 1987. On the use of internal variable constitutive equations in transient forming processes, Int. J. Mech. Sci., 19(2), 95-113.

Haisler, W.E. and Imbrie, P.K. 1985. Numerical considerations in the development and implementation of constitutive models. Nonlinear Constitutive Relations for High Temperature Application, NASA, 169-185.

Hornberger, K., Stamm, H. Arya, V.K. and Huber, W. 1987. Numerical integration and implementation of viscoplastic models into finite element codes. Computational Plasticity - Models, Software and Applications, Pineridge Press, I, 477-490.

Hughes, T.R.J. and Taylor, R.L. 1978. Unconditionally stable algorithm for quasi-static elasto-viscoplastic finite element analysis. Computer and Structures, 8, 109-173.

Kumar, V. Morjaria, M. and Mukherjee, S. 1980. Numerical integration of some stiff constitutive models of inelastic deformation. J. Engng. Materials and Technology ASME, 102 (Jan. '80), 92-96.

Lemaitre, J. and Chaboche, J.L. 1988. Mécanique des Matériaux Solides, 2nd ed., Dunod-Bordas.

Lush, A.M., Weber, G. and Anand, L. 1989. An implicit time-integration procedure for a set of internal variable constitutive equations for isotropic elasto-viscoplasticity. Int. J. of Plasticity, 5, 521-549.

Marchand, N.J. and Moosbrugger, J.C. 1991. Non-linear structural modeling for life predictions: physical mechanics and continuum theories. Int. J. Pres. Ves. & Piping, 47, 79-112.

Meric, L. and Cailletaud, G. 1991. Intégration de lois de comportement en viscoplasticité. Conf. on New Advances in Computational Structural Mechanics (Preprints).

Owen, D.R.J. and Hinton, E. 1980. Finite Elements in Plasticity: Theory and Practice. Pineridge Press Ltd..

Perzyna, P. 1963. The constitutive equations for rate sensitive plastic materials. Quat. Appl. Math., 20(4), 320-332.

Pohé, J. and Bruhns, O.T. 1992. On a constitutive law for polycrystalline ice based on the concept of internal variables. IAHR Ice Symp., 49-60.

Rizkalla, M. amd Mitri, H.S. 1991. An elasto-viscoplasticity model for stress analysis of mining excavations. Rock Mechanics as a Multidisciplinary Science, Roegiers (eds), Balkema, 597-606.

Sham, T.L. and Chow, H.W. 1989. A finite element method for an incremental viscoplasticity theory based on overstress. Eur. J. Mech., A/Solids, 8(6), 415-436.

Zienkiewicz, O.C. and Cormeau, I.C. 1974. Viscoplasticity, plasticity and creep in elastic solids - a unified numerical solution approach. Int. J. for Num. Meth. in Engng, 8, 821-845.

Zienkiewicz, O.C. and Taylor, R.L. 1989. The Finite Element Method, Fourth Edition, Vol. 2 Solid and Fluid Mechanics Dynamics and Non-Linearity, McGraw-Hill Book Company.

Table 1 - Integration methods for time-dependent models

(with $\dot{X} = \dot{X}[X, t]$ and $X_n = X$ at t_n)

Methods	Equations	References
<u>Explicit schemes:</u>		
First-order Euler	$X_{n+1} = X_n + \Delta t_n \, \dot{X}_n$ with $\dot{X}_n = \dot{X}$ for (t_n, X_n)	Zienkiewicz & Cormeau (1974)
Modified Euler	$X_{n+1} = X_n + 0.5\Delta t_n \, [\dot{X} + \dot{X}_{n+1}]$ with $\dot{X}_{n+1} = \dot{X}$ for $(t_{n+1}, X_{n+1};$ *first estimate)*	Chan et al.(1985) Chaboche (1987)
Second-order Euler	$X_{n+1} = X_n + \Delta t_n \, \dot{X}_n + 0.5 \, \Delta t_n^2 \, \ddot{X}_n$ with $\ddot{X}_n = \left(\dfrac{\delta \dot{X}}{\delta t}\right)_n + \left(\dfrac{\delta \dot{X}}{\delta X}\right)_n \dot{X}_n$	Chaboche (1987) Meric & Cailletaud (1991)
Adams-Bashforth	$X_{n+1} = X_n + \Delta t_n \displaystyle\sum_{i=1}^{m} \beta_i \, \dot{X}_{n+1-i}$ with β_i : *coefficients of the serie expansion*	Kumar et al. (1980) Meric & Cailletaud (1991)
Runge-Kunta (Fourth-order)	$X_{n+1} = X_n + 1/6 \, (m_1 + 2m_2 + 2m_3 + m_4)$ with $\quad m_1 = \Delta t_n \dot{X}_n$ $\quad m_2 = \Delta t_n \, \dot{X}_{n1}$ $\quad m_3 = \Delta t_n \, \dot{X}_{n2}$ $\quad m_4 = \Delta t_n \, \dot{X}_{n3}$ where $\dot{X}_{n1} = \dot{X}$ for $(t_n + 0.5\Delta t_n, \; X_n + 0.5m_1)$ $\quad \dot{X}_{n2} = \dot{X}$ for $(t_n + 0.5\Delta t_n, \; X_n + 0.5m_2)$ $\quad \dot{X}_{n3} = \dot{X}$ for $(t_n + \Delta t_n, \; X_n + m_3)$	Dhatt & Touzot (1981) Boyle & Spence (1983) Derrick & Grossman (1987)

Table 1 - Integration methods for time-dependent models (continued)

(with $\dot{X} = \dot{X}[X, t]$ and $X_n = X$ at t_n)

Methods	Equations	References
Implicit schemes:		
θ-method	$X_{n+1} = X_n + \Delta t_n[(1-\theta)\dot{X}_n + \theta\dot{X}_{n+1}]$ *with* $0 \le \theta \le 1$	Chang et al. (1985) Sham & Chow (1989)
Adams-Moulton	$X_{n+1} = X_n + \Delta t_n \sum_{i=1}^{m} \gamma_i \dot{X}_{n+1-i} + \Delta t_n \gamma_m \dot{X}_{n+1}$ *with* γ_i : *coefficients of the serie expansion*	Meric & Cailletaud (1991)
Predictor-Corrector	*Predictor:* $X_{n+1,o} = \sum_{i=1}^{m} \alpha_i X_{n+1-i} + \beta_i \Delta t_n \dot{X}_{n+1-i}$ *Corrector:* $X_{n+1,y+1} = \sum_{i=1}^{m} (\nu_i X_{n+1-i} + \gamma_i \Delta t_n \dot{X}_{n+1-i})$ $+ \gamma_m \Delta t_n \dot{X}_{ny}$ *where* $\dot{X}_{ny}$ = $\dot{X}$ *for* $(t_{n+1}, X_{n+1,y})$ $\nu_i, \gamma_i, \beta_i, \alpha_i$ = *coefficients of the serie expansion* m = *order* y = *number of iterations* $(y > 1)$	Kumar et al. (1980), Chan et al. (1985) Meric & Cailletaud (1991)

A semi-analytical technique to study deformations of a viscoplastic seam caused by a moving longwall face

P.A. Nawrocki
University of Waterloo, Waterloo, Ontario N2L 3G1

ABSTRACT

A semi-analytical method of calculating stresses within elasto-viscoplastic seam of a
Bingham type is considered. The problem analyzed is a moving boundary one, with
boundary and compatibility conditions formulated on the moving boundaries. The changes
in stress and deformation in the seam due to change of the opening span are analyzed.
Then, the size of the viscoplastic zone near the opening and its evolution with time are
determined. For the computational part of the solution, the finite difference method is
adopted. Discretization is performed with respect to the time variable. The analytical
formulae defining stresses and strains within the seam for an arbitrary time instant $i\Delta t$
(i=1,2,...) are presented. Several different longwall velocity functions are considered. The
influence of the seam extraction rate on the stability of the seam is discussed.

RÉSUMÉ

Nous considérons une nouvelle méthode semi-analytique pour calculer les contraintes dans
une couche minière. Avant l'affaiblissement, nous supposons une comportement linéaire
et élastique; après, nous utilisons une rhéologie selon la loi viscoplastique de Bingham.
Une méthode d'analyse statique est développée pour le cas où la frontière d'une chambre
d'exploitation se déplace continuellement, en utilisant une formulation basée sur la
compatabilité et les changements de contraintes et de déplacement. L'évolution temporelle
de la zone viscoplastique est résolue en utilisant la méthode des différences finies. Les
équations analytiques qui décrivent les contraintes et les déformations sont présentées,
avec quelques solutions typiques. L'importance de la vitesse d'excavation sur la stabilité
des chambres minières est présenté.

1 INTRODUCTION

Mine safety and productivity are influenced by the speed at which ore is extracted. For a longwall mining system this speed would correspond to the daily progress of the longwall face. If the rock has a significant component of viscous behaviour, one might suppose that the speed of extraction, combined with a viscous constitutive law could help determine safe values of extraction rate, which at the present time are based almost exclusively on empirical knowledge. Including viscous properties has an advantage in that a time factor is introduced into the model. On the other hand, solution times for problems of this class are longer than for elastoplastic models. One approach to improve the computational speed of time-dependent problems is to use a semi-analytical method, and such a method is presented in this paper.

This paper is concerned with the analysis of inelastic deformation of a seam caused by the progressive growth of the opening span adjacent to the seam. This may be viewed as the advance of a longwall face, and it is assumed that the face moves with a known velocity, and that stress redistribution develops as a result of this movement. A quasi-static analysis presented herein corresponds to the initial phase of longwall mining when the opening has been made and boundary conditions on both sides of the opening are symmetric. However, for advanced longwall exploitation symmetry does no longer exist and one face of the opening moves in the direction of the seam whereas stowing material appears on the other side. The changes in stress within the seam due to changes in the geometric configuration of the excavation are analyzed. Then, the size of the viscoplastic zone near the opening and its evolution with time are determined. Finally, it is emphasized that this analysis refers to horizontal or slightly inclined seams.

2 PROBLEM FORMULATION AND ASSUMPTIONS

Consider an elasto-viscoplastic seam with a single opening of width $2a$, as in Fig. 1. The seam is assumed to be compressed by a beam of rock roof of height H transferring its unsupported weight to the seam, thus inducing additional stresses. An overlying roof will be treated as an elastic beam undergoing shear deformation, neglecting inelastic deformation and cracking. It is further assumed that the seam rests on a rigid foundation, so that elastic and plastic deformations beneath the seam may be neglected. The seam material is considered as an elasto-viscoplastic homogeneous and isotropic material of the Bingham type. Its static force-displacement relation in uniaxial compression is assumed to be that shown in Fig. 2 by the solid line (Bieniawski et al., 1969, Crouch and Fairhurst, 1973). The material shows linear elastic behaviour up to the stress level p_m, whereupon viscous effects come into play and a different force-displacement curve is obtained for each displacement or stress rate. A simplified material response will thus be characterized by an elastic stiffness modulus E, a viscosity parameter μ, and maximum and residual strengths p_m and p_r. Making use of fundamental relations for internal forces and denoting
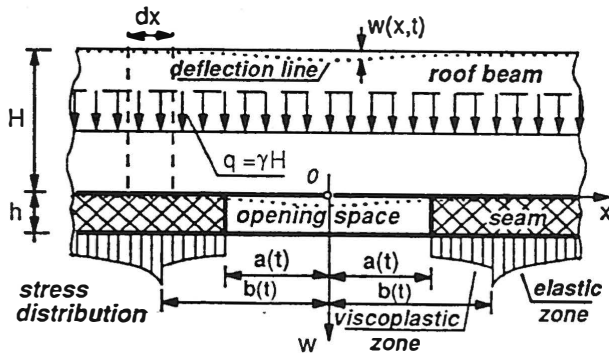
Fig.1 General view of seam geometry.
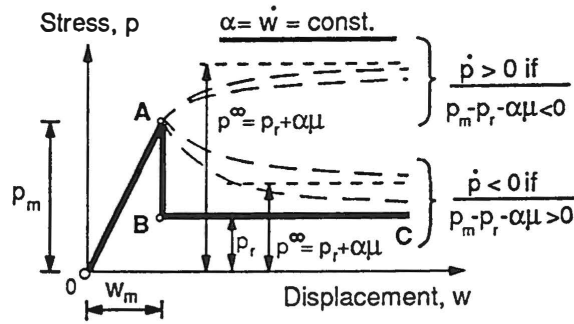
Fig.2 Idealized compression curve and theoretical curves for different stress rates

by $w(x,t)$ the vertical deflection of the roof beam (or the seam), its equation is expressed in the form

$$w'' = d^2w/dx^2 = [p(x)-q]/G \tag{1}$$

where G is the shear modulus of a roof beam; $q=\gamma H$ denotes the specific gravity loading per unit beam length; $p(x)$ is the interaction pressure between the beam and the seam (acting upward), and x is the position along the seam, as shown in Fig.1. Here w'' denotes the curvature of the roof beam. Eqn.(1) is valid within the seam, that is for $x>a$. For the opening space $p(x)=0$ should be assumed. For the specific problem of an elasto--viscoplastic seam Eqn.(1) may be rewritten as

$$
\begin{array}{llll}
Gw''(x,t) = -q & for & 0 \leq x \leq a(t) & (opening) \\
Gw''(x,t) = -q +p(x,t) & for & a(t) \leq x \leq b(t) & (viscoplastic\ zone) \\
Gw''(x,t) = -q +p(x) & for & x \geq b(t) & (elastic\ zone)
\end{array} \tag{2}
$$

The general rate equation of the Bingham model can be presented as $\dot{w}=\dot{w}^e+\dot{w}^{vp}$, where $\dot{w}^e$ and $\dot{w}^{vp}$ denote the elastic and viscoplastic displacement rate respectively. In the elastic regime $(p\leq p_m)$ we have $\dot{w}^{vp}=0$ and the force-displacement response is simply defined by Hooke's law $\dot{w}^e=\dot{p}/E$. However, in the post-peak regime viscous effects come into play and the corresponding constitutive equation is

$$\dot{w} = \dot{p}/E + (p-p_r)/\mu \qquad for \qquad p > p_m \tag{3}$$

For the zone of viscoplastic deformation, $a(t)\leq x\leq b(t)$, according to Eqn.(3), one has $p=p_r+\mu(\dot{w}-\dot{p}/E)$. Using this in (2.2) and replacing the time derivative of p by $G\dot{w}''(x,t)$, the following nonhomogeneous partial differential equation of the third order for the unknown deflection function $w(x,t)$ of the roof beam has been derived for the viscoplastic zone:

68

$$G\frac{\partial^2 w(x,t)}{\partial x^2} + \frac{G\mu}{E}\frac{\partial^3 w(x,t)}{\partial x^2 \partial t} - \mu\frac{\partial w(x,t)}{\partial t} = p_r - q \tag{4}$$

The method applied to solve this equation will now be presented.

3 CONTINUOUS MOTION OF THE LONGWALL FACE - GENERAL SOLUTION

A semi-analytical method has been applied to solve Eqn.(4). We assume that the solution of this equation is known at $t=t_{i-1}$, and the solution at the next time instant $t=t_i$ is then sought. This allows us to approximate the derivative of the unknown displacement function $w(x,t)$ as

$$\partial w(x,t)/\partial t \cong \Delta w/\Delta t = (w_i - w_{i-1})/\Delta t \tag{5}$$

where $\Delta t = t_i - t_{i-1}$, $w_i = w(x,t_i)$, and $w_{i-1} = w(x,t_{i-1})$. Substituting this approximation into Eqn.(4) and using the notation $c_o = (p_r - q)\Delta t/c$, $c_1 = \mu/c$, $c_2 = G\mu/(cE)$, where $c = G(\mu + E\Delta t)/E$, one can reduce Eqn.(4) to the following ordinary differential equation of the second order

$$w_i'' - \mu w_i/c = c_2 w_{i-1}'' - c_1 w_{i-1} + c_o \tag{6}$$

This equation is then solved at the arbitrary time instant, $t_i = i\Delta t$. Its right-hand side is nothing more than a given function of x, and the left-hand side is presented in terms of an unknown function w_i. Although the right-hand side of Eqn.(6) is expected to be known for every $(i-1)$, it is subject to change from one time step to another, and determining this is part of the solution.

Continuous movement of a longwall face with velocity v is equivalent to a continuous increase of the opening span $a(t)$. The growth of the opening span introduces additional stresses in the seam because of increase of the unsupported roof beam length. In the approach advocated in this paper a decomposition of these stress changes to their elastic and viscoplastic components is suggested. This means that for the numerical examples presented later in the paper, every smooth function $a(t)$ is replaced by its equivalent step function. Namely, for every time instant t_i the opening span is changed "instantaneously" by the value $\Delta a = v\Delta t$, producing a purely elastic response in the system. Next the opening span is assumed to remain unchanged during the time interval Δt, producing a viscoplastic stress redistribution within the seam. Because of space limit only the initial solution $w(x,t_i)$ of Eqn.(4) valid for $i=1$, that is for $t=t_1=\Delta t$ can be presented below to show the general approach applied in formulation of the semi-analytical solution of the problem. Details of derivation of the final closed-form solution of the seam deformation problem valid at an arbitrary time instant $t=i\Delta t$, $i=1,2,...,$ can be found elsewhere (Nawrocki, 1993).

For $t=t_i=\Delta t$ the appropriate initial vertical displacement function $w_{i-1}=w(x,t_o)=w(x,0)$ of the seam after loading is (Mróz and Nawrocki, 1989):

$$w(x) = [sae^{s(a-x)} + 1]/E \tag{7}$$

According to this equation one has $w''_{i-1}=qsae^{s(a-x)}/G$, where $s=(E/G)^{1/2}$. Now the following simple form of Eqn.(4) to be solved at the first time instant $t=t_1=\Delta t$ can be written:

$$w'' - \mu w/c = D_o \tag{8}$$

where D_o denotes the constant, $D_o=d/c-q\mu/(cE)$. Note clearly that the general solution $w_i(x)$ of Eqn.(6) is the sum of two solutions: the complementary function $^1w_i(x)$ of the reduced equation, and the particular integral $^2w_i(x)$ of the given equation (6). Moreover, the form of the complementary function $^1w_i(x)$ will remain unchanged at each time instant $t_i=i\Delta t$. However, the form of the particular integral $^2w_i(x)$ is different for each time instant. For $t=t_1=\Delta t$ one has

$$.^1w_i(x) = C_1e^{rx} + C_2e^{-rx}, \qquad .^2w_1(x) = A_o = -D_o/r^2 \tag{9}$$

where $r=(\mu/c)^{1/2}$, and C_1, C_2 are integration constants. The following general equations for the displacement function $w(x)$ are valid in their respective regions (Mróz and Nawrocki, 1989):

$$
\begin{aligned}
w(x) &= -\frac{qx^2}{2G} + C, & 0 \le x \le a(t) & \qquad (opening) \\
w(x) &= C_1e^{rx} + C_2e^{-rx} + A_o, & a(t) \le x \le b(t) & \qquad (viscoplastic\ zone) \\
w(x) &= C_3e^{-sx} + q/E, & x \ge b(t) & \qquad (elastic\ zone)
\end{aligned}
\tag{10}
$$

The boundary and continuity conditions are formulated as follows:

$$
\begin{aligned}
[w] = [w'] = 0 & \qquad @ \quad x = a(t) \\
[w] = [w'] = 0, \quad w = w_m = p_m/E & \qquad @ \quad x = b(t)
\end{aligned}
\tag{11}
$$

Here w' denotes the slope of the roof beam and brackets denote the discontinuity of the enclosed quantity at the specified location. In view of conditions (11), the following formulae have been obtained for the integration constants at $t=t_1=\Delta t$

$$C=\frac{qa^2}{2G}+C_1e^{ra}+C_2e^{-ra}+A_o, \quad C_{1,2}=\frac{(w_m-A_o)r \mp s(p_m-q)/E}{2re^{rb}} \quad C_3=(p_m-q)e^{sb}/E \tag{12}$$

where $b=b(t_1)$ denotes the range of the relaxation zone after the time Δt. It is calculated as the root of the following nonlinear equation

$$C_2 r e^{-ra} - C_1 r e^{ra} - qa/G = 0 \tag{13}$$

In this way the problem of elasto-viscoplastic seam deformation has been solved for $t=\Delta t$. On the other hand, Eqns.(10) together with (12) specify initial conditions for the next time instant $t=t_2=2\Delta t$, and allow the analysis of deformation step by step.

Careful examination of the solutions derived for successive time instants $t_1=\Delta t$, $t_2=2\Delta t$, $t_3=3\Delta t$, ... allows prediction of the solution to the elasto-viscoplastic seam deformation problem at the arbitrary time instant $t_i=i\Delta t$. With the solution presented (Nawrocki, 1993) one can develop a numerical algorithm for calculating stresses and strains within the seam at the arbitrary time instant $t \in \langle t_o, t_f \rangle$, where usually $t_o=0$ and t_f is the final time during which the deformation is studied.

4 NUMERICAL EXAMPLES

The semi-analytical method outlined above has been verified by means of the test example of the elasto-viscoplastic seam with a specified final equilibrium position. We assume that the geometry of the system is fixed, and we also assume that the seam is loaded by the overburden load q_l defined in such a way that the opening span a of the system is its corresponding limiting elastic span, $a=a_l(q_l)$. Such the system remains in equilibrium and no stress redistribution due to the viscosity occurs. Let us now assume that an additional load Δq is applied to this system, whereas the opening span remains unchanged. An instantaneous elastic response of the system is observed and viscoplastic flow is triggered. The viscoplastic zone, $a(t) \leq x \leq b(t)$, of initial length (b_o-a), appears within the seam as the result of its purely elastic response to the applied extra load Δq. The length of this zone gradually increases and stabilizes due to stress redistribution within the seam. Viscoplastic flow stabilizes with stresses and strains asymptotically reaching their ultimate equilibrium values. The following values for the material parameters have been assumed for calculations: $p_m=0.1$MPa, $p_r=0.05$MPa, $q=0.036$MPa, $G=4.31*10^5$N/m, and $E=5.4*10^4$N/m^3. Five different values of the viscosity coefficient have been considered: $\mu_1=1*10^2$, $\mu_2=3*10^2$, $\mu_3=5*10^2$, $\mu_4=7*10^2$, and $\mu_5=1*10^3$ Nsec/m^2.

Numerical results are presented in Fig.3. It can be seen in Fig.3a that some time after the extra load Δq has been applied to the seam its deformation is stabilized to the level of final equilibrium. This time is relatively short for low values of the viscosity coefficient and grows as this coefficient increases. The stress p_a at $x=a$ gradually decreases to its residual value p_r, as shown in Fig.3b. The viscoplastic stress redistribution terminates when stresses reach their ultimate values equal to the residual strength of the seam, p_r. The deflection function is not presented in Fig.3. It is a smoth function along the seam.

According to the general approach outlined above, more complicated longwall velocity
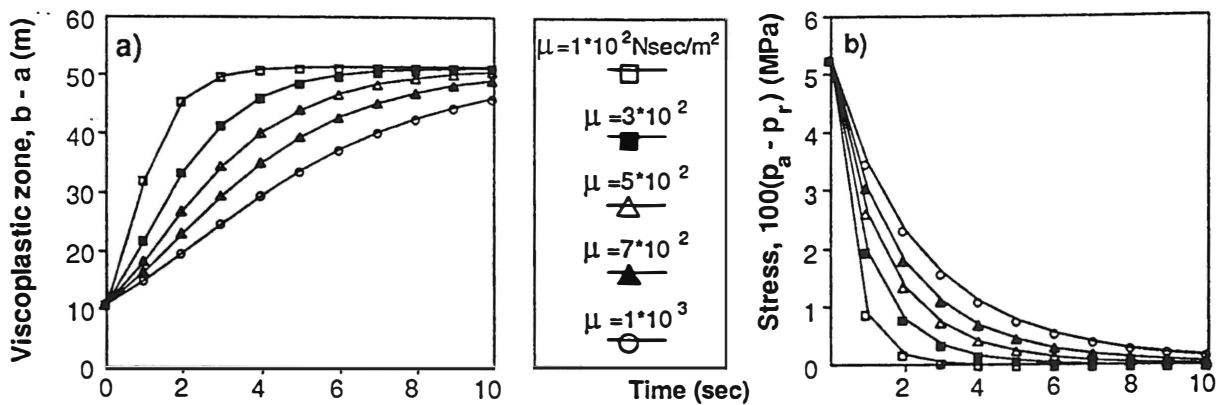
Fig.3. Test example: evolution with time of a) the viscoplastic zone length; b) vertical stress at $x=a$, for five different values of the viscosity coefficient μ.

functions can be considered. Let us consider the deformation of a viscoplastic seam caused by the continuous increase of the opening span, corresponding to the advance of a longwall face with constant velocity v. For every time instant t_i the opening span is abruptly increased by $\Delta a = v \Delta t$ (the elastic loading stage) and then left unchanged for $t = \Delta t$, thus allowing stress relaxation in a system with temporarily "frozen" geometry. This assumed longwall velocity function requires modification of the function $w_{i-1}(x)$ from the form previously presented, so that its appropriate derivatives can be calculated. Then the new form of the fundamental equation (6) can be formulated for any arbitrary time instant t_i. The required modifications involve calculation of $w_i(x)$ as in Eqn.(9) for a new opening span, $a + \Delta a$. This can be achieved by adding an extra elastic component because of span increase to the form $w_{i-1}(x)$ of the solution derived for the previous time step $(i-1)$. The total deflection $w_i(x)$ at an arbitrary time instant t_i can then be presented as the sum of three basic components:

1. Initial vertical displacement of the seam calculated for $a = a_l$ (a_l is the limit elastic span);
2. Sum of all purely elastic increments of this original displacement because of the rapid change of the opening span; and,
3. Sum of all the viscoplastic components of this displacement calculated successively for every $t_i, i=1,2, \dots, f$, where $t = t_f$ denotes the final time instant of interest.

An arbitrary longwall velocity function can now be investigated according to the method outlined above. In this paper only continuous motion of the longwall face terminated after several hours is discussed. The same philosophy, however, can be applied to the continuous motion with constant velocity, or to the continuous motion where the initial acceleration of the longwall face is taken into account in constructing the longwall velocity function. The following values of the material parameters have been assumed in the calculations discussed below: $p_m = 10\text{MPa}$, $p_r = 5\text{MPa}$, $q = 3.6\text{MPa}$, $G = 4.31 \times 10^8 \text{N/m}$, $E = 5.4 \times 10^7 \text{N/m}^3$, and $\mu = 8 \times 10^6 \text{N-sec/m}^2$. The longwall velocity functions used in calculations are presented in Fig.4a.
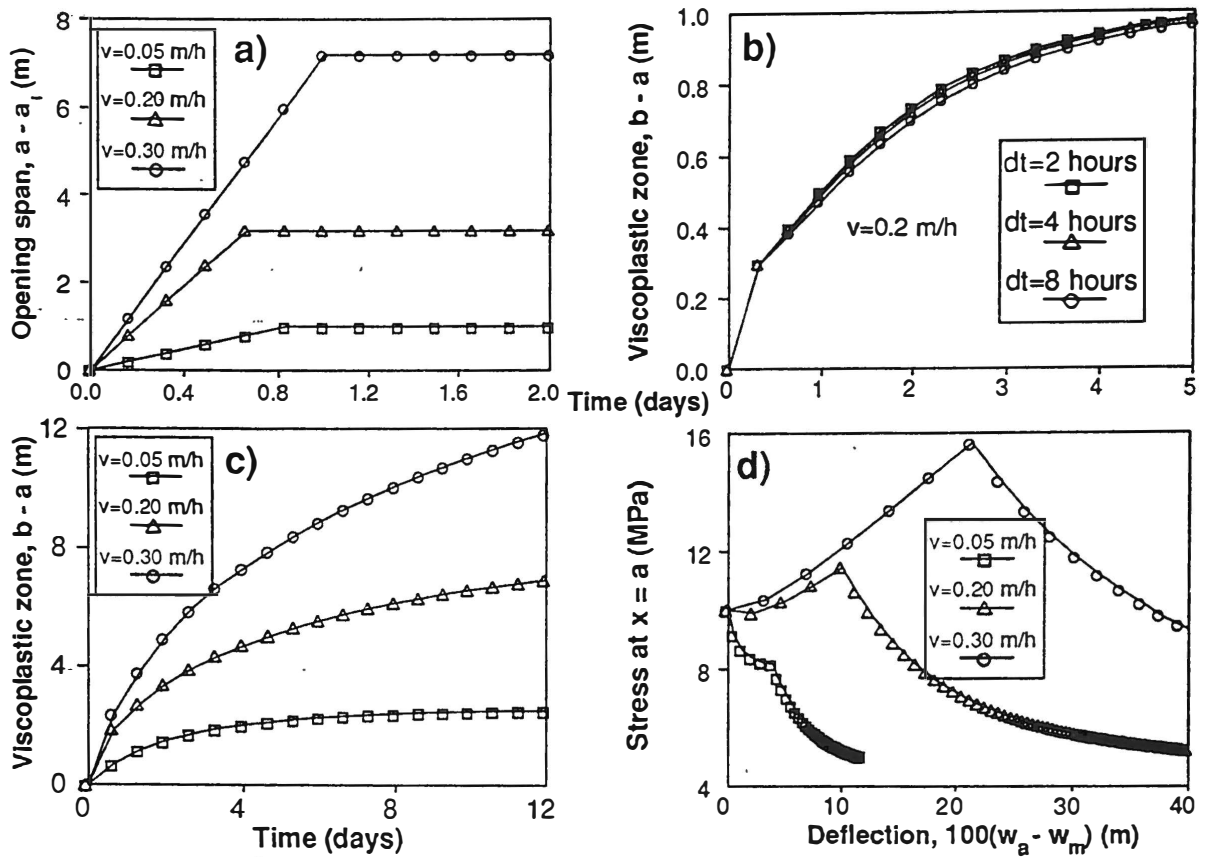
Fig.4. Continuous motion of a longwall face terminated after several hours: a) longwall velocity functions; b) sensitivity of the solution to change in time step Δt; c) growth of the viscoplastic zone; d) force-displacement relations recorded on a moving boundary x=a(t).

A problem to be resolved when the finite difference method is applied to the calculations in question concerns the sensitivity of the solution to the size of time step Δt. From Fig.4b one may see that the solution presented remains stable with respect to Δt. The growth of the viscoplastic zone with time corresponding to the velocity functions of Fig.4a is shown in Fig.4c.The viscoplastic zone starts to develop with a certain growth rate,which gradually decreases during the motion, Fig.4c. The length of the viscoplastic zone gradually attains a limiting value corresponding to the final equilibrium position of the system. The time required for the solution to stabilize grows as the initial velocity of the longwall face increases. Fig.4d shows force-displacement relations at x=a(t), that is on a moving boundary. It must be pointed out that for the approach presented in this paper these relations are not known a priori. This is the case because according to the displacement rate applied the material can exhibit different stress-strain responses, and the displacement rate applied depends on the velocity of the moving longwall face. The various responses ranging from a softening to a hardening response can be obtained according to the value v of longwall velocity. The vertical stress at x=a gradually decreases to the final value equal to the residual strength of the seam.In Fig.4d w_a denotes the deflection of the seam at x=a.

5 STABILITY CRITERIA FOR A SEAM

Instead of deriving the general form of the stability conditions from energy considerations, (Salamon, 1970; Petuchov and Linkov, 1979), an alternative approach has been recommended by Mróz and Nawrocki (1989). They recommended the specification of the instability point on the *a-b* plane, where the opening span *a* is the external control parameter and the position *b* of the elasto-viscoplastic interface defines the system's response. When the external control parameter reaches or exceeds this point, an uncontrollable dynamic deformation and failure process develops and eventually terminates at a new stable opening configuration. Furthermore, for a semi-infinite seam, a brittle-plastic uniaxial model provides a simple stability condition requiring the residual seam strength to be greater than the roof beam pressure, $p_r > q$.

To discuss the effect of longwall velocity on the stability of the seam consider three different speeds of ore extraction: $v=0.18$, $v=0.075$, and $v=0.02$m/h. The semi-analytical approach developed in this paper has been applied to calculate the position of the viscoplastic interface, *b*, corresponding to these speeds. Numerical results are presented in Fig.5. It has been assumed for calculations that $q=3.6$MPa, and the following values of the residual strength have been applied: $p_r=7$, $p_r=3.6$, and $p_r=1$MPa. AB is the reference line plotted to help interpret the results. It can be seen in Fig.5, that for the opening span setup at a reference level, $a=a_{ref}$, the length of the viscoplastic zone increases with a decrease of the longwall velocity. The same statement is true for a decrease of the residual strength. This means that for fast extraction of the seam, concentrations of high stresses appear in the seam close to the longwall face. Slow ore extraction allows much more time for stress redistribution within the seam to occur. Thus, the peak stress $p=p_m$ appearing at $x=b(t)$ is shifted out of the opening wall into the seam, and the corresponding viscoplastic zone of "residual" stresses of the length $(b-a)$ is much larger than it would be for high values of the longwall velocity. Moreover, because instability would have to correspond to the maximum point on the $a=a(b)$ curves as shown in Fig.5, if it could appear, and noting that the slope of these curves decreases with a decrease of p_r, the possibility of the instability occurring grows with a decrease of the residual strength. To verify this conclusion the situation has been considered where the longwall face remains active for 20 hours with $v=0.05$m/h. After that period of time ore extraction has been terminated and the evolution of vertical displacements at $x=a$ has been monitored. The results obtained are shown in Fig.6. It can be seen that for high values of p_r deformation of the system moves asymptotically to the final ultimate value that corresponds to the stable equilibrium position of the system. On the other hand, when p_r is small, vertical deflections grow monotonically and the final destruction of the opening can be expected.

6 CONCLUSIONS

In the case of longwall mining some opposing opinions on the effect of mining velocity on the rock burst occurrence exist. Some researchers claim that slow progress of mining
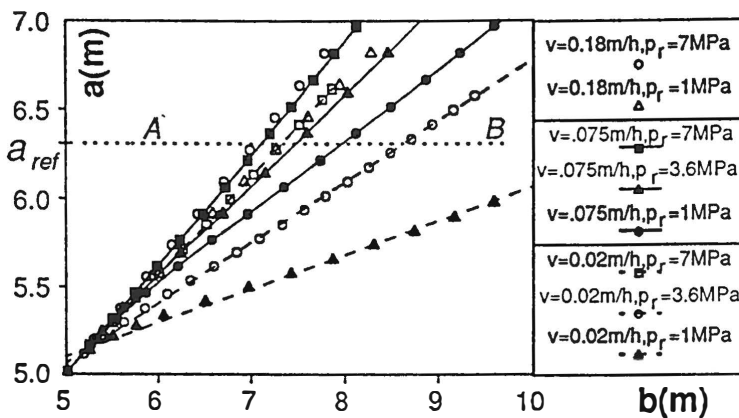
Fig.5. The effect of v and p_r on the development of the viscoplastic zone of deformation.
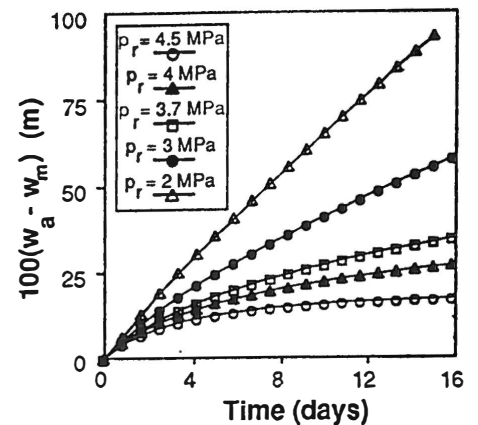
Fig.6. The effect of p_r on the deformation of the seam.

operations favours rock burst occurrence whereas others present just the opposite opinion. The analysis performed in this paper has shown that rapid ore extraction produces zones of high stress concentrations situated close to the longwall face. This situation is assumed to be hazardous by many mining engineers who concentrate their efforts on shifting the zone of high stresses deep into the seam. It has been determined in this paper that this is the natural situation when the longwall velocities are small. The analysis has also shown that for very weak seams (seams with the residual strength p_r lower than the overburden pressure q) deformation of the seam appearing for fixed geometry of the opening grows monotonically, which can lead to the final destruction of the opening. The situation is much different for seams of hard rocks $(p_r > q)$ where strains attain their final asymptotic values after a short period of time.

REFERENCES

Bieniawski, Z.T., Denkhaus, H.G. & Voegler, U.W. 1969. Failure of fractured rock, *Int. J. Rock Mech. Min. Sci.*, **6**, 323-341.

Crouch, S.L. & Fairhurst, C. 1973.'The mechanics of coal mine bumps and interaction between coal pillars, mine roof and floor, Final Report on U.S. Bureau of Mines Res earch.

Mróz, Z.& Nawrocki, P.A. 1989. Deformation and stability of an elasto-plastic softening pillar, *Rock Mech. & Rock Eng.* **22**, 69-108.

Nawrocki, P.A. 1993. Effect of mining velocity on the deformation and stability of an elasto-viscoplastic seam. *Int. J. Num. Anal. Meth. Geomech.* submitted for publication.

Petuchov, I.M. & Linkov, A.M. 1979. The theory of post-failure deformations and the problem of stability in rock mechanics', *Int. J. Rock Mech. Min. Sci. & Geomech. Abstr.* **16**, 57-76.

Salamon, M.D.G. 1970. Stability, instability and design of pillar workings, *Int. J. Rock Mech. Min. Sci.* **7**, 613-631.

DIMENSIONNEMENT DES OUVRAGES SOUTERRAINS DANS LES EVAPORITES
EFFETS MÉCANIQUES DE L'INTERACTION ET DU REFROIDISSEMENT DES CAVITÉS

OULD AMY M., GHOREYCHI M.

*Groupement pour l'étude des Structures Souterraines de Stockage (G.3S)
École Polytechnique, 91128 Palaiseau, France*

RÉSUMÉ

Les évaporites telles que le sel gemme et la potasse présentent un comportement thermo-viscoplastique très marqué, particulièrement sensible à la température. Deux questions relatives au dimensionnement des ouvrages souterrains profonds creusés dans ces milieux (mines, cavités de stockage, etc.) ont rarement fait l'objet d'étude approfondie : l'interaction des cavités rapprochées (galeries, puits, chambres, etc.) et les effets induits par le refroidissement (aérage des mines, circulation de la boue dans les forages pétroliers, forages géothermiques, stockage à basse température, etc.).
A partir d'une modélisation numérique par éléments finis, et sous l'hypothèse des déformations planes, on se propose de calculer les champs des contraintes et des déplacements associés à ces effets. On examinera en particulier les conditions dans lesquelles un ouvrage souterrain profond en milieu thermo-viscoplastique de Norton-Hoff isotrope homogène peut être le siège de sollicitations excessives de compression ou de traction.

ABSTRACT

Evaporites such as rock salt and potash salt have a very significant thermo-viscoplastic behavior, highly sensitive to temperature. Two questions related to dimensioning of deep underground facilities in these media (mines, storage caverns, etc.) have rarely been studied in detail : interaction of neighbouring cavities (galleries, shafts, rooms, etc.) and effects induced by cooling (ventilation of drifts, mud circulation in petroleum shafts, geothermal boreholes, cryogenic storage, etc.).
Using a numerical modelling by Finite Element Method, and under plane strain assumption, we calculate the stress and displacement fields associed to the mentioned effects. In particular, we discuss about the conditions in which deep underground facilities in a Norton-Hoff thermo-viscoplastic medium may be affected by excessive compressive or tensile stresses.

INTRODUCTION

Le souci de sécurité et d'exploitation optimale des ouvrages souterrains a, de tout temps, motivé des études de plus en plus complexes portant sur le dimensionnement de tels ouvrages. Cette exigence est aujourd'hui satisfaite grâce à la grande capacité des ordinateurs et le développement croissant des méthodes numériques.

Le recours à l'outil numérique devient systématique lorsque la rhéologie des géomatériaux considérés présente des non linéarités assez fortes, comme c'est le cas des évaporites (sel gemme, potasse, etc.).

On se propose dans cette contribution de traiter, par la méthode des éléments finis, deux questions rarement étudiées de façon approfondie, intéressant le dimensionnement des ouvrages souterrains profonds creusés dans ces milieux : l'interaction des cavités rapprochées et les effets mécaniques de leur refroidissement. Comme ces deux problèmes ont en commun de faire intervenir la rhéologie des évaporites, un rappel sommaire sur celle-ci permettrait une meilleure compréhension.

Rappels sur la rhéologie des évaporites

Les évaporites possèdent en général un comportement viscoplastique non linéaire, pratiquement sans seuil. On peut donc s'interroger sur l'évolution à long terme des structures souterraines dans ces milieux, en raison de déformations différées importantes et de concentration de contraintes qui diminue en fonction du temps (relaxation des contraintes). Cette aptitude au fluage des évaporites est diversement décrite par les spécialistes. Certaines lois rhéologiques admettent pour le sel gemme l'existence de deux types de fluages : un fluage primaire et un fluage secondaire prépondérant à long terme. Une bibliographie relativement complète (Pouya, 1991), présentant les classiques écoles de pensées, comme celle de Norton-Hoff ou celle de Lemaître-Menzel-Schreiner peut être à ce sujet utilement consultée. Pour notre part, on peut considérer que pour les applications courantes, une loi du type Norton-Hoff suffit puisqu'elle surestime les déformations des structures et se situe donc du côté de la sécurité du dimensionnement des ouvrages souterrains. On adoptera pour les évaporites une loi thermo-élasto-viscoplastique (Pouya, 1991) qui présente les principales propriétés suivantes : absence d'une cohésion mesurable au laboratoire, viscosité décroissante avec la température (loi exponentielle d'Arrhénius), non linéarité vis à vis du déviateur des contraintes, existence d'un fluage primaire. Cette loi rhéologique est décrite par les équations suivantes :

$$\dot{\underline{\varepsilon}} = \dot{\underline{\varepsilon}}^e + \dot{\underline{\varepsilon}}^{vp} + \dot{\underline{\varepsilon}}^{th} \tag{1}$$

$$\dot{\underline{\varepsilon}}^e = \frac{1+v}{E}\dot{\underline{\sigma}} - \frac{v}{E}\dot{\sigma}_{kk}\underline{1} \tag{2}$$

$$\dot{\underline{\varepsilon}}^{th} = \alpha\dot{\theta}\underline{1} \tag{3}$$

$$\dot{\underline{\varepsilon}}^{vp} = \dot{\underline{\varepsilon}}_p^{vp} + \dot{\underline{\varepsilon}}_s^{vp} \tag{4}$$

$$\dot{\underline{\varepsilon}}_p^{vp} = \beta(T)\langle A_p\left[\frac{\sigma_{eq}}{\sigma_0}\right]^{n_p} \exp\left[-\frac{k_p}{T}\right] - \varepsilon_{eq}^p\rangle\frac{\partial\sigma_{eq}}{\partial\underline{\sigma}} \tag{5}$$

$$\dot{\underline{\varepsilon}}_s^{vp} = A_s\left[\frac{\sigma_{eq}}{\sigma_0}\right]^{n_s} \exp\left[-\frac{k_s}{T}\right]\frac{\partial\sigma_{eq}}{\partial\underline{\sigma}} \tag{6}$$

où :

$\dot{\underline{\varepsilon}}$, $\dot{\underline{\varepsilon}}^{e}$, $\dot{\underline{\varepsilon}}_{p}^{vp}$, $\dot{\underline{\varepsilon}}_{s}^{vp}$ représentent respectivement les tenseurs vitesses des déformations totales, des déformations élastiques, des déformations viscoplastiques primaires et des déformations viscoplastiques secondaires ;

$\underline{\sigma}$, σ_{eq}, ε_{eq}^{p}, σ_0 désignent respectivement le tenseur des contraintes, la contrainte équivalente de Mises ($\sqrt{3J_2}$), une déformation également équivalent et une contrainte de référence (1 MPa) ;

T, θ sont respectivement la température absolue et une variation de température ;

E, v, α sont respectivement le module d'Young et les coefficients de Poisson et de dilatation thermique ;

$\beta(T)$, A_p, A_s, K_s, K_p, n_s, n_p sont des constantes du modèle.

En plus des propriétés principales déjà évoquées, on peut ajouter à propos de cette loi deux remarques qui intéressent directement le calcul des structures :
- en l'absence de chargement thermique, et lorsque la structure est soumise à des sollicitations extérieures constantes, les déformations différées provoquent en moyenne une relaxation des contraintes ;
- en présence d'un régime thermique permanent, et sous les hypothèses d'un chargement mécanique extérieur constant et en petites déformations, un régime asymptotique de contraintes s'établit dans toute la structure, avec une évolution stationnaire des déformations (à vitesse constante).
Rappelons que les évaporites, comme la plupart des géomatériaux, ont une faible résistance à la traction, dépassant rarement 1 MPa (Berniaux et al., 1986) alors que leur résistance à la compression peut atteindre 30 MPa.
Enfin précisons que les évaporites tels que le sel gemme, possèdent un coefficient de dilatation thermique relativement élevé (4,2 10^{-5} °C^{-1}), soit environ 3 fois celui de la moyenne des géomatériaux. D'autre part, ils se caractérisent par un module d'élasticité relativement important (typiquement 20000 à 25000 MPa). Il en résulte donc une sollicitation thermique significative (de l'ordre de 1 MPa/°C).

A) INTERACTION DES CAVITÉS

1) Position du problème

L'exploitation des gisements miniers peut conduire au creusement d'un nombre important de cavités s'étalant dans le sens horizontal et dans le sens vertical (exploitation à multi-étages). L'état des contraintes qui règnent dans ce réseau de cavités est le résultat d'une interaction mécanique. Pour une rhéologie plus ou moins complexe, comme celle des évaporites, on peut se demander dans quelle mesure ce type d'exploitation peut poser de problème pour la stabilité mécanique. On sait à l'heure actuelle résoudre semi-analytiquement (Nguyen Minh D. et al., 1992), sous certaines hypothèses, le problème de la cavité circulaire profonde creusée dans un massif salifère semi-infini (fig. 1) et traiter numériquement (Abou-ezzi, 1990) le cas d'une rangée infinie de cavités circulaires creusées à une certaine profondeur du sol (fig. 2).
On se propose dans cette partie de situer la question de l'interaction d'une infinité de cavités (fig. 3) par rapport aux deux problèmes précités. En dehors de critères

énergétiques, on peut examiner la stabilité mécanique sous deux aspects : celui de la convergence et celui de la contrainte orthoradiale maximale sur le pourtour des cavités.

2) Modélisation mécanique effectuée

A partir d'une certaine profondeur (typiquement entre 500 m et 1000 m) dans un massif salifère, on creuse des rangées de galeries rapprochées dont le nombre est suffisamment important pour constituer un réseau infini de cavités [dans le plan perpendiculaire à l'axe des galeries (fig. 3)]. On suppose que les galeries sont assez longues pour que l'hypothèse des déformations planes puisse être valable. On ne s'intéressera pas à l'effet groupé du creusement des cavités sur la subsidence, mais on portera notre intérêt sur l'effet de l'interaction mécanique sur la convergence des cavités et sur l'état des contraintes régnant à leur parois.

L'ensemble des cavités est creusé à température ambiante dans un massif salifère obéissant à la loi décrite précédemment. Les constantes de la loi, identifiant le type de sel gemme envisagé sont consignées dans le tableau 1. Comme nous nous intéressons à l'évolution à long terme, on négligera dans cette partie la phase du fluage primaire.
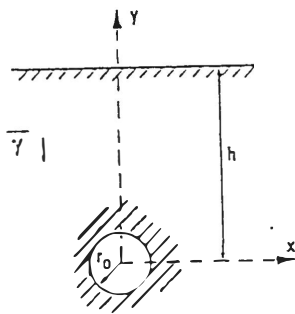
Fig. 1 - Galerie isolée
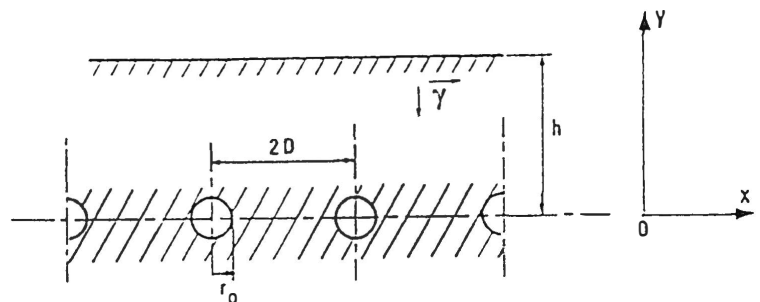
Fig. 2 - Rangée de galeries parallèles
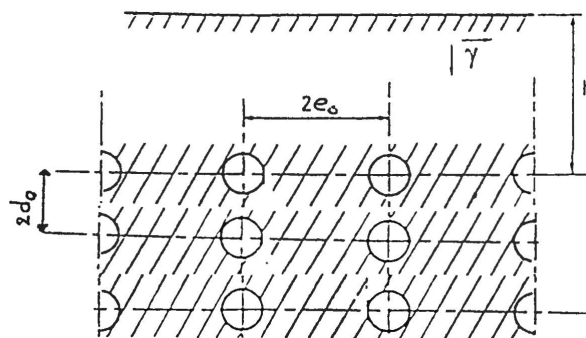
Fig. 3 - Infinité de Rangées de galeries

$\beta(T)$ (Jour^{-1})	A_p	K_p (K)	n_p	A_s (Jour^{-1})	K_s (K)	n_s
$24 \cdot \left[\dfrac{4,67}{\theta+273} - 0,005\right]$	81,82	6229	3,36	0,04356	4755	3,36

Tableau 1 - Jeu des constantes de la loi rhéologique

Adimensionnalisation

Considérons maintenant une cavité centrale à la profondeur h. Compte tenu des diverses symétries, on peut étudier la configuration donnée par la figure 4. Notons σ_0, la contrainte circonférencielle donnée par l'élasticité dans le cas du creusement d'une cavité isolée ($\sigma_0 = 2\gamma h$), ε_0 la déformation qui lui est associée par la loi de Hooke, r_0 le rayon de la cavité et t_0 le temps caractéristique viscoplastique :

Posons :

$$x^* = \frac{x}{r_0} \quad y^* = \frac{y}{r_0} \quad t^* = \frac{t}{t_0} \quad \underline{\underline{\sigma}}^* = \frac{\underline{\underline{\sigma}}}{\sigma_0} \quad \underline{\underline{\varepsilon}}^* = \frac{\underline{\underline{\varepsilon}}}{\varepsilon_0}$$

Une étude détaillée basée sur l'équation d'équilibre, l'hypothèse des petites déformations, la rhéologie du massif et les conditions aux limites, montre (Ould Amy, 1992) que ce problème dépend essentiellement de 3 paramètres :

$\tau_1 = r_0/e_0$ que l'on peut interpréter comme un taux de défruitement horizontal,

$\tau_2 = r_0/d_0$ que l'on peut interpréter comme un taux de défruitement vertical,

n_S qui représente le coefficient de Norton lié à la rhéologie viscoplastique.
Remarquons que l'équation d'équilibre se simplifie :

$$div^*(\underline{\underline{\sigma}}^*) + \frac{r_0 \gamma}{\sigma_0}\vec{j} \approx div^*(\underline{\underline{\sigma}}^*) = \vec{0}$$

(car $\gamma r_0/\sigma_0 = \gamma r_0/2\gamma h \ll 1$ en raison de hypothèse de grande profondeur).
La modélisation effectuée est donnée par la figure 4.

3) Résultats et comparaisons des abaques

Il est clair que si τ_1 et τ_2 tendent tous les deux vers zéro, on est en présence du cas de la cavité isolée et que si τ_2 seulement tend vers zéro, on est en présence cette fois-ci du cas de la rangée infinie de cavités. Donc, pour que la comparaison garde un sens, il faut maintenir ces deux paramètres géométriques dans des planches raisonnables. Traçons alors les convergences verticale et horizontale (fig. 5) et les contraintes orthoradiales aux points I et J (fig. 6) en fonction du temps.
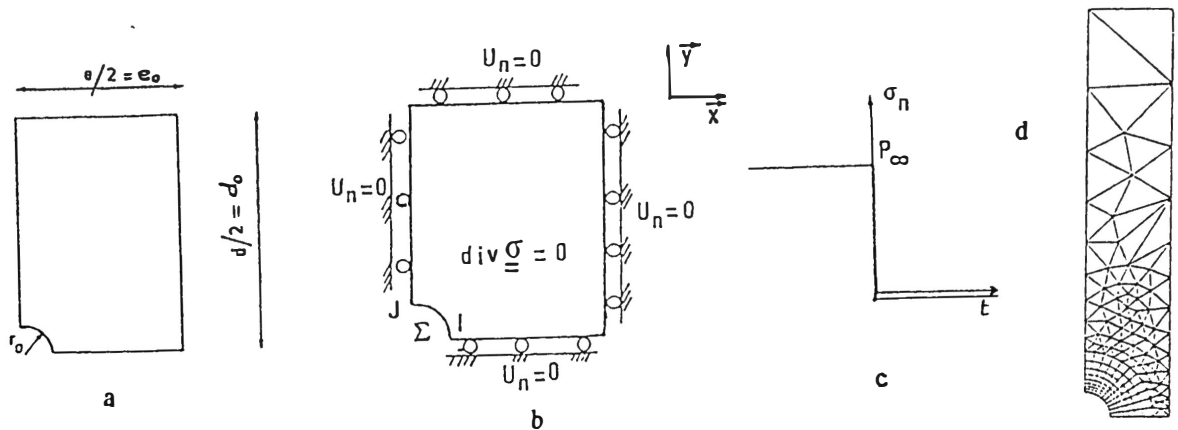
Fig. 4 - Modélisation mécanique effectuée
a- configuration, b- conditions aux limites,
c- simulation du creusement, d- maillage (τ_1=20%, τ_2=8 %)
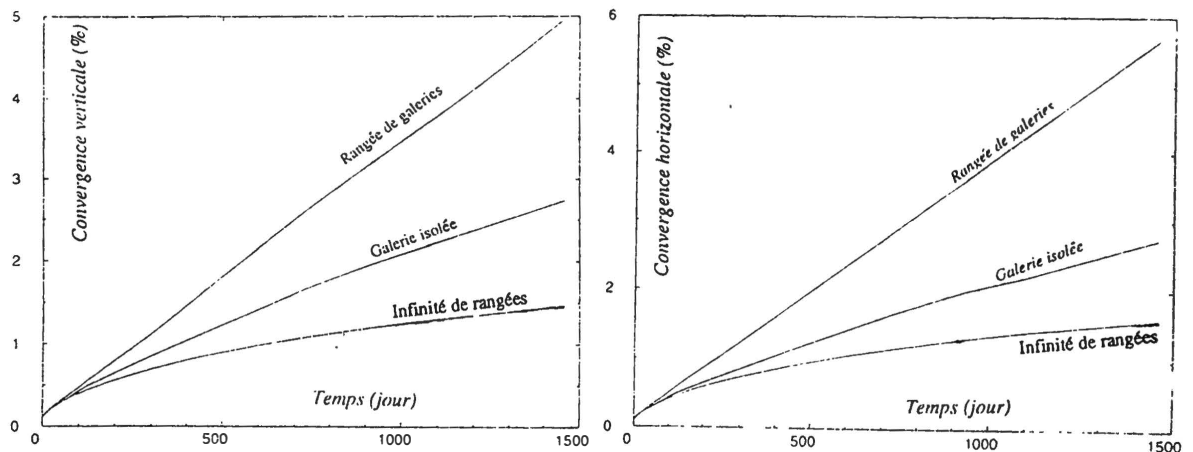
Fig. 5 - Évolution des convergences verticale et horizontale en fonction du temps
$\tau_1 = 20\%$ $\tau_2 = 8\%$ $r_0 = 0,75$ m h = 700 m

Ces figures montrent qu'à court terme les trois problèmes conduisent à des résultats
pratiquement identiques. Mais à partir d'un certain temps (de l'ordre d'une centaine de
jours), l'interaction des cavités se manifeste clairement. L'infinité de cavités conduit à
nettement moins de convergences (dans les deux sens, vertical et horizontal). Ce résultat
qui peut paraître à première vue étonnant est pourtant physiquement compréhensible.
Lorsque l'on creuse une infinité de cavités dans les deux directions, la pression des
terrains se distribue de façon que chaque cavité subisse une "décharge" plus faible de la
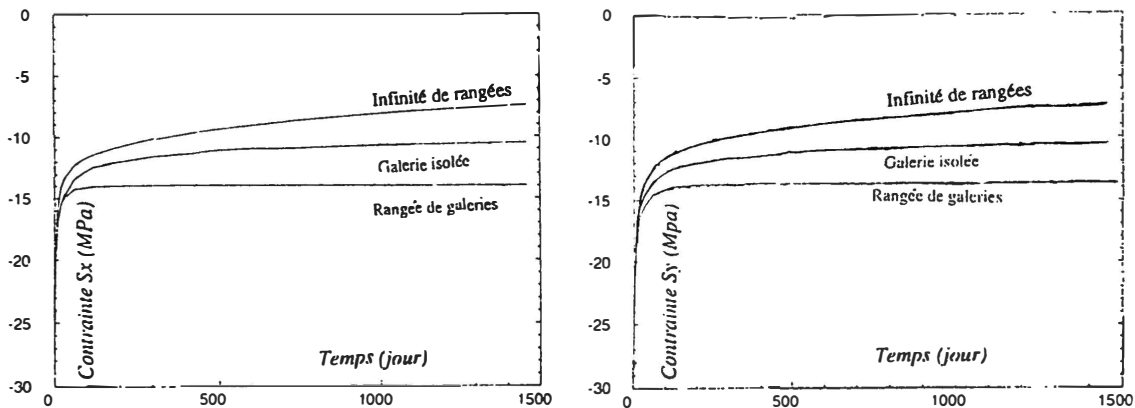
Fig. 6 - Évolution des contraintes aux points I et J en fonction du temps
$\tau_1 = 20\%$ $\tau_2 = 8\%$ $r_0 = 0,75$ m $h = 700$ m

part du massif, contrairement au cas d'une cavité isolée qui prend à elle seule toute la pression du terrain, ou au cas de la rangée de cavités qui, elle, provoque une dissymétrie de l'effort géostatique subi. Cette interprétation est confirmée par l'analyse des contraintes qui fait apparaître une relaxation rapide dans le cas d'une infinité de cavités conduisant à un état asymptotique moins favorable à des déformations viscoplastiques importantes (en raison de la loi de Norton).

Les résultats sur l'interaction mécanique des cavités nous inspirent une analogie avec la fissuration des massifs élastiques : le facteur de concentration des contraintes est maximal pour une rangée de fissures, intermédiaire pour une fissure isolée et faible dans le cas des fissures superposées.

B) REFROIDISSEMENT DES CAVITÉS SOUTERRAINES

1) Problèmes mécaniques associés au refroidissement

De nombreux problèmes mécaniques font intervenir le refroidissement des cavités souterraines, tels que l'aérage des tunnels ou des galeries minières, le stockage cryogénique d'hydrocarbures, le refroidissement des déchets radioactifs dans la phase post-paroxysme thermique et la circulation des fluides dans les forages pétroliers ou encore en géothermie. Toutes ces applications entraînent à des degrés divers une variation négative de la température du massif, évolutive en général dans l'espace et dans le temps. Ce refroidissement transitoire qui s'accompagne donc d'une restitution d'énergie de la part du massif, s'effectue à travers des mécanismes de diffusion et parfois de convection thermiques.

Analyse qualitative des effets mécaniques du refroidissement

Les effets du refroidissement des évaporites peuvent être analysés sous trois aspects : la diminution de la viscosité, la contraction thermique et les constantes de temps associées à la diffusion thermique et à la viscoplasticité.

82

a) Effets de la viscosité

Négligeons, pour simplifier, les déformations dues au fluage primaire. La relation (6) permet d'écrire :

$$\underline{\dot{\varepsilon}}^{vp} = A_s \exp\left[-\frac{k_s}{T}\right]\left[\frac{\sigma_{eq}}{\sigma_0}\right]^{n_s}\frac{\partial\sigma_{eq}}{\partial\underline{\sigma}}, \text{ avec } \sigma_0=1 \text{ MPa} \qquad (7)$$

Pour isoler l'effet de la viscosité, gardons constant l'état des contraintes et choisissons deux distributions de températures T_1 et T_2 ($T_1 > T_2$), alors le rapport des vitesses des déformations associées devient :

$$\eta = \frac{|\dot{\varepsilon}_1^{vp}|}{|\dot{\varepsilon}_2^{vp}|} = \exp\left[-K_s\left(\frac{1}{T_1}-\frac{1}{T_2}\right)\right] = \exp\left[K_s\left(\frac{T_1-T_2}{T_1T_2}\right)\right] \qquad (8)$$

Donc ce rapport est d'autant plus grand que la différence des températures est élevée et que leur produit est faible. Or, pour les ouvrages souterrains creusés dans les évaporites aux profondeurs envisageables (500 m à 1000 m), ces deux conditions peuvent être réunies. Il est donc clair qu'en augmentant la viscosité, le refroidissement diminue sensiblement les vitesses des déformations viscoplastiques, ce qui conduit, à son tour, à un déviateur asymptotique plus faible [compte tenu de la loi de Norton de la relation (7)].

b) Effets de la contraction thermique

La thermoélasticité du sel fait qu'une contraction instantanée se produit lors de toute baisse de température. Les contraintes qui en résultent, pour un comportement linéaire isotrope, sont données par la relation classique :

$$\delta\sigma = E\alpha\delta\theta. \qquad (9)$$

Or, on a vu que pour les évaporites cette sollicitation correspond typiquement à 1 MPa/°C, ce qui est énorme vis à vis de la résistance à la traction 1 MPa. Il y a donc un risque réel de rupture par traction à cause du refroidissement. Lors d'une récente expérience in-situ aux Mines de Potasse d'Alsace (Ghoreychi, 1991), rien qu'une coupure de chauffe a provoqué des fissures longitudinales ouvertes de 2 mm malgré une pression de confinement exercée sur la paroi. Il faut rappeler que la fissuration du massif salifère augmente sensiblement sa perméabilité, ce qui peut remettre en cause le choix du sel comme milieu favorable au stockage souterrain (matériau réputé pour son étanchéité).

c) Effets des constantes de temps

La réponse du massif au refroidissement fait intervenir deux temps caractéristiques. Un temps de diffusion thermique donné par la relation classique :
$$t_d = a^2/c_v$$
où c_v représente la diffusivité thermique et a est une dimension caractéristique.

Le temps associé à la viscoplasticité se déduit, lui, de la relation (7) :

$$t_v = \frac{\varepsilon_0}{A_s \exp\left[-\dfrac{K_s}{T}\right]\sigma_0^{n'}} = \frac{|\sigma_0|^{1-n'}}{EA_s \exp\left[-\dfrac{K_s}{T}\right]}. \qquad (10)$$

Ce temps varie fortement avec le coefficient de Norton (autrement dit avec le type d'évaporite) et la profondeur moyenne de la cavité (à travers σ_0). La comparaison de ces deux temps est déterminante pour prédire le type de sollicitation exercée aux endroits les plus significatifs de l'ouvrage. Si le temps viscoplastique est plus petit que le temps de diffusion alors la relaxation des contraintes sera plus rapide et l'ouvrage pourra être soumis à la compression sur ses parois pendant ce temps. Ce scénario peut se révéler critique. Car, au moment où la traction due au refroidissement sera sensible, une relaxation importante sera déjà produite, ce qui en somme augmente la tendance à la traction. En fait, le calcul des ordres de grandeurs montre que le temps thermique est souvent plus court que le temps viscoplastique, ce qui tend à modérer l'effet de traction.
Il convient d'ajouter à cette analyse que, pour un ouvrage donné (géométrie et conditions aux limites) exécuté en milieu plastique ou viscoplastique, il importe de tenir compte de la manière avec laquelle lui est appliqué le refroidissement (brutal ou progressif, par exemple), qui sous-tend la notion très importante de vitesse de chargement.

2) Application à l'aérage des galeries

L'aérage des galeries est une des applications sur le refroidissement. Une étude récente (Plesel, 1992) abordant le problème du refroidissement d'une cavité sphérique a montré qu'il suffit de très peu de différence entre la température de l'air de ventilation et la température initiale du massif pour faire apparaître de la traction.
Pour examiner cet effet dans le contexte de l'aérage d'une mine, considérons une infinité de galeries identiques creusées à une grande profondeur dans un massif salifère, caractérisées par des sections en fer à cheval (fig. 7). Le sel gemme étudié garde les mêmes propriétés thermo-viscoplastiques que précédemment (tableau 1).

Modélisation

Le champ thermique initial résulte du gradient géothermique naturel (on suppose un profil linéaire en fonction de la profondeur tenant compte des divers conductivités en présence). On modélise la ventilation des galeries par un échange convectif newtonien (température de l'air de ventilation et coefficient d'échange constants). On met en œuvre le code de calcul par éléments finis THERM (Ghoreychi, 1987) pour un modèle linéaire plan transitoire (3 ans d'aérage).
Le champ thermique obtenu est introduit dans un calcul thermo-mécanique (hypothèse d'un couplage indirect qui fait intervenir un chargement mécanique d'origine thermique). Ce calcul se base sur l'hypothèse des déformations planes, les galeries sont supposées infiniment longues. Le champ de contraintes initiales est géostatique isotrope. La modélisation effectuée est donnée par la figure 8.
L'équation des milieux continus, l'hypothèse des petites déformations, les conditions aux limites et initiales, ajoutées à la rhéologie aboutissent, selon la méthode des éléments finis, à résoudre un système d'équations symétrique non linéaire différentiel du premier ordre.

On met en œuvre le programme d'éléments finis GEOMEC (Sabir, 1988) utilisant un algorithme d'intégration dans le temps du type Runge-Kutta d'ordre 2.
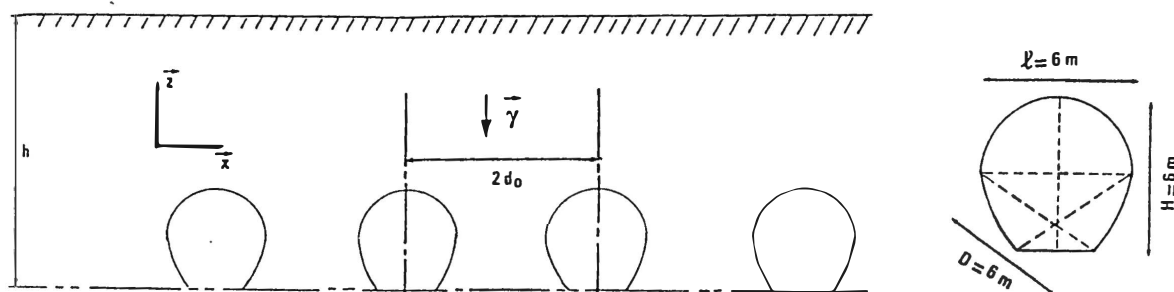
Fig. 7 - Galeries horizontales et parallèles
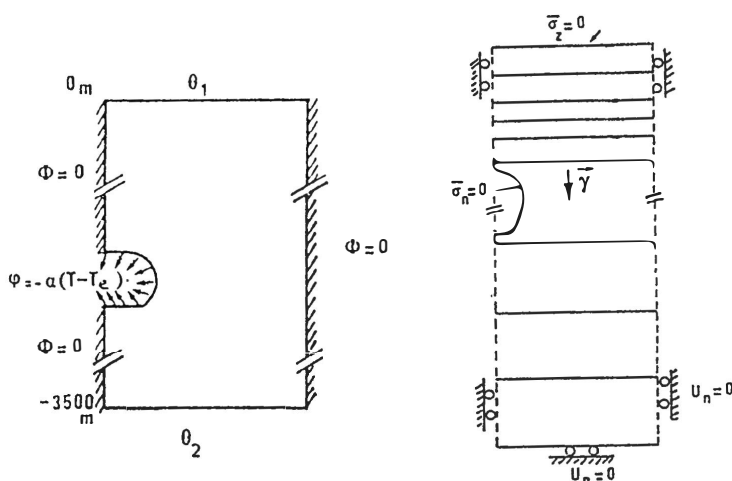
Fig. 8 - Modélisations thermique et thermomécanique de l'aérage
$\alpha=21 W/m^2/°C$, $T_e=25$ °C, $\theta_1=10$ °C, $\theta_2=155$ °C, $d_0=12,5$ m

Résultats

L'examen des résultats montre que l'endroit le plus affecté par l'aérage est la pointe du mur (point I) dans le sens de l'axe de la galerie (contrainte principale suivant $\bar{y}$). L'effet de l'aérage est net aussi bien sur le déplacement (fig. 9) que sur les contraintes. Alors que sans aérage, la contrainte $\sigma_y(I)$ est largement de compression, elle devient rapidement de traction sous l'effet de la ventilation (fig. 10). Il faut remarquer l'importance de la traction en intensité et en extension (celle-ci est métrique et l'intensité atteint une valeur d'environ 2 MPa , soit le double de la résistance en traction).
Les résultats obtenus confirment en outre notre analyse qualitative du refroidissement.
Dans ce cas particulier on a $t_v=3t_d$; la traction est à court terme alors que la compression est à plus long terme. Une dizaine de degrés de différence de températures entre l'air et le massif suffit pour que le risque d'une rupture par refroidissement se manifeste. Enfin ils mettent en évidence l'effet de la géométrie : le toit de la galerie semble mieux résister à la traction (à cause du rayon de courbure) alors que le mur (rayon de courbure infini) en est plus affecté, tous deux pourtant soumis au même flux d'échange. En revanche la tendance

à la traction à court terme (de l'ordre du temps t_d) dans le sens de l'axe de la galerie peut ne pas dépendre de la géométrie de la section de celle-ci.
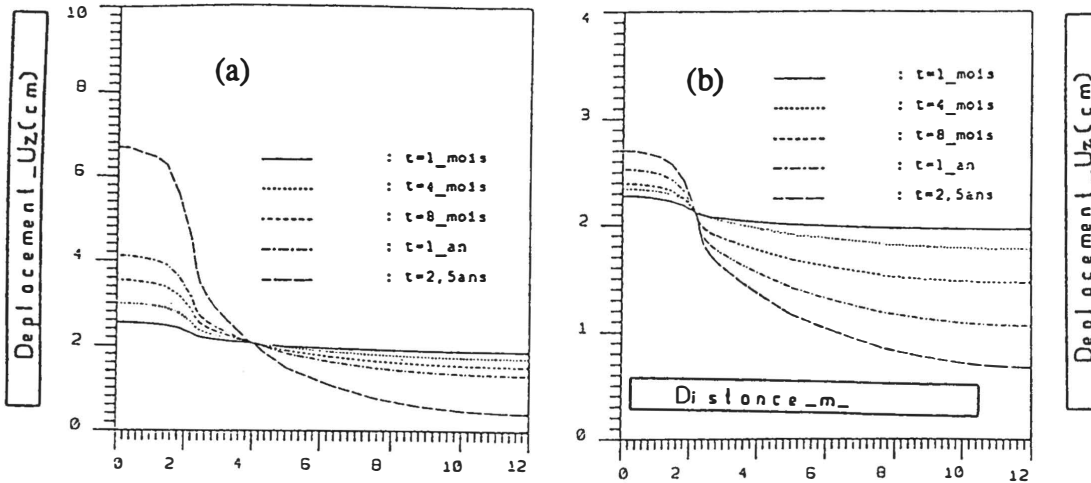
Fig. 9 - Évolution de la montée du mur sans aérage (a) et avec aérage (b) en fonction de la distance pour divers instants
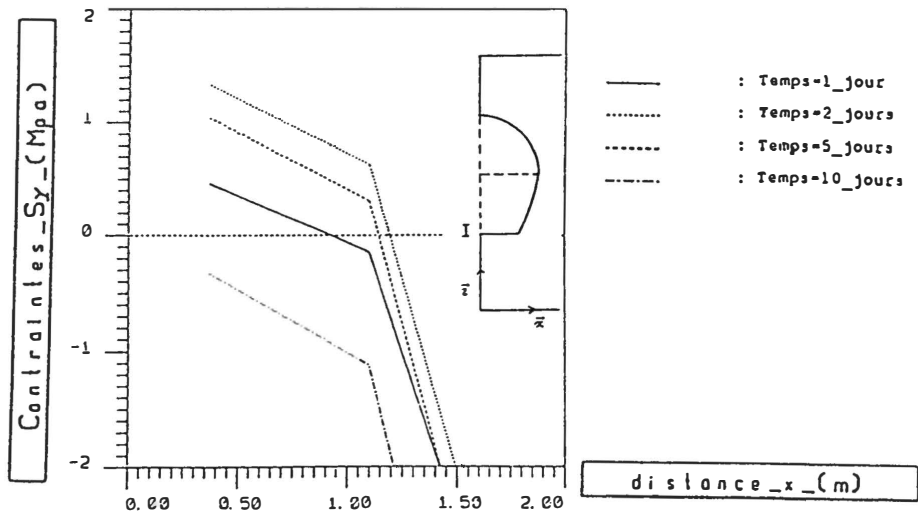
Fig. 10 - Évolution de la contrainte σ_y au point I en fonction de la distance au mur pour divers instants

CONCLUSION GÉNÉRALE

Nous avons examiné dans cette contribution deux questions relatives à la bonne tenue mécanique des ouvrages souterrains profonds creusés dans des massifs thermo-visco-plastiques : l'interaction et le refroidissement des cavités.

Ainsi l'interaction d'une infinité de cavités (plusieurs rangées superposées) semble plus favorable à la stabilité mécanique, comparativement au cas de l'interaction d'une seule rangée de cavités et au cas de la cavité isolée. Elle conduit en effet à moins de concentration de contraintes et à moins de convergence aux endroits les plus significatifs de la structure. Ces résultats obtenus sur les cavités circulaires peuvent être généralisés à d'autres géométries et lois de comportement, ce qui les rend utiles pour optimiser l'exploitation des gisements miniers profonds.

Le refroidissement provoque le développement d'une zone de traction au voisinage du mur où la contrainte dans l'axe de la galerie est susceptible de dépasser la résistance en traction de la plupart des géomatériaux, en particulier les évaporites. Enfin le refroidissement du massif illustre les deux aspects fortement liés de la stabilité (états des contraintes et des déplacements) : il diminue la vitesse de déformation de la roche par le biais de la viscosité et entraîne des contraintes de traction excessives par l'intermédiaire de la contraction thermique. L'étude montre que le risque de rupture par traction sous l'effet du refroidissement doit constituer un élément essentiel de conception et de dimensionnement des ouvrages souterrains.

RÉFÉRENCES

ABOU-EZZI N., NGUYEN MINH D., POUYA A. ; Juin 1991; "Interaction des cavités souterraines dans le sel gemme", 2e Colloque Européen sur les Méthodes Numériques, Madrid.

BERNIAUX J., BONTE G., RENIE D. ;1986; "Mesure des contraintes in situ aux Mines de Potasse d'Alsace", Revue Industries minérales, Mines et carrières techniques, pp. 703-712.

GHOREYCHI M. ; 1987; "Notice technique et mode d'emploi du programme THERM", Rapport LMS-X, École Polytechnique, France.

GHOREYCHI M. ; 1991; "Comportement du sel broyé sous l'effet d'une source de chaleur dans les sondages réalisés dans une mine de sel", 323p., Édition C.C.E., EUR 13638.

NGUYEN MINH D., POUYA A. ; Avril 1992; "Une méthode d'étude des excavations souterraines en milieu viscoplastique. Prise en compte d'un état stationnaire des contraintes", Revue française de Géotechnique, n°59, pp. 5-14.

OULD AMY M. ; 1992; "Modélisation thermomécanique des infrastructures de stockage des déchets radioactifs. Interaction mécanique des cavités et influence de l'aérage des galeries", Rapport G.3S, 98p., École Polytechnique, France.

PLESEL R.; 1992; "Étude du refroidissement des cavités souterraines profondes creusées dans des massifs thermo-viscoplastiques", Mémoire de DEA de Mécanique, Option 7, 36p., École Polytechnique, France.

POUYA A. ; 1991; "Comportement rhéologique du sel gemme. Application à l'étude des excavations souterraines", Thèse de l'École Nationale des Ponts et Chaussées, 203p., France.

SABIR M. ; 1988; "Notice de conception et d'utilisation du programme GEOMEC", Rapport LMS-X, n°3, École Polytechnique, France.

MODELLING HIGH EXTRACTION MINING OF DEEP POTASH DEPOSITS

Euler De Souza
Department of Mining Engineering
Queen's University, Canada

ABSTRACT

A high extraction mining strategy which utilizes salt tailings as backfill for support in deep potash mines is described and modelled in this paper. A two-dimensional and axisymmetric, non-linear, transient, thermo-stress finite element code, named Viscot, has been calibrated and used in the modelling study. Constitutive models and yield criteria for the soft rocks have been determined from laboratory testing and field instrumentation, and the finite element code was used to evaluate induced displacements and stresses during mining, thus permitting an overall assessment of mine stability and integrity during high extraction mining.

RÉSUMÉ

Une stratégie minière à haute extraction qui utilise les rejets salins pour remplissage des mines de potasse profondes est décrite et modellisée dans cet article. Viscot, un logiciel basé sur la methode des éléments finis en bi-demensionnel, avec axisymétrie, non-linéairité, transitoire et thermo-constrainte a été calibré pour modelisation dans cette recherche. Les modèles constitutifs et les critères de rupture pour les roches douces ont été déterminés lors de tests en laboratoire et in situ, et le logiciel d'éléments finis a été utilisé pour évaluer le champ de déformation et de constrainte créé par l'activité minière, donc permettant d'évaluer la stabilité et l'integrité de la mine durant une extraction élevée.

1. INTRODUCTION

With the technology, mining methods and layouts currently utilized in deep soft rock mines, low ore extraction ratios are required to maintain mine stability, to control surface subsidence, and to prevent the occurrence of brine inflows and mining induced seismicity. The need for improved resource recovery, productivity and working conditions are some of the aspects of concern throughout the soft rock industry. A high extraction mining strategy which utilizes salt tailings as backfill for support is modelled in this paper to verify the technical feasibility of increasing the extraction ratio yet maintaining the structural integrity of the mine.

Mine room stability and convergence is dependent on regional stresses and on the geology. A geological section showing the Middle Devonian Evaporite cycles in Saskatchewan is shown in Figure 1. The potash bearing units occur in the Prairie Evaporite Formation and the potash layer that is currently mined occurs at a depth of 1100 meters, with pre-mining stresses approximating 20 MPa. The potash deposit is composed predominantly of medium to coarse grained sylvite and halite crystals, with some carnallite and interstitial clay. The Prairie Evaporite Formation rests conformably on the Winnipegosis Formation and is overlain disconformably by the Dawson Bay Formation (carbonates). The Winnipegosis Formation is a water bearing formation and is one of the possible sources of water that could pose a risk to the mining operations. The Dawson Bay Formation also contains localized pockets of brine and may be interconnected with the waters from the overlying water bearing formations, posing a threat of water inflow and flooding during mining. Naturally, the safety of workers, the possibility of mine flooding and the cost factor involved with the prediction, prevention and control of such occurrences are major concerns of the potash mining industry. Numerical modelling represents one of the means of optimizing operations and predicting some of the risks associated with mining. A modelling program designed to investigate a high extraction mining method utilizing salt backfill was developed in this paper and several possible scenarios of mine design innovation were analyzed using a finite element code. The code was used to simulate the mechanical behaviour, the induced displacements, and the state of stress of the rock strata and underground structures during high extraction mining. Evaluations of room closure rates, roof stability, overall room integrity, the state of stress and long term deformation behaviour of the potash ore, overlying salt rock and salt backfill were made using this code.
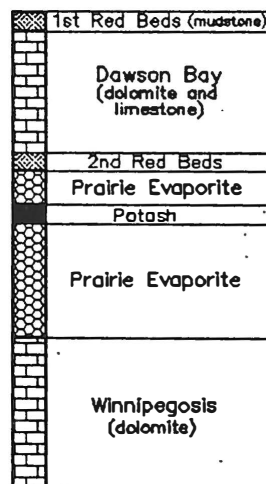
Figure 1. Geology of the Devonian Formations in Saskatchewan

2. DESCRIPTION OF THE NUMERICAL CODE

The numerical code, Viscot, is an adaptation of subroutines given in Owen and Hinton (1980). Viscot is a two-dimensional (plane strain or plane stress), axisymmetric, transient non-linear (viscoelastic or plastic), thermo-stress finite element code, designed to determine the viscoelastic, viscoplastic or elastoplastic deformation of a rock mass due to mechanical and thermal loading. The numerical solution of the non-linear incremental equilibrium equations and constitutive laws which govern the rock behaviour (viscoplastic, viscoelastic or elastoplastic material) within the code is performed by using a Bubnov-Garlekin finite element technique in conjunction with an explicit Euler time-stepping scheme. The viscoplastic material model can be described by Tresca, Von Mises, Drucker-Prager, and Mohr-Coulomb criteria, with or without strain hardening, with an associated flow rule which can be a power or an exponential law. The viscoelastic material model within the code is a temperature and stress dependent law developed specifically for salt rocks. The code can perform plane stress, plane strain and axisymmetric analysis. Isoparametric quadrilateral elements are employed. The elements used include four-noded linear quadrilateral elements and eight-noded quadratic serendipity elements. Isothermal, steady state thermal, or transient thermal stress analysis can be performed using the code. The code was designed to evaluate room closure rates, floor heave and overall room integrity in soft rock mining and to assess the state of stress within a salt backfill material.

2.1 Governing Equations

The governing equations within the code consist of the equilibrium equation, the stress-strain relation, and the equations describing the viscoelastic or viscoplastic deformation. The equilibrium equation takes the form,

$$\frac{\partial \sigma_{ij}}{\partial x_j} + P_i = 0 \tag{1}$$

where P_i is the body force vector and σ_{ij} is the stress tensor, which is related to the strain tensor ε_{ij} by the following relation,

$$\sigma_{ij} = \sigma^o_{ij} + D_{ijkl} (\varepsilon_{kl} - \varepsilon^o_{kl} - \varepsilon^{nl}_{kl}) \tag{2}$$

where σ^o_{ij} is the initial stress, ε^o_{kl} and ε^{nl}_{kl} the initial thermal and inelastic (viscoelastic or viscoplastic) strain respectively, and D_{ijkl} is the compliance elasticity tensor. To obtain a solution of the equilibrium equation 1 given in terms of displacements, the following strain-displacement relationship is employed,

$$\varepsilon_{ij} = \frac{1}{2} \left(\frac{\partial u_i}{\partial x_j} + \frac{\partial u_j}{\partial x_i} \right) \tag{3}$$

The code solves the equilibrium equation 1 in terms of displacements using the Bubnov-Garlekin finite element technique. The boundary conditions employed within this formulation are $u_i = U_i$ on B_1, and $\sigma_{ij}n_j = S_i$ on B_2, where B_1 and B_2 are boundary portions on which displacements and surface tractions are prescribed respectively, U_i are the prescribed displacements, n_j is the outward unit normal vector and S_i are the prescribed surface tractions.

The numerical approximation and solution procedure consists of the following steps. a) Discretization of the region into a network of finite elements. Isoparametric quadrilateral

elements are employed: linear (four-node), quadratic serendipity (eight-node), or quadratic Langrangian (nine-node) elements; b) Formulation of a system of algebraic equations describing the behaviour of various elements; c) Assembly of the element equations into a system of global algebraic equations that incorporate the boundary and initial conditions; d) Solution of the resulting system of algebraic equations and evaluation of stresses, strains and reactions. The non-linear equilibrium equations are solved for a prescribed time by using a time stepping scheme which solves the incremental linearized equilibrium equations at each time step until the final time value is reached or until a steady-state condition exists. The time integration is performed using the Euler explicit time marching scheme (Cormeau 1975, Owen et al 1980). To ensure numerical stability and acceptable accuracy, an automatic scheme for controlling the size of the time step is used in the program.

2.2 Yield Criteria

The onset of plastic behaviour is determined by a yield criterion which can be written as a scalar yield function of the form:

$$f(\sigma) = f(J_1, J_2, J_3) = k \qquad (4)$$

where f is some function and k is a material parameter to be determined experimentally. In general terms, yielding should be independent of the orientation of the coordinate system employed and therefore it should be a function of the three stress invariants given by, $J_1 = \sigma_1 + \sigma_2 + \sigma_3$, $J_2 = -(\sigma_1\sigma_2 + \sigma_2\sigma_3 + \sigma_3\sigma_1)$, and $J_3 = \sigma_1\sigma_2\sigma_3$. It has been further shown (Bridgman 1952) that yielding of a material is independent of the hydrostatic stress. Equation 4 may therefore be modified by stating the yield criterion in terms of the invariants of the deviatoric stresses:

$$f(J'_2, J'_3) = k \qquad (5)$$

where $J'_2 = \{(\sigma'_1)^2 + (\sigma'_2)^2 + (\sigma'_3)^2\}/2$ and $J'_3 = \{(\sigma'_1)^3 + (\sigma'_2)^3 + (\sigma'_3)^3\}/3$. The deviatoric stresses are defined as, $\sigma'_i = \sigma_i - \sigma_m$, where $\sigma_m = (\sigma_1 + \sigma_2 + \sigma_3)/3$.

Four yield criteria (Tresca, Von Mises, Mohr-Coulomb and Drucker-Pragar) are included in the code. The Tresca Yield Criterion states that yielding begins when the maximum shear stress reaches a critical value, Y/2, characteristic of the material. The maximum shear stress is equal in magnitude to half the difference between the algebraic maximum and minimum principal stresses, $\tau_{max} = (\sigma_1 - \sigma_3)/2$. The parameter, k, is determined experimentally. For yielding in uniaxial compression, when $\sigma_1 = k = Y$, is the yield stress, and $\sigma_2 = \sigma_3 = 0$, the Tresca criterion can be written as, $\sigma_1 - \sigma_3 = Y$. For pure shear, $\sigma_1 = -\sigma_3 = k$ and $\sigma_2 = 0$, it follows that k = Y/2. The Tresca criterion can also be expressed in terms of J'_2,

$$2 \cos\theta\sqrt{J'_2} = Y \qquad (6)$$

where θ, referred to as Lode's angle is given by,

$$\theta = \frac{1}{3} \sin^{-1}\left(- \frac{3\sqrt{3}}{2} \frac{J'_3}{J'^{3/2}_2}\right) \qquad (7)$$

The Von Mises Yield Criterion states that yielding occurs when the invariant of the deviatoric stress, J'_2, reaches a critical value, k^2, where k is a characteristic parameter value of the material. Thus, the Von Mises criterion can be written as,

$$(J'_2)^{1/2} = \{[(\sigma_1 - \sigma_2)^2 + (\sigma_2 - \sigma_3)^2 + (\sigma_3 - \sigma_1)^2]/6\}^{1/2} = k \tag{8}$$

The parameter, k, is determined experimentally. The case of pure shear requires, on the use of Equation 8, that k must be equal to the yield shear stress. For yielding in uniaxial compression, where $\sigma_1 = Y$, the uniaxial yielding stress, it follows that $Y = \sqrt{3} k$. Nadai (1937) introduced a physical meaning to the Von Mises yield criterion by defining the so-called octahedral shear stress, τ_{oct}, which is the shear stress on the planes of a regular octahedron, the apices of which coincide with the principal axes of stress. The value of τ_{oct} is related to J'_2 by, $\tau_{oct} = \sqrt{(2J'_2/3)}$. Thus yield can be interpreted to begin when τ_{oct} reaches a critical value, previously defined. Similar to the Tresca criterion, the Von Mises criterion is independent of hydrostatic stress and only depends on the components of the of the deviator stress.

2.3 The Viscoplastic Material Model

When viscoplastic flow occurs, the viscoplastic strain follows rate follows an associated viscoplastic flow rule of the form (Zienkiewicz et al 1974),

$$\dot{\varepsilon}_{vp} = \gamma <\Phi(F)> \frac{\partial F}{\partial \sigma} \tag{9}$$

where γ is a fluidity parameter controlling the plastic flow rate, defined as $1/\mu$, where μ is the coefficient of dynamic viscosity of the material. The term $<\Phi(F)>$ is a scalar function defined as, $<\Phi(F)> = 0$, if $F \leq 0$ and $<\Phi(F)> = \Phi(F)$, if $F > 0$. F is a function forming the condition for viscoplastic yielding, given by Equations 4 and 5, and where $F = f - Y = 0$ at the onset of viscoplastic behaviour. For example, using the Von Mises criterion, F is given by $\sqrt{3} \sqrt{J'_2} - Y$. Two forms of the flow function, $\Phi(F)$, are employed in the code,

$$\Phi(F) = e^{MF/Y} - 1 \tag{10}$$

$$\Phi(F) = (F/Y)^N \tag{11}$$

where M and N are arbitrary prescribed constants. The calculation of the flow vector $\partial F/\partial \sigma$ is more complex, and details of the method are given by Zienkiewicz et al (1974) and Owen et al (1980). Equation 9 can be used to describe the viscoplastic behaviour of the salt and potash in the post-yield phase. A flow function must be selected, as given by Equations 10 and 11. The parameters to be determined include the fluidity parameter γ, the constant M or N, depending on the flow function selected, and the yield stress.

2.4 The Viscoelastic Material Model

The model describing the viscoelastic material behaviour is a baseline creep law, based on a semi-empirical exponential-time law, and was developed using the principles governed by first order kinetics. The creep law has the general form:

$$\varepsilon = \varepsilon_o + \dot{\varepsilon}_{ss} t + \frac{\varepsilon_a}{C} \dot{\varepsilon}_{ss} [1 - \exp(-B C t)] \tag{12}$$

where ε is the total strain, ε_o is the initial strain related to the elastic response due to loading, $\dot{\varepsilon}_{ss}$ is the steady-state creep rate, ε_a is the asymptotic transient strain, t is the time, and B and C are fitting constants. The instantaneous strain, ε_o, for salt rock and potash, is given by, $\varepsilon_o =$

σ/E, where σ is the applied stress and E the Young's Modulus for the rock. For salt backfill, ϵ_o is nonlinearly dependent on the applied stress, and given by, $\epsilon_o = \sigma/(E_i + E_d\sigma)$, where E_i and E_d are parameters defining the stress dependent behaviour of the modulus of deformation of the backfill. The steady state creep rate, $\dot{\epsilon}_{ss}$, is given as,

$$\dot{\epsilon}_{ss} = A\sigma^n \qquad (13)$$

where σ is the applied stress, A a fitting parameter, and n a fitting exponent. The constitutive law given above contains six parameters that need to be evaluated for a particular soft rock.

2.5 The Mohr-Coulomb Material Model

This criterion is a generalisation of the Coulomb friction failure law defined by,

$$\tau = c - \sigma_n \tan\phi \qquad (14)$$

where τ is the shearing stress, σ_n is the normal stress, c is the cohesion and ϕ is the angle of internal friction. This equation can be rewritten in terms of the principal stresses, $\sigma_1 \geq \sigma_2 \geq \sigma_3$, as,

$$(\sigma_1 - \sigma_3) = 2 c \cos\phi - (\sigma_1 + \sigma_3)\sin\phi \qquad (15)$$

The Mohr-Coulomb criterion can also be expressed in terms of the stress invariants and deviatoric stresses as,

$$\frac{1}{3} J_1 \sin\phi + (J'_2)^{1/2}(\cos\theta - \frac{1}{\sqrt{3}} \sin\theta\sin\phi) = c \cos\phi \qquad (16)$$

where the left term represents the effective stress and the right term the yield stress.

3. ROCK PROPERTY DATA

A laboratory testing and a field instrumentation program were developed to investigate all design parameters and engineering properties of the mine rock formations and backfill material in order to establish the input parameters for the numerical simulations described in this paper. A series of tests and procedures were selected and designed to exactly model the physico-mechanical or rheological characteristics of each material as described in section 2. The determination of design parameters under known, calibrated conditions allowed for the simulation and extrapolation to unknown situations or high extraction layouts.

The laboratory testing program, designed to evaluate the basic mechanical properties and nonlinear time-dependent behaviour of the *potash and evaporites*, was based on models developed to investigate the stability conditions of these geological formations underground, and involved the testing of the materials under creep (to determine long term inelastic strain behaviour and time dependent deformation of rock), uniaxial (to estimate the yield function), and triaxial (to define the failure criteria for the materials) conditions. The following material properties have been determined for the potash. Young's modulus: 4150 MPa; Poisson's ratio: 0.3; fluidity parameter γ (equation 9): 6.69×10^{-9} /MPa.sec; N (equation 11): 1.3; A (equation 13): 2.81×10^{-9} MPa^{-n}sec^{-1}; n (equation 13): 1.1; ϵ_a (equation 12): 1.56×10^{-2}; B (equation 12):

174; C (equation 12): 5.0 x 10^{-8} sec^{-1}. The following material properties have been determined for the salt formation. Young's modulus: 4035 MPa; Poisson's ratio: 0.32; fluidity parameter γ: 5.39 x 10^{-9} /MPa.sec; N: 1.0, A: 1.76 x 10^{-9} $MPa^{-n}sec^{-1}$; n: 1.01; ε_a: 2.88 x 10^{-2}; B: 180; C: 5.0 x 10^{-8} sec^{-1}.

An elaborate laboratory testing program was designed to evaluate the basic geomechanical properties and behaviour of the carbonate members of the *Dawson Bay Formation* and of the mudstone members of the *Red Beds*. Uniaxial and triaxial compression tests were used to estimate the strength properties of the materials and to define the experimental parameters describing the failure conditions of rock and tensile tests were used to estimate the behaviour of the Dawson Bay material under tensile conditions known to occur on the lower section of the formation when it is influenced by bending conditions. The following property values have been determined for the limestone formation. Uniaxial strength: 63 MPa; tensile strength: 6 MPa; cohesion: 12 MPa; Poisson's ratio: 0.11; Young's Modulus: 16000 MPa; friction angle: 37°. These values represent reduced data used to describe the in situ behaviour of the rock mass (jointed rock) and calibrated data based on in situ instrumentation. The second red beds demonstrated the following property values. Uniaxial strength: 13 MPa; tensile strength: 2 MPa; Poisson's ratio: 0.13; Young's Modulus: 3200 MPa; friction angle: 35°.

The suitability of the salt material as *backfill* and to be used as a support mechanism was determined by the investigation of its physico-mechanical behaviour, its strength, and its creep behaviour and failure properties. The following material properties have been determined for the backfill material. E_i (modulus of deformation): 19.6 MPa; E_d: 3.2; A (equation 13): 0.7 x 10^{7} $MPa^{-n}sec^{-1}$; n (equation 13): 0.12; ε_a (equation 12): 1.06 x 10^{-2}; B (equation 12): 159; C (equation 12): 5.1 x 10^{-8} sec^{-1}; uniaxial strength: 4.6 MPa; friction angle: 37°.

4. MODELLING STUDIES

The modelling study presented in this section utilizes data from the laboratory testing program, presented in section 3, and data from a field instrumentation program in order to provide practical and rational means of simulating the introduction of a high extraction potash mining method underground. The approach to the modelling study included the following steps: the identification and technical assessment of an alternative layout which could result in improved extraction ratios; the calibration of the numerical model with respect to known conditions underground as established by the field instrumentation program; the modelling of the alternative layout backed by the information gathered in the laboratory and field research programs; and the evaluation to whether such layout can be practically introduced underground.

A review of the various mining methods employed in the potash industry worldwide was performed to identify optional layouts which would permit the conversion from room and pillar mining, currently used in Saskatchewan, to higher extraction methods. The most favourable method to mine the flat lying and continuous deposits of Saskatchewan, which would ensure the integrity of the mine, was the shortwall retreat mining method incorporating salt backfill and yielding pillars (Figure 2). The yielding pillars would serve to provide support close to the mining face and the backfill would provide the required regional support. The proposed layout shown in Figure 2 utilizes block lengths of 914 metres and widths of 256-640 metres, depending on site conditions. The effective web mined in each pass will have a width equivalent to the width of the machine employed (approximately 5.5 metres). The width and length of the yielding pillars would be optimized as experience is gained; initial widths ranging from 2.0 to 4.6 metres
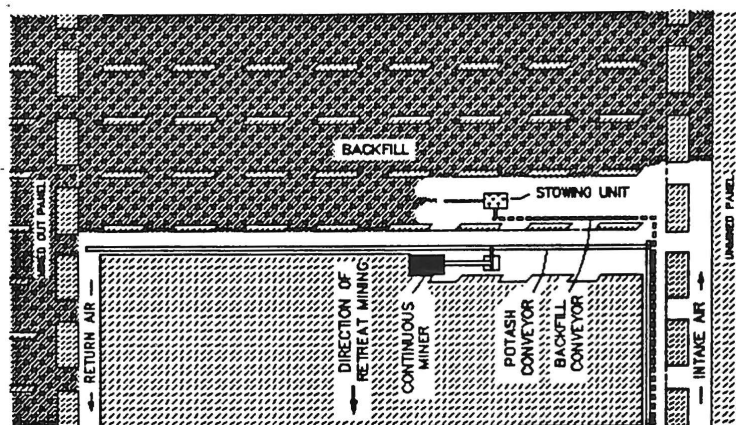
Figure 2. Shortwall Mining

and initial lengths in the order of 5 to 9 metres are suggested. The pillars would be left at every 11 metres of face retreat, that is, at every two passes of the mining machine. Backfilling is performed in the goaf area behind the yielding pillars. Using such layouts, improved panel recoveries would be achievable.

4.1 Code Calibration

The calibration of the finite element code was based on the modelling of an instrumented mine panel. An iterative procedure was employed for the calibration of the code. The method of calibration included the performing of a number of computer runs to first examine the sensitivity of the analysis to each parameter describing a particular material, to examine the sensitivity of the model to the assumptions made to mathematically describe material behaviour, and to determine which parameters should be more carefully evaluated during the calibration of the code according to known field measurements. This would not only assure that a direct correspondence between laboratory determinations and field observations is achieved, but establishes if the assumptions made to derive the analytical models and constitutive relations are accurate and valid to describe the rock masses. Based on this calibration procedure, preliminary field predictions were made, and the inconsistencies existing between field measurements and model predictions were improved at each run. This cycle was repeated several times to improve the correlation between the field and model results to a point where favourable agreement and sufficient accuracy was achieved.

The finite element grid used in the calibration analysis is illustrated in Figure 3. Eight-noded quadratic serendipity elements were used to accurately describe the non linear behaviour of the rock masses. A total of 209 elements, defined by a total of 709 nodes, were used in the discretization procedure. The Dawson Bay Formation, the Second Red Beds, two potash zones, and the Prairie Evaporites were modelled, thus constituting the actual geological setting existing underground (Figure 1). Advantage was taken of the symmetry existing in the underground layout to minimize the size of the model. The vertical boundaries of the model were established at the top of the Dawson Bay Formation and at the mid-height of the Prairie Evaporite below the mining zone. The lateral boundaries were established at the mid-section of the panel and at the mid-section of the barrier pillar, and were treated as planes of symmetry, thereby simulating the array of panels mined parallel to the instrumented panel. The input data included the nodes and nodal coordinates forming each element, the boundary conditions in the form

95
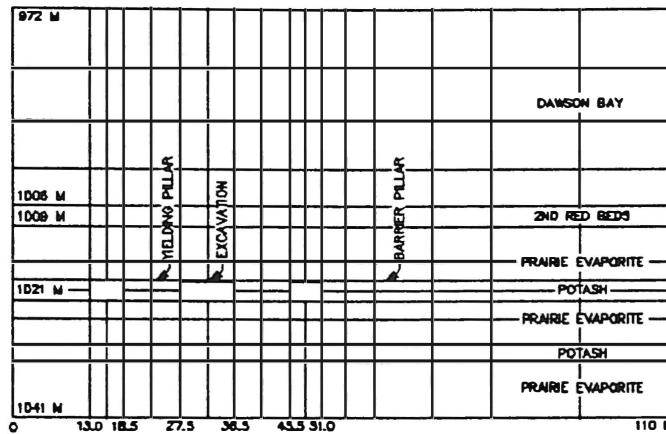
Figure 3. Mesh Used For Code Calibration (Room and Pillar Mining)

of boundary loads and restrained nodes, all necessary material properties (section 3), and the time stepping and load increment parameters. Yielding pillar behaviour was simulated by reducing the modulus and by increasing the Poisson's ratio of the potash rock forming the yielding pillar pattern. Reductions in 50 to 75% of the rock modulus, and an increase in 75% in the Poisson's ratio were used. The pre-mining vertical stress used was 20.6 MPa at the mining depth, with a horizontal to vertical stress ratio of 0.5.

The calibration procedure was performed in several stages. First, the pre-mining stresses were generated from overburden and gravity loading. Loads equivalent to the initial stress were calculated, and then relaxed in a limited time interval to simulate excavation of the panel. The non linear stress-strain calculations were then performed in real time, taking into account the existing field conditions due to room excavation. Each run was designed to simulate the stress and strain conditions occurring since the excavation of the panel, in order to evaluate the conditions encountered prior to, during, and after mining, up to the time when the monitoring program was established in the panel. During correlation of model and laboratory and field measurements, the elastic properties describing the behaviour of the Dawson Bay limestone and Red Bed mudstone were found to be within the range to be expected for these rock formations. The coefficients in the creep equations for the salt, potash and backfill are also very similar to those obtained in the laboratory tests. The values of the coefficient A (Equation 13) were adjusted by a reduction factor of 10^{-1} in view of the expected differences due to scaling, shape and confinement effects. The approach used to establish agreement between the developed model and the field and experimental data has resulted in the following conclusions: a) Favourable correlation between the predictions made using the theoretical models used in the computer code, the material parameters determined in laboratory tests, and the direct field measurements, was achieved; b) All material parameters used during the calibration scheme were based on the experimental data. In the process of fitting the model to the field data, the final values of the model parameters were within the range of values given by the experimental data, which suggests the validity of the laboratory and field determinations; c) Consistent and accurate correlation between the predicted material behaviour and the large scale field measurements could only be achieved when the input model parameters were selected close to the established final values; d) The predicted strata behaviour and failure conditions were in close correspondence with those observed underground. Based on the above discussion it was concluded that calibrated code could be confidently used for the evaluation of a full-scale high extraction underground operation.

4.2 Modelling of a Single High Extraction Panel

The modelling of the shortwall mining method with backfill performed was of a cross-section through an active face with a backfilled gob. The finite element grid used in the analysis is illustrated in Figure 4. A total of 168 eight-noded quadratic serendipity elements were used in the discretization procedure. The lateral boundaries of the model were located 180 metres in the potash seam in advance of the last simulated face in the model and 180 metres back from a 169 metre backfilled gob section, established at the end of the simulation runs. The working face was 11 metres wide, equivalent to the second pass of the miner. The simulation analysis included the determination of the node loads equivalent to the stress condition existing prior to the retreat to a new working face, and then the relaxation of these loads in a prescribed time interval to simulate the retreat of the face by two miner passes. The non linear stress-strain calculations were performed in real time, taking into account the existing field conditions due to room excavation and due to backfilling. Fourteen runs were performed to simulate the retreat of the face from the beginning of the panel, 180 metres into the potash seam. Each run simulated two passes of the miner, each pass being 5.5 metres wide (miner width). After each two pass extractions, a yielding pillar 2 metres wide is left, and the previous excavation is backfilled. Each run simulated a 51.2 hour cycle. This time of retreating 11 metres of face was estimated based on a face 384 metres long and on a miner advance rate of 15 metres/hour. A mining simulation schedule totalling 716.8 hours was thus established to evaluate the ground reactions to active mining conditions in which the face would have retreated from the beginning of the panel, 180 metres into the potash seam.
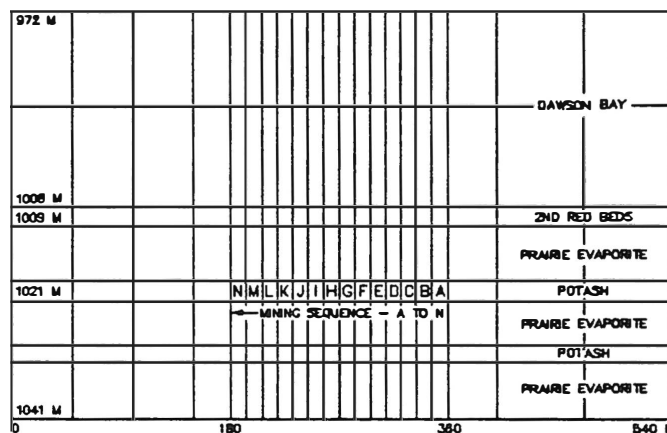
Figure 4. Mesh For a Shortwall Panel

Excavation simulation was performed in a way which the stress conditions established in the end of a face retreat sequence, simulated in an independent computer run, were subsequently used as the initial conditions for a new face retreat, in a new run. Referring to Figure 4, the face retreat was computer simulated in the following manner. In the first run, element A was excavated and the stress/strain conditions due to the development and retreat of the face in two passes were established. The second run was performed using as initial stress conditions the total stresses present due to excavation of the face in the first run (element A). In this run, element A was backfilled and element B was excavated. The stress conditions due to this new configuration were estimated and used in the next excavation run. This procedure was repeated until the fourteenth run was complete to simulate the excavation of the last face in the model (element N), and the sequential backfilling of the previous excavations (elements A to M).

Figure 5 shows the stress conditions along the mine level, in the salt back, and in the Dawson Bay Formation, at the time the last face in the model is developed (element N in Figure 4), and at different times of previous face retreat and backfilling. From a zero stress condition at the face, the stress increased to a maximum value in the abutment zone beyond which it decreased again, and ultimately attained the pre-mining stress level. The peak stress reached magnitudes 1.36 times the original virgin stress level. The deflected position of the peak stress from the face into the unmined seam was due to yield and fracture of the immediate face. The depth from the face at which undisturbed stress conditions were attained was estimated at about 130 metres. The immediate backfilled gob did not carry any superincumbent load at placement time. On the other hand, stress conditions had been developed in the mid section of the gob area (backfill provided partial support), which had been mined and backfilled 358.4 hours prior to the existing face. Further back into the gob area, the backfill, at 716.8 hours after placement,
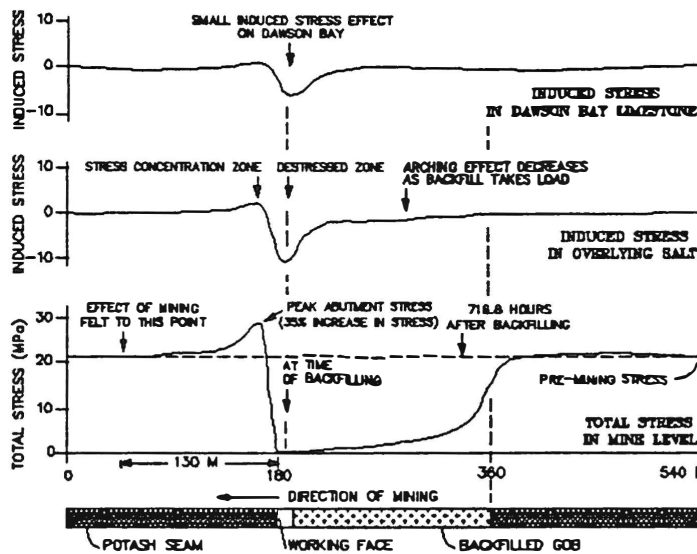
Figure 5. Stress Conditions Around a Shortwall Face

had developed higher support capability. At this time, however, full load development had not yet been achieved. Further modelling has indicated that it takes approximately 7920 hours for the backfill to provide high support to the back for a panel 384 metres wide. The induced stress existing in the overlying salt and limestone formations are also shown in Figure 5. The abutment stresses affect both formations to a small extent. Also, an arching effect, resulting from a zone of stress relief, was noted to develop. This zone of decreasing stress concentration extended from the abutment area onto the gob section, to a depth where the back was still unsupported by the backfill. The influence of those disturbed zones were noted to decrease as the backfill developed load. Figure 6 shows the strain profile occurring across the backfilled section. Approximately 10% maximum strain occurred in the mid panel section before the backfill started to develop load; the strain rate decreased with time as the backfill became stronger. At a time 358 hours after mining, the mid section of the panel had reached 12% strain.

The modelling of multiple high extraction panels was also developed in order to evaluate the general interaction between the backfill and surrounding strata, and to estimate the time required for full backfill load development before the unmined section between two mined out panels could be extracted, thus simulating a sequential retreat strategy. Mine induced stress and strain conditions and backfill load development were evaluated every 360 hours, for a period

of 8640 hours (360 days), to evaluate the long term interaction between the backfill and surrounding strata. The results indicated that high load carrying and support capability was developed within the backfill approximately 11 months after placement. At this point in time, mining of the ore block remaining between the backfilled panels would proceed, as the consolidated backfill would provide the necessary ground support to ensure that stable conditions are maintained during mining. At this time, approximately 26% vertical strain had occurred across the mid-section of each backfilled panel. Approximately 11% maximum strain occurred in the before the backfill started to develop load. The effectiveness of the backfill as a ground support mechanism is indicated by a 74% decrease in potential subsidence, achieved in the mid-section of the panels, 11 months after backfilling. The results obtained from the numerical analyses give an overall indication of the practicality of shortwall mining.
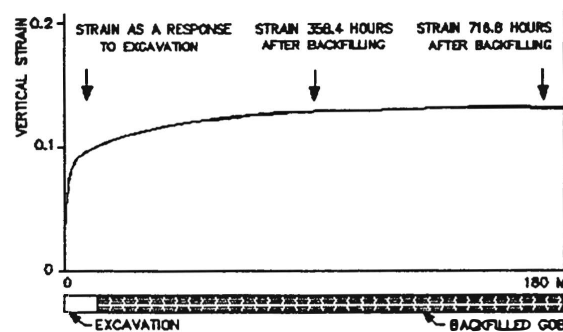
Figure 6. Strain Profile Around a Shortwall Face

5. CONCLUSIONS

This paper presented a procedure developed to model a high extraction mining strategy which utilizes salt tailings as backfill. The finite element code and the constitutive models and yield criteria used to develop the mine simulation models were described, and the iterative procedure developed for the calibration of the numerical model with respect to known conditions underground was introduced. It was noted that only after the calibration study achieved consistent and accurate correlation between the model and the field data that the code could be confidently used for the evaluation of alternative layouts. Although the model results indicated the practicality of high extraction methods, they do not endorse the direct use of the technique underground. Extensive work is still required to evaluate the risk of flooding associated with high extraction mining and extensive controlled field trials would be imperative for verifying the strata behaviour under actual conditions.

REFERENCES

Owen, D.R.J. and Hinton, E. (1980), Finite Elements in Plasticity: Theory and Practice. Pineridge Press Limited, Swansea, U.K., 594 pages.

Cormeau, I. (1975), Numerical Stability in Quasi-Static Elasto/Visco-Plasticity. International Journal for Numerical Methods in Engineering, vol. 9, pp. 109-127.

Bridgman, P.W. (1952), Studies in Large Plastic Flow and Fracture. cGraw-Hill, New York.

Nadai, A. (1937), Plastic Behaviour of Metals in the Strain Hardening Range. Journal of Applied Physics, vol. 8.

Zienkiewicz, O. C. and Cormeau, I. C. (1974), Visco-plasticity - Plasticity and Creep in Elastic Solids - A Unified Numerical Solution Approach. International Journal for Numerical Methods in Engineering, vol. 8, pp. 821-845.

Session 3

Coal Mining

Mines de charbon

Modélisation du comportement du foudroyage par la méthode des éléments distincts : cas d'une longue taille

Al Heib M.M. : Ingénieur en thèse. Ecole des Mines de Nancy-INERIS
Piguet J.P. : Prof. Ecole des Mines de Nancy-INERIS
Ben Slimane K. : Ingénieur INERIS

RESUME

L'article porte sur la modélisation numérique du comportement d'une taille foudroyée en milieu stratifié, et sur son interaction avec le massif. La modélisation vise à étudier particulièrement le processus ou bien le déroulement du phénomène de foudroyage et non pas le mécanisme complet. On étudie le processus de la chute des blocs du foudroyage et ses conséquences pour le reste de l'environnement (affaissements, modifications de chargement etc...). La méthodologie suivante est adoptée en considérant que le calcul se fait en trois étapes principales :

1- une phase de consolidation sans excavation. Pendant cette phase, les joints verticaux ont un angle de frottement très élevé. 2 - une phase simulant l'avancement de la taille. 3 - la dernière phase correspond au foudroyage. Les joints dans la zone foudroyée se voient attribuer un angle de frottement très faible.

Une validation des résultats est établie entre les mesures d'affaissement in situ et le modèle. De plus, une comparaison avec les résultats d'un modèle continu a été réalisée.

ABSTRACT

The model simulates a longwall mining face. The behaviour of rocks mass can be studied by using Distincts Elements method. We are using numerical models for studying the interaction between the rock mass and the mining zone. The model particularly analyses the processus of the goaf phenomena but not the complete mechanism. We study the blocks movement and the consequences for the environment (subsidence, stresses modification, etc...). We analyse the conditions for the first movement of goaf, the evolution and the concerned volume of rock. The methodology adopted follows three main steps :

- a consolidation phase without excavation in which the induced joints have a very high friction angle - simulation of longwall mining excavation. - the third step is the goaf processus. The joints of the goaf zone have very small friction angle.

The validation of the results is set up between the curve of in situ subsidence measurements and the values of subsidence model. Thus, a comparison has been achieved between the results of finite elements models and distinct elements models. The results are encouraging for planification problems.

1. Introduction

En général, les modélisations numériques des excavations minières par foudroyage ne prennent pas en compte la forme géométrique finale de l'assemblage de blocs constitué par le foudroyage des bancs du toit. La zone considérée par ce processus peut être assez importante et son extension dépend de la profondeur, des caractéristiques de la roche, de l'état de contrainte, etc... Plusieurs auteurs (1) ont déduit la forme du foudroyage à partir d'observations in situ et de modélisation physique (2, 3). Il s'agit de blocs plus ou moins séparés par des vides (4). Avant le foudroyage, ces blocs étaient délimités par des plans de stratification d'une part, par un réseau de fissures engendrées par la rupture des bancs du toit (Fig 1) d'autre part.

Nous nous proposons de simuler numériquement le processus du foudroyage et d'en étudier les interactions avec le massif. Une étude de sensibilité aux paramètres géométriques et géomécaniques a été conduite. Nous avons utilisé le code UDEC (ITASCA) pour notre modélisation; celui-ci avait déjà été utilisé par d'autres auteurs pour étudier l'influence d'une taille dans un milieu discontinu (5).

2. Présentation des modèles

2.1. Géométrie du modèle

Le modèle est présenté sur la figure 2. Nous avons considéré que le milieu est stratifié. Des joints horizontaux sont introduits au toit et au mur de la couche de charbon. La distance entre ces joints horizontaux est égale à 25 m pour le haut toit. On estime que l'épaisseur du bas toit est de l'ordre d'une dizaine de mètres et qu'il est composé de plusieurs bancs minces (6). Nous avons modélisé ici un bas toit de 20 m d'épaisseur avec des bancs de 5 m.

Par ailleurs, le toit et le mur sont prédécoupés par des discontinuités verticales, formant avec la stratification des grands blocs de dimensions 25 x 25 m. Elles sont introduites au toit et au mur de la couche exploitée, sur une distance de 50 m seulement à partir de la couche.

La zone du foudroyage prévu est décomposée sous forme de petits blocs. Les dimensions de cette zone sont égales à 65 x 15 m. Des joints plus ou moins verticaux (90° ± 20°) sont introduits et correspondent aux fissures engendrées par la rupture du bas toit. La distance entre ces joints est de 5 m. Les volumes des blocs dans cette zone varient entre 20 et 80 m³ en considérant une épaisseur unitaire du modèle de 1 m, 80 % de ces blocs ont un volume de 25 m³. Ce modèle comprend au total 128 blocs totalement déformables, 2195 éléments et 1874 noeuds. Les éléments au sein des blocs sont de type triangulaire à 3 noeuds.

2.2. Conditions aux limites

Nous avons empêché les déplacements verticaux à la partie inférieure du modèle, ainsi que les déplacements horizontaux aux deux bords du modèle, l'un à cause de la symétrie, l'autre parce qu'il est considéré comme très loin de l'excavation. Le bord supérieur a des

déplacements libres. La taille modélisée est située à 850 m de profondeur. Le modèle est chargé
avec des contraintes verticales dues au poids des terrains sus-jacents.
Le rapport des contraintes Horizontales /Verticales est égal à 0.5.
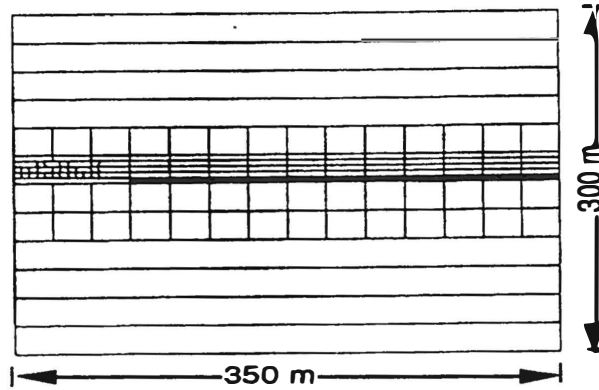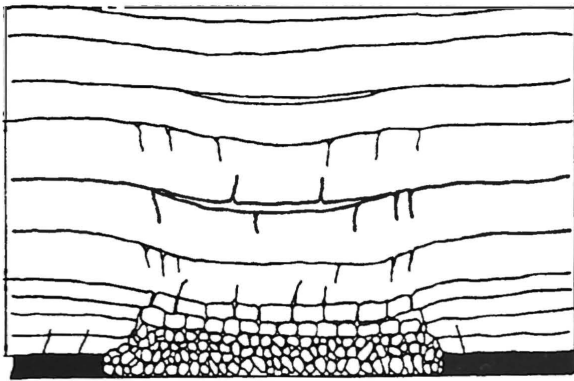
Fig. 1: Répartition des zones au-dessus la taille

Fig. 2 : Modèle d'étude par la méthode des éléments distincts (UDEC)

2.3. Caractéristiques géomécaniques

Les caractéristiques géomécaniques des roches (le toit et le mur en calcaire et la couche
de charbon) et des joints sont représentées dans le tableau 1. En ce qui concerne les joints, ils
sont divisés en trois groupes de caractéristiques différentes :

- les joints horizontaux;

- les joints verticaux à large pas ;

- les joints horizontaux et verticaux dans la zone foudroyée à pas resserré.

Les raideurs normales (K_n) et les raideurs tangentielles (K_s) sont identiques pour les trois

MATERIAUX	E (MPa)	v	K (MPa)	G (MPa)	Kn (MPa/m)	Ks (MPa/m)	ϕi	ϕf
1 : Calcaire	10000	0,1	4500	4200				
2 : Charbon	2000	0,3	1700	770				
3 :Joints horizontaux					10000	10000	50°	50°
4 : Joints Verticaux					10000	10000	89°	50°
5 : Joints de foudroyage					10000	10000	89°	15°

Tableau 1 : Caractéristiques géomécaniques du modèle

102

familles. Nous avons considéré que les joints ne disposent ni de cohésion ni de résistance à la traction.

3. Phases du calcul

Nous avons adopté la méthodologie suivante en considérant que le calcul se fait en trois étapes principales :

.1- une phase de consolidation sans excavation après laquelle nous devons obtenir les contraintes initiales dans le massif avant toute excavation. Pendant cette phase, les joints verticaux ont un angle de frottement initial très élevé égal à 89° ($\tan\phi i = 100$). Ils sont considérés en fait comme des joints fictifs. A la suite de cette phase, nous initialisons à nouveau les déplacements (dûs à la consolidation) à zéro ; les déplacements finaux seront donc uniquement dus à l'excavation.

2- une phase simulant l'excavation et l'avancement de la taille, pendant laquelle nous gardons les caractéristiques mécaniques initiales des joints. Une nouvelle distribution des contraintes s'établira dans les blocs du modèle.

3- la dernière phase correspond au foudroyage. Les fractures induites par l'exploitation commencent à apparaître au toit et au mur. Pour simuler cela, on modifie l'angle de frottement des fractures qui devient égal à 50° (angle final, $\tan\phi f = 1,25$).

Les fractures dans la zone foudroyée (joints horizontaux et verticaux) se voient attribuer un angle de frottement très faible de l'ordre de 15° ($\tan\phi f = 0,25$). Le calcul se poursuit (en augmentant le nombre de cycles) jusqu'à ce que l'on obtienne un nouvel équilibre de l'ensemble des blocs.

4. Résultats et analyses

4.1. Description du mouvement

Nous constatons qu'après le creusement de l'excavation (au terme de 3000 cycles de calcul), les blocs formant la zone foudroyée fléchissent ensemble. Les blocs formant le mur se déplacent vers le vide très rapidement et cessent de se déplacer dans la suite du calcul. Les premiers blocs du bas toit entrent en contact avec le mur après 7000 cycles. Les blocs du haut toit, à 25 m de la couche exploitée, suivent le mouvement. A 12000 cycles, le nombre de blocs qui reposent sur le mur augmente. Des vides apparaissent dans toute la zone de manière aléatoire. Les nouveaux vides sont surestimés car le foisonnement de blocs n'est pas introduit dans les calculs. En raison d'un fort confinement dans cette zone, certains blocs sont stables. Des arcs-boutements se forment par rotation des blocs. L'équilibre total est atteint après 33000 cycles. La forme finale du foudroyage est présentée sur la figure 3. Le déplacement final des blocs du bas toit est égal à l'ouverture de la couche de charbon. Cette forme du foudroyage est comparable à celle qui est observée dans la mine (Fig. 1).

Les fortes concentrations des contraintes de compression enveloppent un volume important. Elles se localisent aux bords de la taille jusqu'à 50 m au-dessus de la couche
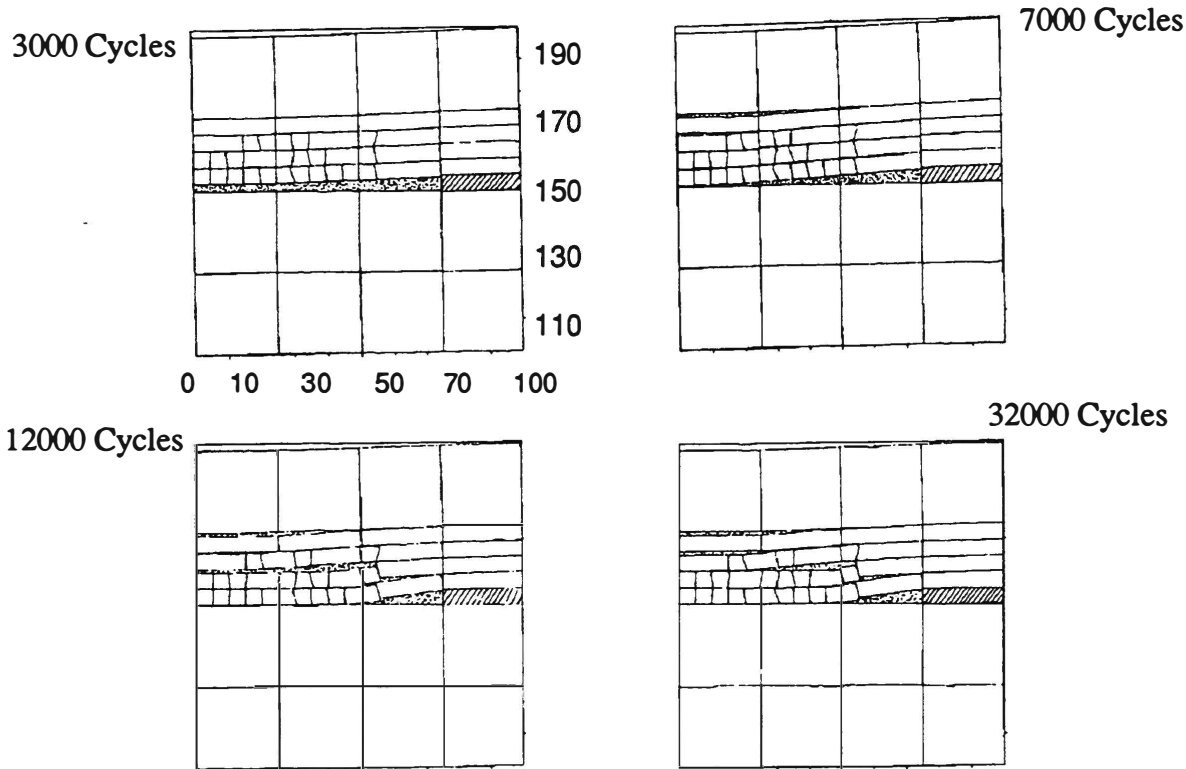
Fig. 3 : Etat des blocs dans la zone foudroyée en fonction du nombre de cycles

exploitée. Elles se trouvent aussi dans le haut toit à plusieurs niveaux (à 70 , 90 et 120 m de la couche exploitée), au milieu de la taille avec des valeurs moins importantes. Les contraintes principales de traction sont associées aux fortes contraintes de compression aux bords de la taille. Elles sont aussi très importantes dans les fibres inférieures des bancs de haut toit et à plusieurs niveaux. La contrainte de traction vaut environ 4 fois la contrainte horizontale initiale qui était en compression. L'extension de la zone détendue, qui peut intéresser pratiquement une grande surface d'un plan de faille ou une discontinuité, peut faciliter un cisaillement sur le plan de faille qui induira une sollicitation dynamique dans les chantiers pouvant se traduire en des coups de terrains, même dans le cas d'une taille isolée (7, 8, et 9). Dans la zone foudroyée, les contraintes de traction varient entre 1 MPa et 2,5 MPa. En revanche, les contraintes de compression varient entre 2 MPa et 25 MPa, pour une contrainte initiale verticale de 20 MPa.

4.4. Comportement d'un banc de stratification

Les bancs de stratification ont un comportement à la flexion semblable au comportement de poutres encastrées. Les contraintes horizontales sur la fibre inférieure sont des tractions. La

valeur maximale est au milieu de la taille. Aux bords de la taille, cette contrainte horizontale s'annule. A la fibre supérieure, entre le bord de la taille et une distance de 100 m, de part et d'autre les contraintes horizontales sont en traction. A partir de 250 m du milieu de la taille, les contraintes horizontales retrouvent leur valeur initiale soit 10 MPa. Les contraintes de traction vont jusqu'à la surface du modèle. Il faut envisager des risques de rupture soit par traction dans la partie inférieure des bancs et aux bords de la taille, soit par cisaillement dans la partie supérieure.

4.5. Courbe d'affaissement

L'affaissement maximal à la surface du modèle, à 170 m de la couche exploitée, est égal à 2 m, soit 40 % de l'ouverture de la couche exploitée (Fig. 4). Cette valeur est nettement plus importante que celle trouvée par la méthode des Eléments Finis (30 cm). Le rapport entre les deux modèles (Eléments Distincts / Eléments Finis) est égal à 7. L'affaissement est nul à une distance égale à 200 m du milieu de l'excavation en Eléments Distincts, alors que cette distance est de 300 m en Eléments Finis. Cette différence s'explique par la présence de la stratification dans le modèle en Eléments Distincts pour lequel on modélise plusieurs bancs qui ont la possibilité de fléchir de façon plus importante que dans le cas des Eléments finis où un seul banc est modélisé.

5. Influence des dimensions du modèle

Le modèle présenté ci-dessus a les dimensions d'un modèle continu étudié par la méthode des Eléments Finis. En modélisation, les dimensions du modèle doivent assurer des résultats indépendants des effets de bords. Pour valider nos calculs à partir de l'affaissement à la surface, nous avons été obligés de construire deux autres modèles numériques avec des limites jusqu'à la surface appelés modèle B et modèle C. Ceux-ci permettent d'étudier l'influence de la hauteur et de la largeur du modèle initial (fig. 2), appelé désormais modèle A.

Les dimensions du modèle B sont égales à 350 x 1000 m, 700 m correspondant aux terrains sus-jacents. Cette partie (350 x 700 m) est supposée homogène, isotrope et sans stratification. Les dimensions du modèle C sont égales à 1000 x 1000 m. Pour les autres données, les deux modèles B et C sont identiques au modèle A.

La comparaison entre les modèles nous permet de constater que les contraintes et les déplacements sont plus importants dans le modèle A (Tableau 2). Les contraintes sont pratiquement multipliées par 2.

L'affaissement au milieu de la taille, à 150 m au-dessus de la couche exploitée (Fig. 4), est 2 et 4 fois l'affaissement maximal des modèles B et C respectivement.

L'affaissement maximal à la surface des modèles B et C est égal à 29 et 14 cm respectivement. L'affaissement est nul à une distance égale à 125 m du bord de la taille pour

Modèle	σ max compression (MPa)	σ max traction (MPa)	Amax (m)
A	172	48	2
B	105	19	1
C	95	29	0,5
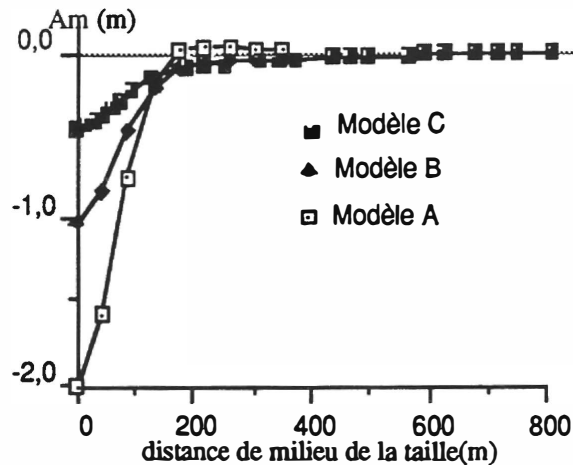
Tableau 2 : Contraintes maximales et affaissement maximal à 150 m au toit de la couche

Fig. 4 : Courbes d'affaissement à une distance verticale de la couche de 150 m

le modèle initial, alors qu'il est à une distance de 625 m du bord de la taille pour le modèle C. En revanche, l'affaissement est pratiquement constant sur toute la limite supérieure dans le cas du modèle B.

En analysant les valeurs d'affaissement en fonction du rapport (largeur / profondeur)[1], celui-ci s'avere différent dans les modèles A, B et C. Pour le modèle A, il est égal à 1 contre seulement 0,18 pour le modèle B. On dépasse donc la largeur critique égale 0,4 H, pour le premier modèle, ce qui n'est pas le cas pour le modèle B.
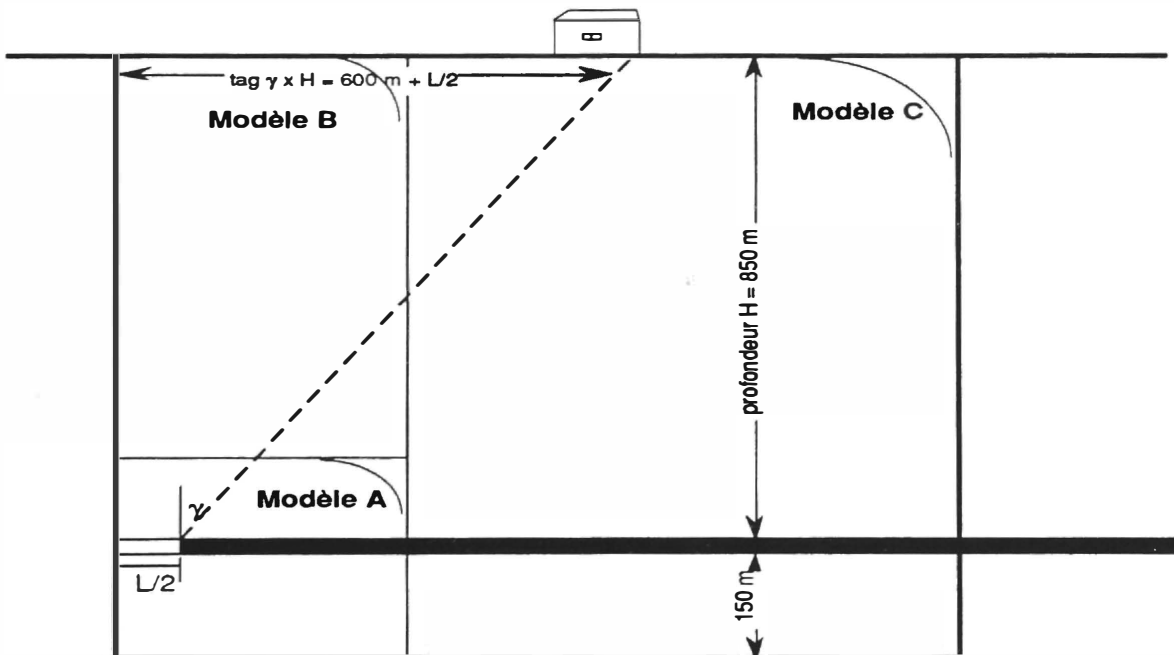
Fig 5 : Limites de 3 modèles en éléments distincts et affaissement induit par l'exploitation d'une taille de 150 m

La figure 5 permet d'expliquer la différence concernant l'affaissement entre ces trois modèles. Si on choisit un angle d'influence "γ" égal à 45°, le modèle A devrait avoir un déplacement induit par l'exploitation nul au-delà d'une distance égale à 225 m. La valeur fournie par le calcul est égale à 200 m. En revanche, l'affaissement maximal à la surface du modèle est supérieur à la valeur qui pourrait être réellement mesurable à la surface du sol.

Nous ne constatons pas un déplacement nul dans le cas du modèle B (Fig. 6), cela correspond aussi aux mesures d'affaissement. La valeur de l'affaissement maximal y est surestimée parce que la largeur du modèle est inférieure à la largeur de la zone d'influence, lors de laquelle les terrains ne s'affaissent plus.

En conséquence, le modèle C permet une estimation de l'affaissement à la surface. L'affaissement maximal est égal à 15 cm soit 3% de l'ouverture de la couche exploitée. Cette valeur est tout à fait représentative d'une taille isolée à 850 m de profondeur.

6. Influence de la largeur du panneau.

On a fait varier la largeur exploitée dans le modèle de 100 m à 500 m. Le modèle employé correspond au modèle B (350x1000 m). La hauteur de la zone foudroyée varie en fonction de la largeur du panneau.

En ce qui concerne les contraintes maximales, la contrainte de traction maximale varie entre 6 MPa et 23 MPa, la première valeur correspond à une taille de 100 m de largeur, les autres valeurs de la contrainte de traction ne dépendent pas de la largeur exploitée. Ces contraintes vont peut-être provoquer une rupture plus ou moins violente dans le cas d'une roche intacte, qui ne résiste pas à des tractions aussi élevées, ou destabiliter des discontinuités existantes.

En ce qui concerne les contraintes principales maximales de compression obtenues dans
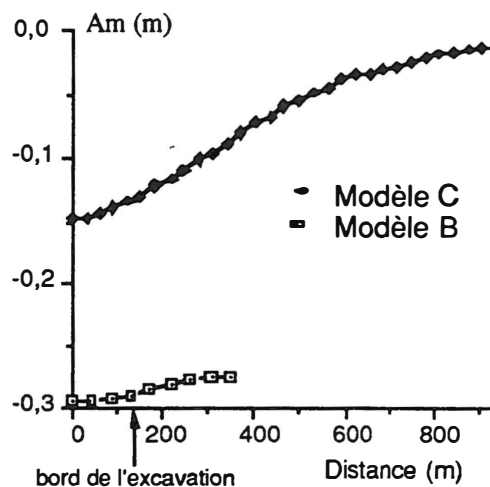
Fig. 6 : Courbes d'affaissements à la surface
pour une taille de 150 m
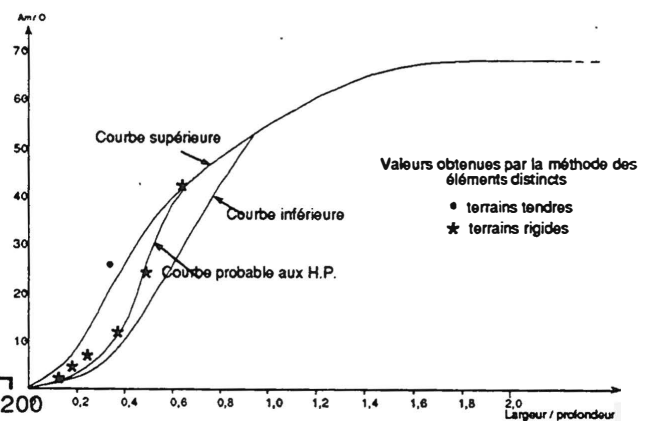
Fig. 7 : Affaissement pour différents
rapports largeur/profondeur

les calculs, elles augmentent linéairement en fonction de la largeur du panneau, et varient entre 80 et 175 MPa. Leurs valeurs sont plus importantes que celles obtenues avec les modèles continus, notamment pour des tailles de petites largeurs.

Les résultats de la modélisation montrent que l'affaissement maximal (Am) à la surface du modèle varie en fonction de la largeur exploitée. Pour une taille de 100 m, l'affaissement maximal à la surface est égal à 10 cm, pour une largeur de 500 m, il est égal à 2,17 m soit 43 % de l'ouverture de la couche exploitée.

La coupe modélisée représente le cas d'une taille des Houillères de Provence (10). Nous avons présenté sur la courbe empirique, les rapports (affaissement maximal / ouverture) obtenus par la modélisation en milieu discontinu (Eléments Distincts) (Fig. 7). Nous constatons une bonne concordance entre les courbes de mesures et les valeurs de la modélisation.

7. Etude paramètrique

Des études de sensibilité sont réalisées sur les paramètres qui déterminent la forme prise par le foudroyage, tels que la taille des blocs dans la zone du foudroyage ou la distance entre les joints horizontaux dits de stratification. Suivent des études qui concement les caractéristiques des joints comme l'angle de frottement, la raideur tangentielle et la raideur normale et enfin, l'influence du tenseur des contraintes initiales avec la présence d'un banc de caractéristiques différentes du reste du massif.

La densité de stratification influence les résultats. Deux familles sont mises en évidence : les modèles à bancs minces et les modèles à bancs d'une épaisseur importante. L'affaissement maximal est égal à 2,75 et 0,5 m pour des bancs de 5 et 150 m respectivement.

La taille des blocs dans la zone foudroyée semble avoir un effet qui se limite à cette zone et qui pratiquement disparaît à l'échelle du massif.

L'angle de frottement ainsi que le tenseur initial des contraintes modifient le mode de foudroyage et surtout la contrainte horizontale. Trois modes de foudroyage ont été observés selon la valeur du rapport des contraintes initiales (K). L'influence de l'angle de frottement se manifeste dans la zone entourant la région foudroyée où les contraintes dépassent le critère de rupture et dépendent donc de la valeur choisie pour l'angle de frottement.

Les raideurs normale et tangentielle sont aussi des paramètres qui modifient le comportement du massif après l'excavation. Des raideurs normale et tangentielle très élevées empêchent la formation du foudroyage localement et la continuité des bancs est assurée. L'affaissement à la surface du modèle diminue jusque quasiment zéro dans les cas où ces valeurs sont très élevées. La raideur tangentielle a un rôle moins important que la raideur normale.

Dans notre cas, il apparaît que certains paramètres tels que la raideur tangentielle et la taille des blocs dans la zone de foudroyage ne nécessitent pas d'être estimés avec une grande précision. En revanche, le tenseur initial de contraintes, la densité de stratification et la raideur normale nécessitent une investigation plus importante pour pouvoir obtenir des résultats

8. Conclusion

La méthode des Elément Distincts employée semble particulièrement adaptée à ce problème de modélisation. Nous avons pu montrer l'efficacité de cette méthode de modélisation surtout en ce qui concerne l'affaissement à la surface de l'exploitation. Les modèles permettent d'estimer la courbe d'affaissement. Ce qui était impossible dans le cas des modèles en milieu continu malgré les hypothèses sur les caractéristiques mécaniques des terrains. De plus, nous avons décrit les mouvements des blocs et de bancs de stratification qualitativement. La distribution des contraintes dans le massif, peut correspondre à celle engendrée après l'exploitation dans un milieu stratifié.

Il faut signaler que les résultats de ces modèles sont très différents des résultats obtenus à partir d'un modèle en milieu continu, principalement pour les trois points suivants :

1- les valeurs des contraintes maximales aux bords et au milieu de la taille; 2- la distribution des contraintes après l'exploitation; 3- l'affaissement à la surface.

Les dimensions du modèle sont très importantes pour la qualité des résultats. Elles jouent un rôle essentiel sur le comportement du foudroyage, les contraintes et l'affaissement à la surface.

[1] Largeur : la largeur du front de la taille.

Profondeur : la profondeur à laquelle se trouve la taille.

[2] Cette courbe résulte de nombreuses études statistiques effectuées entre 1977 et 1980 à partir des données issues de mesures le long du canal de Provence.

Bibliographie :

1. **LABASSE H. 1973** : Les pressions de terrains dans les carrières souterraines. Coups de toit et coups de charge. Rev. Industrie Minérale, 3 : 141-160.

2- **LINGLI Z. 1990** : Contribution à l'étude du foudroyage en travaux miniers par modélisation physique en matériaux équivalents INPL-NANCY.

3. **WOLD M.B. 1985** : A blocky physical model of longwall caving under strong roof conditions 26Th US Symposium on Rock Mechanics / Rapid City p.p. 1007-1015.

4. **PENG S.S. & CHANG H.S. 1984** : Longwall Mining New York Wiley.

5. **CHOI S.K. & COULTHARD M.A. 1990** : Modeling of jointed rock masses using the distinct element method. CSIRO Division of Geomechanics, Melbourne AUSTRALIA p.p. 471-477.

6. **CHAMBON C. 1985** : A la recherche d'un critère pour le calcul de la force portante du soutènement dans une taille, Rapport interne, Laboratoire de Mécanique des Terrains, France.

7. **BENSLIMANE K. 1990** : Sismicité induite et exploitation. Etude CECA n°7220-AF/308. Rapport Final 45p.

8. **REVALOR R. 1991** : La maîtrise des coups de terrains dans les exploitations minières. Thèse INPL 135 p.

9. **KNOL P. & KUHNT W. 1988** : Seismological and geotechnical investigations of the mechanics of Rockbursts. Proc. 2nd Int Symp. "Rockbursts and sismicity in mines", Minneapolis.

10. **ARCAMONE J. 1980** : Méthodologie d'étude des affaissements miniers en exploitation totale et partielle. Thèse INPL. 100 p.

MODELING OVERBURDEN RESPONSE TO LONGWALL MINING

J. A. Siekmeier and K. M. O'Connor
U.S. Bureau of Mines, Twin Cities Research Center

ABSTRACT

This paper presents research, conducted by the U.S. Department of the Interior, Bureau of Mines (Bureau), on modeling overburden response to longwall mining in Illinois. The goal of this research is to define the probable mechanics of rock mass failure over longwall coal mines. The commercially available Universal Distinct Element Code[1] (UDEC) is being used to simulate the plane strain response of a 900-meter-long 200-meter-thick slice of horizontally bedded sedimentary rock along the centerline of a longwall panel. A procedure has been developed to systematically locate horizontal discontinuities within the model based on drill-core logs and rock-mass ratings. Simulated displacements along these discontinuities are consistent with those obtained using time domain reflectometry (TDR). In agreement with previous studies, it has been found that these horizontal discontinuities affect both the magnitude and curvature of the surface subsidence profile.

RÉSUMÉ

Cette communication présente un compte-rendu de recherches faites par le U.S. Bureau of Mines, sur la modélisation de comportement de terrains au-dessus d'une mine par longue taille de l'Illinois. Elle précise le mécanisme de rupture au-dessus de ces chantiers de charbonnage. Le logiciel Universal Distinct Element Code (UDEC) est utilisé pour simuler en 2-D une tranche de strates horizontales faisant 900 m de long avec 200 m d'épaisseur sur la ligne centrale d'une longue taille. Un processus a été mis au point pour placer systématiquement des discontinuités horizontales au modèle à partir des résultats de forages et des évaluations de massifs rocheux. Les déplacements des discontinuités modélisées par UDEC s'accordent avec ceux de la méthode de surveillance "time domain reflectometry" (TDR). Confirmant des recherches antérieures, ces discontinuités influencent l'ampleur et la courbure du profil de la surface.

---

[1]Mention of a product does not imply endorsement by the Bureau of Mines

INTRODUCTION

Subsidence over high-extraction coal mines affects both natural topography and constructed facilities. It has long been hoped that more accurate subsidence-prediction methods would be developed to allow greater resource sharing by predicting and avoiding impacts on sensitive surface areas. To increase the sensitivity of the influence-function technique (Brauner, 1973) to site specific geology, a method to incorporate rock-mass caving and bulking characteristics is being developed. Also, since it has been determined that the influence-function technique must include an intensity function that defines the boundaries and intensity of the zone causing subsidence (Triplett and Yurchak, 1990), the boundary and character of the cave zone is being sought. The cave zone is hypothesized to extend several mined thicknesses into the immediate roof and be composed of caved material that bulks to fill the mine void and subsequently consolidates due to overburden load. Time-domain reflectometry (Dowding et al, 1988) and surface survey measurements are used to provide benchmarks for the analytical research.

MODELING METHODOLOGY

The methodology applied to this study was patterned after the guidelines outlined by Starfield and Cundall (1988) who encouraged researchers to remember that the focus of the numerical analysis should be on gaining an understanding of the mechanisms that characterize the system and not on obtaining unique numeric values for specific parameters. Hart and Cundall (1992) go on to explain that this is accomplished by using the computer model as a laboratory to perform experiments on the system. This can result in an improved understanding of mechanisms, knowledge of parameter dependence, and a means by which to check theories or hypotheses. Ultimately, the new knowledge may lead to new theories or simple conceptual models that then can be used in design (Hart and Cundall, 1992). In the present study, the UDEC analysis increases understanding of subsidence over longwall coal mines allowing influence-function prediction to be improved.

The Universal Distinct Element Code (UDEC) (Itasca, 1992) is being used to perform desk top experiments and identify parameters that significantly influence model behavior. The computer code allows internal deformation of discrete blocks and also allows large displacements and separations along discontinuities. UDEC utilizes the distinct-element method which is a particular type of discrete-element method that uses deformable contacts and an explicit time-stepping solution of the equations of motion (Cundall and Strack, 1979). Output in the form of displacements, velocities, and stress distributions can be compiled into movies that make it possible to visualize the influence of various parameters on rock-mass response. The surface subsidence profiles of the model can be compared with actual profiles surveyed in the field. TDR monitoring cables can be simulated in the model and the shear displacement along horizontal discontinuities compared with TDR measurements. Displacement profiles generated by the model in the immediate roof are considered indicative of the intensity function. Once the important parameters have been identified by computer modeling they will be quantified by field and laboratory measurements and used to improve the accuracy of influence-function prediction.

SIMULATION OF HORIZONTAL DISCONTINUITIES

The distinct-element model is composed of deformable blocks separated by discontinuities. Since it is hypothesized that caving and bulking are affected by the location and character of discontinuities within the rock mass, Bureau researchers are using the modified Rock Mass Rating (RMR) system

(Bieniawski, 1989; Golder, 1989) to systematically define the location of horizontal discontinuities in the model. A commercially-available computer spreadsheet program is used to calculate a RMR for each lithologic bed based on drill-core logs and engineering property tests. The RMR is used to calculate a eformation modulus and bending stiffness for each lithologic bed identified in the boring logs. Large contrasts in the bending stiffness between adjacent lithologic beds have been shown to correlate with horizontal shear displacements measured using TDR (Siekmeier, et. al., 1992). Thus the locations of these large contrasts in bending stiffness are used to define horizontal discontinuities in the distinct element model.

The RMR includes six basic parameters plus adjustments described by three additional parameters.

<u>Basic Parameters</u>

Intact rock strength	R_{IRS}	(0 to 15)
Drill core quality	R_{RQD}	(0 to 20)
Spacing of discontinuities	R_{JS}	(0 to 20)
Condition of discontinuities	R_{JC}	(0 to 30)
Groundwater condition	R_{JW}	(0 to 15)
Orientation of discontinuities	R_{JO}	(-12 to 0)

<u>Adjustments</u>

Blasting damage	A_B	(0.8 to 1.0)
In situ stress or stress change	A_S	(0.6 to 1.2)
Presence of major faults or fractures	A_F	(0.7 to 1.0)

$$RMR = [R_{IRS}+R_{RQD}+R_{JS}+R_{JC}+R_{JW}+R_{JO}] \times A_B \times A_S \times A_F \qquad (1)$$

These parameters are determined directly from boring logs or inferred using other site data and engineering judgement. The need for subjective engineering judgement and interpretation is due to the fact that data may have been collected in a form that is not directly transferable to the parameters listed above.

The in situ deformation modulus (E) of each lithologic bed is estimated using the relationship proposed by Serafim and Pereira (1983) for RMR < 50. Figure 1 shows the correlation between this estimated RMR modulus and the dynamic modulus determined from the sonic velocity. Note that there is an order-of-magnitude difference in the scale, but that the location and relative size of the spikes on the signatures are similar.

$$E = 10^{[(RMR-10)/40]} *1000 \quad <MPa> \qquad (2)$$

The moment of inertia (I) per unit width (1) is determined for a given bed thickness (t).

$$I = \frac{1 \times t^3}{12} \quad <m^4/m> \tag{3}$$

The bending stiffness per unit width of each lithologic bed is the product of the in situ deformation modulus and the moment of inertia of the bed.

$$BENDING\ STIFFNESS = E\ I \quad <MPa\text{-}m^4/m> \tag{4}$$

The bending stiffness can be graphically displayed and used to interpret the character of the overburden. The thicknesses of the lithologic beds in Figure 1 are indicated by the distance between horizontal lines in the RMR and bending stiffness histograms. Note that the bending stiffness is heavily dependent on the bed thickness via the moment of inertia so that thick beds dominate the graphical stiffness histogram. The logarithmic scale is used to allow the location of thin beds of low stiffness to be seen. Adjacent lithologic beds with relatively large bending stiffnesses are grouped together to form geostructural elements, which are defined in Figure 1 by the horizontal lines that cross the figure. These horizontal lines are used as block boundaries in the distinct-element model.

Figure 2 shows TDR displacements compared with the location of the horizontal discontinuities defined in Figure 1. The TDR signatures were recorded as the longwall face approached and advanced past the borehole and show the positions at which cable deformation has occurred. The regularly spaced spikes that do not lengthen during rock mass deformation are crimps placed in the cable prior to grouting the cable into the borehole and are used as reference points. The figure shows that horizontal shear displacements tend to be localized at the top and bottom of the geostructural elements formed of relatively thick shale, sandstone, siltstone, and claystone beds. These locations also correspond to thin limestone, shale, and coal beds. On May 11 the TDR cable was being sheared at depths of 71.4 m, 77.3 m, and 103 m. These localized displacements correspond to thin beds at these depths. The drill core showed a coal from 71.4 to 71.9, a limestone from 76.7 m to 77.2 m, a shale from 102.6 m to 103.0 m, and a sandstone from 103.0 to 103.8 m. The increased spike magnitudes on the May 15 TDR signature show that shearing continued at these locations and ultimately sheared the cable at a depth of 103.0 m. By May 21 additional shear deformations become visible on the TDR signature at depths of 28.7 m, 44.0 m, 49.4 m, 55.7 m, and 61.7 m. The drill core showed a limestone from 27.3 m to 27.6 m, a dark grey shale from 50.3 m to 50.4 m, and a coal from 56.2 m to 56.4 m.

Based on the correlation between the lithology determined from the drill-core log and the actual displacements measured using TDR it is evident that the process of caving and subsidence over this longwall mine involves localized displacements along horizontal discontinuities, and therefore horizontal discontinuities that allow localized displacements need to be included in a computer model attempting to simulate longwall mine subsidence. It may be important to also include vertical discontinuities in the model, but there is currently no way to define their distribution, and therefore a reasonable methodology would need to be developed to estimate their locations.

BOUNDARY CONDITIONS AND MATERIAL PROPERTIES

A two-dimensional, plane-strain, distinct-element model was used to simulate the longitudinal profile of a longwall panel. The model was composed of 26 deformable blocks stacked as a layer-cake to simulate a horizontally bedded rock mass. The blocks represent the geostructural elements defined earlier and are composed of finite-difference triangles. The mass of each triangle was accelerated by gravity while being confined by horizontal stresses. The horizontal stress was assumed to be proportional to the vertical stress at all depths and was varied from 0.5 to 2 to 4 times the vertical stress during different runs.

The deformable block properties are listed in Table 1 and the properties of the horizontal discontinuities are listed in Table 2. These values are considered to be reasonable approximations of the true properties. Future work would investigate the sensitivity of the results to the values selected. The constitutive law that defines shear displacement on the joints assumes a linearly increasing relationship between the applied stress and joint displacement until the applied stress exceeds the Coulomb frictional strength resulting in slip.

RESULTS OF COMPUTER SIMULATIONS

All simulations were performed on a 486/33 MHz microcomputer with 16 Mb of RAM. For this system, the size and complexity of the model was limited by processor speed rather than available memory since run times for models using all available memory were impractical. To simulate longwall mining, blocks were deleted at mine level in a step-wise fashion with steps of 1 meter. Each meter of excavation required 250 to 1000 calculation cycles at 0.3 to 0.5 Hz to transfer the effects throughout the simulated rock mass.

Figure 2 qualitatively compares the shear displacements that occurred at the horizontal discontinuities in the model with the shear displacements measured using TDR. The horizontal discontinuities in the distinct-element model allow displacements to be localized in locations that compare favorably to TDR measurements. Methods are currently being developed that will allow quantitative values to be attached to the spikes on the TDR signatures.

Table 1. - Material Properties

	Density kg/m^3	Bulk Modulus MPa	Shear Modulus MPa	Consitutive Law	Fiction Angle Degrees	Cohesive Strength MPa	Tensile Strength MPa
Soil	1750	107	23	Mohr-Coulomb	30	0	0
Rock Mass	2500	1000	600	Mohr-Coulomb	30	6	2

Table 2. - Horizontal Joint Properties

Normal Stiffness MPa/m	Shear Stiffness MPa/m	Slip Criterion	Friction Angle Degrees	Cohesive Strength MPa
15,000	1,500	Coulomb	10	0

For the purposes of comparison, a model that did not contain horizontal discontinuities was used. Figure 3 compares the longitudinal surface subsidence profiles of models with and without horizontal discontinuities. The figure shows that the horizontal discontinuities have a major effect on the magnitude and shape of the profile. This is because the model containing horizontal discontinuities where slip occurs is much less stiff than the model composed of a homogeneous mass. The surface profile generated by the homogeneous model could be more closely matched to the actual surface measurements if the stiffness of the block material was reduced. However, this type of curve fitting would only allow the model to accurately predict subsidence at a specific site or in areas with very similar geologic characteristics. No knowledge would be gained about the mechanisms responsible for subsidence. The methodology used by the Bureau to incorporate horizontal discontinuities into the distinct-element model provides a more systematic and justifiable approach to approximate the stiffness of the rock mass. Figure 3 also shows the importance of simulating the step-wise excavation of the mine. Step-wise excavation results in a surface profile that more closely matches the profile measured over the end of the panel. Note that when the entire block of coal was removed in one step that the model estimated 2 m of subsidence for a 2 m extracted thickness.

Figure 4 shows the effect of the horizontal stress on the surface subsidence profile. Horizontal stress was found to have little effect on the surface profile during these simulations, however these results are considered preliminary at this time because so few simulations have been done and because the shapes of the profiles are puzzling.

CONCLUSIONS

The commercially-available computer program, UDEC, is being used by Bureau researchers to simulate the response of coal-measure strata to longwall mining. The method used to incorporate horizontal discontinuities into the distinct-element model has been shown to produce results that reasonably simulate localized shearing indicated by TDR measurements. The mechanisms suggested by these numerical experiments indicate that the caving process involves progressive delamination, slip, and separation along horizontal discontinuities between lithologic beds that previously formed a massive laminated linear arch. Kneisley and Haramy (1992), O'Connor and Dowding (1992), Hazen and Sargand (1988), Holt and Mikula (1984), and Nieto et. al. (1983) have also suggested a sequence of main roof caving that is strongly affected by the existence of horizontal discontinuities and thick stiff beds.

REFERENCES

Bieniawski, Z.T. Engineering Rock Mass Classifications. John Wiley and Sons, New York, NY, 1989, 251 pp.

Brauner, G. Subsidence Due to Underground Mining (In Two Parts). BuMines IC 8571 and IC 8572, Washington, D.C., 1973, 56 pp. and 53 pp.

Cundall, P.A. and O.D.L. Strack. A Discrete Element Numerical Model for Granular Assemblies. Geotechnique 29, 1979, pp. 47-65.

Dowding, C.H., M.B. Su, and K.M. O'Connor. Principles of Time Domain Reflectometry Applied to Measurement of Rock Mass Deformation. Int. J. Rock Mechanics and Mining Sciences, Vol. 25, No. 5, 1988, pp. 287-297.

Golder Associates. Geotechnical Study of Rock Mass Classification Parameters for Sydney Coal Field, Nova Scotia. Report to CANMET, DSS Contract No. 09SQ.23440-8-9002, Ottawa, Ontario, Canada, Aug. 1989, 81 pp.

Hart, R.D. and P.A. Cundall. Microcomputer Programs for Explicit Numerical Analysis in Geotechnical Engineering. Presented at the International Seminar on Numerical Methods in Geomechanics, Moscow, Mar. 1992.

Hazen, G.A. and S.M. Sargand, Methods for Assessing Effects of Longwall Mining on Surface Subsidence. Mining Engineering, Vol. 40, No. 6, 1988, pp. 451-454.

Holt, G.E. and P.A. Mikula. Evaluation of Subsidence Prediction Methods for Coal Mining in Eastern Australia. Australian Coal Industry Research Laboratories, Published Report 84-15, 1984, 168 pp.

Itasca Consulting Group. UDEC Version 1.8. Vol. 1 and 2, June 1992.

Kneisley, R.O. and K.Y. Haramy. Large-Scale Strata Response to Longwall Mining: A Case Study. BuMines RI 9427, Washington, D.C., 1992, 25 pp.

Nieto, A.S., D. Stump, and D.G. Russel, A Mechanism for Sinkhole Development Above Brine Cavities in the Windsor-Detroit Area, Proceedings, Sixth International Symposium on Salt, Vol. 1, 1983, pp. 351-367.

O'Connor, K.M. and C. H. Dowding. Distinct Element Modeling and Analysis of Mining-Induced Subsidence. Rock Mechanics and Rock Engineering, Vol. 25, 1992, pp. 1-24.

Serafim, J.L. and J.P. Pereira. Considerations of the Geomechanics Classification of Bieniawski. Proceedings, Intl. Sym. Eng. Geol. Underground Constr., A.A. Balkema, Boston, MA, 1983, pp. 33-34.

Siekmeier, J.A., K.M. O'Connor, and L.R. Powell. Rock Mass Classification Applied to Subsidence Over High Extraction Coal Mines. Proceedings, Third Subsidence Workshop Due to Underground Mining, Syd Peng, Ed., West Virginia University, Morgantown, WV, June 1-4, 1992, pp. 317-325.

Starfield, A.M. and P.A. Cundall. Towards a Methodology for Rock Mechanics Modeling. Int. J. Rock Mech. Min. Sci. and Geomech. Abstr., 25 (3), 1988, pp. 99-106.

Triplett, T.L. and D.W. Yurchak, Inclusion of as Intensity Function for Subsidence Prediction in Illinois, Proceedings, Third Conference on Ground Control Problems in the Illinois Coal Basin, Mt. Vernon, IL, August 1990, pp. 276-284.

HORIZONTAL LINES DEFINE BOUNDRIES OF GEOSTRUCTURAL ELEMENTS
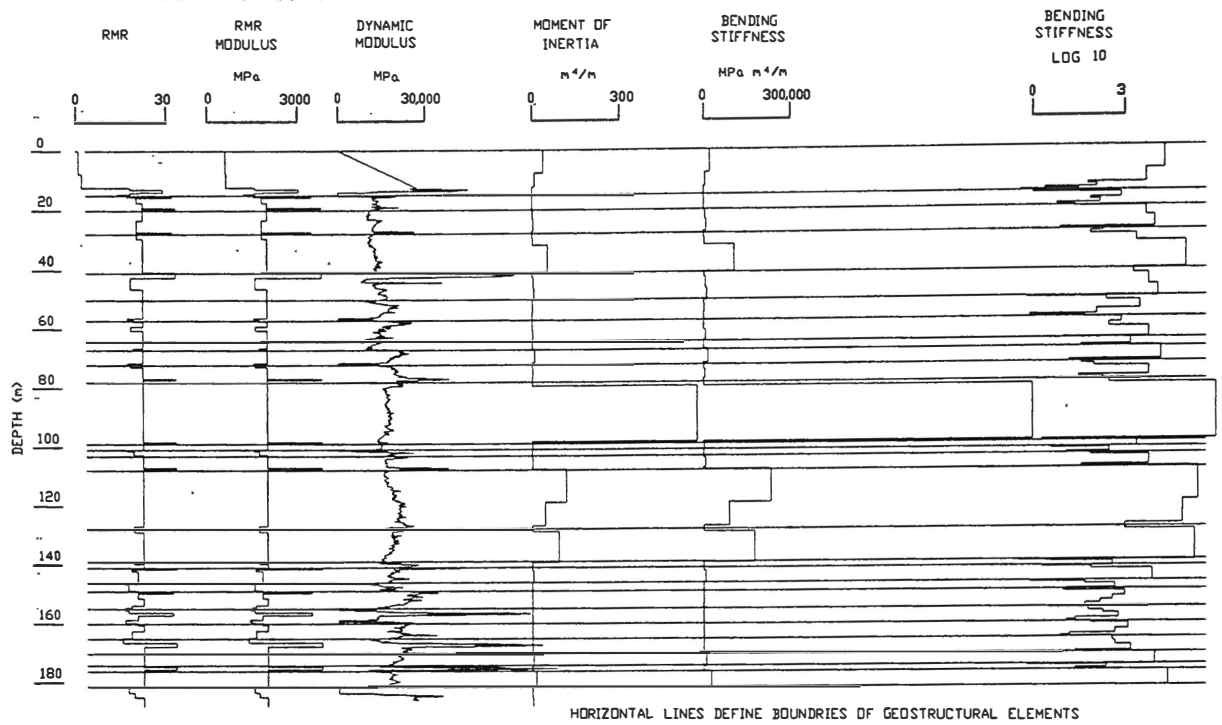
FIGURE 1: HORIZONTAL DISCONTINUITIES DEFINED BY BENDING STIFFNESS LOG10

MINE ROOF IS AT A DEPTH OF 181 M   HORIZONTAL LINES DEFINE BOUNDRIES OF GEOSTRUCTURAL ELEMENTS
* TDR REFLECTION DUE TO PREEXISTING CRIMP
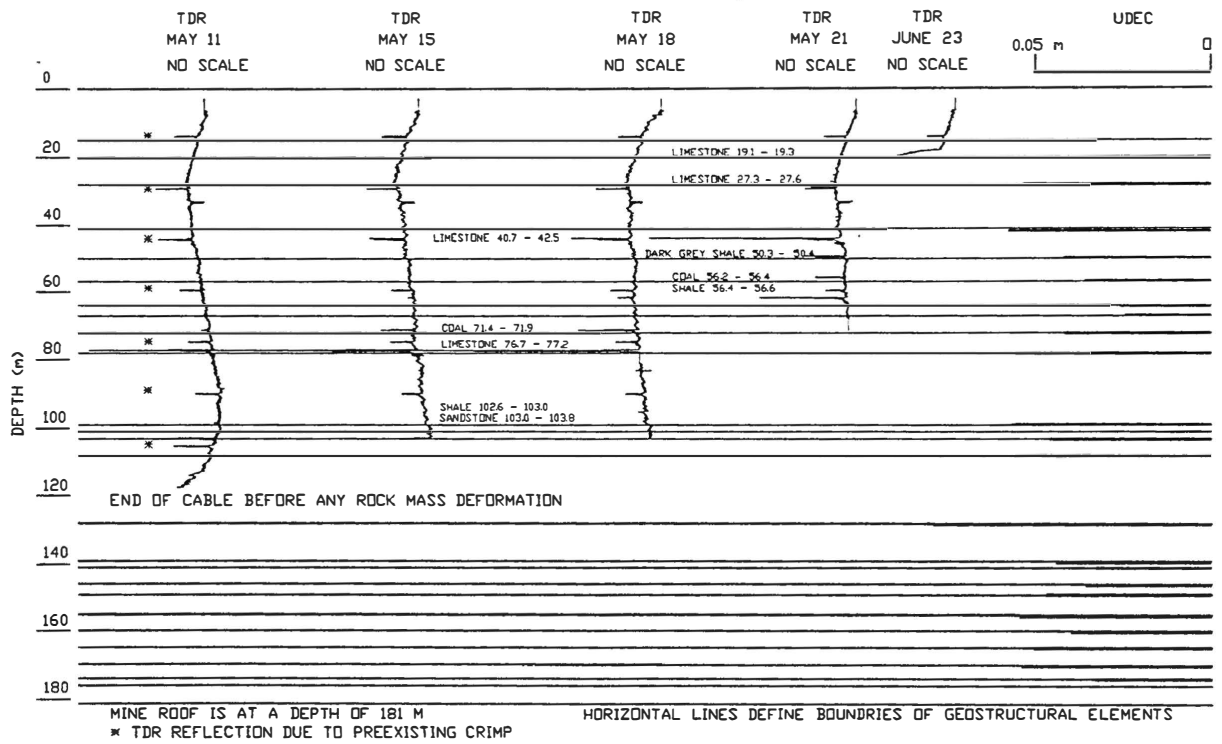
FIGURE 2: RELATIONSHIP BETWEEN GEOSTRUCTURAL ELEMENTS, TDR, LITHOLOGY, AND UDEC

117

VERTICAL EXAGGERATION OF 100

REFERENCE SURFACE

NO HORIZONTAL DISCONTINUITIES

WITH HORIZONTAL DISCONTINUITIES

MEASURED PROFILE
OVER END OF PANEL

LOCATION OF MINE

START OF STEP-WISE EXCAVATION   END OF STEP-WISE EXCAVATION

EXCAVATED AS SINGLE BLOCK

DEPTH (m)
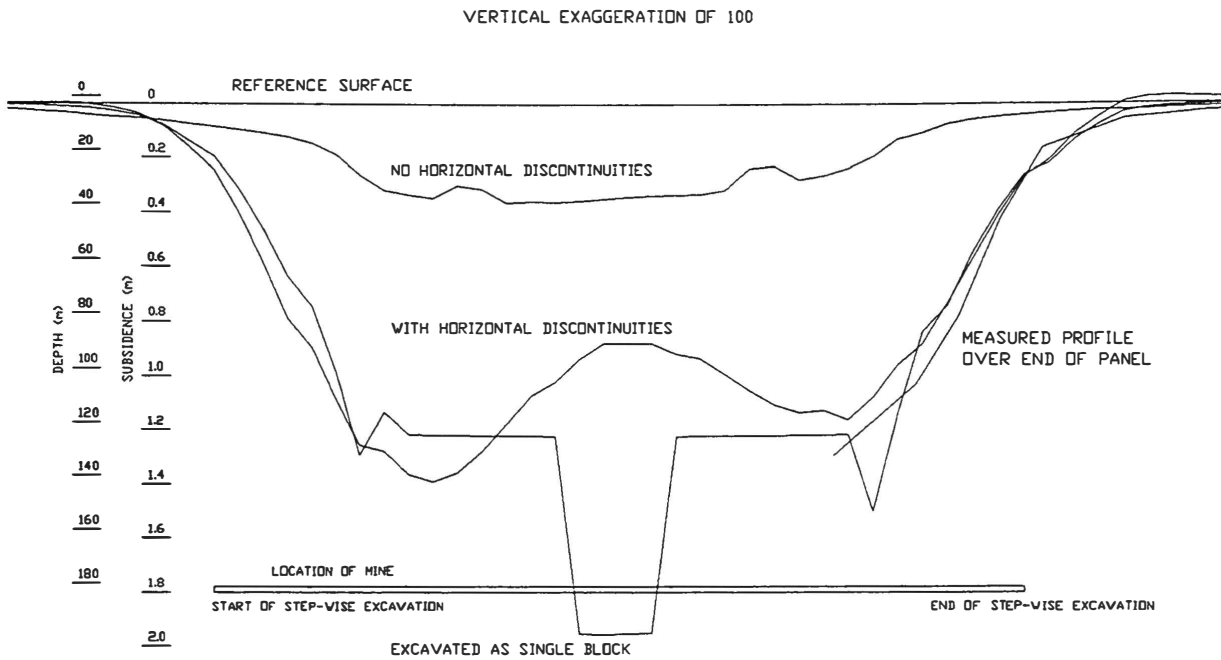
SUBSIDENCE (m)

FIGURE 3: LONGITUDINAL SUBSIDENCE PROFILES GENERATED BY MODEL COMPARED TO MEASURED

VERTICAL EXAGGERATION OF 100

REFERENCE SURFACE

HORIZONTAL STRESS = 0.5 × VERTICAL STRESS

MEASURED PROFILE
OVER END OF PANEL

HORIZONTAL STRESS = 4 × VERTICAL STRESS

HORIZONTAL STRESS = 2 × VERTICAL STRESS

LOCATION OF MINE

START OF STEP-WISE EXCAVATION   END OF STEP-WISE EXCAVATION

DEPTH (m)
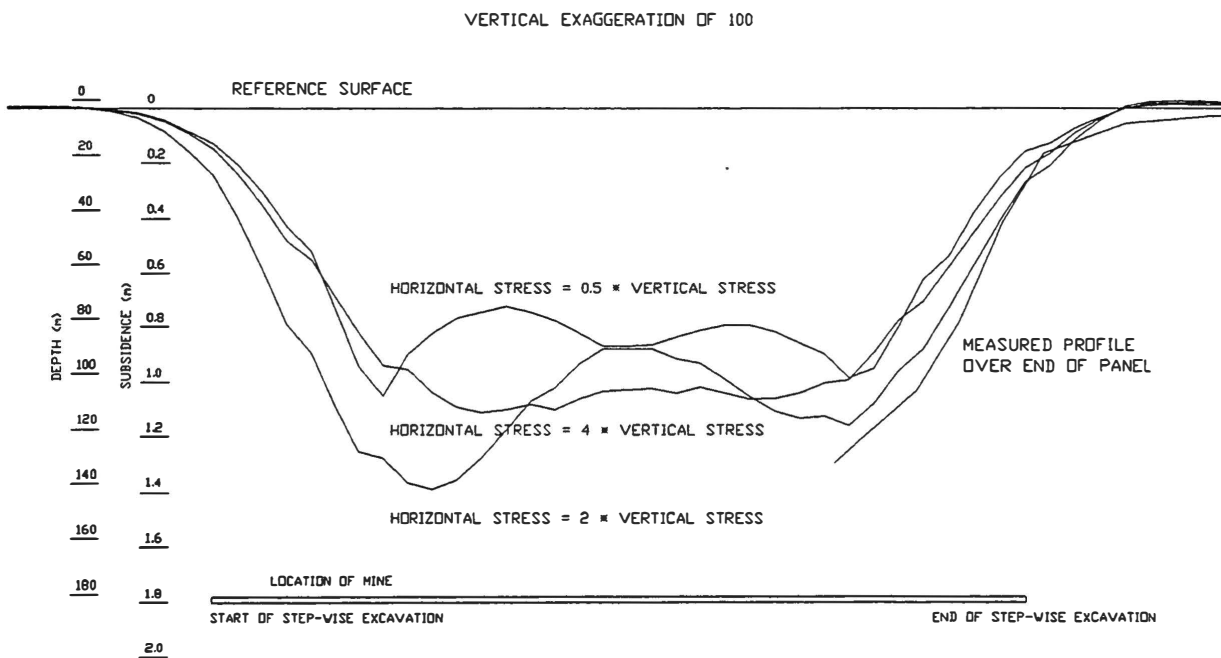
SUBSIDENCE (m)

FIGURE 4: LONGITUDINAL SUBSIDENCE PROFILES FOR DIFFERENT HORIZONTAL STRESSES

NEW DEVELOPMENTS IN MULSIM/NL—A BOUNDARY ELEMENT METHOD PROGRAM FOR STRESS ANALYSIS OF COAL MINES

By R. K. Zipf, Jr.
U.S. Bureau of Mines
Denver, Colorado, USA

ABSTRACT

MULSIM/NL is a three-dimensional Boundary Element Method (BEM) program with three distinguishing features: 1) nonlinear material models, 2) multiple mining steps, and 3) energy release and strain energy computations. Existing BEM programs do not treat gob formation and passive support installation correctly. A new capability, element birth, allows MULSIM/NL to compute better estimates of stresses and displacements in gob and inserted materials. The program retains a displacement at birth for each element that offsets the prescribed stress-strain relationship for elastic elements. Stress-displacement calculations in multiple mining step problems exhibit path dependency and show a strong step-size dependency. Computed stresses oscillate with large mining step sizes. Preliminary studies show that using the lower stress values from an oscillating stress profile provides a good estimate of the stress profile obtained using smaller mining steps.

INTRODUCTION

The U.S. Bureau of Mines seeks to reduce ground control hazards and accidents through improved mine design. Numerical models can provide design engineers with a tool to evaluate the structural response of alternate mine designs. The relative merits of these alternate designs can then be judged from a ground control perspective.

MULSIM/NL, now available to the mining community (1,2) from the Bureau, is a three-dimensional BEM program for stress analysis of coal mines and thin metalliferous veins. Three main features distinguish MULSIM/NL from its predecessors: 1) nonlinear material models, 2) multiple mining steps, and 3) energy release and strain energy computations.

This paper describes the development of an element birth capability, analogous to the element birth option found in many finite element method programs. The element birth capability enables MULSIM/NL to simulate 1) gob formation, 2) backfilling; 3) packwall construction, and 4) supplemental support installation with no significant increase in modeling complexity. Two examples illustrate the use of this new feature.

CURRENT CAPABILITIES OF MULSIM/NL

MULSIM/NL uses the displacement-discontinuity approach (3) to calculate three-dimensional stresses and displacements around tabular deposits such as coal seams. References 1, 2, and 3 explain the theory and operation of the program. MULSIM/NL can analyze from one to four parallel seams having any orientation with respect to the Earth's surface. These seams must lay far below the surface, since topographic or free surface effects are neglected. The user models each seam with a coarse-mesh grid of blocks (up to 50 by 50) that contains an embedded fine-mesh grid of elements (up to 150 by 150). The coarse-mesh blocks cover a large area of a mine layout, while the fine-mesh elements cover a central area where the user wants greater detail.

Nonlinear material models

MULSIM/NL assumes that a continuous, homogeneous, linear elastic rock mass surrounds the seam(s). Unlike prior versions of the program (3,4,5) which assume a linear elastic stress-strain relationship for the in-seam materials, MULSIM/NL now permits various nonlinear material models for the in-seam material. Figure 1 shows the six models available for the in-seam material including (1) linear elastic for coal, (2) strain softening, (3) elastic plastic, (4) bilinear hardening, (5) strain hardening, and (6) linear elastic for gob. The first three are intended for the unmined in-seam coal material, while the latter are for the broken gob material left in the wake of full extraction mining (1,2). Recent work by Maleki (6) and Pappas and Mark (7) provides a basis for selecting input parameters to the strain softening and strain hardening models.
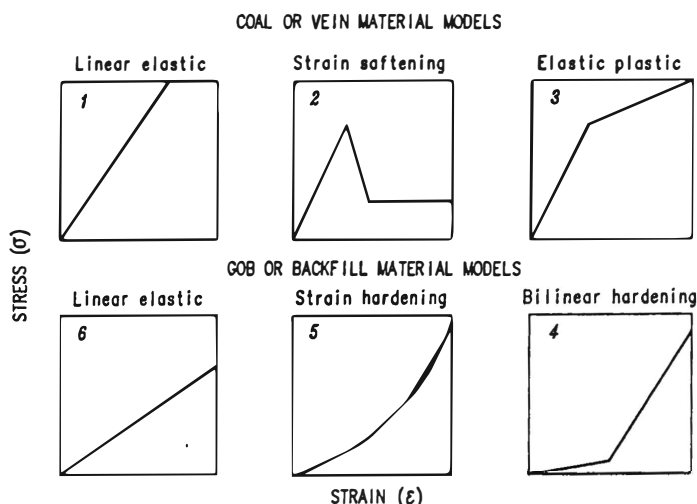
Figure 1.—Stress-strain models for MULSIM/NL

Multiple mining steps and energy release calculations

MULSIM/NL has a multiple mining step capability to simulate the various stages of mine development. With this feature, the user can compute and examine stress and displacement changes induced by mining. Such changes are more comparable to field measurements that usually record stress and displacement changes as opposed to total, or absolute, stresses and displacements. The multiple mining step feature can decrease computation time, since the computed stresses and displacements for one step become the starting point for the solution of the next step in the iterative equation solving process. This feature also provides an essential basis for the new element birth capability.
Based on stress and displacement changes between mining steps, MULSIM/NL computes Energy Release Rate (ERR), using the derivations of Salamon (8). ERR may serve as an indicator of coal mine bump risk (9). MULSIM/NL also calculates other strain energy quantities that may also serve as indicators of coal mine bump potential (1,10).

NEW ELEMENT BIRTH CAPABILITY IN MULSIM/NL

With its nonlinear material models and the multiple mining step capability, MULSIM/NL can efficiently simulate many complex and changing mining scenarios. However, when elastic elements are added subsequent to excavation, such as with passive support systems, MULSIM/NL may compute misleading stress and displacement values. Some examples of structural components added subsequent to excavation include 1) passive supplemental support installation such as cribs, 2) packwall construction, 3) gob formation, and 4) backfilling. The problem becomes most clear with passive supplemental support installation.

Suppose that coal elements are removed during some step in a MULSIM/NL model. In the mined-out elements, the stress, s, is zero, and the element displacement is some value d. Now suppose that in a later step a linear elastic element, to simulate a crib, is added to replace one of the mined-out elements. MULSIM/NL will calculate, for that element, a stress value s', that is greater than zero, and a displacement d', that is less than d. Therefore, without an element birth option, MULSIM/NL suggests that installation of the crib will cause the element displacement to decrease, as if the roof and floor were actively pushed apart. In addition, stress appears on the crib at the moment of installation. Such behavior does not adequately reflect field observations.

The problem arises because MULSIM/NL without element birth does not consider true stress path dependency even though it has a multiple mining step capability. MULSIM/NL without element birth treats each mining step as a separate problem. As stated earlier, stresses and displacements from the previous step provide the initial guess in the iterative equation solver for the current step. However, the new stresses and displacements for the next step are independent of those from the prior step. For any given mining geometry, MULSIM/NL will calculate the same stresses and displacements whether that geometry is created in one mining step or one hundred steps.

To address this problem, MULSIM/NL now incorporates an element birth capability. When an elastic element is added back, or when an elastic element changes properties from one set to another, MULSIM/NL with element birth will compute a displacement at birth, D_B. As shown in figure 2, D_B simply offsets the prescribed stress-displacement (strain) relationship.
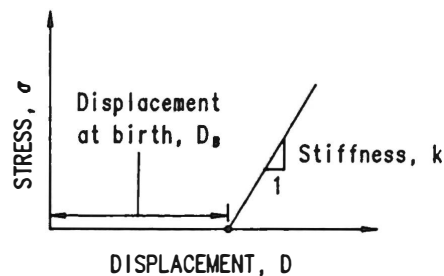
Figure 2.—Prescribed stress-displacement (strain) relation for element offset by D_B.

Implementation of element birth

The element birth capability changes the boundary conditions in the formulation of MULSIM/NL (1). In this program, the fundamental boundary-element equation relating induced stress components [T] to total displacement $[D_T]$ is

$$[T] = [TC][D_T], \tag{1}$$

where [TC] is an n x n matrix of infinite body stress influence coefficients, and [T] and $[D_T]$ are n dimensional vectors. $[D_T]$ is comprised of two parts given as

$$[D_T] = [D_B] + [D_I],$$ (2)

where $[D_B]$ is the displacement at birth, and $[D_I]$ is the displacement increment beyond birth. When an elastic element is created at a given mining step in a MULSIM/NL model, the program will use the total displacement from the previous step as the displacement at birth for the current and subsequent mining steps. Stated mathematically,

$$D_{B \text{ (later steps)}} = D_{T \text{ (last step)}}$$ (3)

for those elastic elements created this step. D_B then remains constant in all subsequent mining steps or until the material properties for that element change yet again.

Two total-stress boundary conditions apply to the fundamental boundary-element equation given by equation (1). The first condition for the mined-out elements is

$$[T] + [P] = [0],$$ (4)

where [P] is the far field primitive stress. This condition makes the total stress in the open areas zero, [0]. The second condition for the elastic elements is

$$[T] + [P] + [K]^T [D_I] = [0],$$ (5)

where [K] is the element stiffness. (The element stiffness, [K], is derived from a secant modulus determined with the prescribed stress-strain relation for the element.) For the nonlinear material models, K is a function of D_I; therefore, the boundary condition given by equation (5) is nonlinear.

Implementation of the new boundary conditions into a BEM program such as MULSIM/NL requires two major programming changes. First, the program must determine when new elastic elements are created, and then store D_T from the prior mining step as the D_B for current and subsequent mining steps. Second, the program must compute D_I from equation (2), and use D_I in the boundary condition equation (5). The element birth option does not cause significant changes to the program input; however, it does increase memory requirements and computational efforts. This new capability enables MULSIM/NL to use existing information in a better way, in order to calculate more realistic stress and displacement values throughout a mine model.

Example 1 - packwall construction

A current Bureau research project seeks to develop novel longwall coal mining methods that achieve 100% extraction and meet current regulatory requirements for safety. Such technology might help mitigate adverse effects from subsidence and multiple seam interactions as well as prevent sterilization of valuable natural resources. One concept under consideration involves the construction of packwalls in lieu of gateroad pillars. Figure 3 shows a MULSIM/NL model illustrating the concept.

In this novel method, panel development begins by advancing an 18-m-wide entry. Construction of two packwalls, 2.4-m wide, follows the wide entry development as quickly as possible. This model assumes that packwall construction lags 18 m behind the wide entry face. The packwalls separate the wide entry into three narrow entries, 4- to-
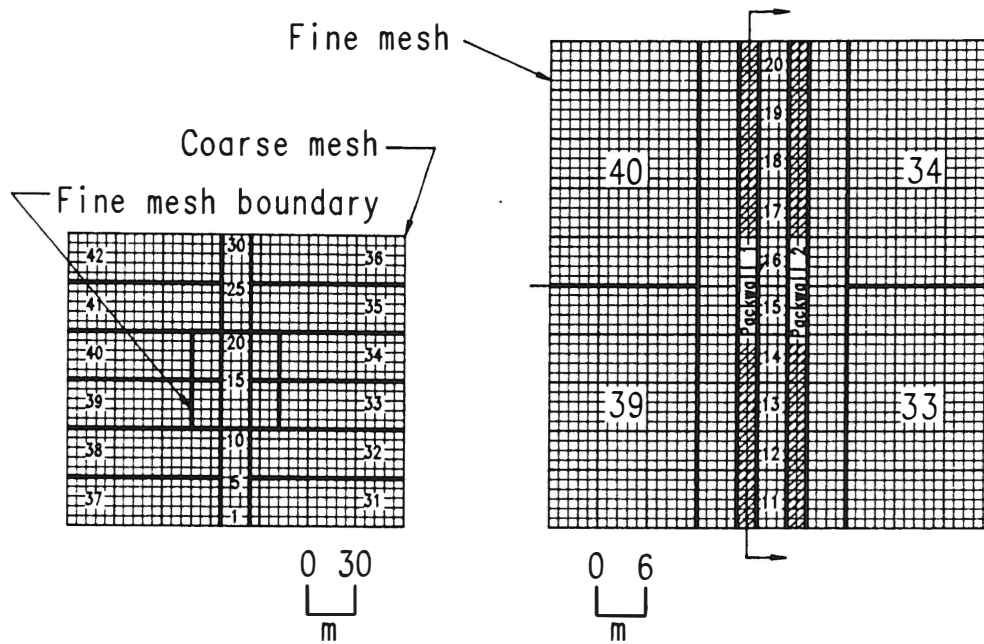
Figure 3.—MULSIM/NL model of packwall construction and mining showing coarse mesh on left and fine mesh on right and cross-section location through packwall 1. Numbers are mining steps for large step model.

5-m wide. As in conventional longwall mining practice in the United States, the entry system serves first as a headgate, and then as a tailgate as adjacent panels are retreated.

The MULSIM/NL model has 42 mining steps. Packwall construction occurs in steps 1 through 30, during which the wide entry and the packwall both advance 6 m (5 element widths) per step. First panel mining begins in step 31 and ends in step 36, while second panel mining begins in step 37 and ends in step 42. Gob formation lags 30 m behind the longwall face, i.e., elements for 30 m behind the face are modeled as open elements. Two different cases are compared with this model: one without and one with the element birth capability. In the first, packwall and gob elements are simply turned-on in the appropriate step, and in the second, packwall and gob elements will have a displacement at birth, D_B.

Figure 4 shows computed stresses and displacements along the axis of packwall 1 for three different mining steps, namely, 1) during packwall construction at step 20, 2) after first panel mining at step 36, and 3) after second panel mining at step 42. Stresses and displacements with and without element birth show significant differences.

As shown in figure 4A, stresses in the packwall reach an anomalous peak of 70 MPa immediately upon construction of the packwall, 18 m behind the entry face. About 30 m behind the face, stresses decrease to a level of about 35 MPa. These calculations also indicate that as mining progresses, stresses on the packwall increase from about 35 up to 55, and then to 85 MPa for a total increase of 50 MPa. (Stresses tend to decrease slightly at the edge of the fine mesh where it interacts with the coarse mesh.)
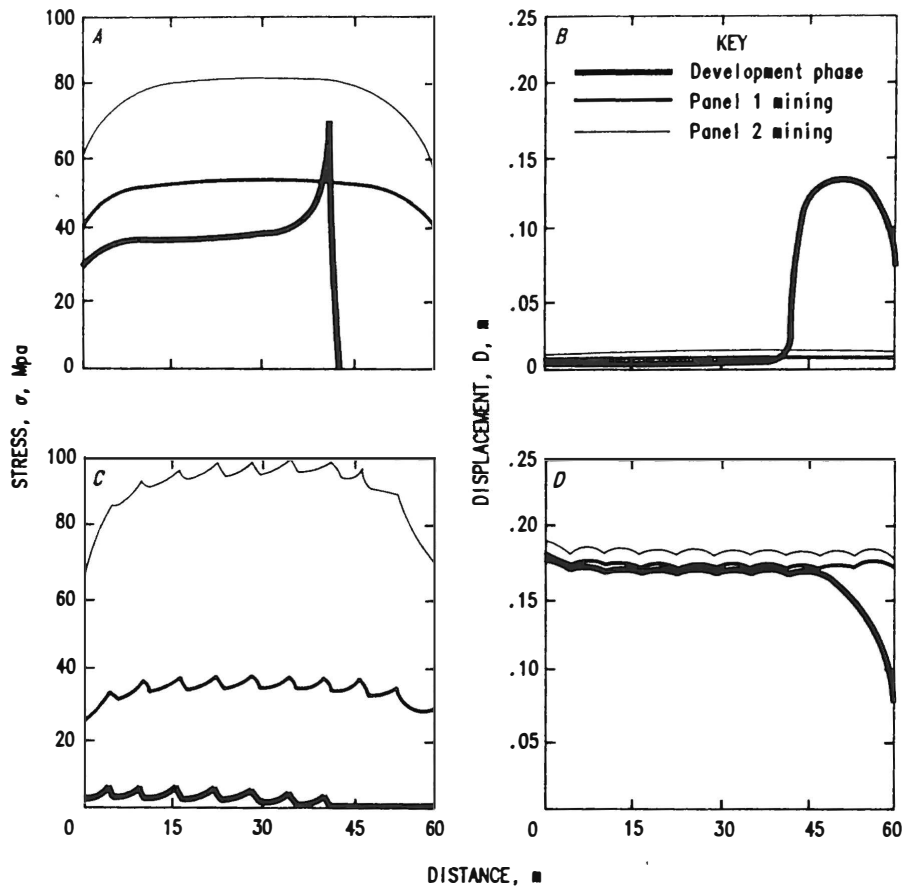
Figure 4.—Stresses and displacements without element birth (A and B)
and with element birth (C and D) in cross-section through packwall 1.

Displacement behavior without element birth (figure 4B) also exhibits unrealistic
behavior. In the 18 m between the entry face and the packwall, the opening sees about
0.14 m of displacement; however, after placement of the packwall, the displacement in
the 18 m gap decreases to about 0.01 m. These computations would suggest that the
roof-to-floor convergence decreases upon installation of the packwall, and such behavior
does not reflect reality.

With the element birth option, the stress and displacement behavior of the packwall
becomes much more realistic. As shown in figure 4C, stresses start at 0 MPa at the end
of the packwall near the face and gradually rise to about 3 MPa at about 30 m behind the
entry face. As mining progresses, stresses in the packwall increase from about 3 up to
35, and then to 95 MPa for a total increase of 92 MPa. Thus, using the element birth
capability leads to higher estimates of total stress, and the total stress increase, on the
packwall. However, the implications and validity of this conclusion require further study.
Between the entry face and the packwall, maximum opening displacement is about 0.17
m. After placement of the packwall, displacements (figure 4D) remain at or above this
level, and they continue to increase in subsequent mining steps.

Figure 4C shows that when using the element birth capability, stresses in the packwall exhibit a peculiar waviness on development and throughout subsequent mining steps. The behavior arises because stress and displacement computations with the element birth capability are step-size dependent.

To illustrate this step-size dependence, Figure 5 replots the stresses from figure 4C at an exaggerated scale. Again, these stresses are along the axis of packwall 1 during the development phase, and they are computed using a large mining step of 6 m per step. Figure 5 shows, that when using large mining steps, the computed stresses oscillate up to 4 MPa in magnitude. However, by decreasing the step size, advancing the face and packwall 2.4 m per step, oscillations in the computed stresses decrease to approximately 1 MPa.

The step-size dependence of the calculations suggest that a large number of mining steps, hence a large amount of computer time, is required in order to obtain acceptable results. For practical engineering purposes though, fewer mining steps may provide acceptable results. As shown in figure 5, using the lower stress values from the oscillating curve will approximate the smoother stress values obtained using a smaller mining step size.

Figure 5.—Stress in packwall 1 during development using large versus small mining steps.

Example 2 - gob formation

Modeling of gob formation provides another example of the potential benefits of the element birth capability. Figure 6 shows a MULSIM/NL model of longwall panel extraction. The longwall face retreats from right to left using 13 steps in the large step model and 36 steps in the small step model. In other words, the face retreats and the gob forms in 30 m (10 element widths) increments in the large step model and in 6 m (2 element widths) increments in the small step model. Two different cases are compared using both step sizes, one with the element birth capability for the gob elements, and one without it.

The model assumes that elements remain open for 30 m behind the face, i.e., gob formation lags the face by 30 m. Assuming that a swelling-consolidation mechanism (2) for gob formation applies, first, the surrounding rock breaks up and swells to fill the mining void in this 30-m zone, and then begins to consolidate and take on load beyond this 30-m zone.

Figure 7 shows computed stresses and displacements using the small step models, when the longwall face position is 30 m inside the fine mesh edge. (Figure 6 indicates the section location). Without the element birth capability, stresses rise rapidly in the gob to in situ levels. Also shown is a small rear abutment peak even though the model uses a strain-hardening material for the gob. In addition, computed displacements in the gob are less than the displacements calculated in the 30 m gap. This stress-displacement
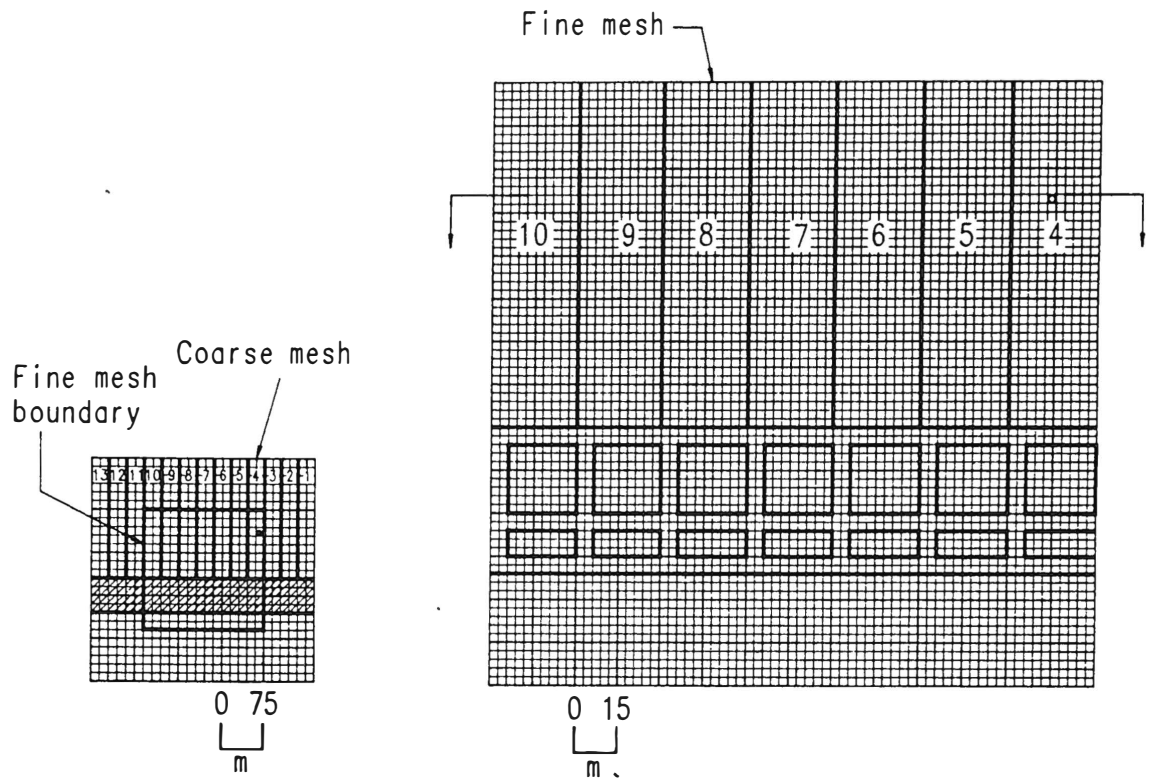
Figure 6.—MULSIM/NL model of gob formation in longwall panel showing coarse mesh on left and fine mesh on right and cross-section location through the gob. Numbers are mining steps for large step model.
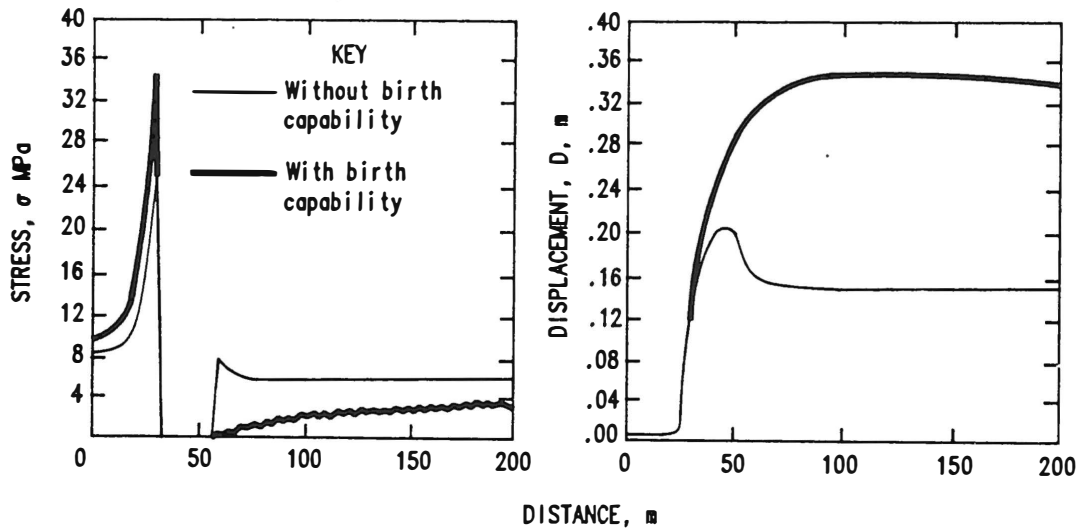
Figure 7.—Stresses and displacements into gob behind longwall face using small step models.

behavior does not simulate expected behavior. With the element birth capability,
computed stresses in the gob rise gradually over a distance of 100 m to about one-half of
the in situ stress level.

Displacements in the gob continue to increase above the levels calculated in the 30 m
gap. Because of the increased displacement levels in the gob, the model computes higher
stress levels in the surrounding coal. Examination of stress profiles in the solid coal
ahead of the longwall face suggests that using the element birth capability results in a 18
to 45% increase in the computed stress level. Therefore, stress computations with BEM
models not having element birth may tend to underestimate stress levels in nearby
unmined structures.

As in the packwall example, these computations,
too, exhibit a step-size dependence. Figure 8
replots from figure 7 the computed stresses in
the gob using the element birth capability with
small mining steps. As mentioned earlier, the
face and gob positions move in 6 m (or two
element width) increments per mining step in
this model. Also shown on figure 8 are
computed stresses with large mining steps, where
the face and gob positions move in 30 m (or 10
element width) increments per step. The
computed stresses show large oscillations;
however, they can still be useful for practical
engineering purposes. Using the lower stress
values in the oscillating curve will approximate
the smoother stress values obtained using a
smaller mining step size.
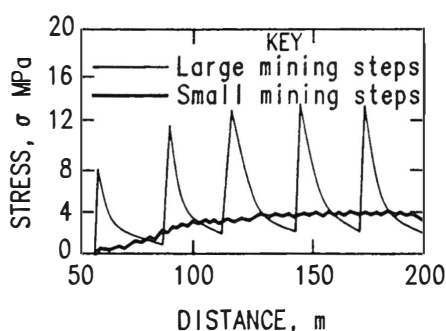
Figure 8.—Computed stresses in gob
using large vs. small mining step
models.

SUMMARY

Program MULSIM/NL is a practical tool for the coal mining engineer with which to
analyze the stresses in an underground mine. MULSIM/NL has many useful features that
lead to realistic stress calculations, such as nonlinear material models and multiple mining
steps. Use of the nonlinear materials can lead to very realistic simulations of coal mine
pillar behavior.

Recent research has developed an element birth capability that enables MULSIM/NL to
more realistically simulate 1) gob formation, 2) packwall construction, 3) supplemental
support installation, and 4) backfilling. This new capability does not increase modeling
complexity significantly; rather, it allows the BEM model to make better use of existing
input information. With the new element birth capability, the stress-displacement
calculations in multiple mining step problems are path dependent.

Two problems, the packwall example and the gob formation example, illustrate the use
and benefits of the new element birth capability. For the packwall example, the use of
element birth provides a more realistic calculation of the stress increases. The new
calculation method leads to higher estimates of total stress and total stress increase on the
packwall. Similarly, the use of element birth in the gob formation example leads to

better simulations of stress and displacement behavior in the gob. Computations using
element birth are step-size dependent. Computed stresses tend to oscillate when using
larger mining step sizes. However, preliminary studies indicate that using just the lower
stress values from an oscillating stress profile provides a reasonable estimate of the stress
profile obtained using smaller mining steps.

At present, using the element birth capability in MULSIM/NL can require large numbers
of mining steps, hence large amounts of computing time. Future research will
concentrate on practical ways to decrease computing time requirements. Parallel
computing may offer the most promising avenue in that regard. These developments will
lead to new releases of MULSIM/NL and better computer stress analysis tools for
practical coal mine engineering.

REFERENCES

1. Zipf, R. K. MULSIM/NL Theoretical and Programmer's Manual. BuMines IC 9321, 1992 52 pp.

2. Zipf, R. K. MULSIM/NL Application and Practitioner's Manual. BuMines IC 9322, 1992 48 pp.

3. Sinha, K. P. Displacement Discontinuity Technique for Analyzing Stresses and Displacements Due to Mining Seam Deposits. Ph.D. Thesis, Univ. MN, Ann Arbor, MI, 1979, 311 pp.

4. Beckett, L. A., and R. S. Madrid. MULSIM/BM - A Structural Analysis Computer Program for Mine Design. BuMines IC 9168, 1988, 302 pp.

5. Donato, D. A., MULSIM/PC - A Personal-Computer-Based Structural Analysis Program for Mine Design in Deep Tabular Deposits. BuMines IC 9325, 1992, 56 pp.

6. Maleki, H. In Situ Pillar Strength and Failure Mechanisms for U.S. Coal Seams. Paper in Proceedings of the Workshop on Coal Pillar Mechanics and Design, A. T. Iannacchione, C. Mark, R. C. Repsher, R. J. Tuchman, and C. C. Jones, eds., BuMines IC 9315, 1992, pp. 73-77.

7. Pappas, D. M., and C. Mark. Behavior of Simulated Longwall Gob Material. BuMines RI, to be published.

8. Salamon, M. D. G., Energy Considerations in Rock Mechanics: Fundamental Results. J. S. Afr. Inst. Min. Metall., v. 84, No. 8, 1984, pp. 233-246.

9. Zipf, R. K., and K. A. Heasley. Decreasing Coal Bump Risk Through Optimal Cut Sequencing with a Non-Linear Boundary Element Program. Proc. 31st U.S. Symp. on Rock Mech., 1990, pp. 947-954.

10. Heasley, K. A. An Examination of Energy Calculations Applied to Coal Bump Prediction. Proc. 32nd U.S. Symp. on Rock Mech., 1991, pp. 481-490.

NUMERICAL SIMULATION OF MAIN ROOF BEHAVIOR IN LONGWALL MINING

Duk-Won Park, Yong-Ming Jiang, Seong-Min Lee, and Debasis Deb

*Dept. of Mineral Engineering, The University of Alabama
Tuscaloosa, AL 35487-0207, U.S.A.*

ABSTRACT

Longwall mining has established its popularity worldwide due to higher productivity and better safety standards. But the operational system of a longwall mine is extremely complex, expensive, and requires great caution for reliable and efficient outcomes. The threat to this mining technique may arise when a thick and strong main roof such as sandstone is encountered. In this paper, an extensive study of main roof characteristics using numerical simulation techniques is included. A large-scale three-dimensional finite element longwall mine model and a small, but detailed, model were established in this study to observe the main roof behavior and its effects on shields in an entire longwall panel. The main roof composed of sandstone was considered as an elastic plate, whereas the immediate roof, overburden, coal seam, and floor were created using hexa-elements in modeling. The gap elements or friction elements were utilized where separation of roof strata occurred, and fractures were developed. With the help of the finite element analysis, the major characteristics of main-roof breakage and the effects on the shields, such as the failure modes of the main roof and the shield support were analyzed.

The main roof was considered as a large plate, and simulated using plate elements. A crack in the main roof and the strata separation between two layers were simulated using gap elements.
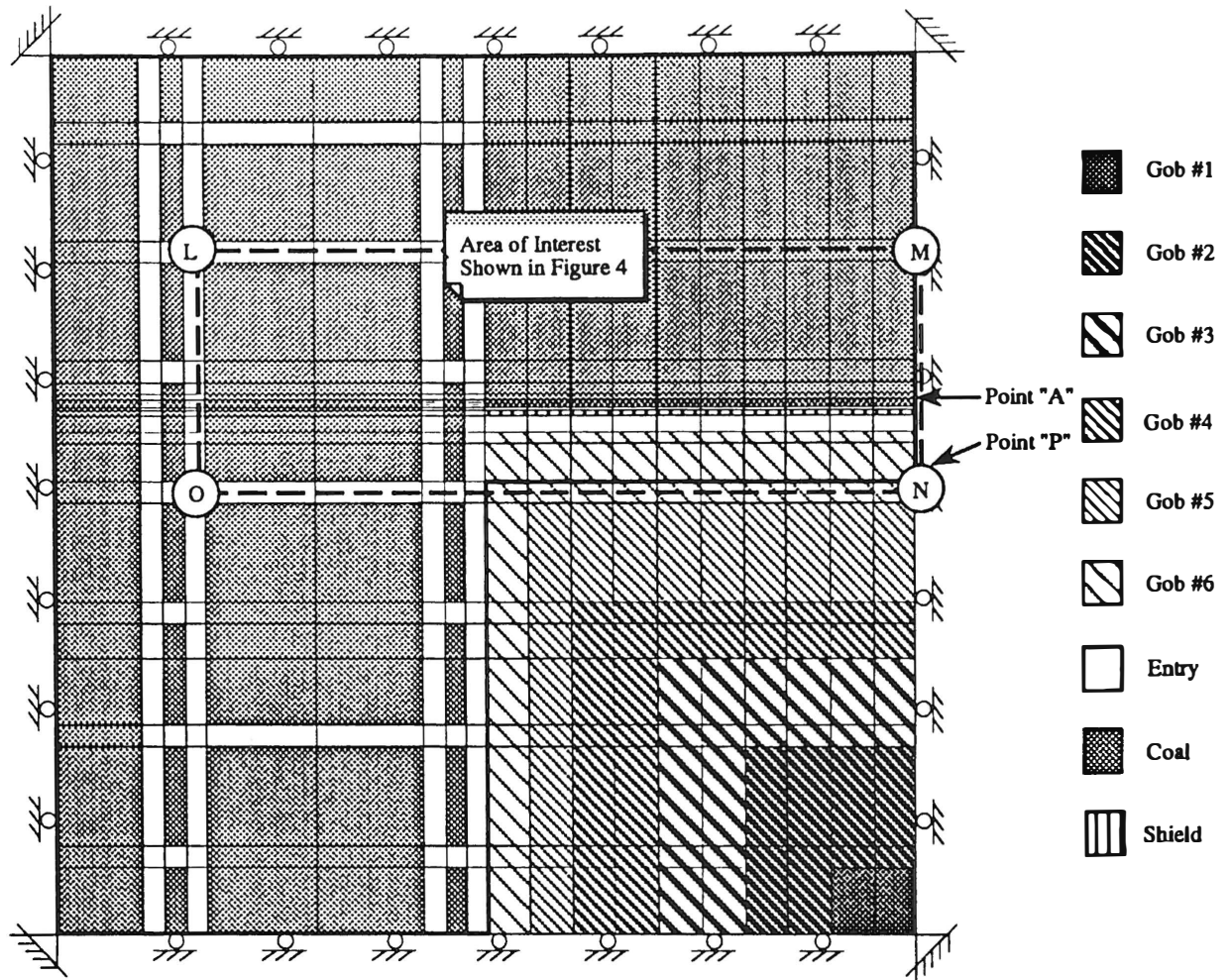
Figure 1. Plan view of finite-element model.

Small-area model

In order to study responses of longwall shield supports under different conditions, a small model with a detailed shield structure was developed. Figure 2 illustrates the side-view of the small model configuration and the corresponding dimensions. A Gullick Dobson, two-leg, 600-ton shield was modeled in this study. The canopy, caving shield, lemniscate links, and base were modeled according to the actual size and shape of the shield using equivalent solid elements. The two double-telescopic hydraulic legs of the shield were modeled using rod elements. The non-linear behavior of the shield was considered to account for the initial elastic displacement with the dead load of the overburden (Park, et al., 1992). The total number of elements consisted in the model was 1,260, including 198 plate elements, 95 gap elements, and 2 rod elements.

INTRODUCTION

Main roof behavior has been studied as a part of the ground control research program for the Warrior Coal Field (Park, et al., 1989, 1991, and 1992). Most of the previous studies utilized two- or three-dimensional finite element models that simulated a limited area. A cantilever beam was always assumed as the main roof in the studies. As a result, the analyses are more likely to represent the center area of the panel. From location to location across the panel width, the behavior of the main roof is different depending on the boundary effects of the longwall face, which includes the effects of yield and abutment pillars at both sides. Pothini, et al., (1989) demonstrated that the severe loading condition on the shield did not always occur in the center of the longwall face, but more likely depending on failure modes of the main roof.

In this study, a large-scale three-dimensional finite element longwall panel model and a detailed small shield structure model were established to study the main roof behavior and its effects on shields in an entire longwall panel. Roof separation and the development of a crack in the main roof were simulated. The analyses of vertical compressive stress on the coal seam and horizontal tensile stress developing in the main roof were performed as well as the effect of the roof behavior on shields. The main emphasis of this study is to determine the displacement, the location of the maximum tensile stress zone, and the initial point of crack generation in the main roof by numerical simulation.

FINITE-ELEMENT MODELING

The large-area three-dimensional finite-element model (large-area model), composed of 5,000 elements, includes a half panel and yield-abutment pillar system. A detailed three-dimensional small-area finite-element model was also used, consisting of a main floor, coal seam, shield structural members, immediate roof, main roof, and additional overburden.

The mine site selected for the analysis is a deep coal mine located in the Warrior Coal Field in Alabama. The mine has longwall panels at a depth of 610 m (2,000 ft). From various research programs carried out at this mine by Park, et al. (1984), physical properties of rock and coal are already known. The longwall panel modeled was 242 m (800 ft) wide, and a yield-abutment-yield-pillar system supported both sides of the panel. The thicknesses of the coal seam and the immediate roof were 1.5 m (5 ft) and 3.1 m (10 ft), respectively. The main roof was 6.1-m (20-ft) thick and consisted of sandstone.

Large-area model

This model was developed for studying the main roof behavior in an entire longwall panel. The plan view, x-y plane, of the mine model covered an area of 242 x 242 m^2 (800 x 800 ft^2). The dimensions of the yield pillar and abutment pillar were 6 x 27 m^2 (20 x 90 ft^2) and 61 x 61 m^2 (200 x 200 ft^2) respectively. Figure 1 shows the meshes used in the model, made-up of 475 eight-nodded hexahedral elements, for the coal-seam level where mining takes place. The width of the half panel is 121 m (400 ft), and the length of the gob is 137 m (450 ft). The remaining length of mined out area is occupied by elements representing longwall shields and unsupported openings. The mesh near the longwall face is refined so that stresses and displacements in the area can be studied in detail. There are 80 shields modeled across the half longwall panel. The top boundary stress condition was determined from the main roof model with 610 m (2000 ft) of overburden strata that was previously analyzed (Park, et al., 1992).
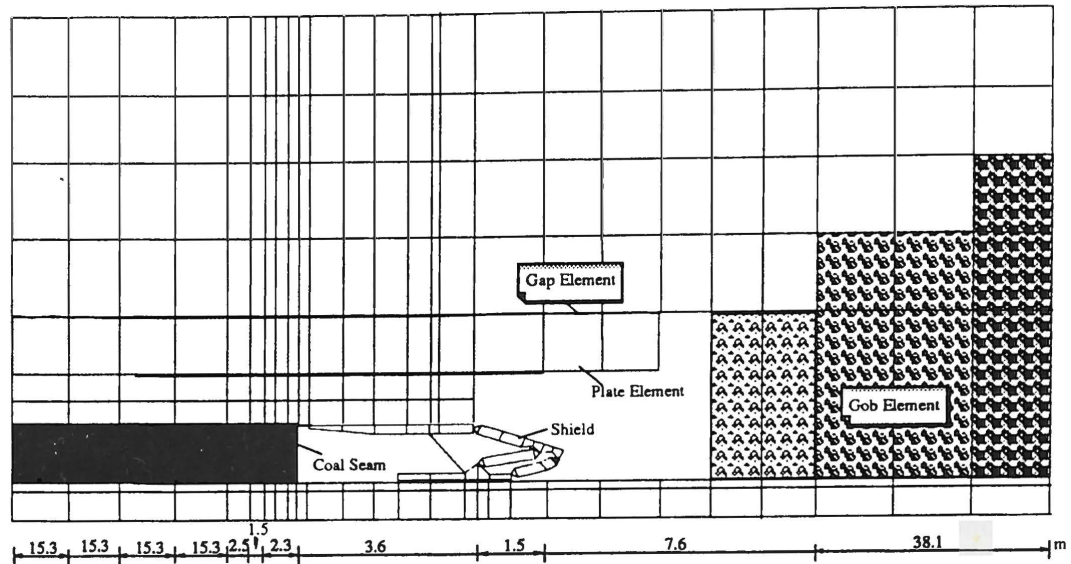
Figure 2. Finite-element model configuration and dimensions.

Failure criteria

For evaluating progressive shear and tensile failures, the Hoek-Brown failure criterion (Hoek and Brown, 1980 and 1988) and the Griffith's theory were used in stress analyses. The Hoek-Brown failure criterion is capable of describing the response of a full-scale rock mass containing discontinuities and variations of material properties. The Griffith's criterion applies for tensile failure. These two criteria have been successfully used for simulating structural behavior of longwall mining (Park, et al., 1985, 1989, 1991, and 1992).

MAIN ROOF BREAKAGE AND ITS SIMULATIONS

Roof separation

The main roof generally refers to the uncaved stronger roof strata above the immediate roof. Before failure it behaves as an elastic plate. When the length of the plate is increased with face advancing, the main roof behaves differently in different periods, showing different stress and displacement distributions. Comparison between two models, which simulated the conditions of the main roof plate of 7.6- and 18.3-m (25- and 60-ft) long, was performed in the study. Figure 3 shows the displacement distributions in the main roof for the two conditions. The results show that the displacement of the main roof at point P in Figure 1 was increased from 10.7 to 19.8 cm (4.2 to 7.8 in.) when the main roof overhang increased from 7.6 to 18.3 m (25 to 60 ft). The development of the displacement in the main roof resulted in a strata separation between the main roof and overburden strata. The separation initiated at the center of panel, point P, when the main roof overhang was approximately 7.6 m (25 ft). The separation continued to extend as the overhang in the main roof plate grew. For instance, the roof separation was extended to the curve ①——①, when the length of the overhang was 18.3 m (60 ft) as shown in Figure 4. The curve was arch shaped and about 7.6 m (25 ft) behind the

supporting line at the middle of the panel. Apparently, the separation was directly related to the growth of overhang in the main roof plate. The results indicate that the separation area continues extending toward the face and pillar direction due to the breakage of the main roof as shown in curve ②——② in Figure 4.

Initiation of main roof breakage

The vertical compressive stresses distributed on the coal seam in the study area were analyzed and are shown in Figure 5. The maximum front abutment pressures did not significantly increase when the main roof plate grew. Approximate 44.5 MPa (6,500 psi) maximum front pressure was found in the area about 1.8 m (6.3 ft) outbye the faceline. However, in the area of the main roof overhang in the gob, the main roof sustained more load for a longer plate. This resulted in a tremendous increase of the maximum moment or tensile stress in the main roof. Figure 6 shows the increased tensile stress in the main roof at cross section A-A' of Figure 4, which was located at the center of the panel, when the main roof plate grew. It can be seen that the maximum tensile stress was distributed the main roof approximately 7 ft inside of the faceline. The maximum tensile stresses of 10 and 12.4 MPa (1450 and 1800 psi) were obtained at the point A for a 4.6-m and 18.3-m (15-ft and 60-ft) long main roof plate, respectively. The relationship between the maximum tensile stress and the length of the plate is shown in Figure 7. The entire tensile stress distribution in the main roof for a 18.3-m (60-ft) plate length is shown in Figure 8(a). From the analysis of the figure, it was found that the maximum tensile stress in each cross section was distributed along the edges of the face and pillar with an arch-like shape. The maximum tensile stress of 12.4 MPa (1,800 psi) occurred at point A, approximately 7 ft inside of the faceline in the middle of the longwall face. According to the Griffith's theory, it is believed that the crack was initiated when the maximum tensile stress was sufficient to cause a tensile crack from point A.
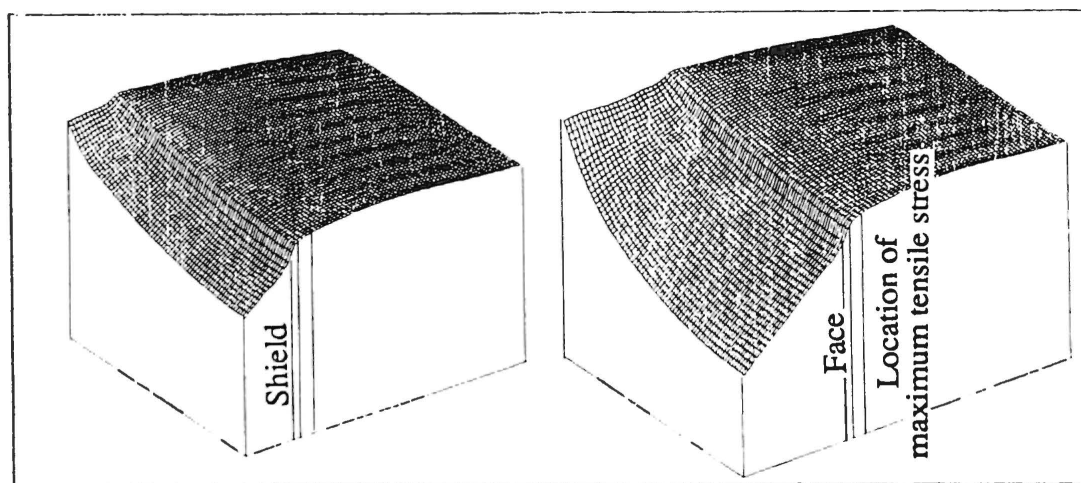
(a) Displacement of main roof when overhang length = 4.6 m (15 ft)

(b) Displacement of main roof when overhang length = 18.3 m (60 ft)

Figure 3. Variations of main roof displacement due to different overhang lengths of the main roof (vertical scale exaggerated).
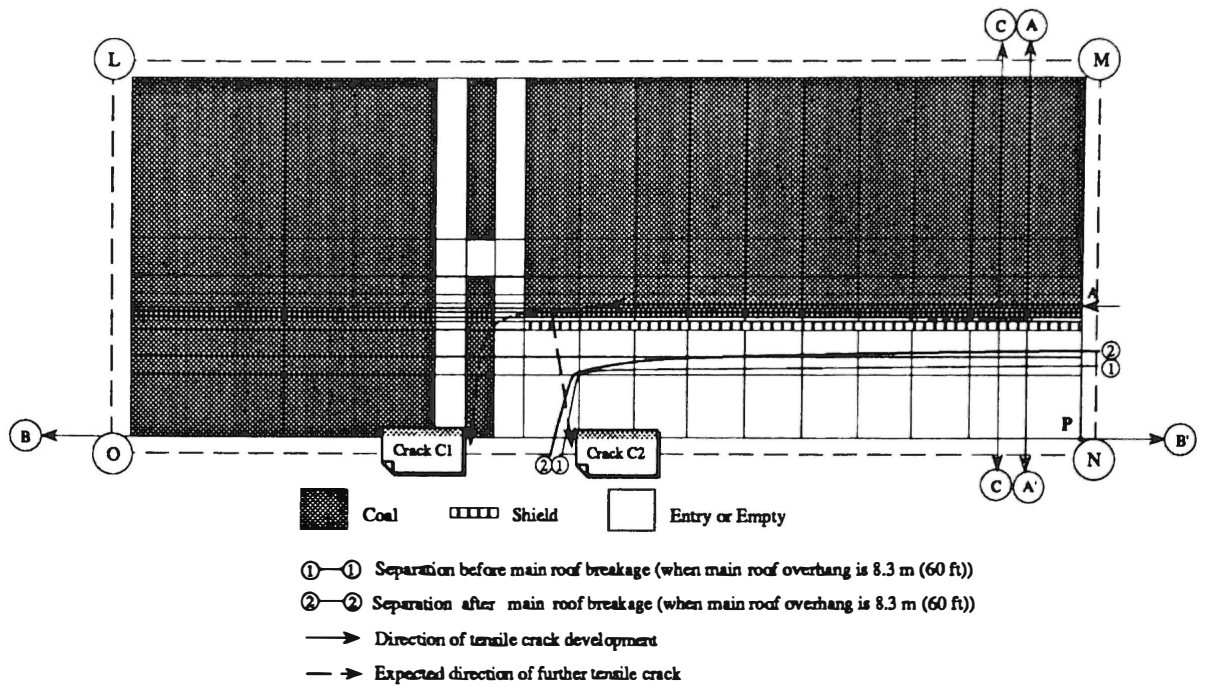
Figure 4. Area of roof separation in the exaggerated figure of box LMNO in Figure 1.
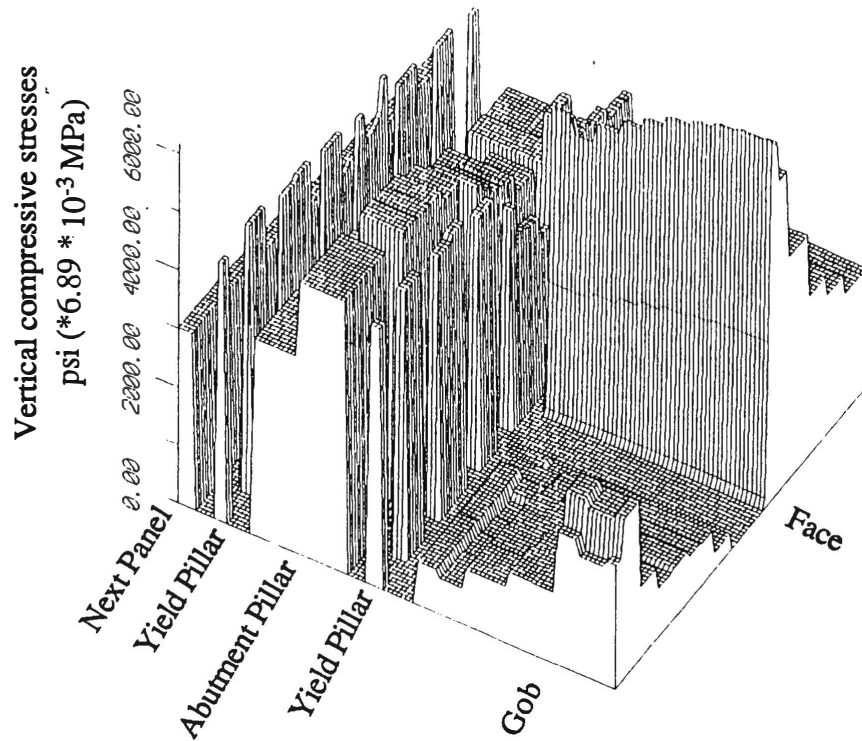
Figure 5. Vertical compressive stresses distributed on the coal seam.
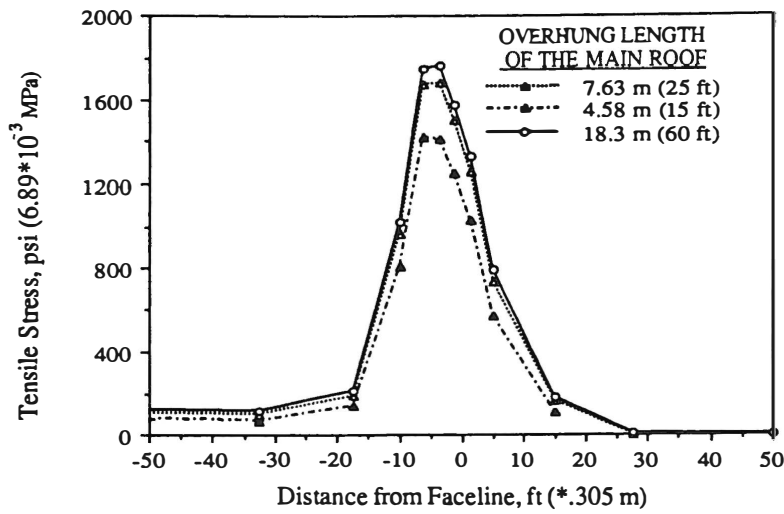
Figure 6. Variation of tensile stress in the main roof due to different lengths of the main roof hanging before breakage in Cross-Section A-A' of Figure 4.
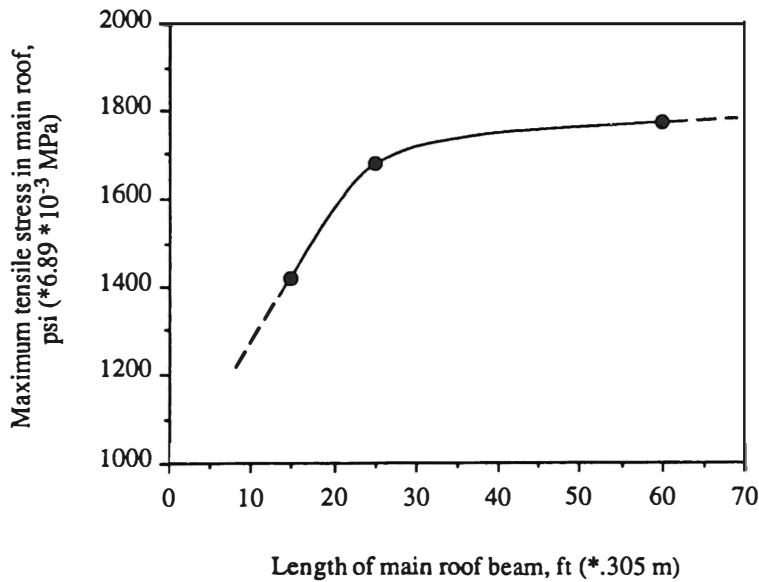
Figure 7. Relationship between maximum tensile stress and overhung length of the main roof.

Failure mode of main roof

The simulation of the crack propagation in the main roof was conducted by progressive iterations. Once the tensile failure occurred, the bending and tensile stress in the failure area were released, and the stresses were transferred and redistributed in each iteration. The

process continued until stress stabilized. Figure 8(a) thru. 8(c) show the tensile stress distribution after a certain number of iterations. The results show that, after the crack initiated form point A, the crack developed toward the head-gate, parallel to faceline until it reached up to 98 m (320 ft) from the center of the panel. With web cutting and face advancing, the crack continued propagating toward the headgate and turned direction towards the back-end of the plate as shown by the dotted line in Figure 4. The main roof breakage closely followed the maximum tensile line shown in Figure 8(a). Thus, as the face advanced, two cracks, C1 and C2, shown in Figure 4 developed in the main roof. The crack line, C1, alone the panel width has an arch-like shape, being farther back from the faceline near the head- or tail- gates. The crack line, C2, developed on the bottom of the main roof just before the roof fell down, initiating from the back end of the main roof toward the face. It should be pointed out that the location of C2 may depend on the shield support conditions. It is probable that, if there was no shield support or low shield setting load, C2 would occur close to the center line of the panel.

ROOF BEHAVIOR AND ITS EFFECT ON SHIELDS

Main roof rebounding

It was verified by monitoring data in the field that the main roof demonstrates a rebounding phenomena when it breaks (Zhu, et al., 1989). Figure 9 shows the comparison of the displacements before and after breakage of the main roof at cross section A-A'. It can be seen that movement near the crack was in the upward direction, resulting in a vertical stress reduction on the coal seam around the crack. However, the displacement at point P was greatly increased, being 19.8 cm (7.82 in.) prior to main roof failure, and 22.7 cm (8.95 in.) after failure. Displacement caused higher roof-to-floor convergence and a higher developing load on the shield.

Load variations on shield

The influence of the wide web cutting was simulated by the small-area model. The 0.76-m (30-in.) web cutting at the longwall face caused stress redistribution in the surrounding strata of the face, roof-to-floor convergence at the face, and increasing load on the shield. The calculated results showed that the developing loads due to the web cutting ranged from 108 to 116 tons before the main roof broke, where the main roof overhang ranged from 7.6 to 18.4 m (25 to 60 ft). It indicates that the increase of the developing load in the shield due to web cutting is not significant as the face advances. However, the behavior of the main roof was much different after the main roof broke. As discussed above, the main roof rebounds when breakage occurs. Then, the broken main roof located behind the crack enters a period of severe movement as the face advances, causing a high developing load on shield. The roof-to-floor convergence was much larger than before the main roof breakage. The developing loads in the shields after the main roof breakage were 1.41 to 1.87 times greater than before breakage.

The developing load distribution on the canopy was also analyzed in the study. Figure 10 illustrates a typical variations of the load distribution on the canopy before and after the main roof breakage. It can be seen that more loading is developed in the rear side of the canopy after the main roof breakage.
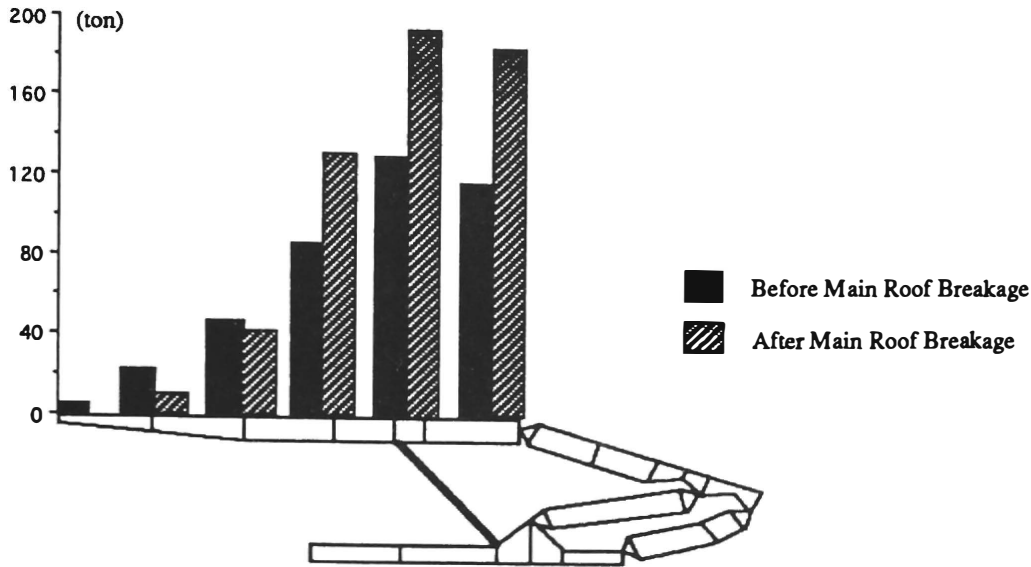
Figure 10. Typical load distributions on shield canopy
before and after main roof breakage.

Influences of coal seam yielding

It was also found that the maximum moments and tensile stresses in the main roof were related to the yielding of the coal seam due to high abutment pressure near the face. The calculated results show that the tensile stress in the main roof increased as much as 1.97 MPa (285 psi) and the location of the maximum tensile stress moved from 1.5 to 3 m (5 to 10 ft) ahead of the faceline when the coal seam yielded at 3 m (10 ft) ahead of the faceline. This indicates that the the location and the crack development path in the main roof is closely related to the coal seam strength.

SUMMARY AND CONCLUSIONS

The analyses using the large-area three dimensional finite-element modeling provides a detailed main roof behavior profile in the entire longwall panel. This study demonstrated that roof separation, main roof breakage, coal seam yielding, web cutting, etc. can be accurately simulated by proper modeling. The results confirm some measured data in previous studies, such as roof rebounding, interval of periodic weighting, and the shape of loading distributions on the shield canopy. It is valuable to define the maximum tensile stress location, the crack propagating in the main roof, and final failure mode. For this specific roof condition, the following conclusions have been reached from the study:

1) The main roof plate initially separated from the overburden strata at the back-center of the panel as the main roof plate grew up to 7.6 m (25 ft) in length. The separation further extended inward with the face advancing and roof breakage.
2) The maximum tensile stress produced in the main roof increased with the increase of main roof plate overhang, and it was distributed along the edges of the faceline and pillar with an arch-like shape. The maximum tensile stress occurred at 2.1 m (7 ft) ahead of the faceline at the center of the panel before the main roof broke. Tensile failure occurred when the

(a) Tensile stress distributions in the main roof
    prior to main roof breakage

(b) Tensile stress distributions after tensile crack
    propagated 48.8 m (160 ft) parallel to face line

(c) Tensile stress distributions after tensile crack
    propagated 98 m (320 ft) parallel to faceline
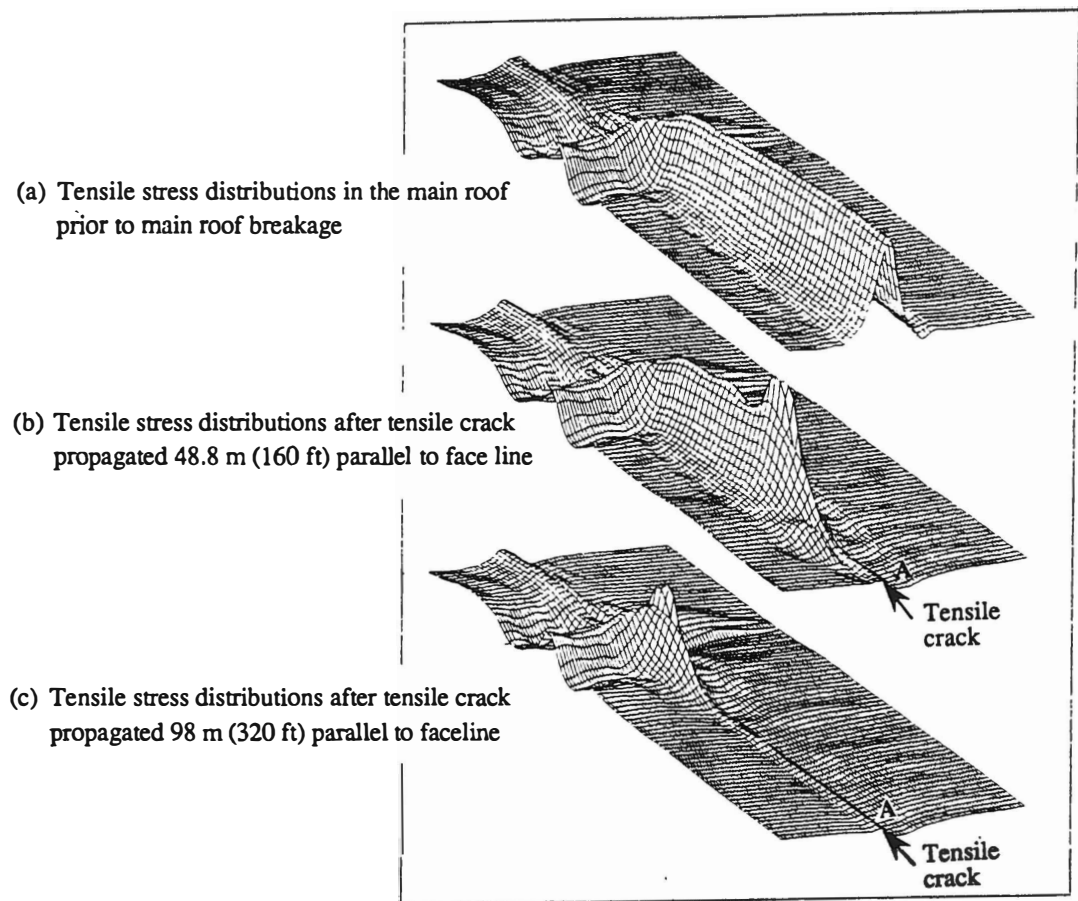
Figure 8. Variations of tensile stress in the main roof
with the propagations of the tensile crack.
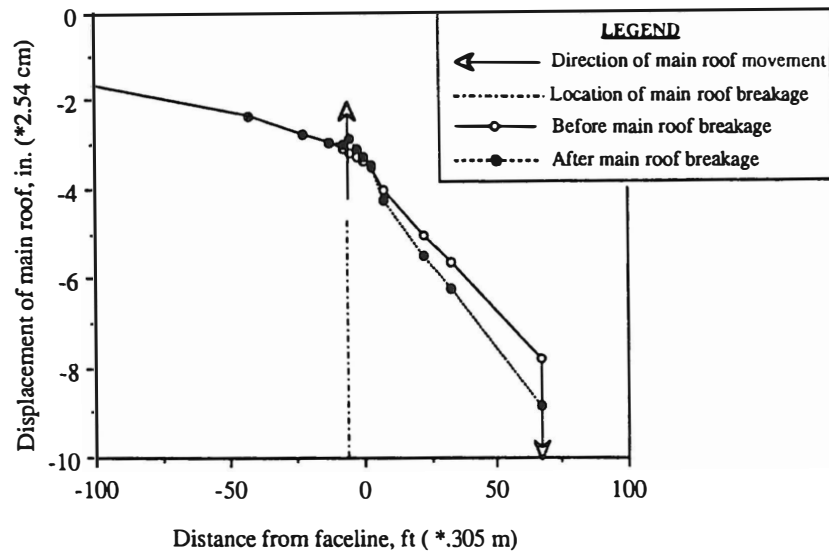
Figure 9. Variations of the displacement of the main roof before and after its breakage.

maximum tensile strength exceeded 12.4 MPa (1,800 psi) when the main roof overhang was 18.3 m (60 ft). It initiated 2.1 m (7 ft) ahead of the faceline in the center of the panel and proceeded parallel to the faceline until it reached approximately 107 m (350 ft) from the center of the panel.

3) It was found that the developing load on the shields were 1.41 to 1.87 times higher during the periodic weighting time than during normal time.

Further studies on the failure modes and their effects on the shield should be conducted.

REFERENCES

Barczak, T.M. and Schwemmer, D.E., 1988, "Stiffness Characteristics of Longwall Shields," Bureau of Mines, Report of Investigations, RI 9154, 14 pp.

Gullick Dobsen, Inc., 1985, *Technical Data for Jim Walter Resources, Inc.*

Hanna, K. and Haramy, K., 1991, "Automated Longwall Mining for Improved Health and Safety at the Foidel Creek Mine," SME-AIME Meeting, Preprint Number 91-165, 8 p.

Hoek, E. and Brown, E. T., 1980, *Underground Excavation in Rock,* The Institution of Mining and Metallurgy, London, 527 pp.

Hoek, E. and E. T. Borwn, 1988, "The Hoek-Brown Failure Criterion - a 1988 Update," *Proceedings,*15th Canadian Rock Mechanics Symposium, Toronto.

Kripakov, N. P., 1981, "Finite Element Analysis of Yield Pillar Stability," *Computers and Structures,* Vol. 13, pp. 575-593.

Park, D.W., R.L. Sanford, T.A. Simpson, and H.L. Hartman, 1984, "Pillar Stability and Subsidence Study at a Deep Longwall Coal Mine," *Proceedings, Second Annual Workshop, Generic Mineral Technology Center, Mine Systems Design and Control,* Reno, NV, pp. 17-50.

Park, D.W. and N. F. Ash, 1985, "Stability Analysis of Entries in a Deep Coal Mine Using the Finite Element Method," *Mining and Technology*, 3, pp. 11 - 20.

Park, D.W. and Gall, V., 1989, "Supercomputer Assisted Three-Dimensional Finite Element Analysis of a Longwall Panel," *Proc. 30th U.S. Symposium on Rock*, W.V.U., Morgantown, pp. 141~148

Park, D.W. and Y.M. Jiang, 1991, "Analysis of a Deep Longwall Face and Support System," *Proceedings, 9th Annual Workshop Generic Mineral Technology Center, Mine System Design and Ground Control*, Lexington, KY, November.

Park, D.W. and S.M. Lee, 1992, "Application of Three-Dimensional Numerical Modeling for Longwall Mine Design, " *121st SME Annual Meeting, Pre-print 92-169*, Phoenix, AZ.

Park, D.W., Y.M. Jiang, and S.M. Lee, 1992, "Interaction of Longwall Shields with Surrounding Strata, " *121st SME Annual Meeting, Pre-print 92-195*, Phoenix, AZ.

Park, D.W., Y.M. Jiang, and S.M. Lee, 1992, "Analysis of Main Roof Behavior and Its Effects to Shields at a Longwall Face," *Proceedings, 10th Annual Workshop Generic Mineral Technology Center, Mine System Design and Ground Control*, Moscow, Idaho, November 15 - 17.

Pothini, R. and S. S. Peng, 1989, "Panel Width Effect on Shield Supports," *Coal,* October, pp. 51 - 54.

Zhu, D. R., M. G. Qiun, and S. S. Peng, 1989, " A study of Displacement Field of Main Roof in Longwall Mining and Its Application," *Proceedings, 30th U.S. Symposium on Rock Mechanics*, Morgantown, WVU, pp. 149 - 156.

Session 4

Subsidence

Affaissement

APPLICATION OF NONLINEAR FINITE ELEMENT METHOD IN PREDICTION OF GROUND SUBSIDENCE DUE TO UNDERGROUND MINING

Yacoub Najjar*, Dar-Hao Chen** and Musharrf Zaman***

* Assistant Professor
Department of Civil, Mechanical, and Environmental Engineering
George Washington University
Washington D.C., 20052

** Graduate Research Assistant, *** Associate Professor
School of Civil Engineering and Environmental Science
University of Oklahoma, Norman, OK 73019

ABSTRACT

A nonlinear Finite Element Method (FEM) is employed to investigate the ground subsidence potential due to mining in an accurate and realistic manner by incorporating an elasto-plastic constitutive model in which the geologic materials are treated as transversely isotropic in both elastic and inelastic ranges. The associated material constants for the constitutive model are obtained by performing a comprehensive series of laboratory tests on cubical specimens under truly three-dimensional loading. A novel algorithm is employed to accurately simulate the excavation sequences. An actual field problem is solved by using the FEM algorithm and a parametric study is conducted to investigate the effects of reduction factors applied to the laboratory determined material properties. The predicted subsidence values are compared with the field measurements and good correlations are obtained.

1 INTRODUCTION

Ground subsidence due to mining is a major problem in the coal industry. The underground mining creates cavities by removing the natural support from the overlying strata. Consequently, successive layers of rock undergo bending under the influence of gravity and may collapsed over the cavity, until finally the movement reaches the surface (Hiramatsu et. al., 1979). Inadequate understanding of strata movements during subsidence has been attributed to damage of many surface structures. As a result, the coal mining industry is forced to take remedial measures to control subsidence by state and federal laws. It is known that a coal mine with a wide area of excavation by the longwall mining technique is difficult, if not impossible, to accomplish without surface subsidence (Hiramatsu, 1983; Siriwardane et. al., 1991). In fact, some mining techniques are designed to accommodate roof collapse as mining progresses (Peng, 1986). To prevent damages to surface structures, it is important to restrict surface subsidence within the allowable limits. Predictions of surface movement and subsidence profile are

important in planning coal mining operations to assess the consequences of the resulting ground movements, if any.

In the present study, a High Capacity (30,000 psig) Cubical Device (HCCD) is used to investigate the behavior of coal under multiaxial loading. An elasto-plastic constitutive model developed by Faruque and Chang (1986) and modified by Najjar (1990) and Chen (1992) is implemented in the nonlinear finite element (FE) code by considering the geologic materials as transversely isotropics both in the elastic and inelastic ranges. Since coals are usually found in nature as a layered material it may be reasonable to treat such materials as transversely isotropic. In this model, a single mathematical function is used to describe both yielding and failure behaviors. The associated material constants in the constitutive model are obtained by performing a comprehensive series of laboratory tests on cubical specimens under three-dimensional loadings. The FE algorithm is used to analyze the ground subsidence problem associated with an actual coal mine and the results are compared with field measurements.

2 CONSTITUTIVE MODEL AND FE ALGORITHM

The algorithm presented by Ghaboussi et. al. (1984) is modified to accurately simulate the excavation sequences. Mining operations are modeled as a multiple step process in which excavations are carried out in steps. In the beginning, all elements are assumed to be active. At a given step, a specified number of elements are removed by deactivating them from the finite element mesh. Also, the stresses present in the excavated elements are redistributed to the unexcavated elements using an iterative technique. The proposed technique is found to converge rather rapidly. The developed algorithm uses an elasto-plastic constitutive model to represent the behavior of overlying strata (i.e., rocks and unconsolidated materials) in a realistic manner. The constitutive model employed is capable of considering unloading and reloading, stress path-dependency, dialatancy, and the effect of intermediate principle stress, which are important for most geologic materials (Chen and Mizuno, 1990). Further details of the testing program and the parameters determination are not given here due to space limitation and can be found in Chen (1992).

2.1 Constitutive Model

The most important feature of the elasto-plastic constitutive model developed is that it accounts for inherent anisotropy, which is an important property of materials like coal. Because the nature of deposition and presence of cracks and bedding planes, coals exhibit a high degree of anisotropy. Another attractive feature of the model is that it accounts for anisotropy even in the elastic range. Further, the model is capable of predicting volumetric response in the compressive as well as in the dilative regions. The yielding and failure behavior are described by a single mathematical function of the form

$$F = \tilde{r}^2 - \left[\alpha \tilde{J}_{1A}^n - \frac{\tilde{J}_{1A}^{2n}}{\beta} + \tilde{K}^2 \right] g(\theta, \tilde{J}_1) = 0 \tag{1}$$

where α, n and K are failure parameters. Also, $\tilde{r}$, $\tilde{J}_1$ and $\tilde{K}$ are non-dimensional quantities given by : $\tilde{r} = r / p_a$, $\tilde{J}_1 = J_1 / p_a$, and $\tilde{K} = K / p_a$, where p_a is the atmospheric pressure and K is

the cohesive strength and $\Gamma = \sqrt{2J_{2D}}$. In these relationships, the three stress invariants J_1, , J_{2D} and J_{3D} of the deviatoric stress tensor S_{ij} are given by

$$J_1 = \sigma_{ii} = \sigma_{11} + \sigma_{22} + \sigma_{33} , \quad J_{2D} = \frac{1}{2} S_{ij} S_{ji} \quad \text{and} \quad J_{3D} = \frac{1}{3} S_{ij} S_{jk} S_{ki} \qquad (2)$$

The hardening behavior of the material used is within the concept of isotropic hardening plasticity. According to this concept, the yield surface, F, is allowed to expand in the stress space. This is achieved by specifying a hardening function β in the form

$$\beta = \beta_1 \, \xi^{\eta_1} \left[1 - \beta_2 \, (r_D)^{\eta_2} \right] \qquad (3)$$

where β_1 , β_2 , η_1 and η_2 are the hardening parameters and $r_D = \xi_D / \xi$. ξ denotes the length of the trajectory of the incremental plastic strain vector and ξ_D is the deviatoric part of ξ, and are defined as

$$\xi = \int \left(d\varepsilon_{ij}^P \, d\varepsilon_{ij}^P \right)^{\frac{1}{2}} \quad \text{and} \quad \xi_D = \int \left(de_{ij}^P \, de_{ij}^P \right)^{\frac{1}{2}} \qquad (4)$$

where $d\varepsilon_{ij}^P$ and de_{ij}^P represent the incremental total and deviatoric plastic strain tensors, respectively.

The variable J_{1A} in Eq. (1) is proposed as

$$J_{1A} = (a_{11} \, \sigma_{11} + a_{22} \, \sigma_{22} + a_{33} \, \sigma_{33}) \qquad (5)$$

where a_{11}, a_{22} and a_{33} are anisotropic coefficients and are positive quantities that can be determined from the stress-strain response under the hydrostatic compression (HC) loading. It may be noted that for an orthotropic material $a_{22} \neq a_{33}$, and for a transversely isotropic material $a_{22} = a_{33}$.

The function g (θ, $\tilde{J}_1$), which accounts for the shape of the yield surface and the failure surface was defined by Faruque and Chang (1986) as follows

$$g(\theta, \tilde{J}_1) = \left[\cos \left(\frac{1}{3} \cos^{-1} (- A \cos 3\theta) \right) \right]^{-2} \qquad (6)$$

where

$$\theta = \frac{1}{3} \cos^{-1} \left[3\sqrt{3} \, J_{3D} / 2 \langle J_{2D} \rangle^{\frac{3}{2}} \right] \qquad (7)$$

and

$$A = \exp (- \gamma \tilde{J}_1) \qquad (8)$$

The variable γ is a material constant that accounts for the variation of the shape of the yield surface on the octahedral plane.

In summary, the developed constitutive model has the following fourteen material constants to describe the anisotropic elasto-plastic material behavior : (1) four elastic constants : $E, E', \vee$ and $\vee'$; (2) two anisotropic constants : a_{22} and a_{33} ; (3) four constants associated with the transition and the yield surface : α, n, k and γ and (4) four constants associated with hardening : β_1 , β_2, η_1 and η_2 . These material parameters were determined by conducting tests along various stress paths (namely, Hydrostatic Compression (HC), Conventional Triaxial Compression (CTC), Simple Shear (SS), Triaxial Extension (TE), and Triaxial Compression (TC) (Desai et. al., 1984)) under various confining pressures. It is important that the constitutive law be valid for all the major stress paths and confining pressures that the material (coal) can experience in reality. Thus, it is desirable that specimens be tested under different anticipated stress paths (Desai et. al., 1984). The anisotropic constants (a_{22} and a_{33}) and hardening parameters (β_1 , β_2, η_1 and η_2) are determined from the HC tests. Also, the unloading-reloading cycles at the same level of confining pressures for different stress paths will be utilized to evaluate the elastic constants (E, $E', \vee$ and $\vee'$). The failure shear strengths for various shear tests are used to compute the yield and/or failure parameters (α, n, k and γ). The detail description of this model and the evaluation of material constants can be found in Chen (1992).

2.2 Finite Element Algorithm

The algorithm for the simulation of excavation into a finite element procedure is summarized and given in the following steps. Step 1: Input data including geometry, element connectivities, material properties and boundary conditions; Step 2: Compute element stiffness matrices (based on the constitutive models adopted) and assemble them to obtain the global stiffness matrix of the domain $[K]_0$; Step 3: Evaluate the equivalent nodal forces due to gravity loading to obtain $(P)_0$; Step 4: Solve $(\Delta U)_0$ from the matrix equation $[K]_0 (\Delta U)_0 = (P)_0$; Step 5: Compute the in situ stresses for each element; Step 6: Deactivate the elements which are to be excavated at the excavation stage number N; Step 7: Restrain the displacements at the nodes that have been completely excavated to zero (i.e., these nodes become inactive nodes). Note that the system would otherwise be singular; Step 8: Recompute the stiffness matrix for the active elements at excavation stage N and assemble them to obtain $[K]_N$; Step 9: Evaluate the external load vector due to gravity load for the active elements at the excavation stage N and assemble them to obtain $(P)_N$; Step 10: Compute the nodal internal resisting force vector (I) from element stress $(\sigma)_{N-1}$; Step 11: Solve the system of equations to obtain $(\Delta U)_N$; Step 12: Compute $(\Delta \sigma)_N$ for each active element at this excavation stage; Step 13: Update $(U)_N$ and $(\sigma)_N$; Step 14: If material nonlinearity is considered, adjust $(\sigma)_N$ to be consistent with the constitutive model used. Otherwise go to step 16; Step 15: Check if convergence is achieved. If it is achieved, then go to step 16. otherwise, go back to step 8 and repeat steps 8 through 15 until convergence is achieved; Step 16: Go to step 6; Step 17: Continue steps 6 to 16 until all excavation stages are completed.

A flowchart that the summarizes important steps involved in the subsidence simulation process and the sequence of operations of these steps are illustrated by Zaman et. al. (1993).

3   ANALYSIS OF SUBSIDENCE AT BLACKSVILLE MINE # 1

An actual coal mine, Blacksville mine # 1, is investigated by using the incremental nonlinear
finite element procedure outlined in the previous section to analyze the associated subsidence
due to mining. This site was also studied by Dahl and Choi (1973), Siriwardane (1985) and later
by Najjar, et. al. (1987). One of the reasons for selecting this site is the availability of field
measurements that can be used to check the accuracy of the FEM results. Numerical predictions
are carried out for two different idealizations of stress-strain responses : (1) stress-strain
behavior of all materials is idealized as linear-elastic; and (2) nonlinear behavior of all materials
is idealized by the Drucker-Prager model with the exception of the coal layer which is idealized
by the elasto-plastic single surface anisotropic model. These idealized cases are referred to in
this paper as case 1, and case 2 respectively. For case 2, the elasto-plastic single surface models
(isotropic and anisotropic) are employed only for the coal layer because the material constants,
which are required for the elasto-plastic constitutive models, were evaluated in this study only
for this material. Cohesion and friction angle values for the other strata were available in the
literature (Siriwardane, 1985). Thus, it was possible to use the Drucker-Prager model for these
strata.

Underground mining at Blacksville # 1 mine adopted the longwall mining method with a face
width of about 450 feet. The coal seam thickness in this area was about 7 feet with a mining
height of approximately 6 feet. The plane strain idealization was used in this study because the
length of the panel was quite large as compared with the panel width. Analysis of a transverse
section close to the center of the panel is considered here for the purpose of subsidence
prediction. The actual and idealized geological profiles are shown in Fig. 1. The finite element
mesh used to discretize the transverse section is shown in Fig. 2. The location of the mine
opening and excavation configuration are also shown in this figure where the dark area
represents the mine opening or the excavated regions. The finite element mesh consists of 477
four-noded isoparametric elements connected to 524 nodal points, including the 12 excavated
elements. The boundary conditions used in this analysis are shown in the same figure. A
summary of the material constants used in the analysis is given in Table 1.

Since laboratory tests usually yield higher strengths than the field strength (Bieniawski, 1968;
Siriwardane, 1985), reduction factors are applied here to Young's modulus (E) and cohesion (C)
to investigate the effects of size and shape on the subsidence magnitude and profile. A
parametric study is performed to investigate the effects of reducing the modulus of elasticity (E)
and cohesion (C). In this parametric study, seven reduction cases are considered. For brevity,
the reduction factors applied to E and C are referred to as RE and RC, respectively.
Numerical/graphical results are presented for subsidence profiles and stress contours. The
parametric study focuses on the effects of material nonlinearity as depicted by the two different
constitutive models adopted and reduction factors on the subsidence magnitudes and profiles.

3.1   Subsidence Profiles

The detailed subsidence profiles for different idealizations, with different reduction factors
applied, can be found in Chen (1992). Only sample results are presented here due to space
limitation. To enhance the comparison of the ground subsidence and roof subsidence profiles,
the excavated region is superimposed on the upper part of all figures. A comparison of the
average subsidence profiles for idealization case 2, including the average of roof and surface
subsidence, with different reduction factors, is presented in Fig. 3. The shape of the average

Table 1 Material Properties Used in the Present Study for Analysis of Blacksville No. 1 Mine

Material	Shale	Limestone	Coal	Shale& Sandstone	Sandstone
Elastic modulus (E) ksi	·500	4000	*	1500	2500
Cohesion (C) (psi)	4041	4041	300	4041	4041
Poisson's ratio (v)	0.2	0.21	*	0.17	0.15
Unit weight γ (pci)	0.08	0.095	0.045	0.085	0.091
α	....	....	80.0	....	....
γ	....	....	45.0	....	....
k (psi)	....	....	300.0	....	....
n	....	....	1.12	....	....
β_1	....	....	1.685	....	....
η_1	....	....	55000	....	....
β_2	....	....	0.91	....	....
η_2	....	....	0.21	....	....

Note : * See Chen (1992) for details.

Depth of Coal at Panel Center is 597 Feet
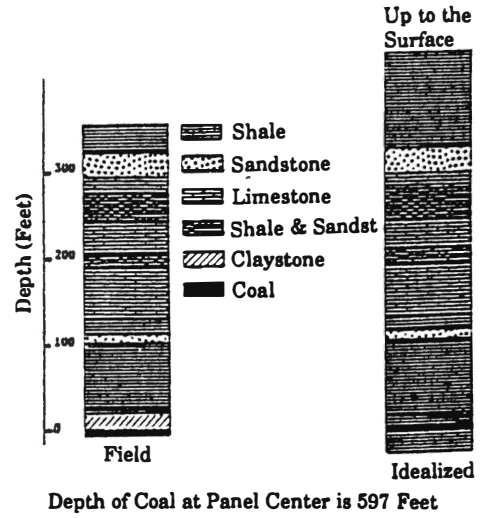
Fig. 1 Field and Idealized Geologic Profiles of Blacksville No. 1 Mine (after Siriwardane, 1985)
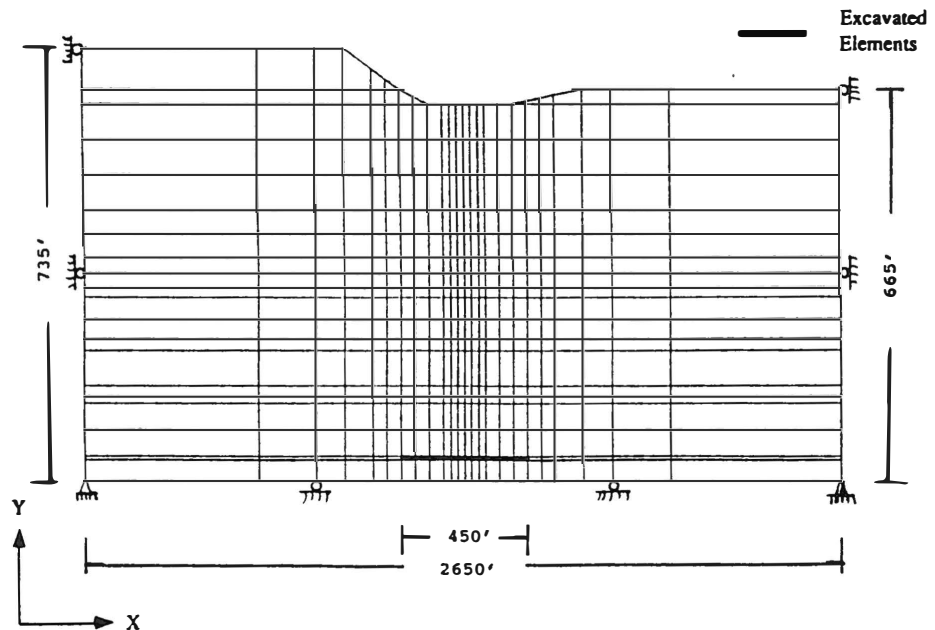
Fig. 2   Finite Element Mesh for the Analysis of Blacksville No. 1 Mine (All Elements are 4-noded Isoparametric Element)

145

subsidence profiles is found to be similar to those of the surface subsidence profiles, but the magnitudes are smaller, as expected, for all reduction cases investigated here. In general, in underground mining, maximum movements are expected at the roof level and they reduce with (vertical) distance from the roof due to arching effect. Thus, the effects of roof collapse or subsidence may or may not cause significant movements of the ground surface depending upon various factors such as geometric and material properties of the overburden and the depth of excavation. Fig. 3 is in agreement with this general remark. The normalized subsidence (s / s_{max}) profiles for average subsidence and surface subsidence for reduction case 6 (RE=0.45, RC=0.2) are presented in Fig. 4, s_{max} being the maximum surface subsidence. The normalized subsidence (s / s_{max}) is defined as the ratio of subsidence at a point (S) and the maximum subsidence of the idealized domain, for a given material idealization. Fig. 4 illustrates that the surface normalized subsidence profiles are in closer agreement with the field data. The measured profile is more localized than the predicted one.

Horizontal Distance Measured From Panel Center (feet)
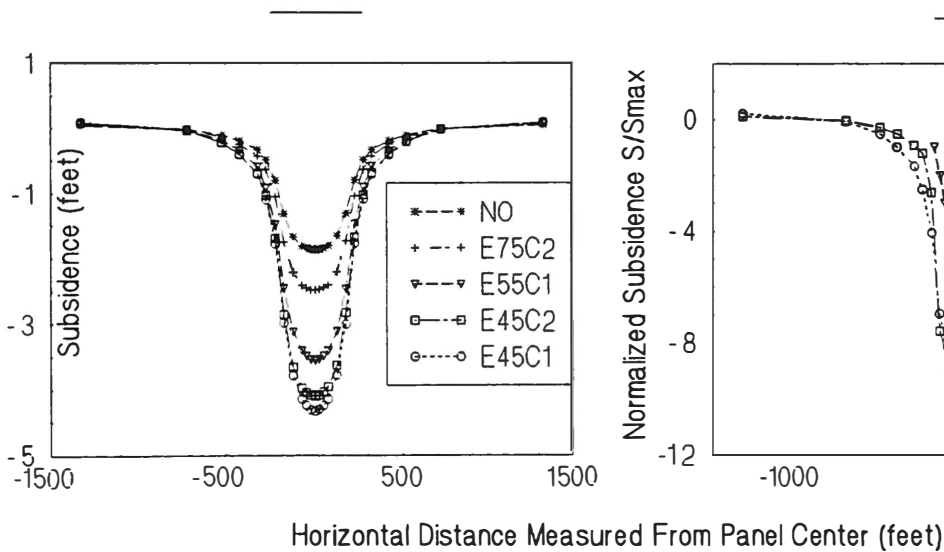
Fig. 3 Comparison of Average Subsidence Profile (Roof and Surface) for Idealization Case 2 by Using Different Reduction factors
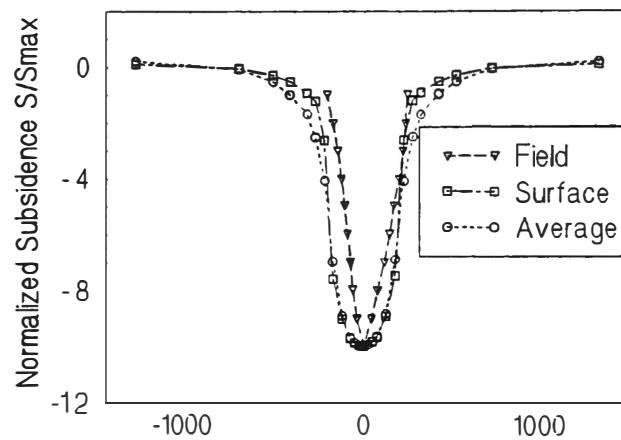
Fig. 4 Comparison of Normalized Average (Roof and Surface) and Surface Subsidence Profile for Idealization Case 2 (RE=0.45, RC=0.2)

3.2 Stress Distribution

The distribution of vertical stresses σ_{yy} under the in situ condition (before excavation) and after excavation, for idealized cases 1 and 2 (RE=0.45, RC=0.2) is shown in Figs. 5 and 6. The contours showing the distribution of shear stresses τ_{xy} are presented in Fig. 7. It is observed that the changes in the stress profile, from the in situ condition to the excavated condition are significant in the region close to the excavation and it gradually becomes insignificant in regions away from the excavated areas. This is why the stress distribution in the region X < 300 feet and X > 2350 feet is not shown here. Also, it may be noted that the origin is chosen at the lower left corner because of the uneven ground surface. In view of Figs. 5,6 and 7 , the following observations can be made :

1. The magnitude of vertical stresses σ_{yy} is almost zero at the mine roof, as expected. Ideally, σ_{yy} at the roof should be zero, but in finite element analysis, the stresses represent the values at the element integration points and not on the roof surface. Thus, some discrepancy is expected. Alternatively, it is possible to use the interpolation technique to obtain stresses at the element nodes. At both ends of the opening, σ_{yy} increases by about 1.7 times from those of the in situ values. This is because the overburden forces at the top of the excavated region are transferred to the unmined regions making the stresses concentrated at the ends of the opening.

2. Compressive stresses are predominant in the central region above the excavation (350 to 550 feet from the ground surface) while tensile stresses are developed in the region just above the excavated area. This phenomenon is similar to a beam which is subjected to downward forces resulting in compression at the top of the beam and tension at the bottom. Also, small tensile stresses are developed in the regions underneath the excavated areas (not shown in figures), due to the upheaving effect at the mine floor caused by the removal of the natural support.

3. The magnitude of shear stress τ_{xy} is drastically increased by as much as 55 times from those under the in situ condition (before excavation). This illustrates the mechanism of subsidence caused by the excavation and leading to the loss of shear strength of the overburden strata.

4   SUMMARY OF OBSERVATIONS

From the discussion of the numerical results, the observations can be summarized as follows :

1. The nonlinear finite element algorithm, along with the elasto-plastic constitutive model, employed in this study provides a useful tool for analysis of subsidence due to underground mining.

2. Linear analysis under-predicts the measured surface subsidence values, as expected.

3. The material constants determined from laboratory tests need to be reduced by a desired
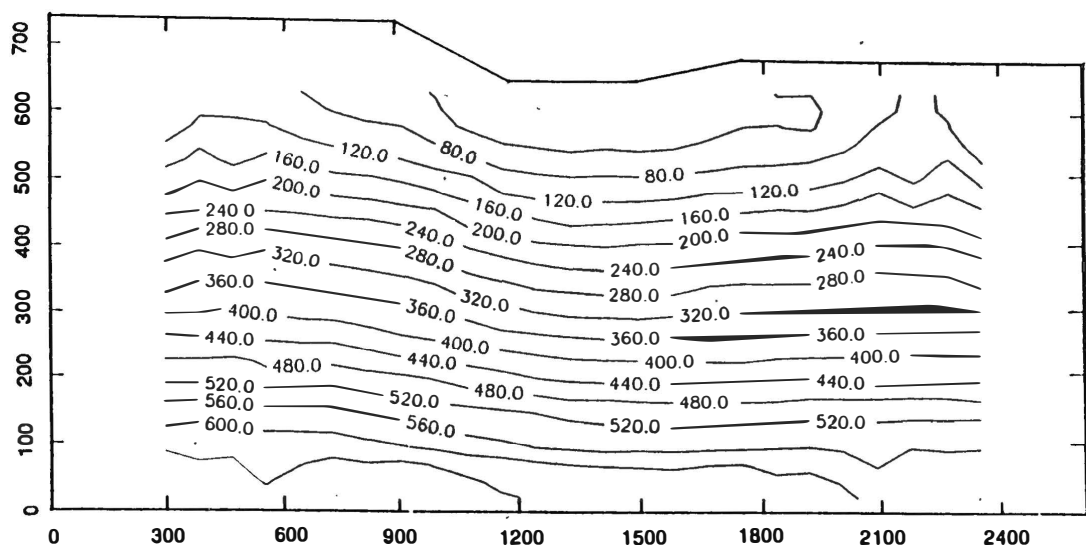
Fig. 5   Distribution of Vertical Stresses σ_{yy} (psi) in Overlying Strata Before Excavation

147
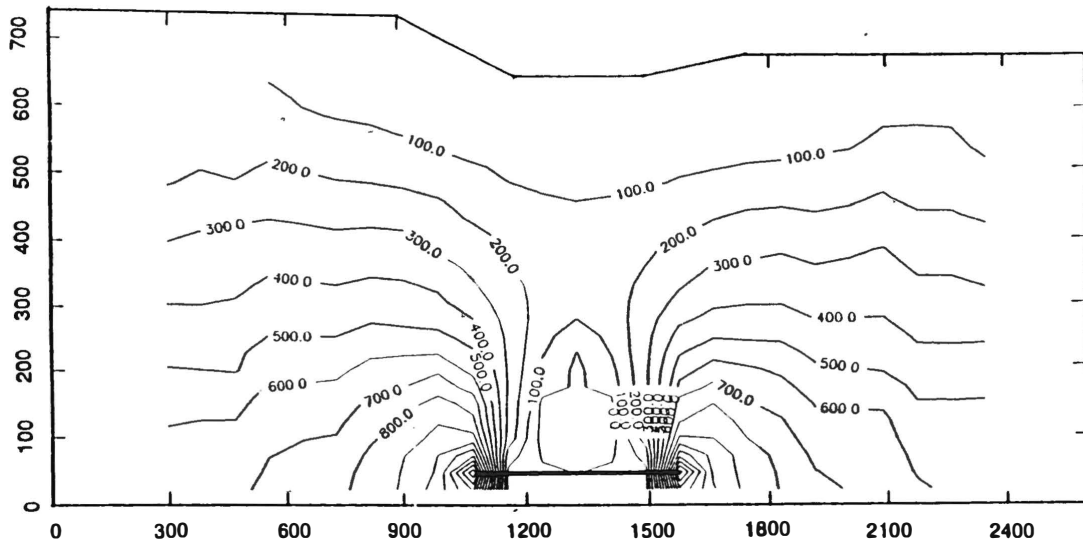
Fig. 6   Distribution of Vertical Stresses σ_{yy} (psi) in Overlying Strata After Excavation by using
Idealization Case 2 (RE=0.45, RC=0.2)
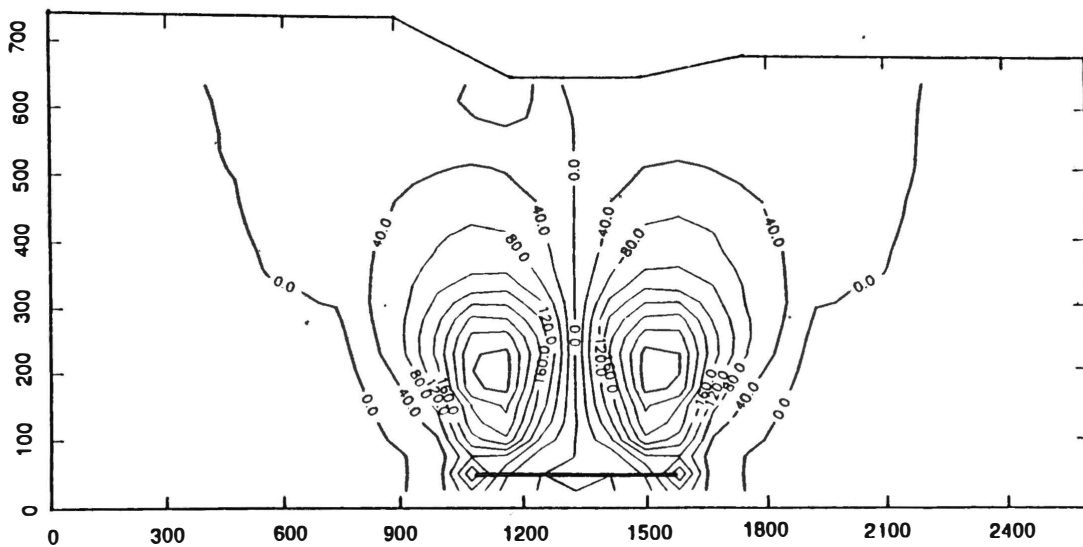
Fig. 7   Distribution of Shear Stresses τ_{xy} (psi) in Overlying Strata After Excavation by using
Idealization Case 2 (RE=0.45, RC=0.2)

factor in order to account for the specimen size and shape effects as compared to the
conditions existing in the field. From the parametric study conducted here, involving
reduction factors applied to E and C, it was found that the maximum value of subsidence is
more sensitive to E than to C when the reduction factors range between 1 to 10. However,
when C alone is reduced by a significant amount (by a factor of 100), this also increases the
subsidence value drastically.

4.   The differences in predicted subsidence values for all idealizations are relatively small

148

(approximately 5%) because the coal layer and the excavated area are rather small compared to the total material domain. The subsidence profile obtained by using the transversely isotropic (idealization case 2) constitutive model for the coal provides better correlation with respect to the field values.

ACKNOWLEDGEMENTS

REFERENCES

Bieniawski, Z.T. (1968), "The Effect of Specimen Size on Compressive Strength of Coal," Int. J. Rock Mech. Min. Sci., Vol, 5, pp. 325.

Chen, Dar-Hao (1992), "Three-Dimensional Testing and Constitutive Modeling of Coal for Analysis of Ground Subsidence Due to Mining," M.S. Thesis, School of Civil Engineering and Environmental Science University of Oklahoma, Norman, Oklahoma.

Chen, W.F. and Mizuno, E. (1990) , Nonlinear Analysis in Soil Mechanics (Theory and Implementation, Elasevier Science Publishers B.V., Netherlands.

Desai, C.S. and Siriwardane, H.J. (1984), Constitutive Laws for Engineering Materials with Emphasis on Geological Materials, Prentice-Hall, New Jersey.

Dahl, H.D. and and Choi, D.S. (1973), "Some cases of Mine Subsidence and its mathematical modeling," Proc. of Fifteenth Symposium on Rock Mechanics, Custer Park, SD. pp. 1-21.

Faruque, M.O. and Chang, C.J. (1986), "New Cap Type Model for Failure and Yielding of Pressure Sensitive Materials", J. Eng. Mech. Div., ASCE, Vol. 112, pp. 1041-1053.

Ghaboussi, J. and Pecknold, D.A. (1984), "Incremental Finite Element Analysis of Geometrically Altered Structures," Int. J. for Num. Met. in Eng., Vol. 20, pp. 2051-2064.

Hiramatsu, Y., Okamura, H. and Sugawara, K. (1979), "Surface Subsidence and Horizontal Displacement Caused by Mining Inclined Coal Seams," Proc. of 4th Int. Congr. Rock Mech., Vol. 1, ISRM.

Hiramatsu, Y. (1983), "Deep Underground Excavations Especially Tunnels, Coal Mining and Subsidence Cause by Them," Proc. of 5 th Int. Congr. Rock Mechanics, Vol 3, pp. G167-G183, Melbourne.

Najjar, Y.M., Zaman, M.M. and Koragappa, N. (1987), "Ground Subsidence in Oklahoma Due to Mining : Potential problems and Numerical Modeling," Report, School of Civil Engineering and Environmental Science University of Oklahoma, Norman, Oklahoma. 86p.

Najjar, Y. M. (1990), "Constitutive Modeling and Finite Element Analysis of Ground Subsidence Due to Mining," Ph.D. Dissertation, School of Civil Engineering and Environmental Science University of Oklahoma, Norman, Oklahoma.

Peng, S.S. (1986), Coal Mine Ground Control. 2nd ed., John Wiley & Sons , New York.

Siriwardane, H.J.(1985), "A Numerical Procedure for Prediction of Subsidence Cause by Longwall Mining," 5th In. Con. on Numerical Methods in Geomechanics, Nagova, Japan, pp. 1595-1602.

Siriwardane, H.J. and Amanat, J. (1991), "Displacement Based Approach for Prediction of Subsidence Caused by Longwall Mining Using Numerical Methods," Proc. of the 7th Int. Con. on Computer Methods and Advances in Geomechanics, Cairns, 6-10 May, 1991, pp. 1387-1392.

Zaman, M., Kukreti, A. and Chen, D.H. (1993), "Numerical Modeling Of Mining Induced Subsidence", Proc. 2nd Asian-Pacific Conference on Computational Mechanics. Sydney, Australia, Aug. 3-6, 1993 (in press).

MODELING OF CONCRETE MASONRY WALL SUBJECTED TO LONGWALL SUBSIDENCE

D. Dutta, S. S. Peng, and Y. Luo
Department of Mining Engineering
West Virginia University
Morgantown, WV 26506
USA.

ABSTRACT

By using linkage element concept for mortar joints, concrete-block masonry wall subjected to subsidence was modeled as a two dimensional, linear, plane stress problem. Smear cracking technique is used to investigate crack initiation and propagation in the wall. Cracking of the wall is confined to mortar joints in a stepped pattern. Effects of locations of maximum curvature, radius of curvature, and length to height ratio of wall are studied and it is found that these quantities are related to the maximum tensile stress on the wall by second order polynomial functions.

INTRODUCTION

Most of the houses in rural USA affected by subsidence have wood-framed superstructures sitting on concrete-block masonry basements. Due to underground longwall mining, these basements develop cracks mostly along the mortar joints. Once these mortar joints are cracked, they open up resulting in the total damage of the basement walls. While there is no exact damage criterion to assess the potential damage to this type of basement, references of damage criteria for residential houses are found in the compiled work of Bhattacharya and Singh (1984). They have reported that radius of curvature from 3 to 20 km is capable of cracking a residential structure. Peng (1992) reports that a radius of curvature of 5.1 km can cause damage to wooden-superstructures. Karmis et al. (1990) considers a radius of curvature 12.2 km as critical. Not only there is no available criterion for concrete block masonry walls, many questions, such as, the location and propagation of crack in the wall, effect of radius of curvature on length to height ratio of the wall, effect of location of maximum curvature along the wall, stress distribution in the wall, effect of openings in the wall, etc., still remain unanswered.

To investigate some of those unanswered issues, numerical analysis is the only recourse because concrete-block masonry is a complex material consisting of an assemblage of brick and mortar joints. The mortar joints act as planes of weakness due to their low tensile and shear strengths.

This paper describes the methodology and results of a finite element technique to investigate the mechanisms of crack development in concrete block walls caused by underground longwall coal mining.

TYPES OF CRACKING IN MASONRY

In the field, it was found that the cracks in the four concrete-block masonry walls were mostly stepped cracks and a few vertical cracks (Luo et al., 1992). Only two horizontal cracks running along the mortar joints and spanning through the entire wall were observed. Twelve major cracks of width 25 mm or more were mostly stepped. Besides that, small cracks of width less than 6 mm were observed near the doors, windows, and at the corners of chimney.

Out of the twelve major cracks, only one crack initiated from the bottom of the wall and propagated upwards. This crack was believed to have been caused by ground strain

combined with sagging (concave) curvature. All the other eleven major cracks initiated from the top of the wall and propagated downwards. They had wider openings on the top than at the bottom. Once the cracks reached the ground level, relative horizontal displacements and slopes on two sides of the wall further increased their widths.

It is clear that the concrete block masonry structures are mostly affected by hogging (convex) curvature which causes tensile stresses on the top of the wall. These stresses cause cracks starting from the top of the wall and propagating downwards. For the ungrouted wall mostly found in the residential structures, the failure pattern tends to be stepped. This pattern predominates although occasionally there was a mixed mode of failure with the cracks extending from one of the head (vertical mortar) joints and passing through one of the blocks instead of following the mortar joints around the block.

FINITE ELEMENT FORMULATION

Early works on finite element formulation of masonry wall considered mortar and bricks as same unit with average mechanical properties (Rosenhaupt and Sokal, 1965; Saw, 1974). Elastic analysis with bricks and joints being modeled separately is found in the work of Ali and Page (1985). Non linear behavior of masonry wall was modeled by Page (1978) and Ali and Page (1988). When bricks and mortars were modeled separately, both bricks and mortars were considered to be two dimensional isoparametric elements. Page (1978) first formulated mortar joints in the masonry wall by using Goodman et al.'s (1968) concept of joint element which was derived from the work on linkage element by Ngo and Scordelis (1967). He did not provide details of element stiffness matrix and strain displacements matrix. However, he has given the relationship between mortar stiffness and mortar elastic properties.

In the current study, the behavior of masonry is modeled using four nodes isoparametric plane stress elements for concrete-blocks which are connected to the mortar modeled by linkage elements. Stiffness matrix and strain displacement matrix for mortar have been derived using linear interpolation functions for displacements. For the bed joints in the masonry having a thickness t and length L between two head joints, shear (ϵ_s) and normal (ϵ_n) strains are given by (Yuan and Chua, 1992),

$$\epsilon_s \approx \frac{u_r}{t}, \qquad\qquad \epsilon_n \approx \frac{v_r}{t} \qquad\qquad (1)$$

where, u_r and v_r are the relative displacements along the horizontal and vertical

directions, respectively.

The relative displacements are related to the nodal displacements by linear interpolation functions which are the same as that used for one dimensional element. Thus, the strain displacement matrix B is,

$$\begin{Bmatrix} u_r \\ v_r \end{Bmatrix} = \frac{1}{t} [N]\{q\}, \quad \text{and} \quad B = \frac{1}{t} [N] \tag{2}$$

where, [N] is the matrix of interpolation functions and $\{q\}$ is the vector of nodal displacements. The constitutive matrix given by Page (1978) is,

$$[C] = \begin{bmatrix} k_s & 0 \\ 0 & k_n \end{bmatrix} \tag{3}$$

$$k_s = \frac{ET}{t} \quad \text{and} \quad k_n = \frac{GT}{t} \tag{4}$$

where, E and G are the Young's and shear modulii of the mortar, and T is the thickness of the wall. The stiffness matrix of the mortar element is,

$$[k] = \int_{-L/2}^{+L/2} [B]^T [C] [B] \, t \, dL \tag{5}$$

Smear cracking approach

Initiation and propagation of cracks in the masonry wall is modeled by smear crack technique (Ali and Page, 1988). Use of smear cracking method overcomes the inherent difficulties present in the discrete cracking model in which the topology of the finite element mesh must be redefined each time a crack is formed or propagated. But in case of smear cracking technique, the material properties of the cracked element are changed each time a crack is formed. This method represents crack as a stress discontinuity rather than a physical separation between two elements. For the two dimensional incremental linear model of mortar joints,

$$\begin{Bmatrix} dv \\ d\sigma \end{Bmatrix} = [C] \begin{Bmatrix} d\epsilon_s \\ d\epsilon_n \end{Bmatrix} \tag{6}$$

where, dv, $d\sigma$, and $d\epsilon_s$, $d\epsilon_n$ are the incremental stresses and strains, respectively.

153

When the normal stress in the head joint or shear stress in the bed joint is more than the tensile or shear strength, respectively, of mortar, a crack is formed. To model a crack, k_n is reduced by a factor 10^{-3} and k_s is reduced by factor 0.1 (Ali and Page, 1988).

Strength of mortar

The S type mortar is mostly used for residential construction. ASTM standard mandates an average compressive strength of eight 50.8 mm mortar cubes to be more than 26.5 MPa. There is no ASTM standard for tensile or shear strength of mortar.

Literature research revealed that the tensile and shear strengths of mortar vary over a wide range. Mortar tensile strength lies between 0.5 MPa and 0.8 MPa and shear strength is a function of compression. The cohesion of mortar lies between 0.3 and 0.8 MPa. Angle of internal friction of mortar is approximately 32˚.

SETUP OF THE CURRENT ANALYSIS

A linear model was adopted to investigate initiation and propagation of cracks and influence of a few factors affecting induced stresses on a masonry wall. A linear model is suitable for this kind of analysis because induced stresses are very low. For low stress level, stress-strain relationship of concrete-block and masonry is linear (Page, 1978; Ali and Page, 1988). Finite element analysis of concrete-block masonry wall was carried out in two stages. In the first stage, initiation and propagation of cracks on a 14.6 m wall of a house basement subjected to subsidence was studied. The wall was 2.4 m high having a running bond of concrete-blocks. The dimensions of the blocks were of standard size, i.e., 396.9 mm long by 193.7 mm wide by 193.7 mm thick. The mortar thickness was also standard, i.e., 9.525 mm. Actual locations of three major cracks in the wall and ground displacements along the side of the wall were known.

Figure 1 shows the finite element mesh of the wall, having a window on the top of the wall, studied in the first stage. The wall is on the top of a 609.6 mm high and 396.9 mm thick continuous concrete footing. Below the concrete, a 609.6 mm of soil is included in the finite element analysis. Instead of applying actual displacements below the soil, relative displacements were imposed at the bottom boundary. Due to this, a bottom corner was restricted in vertical movements but allowed to move freely in horizontal direction. Base displacements were applied below the soil in three steps. For each step, only mortar joints were checked for failure. For head joints, tensile strength criterion

was chosen and tensile strength of mortar was assumed to be 0.70 MPa. Initially, for the bed joints near the window, any joints exceeding shear stress of 0.4 MPa were assumed to have cracked. Table 1 shows the material properties used in the model.

In the second stage, effects of radius of curvature, length to height ratio, and location of maximum curvature were studied. The wall was assumed to have no openings. For changing the length to height ratio, only the length of the wall was varied and height of the wall was kept at 2.4 m.

RESULTS AND DISCUSSION

Figure 1 shows three actual cracking in the wall observed in the field. Crack #1 and #2 had hair line width going down three blocks from the bottom of the window when the measured radius of curvature was 6.1 km. In the analysis, when base displacements resulting a radius of curvature of 6.1 km was imposed, only two head joints and eight bed joints were found to have cracked after the first run (shown as 1 in Figure 1). Initiation of crack #1 matched with, but initiation of crack #2 moved one block away from that of the actual crack observed in the field. It was found that if all the eight bed joints were allowed to crack in FE analysis, crack would propagate horizontally along the bed joints. To prevent this, only two bed joints connecting to two cracked head joints were allowed to crack.

In the second run, the base displacements were chosen such that the imposed radius of curvature was 5.1 km. Eight head joints exceeded 0.7 MPa tensile stress (shown as 2 in Figure 1). Initiation of crack #3 matched with the field observation. Cracking of bed joints were not considered any more. Rather, cracking was imposed on bed joints connecting to those head joints which showed a stepped pattern. In the third run (shown as 3 in Figure 1), base displacements were chosen such that the imposed radius of curvature was 4.1 km. Fifteen head joints were found cracked.

In the second stage, FE analyses were done to investigate effects of radius of curvature, location of curvature, and length to height ratio. Figure 2 shows less-than cumulative frequency distribution of stresses in the head joints of the wall when L/H = 6 and R = 6.1 km. Figure 2 shows that 45 percent of the elements were under compression. If the wall is assumed to be a pure Timoshenko's deep beam (Timoshenko, 1957), the neutral axis will be at the center of the wall resulting in 50 percent of head joints experiencing compression. So, it can be concluded that the neutral axis of the masonry wall under bending is at the lower edge of the beam. For different L/H ratios, locations of

155

curvature, and radii of curvature, it was found that 43 to 45 percent of head joints are under compression. As L/H ratio decreases, percentage of elements under compression decreases from 45 to 43 percent.

Tensile stress distribution contour map from FE analysis showed that the stresses in the wall decrease as the location of maximum curvature goes away from the center of the wall and that the location of maximum curvature versus maximum tensile stress in the wall are inversely related by a second order polynomial function (Figure 3).

Figures 4 and 5 show variations of maximum tensile stress in the wall with radius of curvature and length to height ratio, respectively. These variations can be related by,

$$\sigma_t = a_1 + b_1 R + c_1 R^2 \tag{7}$$

$$\sigma_t = a_2 + b_2 (L/H) + c_2 (L/H)^2 \tag{8}$$

where, σ_t is the maximum tensile stress in the top of the wall, R is the radius of curvature, and a_i, b_i, and c_i (i = 1, 2) are constants. Tables 3 and 4 show values of a_i, b_i, and c_i.

CONCLUSION

Modeling of concrete block masonry wall subjected to subsidence revealed some new insights. Modeling of mortar joints by linkage elements is capable of detecting crack initiation in the mortar. Smear cracking approach shows propagation of cracks in the wall when only few joints are cracked. As more joints are cracked, cracking tends to occupy a larger area in the wall, instead of restricted to the stepped pattern as observed in the field. Effects of radius of curvature, locations of maximum curvature on the wall, and length to height ratio of the wall can be related to the maximum tensile stress on the top of the wall by second order polynomial functions. Current investigation is being continued to study the effects of openings (doors and windows) in the wall and to formulate empirical equation to predict stress distribution in the concrete block masonry wall subjected to subsidence.
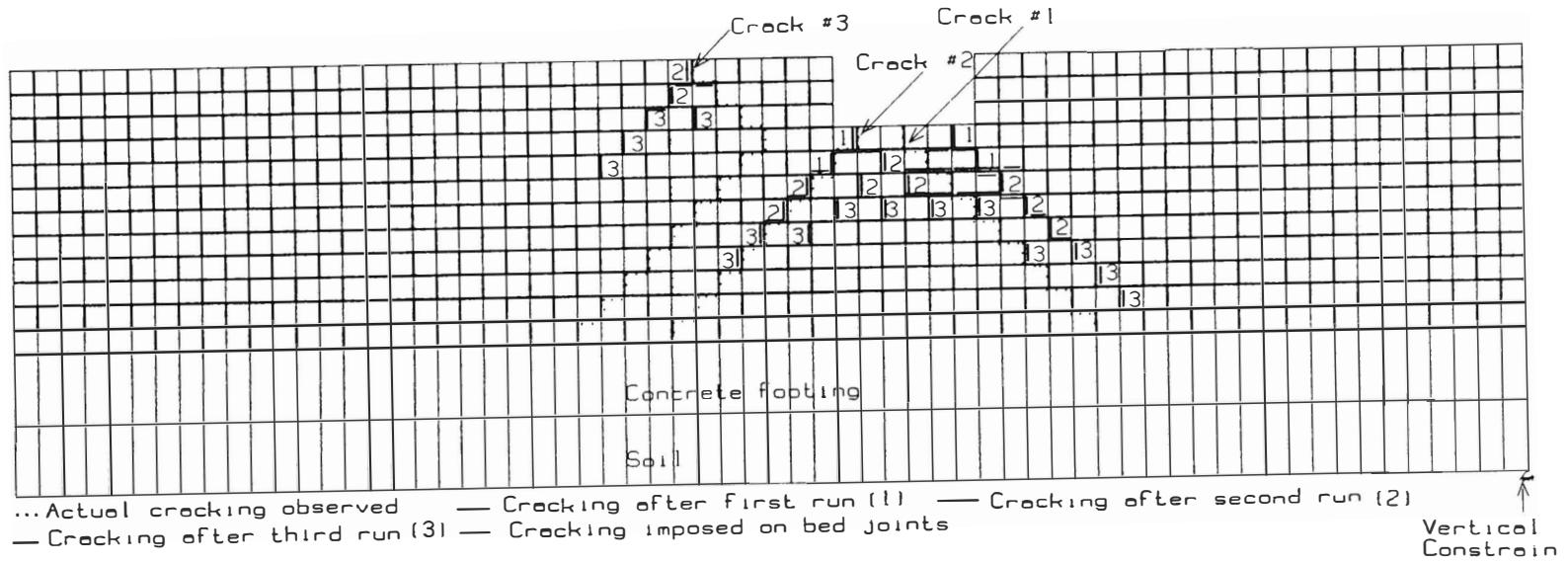
Figure 1 Finite element mesh and cracking in the wall

Table 1 Material properties used in FEA

Materials	E, MPa	Poisson's ratio	Unit weig kg/cu.m.
Brick	14704	0.16	1083
Mortar	7402	0.21	2568
Soil	30	0.35	1608
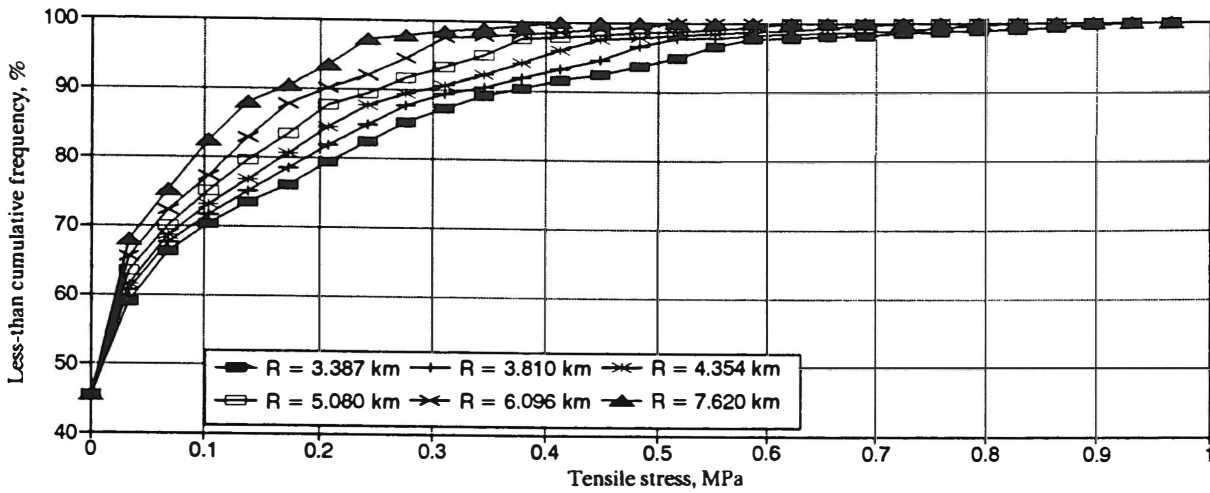
Figure 2 Distribution of less-than cumulative frequency of stresses in the head joints

$$\sigma_t = -0.0146 + 2.1384\xi - 2.2239\xi^2$$

σ_t is maximum tensile stress in the wall
ξ is the location of curvature in terms of wall length
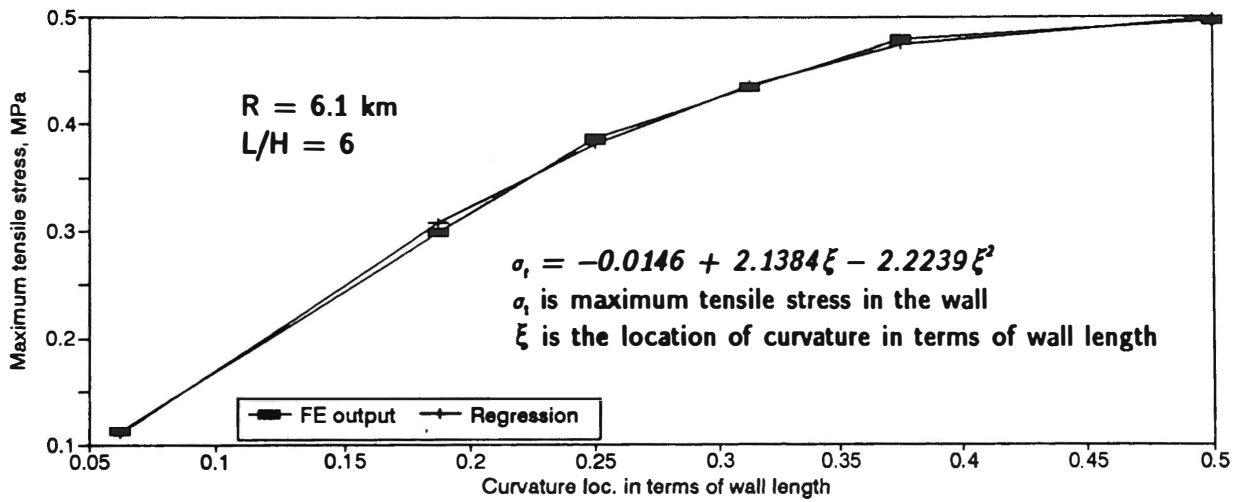
Figure 3 Location of curvature vs. maximum tensile stress in the wall

158
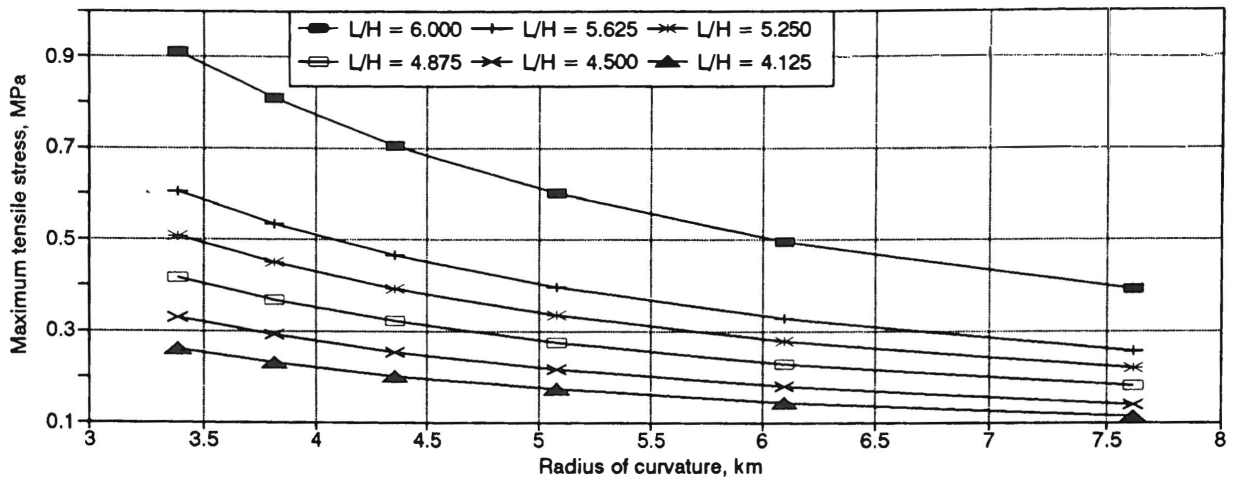
Figure 4 Radius of curvature vs. maximum tensile stress in the wall
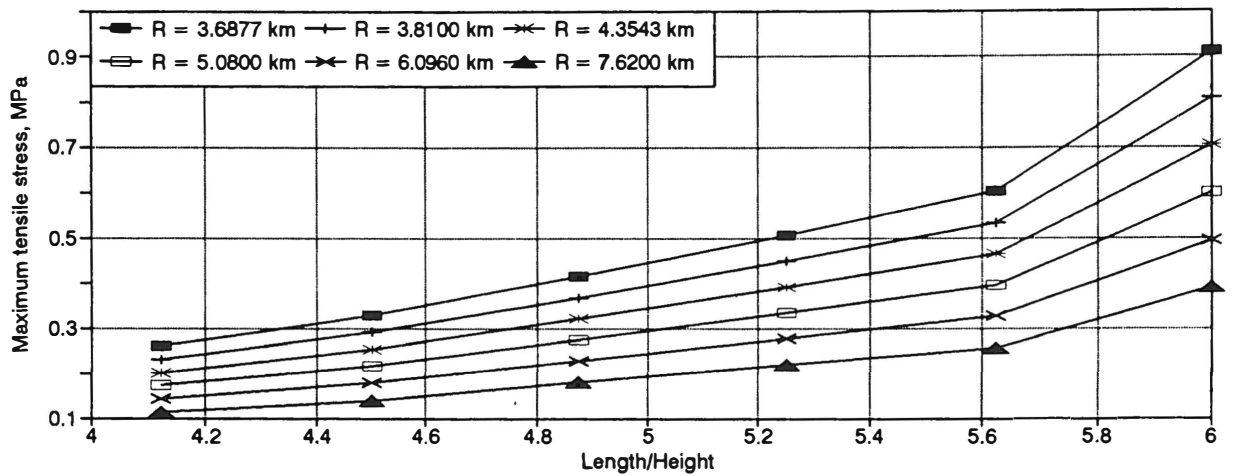
Figure 5 Length to height ratio vs. maximum tensile stress in the wall

Table 2 Values of a1, b1, c1 for different L/H ratio

L/H	a1	b1	c1
6.000	1.8900	-0.3700	0.0228
5.625	1.2500	-0.2469	0.0152
5.250	1.0500	-0.2050	0.0126
4.875	0.8616	-0.1680	0.0103
4.500	0.6844	-0.1339	0.0082
4.125	0.5366	-0.1044	0.0064

Table 3 Values of a2, b2, c2 for different radius of curvature

R, km	a2	b2	c2
3.387	2.8400	-1.2688	0.1568
3.810	2.5260	-1.1261	0.1391
4.354	2.2090	-0.9841	0.1215
5.080	1.8931	-0.8424	0.1038
6.096	1.5655	-0.6961	0.0858
7.620	1.2600	-0.5587	0.0686

REFERENCES

Ali, S. and A. W. Page (1985), *An elastic analysis of concentrated loads on brick work*, J. Masonry Inst., No. 6, pp. 9-21.

Ali, S. and A. W. Page (1988), *Finite element modeling of masonry subjected to concentrated load*, J. Struct. Engg., Vol. 114, No. 8, pp. 1762-1774.

Bhattacharya, S., M. M. Singh, and C. Y. Chen (1984), *Proposed criteria for subsidence damage to buildings*, Proc. 25th Symp. on Rock Mech. Northwestern U., Evanston, IL., AIME, New York, NY, June, pp. 747-755.

Goodman, R. E., R. L. Taylor, and T. L. Brekke (1968), *A model for the mechanics of jointed rock*, J. Soil Mech and Found. Div., ASCE, Vol. 94, SM3, pp. 637-659.

Karmis, M., Z. Yu, and A. Jarosz (1990), *Design consideration for subsidence control*, Int. J. of Mining and Geol. Engg., Vol. 8, No. 4, pp. 357-368.

Luo, Y., S. S. Peng, and D. Dutta (1992), *Some mitigative measures for protection of surface structures affected by ground subsidence*, Proc. 3rd. Workshop on Surface Subsidence due to Underground Mining, June, Morgantown, WV., pp. 129-138.

Ngo, D. and A. C. Scordelis (1967), *Finite element analysis of reinforced concrete beams*, J. Am. Concrete Inst., Vol. 64, No. 3, pp. 152-163.

Page, A. W. (1978), *A finite element model masonry*, J. Struct. Div., ASCE, Vol 104, No. 8, pp. 1267-1274.

Peng, S. S. (1992), *Surface Subsidence Engineering*, SME, Littleton, CO., pp. 153.

Rosenhaupt, S. and Y. Sokal (1965), *Masonry walls on continuous beams*, J. Struct. Div., ASCE, Vol. 191, No. ST1, pp. 155-171.

Saw, C. B. (1974), *Linear elastic finite element analysis of masonry wall on beams*, Buldg. Sc., Vol 9, pp. 299-307.

Timoshenko, S. (1957), *Strength of Materials-Part 1*, D. Van. Nostrand Co. Inc., London, England, pp. 341.

Yuan, Z. and K. M. Chua (1992), *Exact formulation of axisymmetric interface element stiffness matrix*, J. Geotech. Engg., Vol. 118, No. 8, pp. 1264-1271.

Keynote Address

The evolution of numerical modelling in Canada for mining applications - Developments in CANMET and elsewhere

By

John E. Udd

THE EVOLUTION OF NUMERICAL MODELLING IN CANADA FOR MINING APPLICATIONS - DEVELOPMENTS IN CANMET AND ELSEWHERE

J.E. Udd and Y.S. Yu
Mining Research Laboratories, CANMET, Energy, Mines & Resources

ABSTRACT

Numerical methods of stress analysis were introduced into Canadian mining research in the mid-1960's. Because of the great advances that have been made in computer technology, numerical modelling techniques have evolved rapidly. Today the technology is becoming a regular feature of the design of underground structures.

The purpose of this paper is to provide a record of the developments which have taken place in Canada since the method was first introduced.

RESUME

C'est au milieu des années 60 que les méthodes d'analyse numérique des contraintes ont commencé à être utilisées dans la recherche minière au Canada. En raison des progrès fulgurants de l'informatique, les techniques de modélisation numérique ont connu un essor rapide. De nos jours, cette technologie est un élément essentiel du processus de conception de structures souterraines.

Le présent exposé a été rédigé en vue de faire le point sur les progrès réalisés au Canada depuis l'introduction de la méthode.

INTRODUCTION

During the last decade especially, the mining industry has increasingly turned to the use of numerical modelling techniques in order to assess new mining configurations which permit increased extraction ratios while, simultaneously, maintaining structural stability and safety. The use of numerical models permits very rapid assessments of both the short and long-term structural stabilities of underground openings and an identification of potential problem areas in advance. Consequently, corrective measures can be taken in order to achieve better design and safer working environments.

Today, in 1993, the techniques have become so powerful, and so cost-effective and relatively inexpensive, that it is common that several, and perhaps many, alternative configurations may be studied in order to determine the one that is the optimal when viewed from several different aspects. Numerical modelling has made the heretofore next-to-impossible a normal part of mine design.

The Mining Research Laboratories of CANMET, Energy, Mines and Resources Canada, has been engaged, for over twenty-five years, in the application and development of numerical models for the analyses of stresses, deformations, and stabilities around mine openings, such as underground stopes, pillars and pit slopes. Initially, the finite element technique was used. Later, the boundary element and distinct element methods for modelling jointed rock masses, were also adopted.

The finite element method was introduced by the aerospace industry in the United States of America in the early 1950's. It became a common tool for both mechanical and civil engineers in the next decade, and was used for the analysis of stresses in mechanical parts and engineering structures. In the late 1960's, the Canadian Mines Branch (now CANMET) examined the technique and thought that it could be a very flexible, powerful and versatile engineering tool for analyzing the stresses around excavations in rock masses. Subsequently, the then traditional methods of physical modelling and photoelastic analyses were rapidly replaced by the finite element technique. (The senior author was among "the last of the photoelasticians".) As computer technology advanced, and as programs become more user-friendly and suitable for smaller computers, numerical modelling gained recognition from mining operators. Today, it is an indispensable engineering tool for both ground control and mine planning. It has progressed from being in the domain of specialists to being usable by personnel at the mine-site.

NUMERICAL MODELLING IN THE 1960's

A literature search using databases, such as "MINTEC", and "EI Compendix", has

revealed very little concerning the development of numerical modelling techniques, and applications to mining, in Canada, in the 1960's.

It is clear, however, that the Mines Branch was the pioneer. In the mid 1960's, a CDC 3200 series computer was installed at the headquarters of the Department of Energy, Mines and Resources, on Booth Street, in Ottawa. At the time, stress analyses of two-dimensional openings were conducted using the classical techniques of applied mathematics, photo-elasticity, and physical modelling. The first finite element program used to analyze the stresses around mine structures was written by K. Waranica of the Fuels and Mining Practice Division of the Mines Branch in 1966-1967 and was published in 1969 [Yu and Coates, 1969]. The program was written in Fortran and was based on a static, linear elastic formulation. In the trials, a numerical solution for a classic example was compared with a photoelastic solution and was found to be in good agreement [Yu, Gyenge and Coates, 1969]. Subsequently, the other stress analysis techniques used at the Mines Branch were very rapidly replaced by the finite element method.

In retrospect, it is hard to image the limitations that were placed on analyses by the computers of the 1960's. Maximum memory capacities of only 32K, and computers that were very "slow" by present standards, made the analysis of a two-dimensional model with a few hundred nodes and elements a big achievement! At the time, several days were required to prepare the input data for even a simple model. Afterwards, as many as several weeks were required in order to interpret the results manually. The pre- and post-processing facilities which are common today were virtually non-existent. Today, three-dimensional and complex mine models with up to 40,000 - 50,000 degrees of freedom can be solved routinely.

Subsequent to CANMET's first program, a crude mesh generator and a post processor for plotting stress trajectories, point contours of the principal stresses, and excavation displacements were developed in-house to speed up the analytical process [Yu and Coates, 1968].

In the development of the first models at CANMET, our organization was very much indebted to Edward Wilson, then a Lecturer of UCLA, who made available to us a number of programs which were subsequently modified for mining applications. These included: WILAX, a two-dimensional plane and axisymmetric Finite Element code, in the late 1960's; and SOLIDSAP, a linear Finite Element program with both two-dimensional and three-dimensional applications, in 1972. CANMET's present SAP2D and SAP3D programs resulted from modifications to the latter.

The Mines Branch also used NAOS, a two-dimensional Finite Element code with arbitrary loading. This was originally developed by Dunham et al, in 1967 (Dunham et

163

al, 1967).

One of the first applications of the finite element model, in Canada, to simulate mine structures was the work done for the Hilton Mine, at Shawville, Quebec [Yu, Barron and Toews, 1969]. The Hilton Mine was an open pit iron mine then in the final stages of mining. As the open pit was deepened the stability of the north wall became the main concern of the mine operator. A cooperative research project was developed between the company and the Mining Research Laboratories to monitor stability conditions in the pit walls. As a first step, a triangulation monitoring system was designed and installed. The field measurements were monitored over a two year period and were then compared with predictions derived from modelling. The results were very satisfactory, and were helpful in the successful completion of the pit operations.

NUMERICAL MODELLING IN THE 1970's

As mentioned, in the late 60's the numerical models used were based primarily on simple, static, linear elastic conditions. During the 1970's, however, more versatile models which included a provision for geological features, imhomogenities, and anisotropy were developed at CANMET and elsewhere (Toews and Yu, 1973, 1974]. In the United States of America, the EPFE code, a two-dimensional non-linear "progressive failure" Finite Element code, was developed by Sandhu, Wu, and Harper at Ohio State University (Sandhu et al, 1973). The well-known MINTAB program, based on the Displacement Discontinuity method, was developed for applications to tabular orebodies by S.L. Crouch of the University of Minnesota (Starfield and Crouch, 1973). Both have been used by CANMET.

Within CANMET, numerical modelling was successfully applied to a comprehensive analysis of the effects of underground stoping operations on the stabilities of the pit walls above the underground mine in 1974-76, at the Kidd-Creek Mine (then known as Texasgulf) [Yu, 1978]. An underground stability assessment, using the finite element technique, was also carried out for multi-seam mining operations in the Elliot Lake uranium camp (Yu and Hedley, 1977).

The finite element method was also applied to predicting the subsidence above flat-lying and steeply dipping orebodies [Vongpaisal and Coates, 1975]. The work was done at McGill University in a Ph.D. Thesis [Vongpaisal, 1973] and was carried out under the supervision of the late Dr. Coates, the Head of the Mining Research Laboratories at the time. Dr. Vongpaisal, after working for Falconbridge Limited, at their Sudbury operations, became a member of the CANMET organization. Falconbridge, it must be noted, was the Canadian pioneer in using numerical modelling techniques for applications in ground control and mine design.

CANMET's expertise was used internationally in the 1970's: in the work that was done in cooperation with Prof. Richard Call, of The University of Arizona, to develop an optimum design for the Tazadit open pit mine in West Africa [Yu and Toews, 1973]; in the work in attempting to back analyze the world famous pit slide at the Chuquicamata open pit in Chile [Yu and Coates, 1979]; and, in CANMET's well-known pit slope project [Sage, Toews and Yu, 1978].

Also in the 1970's, a number of other applications of finite element techniques to geotechnical problems in civil engineering were reported in Canada. As an example, two dimensional finite element analyses of representative horizontal and vertical sections of the Niagara Gorge were carried out at the University of Toronto by McLennan and Roegiers, in 1976 [McLennan and Roegiers, 1976].

Other applications at CANMET included the study of the stress-strain distribution around a cylindrical Borehole, which led to the derivation of an equation for optimizing borehole locations in order to improve accuracies of in-situ stress measurement techniques and studies of the mechanisms of rock anchors and analyses of block flow slope instabilities around axisymmetric slopes [Coates and Yu, 1978].

Late in the 1970's, a joint research project was undertaken by CANMET and INCO, at Sudbury, to evaluate and to develop numerical techniques suitable for the modelling of the 830 orebody at the Copper Cliff South Mine. The model used was based on an earlier version of MINSIM which had been developed, using the Development Discontinuity method, at the Goldfields Mine in South Africa by S.L. Crouch of the University of Minnesota [Starfield and Crouch, 1973]. The enhancements which were developed and incorporated into MINSIM at CANMET included: a large mine grid; the behaviour of backfill material; provision for a non-homogeneous ore body; hangingwall/footwall material behaviours; and a new numerical procedure for evaluating off-reef stresses. This model was later referred to as MINTAB [Yu and Toews, 1981]. Even though significant improvements had been made, however, CANMET's MINTAB was judged to be still inadequate for modelling the massive and complex 830 ore body. The mine geometry was so complex as to require real three dimensional simulation. Consequently, INCO then embarked on their own research program to develop numerical techniques suitable for their applications. The result, was the development, by INCO, of a linear three-dimensional boundary element program in the 1980's.

In the Numerical modelling of mining excavations in rockmasses that are assumed to be linearly elastic, the Boundary Element method has distinct advantages over domain discretization methods, such as Finite Elements. Mining engineering problems typically involve infinite or semi-infinite domains. Boundary Element models, which have unknowns only on the boundaries of excavations, are very efficient in terms of the number of elements needed in order to effect a solution.

165

One form of the indirect boundary element technique that provides an elegant representation of cracks and faults in both two-dimensional and three-dimensional elastic bodies is the Displacement Discontinuity method. This has become a very useful tool for simulating pillar extraction schemes in tabular orebodies and has also been extended to model the rate-dependent behaviour of a jointed rock mass [Crawford and Curran, 1983]. In the latter, the intact rock is assumed to behave as a linear viscoelastic material while the joints are assumed to follow a non-linear rate dependent behaviour. An efficient multigrid solution of boundary element models of cracks and faults, in order to improve computational efficiency has also been reported recently [Peirce, 1991].

VISCOELASTIC/VISCOPLASTIC STRESS ANALYSIS FOR POTASH MINES

In 1984, the potash industry in Saskatchewan required a numerical model to model the behaviour of the strata of underground potash mines This would provide a tool for quantitative assessments of the stabilities and, hence, the safeties of proposed new layouts; in particular for novel concepts such as multi-seam mining, or longwall extraction, which would otherwise be difficult to assess. The software, known as GEOROC, was developed subsequently through a Government of Canada contract to RE/SPEC Ltd. of Calgary [Fossum el al, 1985]. GEOROC is a two-dimensional finite element program which is based on a linear viscoelastic formulation and three constitutive laws, namely: the power law, the Norton law, and the exponential-time law describing creep material behaviour. The program has now been distributed widely to most of the Canadian potash industry.

GEOROC was originally designed for mainframe or mini computers. Its pre- and post-processing modules were not user- friendly. By the late 1980's, however, advances in micro-computers and the demands for portability and accessibility of software by the mining industry, spurred further development of the software to permit its use with personal computers. As a result, VISROCK, and a number of other two-dimensional personal computer-based software packages were developed [Wan and Yu, 1991].

VISROCK was developed with the financial support of the Potash Corporation of Saskatchewan. It is a two-dimensional elasto-viscoplastic finite element program developed for the analysis of stresses in potash mine structures in rocks with time dependent behaviour. State-of-the art graphics and pre- and post-processors are incorporated into the program. The model is aimed at the phenomenological reproduction the main features of the creep behaviour of potash. This is done by blending the notion of viscoplastic regularization with the concepts of strength degradation via cohesion and friction softening [Wan, 1992]. The yield surface is based on either the von Mises, Mohr-Coulomb, or Drucker-Prager criteria to characterize material strength; while time-dependent plastic deformations follow either a simple power law or an exponential

decay.

Research and development of a time-dependent finite element model for potash mining applications have also been carried out in the Department of Civil Engineering, of the University of Manitoba [Sepehr and Stimpson; 1988]. The model developed, based on viscoelastic/ viscoplastic material behaviour, is very realistic. It has been specifically designed to include those capabilities required in order to model the complex fabric of the stratified and jointed rocks associated with potash mining. It includes an ability to model time-dependent closures of excavations. It is not clear, however, whether or not user-friendly pre- and post-processors have been incorporated into it.

NUMERICAL MODELLING OF TAR SANDS

The software known as NEAT (Nonlinear Effective Stress Analysis for Tarsands) was probably one of the first models ever developed in Canada for tar sands mining applications. It is a two-dimensional finite element program. It was developed for CANMET, in 1979, through a contract to Thurber Consultants Limited, of Edmonton, (Thurber Consultants Ltd., 1979). Subsequently, a number of other organizations began to develop numerical models for oil sands mining applications. These were: the Universities of Alberta and British Columbia, and the Computer Modelling Group of Alberta [Byrne and Janzen, 1984, Vaziri, 1988, Fung, Buchana and Wan, 1992, Wan, Chan and Kosar, 1992]

ADVANCES TO NUMERICAL MODELS FOR MINING APPLICATIONS IN THE 1980'S AND 1990'S

Three-dimensional stress analyses of mine structures

Numerical modelling did not become sufficiently powerful and flexible as an engineering tool, to the point that a ground control engineer could use it in his or her routine work, until recently. At the beginning of their development, stress analyses of three-dimensional complex mine structures were exclusively in the domains of specialists. Typically, such three-dimensional models could only be run on large main frame computers, and at very high computing costs. Because of the costs and the times required, applications were rare.

By the 1980's, however, advances in micro-computer technology made possible a number of initiatives in the development of three-dimensional models of mine structures. The principal organizations in Canada that have been involved are: the University of Toronto;

167

INCO, at Sudbury; Mine Modelling Limited, Sudbury; the University of New Brunswick; McGill University; and CANMET.

Today, in 1993, three-dimensional stress analyses of complex mine structures are very much more efficient and economical. The tool is now widely accepted by the mining industry.

University of Toronto:

EXAMINE³ᴰ is a three-dimensional data visualization and stress analysis package developed at the Data Visualization Laboratory of the University of Toronto. The components of EXAMINE³ᴰ include: a geometry modeller with tools for modelling mine stopes, drifts and haulageways; material interfaces, fault and dykes; and the automatic generation of boundary element meshes for three-dimensional stress analyses. The computer engine is based on a direct three-dimensional boundary element formulation incorporating 8 and 4-noded quadrilaterals and 6 and 3-noded triangles. This development resulted from a five-year Industry/NSERC research grant awarded to both Queen's University and the University of Toronto [Corkum, Curran and Grabinsky, 1991]. Further research and development is presently under way in order to make the package more user-friendly.

INCO Limited:

Through the first Canada/Manitoba Mineral Development Agreement, signed in 1984, the three-dimensional boundary element program known as BEAP was developed by INCO, at their Thompson, Manitoba, operations. The engine's formulation is based on a 9-noded non-conforming element which is very suitable for mining applications and for handling very large and complex openings, such as stopes. Since then, a great deal of effort has been directed to streamlining the computer program into the package known as BEAP3D. State-of-the-art three-dimensional graphics for pre- and post-processing have been incorporated. At present, the package can be integrated into the mine design process. It is very user-friendly in a personal computer Windows environment. The software has been licensed to a number of organizations including: the Detour Lake Mine; the Kidd Creek Mine of 'Falconbridge; the Noranda Technology Centre; the Dickenson Mine; Laval University; SRK of South Africa; and the Thailand Mining Development Corporation. GEMCOM Services, of Vancouver, is the official agent for its distribution, both nationally and internationally.

Under the first Canada/Ontario Mineral Development Agreement, signed in 1985, a major effort was also made to develop a three-dimensional boundary element program

for the simulation of large backfilled stopes at depth. The project was undertaken by INCO, at their Sudbury, Ontario, operations. A three-dimensional boundary element program, MINE3D, based on the theory of incremental plasticity, was developed. In MINE3D, the element geometries are based on a grid of parallelepipeds. The main reason for the selection of this option was that much larger problems can be solved with comparable storage and coefficient calculation requirements. Pre- and post processors were incorporated into the software. At present, because the program requires large disk storage space it can not be used for large-sized mining geometries in a personal computer environment. Research continues in order to improve both the efficiency and the accuracy of modelling large mine geometries.

Mining Research Laboratories - CANMET:

At the Mining Research Laboratories of CANMET there were also a number of developments in three-dimensional stress analyses of mine structures in the 1980's. The program known as SAP3D, which is a static, linear elastic finite element program, and based extensively on an earlier version of Wilson's SAP4 program, was optimized in order to be useful for large problems, requiring up to 30,000 degree of freedom [Toews, Yu and Wong, 1989]. An 8-noded isoparametric element is used in SAP3D. The software has been used in a number of cooperative mining research projects [Yu el al, 1988, Bétournay et el, 1988].

Also at CANMET, an effort was also made to enhance and modify the BMINES Code; which is a general-purpose finite element package with a good selection of material models. BMINES was developed by the United States Bureau of Mines in the 1970's (Von Dillen, Fellnes and Ewing, 1981) and was generously provided to CANMET. It has a good collection of elements in its library, e.g., 8, 20 or variable-noded solid elements. Currently, the program is being used on a Sun Sparcstation. It is capable of handling very large mine geometries, and has been used extensively. The package is not user-friendly and requires state-of-the-art graphics for pre- and post-processing.

McGill University

Since 1986, the Numerical Modelling Group of the Department of Mining and Metallurgical Engineering at McGill University has developed a series of numerical models for a variety of applications in Mining and Geomechanics. Seven numerical models have been so far developed by the Group under the supervision of Dr. H.S. Mitri. These are: S4 (Mitri and Hassani, 1988); MSAP2D (Chau et al, 1988); CABS (Mitri and Rajaie, 1990); VISA2D (Rizkalla and Mitri, 1991); SATURN (Fotoohi and Mitri, 1991); MINE-PAL (Suriyachat and Mitri, 1991) and; GENA3D (Zhang and Mitri,

1992). The series employs linear, non-linear and time-dependent finite element formulations, except for SATURN, which is based on indirect boundary element method with nonlinear displacement discontinuity method. All of the programs are equipped with graphical pre- and post-processors. Work is currently underway to introduce a numerical modelling capability of more complex constitutive models for fractured rocks and anisotropic rockmasses.

University of New Brunswick:

At the Department of Surveying Engineering of the University of New Brunswick, in Fredericton, work to develop numerical models to simulate ground subsidence and to predict dam deformations has been carried out. The software known as FEMMA (Finite element model for multi-purpose applications) has been developed in two main versions: FEMMA 2.0 and FEMMA 3.0. These are for two- and three-dimensional linear elastic and visco-elastic analyses, respectively. The two-dimensional version has been adapted for personal computers, while the three-dimensional version is still only usable on a mainframe. It is not clear whether the software packages have user-friendly pre- and post-processors.

Mine Modelling Limited:

Mine Modelling Limited is a very young company, headed by Dr. T. Wiles, who was formerly associated with INCO, at Sudbury. Dr. Wiles has concentrated his research efforts on increasing the robustness of his three-dimensional boundary element program known as MAP3D. Based on limited information, MAP3D seems to be a user-friendly modelling package.

ONGOING RESEARCH AND DEVELOPMENT AT CANMET

To further improve numerical modelling capabilities for both mining and geotechnical applications, work continues at CANMET to integrate a three-dimensional boundary element model with a finite element face. A full integration of a three-dimensional finite element package with the mine design process, for treating non-linear problems including the viscoplastic behaviour of mine structures, is also being considered.

The technology of a block-spring model for analyzing jointed rocks is also being developed [Wang, 1992, Wang, 1991, Wang and Garga; 1990]. Our Block-Spring Model BSM is a numerical technique recently developed for the analysis of the stress and deformation behaviour of a jointed rock mass. The model simulates the rocks by an

assemblage of blocks which can be any shapes of polygons (in the two-dimensional case). The blocks are assumed to be in contact, but can separate or rejoin. The algorithm of the model is formulated on the basis of the equilibrium conditions of the blocks. It is a static procedure for solving static problems in the rock mass. Theoretically, the model constructs and solves a global stiffness matrix. An iterative procedure is employed so that large displacements of blocks can be simulated. Potential applications of BSM are: the analyses of stresses and deformations in jointed rock masses; the modelling of large displacements of rock blocks, eg., sliding and joint separations; the prediction of unstable blocks around mine openings; the simulation of the effects of rock bolts and cable bolts; modelling of ground water; the simulation of mining sequences; and the analysis of surface linings around rock excavations such as shotcrete and steel set. Ultimately, the model will be extended into three-dimensions.

CONCLUSIONS

Computer simulation is now playing an increasingly important role in evaluating both the short-term and long-term structural stabilities of underground openings, and in ground control studies related to mine design and layout. To make numerical modelling packages more acceptable to mining engineers, however, these must be fully integrated into the mine design process. This is particularly true for three-dimensional modelling.

Progress in the past two decades has been spectacular. As mentioned in the paper, a number of organizations have been involved. At this point, however, it would be very valuable were we able to achieve a greater collaboration and coordination of efforts in Canada. In the final analysis, whatever programs are used should be as user-friendly as possible and suitable for use on the computers which are normally available at mine sites.

ACKNOWLEDGEMENTS

REFERENCES

Bétournay, M.C., Yu, Y.S & Thivierge, S.; A Case Study of Surface Crown Pillars: The Niobec Mines. Proc. 28th U.S. Rock Mechanics Symposium, Tucson, Arizona. June 29 -July 1, 1988.

Byrne, P.M. & Janzen, W.; A Computer Program for Non-linear Analysis of Stress and Deformation in Oil Sand Masses; Soil Mechanics Series No. 80, Dept. of Civil Engineering, University of British Columbia , Vancouver, 1986.

Chau, K.S., Mitri, H.S., Hassani, F.P. & Scoble, M.J., A Finite Element Model of Stress Analysis of Underground Openings. Proc. of First Cdn. Conf. on Computer Applications in the Mineral Industry, Quebec City, March 7-9 (1988) 259-268. A.A. Balkema Publishers.

Coates, D.F., & Yu, Y.S.; Three-dimensional Stress Distribution Around a Cylindrical Hole and Anchor; Proc. 2nd Congress of ISRM, Belgrade, Yugoslavia, 1970.

Coates, D.F., & Yu, Y.S.; Rock Anchor Design Mechanics; Mines Branch Research Report R233, Energy, Mines and Resources Canada, 1971.

Corkum, B.T., Curran, J.H., & Grabinsky, M.W.; EXAMINE3D: A three-dimensional Visualization Tool for Mine Datasets; Proc. 2nd Canadian Conference on Computer Applications in the Mineral Industry; Vancouver, Canada, September 15-18, 1991.

Crawford, A.M. & Curran, J.H.; A Discontinuity Displacement Approach to Modelling the Creep Behaviour of Rock and its Discontinuities; Int. J. for Num. and Analytical Methods in Geomechanics, Vol. 7, pp 245-268, 1983.

Diering, J.A.C. & Yu, Y.S.; Three-Dimensional Stress Analysis: A formulation for Mining Problems; Computers and Geomechanics, Vol. 5, pp 151-170, 1988.

Dunham, R.S., et al; Finite Element Analyses of Axisymmetric Solids with Arbitrary Loadings, Technical Rep. #67-6, Civil Engineering, Univ. of California, Berkley, 1967.

Hedley, D.G.F., Herget, G., Yu, Y.S., & Miles, P.; CANMET Rock Mechanics Research at Kidd Creek Mine; CANMET Report 79-11; Energy, Mines and Resources, Canada, 1979.

Fossum, A.F. et al; GEOROC: A Numerical Modelling Package for Designing Underground Openings in Potash; CANMET Project No. 310104; Energy, Mines and Resources Canada, 1985.

Fotoohi, K. & Mitri, H.S., A Boundary Element Approach to Problems of Mining Through or Near Discontinuities. Proc. 2nd Conf. on Comp. Appl. in Mineral Industry (CAM'91). Vancouver, B.C., Sept. 15-18 (1991), 785-796. Sponsored by UBC and CIM.

Grant, D.R., Hudyma, M.R., & Diering, J.A.C.; Three-Dimensional Stress Analysis Using BEAP; Proceedings 2nd Canadian Conference on Computer Applications in the Mineral Industry; Vancouver, Canada, September 15-18, 1991, pp 643-654.

McLennan J.D. & Roegiers, J.C.; Stress Conditions Around the Niagara Gorge; Proc. 3rd Symp. Engineering Applications of Solid Mechanics; Toronto, Canada, June 7-8,

1976.

Mitri, H.S. & Hassani, F.P., Nonlinear Finite Element Analysis of Mine Roadway Arch Support Systems. Computers & Structures, 29, No. 3 (1988) 355-364

Mitri, H.S. & Rajaie, H., Stress Analysis of Rock Mass with Cable Support - A Finite Element Approach. Proc. Conf. on Stresses in Underground Structures. Ottawa, October 2-3 (1990) 110-119. Supply and Services, Canada, (1990) ISBN 0/660/13724/0

Peirce, A.P.; Efficient Multigrid Solution of Boundary Element Models of Cracks and Faults; Int. J. for Num. and Analytical Methods in Geomechanics, Vol. 15, pp 549-572, 1991

Rizkalla, M. & Mitri, H.S., An Elasto-Viscoplastic Model for Stress Analysis of Mining Excavations. Proc. 32nd U.S. Rock Mechanics Symposium, Norman, Oklahoma, July 10-12 (1991) 597-606. A.A. Balkema Publishers.

Sandhu, R.S., Wu, T.H., & Hooper, J.R.; Stresses, Deformation and Progressive Failure of Non-Homogenous Fissured Rock, OSURF-3177-73-IF, Vol. 1, Ohio State University, March 1973.

Sepehr, K. & Stimpson. B.; Potash Mining and Seismicity: A Time-Dependent Finite Element Model; Int. J. Rock Mech. Min. Sci. & Geomech. Abstr. Vol. 25, No. 6, pp. 383-392. 1988.

Starfield, A.M. & Crouch, S.L.; Elastic Analysis of Single Seam Extraction; New Horizons in Rock Mechanics, edited by Hardy, H.R. and Stefanko, R.; ASCE, NY, 1973

Suriyachat, P. & Mitri, H.S., A Nonlinear Numerical Model for 2-D Stability Analysis of Mine Structures. Proc. 2nd Conf. on Appl. in Mineral Industry (CAMI'91). Vancouver, B.C., Sept. 15-18 (1991), 773-784. Sponsored by UBC and CIM.

Szostak-Chrzanowski, Anna, & Chrzanowski, Adam; Use of 'FEMMA' in 2-D and 3-D Modelling of Ground Subsidence; Proc. 2nd Canadian Conference on Computer Applications in the Mineral Industry. Vancouver, Canada, September 15-18, 1991.

Thurber Consultants Ltd.; Computer Model for Stress-strain Analysis of Tarsands; CANMET Contract Report No. 23440-8-9012, 1979.

Toews, N.A. & Yu, Y.S.; SAP2D Documentation - 2-D Linear Elastic Finite Element Computer System; Divisional Report MRC IR 72-144; Mining Research Laboratories, Energy, Mines and Resources Canada, 1972.

Toews, N.A. & Yu, Y.S.; Documentation of a Computer Program for Automatic Mesh Generation for the 2-D Finite Element WILAX; Mines Branch Research Report R272; Mining Research Laboratories, Energy, Mines and Resources Canada, 1973.

Toews, N.A., Yu, Y.S. & Wong, A.; SAP3D Documentation - A 3-D Linear Elastic Finite Element Program, Divisional Report MRL 89-07(TR), Mining Research Laboratories, Energy, Mines and Resources Canada, 1989.

Vaziri, H.H.; Finite Element Analysis of Oil Sands Subjected to Thermal Effects; presented at the 37th Annual Technical Meeting of the Petroleum Society of CIM held in Calgary, Alberta, June 8-11, 1986.

Vaziri, H.H.; Coupled Fluid Flow and Stress Analysis of Oil Sands Subject to Heating;

The Journal of Canadian Petroleum Technology, Vol. 27, No.5, September-October,
1988.

Von Dillen, D.E., Fellner, R.W., & Ewing, R.D.; Modernization of the BMINES
Computer Code, Contract Report, Bureau of Mines, United States Department of the
Interior, PB03-22156, 1981

Wan, G.R., Chan, D.H., & Kosar, K.M.; A constitutive Model for Effective Stress-
Strain Behaviour of Oil Sands; The Journal of Canadian Petroleum Technology, Vol. 30,
No.4, July-August, 1991.

Wan, G.R. & Yu, Y.S.; A Softening Elasto-Viscoplastic Model for Potash Mines;
presented to the 94th CIM Annual General Meeting, Montreal, April 26-30, 1992.

Wan, G.R.; VISROCK - An Elasto-Viscoplastic Program for Rocks Theoretical Manual;
Version 1.0, Divisional Report MRL 92-036(TR); Mining Research Laboratories,
Energy, Mines and Resources Canada, 1992.

Wang, B.; A Block Spring Model for Jointed Rocks; Ph.D. Thesis, University of
Ottawa, Canada, pp 204. 1991.

Wang, B.; Introducing BSM: A Computer Program of the Block-Spring-Model for
Analyzing Jointed Rocks; Divisional Report MRL 92-124(INT); Mining Research
Laboratories, Energy, Mines and Resources Canada, 1992.

Vongpaisal, S.; Prediction of Subsidence Resulting From Mining Operations; Ph.D.
Thesis, McGill University, Department of Mining and Metallurgical Engineering, 1973.

Vongpaisal, S. & Coates, D.F.; Analysis of Subsidence from Inclined Workings; Proc.
10th Canadian Rock Mechanics Symposium, Queen's University, Sept. 2-4, 1975.

Wiles, D.T.; Issues of Ease of Use, Error and Accuracy Control in MAP3D Mining
Analysis Program in 3-Dimensions. Proc. 2nd Canadian Conference on Computer
Applications in the Mineral Industry; Vancouver, Canada, September 15-18, 1991.

Wilson, E.L.; SOLID SAP - A Static Analysis Program for Three-Dimensional Solid
Structures; Structural Engineering Laboratory, UCLA, UC SESM 71-19, September 1971

Yu, Y.S.; Finite Element Modelling at the Kidd Creek Mine; Timmins, Ontario.; Proc.
3rd Symp. Engineering Applications of Solid Mechanics; Toronto, Canada, June 7-8,
1976.

Yu, Y.S., Barron, K. & Toews, N.A.; Stress and Deformation in a Hilton Mine Model;
Division Report MR 69/58-ID; Mining Research Laboratories; Energy Mines and
Resources Canada, 1969.

Yu, Y.S., Bétournay, M.C., Larocque, G.E., & Thivierge, S.; 1988; Pillar and
Stope Stability Assessment of the Niobec Mine Using the Three-Dimensional Finite
Element Technique. Proceedings 15th Canadian Rock Mechanics Symposium, University
of Toronto, October 3-4, 1988.

Yu, Y.S., Closset, L. & Diering, J.A.C.; A Boundary Element Application Package
for Three Dimensional Stress Analysis of Mine Structures.; Proceedings - Stresses in
Underground Structures, CANMET, Energy, Mines and Resources Canada; October 2-3,
1990.

Yu, Y.S. & Coates, D.F.; A computer Program for Checking Input data by Plotting for

the Finite Element Method of Analysis; Divisional Report MR 68/15 LD; Mining Research Laboratories, Energy Mines and Resources Canada, 1968.

Yu, Y.S., & Coates, D.F.; A computer Program for Plotting Principal Stresses and Displacements; Divisional Report MR 68/54 LD; Mining Research Laboratories, Energy Mines and Resources Canada, 1968.

Yu, Y.S. & Coates, D.F.; Development and Use of a Finite Element Computer Program; Mines Branch Research Report R198; Energy Mines and Resources Canada, 1969. - -

Yu, Y.S., & Coates, D.F.; Analysis of Rock Slopes Using the Finite Element Method; Mines Branch Research Report R229; pp 74; Energy, Mines and Resources Canada, 1970.

Yu, Y.S. & Coates, D.F.; Chapter 23: Canadian Experiences in Simulating Rock Slopes With the Finite Element Method; Rock Slides and Avalanches - Development in Geotechnical Engineering; Vol.14B, pp 709-758. B. Voight (Editor), Elsevier Scientific Publisher, Amsterdam, 1979.

Yu, Y.S., Gyenge, M. & Coates, D.F.; Comparison of Stress and Displacement in a gravity-Loaded 60° slope by Photo-elasticity and Finite Element Analysis; Divisional Report MR 68/20-ID; Mining Research Laboratories, Energy Mines and Resources Canada, 1968.

Yu, Y.S. & Hedley, D.G.F.; A Trial of Monitoring Slope Wall Movement at Hilton Mine Using a High Precision Theodolite; Divisional Report MRC IR 73-18; Mining Research Laboratories, Energy, Mines and Resources Canada, 1973.

Yu, Y.S. & Hedley, D.G.F.; A Model for Multi-Seam Mining of the Dension Mine at Elliot Lake, Ontario; Divisional Report MRP/MRL 77-127(TR); pp 73; Mining Research Laboratories, Energy, Mines and Resources Canada, 1977.

Yu, Y.S. & Toews, N.A.; MINTAB User's Guide - A Mining Simulator for Determining the Elastic Response of Strata Surrounding Tabular Mining Excavations (Version 1.0, 1981). Divisional Report MRP/MRL 81-28(TR); Mining Research Laboratories, Energy, Mines and Resources Canada, 1981.

Zhang, L. & Mitri, H.S., 3-D Modelling of Underground Mine Structures with Backfill. CIM Bull., 85, No. 962 (1992) 89-95

Session 5

Open Pit Mining

Mines à ciel ouvert

Numerical modelling of buckling and ploughing slope instability in surface coal mining

E. Eberhardt
D. Stead

Department of Geological Sciences, University of Saskatchewan, Saskatoon, SK
S7N 0W0, Canada

ABSTRACT

Buckling and ploughing are characteristic failure mechanisms affecting the footwall slopes of surface coal mines. These failures may cause large losses in production, pose serious safety hazards and necessitate extensive deformation monitoring schemes. A brief survey of the factors influencing buckling and ploughing failures is presented based on a detailed examination of the published literature. A critical review of conventional methods of analysis: two-dimensional limit equilibrium, Euler theory, three-hinge buckling and physical modelling; is undertaken. Preliminary results of numerical modelling using finite difference and distinct element techniques are presented using a typical footwall slope and a selected case history.

RÉSUMÉ

Flambage et défoncement sont deux mécanismes de rupture qui affects les flancs des mines de charbon à ciel ouvert. Ces échecs causent peut-être des grands pertes en production, présents des hasards de securité sérieux, et rendre nécessaire des systems de contrôle considérable. Après un examen rigoureux de la littérature publier, une étude des éléments qui influence les ruptures de flambage et défoncement sont présenté. Une critique des méthodes d'analyse conventionnelles tel que "two-dimensional limit equilibrium, Euler theory, three-hinge buckling and physical modelling" sont entrepris. Dans cette comunication les téchniques de deux modèles numérique, "finite difference" et "distinct element" sont présenté.

INTRODUCTION

In surface coal mines, steeply-dipping footwall slopes with strata parallel to the slope face present stability problems as slope heights increase. This requires a better understanding of footwall failure mechanisms. The consequences of slope failure in such environments range from minor coal contamination, production delays and losses, to major safety hazards to both equipment and personnel. Buckling and ploughing mechanisms in footwall slopes may be the major cause of a failure or a component of a complex translational process. Footwall failures involving buckling and/or ploughing failure mechanisms have been reported worldwide. Brawner (1971), Cavers (1981), Hawley et al (1986), and Stacey et al (1990), describe footwall instabilities including buckling failures in the surface coal mines of Western Canada. In Europe, footwall buckling and ploughing failures have been reported by Walton and Taylor (1977), and Walton and Coates (1980), in the U.K.; by Choquet et al (1992), in France; by Serra de Renobales (1987), in Spain; and by Nilsen (1987), in Norway. In addition to buckling failures associated with mining , natural buckling slope failures have been reported in China, Li and Zhang (1990),and in the USA, Watters and Inghram (1982). The major factors influencing buckling and ploughing instability are indicated in Table 1.

In this paper the authors utilize a finite difference code, FLAC, Itasca (1992a) and a distinct element code, UDEC, Itasca (1992b) to investigate the modes of footwall failure mechanisms in non undercut surface coal mine slopes.

CONVENTIONAL METHODS OF ANALYSIS

Brawner (1971) presented one of the first analytical methods for slope design in steep footwall surface coal mine slopes. Stability charts were constructed estimating the allowable footwall slope height as a function of slab thickness, bedding angle, cross joint orientation and friction angle for a failure mechanism involving an upper driving slab acting along a bedding plane and a lower toe wedge formed by a crosscutting discontinuity. This analysis assumes that the blocks are homogenous and isotropic and behave in a rigid translational manner. In practice the varying geomechanical properties within the Coal Measure's slopes may result in a more complex failure mechanism. In particular, the boundary between the steeper surface underlying the main slab and the crosscutting surface may be a region of complex deformation. Walton and Coates (1980), suggested that a Prandtl bearing capacity failure mechanism may be applicable in some cases. Failure may also involve buckling deformation in the upper slab, as remarked by Brawner (1971), in order to allow kinematic release.

Hawley et al (1981), provided a summary of the limit equilibrium techniques used in the analysis of footwall slopes. The method of buckling analysis first adopted in slope

design in surface coal mining was the Euler solution for a column with free ends. A factor of safety against buckling is derived by comparing the critical buckling load against the driving forces acting on the slab. This analysis provides an upper limit on the possible footwall slope height but is limited by the assumption of an elastic,

TABLE 1   Major factors that influence buckling and ploughing slope failures

FACTOR	INFLUENCE
Geometry	
Strata Dip	Varying dip resulting in curvature may promote buckling. Buckling in high slopes may occur at dips as low as 17°, but usually occurs at dips between 25° and 45°.
Slope Height	Increases driving forces. Permeability of slab may decrease with with increase in height due to orthogonal joint closure. Three hinge buckling stability in plane slabs (rigid blocks) increases with increasing height.
Slope Angle	Increase in slope angle reduces stability.
Sectional Curvature	Increased curvature promotes buckling.
Slope Length,L	Increased slope length reduces stability apart from three hinge buckling in rigid plane slabs.
Bedding /Jointing	Stability decreases with reduction in spacing (increase in slenderness ratio L/T).
Spacing Parallel to Footwall Slope	Euler buckling may be limited to spacing <1m. Slabs generally range in thickness from 0.3m to 10m. Thicker slabs may consist of multiple slabs exhibiting bulging and chevron morphology during deformation.
Joint Spacing Orthogonal to Footwall Slope	Reduced joint spacing may reduce incidence of Euler buckling but may increase ploughing instability. Reduced footwall spacing may increase permeability and reduce water pressures. Increased joint spacing may increase driving forces.
Structure	
No. of Joint Sets	Highly jointed toe regions may fail releasing upper slab. Increased jointing may reduce rigidity of slab and promote complex failures.
Orientation of Joints	Joints dipping out of the slope increase potential for bilinear slab failures.
Joints/Thrust Planes	Joints dipping into slope may promote ploughing failure.
Bedding Plane Shears	Reduces shear strength, promotes buckling/ploughing failure.
Folding	Increases buckling potential.
Sedimentary Features	
Cross Bedding	May allow toe release.
Rolls	Increased curvature may promote buckling.
Material	
Lithology	Varies from brittle, more rigid rock types (sandstones, granites limestones) to more plastic or time dependent materials (mudstones, siltstones,schists).
Geomechanics	Materials with high deformation moduli and uniaxial compressive strengths may display typical rigid Euler or three hinge buckling. Low deformation rock types may display non linear behaviour and/or creep. Uniaxial tensile strength of materials at points of slope curvature change may dictate the sudden tensile failure and release of upper slabs. The degree of corner crushing of blocks will be affected by the uniaxial compressive strength.
Water pressures	High water pressures may be necessary for three hinge buckling in planar slabs. Many failures have been reported in dry slopes. High water pressures are often critical particularly in the toe region. Freezing/thawing of snow and rainfall linked with accelerated deformation of failures, Stacey et al (1990).
Time	Range from rapidly moving brittle failures to slow time dependent creep mechanisms, Li and Zhang (1990). Progressive failure may be a factor in long term movements.
Man	
Blasting	Recorded as a possible factor in destabilisation of the footwall by several authors, Stacey et al (1990), and Scoble (1991).
Old Workings	Workings within the footwall may promote buckling, Walton and Coates (1980).

perfectly straight weightless column. The published literature shows that many buckling failures occur in non elastic rocks and in slopes of arcuate section. In natural buckling failures in granites, elastic conditions may be satisfied to some degree but buckling failures in mudstones and foliated rocks may involve non linear deformation. Cavers (1981), points out that the columns are not weightless and the analysis is conservative as a component of the weight of the slab acts to resist movement of the slab outward from the slope during buckling.

Watters and Inghram (1983), and Nilsen (1987), extend the elasticity theory approach to cover flexural buckling of plates in addition to beams. Both authors were concerned with the effects of, and the assessment of high *in situ* horizontal stresses. Nilsen (1987), undertook a sensitivity plate model analysis examining the effect of the magnitude of the horizontal stress (parallel to the strike) on the magnitude of the axial stress (parallel to the dip) required to initiate buckling. As expected, the higher the out of plane stress the more likely buckling is to occur. Nilsen is also one of the few authors to apply probabilistic theory in the design of footwall slopes against buckling failure. It should be noted that several authors, Cavers (1981), and Walton and Coates (1980), comment that they have never observed a Euler type failure in the field or in the case of the latter authors, that Euler theory did not appear to predict buckling satisfactorily on slabs over 1m in thickness.

Cavers (1981), and Cavers et al (1986), describe two methods of analysis for assessing the buckling potential of jointed planar and curved slabs. These methods, based on the principle of three hinge buckling, use force and moment equilibrium equations to assess the stability of a slab cut by three cross joints orthogonal to the slab. The stability of each of the two blocks involved is determined and the required interblock force for stability calculated. The analysis assumes that the individual blocks are rigid. Cavers (1981), notes that the upper slab must yield to provide room for the blocks to rotate requiring the equilibrium equations to be modified to allow for corner crushing of the blocks. The three hinge method has also been applied successfully to the analysis of curved footwall slopes. A limit equilibrium software package, CURVBUK, has been used to analyze several case studies by Cavers et al (1986), and Choquet et al (1992).

Ploughing instabilities involve sliding of an upper slab along bedding in combination with sliding along a discontinuity inclined into the slope resulting in the lifting and rotating of a toe block out of the slope. Footwall failures involving ploughing mechanisms have been reported in Europe by Walton and Coates (1980), and Serra de Renobales (1987), and in Canada by Stacey et al (1990). Hawley et al (1986), provide an analytical method of analyzing ploughing failures using an equilibrium approach.

In addition to numerical analyses, several authors have undertaken physical modelling of buckling and ploughing instabilities using base friction modelling techniques.

Walton and Coates (1980), used this technique to produce charts illustrating the effect of toe joint inclinations on the potential for cross over release or ploughing of the toe wedge. They also showed the effect of slope curvature on buckling. Choquet et al (1992), in a recent study, compared the results obtained with the CURVBUK program to those obtained using a base friction model for a curved footwall slope in France.

NUMERICAL MODELLING

To date little numerical modelling has been undertaken on footwall slopes to investigate the possible failure mechanisms. This paper examines the application of finite difference and distinct element techniques in characterizing footwall failure mechanisms, with emphasis on buckling and ploughing.

Finite difference models

Continuous slab models were analyzed using FLAC, Fast Lagrangian Analysis of Continua, an explicit, finite difference program developed by Itasca (1992a). The models were set up to simulate the mining of a thin coal seam. This was done by dividing the models into three components, a base, a thin bed (footwall) and overburden. After time-stepping the models to an initial equilibrium, the overburden was then decrementally removed. By removing the overburden in small decrements, the length of the unrestrained slab was gradually increased. The models were also constructed so that the dip of the footwall and the thickness of the beds can be varied. FLAC offers a choice of constitutive models to represent the behaviour commonly associated with geologic materials.

An elastic constitutive model was chosen to stimulate Euler buckling. No external forces, such as water pressures, were added to the model thereby restricting the slope (column) to deform under it's own weight. In general, the models set with an elastic constitutive model did not show any indication of a buckling failure.

A second set of models were constructed with a gentle roll in the footwall resulting in a change of dip from 30° to 35°. A Mohr-Coulomb plasticity model was chosen to represent the materials used in this simulation. This is the conventional model used for elasto-plasticity in rock and allows for the representation of a material which is yielding in shear. Failure of the modelled slope occurs at the point where the bedding steepens after the remaining toe support is removed (Figure 1). Above this point the driving slab has moved down the slope. As would be expected, the failure process in the model appears to initiate in tension at the point in the slope where the dip steepens, allowing the rest of the slope to fail in a planar fashion. This corresponds to observations made by Cavers (1980), Walton and Coates (1980), and Serra de Renobales (1987).

thin bed

length : thickness

100 : 1
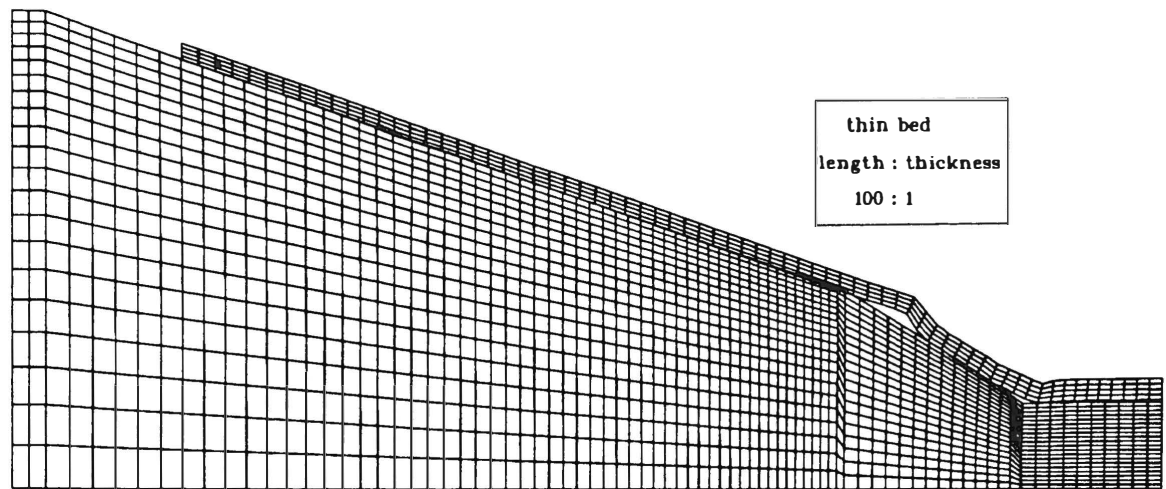
Figure 1   Finite difference model of buckling failure

Distinct element models

Discontinuous slab models were analyzed using UDEC, Universal Distinct Element Code, a distinct element program also developed by Itasca (1992b). The distinct element method prescribes an interface for each block contact within the model. Fully deformable blocks were used in the model to avoid problems of corner crushing. A similar model geometry as illustrated in Figure 1 was used. In addition, the effect of joint crosscutting was modelled. Three different sets of models were constructed: joints perpendicular to the bedding with no crosscutting discontinuities; joints perpendicular to the bedding with a crosscutting discontinuity dipping out of the slope; and joints perpendicular to the bedding with a crosscutting discontinuity dipping into the slope.

A Mohr-Coulomb plasticity model was chosen to represent both the intact rock and the discontinuities. As with the FLAC models, the UDEC models were constructed to allow for the decremental removal of the overburden load. The three different model results are shown in figures 2 to 4. Failure of the slope can be seen in each of the three models. In the first model (Figure 2), in which there was no crosscutting joint, the failure displays a similar mechanism to the failure seen in the Mohr-Coulomb FLAC model. Failure of the modelled slope occurs at the point where the slope steepens, with the upper portion of the slope failing in a planar fashion. Plasticity indicators showed that the blocks at the buckle failed in tension. Figure 3 shows the results of the model in which a crosscutting discontinuity dips out of the slope. As would be expected, this model shows a planar failure along the discontinuity. The major factor influencing the modelling of this type of failure is the shear stiffness and the frictional resistance along

the top of the toe block formed by the crosscutting discontinuity. This is consistent with observations made by Brawner et al (1971). Figure 4 shows the results of placing the crosscutting discontinuity so that it dips into the slope. In this case the toe block is rotated, pushed up and then out. This follows the mechanism of a ploughing failure, corresponding with descriptions given by Hawley et al (1986), and Serra de Renobales (1987).
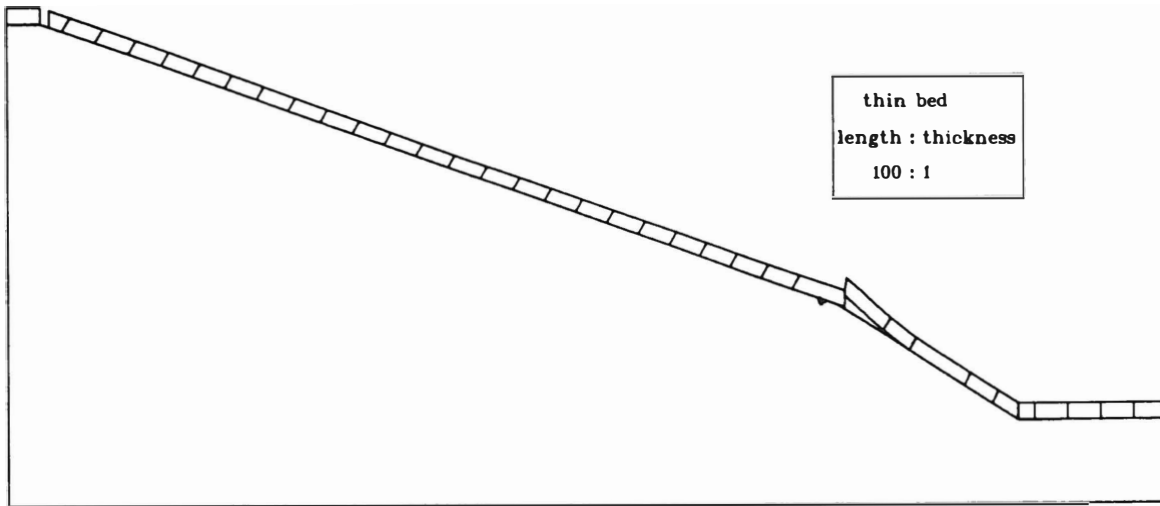
Figure 2   Distinct element model of buckling failure with jointing
oriented perpendicular to bedding
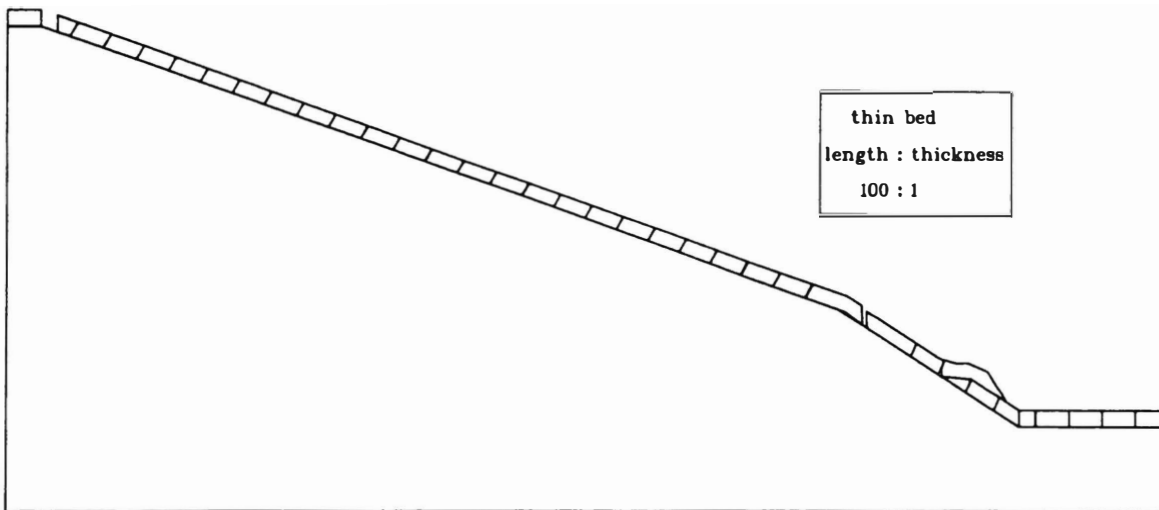
Figure 3   Distinct element model of buckling failure with jointing oriented
perpendicular to bedding and a crosscutting discontinuity dipping out of the slope
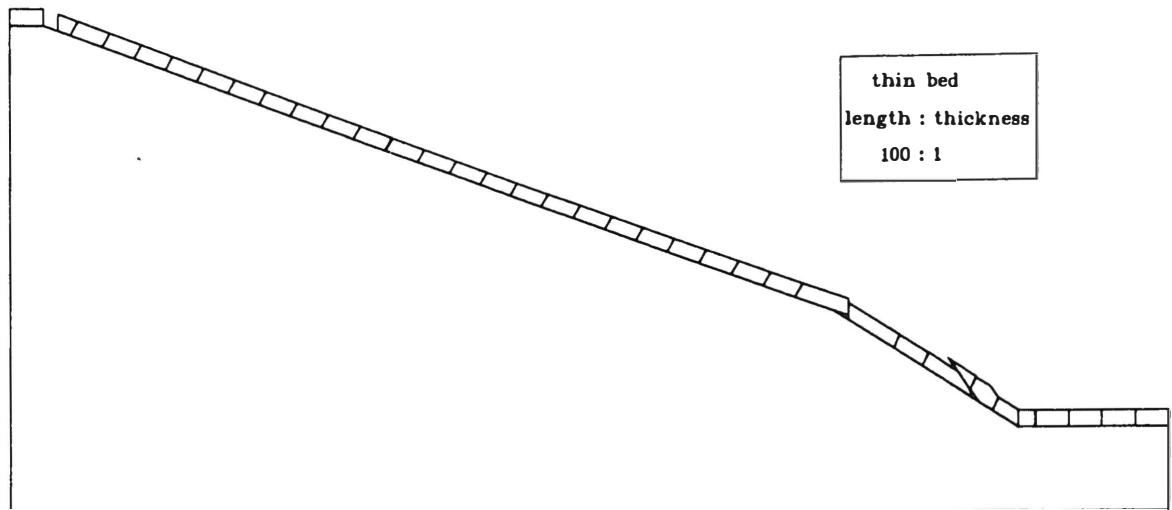
Figure 4   Distinct element model of buckling failure with jointing oriented
perpendicular to bedding and a crosscutting discontinuity dipping
into the slope (deformation 5x magnification)

APPLICATIONS AND LIMITATIONS

The modelling techniques used above were applied to a case study of the 1974 U.K.
Westfield highwall failure as described by Scoble (1981). This case study was chosen
from a limited number of available case studies because of the quantity of information
available on both the geometry of the failure and the material properties. Scoble reports
that witnesses stated that the middle of the face first bulged and then slid down over the
lower part of the slope engulfing a bulldozer at the base of the slope, killing the driver.
Further inspection revealed that the lower part of the face had suffered a slab slide with
buckling occurring at the toe. Figure 4 shows the results of modelling this failure with
UDEC. After the removal of the toe support, plasticity indicators show that tensile
failures occur along the middle of the slope. This corresponds with the witness reports.
Detailed examination of the deformed blocks reveals that buckling occurs in the lower
portion of the slope.

The use of numerical modelling in analyzing case studies has limitations. Input
parameters for material properties have a significant effect on the results. For this type
of analysis, the normal stiffness, shear stiffness and friction angles along the block
interfaces, largely control the modelled failure mechanism. It is important that
numerical modelling techniques are calibrated against measured ground deformation
results and that representative stiffness values, where possible, be obtained by back
analysis of previous buckling instabilities.
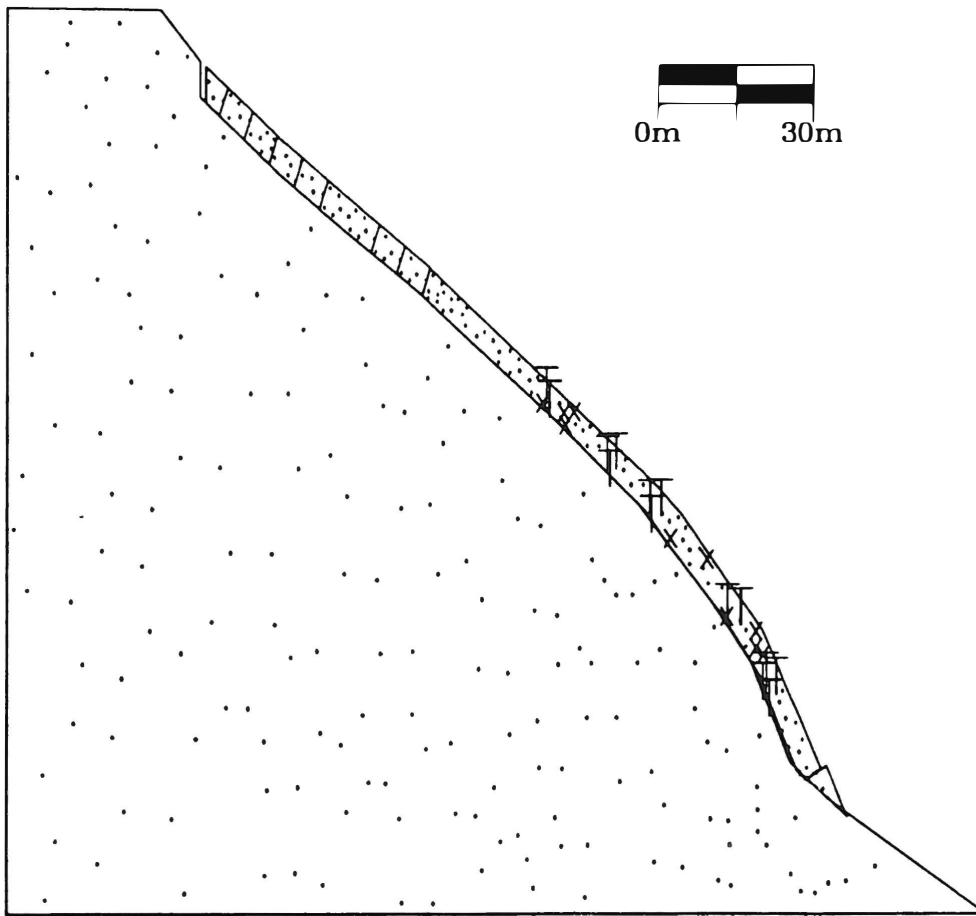
Figure 5   Distinct element model of the 1974 U.K. Westfield highwall
buckling failure (with plasticity indicators)

CONCLUSIONS

This paper reviews the mechanisms of buckling and ploughing failure observed in
surface coal mines. A preliminary numerical modelling study of buckling and
ploughing failure was under taken using finite difference (FLAC) and distinct element
(UDEC) techniques. These models were also used to analyze a buckling failure case
history from the U.K. The results of this numerical modelling study illustrate the
potential for analyzing buckling and ploughing failures in surface coal mines. Further
work is being undertaken to investigate the effect of varying strength and stiffness
values on the failure mechanism. This work demonstrates the usefulness of the finite
difference and distinct element techniques in studying the mechanism and development
of buckling and ploughing failures.

REFERENCES

Brawner, C.O., Pentz, D.L. and Sharp, J.C. 1971. Stability studies of a footwall slope in layered coal deposit. Proc. 13th U.S. Symp. on Rock Mechanics, 329-365.

Cavers, D.S. 1981. Simple methods to analyze buckling of rock slopes. Rock Mechanics, 14, 87-104.

Cavers, D.S., Baldwin,G.J., Hannah,T. and Singhal,R.K. 1986. Design methods for open pit coal mine footwalls. Proc. Int. Symp. on Geotechnical Stability in Surface Mining, Ed. Singhal, Calgary, 79-86.

Choquet, P., Hadjigeorgiou, J., Manini, P., Mathieu, E., Soukatchoff, V. and Paquette, Y. 1992. Analysis of the strata buckling mechanism at the Grand-Baume coal mine, France. Proc. 94th AGM CIMM, Rock Mechanics and Strata Control, Montreal, 136-154.

Hawley, P.M., Martin, D.C. and Acott, C.P. 1986. Failure mechanics and design considerations for footwall slopes. CIM Bulletin, 79, 47-53.

Itasca Consulting Group, Inc. 1992a. FLAC version 3.04.

Itasca Consulting Group, Inc. 1992b. UDEC version 1.8.

Li, Q. and Zhang, Z.Y. 1990. Mechanism of buckling and creep-buckling failure of the bedded rock mass on the consequent slopes. Proc. 6th IAEG Congr., Amsterdam, 2229-2233.

Nilsen, B. 1987. Flexural buckling of hard rock - a potential failure mode in high rock slopes?. Proc. 6th Int. Congr. on Rock Mechanics, Eds. Herget and Vongpaisal, Montreal, 457-461.

Serra de Renobales, T. 1987. Strata buckling in footwall slopes in coal mining. Proc. 6th Int. Congr. on Rock Mechanics, Eds. Herget and Vongpaisal, Montreal, 527-531.

Scoble, M.J. 1981. Studies of ground deformation in British surface coal mines. PhD. Thesis. Dept. of Mining Engineering, University of Nottingham, England.

Stacey, P.F., Bjornson, B. and Parsons, D. 1990. Mining implications of footwall movement at the Westar Greenhills operation. Proc. 2nd. Int. Symp. on Mine Planning and Equipment Selection, Calgary, 411-421.

Sun Guangzhong. 1982. A testing of a buckling failure of rock mass. Proc. 4th IAEG Congr., New Delhi, II.83-II.90.

Walton, G. and Taylor, R.K. 1977. Likely constraints on the stability of excavated slopes due to underground coal workings. Proc. Conf. on Rock Engineering, Newcastle-upon-Tyne, 329-349.

Walton, G. and Coates, H. 1980. Some footwall failure modes in South Wales opencast workings. Proc. 2nd Int. Conf. on Ground Movements and Structures, Cardiff, 435-448.

Watters, R.J. and Inghram, B.J. 1983. Buckling failure of granite slabs in natural rock slopes as an indication of high residual stresses. Proc. 20th. Eng. Geol. and Soils Eng. Symp., Boise, 83-96.

INTERPRETATION OF NON-STRUCTURAL SLOPE FAILURE IN OPEN-PIT MINING - A NUMERICAL MODELLING APPROACH

C.M. Tsomondo and H.S. Mitri

Department of Mining and Metallurgical Engineering
McGill University
Montreal, Quebec, H3A 2A7

ABSTRACT

Pit slope failure can take several forms of varying complexity. Of particular importance is a non-structurally controlled failure in open pit mines located within high lateral stress regimes which cannot be predicted by analytical methods. This paper presents a technique of analyzing numerical modelling output data (stresses and displacements) to determine the mechanisms and modes of non-structural slope failure in open pits. A loci of zero vertical displacements within the critical slope demarcates a zone of low confinement. Uni-directional horizontal displacement vectors tend to "open" these unconfined zones. Loci of maximum vertical displacement vectors also occur close to the slope face and only within the lower benches causing a precursor instability in the pit slope. The analysis indicates the presence of multi-step progressive failures as the mode of non-structural slope failures in geodynamic regions. The method was successfully used in a back-analysis of a historical non-structurally controlled slope failure at Jeffrey Mine at J.M. Asbestos Inc., Asbestos, Quebec.

RESUMÉ

La rupture de la pente-enveloppe d'une fosse est de forme et de complexité variable. En ce domaine il faut porter une attention particulière à toutes ruptures structuralement non-contrôlées et localisées dans une zone de fortes contraintes latérales, car elles ne peuvent être détectées par les méthodes analytiques. Nous présentons ici une technique d'analyse des données de modélisation numérique (contraintes et déplacements) qui permet de déterminer les mécanismes et les modes de rupture. Sur un pente limite, c'est le lieu géométrique des déplacements verticaux nuls qui indique la zone de faible confinement. Un déplacement unidirectionnel horizontal provoque "l'ouverture" de ces zones non-confinées. Les vecteurs de déplacement vertical maximum apparaissent à proximité de la surface de la pente, aux gradins inférieurs seulement, annonçant ainsi une instabilité de la pente-enveloppe. Dans les régions géodynamiques, l'analyse démontre la présence de ruptures à développement progressif, lesquelles provoquent la rupture de la pente. Cette méthode fût utilisée avec succès lors d'une analyse rétrospective de la rupture de la pente-enveloppe à la mine Jeffrey de la J.M. Asbestos inc., Asbestos, Québec.

INTRODUCTION

The main objective in the optimal design of the final pit slope angle is to maximize the slope angle without compromising on the safety and the possible economic losses that may occur due to a slope instability. The steepening of the pit slopes minimizes the waste removal thus reducing the stripping ratios. The net effect is two-fold, namely it increases the mineable reserves for a fixed pit limit due to mining of deeper levels and less equipment capitalization as less material is required to be moved. Both these factors improve the net present value of the mine property.

Due to potentially expensive economic penalties resulting from slope failure, it is necessary to identify and evaluate the unstable zones. This calls for an integration of slope stability assessment in the overall mine design. Several authors who dealt with the problem of slope stability analysis have placed emphasis mainly on the geotechnical controls of the slope rock masses. The variability of the lithologies, types of discontinuities and their location and orientation with respect to the pit crestline are considered critical. Groundwater pressure and seismicity occupy supplementary roles in these slope failures.

The shallow nature of open pit mines has led to the generalized assumptions that ground in-situ stresses are unimportant. This is unfortunately not universal, in particular, when dealing with open pit mines in terrains of higher lateral stresses than the gravity loading. This paper pursues this field and through the use of a back analysis case study illustrates how numerical modelling methods can be used to predict complex, non-structural failures.

NUMERICAL ANALYSIS OF SLOPE STABILITY

The traditional geotechnical site investigations in open pit mines is hinged to the identification of one or more potential failure modes. In hard rock mines these failure modes tend to be structurally controlled; consisting of loose blocks that could be triggered into sliding along one or more planes, or topple. In soil and/or weathered slope profiles, failure has been postulated to be either non-circular or circular arc.

The principle of stability analysis is based on drawing stereographic projections of the discontinuities and the local pit slope on stereonets [*Hoek & Bray, 1984*]. The diagrams will indicate the failure mechanisms that are kinematically unstable. A deterministic approach of static limiting equilibrium is used to find the safety factor (i.e. ratio of failure resisting forces to disturbing forces). The use of statistical data allows for a quantitative assessment of the structural control. The variability of the discontinuities in dip angle, orientation, spacing, continuity and in-fill material type can now be studied. These analytical methods are successful in the interpretations of about seventy-five percent of all pit slope failures [*Ross-Brown, 1979*].

Some slope failures both in rock and soil material are not structurally controlled. They do not follow any well-defined failure surfaces hence cannot be analyzed by the analytical method. This is specially true in blocky rock masses with no dominant controlling discontinuities. The rock is stiff such that it resists both non-circular and circular failure modes.

These failures are generally rare worldwide but in geodynamic terrains where the pre-mining horizontal stresses exceed the vertical, the phenomenon seems prevalent. The high horizontal stresses are due to either residual thrust tectonic stresses; or isostatic disequilibrium resulting from unloading of the ice sheets or both. Underground stress measurements in Canadian hard rock mines that have been conducted by CANMET at depths of 60 to 1890 metres [*Arjang,1991*] confirm that most of the Canadian Shield as well as the St. Lawrence Valley exhibit these high lateral stresses.

Since some large open pit mines located in the above described areas can have depths of over 200 metres, it implies that their stability is influenced by the pre-mining stresses. Corresponding depth stresses can be assumed in open pit mines within the same geographic region as the underground mines in which measurements were taken.

Numerical modelling methods such as the finite element and/or distinct element methods are suitable for analyzing and predicting potential slope failure zones in non-structurally controlled pit slopes [*Dolezalova, 1984*]. This study employs a static linear elastic finite numerical modelling software called e-z Tools. The software is based on its earlier version developed by *Chau et al (1988)* known as MSAP2D at McGill University. The software permits the simulation of ground stresses, displacements and safety levels of a multi-lithological, multi-benched vertical section of the pit slope. Several theoretical parametric studies were conducted using the software. It was then decided to test the validity of the results by performing a back analysis on the J.M. Asbestos mine (Quebec) southern hanging wall massive slope failure of 1971. The objective was to determine the ground stress conditions and the rock mass mechanical properties (cohesion and internal friction angle) that existed at time of failure.

CASE STUDY: J.M. ASBESTOS SOUTHERN HANGING WALL FAILURE (1971)

The orebody is a massive elliptical chrysotile deposit measuring some 1100 x 600 metres in plan and dipping south-east at 65°. The geology consists of serpentinised peridotite and dunites overlain by gabbroic and volcanic sequences and slate [*Labbe, 1979*]. The deposit is ophiolitic and the whole area was previously covered by an ice cap during the Ice Age. Thus, both residual tectonic stresses and ice unloading induced stresses are expected to be present.

Section Analyzed

A vertical section through the centre of the southern hanging wall instability zone trending at 135° is considered. At the time of failure the section consisted of five berms interspaced over a 248 metre pit depth. The overall pit slope angle was 25°. The slip scarp occurred at 26-30 m behind the pit crest and the toe of failure was about 16 m above the pit floor [Figure 1]. The failure plane cut across both the bedding plane and the main shear zone. The slope geometry (strike and dip) and the discontinuities orientation and dip angle suggest a structurally stable slope according to the analytical methods of slope stability. Thus the traditional thinking has attributed the failure solely to groundwater pressure. While this may have been a factor as a pushing force directed down the slope; there existed no defined slip plane at the bottom through which the groundwater would have exerted an uplifting pressure on the overlying rock mass. Other contributory factors should have existed!

188
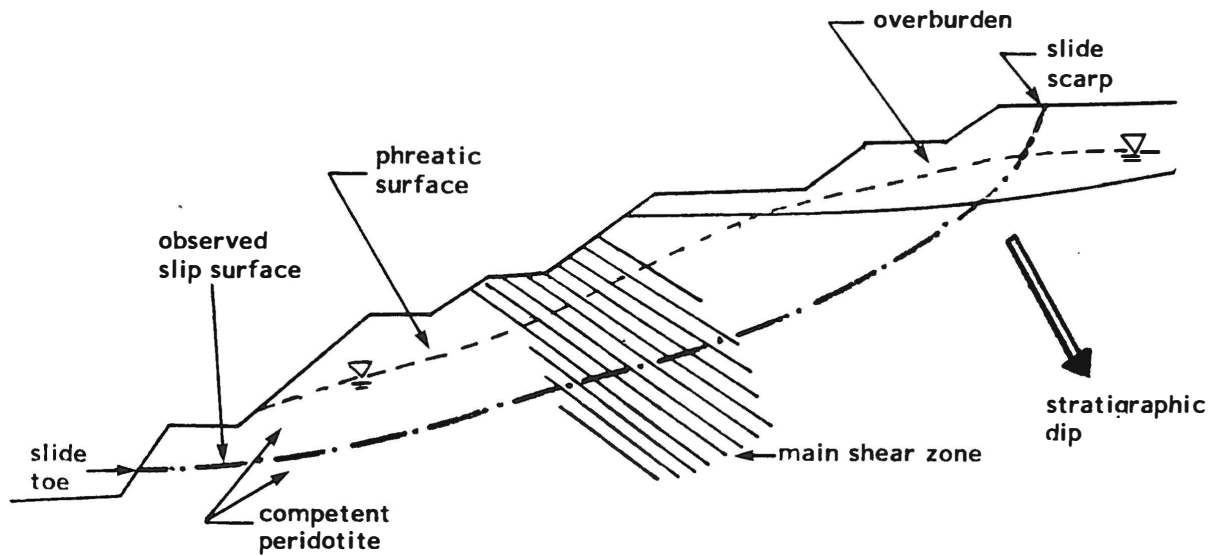
Figure 1   Southern hanging wall failure geometry [*Adapted from Sharp et al., 1978*]

The open pit problem domain is defined as either at locations where the excavation displacements or the excavation induced stresses are zero, that is, at infinite. Truncation of the domain is necessary to reduce computational costs hence boundary conditions are imposed at the fictitious boundaries. The outer boundaries have been set at the following distances:

1. ten times the height of the excavation in the horizontal direction i.e. 2500 metres and
2. six times the height in the vertical direction i.e. 1500 metres.

The vertical axes at the fictitious boundaries are fixed in the x-direction and free in the y-direction. Conversely, on the lower horizontal boundary the y-axis is fixed with x free to move. The slope and the upper horizontal surface are free. These conditions have a trade-off finite element analysis error of less than 10 percent [Toews et al.,1975].

Natural Stresses

Primary stresses result from superposition of two kinds of stresses, namely gravitational and tectonic. The state of the initial stresses, prior to the excavation is essential. However, these are difficult to find since the rock mass varies significantly over the mine structure. A weighted rock unit weight,γ_{ave} has been used in this analysis to calculate the gravitational stress, σ_y given by the formula:

$$\sigma_y = \gamma_{ave} H \qquad (1)$$

where H is the depth of rock mass below surface.

189

The Quebec Eastern Townships is located in an area where the tectonic stresses are greater than the gravitational stress. Such areas are known as geodynamic and their average horizontal stress has been defined by an empirical equation [*Theil,1989*] as:

$$\frac{\sigma_x + \sigma_z}{2} = 9.31 + 0.05H \ MPa \tag{2}$$

Arjang (1991) also derived a formula for the average horizontal stress,σ_{ave} which is given by:

$$\sigma_{ave} = 5.91 + 0.0349H \ MPa \tag{3}$$

Using this background information the horizontal in-situ stress has been simulated for a variety of magnitudes namely for the following stress ratios, k: 1.0, 1.5, 2.0, 3.0 and 4.0 of the vertical stress. A finite element mesh consisting of 2637 elements (2751 nodes) has been generated to examine the stability of the pit slope [Figure 2]. This mesh is graded such that the highest mesh density is around the excavation's critical zone. In this region the elements are approximately 8 m by 9 m in size. The mesh density used is near the maximum (4000 elements) that could be run on the coreprocessor and it takes about 4.5 hours to complete the execution on an IBM PS/2 Model 70 386 16MHz machine.

Geomechanical Data

This was obtained partly from literature on the mine that documented the slope failure under investigation as well as typical Quebec lithologies belonging to the same Appalachian sequence. For the purpose of numerical modelling, the geomechanical classification of the rock masses was done using the Bieniawski ratings as indicated in Table 1. The Young's modulus, E_{ave} was then calculated for each rock mass rating, RMR, (where RMR$\geq$55%) of the different lithologies according to the formula proposed by *Brady & Brown, 1985*:

$$E_{ave} = 10^{\frac{(RMR - 10)}{40}} \tag{4}$$

Table 1   Derived Young's moduli from RMR

	Slate	Overbdn	Peridotite	Gabbro	Basalt
σ_c (15)	12	1	12	12	12
RQD (20)	17	8	13	17	13
JS (30)	20	0	20	25	17
JN (25)	12	0	12	12	10
Groundwater(10)	4	4	4	6	4
RMR	65	13	61	72	56
E..(MPa)	23714	-	18836	35481	14125
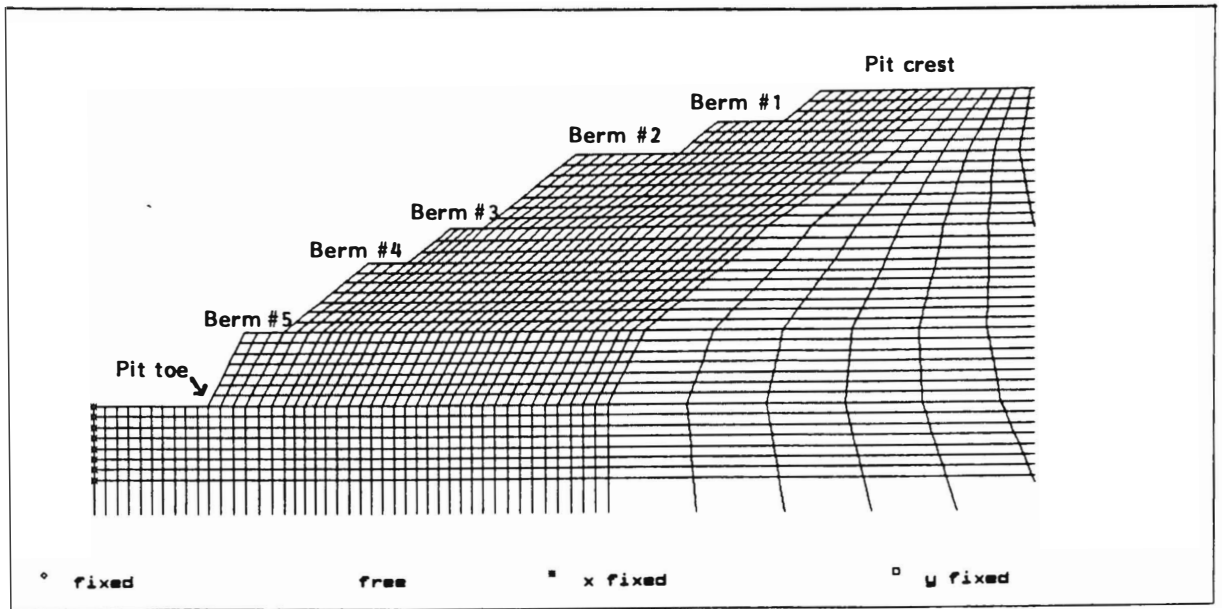
Figure 2   Slope finite element mesh

This method was preferentially chosen because it is more practical and representative of the field rock properties compared to the use of laboratory determined Young's moduli of elasticity of intact rocks.

The failure zone had a wide shear dipping sub-parallel to the geology. Hence the rock masses in this zone were treated as transversely isotropic with the angle of orthotropy being equal to the dip of the shear zone.

Numerical Results

Slope Stresses Analysis

A parametric study of the slope stress type and distribution was conducted for the above mentioned in-situ stresses. The terms "radial" and "tangential" are used for sub-horizontal and sub-vertical re-distributed principal stresses respectively. Four plots of ratios of the tangential stress, σ_t to the in-situ lateral stress, σ_H with respect to relative distances from the pit slope face are illustrated in Figure 3. The curve for the stress ratio at the slope toe indicate high values at the slope face elements decreasing to unity for far field elements. A curve for finite elements 16 m above the pit toe has a stress ratio of 0.98 at the face element and then a sharp decrease to 0.32 for the next element beyond which the ratio increases gradually to unity for far field elements. For elements located at levels of greater than 24 metres above the pit toe, the stress ratios increase from zero at the face elements to unity for far field elements.

The results indicate that where the stress ratio, σ_t/σ_H is unity or greater then the slope is under confinement. Conversely, when the ratio is less than unity the ground is de-stressed and susceptible to failure.
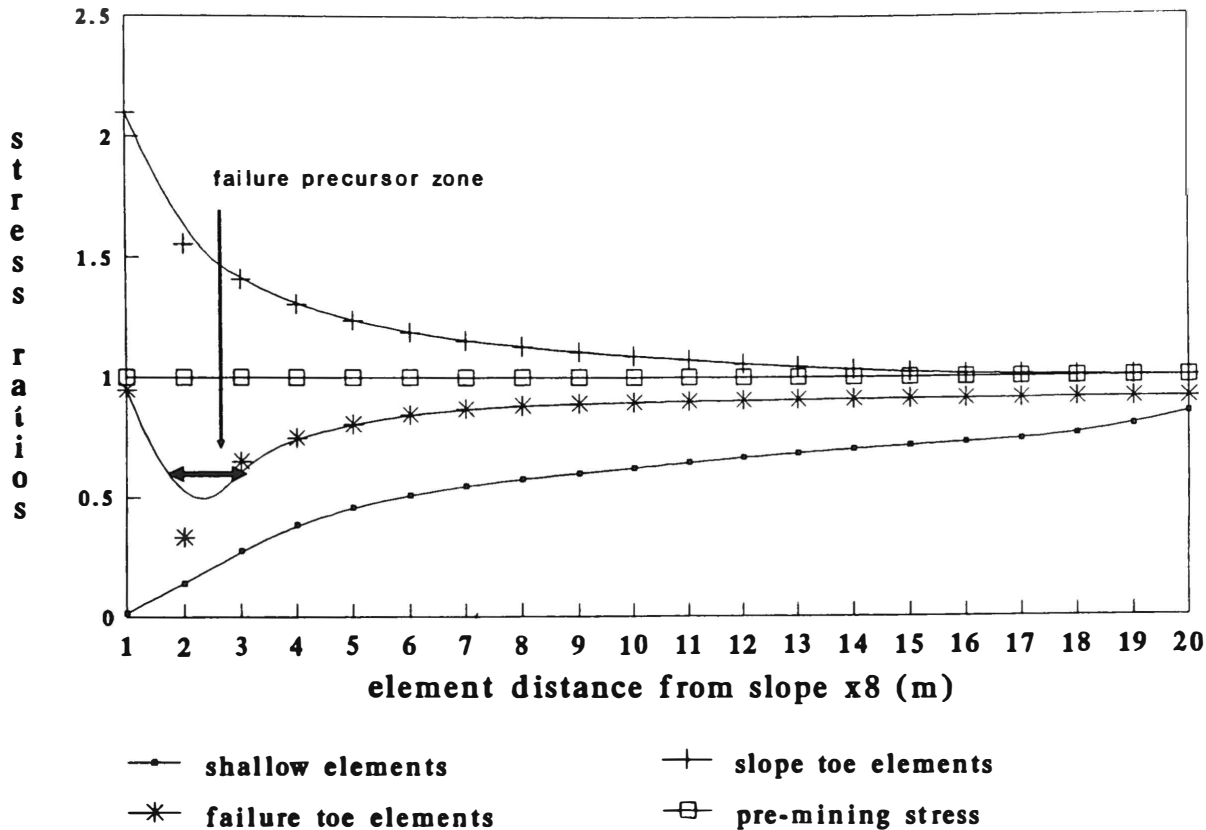
Figure 3   Slope stress ratio variation for k=3

The radial stresses are everywhere less than the tangential stresses and they linearly increase from zero at the slope face to maximum values corresponding to the gravity stresses. In the lowest berm some radial stress values are of opposite sign reflecting tension. Their direction is perpendicular to the slope face and hence also parallel to the direction of maximum displacements namely the horizontal. Since rock is weak in tension, the location of these stresses is an indication of potential incipient failure. The failure mode would be separation of the rock mass in a direction parallel to the slope face i.e. slabbing. A Mohr-Coulomb safety level plot did show these tension zones to be the first to fail [Figure 4]. Some tension existed in the toe of the second berm which marks the overburden-peridotite contact. This is probably due to the strong contrast in the materials stiffness properties.

Slope Displacements Analysis

The resultant displacements in the slope are towards the excavation. On the pit floor they point upwards reflecting gravity relief due to mining and physically cause floor heaving.

A method was devised to analyze the behaviour of these resultant displacements. They were resolved into their horizontal and vertical components as U_x and U_y respectively. The behaviour of each component was then studied and the following trends were observed: The U_x variation with distance from the slope face is exponentially decreasing. It decreases to zero at the fictitious boundary.

Everywhere in the slope, the U_x displacements are towards the excavation. The U_x increases with depth in the zone of the total slope height as well as with increase in the horizontal in-situ stress. The U_y displacements variation with distance from the slope face is more complex and tend to depend on both the in-situ stress and the elevation of the nodes being considered.
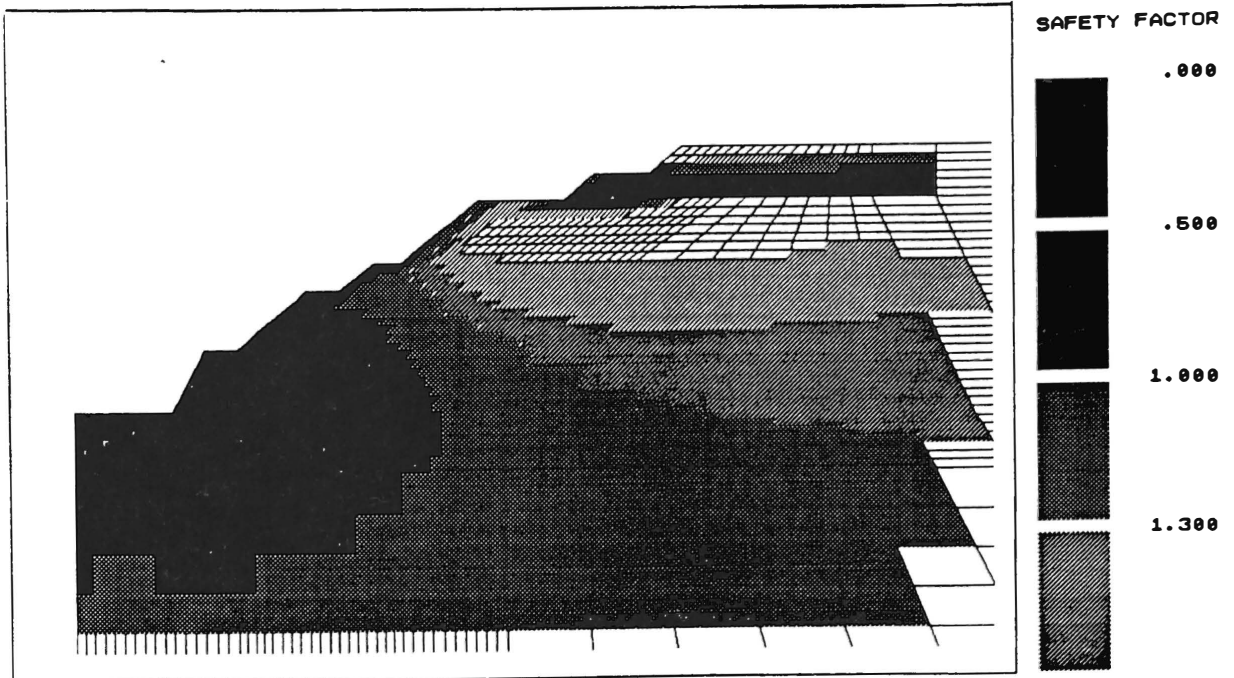
Figure 4   Slope safety levels using Mohr-Coulomb criterion (k=3)

A parametric study on the in-situ stress ratios indicate a decreasing trend in the positive U_y displacements with increase in k value for the pit toe elements [Figure 5]. The curve for k=3 indicate a negative U_y at the toe node, gradually increasing to a small positive U_y and subsequently increases negatively. This stress ratio is considered to be close to the critical situation where the U_y displacements are zero at the pit toe.

The vertical displacements at different levels of the pit slope were then analyzed using the critical stress ratio of three [Figure 6]. At or near the slope face the displacement vectors, U_y are pointing upwards for nodes at lower elevations such as the bottom berms #4 and #5. The positive U_y decrease in magnitude with increase in distance form the slope face to a point where U_y becomes zero. Beyond this point U_y become negative and increase in magnitude with distance up to the fictitious boundary. Similar to U_x, the magnitude of U_y increase with depth of mining. For levels near the surface, for example berm #2, U_y is entirely downward pointing. This is a consequent of gravity loading being the dominant force at such shallow levels.

The toe node is displaced downwards whilst the toe berm (berm #5) is displaced significantly upwards. This indicates a point on the slope where zero displacement exists. That location is critical in defining the *toe* of the slope failure.
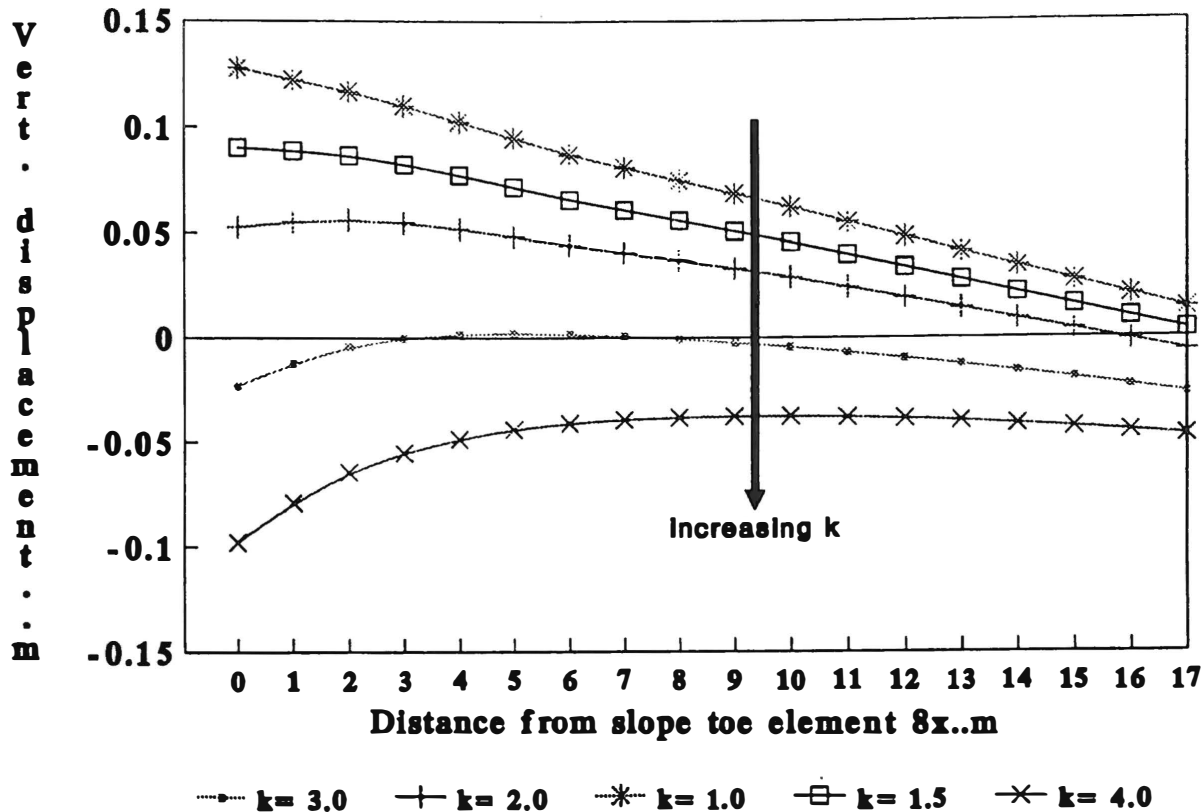
Figure 5   Vertical displacements at pit toe level for different k ratios

The above trends of U_y with distance from the slope face identifies stationary points (zero displacements). These are unconfined points or elements with shearing occuring on either side since the nodal displacements are opposed. When combined with a uni-directional U_x this cause material separation as differential displacements exists between any two row elements. The zero U_y points mark potential "failure points" which when connected for successive rows of finite elements form a continuous locus that daylights on the slope face in the second berm.

The location of the maximum U_y away from the slope face in the pit toe berm indicates a locus of "column" of elements within the slope that is moving upwards more than the columns on either side. Secondly this column is displaced towards the slope face more than its neighbouring element that is away from the slope. This implies that the face elements are being "pushed" towards the excavation and the maximum U_y locus represent separation in the rock mass. The slope face elements are therefore likely to fail in this region.

For lower values of k, the "discontinuities" (i.e. zero U_y displacements loci) are steeper and start lower in the pit face whilst at the same time they occur furthest from the pit toe. This implies that the slope is stable above the incipient point of "discontinuity". The incipient point occurs below that of higher k values implying that the lower k ratio pit goes deeper before stress related failure exists. The steep dip and long distance from the toe of the low k "discontinuity" means that failure is unlikely as there are less chances of this plane daylighting in the slope and the slope tends to remain stable.
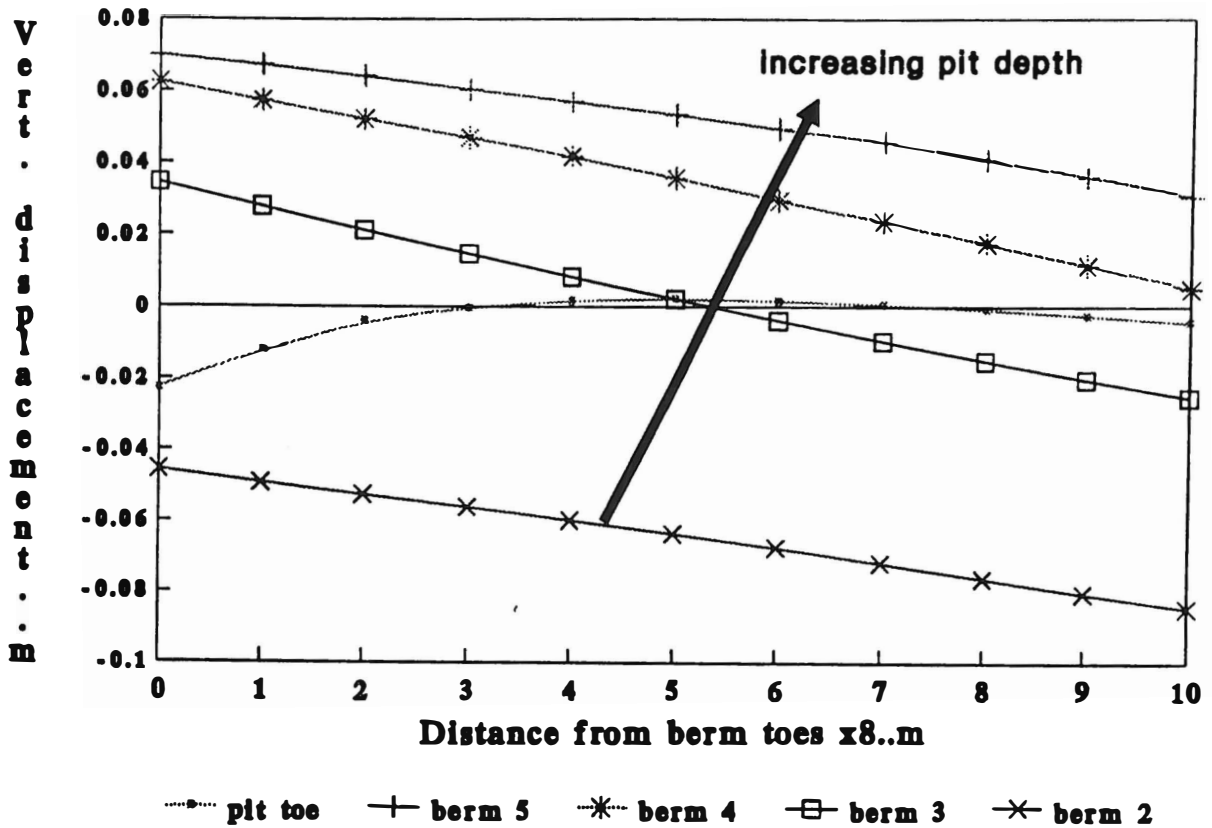
Figure 6   Vertical displacements at different levels (k=3)
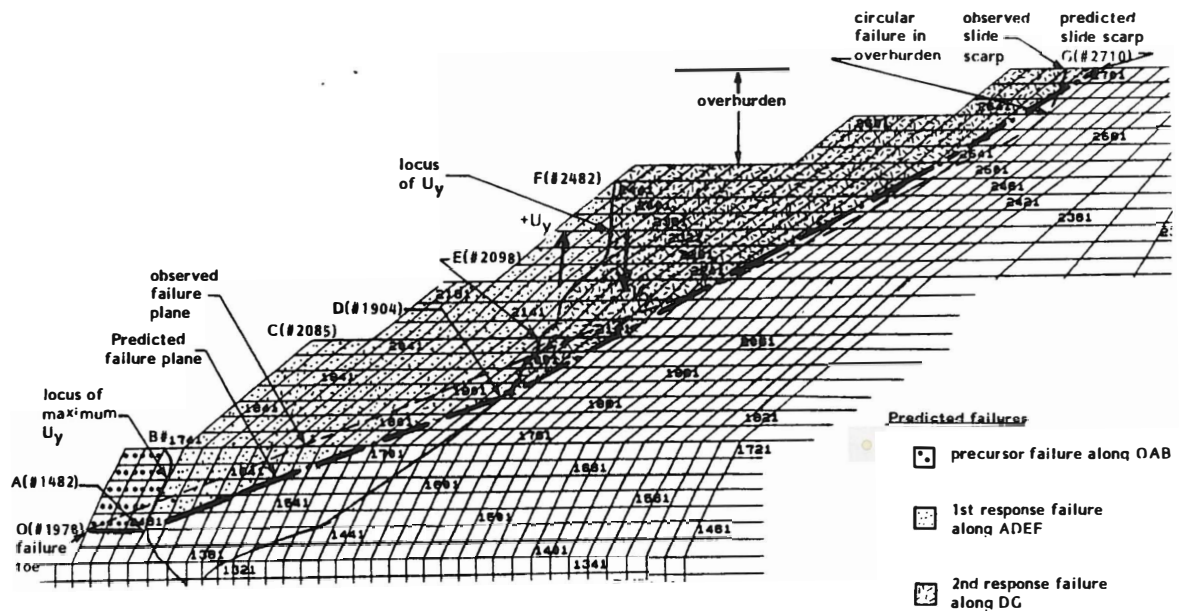
Figure 7   Comparison of actual and predicted failure planes

As the k value increase, the point of incipient failure moves up the slope face towards the surface hence a greater volume becomes prone to failure. At depth, the "discontinuity" rapidly shifts upwards towards the pit toe such that less material now sits above this surface. The probability of daylighting at the pit toe increases reflecting less buttressing force and a higher potential of failure. Since the higher k value creates a plane of maximum U_y away from the face within the rock mass, as discussed earlier, this amounts to another separation plane which is more susceptible to failure. The net result of such a toe failure would be to destabilise the zone behind the toe area such that failure would propagate upwards and backwards till it intersects the zero U_y displacement "discontinuity" upon which failure follows the locus of zero U_y.

At shallow depths it leaves a very steep post failure slope such that the material cannot stand, hence it too fails to its internal friction angle. In consequent it propagates to the upper ground surface.

Simulation of Southern Hanging Wall slope mechanism

Simulations of the material safety levels based on Mohr-Coulomb criterion was executed and it showed failure in the area above the zero U_y displacements. A sensitivity analysis was performed through variation of material properties (cohesion and friction). The best results were obtained by the material property set:
peridotite: internal friction angle of 37° and cohesion of 0.3 MPa; and overburden: internal friction angle of 20° and cohesion of 0.1 MPa. The result is illustrated in Figure 4.

The following is suggested as the most likely mode of failure:
A "tension" crack (for k=3) exists along the following nodes:1380, 1431, 1482, 1535, 1586, 1638, 1690 and 1741 which trace out a reverse S shape [Figure 7]. The node number 1482 marks the closest distance (30 metres) of the tension crack from the pit slope before the crack swings away to nodes 1431 and 1380 respectively. It is reasonable to assume failure will not go lower than this point such that the initial failure plane of the zone in front of the tension crack is through nodes 1479, 1480, 1481 and 1482. This assumption is supported by the Mohr-Coulomb safety level plot which shows the elements sitting on the above nodes to be in failure [Figure 4].

When this failure had occured, a new slope face was created denoted by A(#1482), B(#1741) and C(#2085). This created an excessive berm height as well as a steeper inter-berm angle (45°) greater than the internal friction angle of the rock mass. Consequently this slope failed back to a slope angle governed by the internal friction angle (37°). Support to this conclusion is highlighted again by the safety level contour of 0.5 to 1.0 [Figure 4].

The internal friction angle was used to draw in the failure plane from node #1482. The line intersects the failure plane predicted by the analysis of vertical displacement vectors at D(#1904 node). The failure then follows this line through point E(#2050) to daylight at F(#2098) on the pit slope face.

The zone above point E (#2098) after this second failure was again left at a higher inter-berm angle such that it failed as described earlier, to the internal friction angle. A plot of safety levels indicates a safe zone in this second berm. In reality this does not exist since the toe loss will introduce instability as overhangs are improbable in this rock mass. This failure will propagate upwards along the 35-37° angle to daylight on the upper surface at G(#2710) at 60 metres behind the original pit

crest.

The actual 1971 failure surface was then plotted on the same section for comparison and to determine the variability of the finite element approach from the actual [Figure 7]. The results indicate a very good agreement between the actual and the predicted failure planes. The difference in the location of the slip plane scarps on the ground surface is due to a circular failure occuring in the overburden horizon. This mode is not simulated by this numerical method.

Conclusions

A finite element model (e-z Tools) has been successfully used to do a back analysis on a non-structurally controlled J.M. Asbestos southern hanging wall failure of 1971. Numerical modelling is therefore a useful tool in the prediction of failure zones and their evaluation during the design and life of the mining operation.
The failure was most probably a multi-step event consisting of a precursor failure at the toe, followed by a response failure to the rock mass internal friction angle, then a failure along a zero vertical displacement locus which was followed by another response failure to surface. The response failures are likely to have included toppling mechanisms since the high face would be structurally prone to this failure mode.

A parametric study indicated an in-situ stress ratio of horizontal to vertical of three to be the most likely to have operated in this failure. The peridotite coefficients in the Mohr-Coulomb failure criteria of internal friction, $\phi=37°$ and cohesion,$C=0.3$ MPa was deduced.

References

1.   Arjang, B., 1991. Pre-mining stresses at some hard rock mines in the Canadian Shield. CIM. Vol. 84, No. 945. pps. 80-86.

2.   Brady, B.H.G. and Brown, E.T., 1985. Rock Mechanics for Underground Mining. Publ. Allen & Unwin Inc., London, U.K.

3.   Chau, K.S., Mitri, H.S., Hassani, F.P. and Scoble, M.J., 1988. A finite element model for stress analysis of underground openings. Proc. of First Can. Conf. on Computer Applications in the Mineral Industry, Quebec City, March 7-9, pps. 259-268, A.A. Balkema Publishers.

4.   Dolezalova, M., 1984. Stability problem of a 210 m deep open pit mine. Proc. 6th Conference on Soil Mechanics and Foundations Engineering, Budapest, pps. 601-608.

5.   Hoek, E. and Bray, J.W. 1984. Rock Slope Engineering, IMM, London, U.K.

6.   Labbe, M., 1979. Mining Operations (drilling and blasting) in Third Open Pit Operators Conference, June 10-13, CIM.

7.   Ross-Brown, D.M., 1979. Ch.12 "Analytical Design" in Open Pit Mine Planning and Design. AIME, pps. 161-183.

8.   Sharp, J.C., Ley, G.M.M. and Sage, R., 1977. Pit slope manual. Chapter 4: Groundwater, CANMET, CANMET Report 77-13; Nov.

9.   Thiel, K., 1989. Chapter 2: General Characteristics of Rocks and Rock Masses. In Rock Mechanics in Hydroengineering, pps. 25-29.

10.   Toews, N.A and Yu, Y.S., SAP2D Documentation, (1975), Version 2-D Linear Elastic Finite Element Computer System, CANMET, Ottawa, p. 84.

TOPPLING AND SLIDING OF BLOCKS UNDER DYNAMIC LOADING

M. Y. Ma
Clarkson University, Potsdam, NY, U.S.A.

M. R. Yeung
Woodward-Clyde Consultants, Oakland, CA, U.S.A.

ABSTRACT

The Discontinuous Deformation Analysis (DDA) was applied to study the dynamic behavior of two block systems with inclined bases. The input dynamic loading was in the form of sinusoidal acceleration of the base. It was found that the dynamic loading is destabilizing and that the blocks in the block systems generally exhibit cyclic behavior. In the case of one block on an inclined base, movement of the base in the upslope direction was found to be more destabilizing than that in the downslope direction. Moreover, the more slender the block is, the more it rotates and slides in a given amount of time. As in the static case, smaller friction angles tend to promote sliding and inhibit toppling. It was also found, at least for the cases studied, that the frequency of the base motion has a relatively small effect on the behavior of the block. Furthermore, if a block slides, topples or simultaneously slides and topples under static loading, it will likely behave similarly under dynamic loading. A block stable under static loading will likely slide and topple simultaneously under dynamic loading. Finally, for a system of rectangular blocks on a stepped base, all blocks slide and topple (upslope or downslope) simultaneously.

INTRODUCTION

Toppling and sliding of rock blocks is a common rock slope failure mechanism. Various idealized block systems have been used to model this mechanism. Two such systems are a single block on an incline and a system of rectangular blocks on a stepped base. Yeung and Goodman (1992a) studied the one-block-on-an-incline problem using the Discontinuous Deformation Analysis (DDA), a numerical modeling technique for discontinuous block systems, and derived charts predicting the initial behavior of the block. The problem of toppling and sliding of a system of rectangular blocks on a stepped base was analyzed by Goodman and Bray (1976) using a limit equilibrium approach, and by Yeung and Goodman (1992a) using DDA. These analyses were for static loading conditions. Ma, et al (1992) showed that the DDA method can be applied to analyze block systems under dynamic loading by comparing DDA results with theoretical predictions of the dynamic behavior of a two-block system. This capability of DDA to model dynamic behavior was used to study the behavior of the two block systems mentioned above under dynamic loading in the form of horizontal shaking of the base. This paper presents the results of this study.

METHODOLOGY

DDA was used to analyze the dynamic behavior of the two block systems. Shi (1992) gives a complete theoretical development of this numerical modeling technique. Some example applications of DDA can be found in papers by Yeung and Goodman (1992a and 1992b). DDA and the well-known Distinct Element Method (DEM) can handle similar kinds of problems. However, DEM's ability to model real time dynamic behavior is questionable because it is an explicit method that uses fictitious forces and artificial damping to control numerical instability. In DDA, on the other hand, the displacements and strains of the blocks in each time step are computed by solving implicitly a system of simultaneous equilibrium equations. Since this system of equations is derived from minimizing the total potential energy of the block system, its solution satisfies equilibrium at all times. Furthermore, a complete kinematic theory in DDA governs how blocks interact. Because DDA is inherently stable, it does not require artificial forces for stability, and should therefore model real time dynamic behavior accurately.

The dynamic loading applied to the block systems was in the form of sinusoidal horizontal acceleration of the base. A sinusoidal base acceleration was selected for simplicity. For practical problems, real earthquake motions can be input as base motion. The frequency and initial direction of the dynamic loading were varied to study their effects on the failure mechanism. In addition, the effects of block system geometry and friction angle were also investigated. By tracking the displacements and rotations of the blocks in a system, different behavior (sliding only, toppling only, sliding and toppling simultaneously, and stable) can be identified.

ONE BLOCK ON AN INCLINED BASE

Nine cases were investigated in which a rectangular block on an inclined base was loaded by horizontal shaking of the base. In all cases, the base inclination was 30°, and the length of the block was 1.73 m. Table 1 lists the different combinations of friction angle, ϕ, δ (δ is defined as the arctangent of the length to height ratio of the block), and frequency and initial direction of the base motion used. Also given in Table 1 is the static behavior of the block on a stationary base.

Table 1: Summary of DDA Results for One Block on an Inclined Base

| Case | ϕ (degree) | δ (degree) | Base Motion | | Rotation after 1 second (degree) | Displ. after 1 second (m) | Static Behavior |
			Freq. (Hz)	Initial Direction			
1	35	30	2.5	Right	-17.5	-0.55	Stable
2	35	35	2.5	Right	-7.5	-0.34	Stable
3	35	40	2.5	Right	-5.5	-0.29	Stable
4	35	35	2.5	Left	-0.7	-0.32	Stable
5	35	35	1.0	Right	-2.5	-0.46	Stable
6	35	35	4.0	Right	-3.6	-0.31	Stable
7	25	25	2.5	Right	-11.5	-0.63	S+T or S only
8	25	35	2.5	Right	-0.3	-0.28	S only
9	35	25	2.5	Right	-9.5	-0.01	T only

Note: S = Sliding; T = Toppling.

DDA results are plotted in Figures 1 and 2. Plotted against time on these figures are the sinusoidal input base displacement (positive is to the right), the displacement of the downslope corner of the block (positive is to the right), and rotation of the block (positive is clockwise). The displacement scale shown in these figures is for the block displacement only. The base displacement starts at zero initially. The positions of the block after 0.25, 0.5 and 1.0 second of dynamic loading for representative cases (cases 1, 2, 4, and 8) are shown in Figure 3. (The initial position of the block is indicated by dashed lines in Figure 3.) As can be seen from Figures 1 and 2, the block exhibits cyclic behavior under dynamic

shaking of the base in most of the cases. In case 1, for example, the cyclic behavior of the block can be interpreted as having the same frequency as the input base motion. Furthermore, the block and base motions can be interpreted as being in phase.
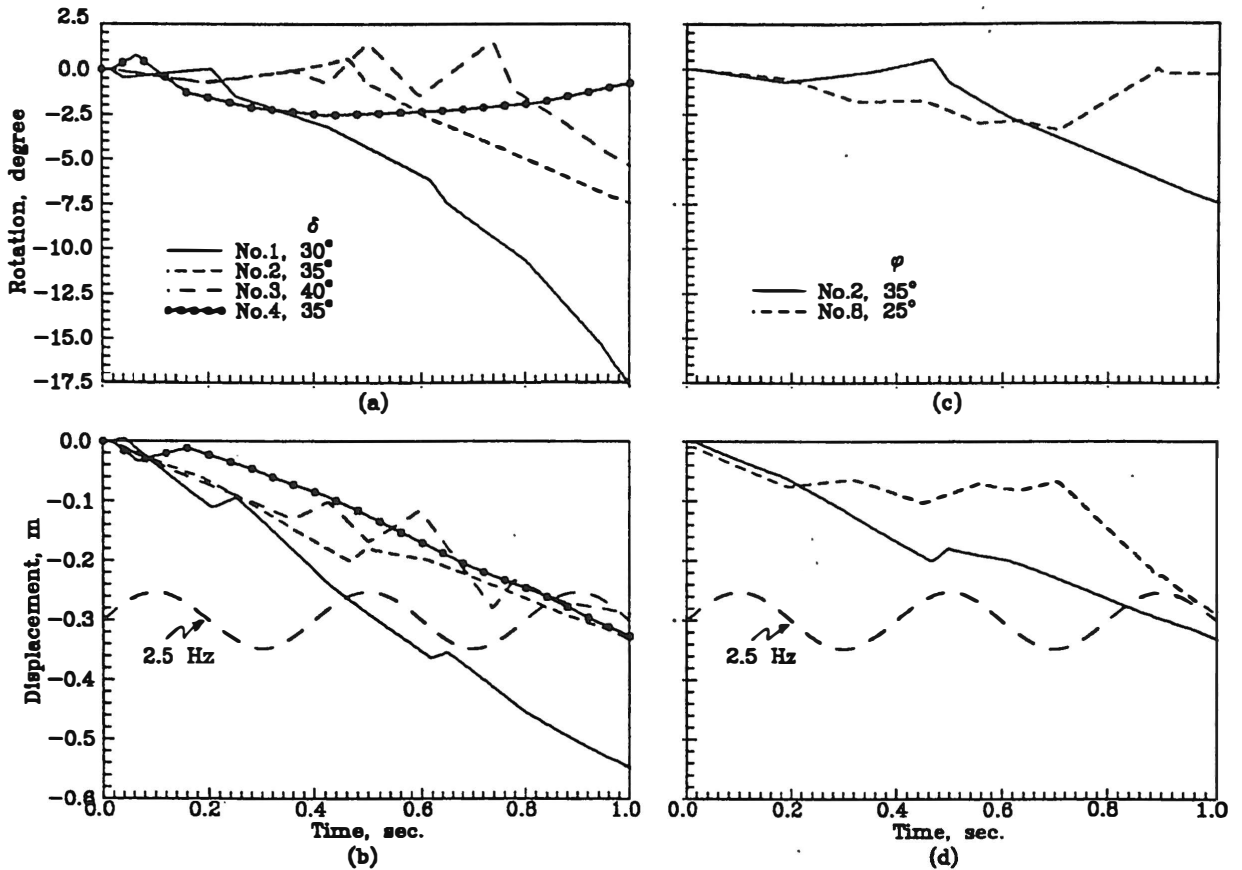
Figure 1 DDA Results for One Block on an Incline

Effects of Block Geometry and Friction Angle

The effect of block geometry as represented by the angle δ can be seen from DDA results for cases 1 through 3. As illustrated by Figures 1(a) and 1(b), the cyclic behavior is more pronounced as δ increases, or if the block is less slender. Moreover, the smaller δ is, or the more slender the block is, the more the block slides and rotates, as shown clearly by DDA graphic output in Figure 3. While the block in cases 1 through 3 are stable under static loading, it fails by toppling and sliding simultaneously under dynamic loading. This shows that dynamic loading is destabilizing to a block on an incline.

Comparing DDA results from cases 2 and 8 (see Figures 1(c) and 1(d)), it can be seen that the cyclic behavior is more pronounced in case 8 in which the friction angle is smaller, and that the block rotates less after 1 second in case 8 because smaller friction promotes sliding

and therefore inhibits toppling.
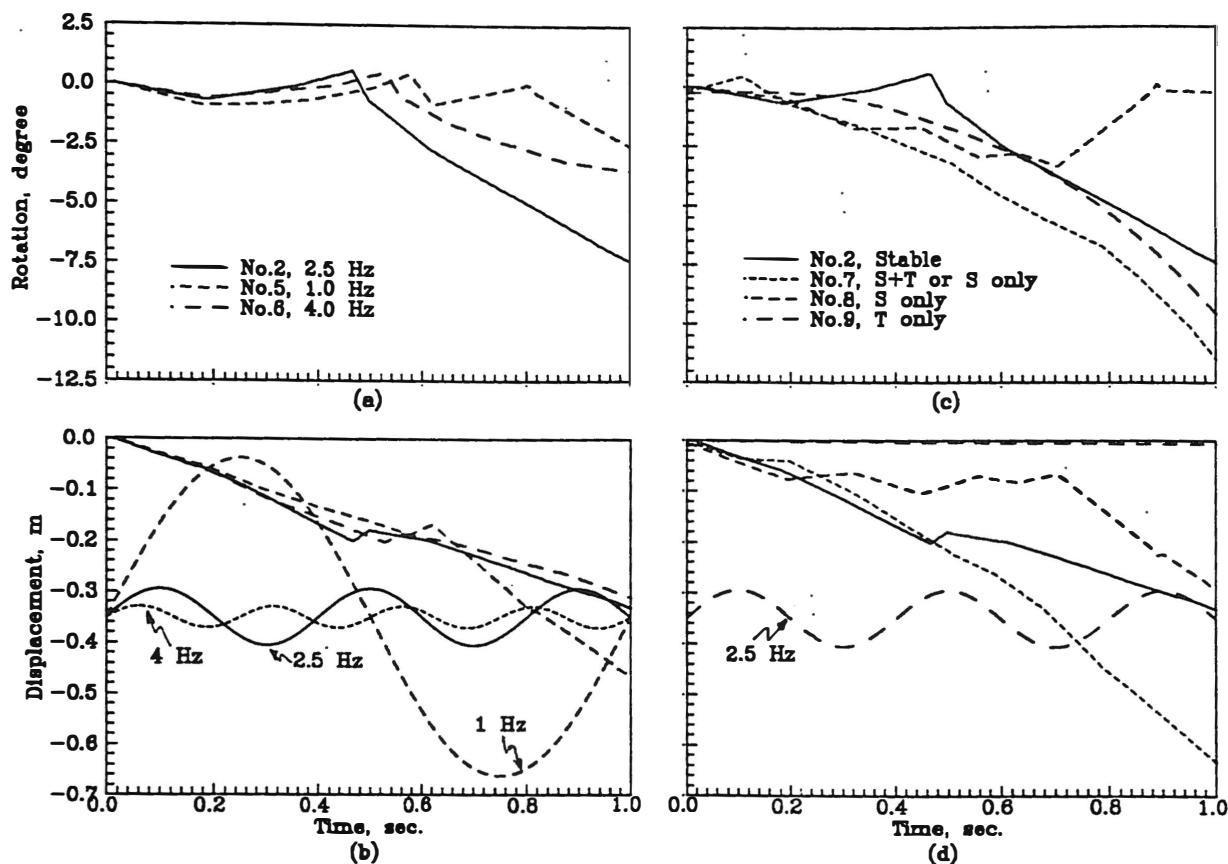
Figure 2 DDA Results for One Block on an Incline (Continued)

Effects of Initial Direction and Frequency of Base Motion

Cases 2 and 4 are identical except for the initial direction of base motion. As shown by Figures 1(a) and 1(b), the block slides and rotates more in case 2, in which the initial direction of base motion is to the left, than in case 4, in which the initial direction is to the right. This is reasonable because movement of the base to the right induces an inertial force in the block in the downslope direction, which is destabilizing. Furthermore in case 4, the block rotates upslope when the base moves to the left initially, and the magnitude of the block rotation decreases as the magnitude of the block displacement increases with time.

Different frequencies of base motion (while keeping the maximum acceleration constant) were used. They are 1.0, 2.5, and 4.0 Hz in cases 5, 2, and 6 respectively. As shown by Figures 2(a) and 2(b), the behavior of the block in all these cases is similar, although the cyclic behavior is more pronounced in case 5. From this observation, one may speculate that

Case 1

Case 2

Case 4

Case 8
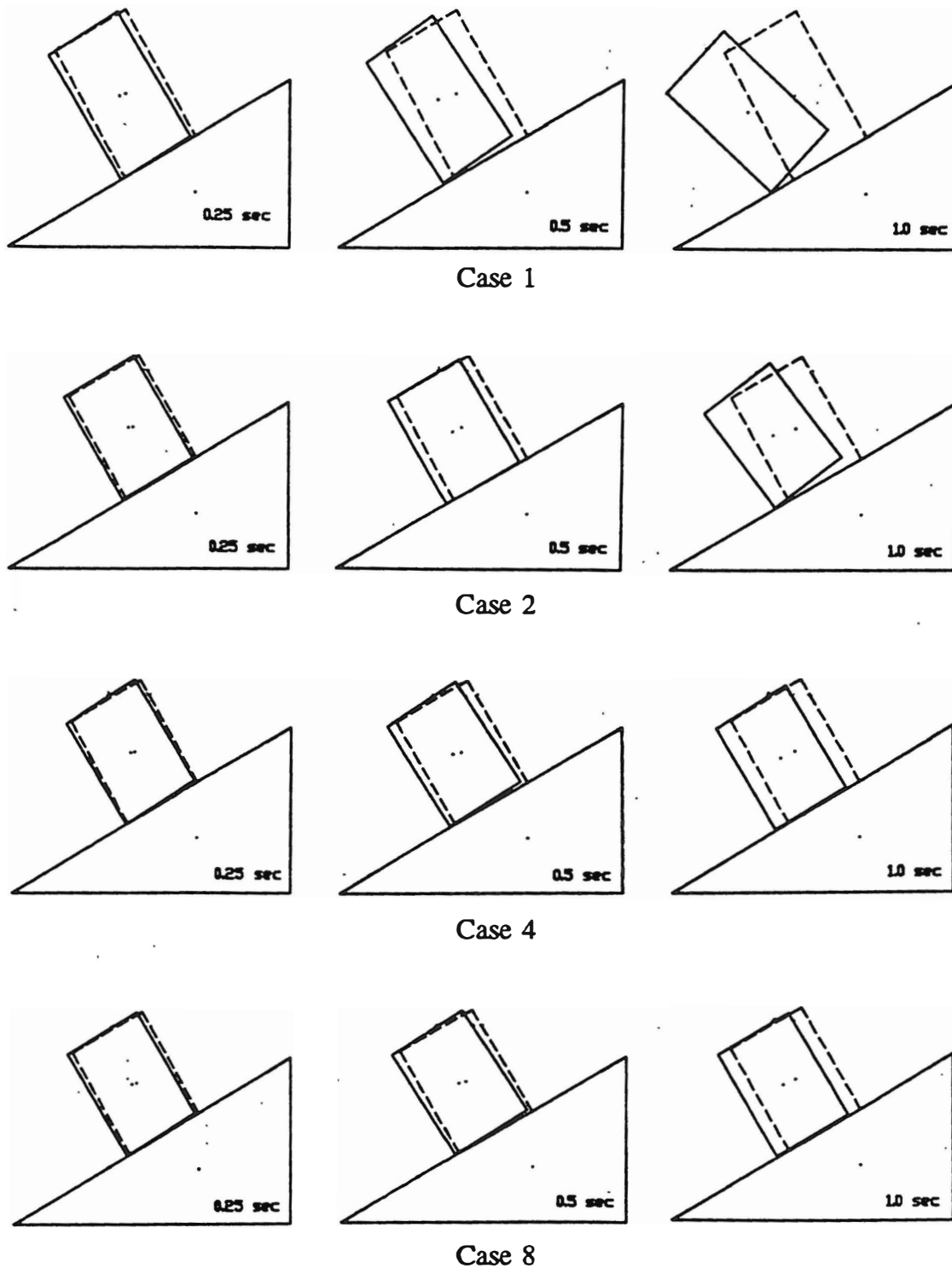
Figure 3 DDA Graphic Output for One Block on an Incline

there is a resonant frequency for every block geometry at which the block will oscillate violently with the input base motion.

Dynamic Behavior vs. Static Behavior

The blocks in cases 2, 7, 8, and 9 have different static behavior. Under static loading, the block is stable in case 2, slides and topples simultaneously or slides in case 7, slides only in case 8, and topples only in case 9. As can be seen from Table 1 and Figures 2(c) and 2(d), the behavior of the block after 1 second of dynamic loading is the same as the static behavior in cases 7, 8, and 9. In case 2, however, the block, which is stable in the static case, fails by sliding and toppling simultaneously. In fact, a block slides and topples simultaneously under dynamic loading in all cases in which the block is stable statically.

RECTANGULAR BLOCKS ON A STEPPED BASE

A system of rectangular blocks on a stepped base is loaded dynamically with the same sinusoidal horizontal motion having a frequency of 2.5 Hz as in the one-block-on-an-incline case. The rotations and displacements of the blocks after selected elapsed time intervals for all the blocks are plotted in Figures 4(a) and 4(b) respectively. In addition, the configuration of the block system after 0.0, 0.15, 0.30, and 0.50 second of loading are shown in Figure 5.
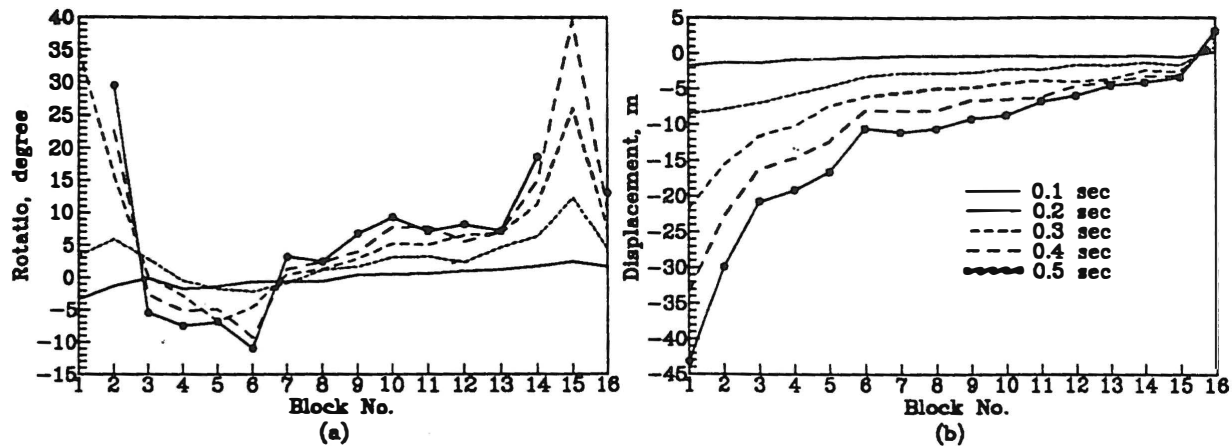
Figure 4 DDA Results for Rectangular Blocks on a Stepped Base

It can be seen from Figures 4 and 5 that a block generally slides more if it is located more downslope. Blocks 3 through 6 rotate downslope, while all others rotate upslope. The behavior of this block system under dynamic loading is much different from that under static loading. While different zones of behavior (sliding only, sliding and toppling simultaneously, toppling only, and stable) can be distinguished under static loading, all the blocks slide and topple (upslope or downslope) simultaneously under dynamic loading.
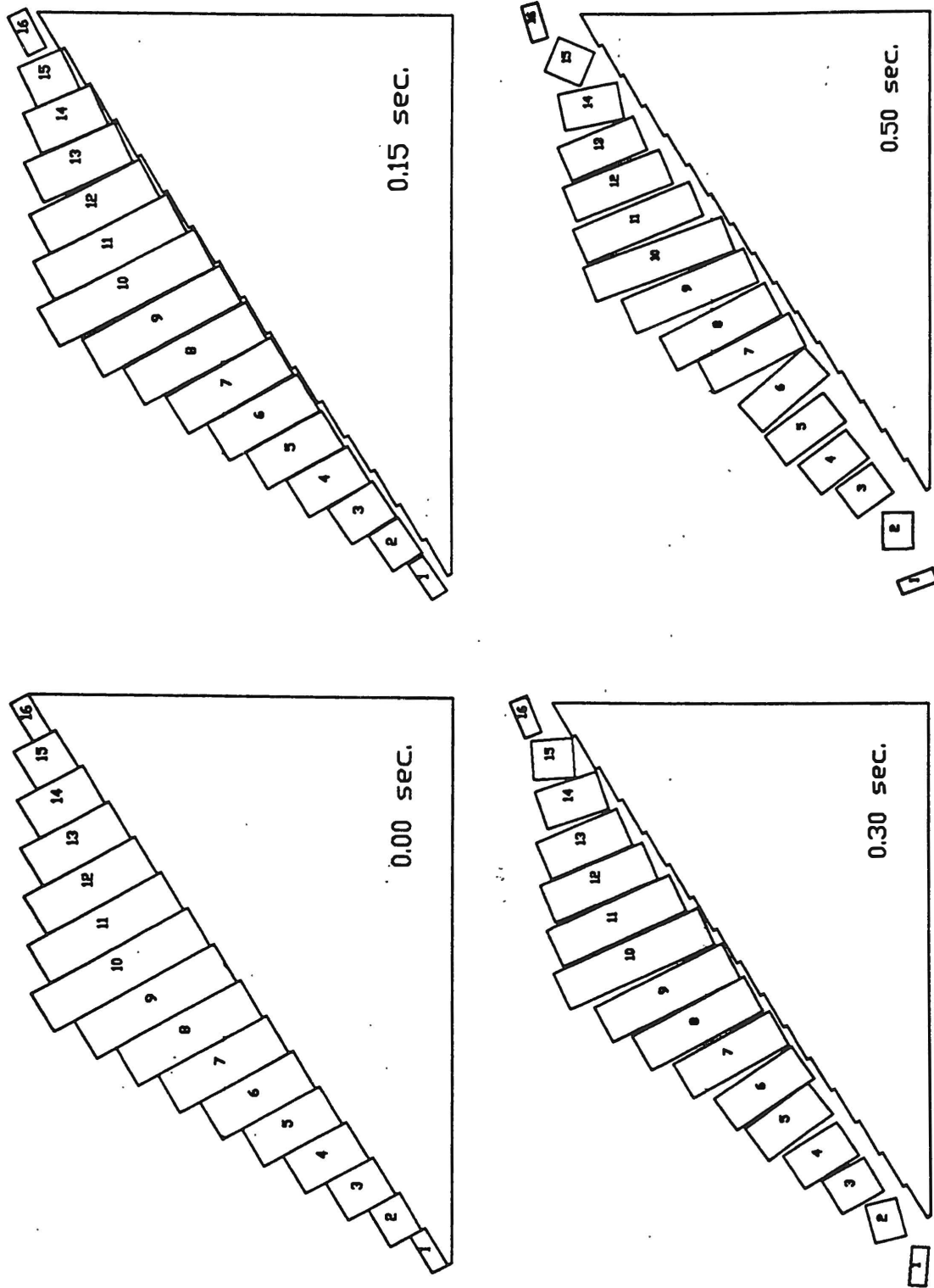
Figure 5 DDA Graphic Output for Rectangular Blocks on a Stepped Base

CONCLUSIONS

DDA is shown by the results presented in this paper to be a powerful numerical modeling technique for the statics and dynamics of block systems. It provides insights into the dynamic behavior of the two block systems studied - one block on an incline and a system of rectangular blocks on a stepped base. Because the behavior of blocky systems is very complicated, close-form solutions are very seldom available. As a result, numerical methods such as DDA or physical modeling techniques are usually applied to obtain behavior mechanisms of block systems. However, DDA has advantages over physical modeling because it is cheaper and less time-consuming. Moreover, DDA gives the displacement of a system which is an important, and maybe the only, measure of stability of the system under dynamic loading (Newmark, 1965, and Seed, 1966). Knowing the critical displacement and rotation of a rock slope under dynamic loading, stabilization schemes can be developed. With further development and validation by actual case histories, DDA should become a comprehensive design tool for engineers dealing with discontinuous systems.

REFERENCES

Goodman, R. E. and Bray, J. W., 1976. Toppling of rock slopes. *Proc. Specialty Conference on Rock Engineering for Foundations and Slopes*, ASCE, Boulder, Colorado, pp. 201-234.

Ma, M. Y., Yeung, A. T. and Huang, A.B., 1992. Seismic stability of Landfill, ASCE *Ninth Eng. Mech. Conf.*, Texas, pp. 721-724

Newmark, N. M., 1965. Effects of earthquakes on dams and embankments. *Geotechnique* 15 (2). pp. 139-160.

Seed, H. B., 1966. A method for earthquake resistant design of earth dams. *J. Soil Mech. Found Div.* ASCE, 92 (SM1) , pp. 13-40.

Shi, G.-H., 1992. Block System Modelling by Discontinuous Deformation Analysis, Computational Mechanics, London, England.

Yeung, M. R. & Goodman, R. E., 1992a. Multi block stability analysis using the DDA method. *Proc. International Conference on Fractured and Jointed Rock Masses*, Lake Tahoe, California.

Yeung, M. R. & Goodman, R. E., 1992b. Use of Shi's discontinuous deformation analysis on rock slope problems. *Proc. ASCE Specialty Conference on Stability and Performance of Slopes and Embankment-II*, Berkeley, California, Vol.1, pp. 461-478.

The influence of underground workings on slope instability : A numerical modelling
approach

D. Stead
B. Benko

Department of Geological Sciences, University of Saskatchewan, Saskatoon, SK,
S7N 0W0, Canada

ABSTRACT

The influence of underground workings on the stability of surface slopes ranges from the
progressive or sudden collapse of shallow old workings to subsidence coincident with
deeper underground mines. Both natural and man-made slopes may be destabilized due to
the effects of such underground works. Considerable research has been undertaken
particularly related to surface coal mine slope instability using empirical and equivalent
physical model approaches. This paper describes the application of finite difference and
distinct element modelling techniques to the prediction of the effects of underground
workings on surface slopes.

RÉSUMÉ

Les effets d'exploitations aux mines souterraines sur l'équilibre des flancs aux surfaces
varient entre l'effondrement soudain ou graduel aux vieux mines de peu profondeur et
l'affaisement associer avec les mines souterraines qui sont plus profonds. Les flancs
naturelles et construits sont peut-être déstabilisés à cause des effets d'exploitations aux
mines souterraines. Beaucoup des recherches sur les effets d'instabilité aux flancs des
mines de charbon à ciel ouvert étaient entrepris employer des façons d'analyse
empiriques et des modèles physiques. Dans cette communication les deux modéles,
"finite difference" et "distinct element" et l'application de ces techniques aux prédictions
des éffets d'exploitations aux mines souterraines sont décrits.

INTRODUCTION

The design of slopes in soils and rock is generally undertaken using conventional limit equilibrium techniques with the production of a factor of safety or a probability of failure. These methods do not directly allow for an assessment of the effects of mining induced ground deformation on the stability of a slope. In this paper the authors review previous work undertaken to characterize the effects of undeground workings on surface slopes and examine the application of the finite difference code, FLAC, (Itasca, 1992a) and the distinct element code, UDEC, (Itasca, 1992b) to stability assessment of slopes affected by underground mining.

PREVIOUS WORK

The presence of old workings within or beneath excavated slopes has been recognized as a contributing factor to slope instability in numerous surface coal mines. Walton and Taylor (1977) described the influence of old room and pillar workings and ancient workings termed "bell pits" on slope stability in the United Kingdom. They divide the effect of underground mine workings on slopes into workings encountered within the slopes or beneath the level of the slopes. The extent of void migration, the degree of pillar collapse or pillar "robbing", failure of the roof and floor strata and the bulking of failure debris must be considered.

Garrard and Taylor (1984) investigated collapse mechanisms of shallow underground coal mine workings using stereophotographic techniques and field observations. They comprehensively documented data on over 151 collapsed workings at 18 opencast coal sites in the U.K. Their study concentrated on void migration and collapse mechanisms of old shallow room and pillar coal workings at less than 75m depth. Over 60 variables on each working were recorded and statistically analyzed. Stead (1984), and Scoble (1981) recorded data on over 240 slope failures at surface coal mines within the United Kingdom. They showed that underground workings were a possible contributary factor in over 25% of the instabilities. Several major failures were related to active longwall mining activity beneath the sites.

The effect of deeper underground mining on surface slope instability has been reported worldwide. Malgot et al (1986) and Rybar and Malgot (1982), describe the activation and reactivation of major block slides in Czechoslovakia due to the mining of brown coal beneath slopes without backfilling. The impact of subsidence on slope instability was recognized in a comprehensive engineering geological mapping program that produced zonal instability assessment maps. Rybar et al (1990) document a major open pit rock slide in a tin mine due to underground mining 50-150m beneath the pit bottom. Singh and Singh (1992) used equivalent material physical modelling to simulate the

effect of underground panel excavation on slope instability in overlying open pit slopes. The appearance and development of major tension cracks within the model mine slopes were photographed as underground mining progressed.

Numerous workers have applied numerical modelling techniques in the study of subsidence associated with the longwall mining of coal. Coulthard and Dutton (1988) compared the application of the finite difference code, FLAC, and the distinct element code, UDEC, to the numerical modelling of subsidence induced by underground coal mining. The non linear constitutive models in these codes were believed to allow a better simulation of the behaviour of roof strata and to have potential in the prediction of surface subsidence. Similar studies, comparing the subsidence monitoring records and predicted subsidence from distinct element models were undertaken by Connor and Dowding, (1990,1992). These studies have all been undertaken on a model with flat terrain and horizontal strata. Jerran and Adamek, (1988) investigated the subsidence due to excavation of horizontal longwall panels beneath sloping terrain in Pennsylvania. They used an empirical-based United States Bureau of Mines subsidence prediction model to compare numerically derived subsidence with measured data. It was noted in this study that the magnitude and direction of subsidence movements were significantly affected by the topographic slope. Small horizontal adjustments were observed after the cessation of vertical movement which were believed to represent the reaction of the surface to changes in slope induced by subsidence.

To date, very little numerical modelling has been undertaken to simulate the effects of underground workings on slope stability. Watters et al (1990) undertook a finite difference numerical modelling exercise to show the effects of abandoned underground workings within an open pit gold/silver mine. They utilized the FLAC code to illustrate areas undergoing plastic yield and tension around the underground workings. The alignment of such tension zones predicted a potential failure surface which was then analyzed using a conventional 2-D limit equilibrium analysis.

NUMERICAL MODELLING

In this paper, the authors present the results of modelling the effect of underground longwall and room and pillar coal workings on surface mine slopes using the finite difference code, FLAC. The potential application of the distinct element code, UDEC, is discussed and preliminary results shown illustrating the effect of an old working on a typical surface coal mine bench.

Effect of room and pillar stability on surface mine slopes.

The finite difference code, FLAC (Fast Lagrangian Analysis of Continua) is used to

model the effect of room and pillar instability on a surface mine slope. FLAC is a two-dimensional explicit finite difference code which simulates the behaviour of materials that may undergo plastic flow when their yield limit is reached. Non linear constitutive material models embodied in this code enable a more realistic representation of the rock material. FLAC is particularly useful in mining applications because it enables progressive collapse to be simulated as excavation proceeds.

In this simulation two levels of room and pillar mining are present beneath a slope. The slope is at a limit equilibrium state with a face angle of 60 degrees. The influence of progressive pillar collapse on the slope stability is investigated. The first level of mine workings is at 20m depth beneath the slope toe, the second at 30m depth (Figure 1). The span of rooms is 3m and the height 2m. The pillars are 4.5m in width. The simulation employs a combination of the Mohr-Coulomb constitutive model and ubiquitous joint model. The Mohr-Coulomb model is applied to the slope and near surface material, the ubiquitous joint model represents the horizontally bedded coal bearing strata.
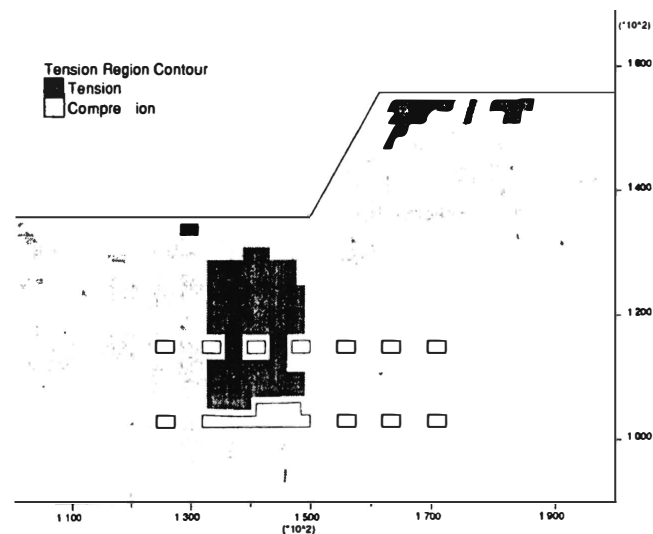
Figure 1   Plot of tension zones after the second pillar collapse

The progressive pillar collapse was simulated in the deeper level of workings, 30m below the slope base by removing the appropriate pillar material zones. This procedure was continued until active collapse in the model occurs. First the pillar closest to the slope toe was assumed to undergo progressive collapse. The pillar collapse was simulated by successive removal of 1m x 1.5m grid zones in three steps. After the third step, general tension failure occurred in the roof, spanning over 7.5m. The zones representing this part of the model were deleted in order to make further stepping

possible (Figure 1). After the deletion of the model zones representing the failed
material, the model was stepped to equilibrium. The next pillar to collapse was assumed
to be the neighbouring pillar in the direction away from the toe. This was again
removed in three steps. After the third step (total collapse of the second pillar), a
progressive failure developed in the roof and slope. Figure.1 shows a plot of the region
of tension in the model at this stage. Well developed tension zones behind the slope
face are present, indicating the incipient yielding instability of the slope. Figure 2 shows
a more detailed view of the slope. A well developed concentration of shear strain
behind the slope face suggests the potential location of the failure plane. The
mechanism of the slope instability during the progressive pillar collapse is a "cyclic
progression". The displacements produced by each step of pillar collapse induce an
adjustment and subsequent stabilization of the slope in a new limit equilibrium state
until the final collapse. This cycle is more pronounced as the pillar collapse progresses.
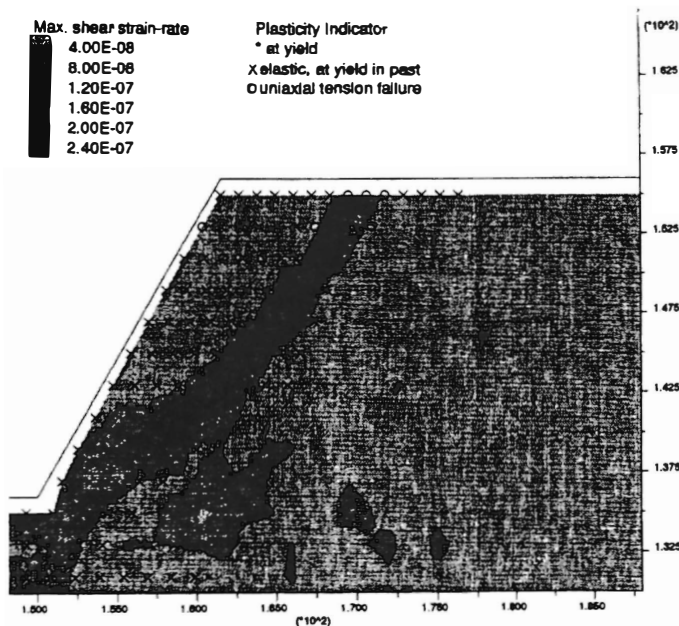
Figure 2   Plot of shear strain rate and plasticity state

Effect of longwall mining on slope deformation

The effect of advancing longwall mining on slope instability was also investigated with
the finite difference code, FLAC. In a similar manner to the previous application, a
slope standing at 60 degrees in a limit equilibrium state served as the starting point. A
combination of Mohr-Coulomb and ubiquitous joint constitutive model was again used.
The longwall mining activity was represented by excavation of appropriate material
zones from the model. The excavation sequence started 20 metres away from the toe at

50 metres depth. Two model simulations were performed using identical geometry and material properties:

(1)   the effect on slope instability of longwall mining with old collapsed room and pillar workings present beneath the slope level;

(2)   the effect on slope instability of longwall mining without previous mining activity.

The longwall was advanced towards the slope to simulate the least favourable situation for slope stability.

The collapse of the old room and pillar mines was simulated by deleting zones above the existing rooms and filling the previous openings with weak Mohr-Coulomb fill material. The height of void migration from the original level was given a random distribution, resulting in final void location at different levels (Figure 3.). The void migration for the room and pillar mine was performed before the longwall mining was introduced. No major influence on the slope stability was observed. In the next stage, the advance of longwall mining was simulated. After each excavation step the model was brought to equilibrium, requiring deletion of zones that failed in tension in the roof of the workings. This resulted in an "arch-shaped" zone as shown in Figure 3. This figure shows also the plasticity indicators after 26 meters of longwall advance towards the slope.
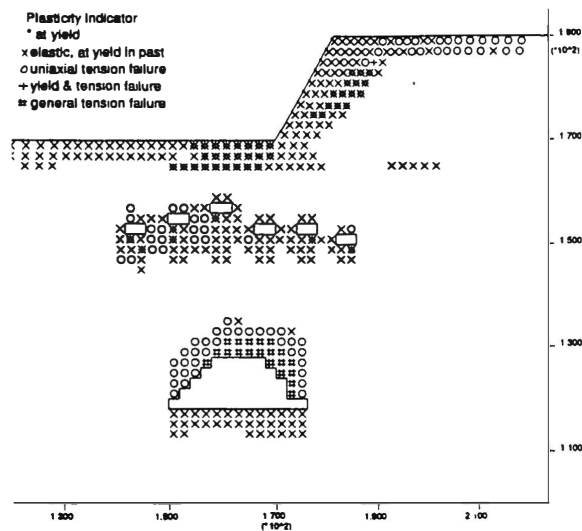
Figure 3   Plasticity state with collapsed room and pillar mine undermined by longwall

Without previous mining activity, the x-displacement pattern together with displacement vectors are presented in Figure 4. Both analyses (with and without old room and pillar workings) demonstrated a clear influence on stability of advancing the longwall beneath
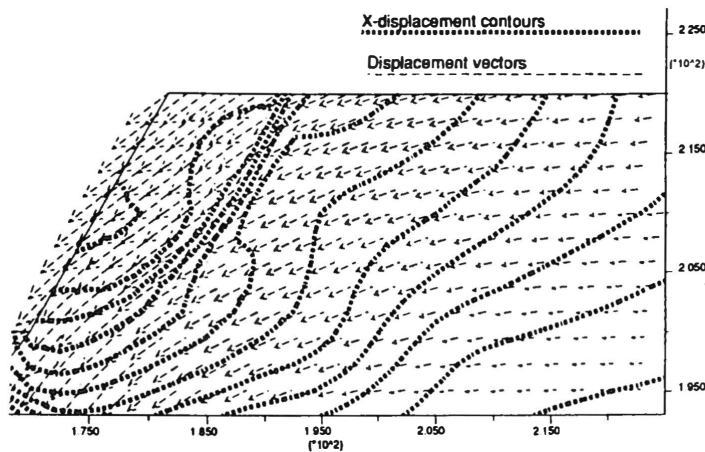
Figure 4   Displacement vectors and contours due to longwall mining beneath a slope

the slope. As confirmed by field observations (Malgot et al,1986), the failure does not display a morphology typical of natural landslides. Very little movement out of the slope is observed. In the numerical model, movement out of the slope would be indicated by a pronounced concentration and higher magnitude of horizontal displacements or displacement velocities in the lower part of slope. This is instead replaced by the subsidence of the slope toe.

Distinct element model

The Universal Distinct Element Code, UDEC, allows the modelling of jointed media and hence is readily applicable to simulating the stability of surface mine slopes undermined by room and pillar workings or open voids. A variety of material constitutive models and a choice of rigid or deformable blocks are available. A simple example is presented in Figures 5 and 6, which illustrate the excavation of an 8m wide room. A Mohr-Coulomb elastoplastic constitutive model was used. Preliminary attempts have been made to simulate the process of void migration by deleting those fully deformable joint bounded blocks which show excessive movement into the excavation. As the model is stepped, the area of tension progresses towards the surface and if a weak soil cover were present might result in a surface crown hole collapse. To simulate the effect of bulking phenomena, blocks can be assigned the properties of fill instead of being deleted entirely. It is interesting to note the tension zone extending to the surface (Figure 5). As would be expected, due to low overburden stresses, yield is restricted, unless highly weathered weak materials are present, and failure is mainly by roof migration rather than pillar collapse. This agrees with the conclusions of Garrard and Taylor, (1984). After simulation of void migration, a surface mine slope was

213

progressively advanced towards the workings. As the distance between the slope face and the workings decreases, the tension zone increases resulting in rockfall from the face and backward tilting of the rock blocks into the crown hole (Figure 6). As the slopeward side of the arch fails the vertical stress is transferred to the other side. It is at this stage that highly weathered/"robbed" pillars could conceivably fail in practice, possibly leading to total failure of a bench slope. The example presented is of thick horizontally bedded strata. The coal bearing strata are often closely laminated. Increasing the number of blocks to represent this situation was impractical in the present study, due to computer memory limitations. This problem can be partially overcome by using a ubiquitous constitutive model for the fully deformable blocks. In the model this results in more yielding in a horizontal direction parallel to the planes of weakness (lamination). Deformation at the slope crest above the workings is obviously critical with regard to nearby structures, pipelines, or excavating equipment. To allow an assessment of the deformation, history plots can be established at varying distance behind the slope. These indicate the existence of a minor subsidence trough above the void. This movement is generally not immediately apparent in the model as it is often masked by the major movement of blocks at the slope face and within the roof of the working.
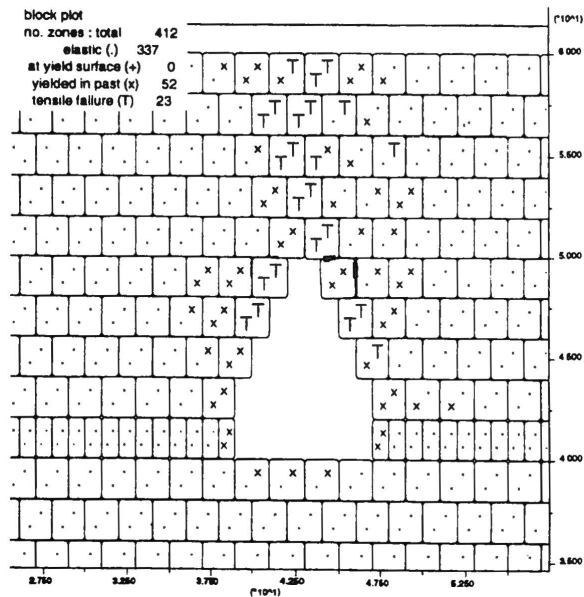
Figure 5   Tension zone above excavation with simulated void migration

Further work in progress includes the application of the UDEC code to assessing the effects of old workings and longwall mining in dipping seams and on structurally controlled slope instabilities.

block plot
displacement vectors
      maximum =   2.165E+00

0   1E 1

shear displacements on joints
max shear disp =   1.886E+00
each line thick =   3.777E-01
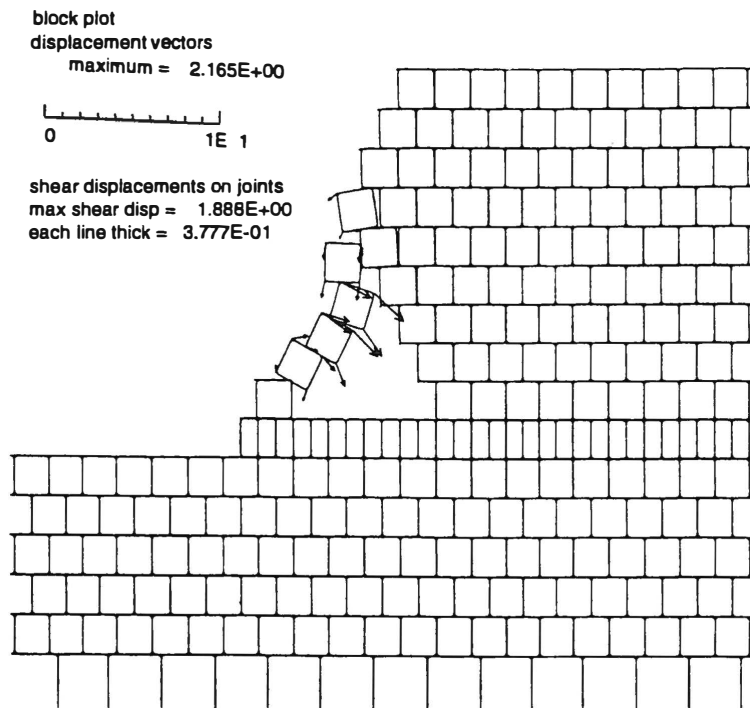
Fig.6   Slope face collapse due to advance of mine slope towards old working

DISCUSSION AND CONCLUSIONS

The finite difference code, FLAC, and the universal distinct element code, UDEC
appear to offer considerable potential in providing an insight into the mechanism of
slope failures involving underground workings. Used in conjunction with conventional
limit equilibrium techniques it is possible to provide a factor of safety for failure
surfaces predicted by the numerical model. This surface may in many cases not coincide
with that predicted by critical limit equilibrium failure surface searching routines. Work
is in progress to utilize the pseudo -programming language FISH included in the FLAC
code to integrate the factor of safety limit equilibrium analysis and the finite difference
modelling. An obvious restriction of these models is their lack of consideration of three
dimensional factors. In most cases a two dimensional modelling analysis will provide a
useful indication of the effect of mining on the slope which can then be incorporated
into more conventional design. Calibration of such models against ground deformation
measurements is advisable wherever possible. In critical slopes, the use of three
dimensional modelling and limit equilibrium techniques might be appropriate if
sufficient input data were available.

REFERENCES

Connor K.M. and Dowding, Ch.H. 1990. Monitoring and simulation of mining-induced subsidence. In " Mechanics of Jointed and Faulted Rock", Rossmanith (ed), 781-787.

Connor, K.M. and Dowding,Ch.H. 1992. Distinct element modelling and analysis of Mining - induced Subsidence, Rock Mechanics and Rock Engineering, 25, 1-24.

Coulthard, M.A. and Dutton, A.J. 1988 Numerical modelling of subsidence induced by underground coal mining. Proc. 29th US Rock Mechanics Symp. "Key Questions in Rock Mechanics", Minneapolis, Cundall et al (eds), 529-536.

Garrard, G.F.G. and Taylor, R.K. 1988. Collapse mechanisms of shallow coal-mine workings from field measurements. In" Engineering Geology of Underground Movements", Bell, Culshaw, Cripps, and Lovell (eds), Geol. Soc. Eng. geol. Special Public. No.5, 181-192.

Itasca Consulting Group, Inc., 1992a FLAC version 3.04.

Itasca Consulting Group, Inc., 1992b UDEC version 1.8.

Jeran, P.W. and Adamek,V. 1988. Subsidence due to undermining of sloping terrain: A case study. U.S. Bureau of Mines, Rep. of Invest., 9205, 10pp

Malgot, J., Baliak, F. and Mahr, T. 1986. Prediction of the instability of underground coal mining on slope stability in the Vtacnik mountains. Bull. IAEG. Geol. No.33, 57-65.

Rybar, J., Kostak, B. and Uher, M. 1990. Deep seated rockslide initiated by ore mining. Proc. 6th IAEG Cong., Amsterdam, 2681-2686.

Rybar, J. and Malgot, J. 1982. Engineering geology in the exploitation of mineral deposits. Proc. 4th IAEG Cong., New Delhi, 333-343.

Singh, T.N. and Singh, D.P. 1992. Prediction of instability of slopes in an opencast mine over old surface and underground workings. Int. Jour.Surface Mining and Reclamation 6, 81-89.

Scoble, M.J. 1981. Studies of ground deformation in British surface coal mines. PhD Thesis. Dept of Mining Engineering, University of Nottingham England.

Stead, D. 1984. An evaluation of the factors governing the stability of surface coal mine slopes, PhD. Thesis. Dept of Mining Engineering, University of Nottingham, England.

Walton, G and Taylor, R.K. 1977. Likely constraints on the stability of excavated slopes due to underground coal workings. Proc. Conf. on Rock Engineering, Newcastle-upon-Tyne, 329-349.

Watters, R.J. Rehwoldt, E. and Coulthard, J. 1990. Effects of abandoned underground workings on open pit slope design, Proc. 31st US Rock Mechanics Symp., Golden, "Rock mechanics contributions and challenges, Hustrulid & Johnson (eds). 721-728.

Session 6

Hard Rock

Roche dure

NUMERICAL MODELLING FOR THE EVALUATION OF THE ROCKBURST POTENTIAL OF AN UNDERGROUND EXCAVATION

Richard SIMON, Michel AUBERTIN, Denis E. GILL
École Polytechnique, Montréal, Qc, Canada, H3C 3A7

ABSTRACT

This paper shows how numerical modelling has been used for assessing the rockburst potential of an underground excavation with a recently developed methodology, which is also briefly presented. Numerical methods serve as tools in the back-analyses of a real rockbursting case that occurred in a northwestern Québec mine. The finite element method is used for the evaluation of the stress state in the rock structure under consideration; several 2D analyses and a few 3D analyses results have indicated that the structure was unstable. On the other hand, an estimation of the stable surrounding rock mass stiffness was made by performing numerical stress analyses with the boundary element method. The back-analyses show that numerical modelling can be an asset for evaluating the rockburst potential of underground excavations.

RÉSUMÉ

Cet article montre comment la modélisation numérique peut servir à l'évaluation du potentiel de coups de terrain d'une excavation souterraine, à l'aide d'une méthodologie récemment établie et brièvement présentée. La modélisation est utilisée pour effectuer des rétro-analyses d'un cas réel de coup de terrain qui s'est produit dans une mine souterraine du nord-ouest québécois. La méthode des éléments finis a été employée pour évaluer l'état de contraintes dans la structure étudiée. Plusieurs analyses bi-dimensionnelles et quelques analyses tridimensionnelles ont mené à la conclusion que la structure était instable. D'autres analyses de contraintes par la méthode des éléments frontières ont servis à estimer la rigidité du massif au pourtour de la structure instable, estimation nécessaire à l'évaluation du potentiel. Les rétro-analyses démontrent que la modélisation numérique peut être un outil appréciable pour l'évaluation du potentiel de coups de terrain.

1 INTRODUCTION

Rockbursting is one of the major rock mechanics problems facing the mining industry. A rockburst is a sudden rock failure characterized by the breaking up and expulsion of rock from its surroundings, accompanied by a violent release of energy (Blake, 1972). Rockbursts may involve: i) slip on pre-existing discontinuities, or ii) fracturing of the rock mass (Brown, 1984). The problem is usually encountered around deep underground excavations in hard rocks. For large operations, various techniques have been developed in order to predict and/or prevent their occurrence (Fairhurst, 1990; Hedley, 1992). However, for small mines such as those found in the Abitibi region, in the northwest part of the Québec Province, these techniques are often difficult to apply because of the costs involved or of the geomechanical characteristics of the mine itself.

For these mines, a methodology has been developed by Gill and Aubertin (1988) - see also Aubertin et al. (1992), and Gill et al. (1993) - in order to evaluate the rockburst potential of existing or future excavations. This methodology is based on a rational and practical engineering approach to the problem, that involves identification of vulnerable rock structures, stability analyses and stiffness comparison between the failed rock and the stable surrounding rock mass.

After a brief description of the methodology, this paper presents the numerical modelling strategy adopted in order to analyze a known rockbursting case. A commercial finite element code (COSMOS/M) and an "in house" boundary element code (FORMSTAB) are used to demonstrate how an actual complex field problem can be approached to evaluate the occurrence of failure, and to establish if this failure is sudden or gradual (Simon, 1992).

2 THE METHODOLOGY

The methodology briefly presented here was developed in order to evaluate the rockburst potential of underground excavations, starting from routine mining and ground control engineering. It includes up to four steps: the zoning, the identification of vulnerable rock structures, the stability analysis and the stiffness comparison when so-called "strain bursts" or "pillar bursts" are expected. More details about this methodology can be found in Gill et al. (1993).

2.1 Zoning

Zoning consists in dividing the rock mass into different sectors in which a specific mechanical behaviour is foreseen (rock mass deformability, strength, etc.). It includes the determination of the location, boundaries and general properties of rock mass in the different zones. All the major geological discontinuities must also be identified at this step.

2.2 Identification of vulnerable rock structures

The methodology considers three broad categories of potentially vulnerable rock structures, namely:

i) An excavation that approaches a major geological discontinuity.
ii) An excavation that goes through a major geological discontinuity or through a zone boundary.
iii) An excavation that follows a major geological discontinuity or a zone boundary.

2.3 Stability analysis

In routine mining engineering, stress analyses are usually performed using an elastic constitutive model for the rock mass; this has been proven to be an adequate approach for most rockburst situations (e.g., Ortlepp, 1983). Rock properties are generally obtained through standard laboratory tests conducted on specimens prepared from appropriate rock samples. Rock mass properties are extrapolated from rock properties by using various relationships that take into account the mechanical effects of scale and of geological discontinuities; relationships based on geomechanical classification ratings are often used for that purpose (Hoek and Brown, 1980; Bieniawski, 1984). The knowledge of the pre-mining state of stress results from in situ measurements or, if unavailable, from empirical relationships such as those proposed by Herget (1987) for the Canadian Shield. The analysis often relies on numerical calculations to evaluate the induced stresses around the openings.

2.4 Stiffness comparison

This step consists in comparing the post-peak stiffness of the unstable rock structure to the pre-peak stiffness of the stable surrounding rock mass. If the value of the post-peak stiffness of the unstable rock structure is larger (in absolute values) than the value of the stable surrounding rock mass stiffness, there is a rockburst potential. A possible way to estimate the latter is to perform numerical stress analyses, as shown in the following.

3 NUMERICAL MODELLING

This methodology was first validated through back-analyses of known non-rockbursting rock structures (Gill and Aubertin, 1988). For the purpose of going one step further in validating the approach, back-analyses of a rockburst that occurred in a northwestern Québec mine have been performed (Simon, 1992). The present paper refers to this case, which is illustrated in Figure 1. This figure is a plan view of a shaft station where two rockbursts occurred (structure A and subsequently, structure B) and produced two low magnitude

219

seismic events. The volume of broken rock was about 75 m³ for structure A and about 40 m³ for structure B. The back-analyses of this case have required numerical modelling for performing the stability analyses of the structures, and for estimating the stable surrounding rock mass stiffness.

One of the methodology objective being to provide a tool that can be used on a day-to-day basis by engineers, and since most of the stability analyses performed for Québec underground mines are limited to two-dimensional analyses, the methodology recommends to start with 2D models.
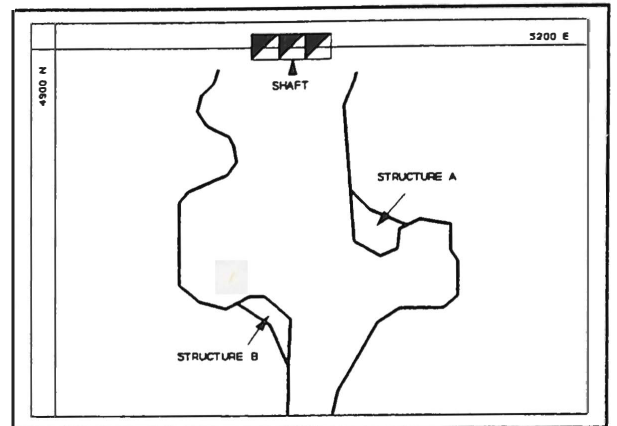
Figure 1. Shaft station where rockbursts occurred in structure A, and in structure B about 2 months later (after Simon, 1992).

3.1 Stability analyses

The stability analyses were only performed on structure A, the first one that failed. It was considered that structures A and B acted as structural elements called "pillars" submitted to high stress concentration. A two-dimensional finite element model was constructed to evaluate the stress state in these structures. Figure 2 shows the modelled excavation in plan and cross sections, and Figure 3 shows the finite element model consisting in 2056 rectangular 8-nodes elements. This type of element usually gives more accurate results than triangular elements in plane strain analyses (Brebbia and Connor, 1974; Rao, 1989; MacNeal, 1990; Pepper and Heinrich, 1992). Note that only a quarter of the excavation is modelled due to the symmetry of the idealized excavation. To simulate in the 2D analysis the high stresses in these three-dimensional "pillars", the strategy adopted was to increase their elastic modulus by a value equal to the ratio A_1/A_2 as shown in Figure 4. In this case, the ratio was about 4. Table 1 summarizes the hypotheses and data used in the first analysis.

Table 1.
Initial conditions and hypotheses adopted for the
2D finite element analysis

E_1 (GPa)	E_2 (GPa)	Co (MPa)	m	S	ν	σ_v (MPa)	σ_h (MPa)	Pillar mesh	Element type	Type of analysis
53	237	229	11	0,07	0,3	22	83	24 X 24	8-nodes rectangular	Plane strain

where E_1, E_2 are the rock mass and pillar elastic modulus, Co, the intact rock uniaxial compressive strength, m and S, the Hoek and Brown failure criterion parameters, ν, the Poisson's ratio, and σ_v, σ_h, the vertical and horizontal pre-mining stresses respectively.
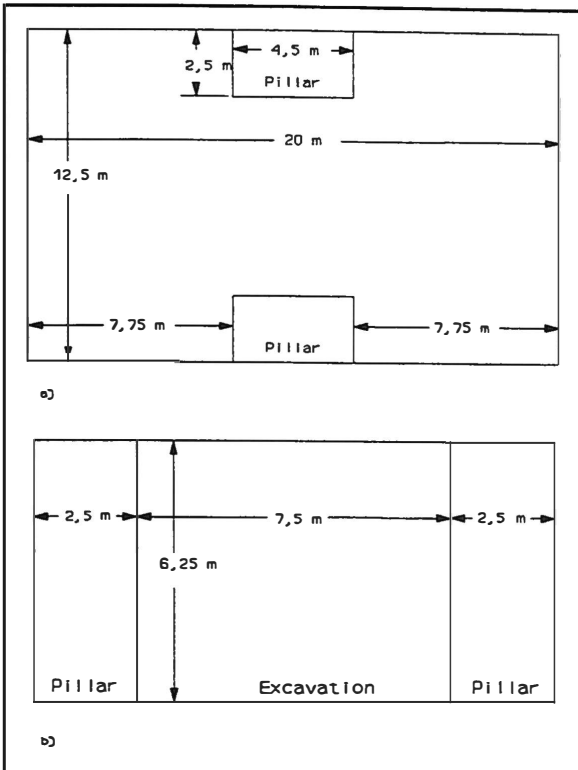
Figure 2. Modelled excavation: a) plan section;
b) cross section (after Simon, 1992).
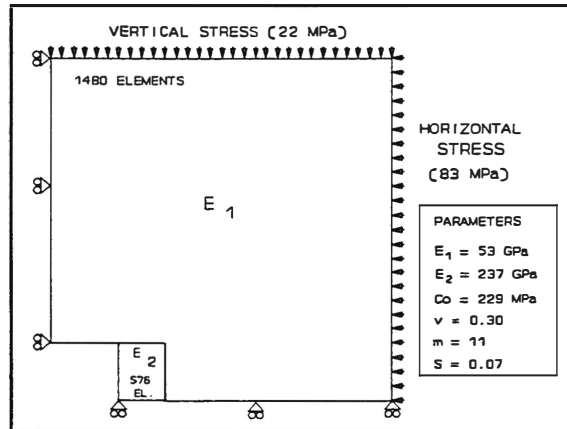
Figure 3. Finite element model used for the stress
analyses (after Simon, 1992).
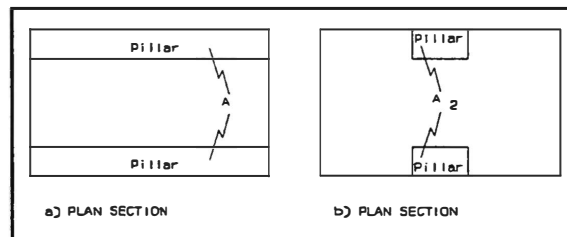
Figure 4. a) Modelled situation in plane strain; b) In
situ situation (after Simon, 1992).

This model was analyzed in plane strain with a commercial finite element code
(COSMOS/M) using the GEOSTAR module. GEOSTAR is a proprietary 2D and 3D
geometric modelling program for applications on micro-computers and mini-computers. It
performs as a complete pre and postprocessing program for the COSMOS/M family of finite
elements analysis modules (SRAC, 1992).

The results of this first analysis, shown in Figures 5a to 5c, indicate that tensile failure and
shear failure due to deviatoric compressive stresses were obtained when using the Hoek and
Brown (1980) failure criterion. This analysis also shows that failure can be attributed
mostly to the tensile stresses. Unfortunately, because no tests were performed directly on
the local rock, most of the data used in this analysis were obtained from other locations of
the mine where geology was considered comparable. In order to evaluate the effect of the
imprecision and possible dispersion of the available data, parametric sensitivity analyses
were performed to cover most of the envisioned properties spectrum. The influence of
several parameters was studied in these analyses, namely: the pre-mining horizontal stress
(σ_h), the "pillars" relative area (which affects the stress concentration factor), the Poisson's
ratio (ν), the intact rock uniaxial compressive strength (Co) and the Hoek and Brown failure
criterion parameters for the rock mass (m & S).

221
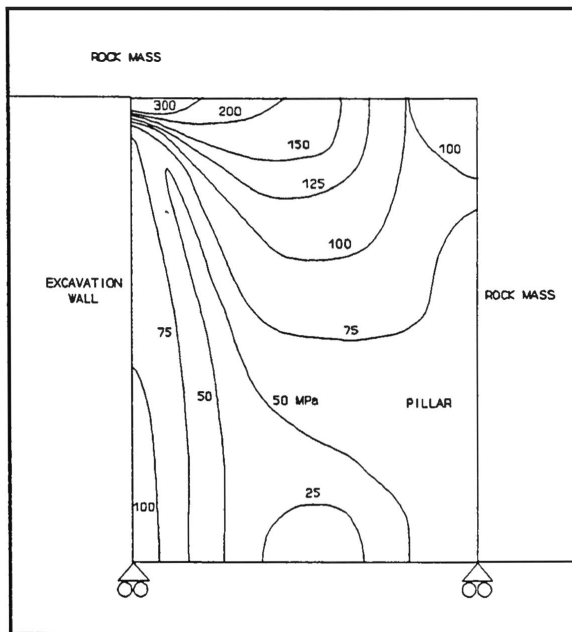
Figure 5a. Contours of the deviatoric stress component (σ_1-σ_3) obtained from the 2D stress analysis.
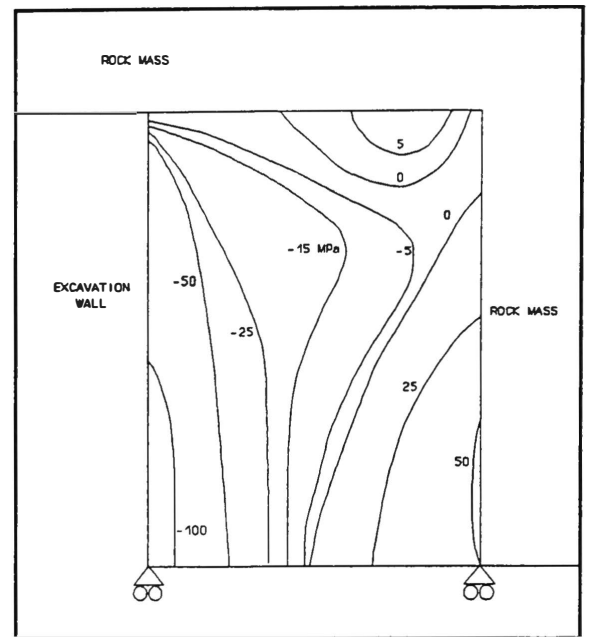
Figure 5b. Contours of the minor principal stress (σ_3) obtained from the 2D stress analysis.

- Pre-mining horizontal stress

The initial pre-mining vertical and horizontal stresses used in the first analysis were obtained from in situ measurements made on upper levels. In all the analyses, the vertical stress was considered to be approximately equal to the vertical earth pressure. However, the major principal horizontal stress value used in this first analysis (i.e. 83 MPa) is much higher than the average maximum horizontal stress value at this depth compiled by Herget (1987) for the Canadian Shield. Accordingly, three other analyses were then performed with different horizontal stresses, using Herget (1987) upper and lower limits (σ_h = 43 MPa and σ_h = 29 MPa), and as a limiting case, an horizontal stress equal to the vertical stress (σ_h = 22 MPa).
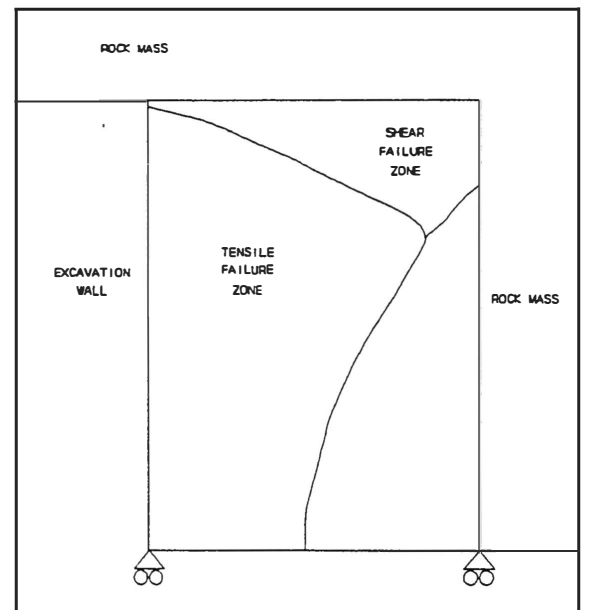
Figure 5c. Failure zones in the pillar using the Hoek and Brown (1980) failure criterion.

For σ_h = 43 MPa, tensile failure and shear failure due to deviatoric compressive stresses were obtained for the average properties values (Table 1), and for the other geomechanical properties considered in the following. For σ_h = 29 MPa, the structure was found to be

222

stable for the average properties values, but shear failure was obtained when these values were lowered by 10%. Likewise, for $\sigma_h = 22$ MPa, the structure was stable for the average geomechanical parameters values, but shear failure was obtained when these values were lowered by 15%.

- Pillar area

Since the geometry of the excavation was simplified in the numerical analysis to facilitate the modelling task, and since there was no certainty as to the real "pillar" size, analyses were performed in order to evaluate the influence of the "pillar" area. According to the strategy adopted in the 2D analyses, the modification of the "pillar" area in the model was accomplished by increasing or decreasing its elastic modulus. The initial "pillar" area was about 11 m^2. Two analyses were performed for areas of 7,5 m^2 and 25 m^2. Again, tensile and shear failures were obtained for both of these cases.

- Poisson's ratio

The measured value of ν is 0,30. Two analyses were also performed for $\nu = 0,15$ and $\nu = 0,40$. The Poisson's ratio affects mostly the minor principal stress values (σ_3), but has little effect on the results of the stability analyses. Again, tensile and shear failures were obtained for both cases.

- Geomechanical parameters

The geomechanical parameters that were varied are the uniaxial compressive strength (Co), and the Hoek and Brown failure criterion parameters (m, S). Stability analyses were performed to cover most of the envisioned properties spectrum (Co=180 to 260 MPa; m=3 to 11; S=0,01 to 0,1). Both tensile and shear failures were obtained for these variations.

3.2 Estimation of the stable surrounding rock mass stiffness

The local excavation stiffness for the stable surrounding rock mass can be estimated by performing other types of numerical analyses, as illustrated on Figure 6a and 6b, where the model dimensions are the same as those of the excavation. A normal internal pressure P_i is applied to the walls and the tangential deformation (ϵ_t) at different locations identified by points A are computed. Analyses are performed for different values of P_i; the slope of the graph of P_i versus $\Delta\epsilon_t$ represents the local excavation stiffness for the stable surrounding rock mass under the usual hypothesis of 2D modelling (Gill et al., 1993). The model presented in Figure 6a would be used for the fracturing of a portion of the excavation, and the model in Figure 6b would be used for a "side pillar" failure. Both cases can be considered as possible representation of the actual situation depending on the failure initiation mode.
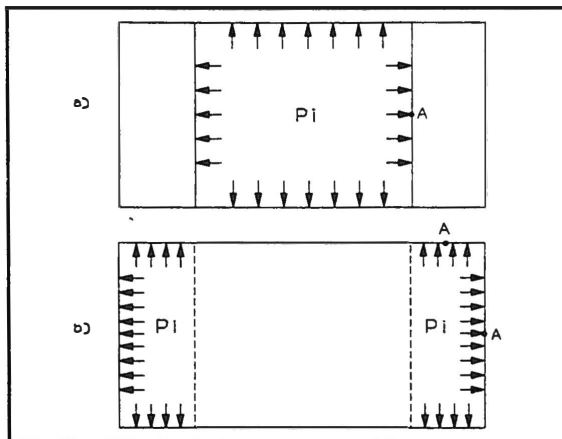
Figure 6. Models used to estimate the local stiffness for the stable surrounding rock mass.
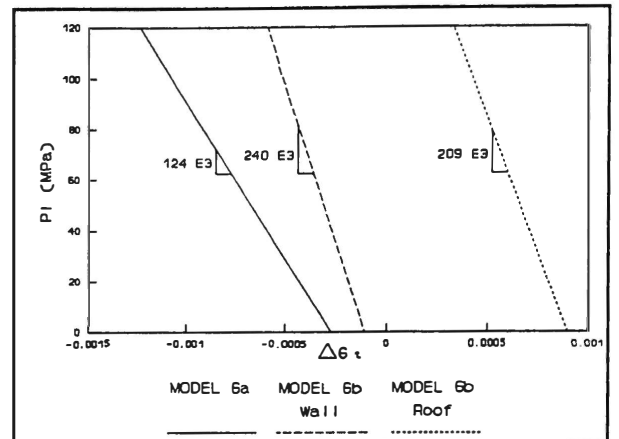
Figure 7. Results of the stress analyses performed to obtain the local stiffness of the stable surrounding rock mass (after Simon, 1992).

The analyses were performed with the models illustrated on Figure 6 using an "in house" boundary element program named FORMSTAB, which has been developed from the BOUDEM code presented in Appendix 4 of Hoek and Brown (1980). The results of these analyses are plotted on the graph in Figure 7. This gives a local stiffness for the stable surrounding rock mass ranging from 124 GPa to 240 GPa. This stiffness was compared with the post-peak modulus of the failed rock obtained from the empirical relationships of Brady and Brown (1981). The comparison led to the conclusion that there was a rockburst potential in this case.

4 DISCUSSION

One of the major uncertainty often encountered while performing numerical modelling in mining is the lack of specific geomechanical data. The case analyzed in this paper is no exception. In fact, as previously mentioned, most of the data used to perform these analyses were obtained from other locations in the mine where geology was considered comparable. This led to several uncertainties in the evaluation of the rock mass mechanical properties. Nevertheless, the parametric sensitivity analyses allowed to cover most of the envisioned properties spectrum and pre-mining stress conditions. As it was shown with these analyses, failure was obtained for the vast majority of the studied cases. And for the cases where stability was foreseen, lowering the average geomechanical parameters values by a small percentage would again lead to instability. Thus, these analyses lead to the conclusion that failure of the structure was most likely to occur, and in a usual engineering approach, the structure would have been considered unstable.

The results of the stability analyses also showed that both tensile and shear failures were obtained. However, rockburst phenomena are usually attributed to shear failure due to compressive stresses or to fault-slip along geological weakness planes. Albeit these

considerations, Hasegawa et al. (1989) have reported that tensile failure can produce low magnitude seismic events and damage in nearby openings. Hedley (1992) also reports a case where a small rockburst in a hanging wall may have been trigger by tensile failure. In the case studied here, the tensile failure region (which was close to the opening) may have triggered the global failure of the structure, that may have been the result of a shear failure since elements in the "pillar" core failed due to the compressive deviatoric stresses.

The high tensile stresses in the structure originated from the very high pre-mining horizontal stress. This horizontal stress value was based on only a few in situ measurements made on upper levels. Unfortunately, it was impossible to assess the real horizontal stress at this depth. The real stress could be much lower than the one used for the initial analysis. The sensitivity analyses showed that with a lower pre-mining horizontal stress, the tensile failure region would vanish, but shear failure could still be possible.

To model a complex three-dimensional geometrical problem in two dimensions, simplification assumptions had to be made. The surrounding openings (shaft and drift) were disregarded, although their influence might not have been negligible. In addition, it was not sure that the strategy adopted to induce the stress concentration in the structure would bring a good estimation of the real stress state. To verify this aspect of the modelling work, the finite element software was installed on a more powerful computer, and a 3D model (based on the geometry shown in Figure 2) was constructed. Figure 8 shows a comparison of the major principal stress (σ_1) along the structure central axis obtained for 2D and 3D analyses results. This figure indicates that the 2D model gives a good estimation of the stress state at the "pillar" centre. However, the 2D estimation seems to be less accurate at the structure boundaries (roof and floor). This might be attributed to the fact that adjacent elements at the boundary have different elastic modulus, hence creating a higher gradient in the stress field. The same phenomenon was observed at the other boundary of the structure and of the rock mass. Nonetheless, the 2D model overestimates the stress state in the pillar, thus giving a conservative solution. This is in accordance with the usual goal of 2D modelling, which is to obtain results on the conservative side, although as close to reality as possible. Many examples of such modelling ideology can be found in the literature, where 2D modelling results gave conservative estimations of 3D modelling results (e.g., Pariseau and Sorensen, 1979; Potvin et al., 1989). Still, close attention to the simplification assumptions is needed to make sure that the 2D model does not underestimate the stress state or overestimate the safety factor of the structure (e.g., Moon and Lee, 1991). Overall, the 2D modelling was regarded as satisfactory considering the relative precision of the data used.

One major concern in numerical modelling is the accuracy of the computed results. Several analyses were performed to find the pillar mesh size that would be accurate without being too costly in CPU time. A way to determine the accuracy of the model is to refine the mesh until the results variations stays within an acceptable range. It was found that a 24 x 24 mesh in the pillar gives accurate results for the 2D modelling. The iterative process to

determine the results accuracy can be however very arduous, especially for 3D analyses, since a single analysis may take many hours to compute. Unfortunately, due to software limitations, the 3D model had to be constructed with a much coarser pillar mesh size. Nevertheless, another 3D analysis was performed with a somewhat finer mesh size and the results showed that there was no significant variations in the stress results.
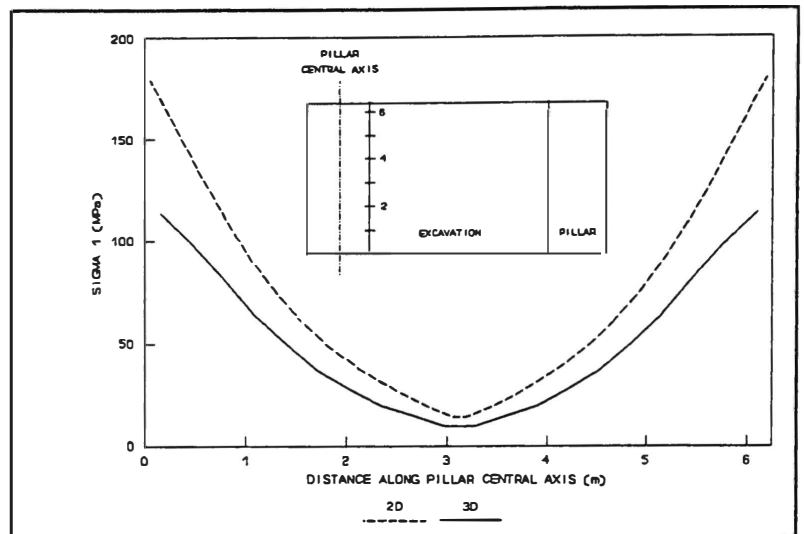
Figure 8. Comparison of the major principal stress (σ_1) along the structure central axis obtained from the 2-D and 3-D analyses.

5 CONCLUSIONS

The back-analyses presented in this paper illustrate how numerical modelling can be used for the preliminary evaluation of the rockburst potential. In an actual rockbursting case, the 2D stress analyses performed with the finite element method showed that there was a great probability of failure of the structure. It was shown that these 2D stress analyses compare fairly well with more realistic 3D analyses. Other numerical stress analyses were performed with the boundary element method to estimate the stable surrounding rock mass stiffness. From the latter results, it was concluded there was a potential for rockbursting.

ACKNOWLEDGEMENTS

REFERENCES

Aubertin, M., D.E. Gill, R. Simon 1992. Évaluation du Potentiel de Coups de Terrain dans les Mines; Phase II - Validation de la Méthodologie Proposée. Rapport Final présenté à l'Institut de Recherche en Santé et Sécurité au Travail (IRSST), Septembre 1992.

Bieniawski, Z.T. 1984. Rock Mechanics Design in Mining and Tunnelling. A.A. Balkema.

Blake, W. 1972. Rockburst Mechanics. Quarterly of the Colorado School of Mines, 67, 1, 1-64.

Brady, B.H.G., E.T. Brown 1981. Energy Changes and Stability in Underground Mining: Design Application of Boundary Elements Methods. Trans. Int. Min. Metall., 90, A61-A68.

Brebbia, C.A., J.J. Connor 1974. Fundamentals of Finite Element Techniques. John Wiley and Sons.

Brown, E.T. 1984. Rockbursts: Prediction and Control. Tunnels and Tunnelling, April, 17-19.

Fairhurst, C. (Ed.) 1990. Proc. 2nd Int. Symp. on Rockbursts and Seismicity in Mines. A.A. Balkema.

Gill, D.E., M. Aubertin 1988. Évaluation du Potentiel de Coups de Terrain dans les Mines d'Abitibi. Rapport de recherche de l'URSTM présenté à l'Institut de Recherche en Santé et Sécurité du Travail (IRSST).

Gill, D.E., M. Aubertin, R. Simon 1993. A Practical Engineering Approach to the Evaluation of Rockburst Potential. Proc. Third Int. Symp. on Rockbursts and Seismicity in Mines, Kingston, Ont. (to be published).

Hasegawa, H.S., R.J. Wetmiller, D.J. Gendzwill 1989. Induced Seismicity in Mines in Canada - An Overview. Pure and Applied Geophysics, 129, 423-453.

Hedley, D.G.F. 1992. Rockburst Handbook for Ontario Hardrock Mines. CANMET Special Report SP92-1E.

Herget, G. 1987. Stress Assumptions for Underground Excavations in the Canadian Shield. Int. J. Rock Mech. Min. Sci., 24, 95-97.

Hoek, E., E.T. Brown 1980. Underground Excavations in Rock. Inst. Min and Metall, London.

MacNeal, R.H. 1990. The Shape Sensitivity of Isoparametric Elements. Proc. 6th World Congress on FEM, Robinson, J. (ed.), 520-529.

Moon, H.K., H.K. Lee 1991. A 3-D FE Model of a Shaft-Tunnel-Tunnel Intersection and Comparison with a 2-D Model. Proc. 7th Int. Cong. Rock Mech., ISRM, 2, 1331-1334.

Ortlepp, W.D. 1983. The Mechanics and Control of Rockbursts. Rock Mechanics in Mining Practice. Budavari (ed.), SAIMM, Johannesburg, 257-282.

Pariseau, W.G., W.K. Sorensen 1979. 3D Mine Pillar Design Information from 2D FEM Analysis. Int. J. for Numerical and Analytical Methods in Geomech., 3, 145-157.

Pepper, D.W., J.C. Heinrich 1992. The Finite Element Method: Basic Concepts and Applications. Hemisphere Publ. Corp.

Potvin, Y., M.R. Hudyma, R.C.T. Pakalnis 1989. Comparison of Two Dimensional and Three Dimensional Boundary Element Numerical Models. 91st CIM Annual General Meeting, Quebec City (Qc), 20 p.

Rao, S.S. 1989. The Finite Element Method in Engineering. 2nd ed., Pergamon Press.

Simon, R. 1992. Validation d'une Méthodologie d'Évaluation du Potentiel de Coups de Terrain dans les Mines. Mémoire M.Sc.A., Département de génie minéral, École Polytechnique de Montréal.

SRAC 1992. Geostar User Guide. Version 1.65a, Fourth Edition, Structural Research and Analysis Corporation, California, USA.

A STRAIN ENERGY APPROACH FOR THE PREDICTION OF ROCKBURST POTENTIAL IN UNDERGROUND HARD ROCK MINES

H.S. Mitri, F.P. Hassani and R. Kebbe
Department of Mining and Metallurgical Engineering
McGill University, Montreal, Quebec, Canada H3A 2A7

ABSTRACT

Following the lines of thought that rockburst phenomenon is primarily due to sudden release of strain energy, an existing finite element model which is developed at McGill (and called MSAP2D) is modified to enable the calculation of strain energy density distribution around mine openings at depth. The new version of the model calculates the strain energy density stored in each element. This information is then sent to the postprocessor. The new postprocessor displays five levels of strain energy density. Such a picture can serve as a basis for locating areas of high strain energy build-up and hence potential rockburst occurrence. The use of this approach is demonstrated by reference to a case study of a narrow vein ore body in Campbell Red Lake Mine, Balmertown, Ontario.

RÉSUMÉ

En se basant sur l'hypothèse que le phénomène de coup de terrain est principalement dû au relâchement soudain d'énergie de deformation, un modèle existant d'élements finis développé à McGill (nommé MSAP2D) est modifié pour permettre le calcul de la distribution de densité d'énergie de deformation autour des ouvertures de mines en profondeur. La nouvelle version du modèle calcule la denisité d'énergie de deformation emmagasiné dans chaque élement. Cette information est ensuite relayée au post-processeur. Le nouveau post-processeur montre cinq niveaux de densité d'énergie de deformation. De tels résultats sont utiles pour identifier des endroits de grandes accumulation d'énergie de deformation menant à la rupture violente du massif rocheux. Cette approche est appliquée à une étude de cas d'une veine étriote de la mine Campbell Red Lake à Balmertown en Ontario.

INTRODUCTION

Concern has grown in recent years over the continued incidence of rockbursts in underground Canadian mines. The cause of these rockbursts is not a natural occurrence like earthquakes. It is due to mining operations and specifically the shattering of support pillars. Despite mounting research, little is understood about rockbursting and its alleviation. It is generally agreed that rockbursts result from sudden, uncontrolled releases of energy within a volume of highly stressed rock. Rockbursts are recorded by a multi-channel microseismic system that gives relatively accurate locations for both small and large seismic events. An energy balance approach is used to evaluate the source of energy liberated in a rockburst. All sources of energy entering the system are balanced against how the energy could be dissipated and the excess of energy will be liberated as seismic energy. It is discovered that the post-failure behaviour of brittle rocks is either violent or non violent, depending on the stiffness of the loading machine. A number of source location techniques have been developed. Most use the arrival time of the compressional waves to successive geophones or accelerometers. When full seismic waveforms are recorded, the separation of compressional and shear waves is used to determine source locations. In many mines, microseismic systems indicate those areas of the mine which are rockburst-prone and a build up in microseismic activity sometimes precedes a large rockburst. Computer models also indicate locations which are highly stressed and rockburst-prone.

Recognized as having complex and divergent modes of origin, rockbursts have been recorded at shallow depths but are more commonly associated with the deep metal mines found within the strong, brittle rocks of the Canadian PreCambrian Shield. The Macassa Mine, Kirkland Lake, as an example, recorded three major rockbursts between July 1985 and January 1986 (Hanson et al., 1987) each measuring over Nuttli 2.0. Inco's Creighton Mine, Sudbury, has documented 897 rockbursts, one of which measured 4.0 on the Nuttli scale in 1984 (Oliver et al., 1987). The Campbell Red Lake Mine, Balmertown, which has experienced rockbursts since the 1960's, recorded a series of rockbursts in December 1984 so severe that mining had to be discontinued in one particular ore zone (Makuch et al., 1987).

There are two common approaches to the alleviation of rockburst [Hedley,1987]. One approach, sometimes referred to as strategic, is to diminish the severity of the rockburst by avoiding remnant pillars and longwall face configurations, using sequenced extraction and mining away from, rather than towards, a major weakness plane. The second approach, sometimes referred to as tactical, is to accept that some rockbursts are inevitable, but seeks either to limit the extent or the timing of the damage. In access drifts, the concept of lacing is introduced. This concept consists of mild steel grouted rebar, wire mesh and flexible steel cable over the mesh and connected to the rebars in a diamond pattern. It is found that this type of support system, when subjected to nearby rockburst, allowed the wall rocks to rapidly converge inwards while still maintaining the integrity of the drift [Hedley,1987]. Friction type (e.g. Split Sets and Swellex) support systems with wire mesh have been found to be effective in rockburst conditions in Canadian mines. The control of the volumetric closure of a stope is also found to limit the severity of rockburst. Backfill or other support systems between hanging wall and footwall both limit stope closure and absorb energy otherwise liberated as seismic energy.

The initial results of destress blasting were encouraging but this practice was discontinued when it was thought that no excess energy was being released other than that of the explosive. However, destress blasting is continued in North American mines (Coeur d'Alene, USA, Campbell Red Lake, Sudbury

and Kirkland Lake, Canada) with apparent success.

The concept of destressing is to fracture highly stressed pillars with explosives thereby reducing the deformation modulus and the stress they can support. This in turn allows the hanging wall and footwall to converge with the resultant change in potential energy. In many mines, rockbursts occur shortly after destress blasts and large production blasts, due to stress transfer. In some cases it may be possible to control the timing of a rockburst by such blasting. The benefits of theses tactical techniques are realized in the short-term.

NUMERICAL MODEL MSAP2D

A finite element model, based on the 4-node isoparametric quadrilateral element, has been previously developed at McGill to enable a 2-D linear elastic analysis of underground and surface mining excavations on a microcomputer system (Chau et al., 1988). The model, called MSAP2D, was designed to serve as a user-friendly tool, with extensive data visualization capabilities. MSAP2D consists of five modules: ZONE, PRESAP, MESH2D, SAP2D and POSTSAP.

PRESAP is a mesh generation program for the core program MSAP2D. It reads a simple datafile and generates the required datafile for program MSAP2D. The data for program PRESAP can be checked graphically by program ZONE which displays the geometry of the problem, its geology, intended mesh grading and boundary conditions. MESH2D is a graphic program for checking the geometry of the structure, generated mesh, boundary conditions, mining sequences as well as material types simulated can all be graphically displayed and checked. MSAP2D is the main finite element program of the system. Displacements of nodal points as well as stresses at prescribed locations are computed. The new version of the code presented herein calculates the strain energy density stored in each element. POSTSAP is a postprocessing program designed to interpret the output from program MSAP2D. Nodal displacements and principal stresses are displayed. Moreover, failure criteria are incorporated to permit checking the safety level of a mine design. The new version of the postprocessor presented herein reads the strain energy density in each element and then calculates the difference between the maximum and minimum strain energy densities in a given problem domain. This difference is then subdivided into five equal segments to reflect five strain energy density ranges in the domain. In this way, elements storing relatively higher strain energy can be easily identified. The use of this feature, in determining the locations of potential rockburst and associated failure modes, is demonstrated through a case study of crown pillars in a narrow vein ore body in Campbell Red Lake mine.

FINITE ELEMENT EQUATIONS

The two-dimensional, quadrilateral isoparametric element shown in Fig. 1 is used in the finite element formulations. It offers the advantage of handling curved and arbitrary geometric shapes. The isoparametric formulation expresses both the displacements $(u,v) = \{a\}^T$ and the geometry $(x,y) = \{x\}^T$ of the element by the same interpolation shape functions $N_i(i=1,2,3,4)$. Thus,

$$\{u\} = [N] \{u^e\} \tag{1}$$
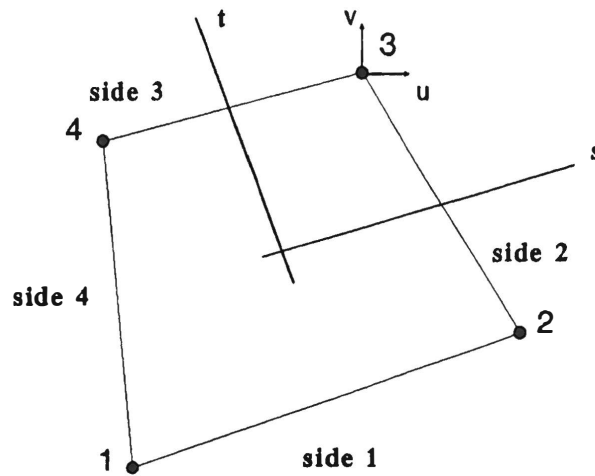
Figure 1 Quadrilateral isoparametric element

$$\{x\} = [N]\,\{x^e\}$$ (2)

$$N_i = \tfrac{1}{4}\left(1+\xi\xi_i\right)\left(1+\eta\eta_i\right)$$ (3)

where

$\{u^e\}^T$	=	nodal displacements $(u_1, v_1, u_2, v_2, u_3, v_3, u_4, v_4)$
$\{x^e\}^T$	=	nodal coordinates $(x_1, y_1, x_2, y_2, x_3, y_3, x_4, y_4)$
ξ, η	=	natural coordinates
ξ_i	=	$(-1,+1,+1,-1)$
η_i	=	$(-1,-1,1,1)$

The strain-displacement relationship at any point within the element can be expressed as:

$$\{\varepsilon\} = [B]\,\{u^e\}$$ (4)

where $\{\varepsilon\}$ is the strain vector and [B] is the strain-displacement matrix and is obtained by taking appropriate derivation of N_i. The total stress at any point due to gravitational load and in situ stress can be calculated from:

$$\{\sigma\} = [D]\,\{\varepsilon\} + \{\sigma^0\}$$ (5)

where

$\{\sigma\}^T$	=	$(\sigma_{xx}, \sigma_{yy}, \sigma_{xy})$	=	stress vector
$\{\sigma^0\}^T$	=	$(\sigma^0_{xx}, \sigma^0_{yy}, \sigma^0_{xy})$	=	in situ stress vector
[D]	=	stress-strain elasticity matrix		

231

The plane strain elasticity matrix $\overline{[D]}$ for an orthotropic material in a local N-S coordinate system making an angle with global x-axis of the cartesian frame of reference is transformed to global coordinates by the relation

$$[D] = [T]^T \overline{[D]} [T] \tag{6}$$

$$\overline{[D]}^{-1} = \begin{bmatrix} \dfrac{1}{E_N} & \dfrac{-\nu_{NS}}{E_N} & 0 \\[2mm] \dfrac{-\nu_{SN}}{E_S} & \dfrac{1}{E_S} & 0 \\[2mm] 0 & 0 & \dfrac{1}{G_{NS}} \end{bmatrix} \tag{7}$$

and

$$[T] = \begin{bmatrix} c^2 & s^2 & cs \\ s^2 & c^2 & -cs \\ -2cs & 2cs & c^2 - s^2 \end{bmatrix} \tag{8}$$

where

    $c = \cos\beta$

    $s = \sin\beta$

    β = the angle between x-axis and N-axis

In the above, [T] is a transformation matrix from local N-S system to the global x-y system and is derived elsewhere (Cook, 1989). E_N and E_S are moduli of elasticity in N and S directions respectively and G_{NS} is the shear modulus in N-S plane having the Poisson's ratios ν_{NS} and ν_{SN}.

The element stiffness matrix can be derived from the Principle of Virtual Work or the Potential Energy Theorem.

The 8 x 8 - element stiffness matrix [Kᵉ] is calculated by numerical integration using (2 x 2) Gauss quadrature scheme as follows:

$$[K^e] = t \sum_{i=1}^{2} \sum_{j=1}^{2} [B(\xi_i, \eta_j)]^T [D] [B(\xi_i, \eta_j)] \, | J(\xi_i, \eta_j) | \tag{9}$$

where

$$\xi_1 - \eta_1 - -\frac{1}{\sqrt{3}} \ , \ \xi_2 - \eta_2 - +\frac{1}{\sqrt{3}} \ , \ |J| = \text{determinant of the Jacobian matrix which is a}$$

function of ξ and η, and t = thickness of the element.

The element load vector {P} is composed of several load vectors. Its complete form is given by:

$$\{P\} - \{F^b\} + \{F^t\} - \{F^{\sigma 0}\} \tag{10}$$

where

$\{F^b\}$	=	load vector due to own weight of the rockmass
$\{F^t\}$	=	load vector due to boundary tractions
$\{F^{\sigma 0}\}$	=	load vector due to in situ stresses

The global stiffness matrix and load vector hold a set of equilibrium equations
which are solved for the nodal displacements by Gauss elimination method (Bathe, 1982).

The average strain energy density in each element U_d^e is then calculated (Mitri and Suriyachat, 1990). This is done by dividing the total strain energy stored in the element U^e by its volume V^e. It can be shown that

$$V^e - t \sum_{i-1}^{2} \sum_{j-1}^{2} |J(\xi_i, \eta_j)| \tag{11}$$

and

$$U^e - \frac{1}{2} \{u^e\}^T \sum_{i-1}^{2} \sum_{j-1}^{2} [B(\xi_i, \eta_j)]^T [D] [B(\xi_i, \eta_j)] |J(\xi_i, \eta_j)| \{u^e\} \tag{12}$$

Thus

$$U_d^e - \frac{U^e}{V^e} \tag{13}$$

CASE STUDY : CAMPBELL RED LAKE MINE

The ore body consists of Chlorotic rock and Andesites adjacent to each other. The average dip angle is 65 degrees. Ore is mined by cut-and-fill method, in 8-foot lifts, and the levels are 150 feet apart. Drifts have generally a cross section of 9 by 9 feet. The general mining practice for cut-and-fill stopes at Campbell is to drift an ore in order to define the horizontal limits. Once it is determined, a bypass drift is driven 30 feet on the projected footwall side of the ore drift. The ore drift has a further 9 to

20 feet of backs taken down in order to prepare it to be accessed by either chutes or drawpoints from the bypass drift. Once access is established, the ore drift is filled with a cement plug along its length so that the stope beneath it can be mined up to the level. The entire bypass drift is also cemented as a mean of containing the bursts. Drawpoints to access the stope are driven on 50-foot centres, which is the maximum distance that the blasted ore can be mucked by scoop remotely. The sill is mined from the centre out in 50 foot sections, depending on how well it holds out before requiring fill. Holes are drilled up from the stope by using a longhole machine. Initially a slot is blasted to open up the ground to " mass blasting ". Several thousand tons are blasted at once and then mucked remotely.

Sections Analyzed

The 1761, 1661 And 1541 stopes are located in the G zone at Placer Dome Campbell Red lake mine. Their depths are 2227, 2400 and 2745 feet respectively below ground surface. Ten sections at 45 feet interval, from 5350 N to 5750 N, were provided by Campbell mine. Sections 5545 N and 5650 N, located between levels 7500 and 8345, were used in this case study. The modelling results include strain energy density concentrations in the crown pillars and walls of the three stopes mentioned above. The bottom of the sections analyzed is 2745 feet below ground surface. The vertical in situ stress is given by the depth below ground surface times the unit weight of the rock mass and the horizontal-to-vertical in situ stress is 1.7. Thus,

$$\sigma_v = 3294 \text{ psi}$$
$$\sigma_h = 5560 \text{ psi}$$

Section 5545 N is located between 4250 E and 4650 E. Mining activities took place between levels 7500 and 8345. The average dip angle of this section is about 65 degrees. This section consists of 3 stopes and 2 crown pillars with the dimensional properties given in Table 1.

Table 1 : Dimensions of Stope Sections Analyzed

Section	Dimension (ft)	1761 Stope	1661 Stope	1541 Stope	Lower Crown Pillar	Upper Crown Pillar
5545 N	Height (ft)	69	109	127	76	64
	Average Width (ft)	58	30	22	58	22
5650 N	Height (ft)	-	113	141	75	-
	Average Width (ft)	-	27	30	21	-

A finite element mesh consisting of 2904 elements and 2745 nodes has been constructed for Section 5545N. The finite element model has a width of 581 feet and a height of 845 feet, (see Figures 2 and 3). Section 5650 N is located between 4290 E and 4650 E. Mining activities took place between level

7500 and elevation 8345. The average dip angle is about 65 degrees. This section consists of 2 stopes and a crown pillar and its dimensions are listed in Table 1. The finite element model has the same dimensions as that of section 5545 N but the mesh has 2584 elements and 2745 nodes (see Figures 4 and 5). The ore material consists of Chlorotic rock and Andesites and the geomechanical data, provided by Campbell Redlake Mine, is recorded in Table 2. Unfortunately, no data was available regarding the rock strength parameters (e.g. m, s and σ_c for Hoek-Brown criterion).

Table 2 : Geomechanical Data

Material	E (psi)	Unit Weight (lb/in³)	Poisson's Ratio
Chlorotic Rock	8340000	0.092	0.15
Andesite	11960000	0.097	0.21
Host Rock	11368000	0.1	0.20
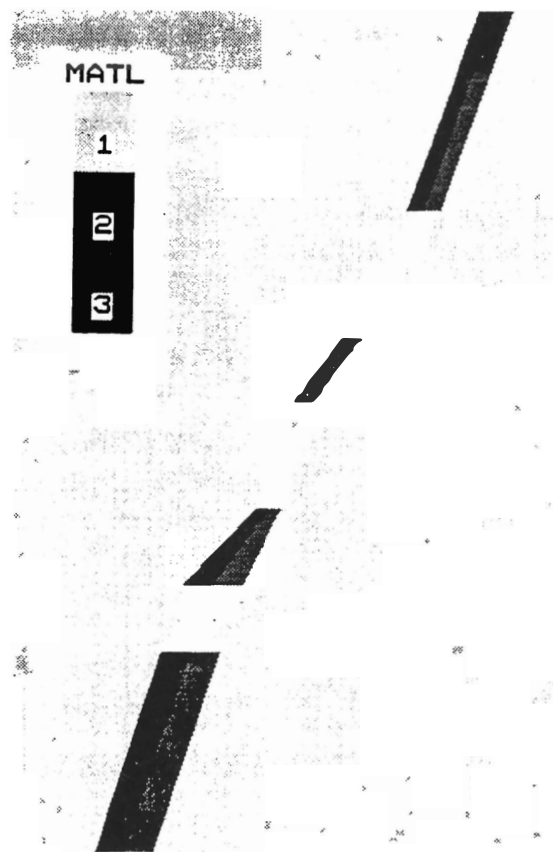
Figure 2   Material types of section 5545N
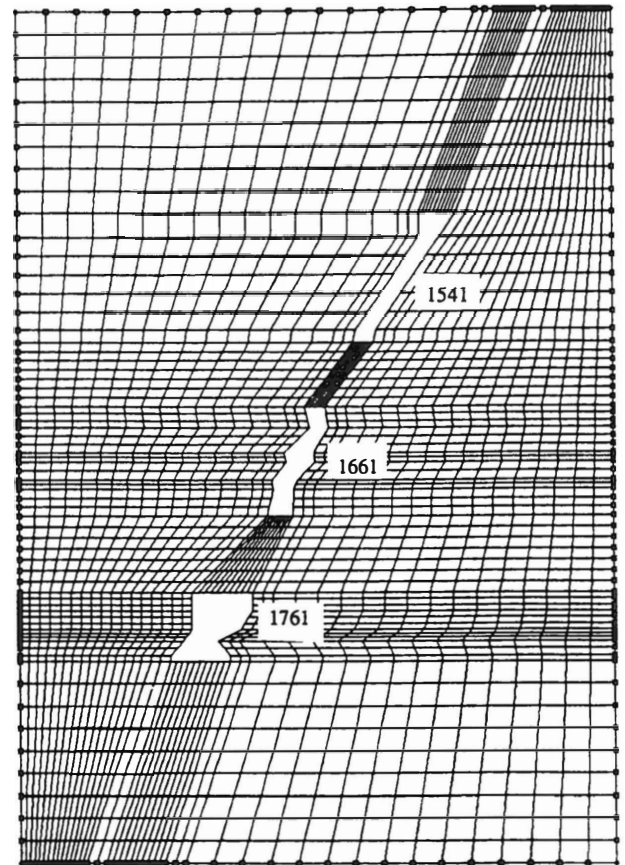
Figure 3   Finite element model of section 5545N

235
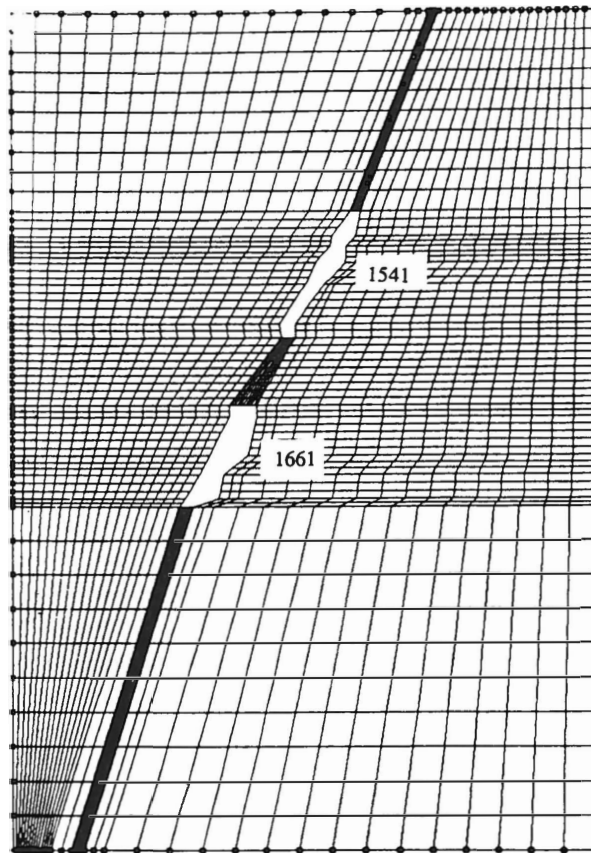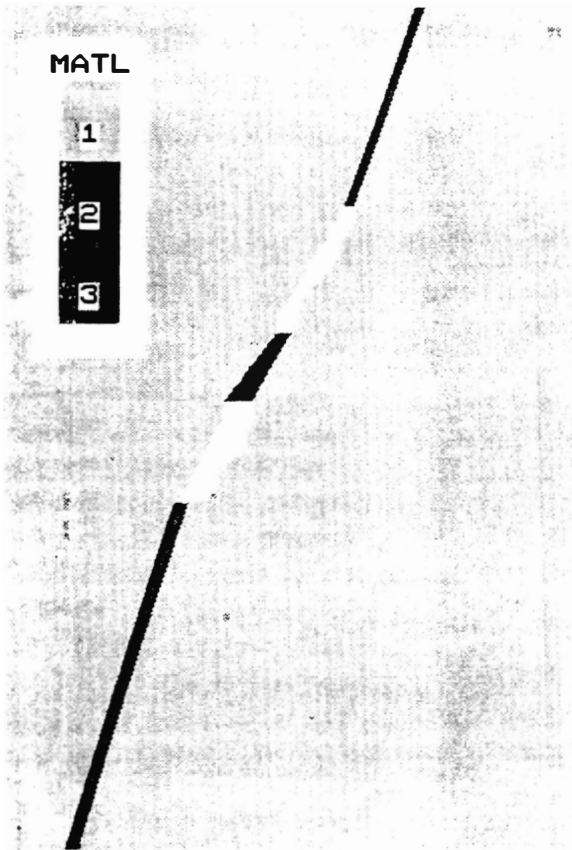
Figure 4 Material types in section 5650N

Figure 5 Finite element model of section 5650N

Tables 3 and 4 give the values of strain energy density, stored in the finite elements, at the locations indicated in Figures 6 and 7, for sections 5545 N and 5650 N respectively.

Table 3: Strain Energy Density (lb.in/in²) around mine stopes - Section 5545N

Point	A	B	C	D	E	F	G	H	I	J	K	L
Strain Energy Density	13.2	10.4	23.6	38.2	49.9	48.5	11	12.4	61.8	88.2	80.6	64.3

236

Table 4: Strain Energy Density (lb.in/in²) around mine stopes - Section 5650N

Point	A	B	C	D	E	F	G	H
Strain Energy Density	12.1	9.2	52.1	88.1	84.7	90.2	9.4	9.6

The strain energy density of the above elements is represented graphically in Figures 6 and 7 respectively. In these figures, level 1 represents the highest strain energy density (solid black). It can be seen clearly that strain energy density is highest at the back of stope 1661 and at the bottom of stope 1541, of both section 5545 N and section 5650 N. These results conform with previous observations reported by Campbell Red Lake mine. The advantage of the present method is that it doesn't require data on the strength of the rock to examine its conditions (i.e. strain energy build-up). The highest strain energy density, in the section 5545 N, is found at the upper sill pillars even though the in situ stress at this level is less than it is at the lower sill pillar. It can then be conducted from the results that if and when the occurrence of rockbursts is imminent, it is the back of stope 1661 that is prone to rockburst

It can be concluded from the numerical modelling results that (a) it is the back of stope 1661 that is prone to rockburst, and (b) if and when rockburst occurrence is imminent it will likely do so with a shear failure mode in the upper crown pillar as illustrated in Figures 6 and 7. There is obviously a need, at this stage, for a strain energy-based failure condition against which one should compare the calculated, or existing, strain energy levels. With the help of strain energy failure criterion, one can assess what may be termed as "rockbursts safety levels". Further investigation is currently underway using laboratory testing.

CONCLUSIONS

A strain energy-based postprocessor for 2-dimensional finite element analysis has been developed to help identify areas of rockburst potential around mine stopes at depth. The existing model developed at McGill, called MSAP2D, has been modified to calculate the average strain energy density in each element and send this information to the postprocessor.

The latter calculates the range between maximum and minimum energy densities and divides it so that 5 different levels of strain energy density can be graphically displayed. The locations of highest strain energy levels displayed, are considered to indicate where a rockburst might occur and the type of failure modes. The usefulness of the postprocessor is demonstrated through a case study of highly-stressed sill pillars in a narrow-vein orebody at Campbell Red Lake Mine, Balmertown, Ontario.

ACKNOWLEDGEMENTS
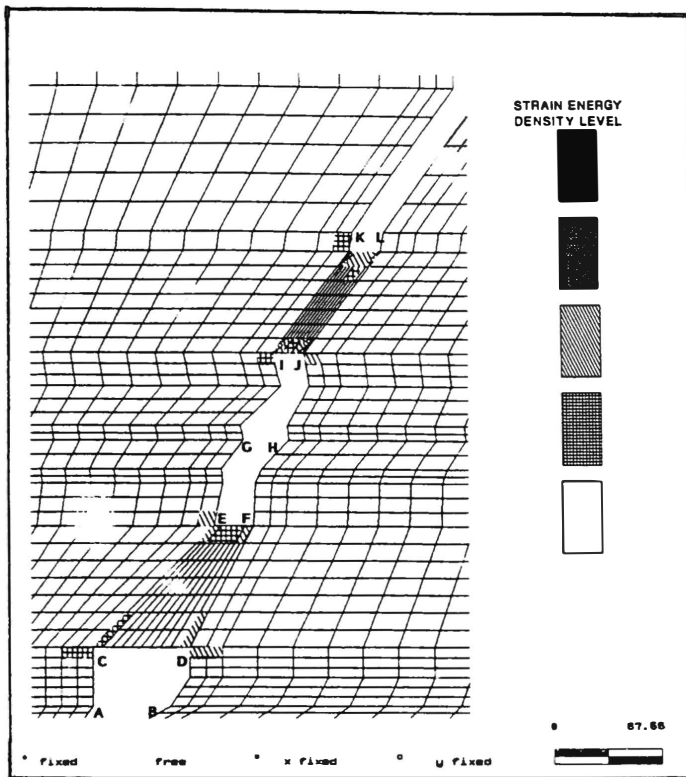
Figure 6   Strain energy density
levels of section 5545N

Figure 7   Strain energy density
levels of section 5650N
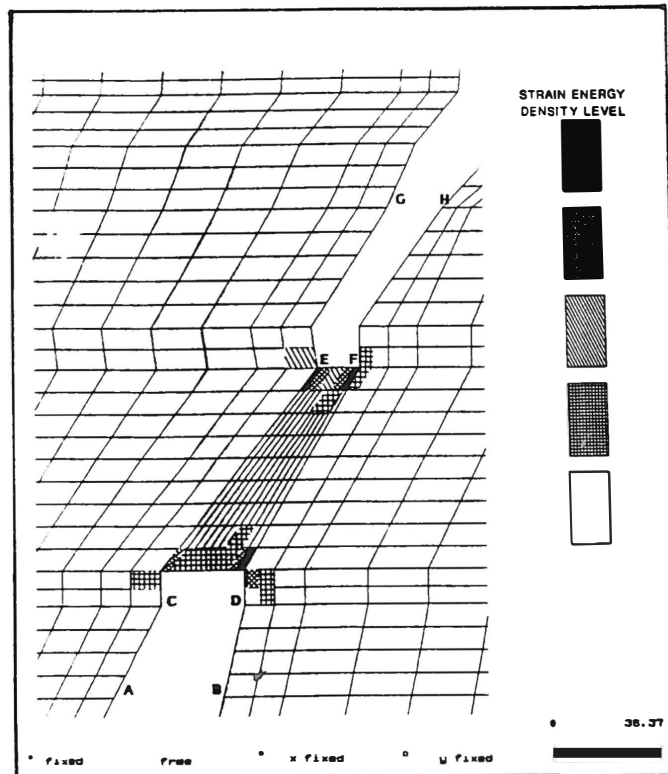
REFERENCES

Bathe, K.J., 1982. Finite Element Procedures in Engineering Analysis, Prentice-Hall, Inc., Englewood Cliffs, New Jersey.

Chau, K., Mitri, H.S., Hassani, F.P. and Scoble, M.J., 1988. A Finite Element Computer Model for Stress Analysis of Underground Openings. Proc. 1st Can. Conf. Comp. Appl. in the Mineral Industry, Quebec, March 7-9, pp. 259-268.

Cook, R.D., 1989. Concepts and Applications of Finite Element Analysis. Wiley, New York, 3rd Ed. Hanson, D., Quensel, W. and Hong, R., 1987. Destressing a Rockburst Prone Crown Pillar-Macassa Mine, CANMET, Elliot Lake, MRL 87 (TR).

Makuch, A., Neumann, M., Hedley, D. and Blake, W., 1987. Practical Applications of Pillar Destressing at Campbell Red Lake Mine, 8th Underground Operators Conf., Can. Inst. Ming. Metall., Elliot Lake.

Mitri, H.S., Scoble, M.J. and McNamara, K., 1988. Numerical Studies of Mine Pillars in Highly-Stressed Rock. Proc. 41st Can. Geotech. Conf., Kitchener-Waterloo, Ontario, Oct. 5-7, pp. 50-56.

Mitri, H.S. and Suriyachat, P., 1990. Energy-Based Postprocessor for 2-D F.E.A. of Mine Openings. Proc. Int. Conf. on Struct. Engng. and Computation, April 25-28, pp. 917-925.

Hedley, D.F.G., 1987 Catalogue of Rockburst Literature. - CANMET report.

Hedley, D.F.G., 1990 A Five-Year Review of the Canada-Ontario Industry Rockburst Project-CANMET report.

Session 7

Ground Support

Soutènement

A CABLE BOLT MODEL AND ITS IMPLEMENTATION INTO UDEC AND FLAC

G. Tan
Mines Research, INCO Ltd.
W. F. Bawden
C. Pelley
Queen's University at Kingston, Canada

ABSTRACT

In this paper a new cable bolt model is presented. It is assumed that cable bolt performance is mainly determined by the interaction between the cable strand and grout. This interaction, in turn, is dependent on the cable's external geometry, rock mass properties, grout properties and in-situ stresses. Equations for two critical cable bolt loads — the linear elastic limit load and the ultimate bond load — are given. The load-displacement for 7-strand cable bolts is derived based on these loads and analysis of displacements. The model has been implemented into UDEC and FLAC. Test runs on the Winston Lake Mine quasi-AVOCA-longhole stope stability problem have shown good results.

1 INTRODUCTION

Since contrasting results have been reported in the use of cable bolts for the support of underground excavations, considerable research work has been carried out in the laboratory and in situ to understand their behaviour under uniaxial loading conditions (Stillborg,1984; Fuller et al.,1983,1988,1990; Goris et al.,1987,1989; Bawden, Reichert and Hyett, 1992; Reichert, 1991; Hyett, Bawden and Reichert, 1992; Kaiser, Yazici and Nose, 1992; Yazici and Kaiser, 1992). Some factors affecting cable bond have been pointed out to be:

(1) the type of cable, its method of construction, the number and diameter of strands, and the surface properties of strands;
(2) the strength and stiffness of cement grout;
(3) the bonded length of cable;
(4) the borehole diameter and the position of cable in borehole;
(5) the degree of confinement provided by surrounding rock mass;
(6) the in-situ stress condition.

Currently there are 3 approaches to model cable bolt behaviour. One uses an equivalent material approach (Sharma and Pande (1988)) to change the rock mass properties. The other uses a specially designed "cable bolt" structural element explicitly, such as those in some FEM programs. The third uses a "cable bolt model" to simulate the interaction between the cable bolts and the rock mass, such as St. John and Van Dillen's (1983) model used in UDEC and FLAC. In this way, there is no explicit "cable bolt element". The cable bolt's effect is considered interactively during the iteration process. It is reasonable to believe that, with a good model, this latter approach can simulate cable bolt behaviour most closely. Due to the incremental and interactive aspect of this approach, it is more suitable for time dependent solvers such as those used in UDEC, FLAC and other dynamic, plastic and visco-plastic programs. The model discussed in this paper is used in the third approach.

2 ANALYSIS OF ELASTIC STRESS STATE IN GROUT

Fig.1 shows 3 typical load-displacement curves from cable bolt pull tests. As one can see, between O and A, the relation is very linear. Refer to the corresponding load, F_e, as linear elastic limit load. After passing A, there are three possibilities: for simplicity, call these "hardening", "constant" and "softening" respectively. For these three general situations, the ultimate bond load, or post-elastic load,

Figure 1

could be larger than, equal to or smaller than the elastic load. From an engineering point of view, the elastic limit load and the ultimate bond load as well as their corresponding displacements are of primary importance.
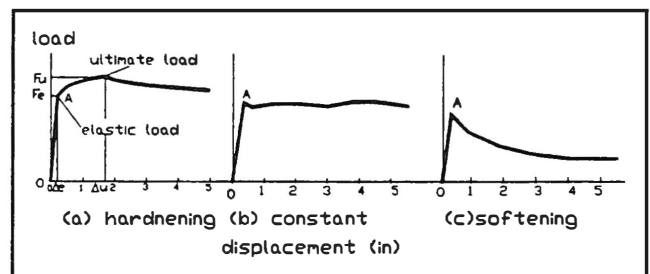
Under the pulling load there will be 3 stress components generated on the contact surface due to its geometry (Fig.2). Their relation is (see Tan, 1993):

$$p_r(z) = 0.2378h\, p_z(z)/\pi a$$
$$p_\theta(z) = 0.1944h\, p_z(z)/\pi a \qquad (1)$$

where a—radius of the cable strands; h—cable pitch length. From Eqn.(1) it can be shown that the hoop shear stress is 5 times as large as the axial shear stress. This may be useful in explaining why sand grout performs better than plain grout in helping to chose the optimum sand size distribution.

Laboratory tests (Reichert, 1991) show that the confinement stiffness greatly affects cable bolt bond capacity. To analyze the effect of confinement stiffness and stress field on cable bolt bond capacity, 2-D thick wall cylinder theory is used (Fig. 3). Radial displacement and stress on the outer wall of grout should be equal to those on the inner wall of the confining material. Using thick wall cylinder theory, it is easy to find that (Tan, 1993):

$$p_2^r(z) = C1/(C2+C3)\, p_1^r(z) \qquad (2)$$

Figure 2

where C (C= C1/(C2+C3)) is referred as confinement factor, it is a function of rock mass Young's modulus and Poisson's ratio, grout Young's modulus and Poisson's ratio and the diameters of cable and borehole. As confinement increases, C becomes larger and so does p_2^r. An increase in p_2^r will increase the threshold for the tensile hoop stress, (σ_θ), cracks the grout annulus.
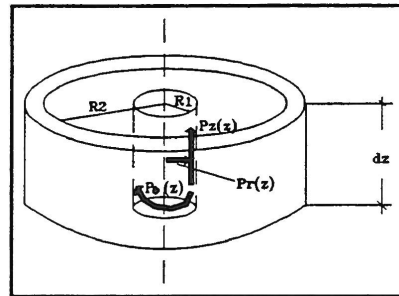
Radial stresses around the cable borehole in a stope consist of in-situ field radial stress $p_2^{rf}(z)$ and confinement induced radial stress $p_2^{r\,conf.}$: $p_2^r = p_2^{rf} + p_2^{r\,conf.}$. When the in-situ stress, p_2^{rf}, is compressive, (positive), it is equivalent to increasing the total confinement (ie. radial stiffness) and hence increasing bond. If the field stress becomes less compressive in magnitude during mining, cable bolts will lose some bond capacity.

We can now look at the elastic stress state in grout. It can be shown that, for a thick wall cylinder subjected to an internal pressure, p_1^r, and an external pressure (confinement induced plus field stress), p_2^r, the radial normal stress and the hoop normal stress in the grout cylinder are (using compressive stress as positive):
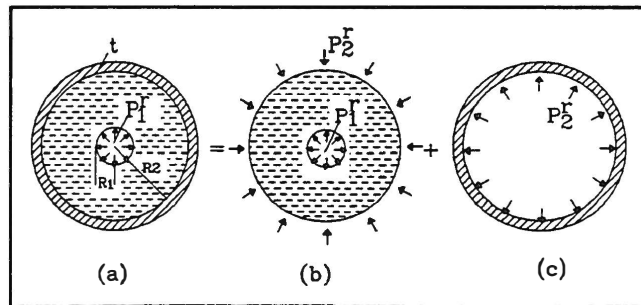
Figure 3

$$\sigma_r = p_1^r \frac{(\frac{R_2}{r})^2 - 1}{(\frac{R_2}{R_1})^2 - 1} + p_2^r \frac{1 - (\frac{R_1}{r})^2}{1 - (\frac{R_1}{R_2})^2}, \qquad (3)$$

$$\sigma_\theta = -p_1^r \frac{(\frac{R_2}{r})^2 + 1}{(\frac{R_2}{R_1})^2 - 1} + p_2^r \frac{1 + (\frac{R_1}{r})^2}{1 - (\frac{R_1}{R_2})^2}, \qquad R_1 \leq r \leq R_2 \qquad (4)$$

Hoop shear stress induced by hoop shear force $p_\theta(z)$ is:

$$\sigma_{rz}(z,r) = \frac{R_1}{r} p_z(z), \qquad R_1 \leq r \leq R_2 \tag{5}$$

Axial shear stress induced by axial shear force $p_z(z)$ is:

$$\sigma_{r\theta}(z,r) = \frac{R_1^2}{r^2} p_\theta(z), \qquad R_1 \leq r \leq R_2 \tag{6}$$

In Eqn.(3),(4),(5) and (6), R1, R2 are the radii of the cable and the borehole respectively. R1 $\leq$ r $\leq$ R2 represents the grout. These stresses are shown in Fig.4.

3 DETERMINATION OF LINEAR ELASTIC LIMIT LOAD

Linear elastic limit load depends on confinement, stress level, grout quality and embedment length. It is too complicated for an analytical solution at this point. But we can consider two extreme situations — no confinement and complete confinement. The "no confinement" case results in an induced radial pressure at the grout outer wall $p_2^r = 0$, while the "complete confinement" results in the radial displacement at the grout outer wall $u_r^{R2} = 0$. We must now determine the

Figure 4

elastic limit load corresponding to these two extremes, (minimum and maximum), and then for different confining loads between the extremes.
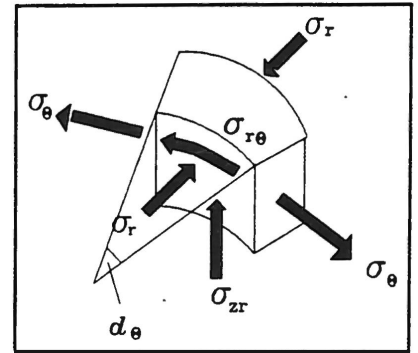
For the no confinement situation, when the radial cracks initiate at the grout-cable contact they propagate unstably outwards. Since there is no external confinement on the grout, the cable bolt will lose capacity immediately. The minimum elastic limit load then equals the initiation load for radial cracks in grout.

$$F_{min} = 2\pi R_1 L^0 (8{\sim}10) \% UCS_g \frac{R_2^2 - R_1^2}{R_2^2 + R_1^2} \frac{\pi a}{0.2378h} \tag{7}$$

where L^0 — embedment length, UCS_g — grout uniaxial compressive strength.

For complete confinement, cable strands would have to completely shear off the grout ridges in order for large displacements to occur. The governing condition for the maximum elastic limit load is then: Shear stress on grout ridges equals shear strength of grout. An acceptable prediction of the shear strength of the grout is that it equals half of the UCS of the grout. The above discussion gives the maximum elastic limit load as:

$$F_{max} = 2\pi R_1 L^0 \frac{50\% UCS_g}{\sqrt{(\frac{0.1944h}{\pi a})^2 + 1}} \tag{8}$$

Laboratory test data (Reichert, 1991) has been checked against the above two equations, all the test results fall between the two lines generated from Eqn.(7) and (8). The result for heatshrink (close to no confinement) falls right on the no confinement line.

Interpolation for F_e^*, the elastic linear limit load of a practical situation where the actual confinement lies somewhere between complete confinement and no confinement is obtained through regression of the test data from Reichert (1991) and Goris (1989). It results in:

$$F_e^* = (0.17 + 0.40\ C_3/(C_2+C_3))(F_{max}-F_{min}) + F_{min} \qquad (9)$$

Eqn.(9) is valid for those cables whose embedment length is equal to 254 mm (10"). Cable tests by Fuller et. al.(1988), Goris(1989), and Reichert, Bawden and Hyett(1992,1991) has shown a linear relation of load capacity with embedment length. From Goris' and Reichert's research, we get an embedment length factor f_l :

$$f_l = 1 + 0.7(L - 0.25)/0.25$$

where L is the actual embedment length (in meter, 10 inch = 0.250 m). For example, a cable with 500 mm (20 in) embedment length will have the elastic limit load as large as 1.7 times (not 500/250 = 2 times) that of 250 mm (10") embedment. Now Eqn.(9) could be written as:

$$F_e = f_l\ F_e^* = f_l\ \{(0.17 + 0.40\ C_3/(C_2+C_3))(F_{max}-F_{min}) + F_{min}\} \qquad (10)$$

4 POST ELASTIC FAILURE MODEL AND THE CABLE BOLT LOAD INCREMENT ΔF

As discussed previously, following elastic failure, the remaining resistance is mobilized by shearing of grout ridges. The post elastic failure model is illustrated in Fig.5.

Under a pulling force, the grout block will begin to move. This movement is resisted by the shear strength of the interface, (i.e. the friction angle, ϕ, and the dilation angle α between the cable and the grout, (Fig.5). Decreasing of confinement (deteriorating ground condition) and field stress (stress changes due to excavation) will result in smaller normal pressure p_r and hence less axial shear resistance p_z and so less cable bonding capacity, and vice versa.
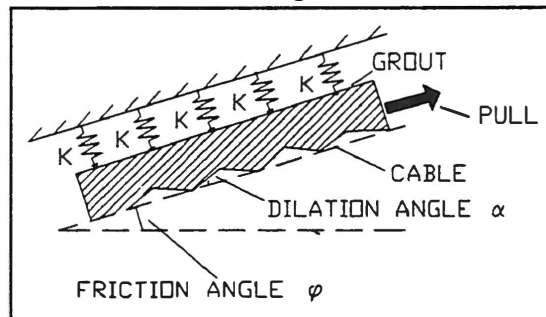
Figure 5

According to the model shown in Fig.5, the post-elastic axial shear bond increment is:

$$\Delta p_z = tg(\phi + \alpha)\ \Delta p_r \qquad (11)$$

The value of $(\phi + \alpha)$ is found about 18°. Δp_r is a function of the UCS_g and a confinement stiffness factor K_c, while K_c is defined as:

$$K_c = p_1^r / u_r^{R1} \qquad (12)$$

where p_1^r is the radial pressure at the grout inner wall, (by the cable), and u_r^{R1} is the corresponding radial displacement, (see Fig.6).

244

The analysis to the wedge gives:

$$K_c = (E_g^{-1} \ln((R1+R2)/2R1) + (2G_s)^{-1})^{-1} \qquad (13)$$

Assume: $\Delta p_r = a_1 + a_2 K_c + a_3 UCS_g$, a regression of the test result of Reichert et al., (1991), and Goris (1989) gives:

$$\Delta p_r = -3.42 + 0.0006 K_c + 0.10 UCS_g \qquad (14)$$

In this equation, Δp_r, K_c, UCS_g and the constant 3.42 are all in the unit of MPa.

Finally the post-elastic cable load increment is:

$$\Delta F = 2\pi R_1 f_l L^0 \Delta p_z \qquad (15)$$

where f_l is the embedment length foctor and $L^0 = 0.25m$.

5 IN-SITU STRESS EFFECT AND THE CALCULATION OF RESULTING CABLE BOLT LOAD INCREMENT

Kaiser, Maloney and Yazici(1992) have found that large stress changes (>25MPa) occurred in the hanging wall of Winston Lake mine as mining proceeded. They expected cable bond strength loss associated with this stress change may range from 50% to 100%.
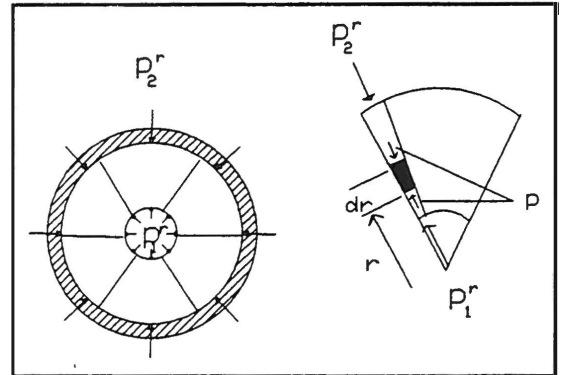
Figure 6

Hyett and Bawden(1993, in preparation) did a systematic laboratory test on the confining stress effect on cable bolt bond strength. Observation of their test results leads to the following conclusions:
(1) In all cases, the higher confining stress results in higher pull load.
(2) No direct relation between grout water/cement ratio and the cable bolt pull load increase due to the confining stress changes.
(3) The increase of the pull load due to the increase of confining stress is more profound in the lower stress level. This is maybe because at the higher stress level, more grout flutes get crushed , so both the friction coefficient and the friction area get smaller.

It is accepted that the cable bolt support system is of a frictional nature due to the geometry of the cable strand. Fig.7 is a conceptual model. The stress change $\Delta\sigma$ will lead to the change of shear stress Δp_z on the contact surface between cable and grout and hence cable bolt load change ΔF_σ. For this simple friction model, the following relation exists:

$$\Delta p_z = \Delta\sigma \, tg \, \varphi \qquad (16)$$

where φ is the friction angle due to the confining stress change. Although the data is scattered

to some degree, the analysis of Hyett and Bawden's test results gives the friction angle φ at around $20 \sim 22^0$. However φ should be left as an input parameter in the implement program, so that it can be changed by the modeller.
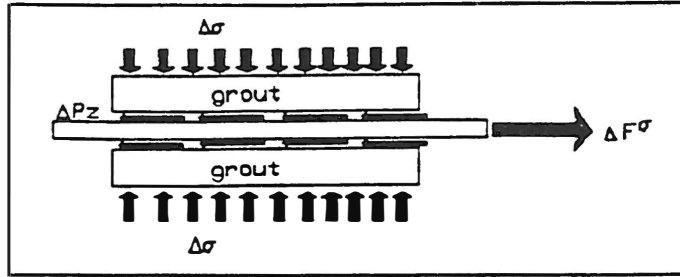
Figure 7

The total pull load increase should then be:

$$\Delta F_\sigma = 2\pi R_1 \, L \, \Delta p_z = 2\pi R_1 L \, \Delta\sigma \, tg \, \varphi \quad (17)$$

where $2\pi R_1 \, L$ is the simplified friction area between cable and the grout, L is cable's embedment length, R1 is the radius of cable bolt.

Now the total cable load force (i.e. total cable capacity) can be found by:
(i) in elastic stage:

$$F = F_e = F_e^* + \Delta F_\sigma \quad\quad (18)$$

(ii) in post elastic stage:

$$F = F_u = F_e + \Delta F = F_e^* + \Delta F_\sigma + \Delta F \quad\quad (19)$$

6 DISPLACEMENT ANALYSIS AND THE CABLE BOLT LOAD-DISPLACEMENT RELATIONSHIP

A theoretical analysis of the displacement is extremely difficult and is believed, at this time, to be practically unrealistic. It is much more complicated than the stress analysis. Since there are 3 different materials (cable, grout and confining materials), and many different failure mechanisms occurring, (e.g. grout cracking and crushing, contact and compression between cable and grout, cable untwisting and plastic deformation of the grout and rock mass, etc.), one would have to make very significant simplifications for a deformation analysis.

Fortunately, both Goris and Reichert's testing show a similar general displacement character, (refer to Fig. 8). It is described below:
(1)Δ_e, the displacement corresponding to elastic limit load, is about $3 \sim 4mm$ for samples of 250mm (10") embedment length. As the embedment length increases, this displacement increases proportionately.
(2) Δ_u, the displacement corresponding to ultimate bond load, occurs at total displacement of about $36 \sim 40mm$ for samples of 250mm embedment length.

If we take $\Delta e = 3mm$, $\Delta u = (3+34) = 37mm$ for a 250mm (10") embedment length. Then for cables with longer or shorter embedment length, a reasonable expansion is:

$$\Delta_e = f_l \times 3mm$$
$$\Delta_u = \Delta_e + 34mm \quad\quad (20)$$

where f_l is the embedment length factor.

246

Most test results show that, following the ultimate bond at about 40mm displacement, the bond may remain nearly level up to 150 mm (6") displacement or more, or it may drop off. For simplicity, it is assumed here that this drop or rise is negligible, and the ultimate bond remains constant. It should be noted, however, that although the so-called "perfect plastic behaviour" is taken, it should not be concluded that this model could only take the constant load path after the ultimate cable load F_u is reached. In fact it can take any load path. This is because the existence of ΔF_σ, the in-situ stress effect, in Equ.(18) and (19).

As shown in Fig.9, there are two load-displacement curves, one for stress state 1, the other for stress state 2. As mining proceeds, if the in-situ stress changes from state 1 to state 2, then the load-displacement path will jump from curve 1 to curve 2, showing a reduction in cable bolt capacity.
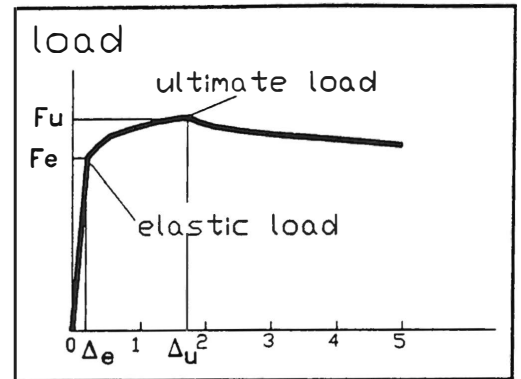
Figure 8

Using Fig. 10, one can construct a cable bolt load-displacement relation by using a multi-segment format. The model consists of 4 straight line segments. Segment 1 is the elastic deformation line. The post elastic failure hardening, (or softening or constant), curve is divided into two segments, segment 2 and segment 3, with the segment break point as shown. Following ultimate bond the curve continues as a horizontal segment, segment 4. This multi-segment format is parallel with the discussion by Potvin et. al.(1989) except the increasing friction curve section in their discussion is represented by two straight segments 2 and 3. Equations for the 4 segments discussed above are:
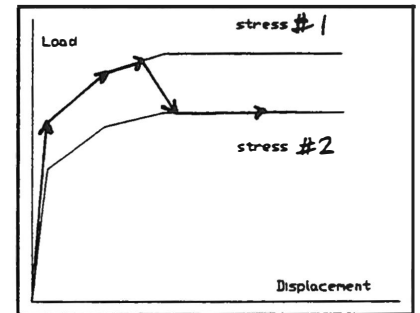
Figure 9

$$
\begin{cases}
F = \dfrac{F_e}{\Delta_e}\Delta, & \Delta \leq \Delta_e & (Seg.1) \\[2mm]
F = F_e + \dfrac{4}{3}\dfrac{\Delta-\Delta_e}{\Delta_u-\Delta_e}(F_u-F_e), & \Delta_e < \Delta \leq \Delta_e + \dfrac{\Delta_u-\Delta_e}{2} & (Seg.2) \\[2mm]
F = F_u - \dfrac{2}{3}\dfrac{\Delta_u-\Delta}{\Delta_u-\Delta_e}(F_u-F_e), & \Delta_e\,\dfrac{\Delta_u-\Delta_e}{2} < \Delta \leq \Delta_u & (Seg.3) \\[2mm]
F = F_u, & \Delta => \Delta_u & (Seg.4)
\end{cases}
\tag{21}
$$

7 IMPLEMENTING THE MODEL INTO FLAC AND UDEC

The above model has been implemented into the 2D numerical stress analysis codes, FLAC and UDEC. Both have been checked against laboratory pull test simulations. Both have also been used to model the Winston Lake Mine problem (Maloney and Kaiser, 1990). Due to space limitation, only UDEC model is discribed herein.

The Winston Lake Mine ore body is located within the Big Duck Lake volcanic sequence . The

ore body varies in thickness from 2 to 20m horizontally, averaging 7m and dips at 50° to the east. A gabbroic intrusion forms the immediate hanging wall except in the thinner ore zone (60% of the ore body) where a thinly banded cherty ash, up to 20m thick, lies intermediate. The immediate footwall also varies, being either an altered mafic flow or an altered rhyolite. The ore zone contacts are generally sharp and commonly marked by a 1 to 3mm chloritic seam.
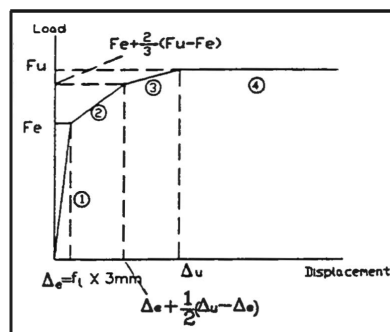
Figure 10

3 major joint sets were observed in the massive ore body.
Set A: − striking N/S, dipping 43°E, parallel to the ore body;
Set B: − striking E/W, approximately vertical;
Set C: − striking N/S, dipping 43°W, perpendicular to the ore body.
In the hanging wall the joints are less pronounced and the rock is more massive.

Ground control problems occur in two fundamental ways:
(1) In narrow stopes, chert delamination from the hanging wall has caused excessive dilution;
(2) In wide overcuts (> 8m) large wedge type failures have occurred.

The model set up is shown in Fig.11. A detailed view is shown in Fig.12. All blocks are fully deformable. The chert layer is modelled by few layers of blocks with the total width 6m. The stope width is 10m, height 20m. Two stopes have been simulated: the lower stope has been excavated and, after some time stepping, backfilled with uncemented waste (properties modelled as 1/10 that of the ore body and 0 strength on joints). Then the top stope has been simulated with or without cable bolts. The chert layer, orebody and the backfill are modelled as Mohr-Coulomb material with different material properties. The hanging wall and the foot wall are modelled elastically. All the property data come from Maloney and Kaiser (1990).

Fig.13 shows the no-cable case result, cherty immediate hanging wall has delaminated and the topsill has wedge failure in the back as observed in the field. Tensile areas appeared both in the hanging wall and the topsill corner (hanging wall side).

Fig. 14 is the cable bolt layout for case 2. Cable spacing in out-of-plane direction is 2m. Average cable toe spacing is 2m. Seven cables are in the topsill back and ten in the hanging wall. The numbers show the locations of the "history monitor variables" in UDEC. Fig.15 shows that the bolts have stabilized the lower part of the cherty hangingwall and a large part of the topsill back. But, the upper part of the cherty hangingwall still delaminates and falls. This matches well with the field observation (Maloney, personnel communication,1993). From Fig. 14 it seems that the cable density in this area is too low and the cable orientation is not favourable, both linked to the location of the cable bolt access drift. Also the low stress level (in the tensile area, especially) has reduced the cable bond capacity in this area. Fig.16 is the stress trajectory plot. It indicates that, in the cherty hangingwall, in the topsill back (up to 5 to 15m) and in the backfill, the stress levels are very low. It also suggests that the back failure is more gravity driven than stress driven. Fig.17,18 & 19 represent the modelled cable bolt axial force change. These curves show that the cables in the back of topsill and in the upper part of hanging wall experienced excessive load changes (some cable loads dropped almost 70%). This change is made possible by a

248

Figure 11

Figure 12

Figure 13

Figure 14

Figure 15

Figure 16

Figure 17

Figure 18

Figure 19

Figure 20

Figure 21

Figure 22
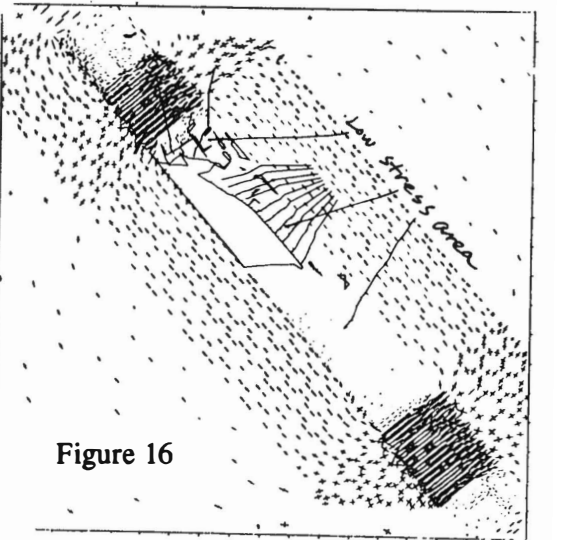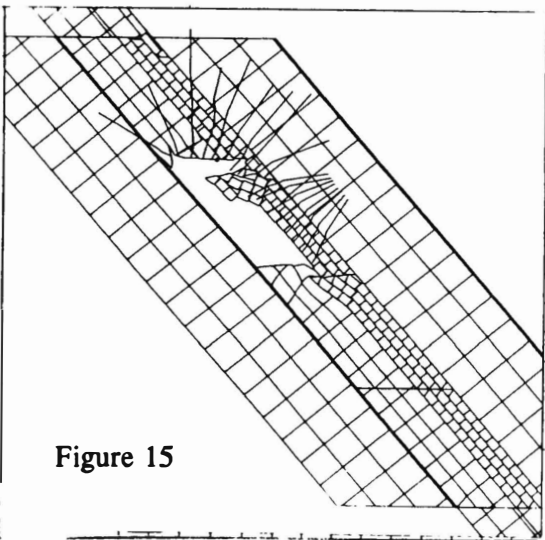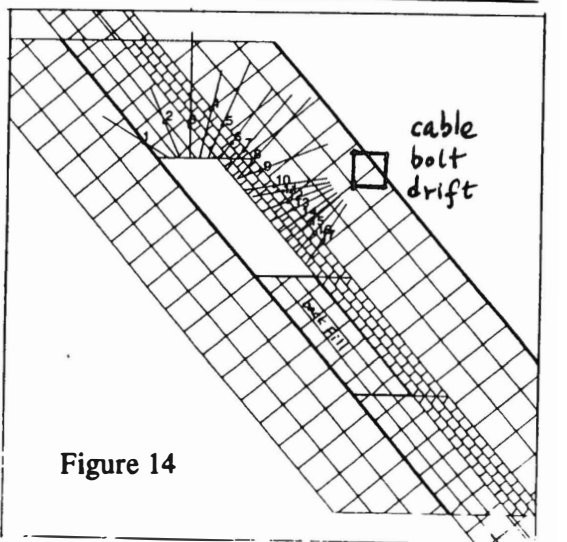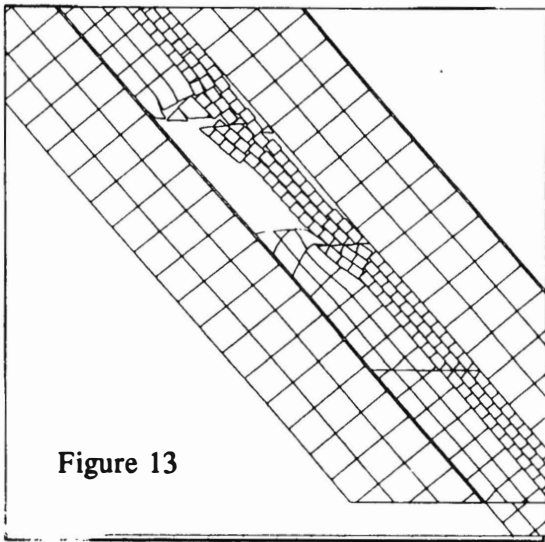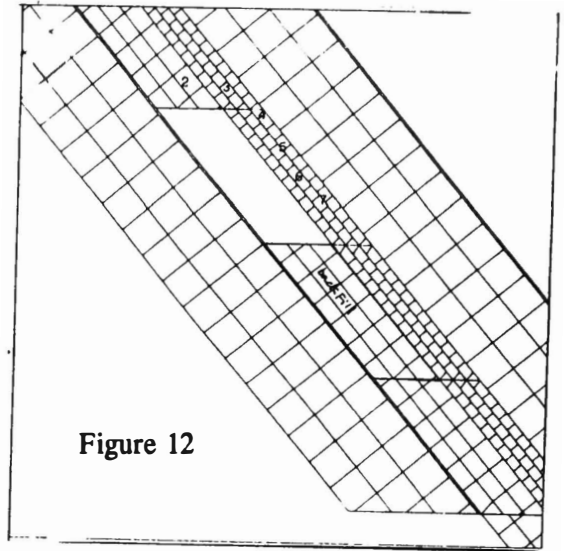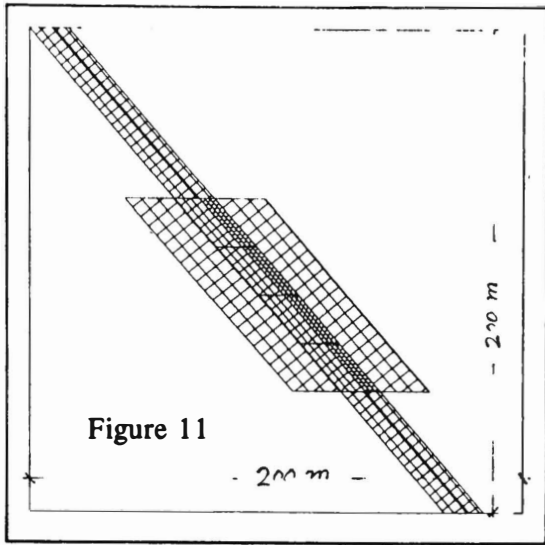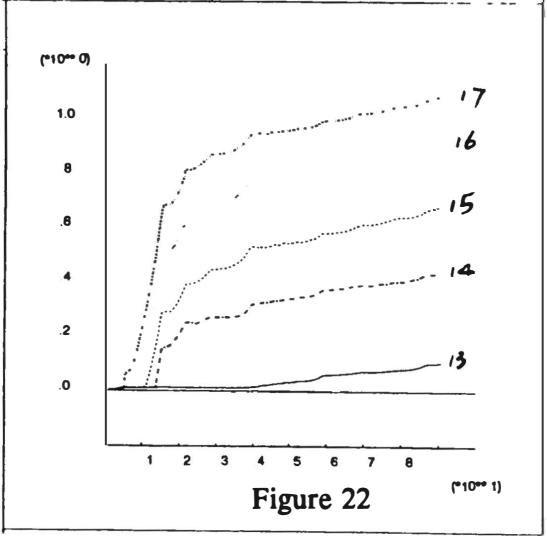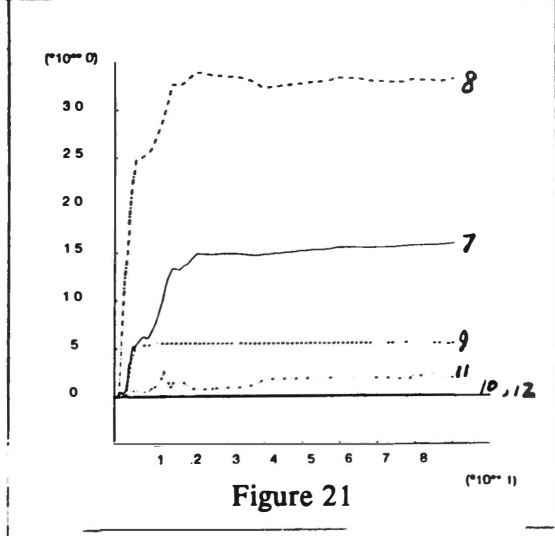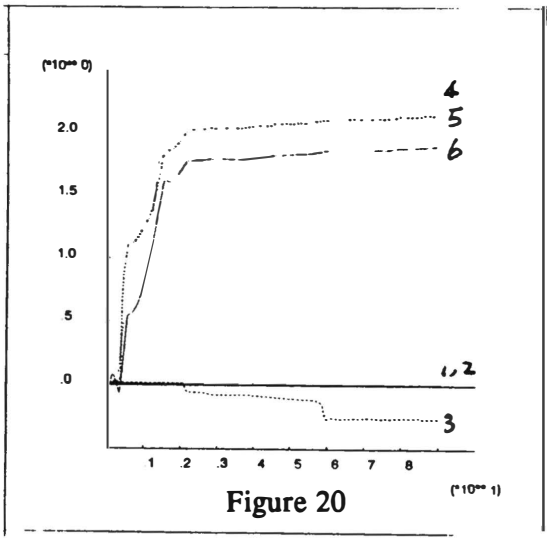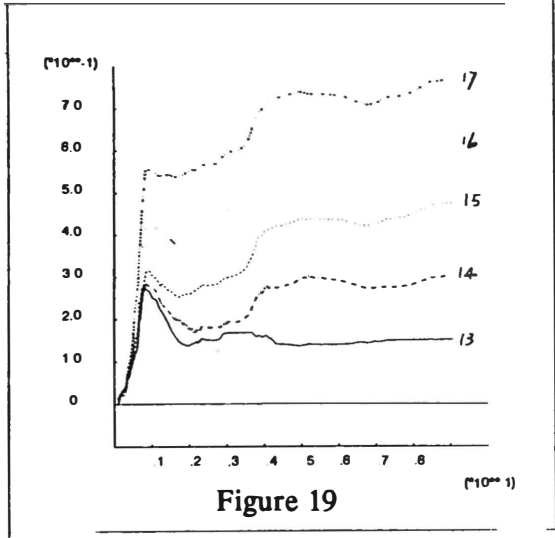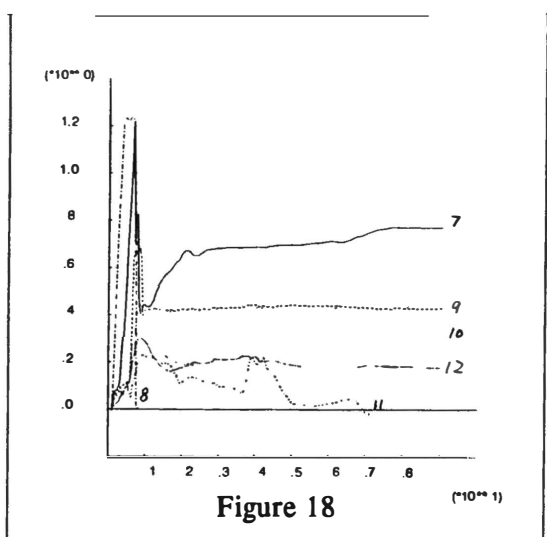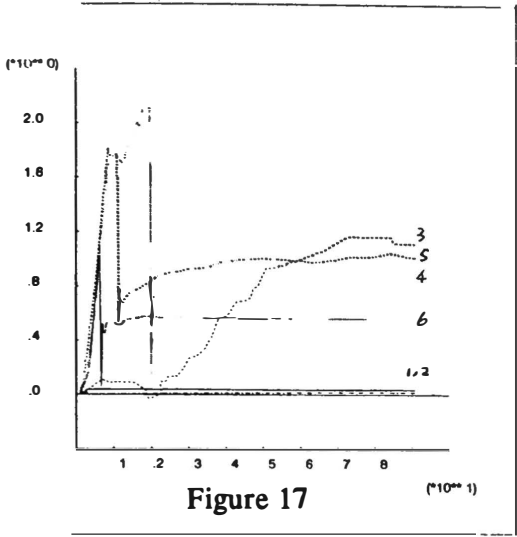
combination of many factors, such as the relative displacement between cable and rock mass, and the field stress change. Fig.19 shows that the cables in the lower part of hangingwall have more stable loads since both the stress and displacement in this area are more constant. From the modelling and the field observation, it seems to be reasonable to conclude that cable bolting alone will only reduce, not eliminate, the dilution from the hangingwall. Relocating the cable bolt access drift above the topsill will benefit the cable bolt orientation and density in the upper part of the hangingwall. And also, installation of cable bolt support in the hangingwall one or two stopes up, in advance of mining, may also help reduce the "push" from the cherty hangingwall near these stopes. More simulations with different cable bolt layouts and different geometries of stopes and hangingwall are undergoing (Tan & Maloney).

Fig.20,21 & 22 represent the modelled cable bolt axial force change using the previously available cable bolt model in UDEC. The parameters used in this simulation are the same as those in the previous one. These curves represent a very stable cable bolt performance, nearly perfectly plastic. This does not agree with field observation (Kaiser, Maloney and Yazici,1992).

8 CONCLUSIONS

(1) The forms of the equations presented for the cable bolt model come from the analysis of the stress state in the grout, the interaction between cable bolt, grout and rock mass, and the cable's geometry. The coefficients in these equations come from the data analysis of cable bolt pull test, in laboratory and field, performed by Reichert (1991), Goris (1989) and Hyett et al. (1993). The model takes account on grout quality, rock mass stiffness, field stresses and borehole diameter, etc.

(2) The input parameters are not difficult to obtain. Other than rock mass properties already required for any rock mechanics numerical model, this cable bolt model only needs the grout Young's modulus, Poisson's ratio (about 0.18), UCS and borehole diameter. If no grout test data is available, grout water/cement ratio usually gives a very reliable estimate (Hyett, Bawden and Reichert, (1992)).

(3) The model has been implemented to UDEC and FLAC. Test runs on Winston Lake Mine quasi-AVOCA-longhole stope hanging wall stability problem have shown that the cable bolt load changes drastically due to the changes in rock mass stress and displacement state. The new cable bolt model allows improved estimation of the cable bolted ground over previously available models.

REFERENCES

1. Evaluation of design bond strength for fully grouted cables, Bawden,W.F., Reichert, R.D., and Hyett, A.J., July 1992, CIM Bulletin Vol. 85, No. 962

2. Cable support design for underground mines, Fuller, P.G., Dight, P.M. & West, D. 1990, 92nd Annual General Meeting of CIM

3. Laboratory pull testing of short grouted cable bolts, Fuller, P.G., Dight, P.M. & West, D. 1988,   4. Cable bolt support in mining — A keynote lecture, Fuller, P.G., 1983, Proceedings of the International Symposium on Rock Bolting

5. Grouted flexible tendons and scaling investigations, Goris,J.M., Conway,J.P., 1987, World Mining Congress, Stockholm, Sweden

6. Laboratory evaluation of cable bolt supports   Part 1 Evaluation of supports using conventional cables, Goris,J.M., 1989 (Internal report)

7. The effect of rock mass confinement on the bond strength of fully grouted cable bolts, Hyett, A.J., Bawden, W.F., Reichert, R.D., 1992, Int. J. Rock Mech. Min. Sci. & Geomech. Abstr., Vol.29, No. 5, pp. 503-524

8. Effect of stress changes on the bond strength of fully grouted cables, Kaiser, P.K., Yazici, S. and Nose, J., 1992, Int. J. Rock Mech. Min. Sci. & Geomech. Abstr., Vol.29, No. 3, pp. 293-306

9. Winston Lake monitoring project (Data report): Support of a hanging wall by cable bolts, Maloney, S.M. and Kaiser, P.K., 1990, (Internal Report)

10. A Laboratory and Field Investigation of The Major Factors Influencing Bond Capacity of Grouted Cable Bolts, Reichert, R.D., 1991, Master Thesis, Queen's University, Kingston, Canada

11. Stability of rock masses reinforced by passive, fully-grouted rock bolts, Sharma, K.G., Pande, G.N., 1988, Int. J. Rock Mech. Min. Sci. & Geomech. Abstr. Vol. 25, No.5 pp 273-285

12. Rockbolts: A new numerical representation and its application in tunnel design, St.John, C.M., Van Dillen, D.E., 1983, 24th U.S. Symposium on rock mechanics

13. Experimental investigation of steel cables for rock reinforcement in hard rock, Stillborg, B., 1984, Doctoral thesis, Lulea University of Technology, Sweden

14. A new cable bolt load-displacement relationship and its implementation into FLAC and UDEC, Tan, G., 1993, Doctoral thesis, Queen's University, Canada

15. Bond strength of grouted cable bolts, Yazici, S. and Kaiser, P.K., 1992, Int. J. Rock Mech. Min. Sci. & Geomech. Abstr., Vol.29, No. 3, pp. 279-292

BEHAVIOR OF A STEEL-LINER-AND-BOLTS SYSTEM UNDER VERY HIGH THERMAL AND MECHANICAL LOADING

François E. Heuze, and Robert P. Swift
Lawrence Livermore National Laboratory, Livermore, CA

Leslie R. Hill, and William H. Barrett
Sandia National Laboratories, Albuquerque, NM

ABSTRACT

This work involved the response of a liner-bolt system installed on the wall of the DIAMOND FORTUNE cavity, a 22-m diameter nearly semi-spherical chamber in tuff, at the Nevada Test Site. DIAMOND FORTUNE is a low-yield nuclear test of the Defense Nuclear Agency which was performed in April, 1992. A 1.4-m square, 2.5-cm thick steel plate was anchored by 9-m long bolts: four 2.5-cm diameter bolts at the corners and a 5-cm diameter bolt at the center. The bolt ends daylighted in a tunnel surrounding the cavity, and were tensioned from there. The system was equipped with 20 data channels for strain, acceleration, contact pressure, and temperature. We relate the thermal analyses and the 3-dimensional dynamic analyses performed for this project, and we present the test results which indicated the excellent response of this system to the high dynamic loads and temperatures.

RESUME

Ce project concerne la réponse d'un blindage d'acier ancré par boulons pré-contraints à la paroi d'une cavité hémisphérique de 22-m de diamètre, sous l'action du tir nucléaire à faible puissance, DIAMOND FORTUNE. Ce test a été effectué dans un tuff volcanique au Centre d'Essai du Nevada, en Avril 1992. Le blindage de 1.4-m sur 1.4-m, épais de 2.5-cm était ancré par 5 barres d'acier longues de 9-m; 4 aux coins, avec un diamètre de 2.5-cm et une au centre, avec un diamètre de 5-cm. Les barres se terminaient dans une gallerie adjacente, d'ou elles pouvaient être tensionées. Le système était doté de 20 canaux d'acquisition de données pour déformations, accélérations, pressions de contact, et température. On présente les analyses thermiques et les analyses dynamiques en 3-dimensions, et on les compare aux résultats de ce test qui révèlent l'excellent comportement du système sous les fortes charges thermiques et mécaniques.

INTRODUCTION AND OVERVIEW

In the early 1980's, the idea was put forth to provide a reusable underground cavity in which a series of low-yield nuclear explosions could be performed for the purpose of research in weapons physics and non-weapon high-energy physics. The concept, now designated as CONVEX (COntained Nuclear Vessel EXperiment), is a joint effort of three DOE laboratories (LANL, LLNL, SNLA), and the Defense Nuclear Agency (DNA). Early studies by Heuze (1983) on HEDEF (High-Energy Density Experimental Facility), a precursor of CONVEX, concluded that a steel-lined rock cavity would offer containment advantages over a free-standing steel vessel. In addition, the steel liner would be pre-stressed against the rock by bolts that daylight in tunnels adjacent to the cavity, as proposed by Heuze and Thorpe (1983). This concept was tested recently, as an add-on to the low-yield nuclear test of the DNA, DIAMOND FORTUNE, executed in an 11-m radius hemispherical underground chamber in tuff, in April 1992. Our experiment was called the CONVEX Liner Add-on.

This paper presents a summary of the data obtained on the CONVEX Liner Add-On, describes numerical simulations of the experiment, and gives comparisons of the measured data and results of calculations. The data analyzed include strains on the tensioned bolts and on the steel liner plate, stresses in the grout/rock backing the liner, temperature on the back of the plate, and accelerations on the plate and in the rock pillar. The quality of the data obtained is very good, and the response features captured by the different data sets are quite similar and reveal the complex nature of the flow field inside the cavity. Calculations were performed using three-dimensional, static and dynamic, finite-element codes, developed at LLNL. NIKE3D, described by Maker et al. (1991), was used to simulate the pre-test bolt tensioning condition. DYNA3D, described by Hallquist and Whirley (1991), provided the dynamic response of the bolt/liner/rock system. Pre-test calculations were performed to guide instrument choice, location and recording ranges, to set the tensioning of the bolts, and generally, to produce confidence that the liner system would survive the environment and remain operational. Post-test calculations were performed with the best estimate of the actual cavity pressure history at the liner plate, obtained from measurements and flow field calculations. Experimental measurements showed that the bolts remained in a tensioned state throughout the duration of the test. Hence, the bolt tensioning used (about 330 Mpa) was sufficient to offset the compressive air blast loading. They also showed that the liner plate maintained firm contact with its grout-rock backing, thus fulfilling the main operational objective of the test.

LINER EXPERIMENT

Configuration and Instrumentation

The liner experimental configuration consisted of a steel plate anchored vertically to the cavity wall by four corner bolts and a centerbolt, with the bolts daylighting in an adjacent "run-around" drift (Figure 1). The cavity rock consisted of volcanic tuff located in the P-tunnel complex at the Nevada Test Site. The plate is 1.4 m square, 2.54 cm thick, and made of A36 steel. The bolts, 2.54 cm and 5.08 cm in diameter at the corners and center, respectively, are about 9 m long and made of 1045 steel. A thin layer of rock-matching grout, about 5 cm thick, was used between the plate and rock to provide a smooth bearing surface for the plate. The bolts were tensioned to about 330 Mpa, less than 50% of their yield strength. This initial pre-tension load was selected on the basis of preliminary calculations indicating that the bolts would remain in tension during the dynamic loading.

The corner bolts were grouted in their boreholes after tensioning. The centerbolt was encased in a 10 cm diameter schedule 40 pipe casing. The annulus between the casing and the bolt was filled with *Vistanex* (an inert non-toxic hydrocarbon polymer made by EXXON Chemical Company) for containment purposes. The casing was cemented in the pillar.
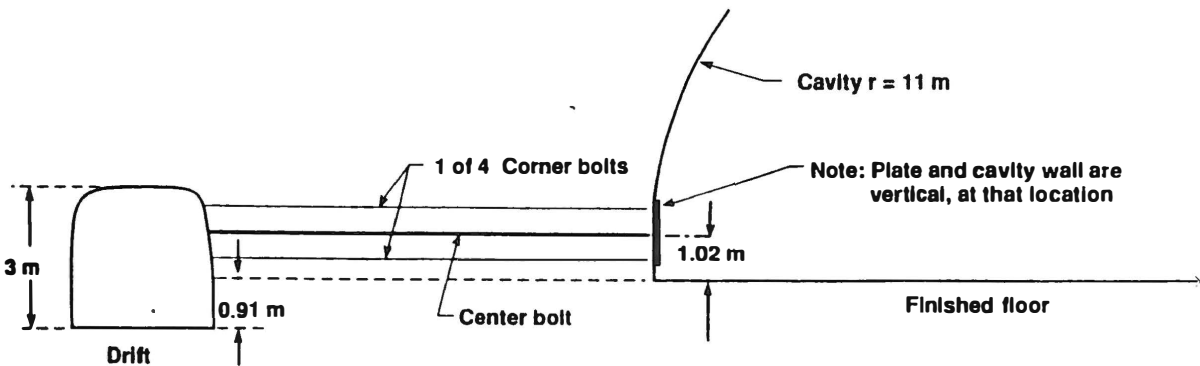
Figure 1. Geometric lay-out of CONVEX Liner Add-On; elevation.

The set of diagnostics, shown in Table 1, was adapted to a 20 data channel allotment to provide the mechanical and thermal response of the liner/bolt/rock system. The desired measurements included: horizontal and vertical strains, acceleration, and temperature on the back of the plate; axial strains and bolt loads for the centerbolt and corner bolts; contact pressure between the plate and the rock; cavity wall pressure; and acceleration inside the 9 m rock pillar separating the cavity and run-around drift.

Table 1. Instrumentation for the CONVEX Liner Add-On.

		Strain	Stress	Accel.	Pressure	Temperature
Plate:	4 Strain Gauges	√				
	1 Accelerometer			√		
	1 Thermocouple					√
Plate/Rock:	2 Toadstools				√	
Center bolt:	4 Strain Gauges	√				
	1 Load Cell		√			
Corner bolt:	2 Strain Gauges	√				
	1 Load Cell		√			
Rock Pillar:	3 Fluid-Coupled Plates				√	
	1 Accelerometer			√		

Summary of Test Results

As indicated in Figures 2 and 3, the salient feature of the test was the fact that the instruments showed the whole system retaining strong tension and contact with the rock throughout the dynamic phase. Figure 2 is the time history of 4 longitudinal strain gauges on

255
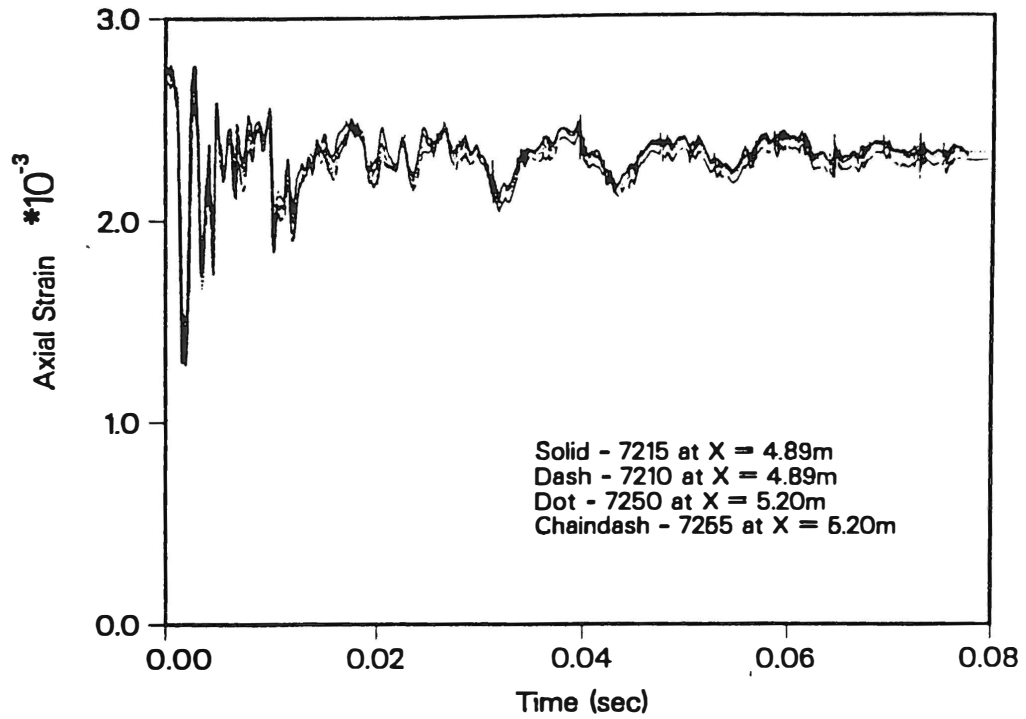
Figure 2. Measured responses of axial strain gauges on the centerbolt.
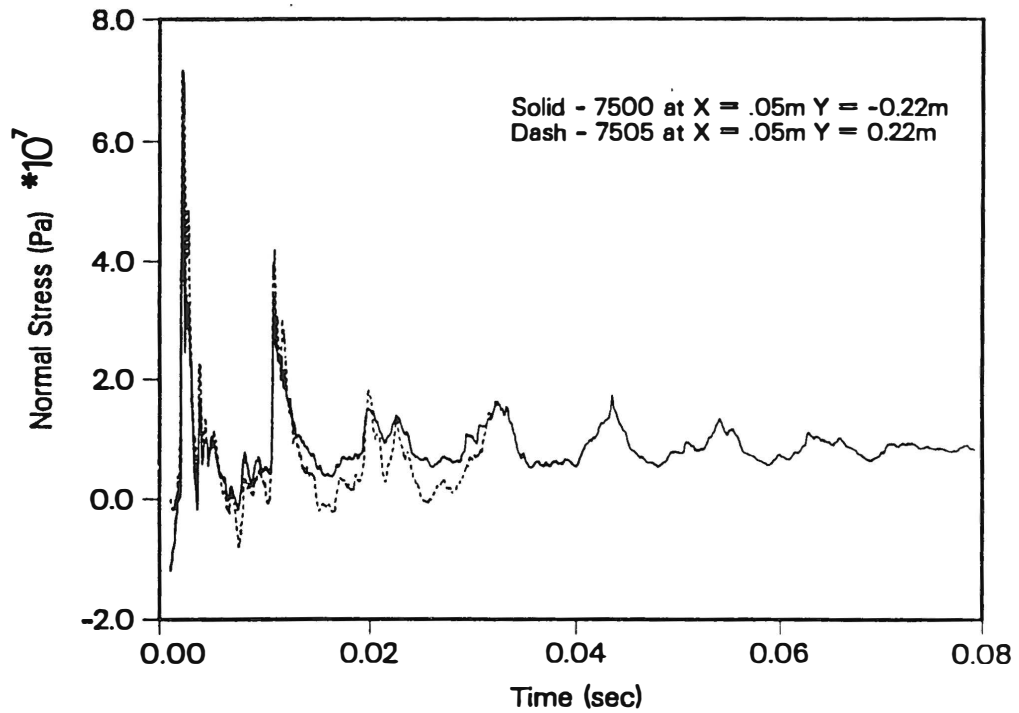
Figure 3. Measured responses of pressure gauges in grout between the liner plate and the rock.

the center bolt within a 30-cm section. The first aspect to note is the excellent reproducibility of the strain records. The second is the fact that the bolt quickly regained up to 80 percent of its original tension, after the first few milliseconds. Such behavior was also true of the only strain-gaged corner bolt (not shown), which retained over 85 percent, of its original tension. Figure 3 shows the time history of the two "toadstool" gages measuring the stress in the grout perpendicular to and behind the plate. The two instruments again gave consistent results, and the remaining gauge at 80 ms shows a strong contact pressure. Another remarkable feature of the test data is the consistency of various stress and strain records in showing the history of cavity pressure oscillations (Figure 4).

Regarding the thermal environment, the strain-gages could operate up to a maximum of 175 C. As shown in Figure 5, more than 10 seconds elapsed before this temperature was reached on the back of the plate. There was no need for temperature correction of gauge readings in the dynamic phase.

CALCULATIONS

Thermal Calculations

The TOPAZ2D finite element code (Shapiro, 1986) was used to estimate the temperatures in the plate, grout, and rock. For simplicity, the grout and rock were given constant thermal temperatures, although temperature-dependent properties of the grout are available (Moss et al, 1982; Zimmerman, 1982). Figure 5 shows the input temperature in the cavity, i.e. on the front side of the liner plate (A), and the expected histories on the back of the plate (B), and in the middle of the grout (C). Clearly the temperature gradients are very high. The actual temperature record (D) was well within the range of expectations, even with a simple model.

The 3-D Mechanical Model

The approach to numerically simulate the CONVEX plate/bolt/rock system consisted of defining the equilibrium state due to bolt tensioning, using NIKE3D, and mapping the equilibrium conditions into DYNA3D as initial conditions for the dynamic response calculations. Views of the three-dimensional model are given in Figures 6 and 7, showing the upper-right quadrant of the system that extends back from the cavity face into the rock. The quadrant geometry reflects the symmetry of the experiment about the axis of the centerbolt. The model extends axially outward, 9 m, to the run-around alcove where the wall buffer plates and holding nuts for the centerbolt and cornerbolt are secured. A total of 22,706 solid-brick elements were used in the static model along with 19 slide surfaces. The dynamic model is identical to the NIKE3D model, plus 2139 additional elements and 4 slide surfaces extending the rear of the model into the grout-enclosed run-around region and beyond into the rock to a range of 50 m. Slide surfaces include the steel bolt-steel plate, steel plate-buffer plate, steel plate-grout, steel bolt-grout, and rock-grout interfaces. Both the centerbolt and the cornerbolts were tied to the nuts and plates at the cavity and rear surfaces. The boundary conditions on the top and right outer rock surfaces allowed no vertical and no horizontal motion, respectively.
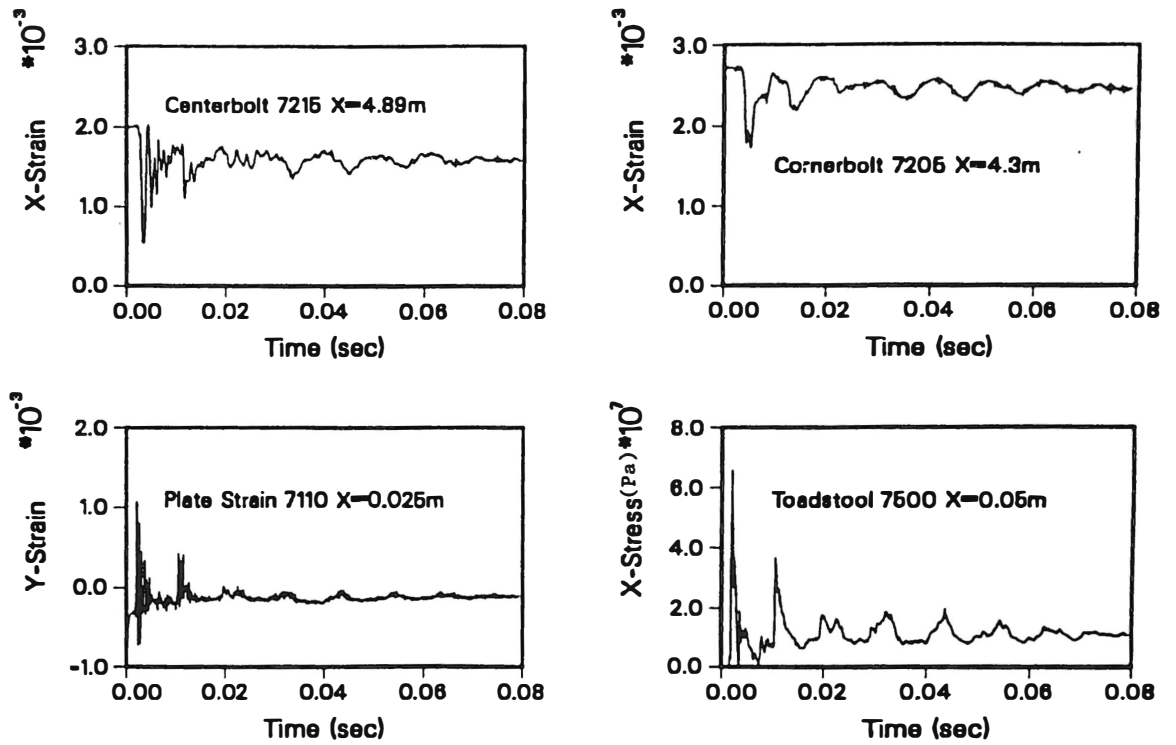
Figure 4: Data sets were consistent in showing cavity pressure oscillations.
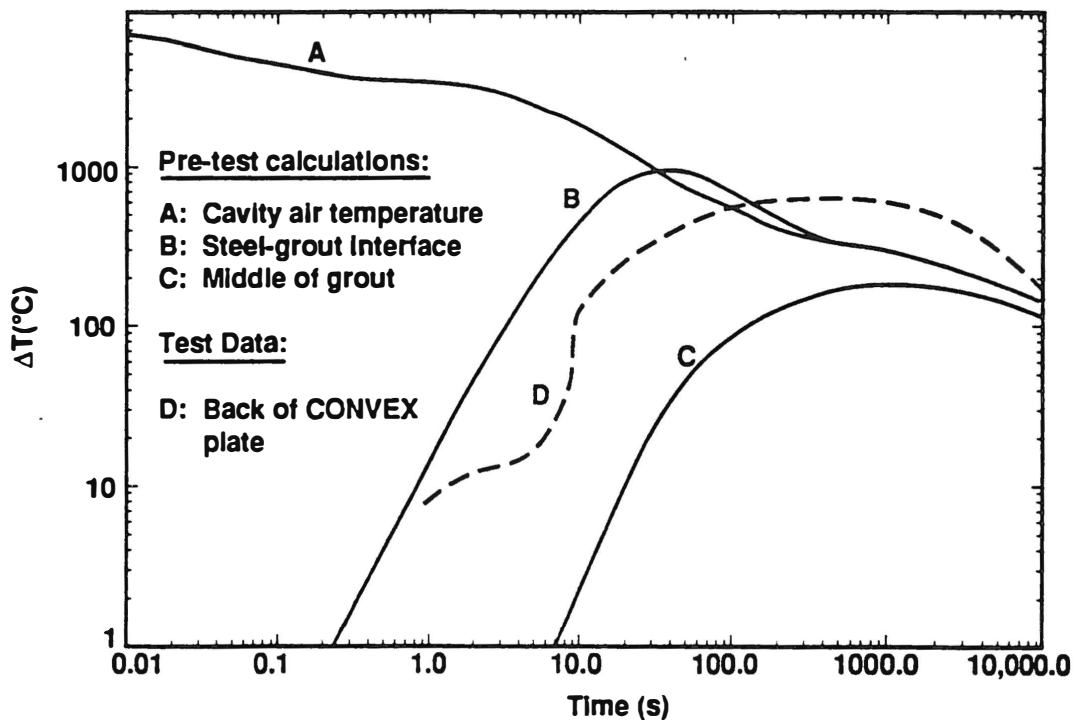
Figure 5: Measured and calculated temperature histories.

258
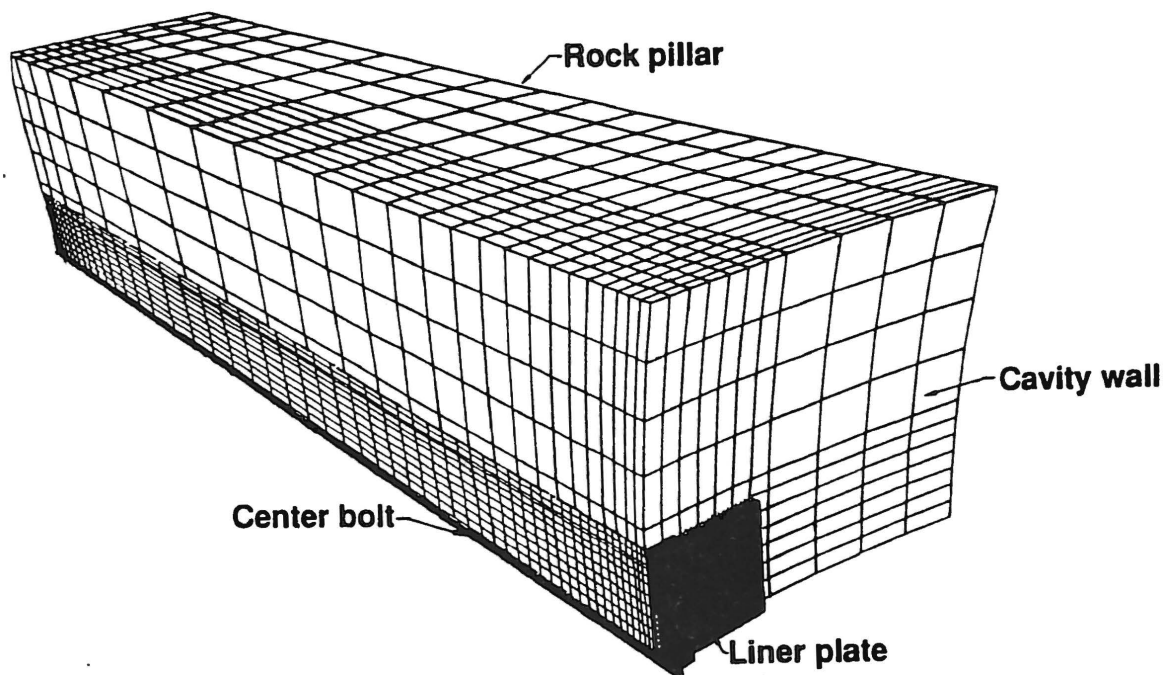
Figure 6: **Complete model for 3-D Mechanical analysis. Note the double curvature of the cavity wall.**
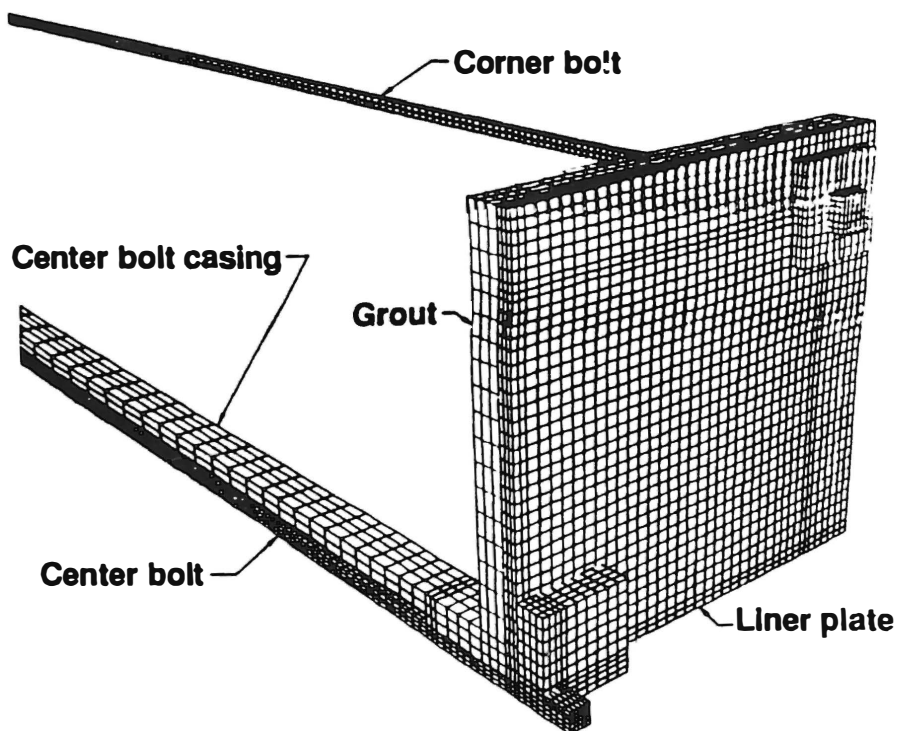
Figure 7: Details of plate, bolts and grout model.

Estimates for the rock material properties required for numerical modeling were obtained from in-situ borehole-jack tests in one of the cable holes of the pillar, along with wave speed and strength measurements on core samples from the pillar. Wave speed and strength measurements also were obtained on core samples of the HLNCC grout used behind the plate.

Equilibrium Condition

The equilibrium outward displacements calculated with NIKE3D for the rear surface of the plate adjacent to the grout, and caused by pre-tensioning the centerbolt and cornerbolt, are shown in Figure 8. The maximum displacement is about 0.45 mm in the elements next to the centerbolt. The stress distribution for the centerbolt and plate indicated maximum compressive and tensile axial values of about -300 Mpa and +430 Mpa, respectively, in the region where the nut fastens the bolt to the plate. These stress levels are well below the elastic yield stress and the entire system is linear. Just behind the plate, at a distance of about 8.5 cm along the length of the bolt, the stress becomes uniform with an axial tension of 325 Mpa (Figure 9) and remains at this level until in the immediate vicinity of the run-around drift wall. This configuration is mapped into DYNA3D as the initial state for the dynamic response calculation. The pseudo-thermal model approach is believed to simulate the stress and strain states associated with bolt tensioning quite realistically. The same conditions would be very difficult to obtain using mechanical force or pressure prescriptions for the bolts, plate and rock exterior surfaces.

Dynamic Response

The dynamic response calculations were carried out to a time of 40 ms. The normal pressure loading function on the plate is given in Figure 10. This function was applied uniformly to the cavity surface and to the plate and bolt surfaces facing toward the cavity.

The comparison of calculation results and test data, shown in Figures 11 to 14, highlights the successes and shortcomings of the calculations. Figure 11 shows that the horizontal (as well as vertical) strains on the back of the plate could be estimated satisfactorily, for the purpose of establishing the type and range of strain gages to be used. Figure 12 shows that the prediction of center bolt axial-strain history at mid-length was pessimistic in terms of the negative effect of the loading on the retained tension. Basically, it is thought that the rock model in DYNA3D did not damp out the shock energy in the liner system as the real rock did. The comparison of calculated and measured axial strain at mid-length on one of the corner bolts (not shown) indicated an even grater disparity between calculations and observations. This also reflects the difficulty in modeling the sequence of bolt tensioning, bolt grouting, and selecting a bolt-grout interface condition after grout curing. Figures 13 and 14 relate to accelerations. The comparison for the back of the plate is satisfactory (Figure 13). But Figure 14, again, clearly indicates a lack of material damping in the calculations.

```
contour values
  A= 2.50e-05
  B= 5.19e-05
  C= 7.87e-05
  D= 1.06e-04
  E= 1.32e-04
  F= 1.59e-04
  G= 1.86e-04
  H= 2.13e-04
  I= 2.40e-04

    (metres)
```
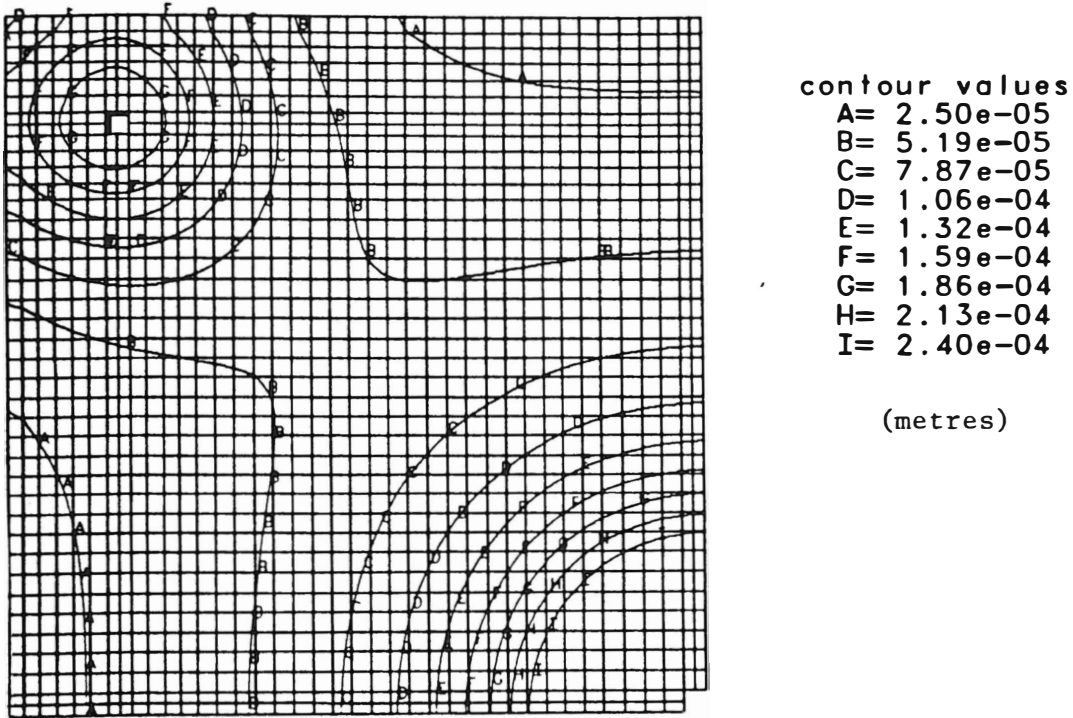
Figure 8: Calculated equilibrium displacement on back of plate, caused by 325 Mpa tension in bolts.


```
contour values
  A= 0.
  B= 7.50e+07
  C= 1.50e+08
  D= 2.25e+08
  E= 3.00e+08

   (Pascals)
```
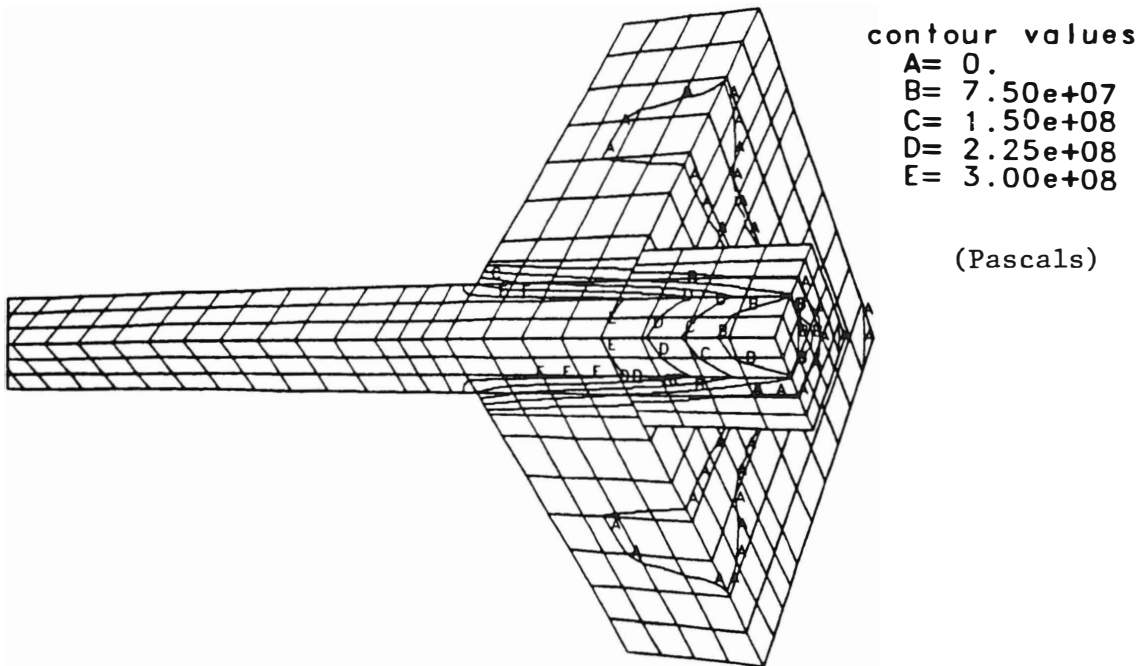
Figure 9: Axial stress distribution in center bolt and plate, at pretensioning.

261
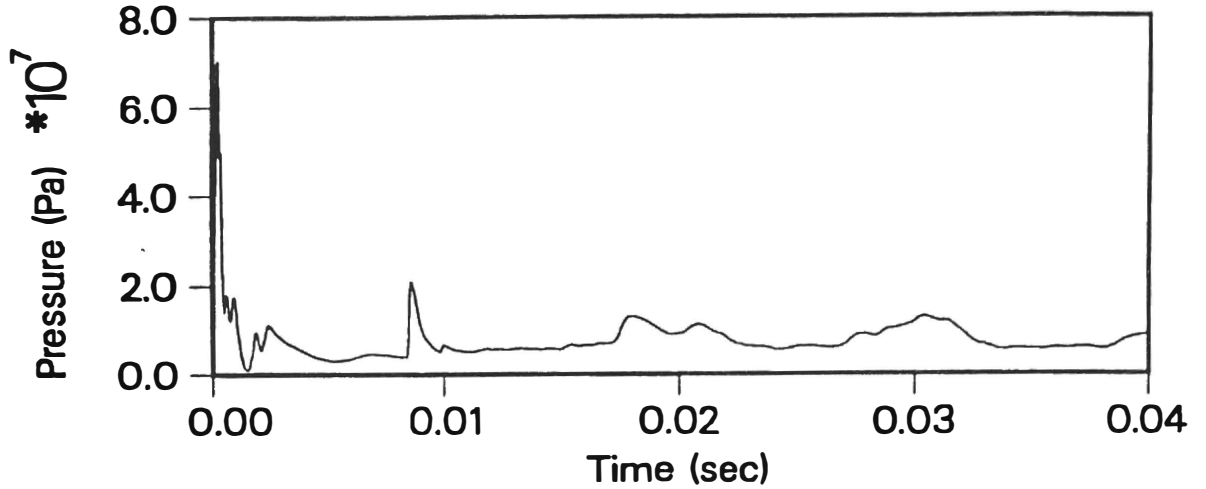
Figure 10: Pressure loading function used for dynamic response calculations.
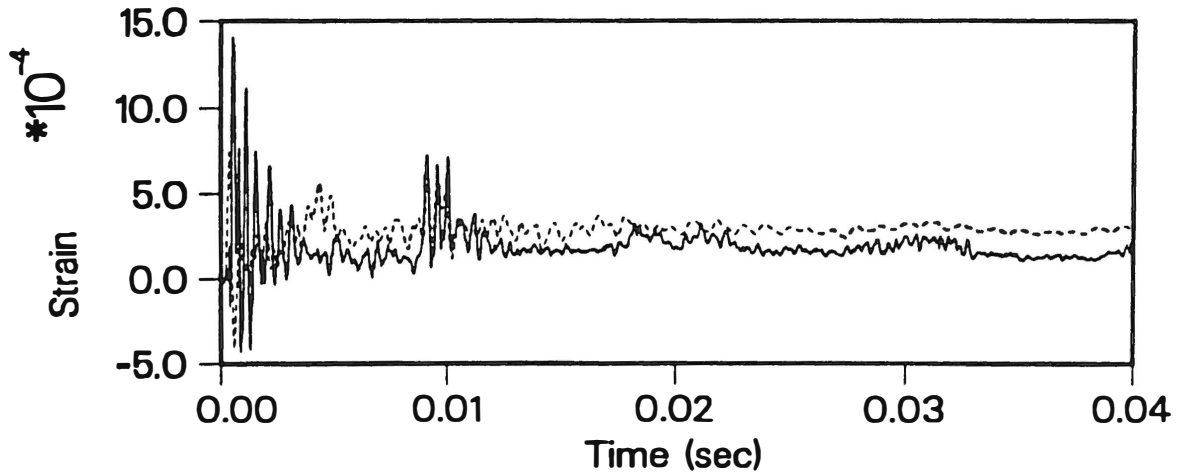
Figure 11: Horizontal strain on back of plate: calculated (dash) vs measured (solid).
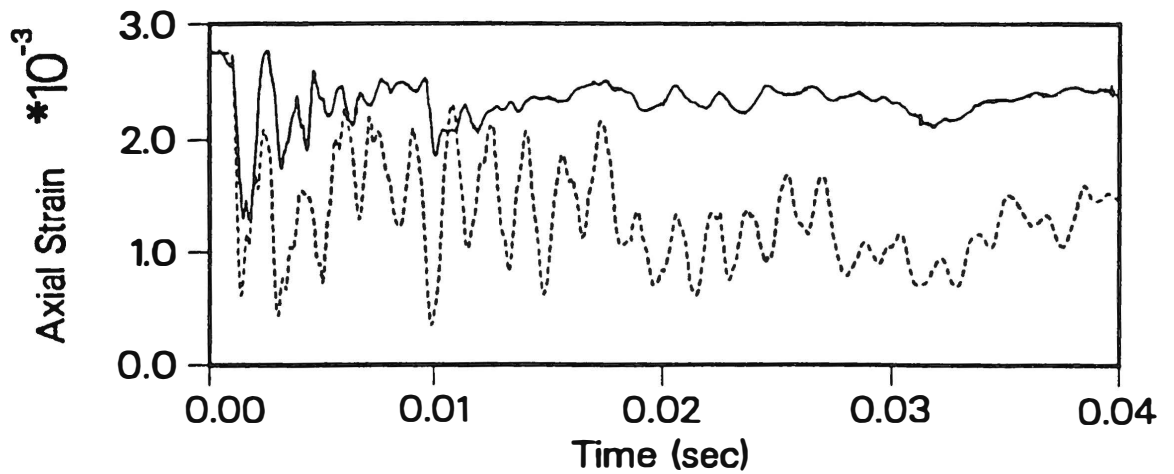
Figure 12: Axial strain on centerbolt, mid length, calculated (dash) vs measured (solid).
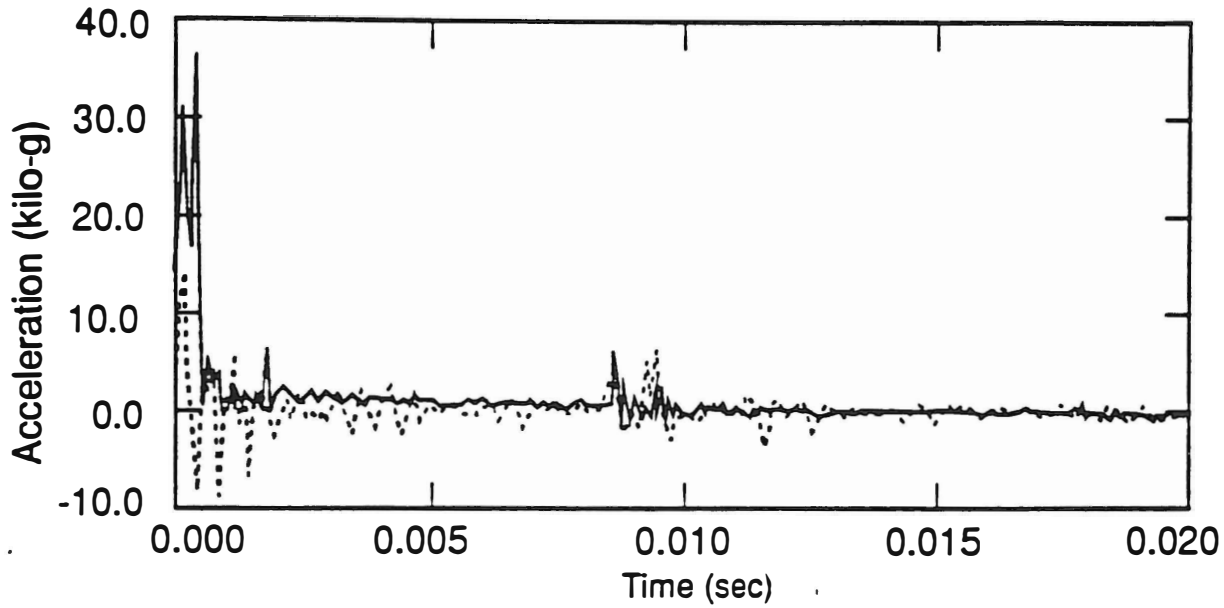
Figure 13: Acceleration on back of plate: calculated (dash) vs. measured (solid).
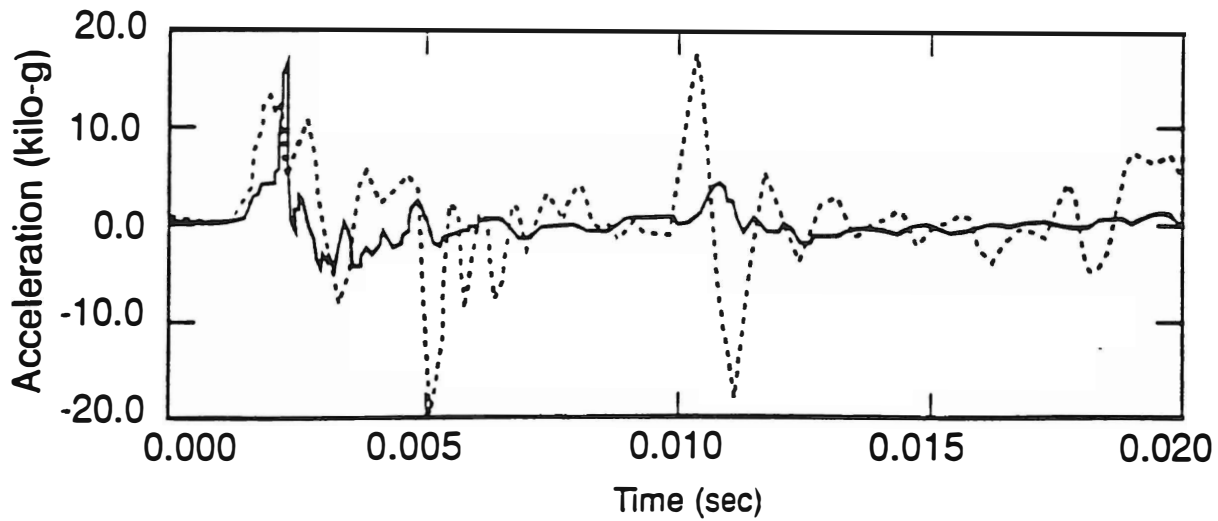
Figure 14: Acceleration at mid-pillar: calculated (dash) vs. measured (solid).

SUMMARY AND CONCLUSIONS

This combined experimental and modeling project was very successful in proving the validity of the concept of a prestressed steel liner and bolt system, for the reinforcement of rock cavities subjected to extreme thermal and dynamic mechanical loading. The instrumentation performed extremely well and provided the essential diagnostics to determine the residual tensions and liner-rock contact pressure. The two-dimensional thermal modeling was very adequate in predicting the plate temperature. The extensive 3-D mechanical modeling highlighted both the power and some of the shortcoming of these models. The comparison of calculational results and test data suggests the need for improvements in the rock material models and in the handling of linked static (pretensioning) and dynamic analyses.

REFERENCES

Heuze, F. E., "Preliminary Structural Investigations for a High-Energy Density Facility", Lawrence Livermore National Laboratory Report UCID-19575 Rev. 1, 37 p., (June, 1983).

Heuze, F. E., and Thorpe, R. K., "Geological Engineering Considerations for a High-Energy Facility, and a Cost Estimate for the Related Conceptual Design", Lawrence Livermore National Laboratory Report UCID-19848, 40 p., (July, 1983).

Maker, B. N.,. Ferencz, R. M, and. Hallquist, J. O, "NIKE3D - A Nonlinear, Implicit, Three-Dimensional Finite Element Code for Solid and Structural Mechanics- User's Manual", Lawrence Livermore National Laboratory Report UCRL-MA-105268, (January, 1991).

Moss, M., Koski, J. A., Haseman, G. M., and Torney, T. V., "The Effect of Composition, Porosity, Bedding Plane Orientation, Water Content, and a Joint, on the Thermal Conductivity of Tuff", Sandia National Laboratories, Albuquerque, NM, SAND 82-1164, 28 p., (November, 1982).

Shapiro, A. B., "TOPAZ2D: A Two-Dimensional Finite Element Code for Heat Transfer Analysis, Electrostatic, and Magnetostatic Problems", Lawrence Livermore National Laboratory Report, UCID-20824, 110 p., (July 1986).

Whirley, R. G., and Hallquist, J. O., "DYNA3D - A Nonlinear, Explicit, Three-Dimensional Finite Element Code for Solid and Structural Mechanics - User's Manual", Lawrence Livermore National Laboratory Report, UCRL-107254, 314 p., (May, 1991).

Zimmerman, R. M., "Conceptual Design of Field Experiments for Welded Tuff Rock Mechanics Program", Sandia National Laboratories, Albuquerque, NM, SAND 81-1768, 26 p., (October 1982).

ACKNOWLEDGMENTS

Étude théorique et expérimentale du comportement à l'arrachement
de câbles cimentés dans le roc

Adil Chennouf
et
Brahim Benmokrane

Département de génie civil, Université de Sherbrooke, Sherbrooke, QC, J1K 2R1

RÉSUMÉ

Ce manuscrit présente les résultats d'une simulation expérimentale en laboratoire et d'une analyse numérique par éléments finis du comportement des câbles d'ancrage cimentés dans le roc soumis à des efforts de traction ou d'arrachement. Dans le modèle numérique utilisé, le contact entre le câble et le coulis de ciment a été simulé à l'aide d'éléments d'interface spéciaux dont les caractéristiques mécaniques ont été tirées des relations contrainte d'adhérence-glissement obtenues de l'étude expérimentale.

Une bonne corrélation entre les résultats expérimentaux et numériques a pu être ainsi obtenue pour les trois types de coulis de ciment considérés.

ABSTRACT

This paper presents the results of a laboratory experimental simulation of rock cement grouted cables loaded in tension. It also includes a numerical analysis using the finite element method. In the numerical model the contact between the cable and the cement grout has been simulated by interface elements. Mechanical characteristics of the interface element have been derived from the bond stress-slip relashionships established from the experimental study. A good correlation between experimental results and those of the numerical analysis has been obtained.

INTRODUCTION

L'utilisation de câbles cimentés dans le roc connaît actuellement un développement très important tant dans les travaux de renforcement de massifs rocheux fracturés que de stabilisation d'ouvrages de génie civil [Stillborg, 1984, Goris, 1991; Hinks et coll., 1990; Mitri et Rajaie, 1991]. Les câbles cimentés offrent la possibilité de renforcer ou de stabiliser des terrains sur de grandes distances (plusieurs dizaines de mètres) et aussi la facilité de la mise en place à partir d'un espace réduit (ex. intérieur des mines, des tunnels, des excavations souterraines, etc.). Dans les travaux de stabilisation d'ouvrages de génie civil, l'utilisation de câbles offre aussi l'avantage de disposer d'ancrages de capacité individuelle de plusieurs milliers de kilonewtons [Hinks et coll., 1990].

La présente étude fait partie d'un projet global, entrepris au Laboratoire de mécanique des roches de l'Université de Sherbrooke sur le comportement des câbles (ou multicâbles) cimenttés dans le roc. Ce manuscrit fait l'objet de résultats d'une étude expérimentale en laboratoire et d'une simulation numérique par éléments finis du comportement de câbles cimentés dans le roc soumis à des efforts de traction. L'étude expérimentale a comporté des essais d'arrachement statiques sur des modèles réduits d'ancrages constitués de câbles injectés sur une courte longueur ancrée avec différents coulis de ciment. Des cylindres en béton ont été utilisés comme milieu rocheux encaissant. Cette étude a permis d'établir des relations du type contrainte d'adhérence-glissement du câble. La courte longueur ancrée considérée ici (4 d) permet d'attribuer un caractère local à ce type de relations (d = diamètre du câble soit 15,8 mm). L'étude numérique par éléments finis a été réalisée à l'aide du progiciel CESAR-LCPC développé par le Laboratoire Central des Ponts et Chaussées (Paris, France). Le contact entre le câble et le coulis a été simulé en utilisant des éléments d'interface spéciaux dont les caractéristiques mécaniques sont tirées des relations contrainte d'adhérence-glissement dérivées de l'étude expérimentale. La simulation numérique entreprise a permis d'illustrer l'effet du glissement entre le câble et le coulis sur la distribution des contraintes de cisaillement le long du câble et aussi d'établir une comparaison avec les charges et les modes de ruptures obtenus expérimentalement.

ÉTUDE EXPÉRIMENTALE

Essais d'arrachement sur des modèles réduits d'ancrage

Les modèles réduits d'ancrage utilisés pour les essais d'arrachement sont analogues à ceux décrits lors d'études antérieures (Benmokrane et coll., 1992). Chaque éprouvette, représentant le modèle réduit, est constituée d'un cylindre en béton (f'_c = 60 MPa, E = 30 GPa). L'ancrage est constitué d'un câble à 7 fils (charge de rupture = 270 kN) scellé dans un trou axial de 38 mm de diamètre foré dans l'éprouvette de béton. Dans ce type d'essais, la rupture des ancrages se produit soit le long du contact câble-coulis de scellement soit dans le câble par atteinte de la charge limite de rupture (Chennouf, 1992). Une vue du type d'éprouvette utilisée dans cette étude est montrée dans la figure 1.
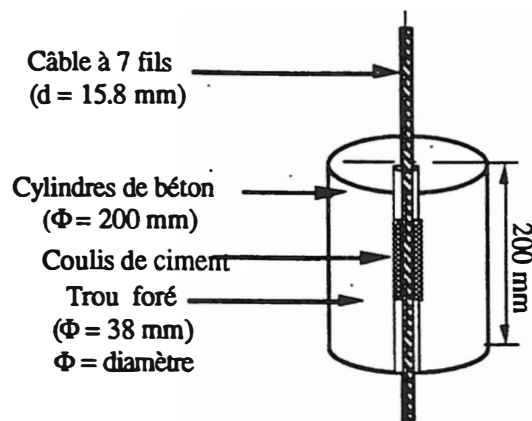
Figure 1: Modèle réduit d'ancrage utilisé

En fait, ce modèle d'ancrage a été utilisé dans le but précis d'examiner l'évolution de la contrainte d'adhérence moyenne mobilisée le long du contact câble-coulis en fonction du glissement. Ainsi, une longueur de scellement très courte (4 d = 65 mm) a été retenue pour justifier l'hypothèse d'une répartition uniforme de la contrainte d'adhérence mobilisée le long du contact câble-coulis.

L'identification des trois coulis de scellement utilisés est montrées dans le tableau 1. Il s'agit de coulis à base de ciment Portland de Type 10 avec l'ajout ou la substitution d'un agent expansif (coulis AC3) et d'un sable (coulis AC6).

Tableau 1   Composition des trois coulis de scellement utilisés

	AC1	AC3	AC6
Eau (E)	1	1	1
Ciment Portland de Type 10	2,22	2,22	2,22
Agent expansif (Poudre d'Aluminium)	-	$1,55 \ 10^{-4}$	-
Sable	-	-	0,95
Eau/Liant (E/C)	0,45	0,45	0,45

Nota: Le dosage de chaque constituant est donné en fonction de la masse d'eau.

Les caractéristiques mécaniques de ces coulis de ciment évaluées après 28 jours de mûrissement sont illustrées dans le tableau 2. L'injection des câbles et la préparation des modèles sont décrites en détail ailleurs (Chennouf, 1992). Les essais d'arrachement ont été réalisés à l'aide d'une presse universelle d'une capacité de 266 kN en traction. Les détails de montage et d'acquisition de données ont été décrits lors d'études antérieures (Benmokrane et coll., 1992).
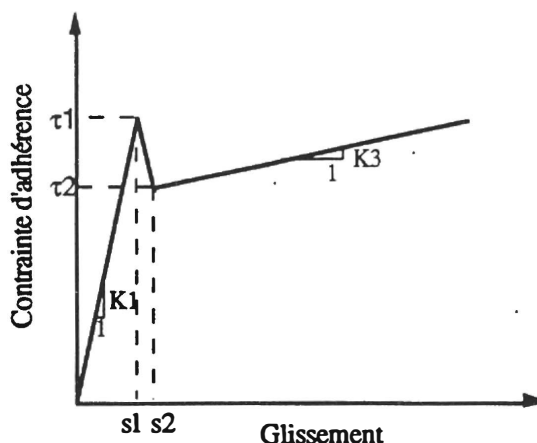
Figure 3 Représentation graphique illustrant les paramètres utilisés dans l'établissement
de relations contrainte d'adhérence en fonction du glissement

ÉTUDE NUMÉRIQUE PAR ÉLÉMENTS FINIS

Introduction

L'étude numérique par éléments finis a été réalisée à l'aide du logiciel CESAR qui fait partie du progiciel CESAR-LCPC. Ce dernier comporte également le pré-processeur MAX et le post-Processeur PEGGY et des programmes utilitaires.

Le logiciel CESAR, est un code de calcul très général basé sur la méthode des éléments finis. Il permet de modéliser un grand nombre de problèmes de génie industriel (calcul des structures) et surtout du génie civil (calcul par phases de construction, hydrogéologie, thermique, mécanique des sols et des roches, etc.)

Pour la simulation du comportementà l'arrachement de câbles cimentés dans le roc, on a utilisé le module TCNL qui traite des problèmes de contact entre solides à comportement non linéaire (élastoplasticité) dans le domaine de la géomécanique..

Formulation par éléments finis :

La figure 4 montre un schéma d'un câble injecté dans une roche. Celui-ci est constitué de trois matériaux (câble, coulis de scellement et roc) et deux interfaces câble-coulis et coulis-roc. Des éléments d'interface spéciaux ont été utilisés pour modéliser les contacts entre les différents matériaux. Leurs caractéristiques géométriques et mécaniques sont décrites plus loin.

Le type d'élément fini utilisé pour représenter le câble, le coulis de scellement et le roc est un élément isoparamétrique quadrilatère à huit nœuds. L'élément est également axisymétrique car la géométrie et le chargement d'un ancrage vertical considérés ici sont axisymétriques.

Dans la formulation de ce modèle, il a été considéré que les trois matériaux constituant l'ancrage (câble d'acier, coulis de scellement et roche) se comportent tel un milieu élastique parfaitement plastique.

268

Tableau 2   Caractéristiques mécaniques des coulis de scellement évaluées à 28 jours de mûrissement

	Résistance en compression f_c (MPa)	Résistance en traction T_O (MPa)	Module d'élasticité E (GPa)	Coefficient de Poisson ν	Cohésion c (MPa)	Angle de frottement Φ (Degrés)
AC1	52,6±4,0 (3)	3,8±0,8 (3)	14,8±0,5 (7)	0,14±0,01 (7)	7,0	40,5
AC3	40,3±0,5 (3)	3,7±0,2 (3)	12,0±1,0 (4)	0,17±0,01 (4)	9,1	20,7
AC6	51,8±3,1 (3)	4,3±0,8 (3)	17,9±0,4 (4)	0,15±0,01 (4)	11,2	27,4

( ): Nombre d'essais

RÉSULTATS

Les ruptures des ancrages se sont produites effectivement au niveau du contact câble-coulis de scellement. Les valeurs moyenne de la contrainte d'adhérence obtenues à la rupture sont illustrées dans le tableau 3 pour l'ensemble des ancrages testés. Ces valeurs ont été calculées en utilisant l'expression suivante:

$$\tau = \frac{P_{rupt}}{\pi\,d\,LA} \qquad [1]$$

avec P_{rupt} = charge de rupture, d = diamètre du câble (15,8 mm) et LA = longueur ancrée.

Tableau 3:   Valeurs moyennes des contraintes d'adhérence obtenues à la rupture des ancrages après 28 j de mûrissement

Coulis	AC1	AC3	AC6
Contrainte moyenne d'adhérence (MPa)	4,2±0,2	4,3±0,1	4,4±0,2

Les courbes contrainte d'adhérence-glissement obtenues [Chennouf, 1992] ont permis de retenir la forme générale illustrée à la figure 3 pour l'établissement des relations contrainte d'adhérence-glissement. Ce modèle est constitué de trois branches linéaires. La première branche correspond à la phase d'avant-rupture de l'ancrage, la deuxième correspond à une chute de résistance et enfin la troisième consiste en une résistance résiduelle du câble à grands déplacements. Les valeurs moyennes des paramètres caractérisant chacune des trois branches du modèle proposé sont illustrées dans le tableau 4.

Tableau 4:   Valeurs expérimentales des paramètres reliant la contrainte d'adhérence au glissement

Coulis	s1 (mm)	$\tau1$ (MPa)	K1(MPa/mm)	s2 (mm)	$\tau2$ (MPa)	K3(MPa/mm)
AC1	2,9±0,3	4,2±0,2	1,4±0,1	-	2,5±0,4	0,03±0,02
AC3	2,8±0,3	4,3±0,1	1,5±0,3	3,1±0,3	2,6±0,5	0,03±0,01
AC6	3,0±0,1	4,4±0,2	1,4±0,2	-	2,6±0,3	0,04±0,02
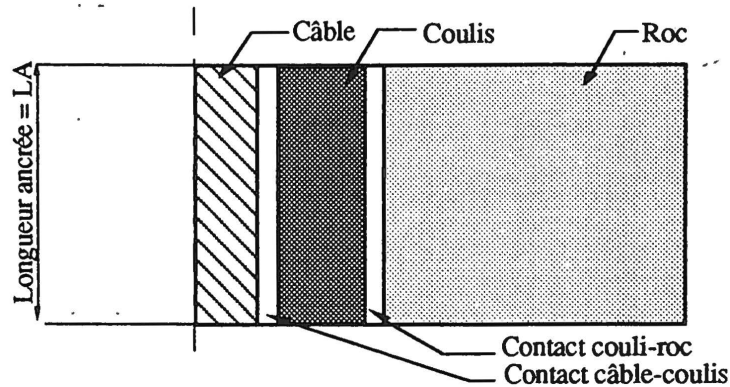
Figure 4: Schéma d'un modèle de câble injecté

Le critère de Mohr Coulomb est utilisé pour indiquer l'écoulement plastique dans le coulis de scellement et dans la roche. Ce critère utilisé pour les sols, les roches et les bétons (Chen, 1983), s'écrit ainsi:

$$F = \sigma_m \sin \phi + \sqrt{J_2} \left(\cos \theta - \frac{\sin\theta \sin\phi}{\sqrt{3}} \right) c \cos\phi \qquad [2]$$

où F est la fonction décrivant l'écoulement plastique, σ_m = le contrainte moyenne, J_2 = le deuxième invariant de la contrainte déviatrice Sij, ϕ = l'angle de frottement interne, c = la cohésion et θ = l'angle de Lode.

En ce qui concerne l'acier, le critère de Von Mises a été retenu et s'écrit comme suit:

$$F = J_2 - K^2 \qquad [3]$$

où K= limite élastique en cisaillement simple.

L'utilisation d'un critère d'écoulement pour l'acier (câble d'ancrage) n'est, en réalité, pas nécessaire pour ce type d'étude car il est considéré que la rupture dans l'acier est atteinte une fois que la charge totale appliquée a atteint la limite d'écoulement plastique du câble.

La résolution numérique d'un problème élastoplastique se traite comme tout problème non linéaire au moyen d'un processus incrémental et itératif.

Simulation des contacts câble-coulis et coulis-roc

La simulation par la méthode des éléments finis des conditions de contact entre le câble d'acier et le coulis de scellement et aussi entre le coulis et le milieu encaissant (adhésion, glissement relatif avec frottement) peut être réalisée par l'intermédiaire d'éléments spéciaux appelés "éléments joints" ou "éléments d'interface". Pour ce faire, les nœuds se trouvant à l'interface acier-coulis et coulis-milieu encaissant sont dédoublés. Aussi, une loi de comportement est associé à ces éléments sans dimension physique.

L'élément joint élastique à ressort de Ngo et Scordellis (1967) est le premier élément qui a été développé pour modéliser l'adhérence entre l'armature et le béton (figure 5a). En se basant sur ce modèle Goodman et al (1968) ont proposé une formulation d'un élément joint plan isoparamétrique à quatre nœuds d'épaisseur nulle (Figure 5b) D'autre part, en 1982, Heuze et Barbour ont présenté une revue générale actualisée des modèles existants et ont

270

proposé un nouvel élément joint axisymétrique. Dans le cas bidimensionnel, le comportement des éléments joints est conventionnellement régi par l'équation suivante:

$$\langle P \rangle = \begin{bmatrix} P_n \\ P_s \end{bmatrix} = \begin{bmatrix} K_n & 0 \\ 0 & K_s \end{bmatrix} \begin{bmatrix} u_{haut} - u_{bas} \\ v_{haut} - v_{bas} \end{bmatrix} \qquad [4]$$

où $\langle P \rangle$ représente le vecteur force nodal par unité de longueur;

K_n et K_s représentent respectivement la rigidité normale et la rigidité tangentielle du joint par unité de longueur.
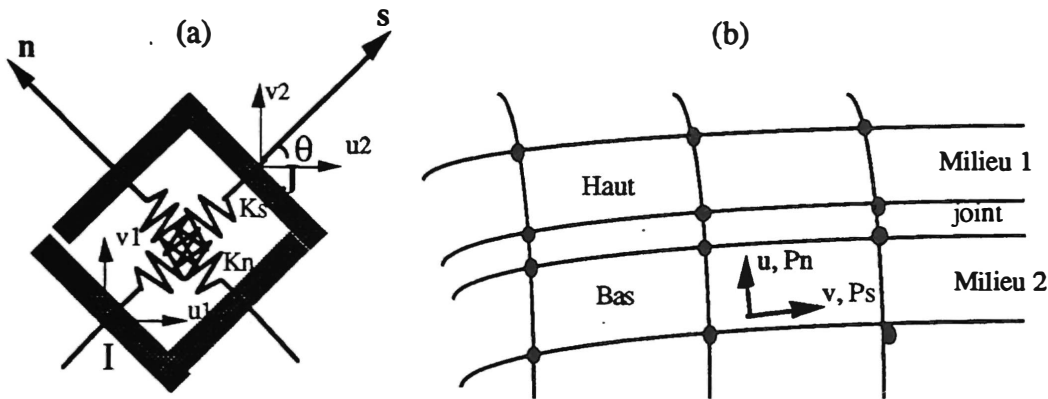
Figure 5 : Modèles d'éléments d'interface (a) Ngo et Scordellis (1967), (b) Goodman et coll.(19968)

Une des principales difficultés posées par cette approche réside dans l'évaluation réaliste de ces deux paramètres (K_n et K_s). En mécanique des roches, ceux-ci sont évalués par un essai de cisaillement direct (Goodman et coll., 1968). Dans le cas des ancrages injectés dans le roc, ces paramètres pourraient être évalués à partir d'essais d'arrachement.

Pour des corps en contact, la rigidité normale Kn prend une valeur assez importante (pénalisation) pour assurer le maintient du contact et éviter le chevauchement. Dans le cas d'adhérence Ks prend une valeur aussi grande que celle de Kn, alors que pour un contact glissant sans frottement Ks est nulle. Dans le cas de l'ouverture du joint on a Kn =Ks = 0 (Buragohain et Shah, 1978).

Le comportement non linéaire des joints est classiquement formulé par une approche élastoplastique (Ghaboussi et coll., 1973). Dans ce cas, deux critères sont utilisés; il s'agit de:

- •un critère de traction pour le contact (ouverture /fermeture du joint): $F_1 = \sigma_n - R_T \leq 0$ [5]
- • un critère pour le glissement avec frottement.

Dans cette étude, le critère utilisé est celui de Mohr-Coulomb: $F_2 = |\tau| - \sigma_n . tg\, \phi - c \leq 0$ [6]

Élément d'interface utilisé

L'élément d'interface utilisé est un élément isoparamétrique quadrilatère à 6 nœuds (figure 6). Cet élément est quadratique suivant la direction tangente et linéaire suivant la direction normale.

Lorsque les matériaux sont en contact, l'épaisseur des éléments d'interface est nulle. Ceci conduit à une singularité numérique. Pour lever numériquement cette singularité, CESAR suppose une épaisseur très petite. Pour un problème axisymétrique, cette dimension est calculée comme suit:

$$e = L.10^{-n} ; \qquad \text{avec} \qquad L = \frac{1}{2}[(Xmax-Xmin)+(Ymax-Ymin)] ,$$

où les grandeurs Xmax, Xmin, Ymax et Ymin, représentent les valeurs extrêmes des coordonnées des nœuds du maillage. Le cœfficient de pénalisation (10^{-n}) a une influence sensible sur le conditionnement de la matrice de rigidité. Par conséquent, sa valeur doit être choisie par expérimentation. Cependant, le code CÉSAR, propose une valeur de 10^{-6} pour les problèmes axisymétriques, ce qui a permis d'obtenir un bon comportement des éléments d'interface.
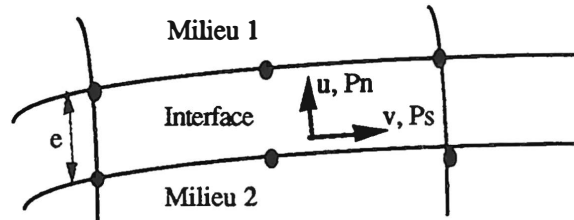
Figure 6: Élément d'interface utilisé

Loi de comportement

Les contraintes sont reliées aux déformations par l'expression suivante

$$\langle\sigma\rangle = [E]\langle\varepsilon\rangle \qquad\qquad [7]$$

avec $\langle\sigma\rangle^T = \langle\sigma_r\ \sigma_z\ \sigma_\theta\ \sigma_{rz}\rangle$ et $\langle\varepsilon\rangle^T = \langle\varepsilon_r\ \varepsilon_z\ \varepsilon_\theta\ 2\varepsilon_{rz}\rangle$ pour un problème axisymétrique.

La loi de comportement utilisée est celle d'un glissement avec frottement de Coulomb:

$$[E] = \begin{bmatrix} 0 & 0 & 0 & 0 \\ 0 & E & 0 & 0 \\ 0 & 0 & 0 & 0 \\ 0 & 0 & 0 & G \end{bmatrix}$$

De plus, la relation contrainte normale-contrainte de cisaillement suit une loi de Coulomb, avec E étant le module d'élasticité de l'élément d'interface.

Caractéristiques de l'élément d'interface

Le comportement mécanique de l'élément de contact est identique à celui du triplet à trois ressorts reliant deux à deux les nœuds en vis à vis (figure 6). La rigidité de ces ressorts est de l'ordre de kE (k= 10^{-n})

Pour le module de rigidité $G = \frac{E}{2(1+\nu)}$, on suppose que $\nu = 0$ et par suite $G = \frac{E}{2}$

Méthode de résolution numérique

Dans la résolution de ce problème, deux types de non linéarité se présentent:

- une non linéarité du type géométrique;
- une non linéarité du type comportement.

La première non linéarité provient de l'indétermination a priori de la surface de contact final. La seconde provient des phénomènes de glissement avec frottement qui peuvent se produire sur la surface de contact et compte tenu de ces non linéarités, la résolution se fait par la méthode incrémentale. Le calcul des incréments successifs de chargement est réalisé à l'aide de deux critères distincts:

- le critère de non-interpénétration;
- le critère de résistance à la traction.

Le critère de non-interpénétration a pour but d'interdire à tout point du matériau de pénétrer à l'intérieur du materiau en contact avec lui. Le critère de résistance à la traction assure la fermeture du contact. En fait, la déplacement suivant la normale extérieure à l'appui est cinématiquement admissible et comme cette séparation n'est pas toujours acceptée, on suppose alors que pour un point M appartenant à un élément d'interface actif : $\sigma_n - R_T \leq 0$; σ_n et R_T représentent respectivement la contrainte normale et la résistance à la traction de l'élément d'interface.

Paramètres mécaniques

Les paramètres mécaniques des matériaux constituant le modèle d'ancrage (câble, coulis de ciment et milieu encaissant) ont été déterminés à partir d'essais en laboratoire décrits plus haut.

Pour les éléments d'interface, en plus des rigidité tangentielles qui ont été déterminées expérimentalement pour les différents coulis étudiés, les autres paramètres requis sont la cohésion et l'angle de frottement. Ces deux paramètres de Mohr-Coulomb peuvent être déterminés à partir d'essais de cisaillement direct. La conduite de tels essais en laboratoire est cependant compliquée et en plus, ces essais ne permettent pas de tenir compte rigoureusement des conditions réelles de l'ancrage (rugosité du trou, confinement, conditions de mûrissement, etc.). Il est proposé ici d'attribuer à la cohésion des éléments de l'interface câble-coulis et coulis-roc respectivement les valeurs de la résistance au cisaillement ultime $\tau_{t\text{-}c}$ ou $\tau_{t\text{-}c}$, déterminées à partir d'essais d'arrachement d'ancrages scellés sur une courte longueur.

APPLICATIONS ET DISCUSSIONS

Les applications présentées ici concernent d'une part, l'évolution de la distribution des contraintes le long de la longueur ancrée en fonction de la charge appliquée et d'autre part, une étude comparative entre les charges et modes de rupture obtenus numériquement et ceux obtenus à l'aide d'essais d'arachement effectués sur les câbles injectés avec les trois différents coulis de ciment.

Une illustration du maillage typique utilisé dans les applications est présenté dans la figure 7.

Le figure 8 présente les courbes de distribution de contraintes d'adhérence, pour les coulis AC1 et AC3, le long de la zone ancrée pour quatre niveaux de chargement. Le premier chargement correspond au comportement élastique, tandis que les trois autres correspondent au glissement du câble au niveau de l'interface câble-coulis.

Un exemple de l'évolution du glissement à différents incréments de chargement est présenté dans la figure 9.

L'examen de ces figures montre les effets de la propagation de la rupture sur les distributions des contraintes le long de l'ancrage. Ainsi, la forme des courbes montre qu'à l'étape 1 de chargement, la distribution des contraintes est exponentielle et que les pics de contraintes sont situées proche de l'extrémité tendue du câble. Cependant, les étapes de chargement 2 et subséquentes indiquent un déplacement des profils de contraintes et des pics de contraintes de plus en plus en profondeur. Ceci est le résultat de la propagation de la décohésion du coulis vers le bas de la zone ancrée à mesure que la charge appliquée augmente.
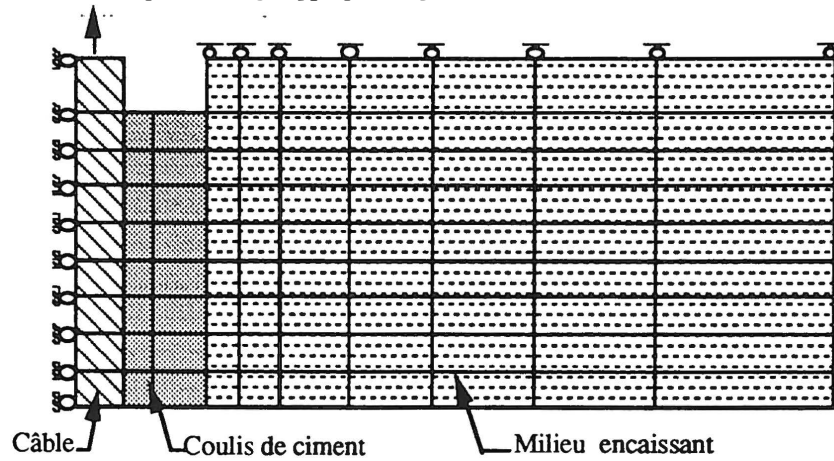
Figure 7: Configuration du maillage typique utilisé dans les applications
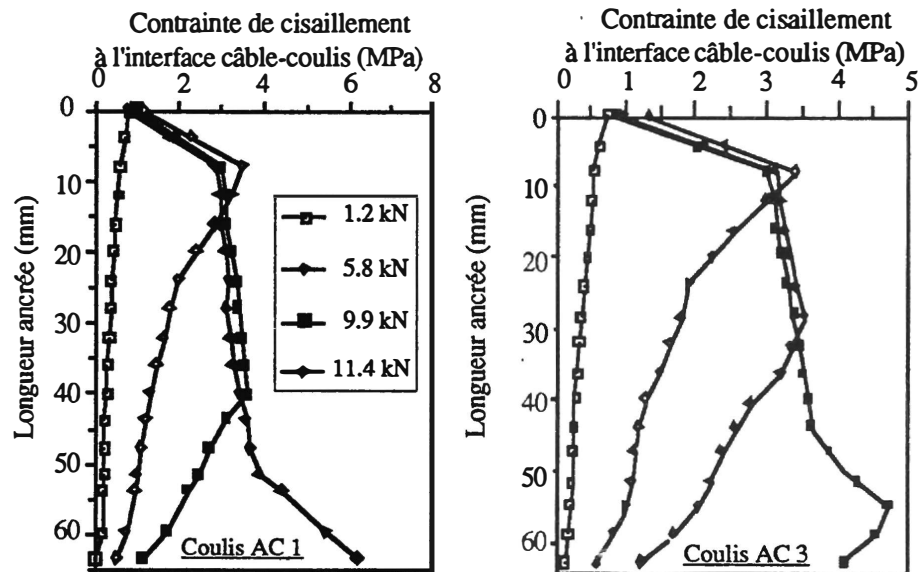
Figure 8: Distributions de la contrainte d'adhérence le long de la zone ancrée pour différents niveaux de chargement obtenues pour les coulis AC1 et AC3

F = 5,8 kN   F = 9,9 kN   F = 11,4 kN
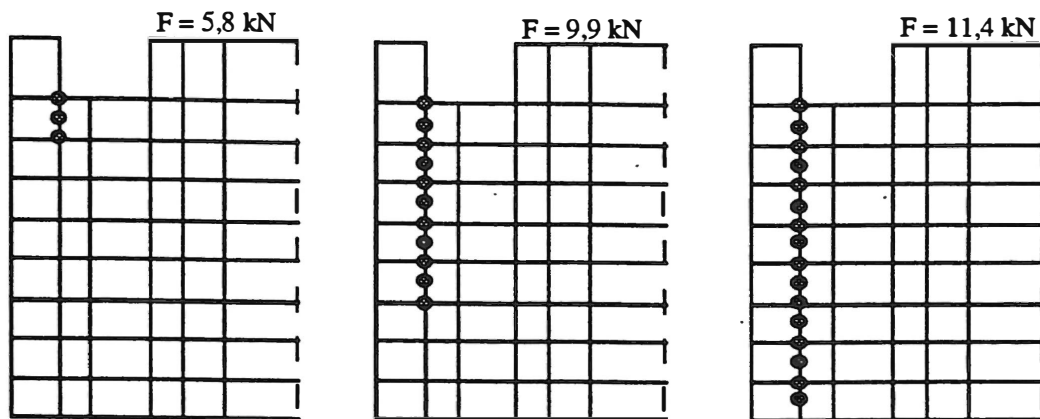
Figure 9: Évolution du glissement au contact câble-coulis en fonction du niveau de chargement (coulis AC1)

Le tableau 5 compare les charges de rupture expérimentales à celles obtenues à l'aide du modèle numérique. On peut constater que les charges de rupture prédites par le modèle sont très proches de celles obtenues à l'aide d'essais d'arrachement. De plus, le mode de rupture des ancrages prédit par le modèle, soit au contact câble-coulis (figure 9), est analogue à celui observé expérimentalement.

Tableau 5:   Comparaison entre les charges de rupture prédites par le modèle et celles obtenues expérimentalement pour les trois coulis de ciment considérés (AC1, AC3 et AC6)

	AC1	AC3	AC6
Modèle numérique	11,4	11,8	11,6
Essais d'arrachement	13,2	13,5	13,8

CONCLUSIONS

Cette étude montre que la simulation numérique par éléments finis constitue un outil très adéquat pour prédire le comportement de câbles cimentés dans le roc. Une bonne concordance a été ainsi obtenue entre les charges et les modes de rupture prédits par le modèle et ceux obtenus expérimentalement sur des câbles injectés avec trois types de coulis de ciment. Le contact entre le câble et le coulis a été simulé à l'aide d'éléments d'interface spéciaux dont les caractéristiques mécaniques ont été déterminées à partir d'essais d'arrachement. Ces essais ont été réalisés sur des câbles injectés sur une courte longueur d'ancrage (4 fois le diamètre du câble), car ils permettent mieux d'établir les caractéristiques mécaniques de l'élément d'interface. De plus, de tels essais peuvent être facilement effectués sur le terrain, ce qui permettra de tenir compte des conditions réelles d'utilisation du câble (qualité des contacts câble-coulis et coulis-roc, confinement du milieu encaissant, conditions de mûrissement, etc.) Ceci du reste rejoint une de nos conclusions établies lors d'une étude antérieure sur des barres d'ancrage cimentées dans le roc (Benmokrane, 1990).

REMERCIEMENTS

Benmokrane, B. (1990) *Etude par Éléments Finis du Comportement à l'Arrachement d'Ancrages Injectés dans le Roc*, Revue canadienne de génie civil, Vol 17, No. 2, p. 129-141.

Benmokrane, B., Ballivy, G. (1991) *Distribution Expérimentale des Contraintes le Long d'Ancrages Scellés dans un Massif Rocheux Soumis à des Charges de Tensionnement*, Bulletin CIM,, No 951, p. 45-52.

Benmokrane, B.,Chennouf, A., Ballivy, G. (1992) *Study of bond strength behaviour of steel cables and bars anchored with different cement grouts*, Proc. of the Int. Symp. on Rock. Support, Sudbury, Ont., A.A Balkema, p.293-301

Bernander, K.G. (1957) *An Investigation of Bond by Means of Strain Measurements in High Tensile Bars*

Buragohain, D.N., Shah, V.L. (1978) *Curved Isoparametric Interface Surface Element*, Journal of the Structural Division, ASCE, V. 104, # ST1, p.205-209.

Chen, W. F. (1983) *Plasticity in reinforced concrete.* McGraw-Hill Book Company, New York

Chennouf, A. (1992) *Résistance à l'adhérence et au glissement des barres et câbles d'ancrage injectés dans le roc avec différents coulis de ciment*, Mémoire de Maitrise, Dépt. de génie civil, Université. de Sherbrooke, 180p

Ghaboussi, J., Wilson, F. L., Isenberg, J. (1973) *Finite element for rock joints and interfaces*, J. of Soil Mech. and Found Div., ASCE, Vol. 99, SM 10, P. 833-848

Goris, J.M. (1991). *Laboratory Evaluation of Cables Supports*, CIM Bul., Vol. 84, No. 948, p. 44-50.

Goodman, R.E., Taylor, R.L., Breeke, T.L. (1968) *A model for the Mechanics of Jointed Rock*, Journal of Soil Mechanics and Foundations Divisions. ASCE, Vol. 14, No. SM3, p 637-659.

Heuze, F.E., Barbour, T.G. (1982) *New Models for Rock Joints and Interfaces*, ASCE, INT. GEOT., ENG., Vol. 108, No. GT5, p. 757-776.

Hinks, J.L., Burton, I.W., Peacock, A.R., Gosschalk, E.M. (nov. 1990) *Post-Tensioning Mullardock Dam in Scotland*, Water Power and Dam Engineering p. 12-15.

Mitri, H.S., Rajaie, H. (March 1991). *Stress Analysis of Rock Mass With Cable Support - A Finite Element Approach.* Professional Development Seminar, Numerical Modelling of Rock Excavations, McGill University.

Ngo, D., Scordelis, A.C. (1967) *Finite Element Analysis of Reinforced Concrete Beams*, ACI Journal, V. 64, # 3, p.152-163.

Stillborg, B. (1984). *Experimental Investigation of Steel Cable for Rock Reinforcement in Hard Rock*, Doctoral Thesis, Division of Rock Mechanics, Lulea University (Sweden), 127 p.

Session 8

Miscellaneous

Autres

DISCRETE PARTICLE MODELLING FOR ANALYSIS OF BOREHOLE STABILITY: APPLICATIONS IN PETROLEUM GEOMECHANICS

S.G. Thallak and K.E. Gray
Center for Earth Sciences and Engineering
The University of Texas at Austin
Austin, Texas - 78712.

ABSTRACT

The theoretical development of the method is briefly described, and a number of problems as applied to borehole stability are given which illustrates the capabilities of the method. The analysis utilizes plane particles simulating a two-dimensional assembly of discs. Particle motions are coupled with Darcy flow through the assembly. Results of the simulations as applied to borehole stability problems suggest a number of behavioral features and deformation mechanisms. The stress distribution around the borehole clearly reflects a type of non-linear elastic behavior with elasto-plastic dilatant mechanisms. The paper also discusses the application of discrete particle method to other problems such as hydraulic fracturing and sand production problems in unconsolidated reservoirs.

RESUME

Le développement théorique de la méthode utilisée dans cet article est brièvement décrit puis quelques applications à la stabilité des puits sont présentées pour illustrer les capacités de cette méthode. Notre analyse utilise des particules planes simulant un assemblage bidimensionnel de disques. Le mouvements des particules est couplé avec l'écoulement de Darcy dans cet assemblage. Les résultats des simulations appliquées aux problèmes de stabilité de puits mettent en évidence un certain nombre de caractéristiques de comportement et de mécanismes de déformation. La distribution de contraintes autour du puits est caractéristique d'un comportement non linéaire avec mécanismes élasto-plastiques dilatants. Cet article aborde également l'application de la méthode des particules discrètes à d'autres problèmes comme la fracturation hydraulique ou les venues de sable dans un réservoir non consolidé.

INTRODUCTION

In loosely consolidated sandstone, forces are transferred through contact between particles; the constitutive relation for such materials is therefore complex. Many laboratory tests are necessary to understand behavior before physical processes in these materials can be modelled. Most of the published studies on behavior of loosely consolidated materials are based on conventional continuum mechanics principles. The continuum models are phenomenological, and are primarily concerned with mathematical modelling of observed phenomenon without detailed attention to their fundamental physical significance. A realistic behavioral law for poorly consolidated sandstones and dense sands requires descriptions of anisotropy, stress path dependency, dilatancy, and confining pressure-dependent moduli. Most current models lack one or more of these aspects, and therefore cannot explore the physical processes that take place because of the particulate nature of the medium, and cannot cope fully with stress rotations, stress history, and dilation effec . These models can only simulate macroscopic response in cases where granular material behavior is reasonably emulated by the continuum constitutive law being used.

An alternative approach is to model the granular medium as an assemblage of particles, where physical processes can be understood more rigorously by looking at the grain-scale level. In geomechanics and mechanics of materials, particulate numerical simulations are called the discrete or distinct element method (DEM), and it is specifically designed to solve problems where continuity between separate elements do not apply. Discrete numerical simulations with particles are currently used in various scientific disciplines, to examine a wide range of physical systems with inherent "granularity". These include stellar dynamics and galaxy formation in astrophysics, fluid turbulence in hydrodynamics, condensed matter mechanics in molecular dynamics, and electrostatic plasma behavior in plasma physics (Hockney and Eastwood, 1981). In addition, the method is used in process engineering to study the flow of granular media in hoppers or down inclined chutes (Campbell and Brennen, 1983; Hawkins, 1983); the development of stresses around tunnel openings in jointed rocks (Lorig and Brady, 1984); non-linear static and dynamic soil structure interaction problems (Ting and Corkum, 1988); and the stress and flow response of naturally fractured fluid reservoirs.

The discrete element method was extended to soils by Cundall and co-workers, using two-dimensional discs (Strack and Cundall, 1978) and three-dimensional spheres (Cundall and Strack, 1979). The DEM and its computer implementations with assemblies of elastic discs are used to study fabric evolution in granular media during loading, and to aid in the development of constitutive relationships for soils (Strack and Cundall, 1978; Cundall and Strack, 1979, and c; Bathurst, 1985; Rothenburg and Bathurst, 1989; Thornton and Barnes, 1986; Ng, 1989). Compared to molecular dynamics calculations, Cundall's treatment has many similarities and some unique differences. Mainly, only particles that are touching each other are analyzed for force calculations in Cundall's method (i.e., only short range forces are considered).

Until recently, DEM approaches considered only dry particulate materials. Harper and Last (1989) developed a flow-coupled DEM, which was designed specifically to evaluate the behavior of fluid-filled blocky media. The blocky media was represented by a set of polygons of arbitrary shape, which interact with their immediate neighbors through planar joints. Hakuno and Tarumi(1988) developed a modified DEM that takes into account pore-water pressure, to analyze liquefaction of saturated sand under seismic excitation. In their analysis, Hakuno and Tarumi simulated the gradual rise of excessive pore-water pressures due to effect of shaking.

In this paper a model considering fluid-induced deformations, which was developed to address the class of flow-coupled problems in granular media as applied to loosely consolidated sandstones in petroleum geomechanics is described. The steady-state pore fluid response has been successfully incorporated into DEM formulation, to simulate fluid-flow induced deformation processes in granular media (Thallak 1991). The same model was also used to address the class of flow-coupled problems related to borehole mechanics (Thallak et al., 1991). This paper briefly presents some of the applications related to petroleum geomechanics using the above developed model. The model considers only two-dimensional disc elements and does not consider excess pore pressure due to change in the pore geometry during the deformations. The model is currently limited to single-phase flow and isothermal problems.

DISCRETE PARTICLE METHOD FOR GRANULAR ASSEMBLIES

The DEM employs an explicit time-finite difference scheme in which each calculation cycle includes the application of two simple force-displacement laws at all disc contacts. Discs in contact can slide with a constant coefficient of friction and can separate if the normal force is reduced to zero. For slippage between discs, Coulomb's friction law is used. The disc accelerations and velocities calculated from Newton's second law are assumed to be constant over a small time step, Δt, and the net forces and moments acting on each disc are updated from force displacement laws applied to the contacts with neighboring discs. In fact, the DEM models a highly-damped transient dynamic mechanical system. It can be imagined as a network of lumped-mass dashpot elements in which damped linear springs connect disc shaped masses. Although the system is dynamic, the transient state approaches a static equilibrium condition if loading rates are kept low enough that inertial disc forces are always a small fraction of the average contact forces acting through the assembly. Kinetic energy is dissipated through introduction of artificial damping; without this damping, the static equilibrium conditions could not be achieved.

FLUID FLOW COUPLING

For purposes of simulating fluid flow in assembly of discs, it is assumed that the state of fluid in each pore can be characterized by an average pressure and that the quantity of fluid transmitted between adjacent voids is proportional to the difference in average pressures. This model of fluid transfer through a granular material is equivalent to flow through a network of interconnected pipes in which nodes of the network are geometrically identified with centroids of voids. Nodes are connected with pipes that transfer fluid according to Hagen-Poissuelle law. The model implies that the transmissibility between two voids is characterized by a pipe transmissibility. It has been shown that the adopted approach to modelling flow through a plane granular material fully emulates Darcy flow in the 2-D representation (Thallak , 1991).

Fluid flow in particulate medium is characterized by developments of microscopic pressure gradients that result in forces acting on particles because of fluid pressure differences in adjacent voids. In the adopted approach to coupling flow and particle motions, the unbalanced body force arising from fluid flow is calculated by integrating pressures acting on surfaces of each particle. The equivalent force is then applied on the particle centroid. The unbalanced body forces cause particle displacements and the latter affect intergranular forces and effective stress.

The computational cycle in the flow coupled DEM model consists of applying boundary fluid pressure, calculating pressure in each void based on the current geometry of voids, updating particle positions due to unbalanced forces, next increment of boundary fluid pressure is applied. This approach has only been developed for steady-state and single-phase flow at the present time. Figure 1 shows the general outline of flow-coupled DEM and the local equilibrium scheme of the particles under both contact and pore fluid pressures. The detailed descriptions of the mode of coupling and verification of the model is given elsewhere.

BOREHOLE STABILITY

The following generic approaches to borehole stability analysis have been in practice in the last couple of decades: empirical approaches based on observation and collection of experience, analytical approaches based on continuum mechanics formulation, numerical approaches including finite element methods and boundary element techniques. All these approaches are based on continuum principles, using a constitutive model to represent formation deformation and yield behavior. In this paper, we have treated the medium as an assemblage of particles, rather than as continuum, as this permits exploration of the actual mechanisms involved. These simulations are carried out with an intention to explore the mechanics of deformation, yield, and load transfer around a borehole in a discrete assembly of particles. Also some of the simulations presented below are a class of flow-coupled problems related to borehole mechanics including topics such as hydraulic fracturing, wellbore stability, and solids production simulations. The flow-coupled discrete particle model discussed above has been used to investigate hydraulic fracturing and production processes in unconsolidated formations. Considering that solids production undoubtedly leads to permeability alterations, the mechanism of this phenomenon, one way or another, is associated with creation of new flow channels in the material surrounding the

a). b).

Modelling of Pore Water
Pressure In Pore 2

d).

contact vector

particle

..... flow channel

c).

U$_i$ - Pore Pressures in the voids   P$_i$ - Contact Normal Forces
T$_i$ - Contact Tangential Forces;   TF$_1$ & TF$_2$ - Net Force Components
F$_1$ & F$_2$ - Net Body Forces. M - Net Moment acting at Disc Centroid

for particle i.contact forces are
summed over neighbours m,n,p,q
and pore pressures are summed
over pores 1,2,3,4

Figure 1. General outline of the flow-coupled DEM and local equilibrium scheme:
   a) identification of associated flow network; b) calculation of body forces due
   to pore pressure; c) local equilibrium scheme of a disc; d) nature of contact

borehole. This can occur either as a result of shear deformations and plastic flow of sand near the borehole or as a consequence of sand washout through wormholes. Both are not mutually exclusive and there may be zones of material around the borehole where permeability is enhanced through different mechanisms.

If plastic flow of sand is the primary mechanism of sand production, the influx of sand grains into the well must be an intermittent process. The hypothesis of an intermittent plastic flow as a mechanism of solids production needs careful analysis of conditions leading to termination and activation of flow. Termination of solids production can be attributed to arching of sand around perforations. Activation or initiation of plastic flow can be attributed to fluid flow/hydrodynamic

drag force and to disturbances related to drilling and operations which lead to destruction of sand arches around perforations. In the following section, initial work on formation of arches and mechanisms of destruction both in cohesive and cohesionless assemblies of discs is presented. The results presented are based on discrete particle simulations with 2-D disc assemblages. The isotropically compacted dense assembly is shown in Figure 2. The disc size distribution corresponds to a log-normal distribution and was taken for a prescribed particle size distribution.

Borehole simulation using DEM

A two-dimensional borehole is simulated by removing some particles that fall in a user defined circular area near the center of the assembly. The centrally located mass of grains is removed from a disc assemblage that is already consolidated to a dense state. Removal of these particles creates an imbalance in the force system, resulting in slip and disintegration of contacts between the grains surrounding the opening. Calculation cycles are iterated slowly until the system comes to equilibrium, which allows the progressive loosening of grains around the opening. This approach permits the study of the mechanisms of the processes around a borehole in a granular
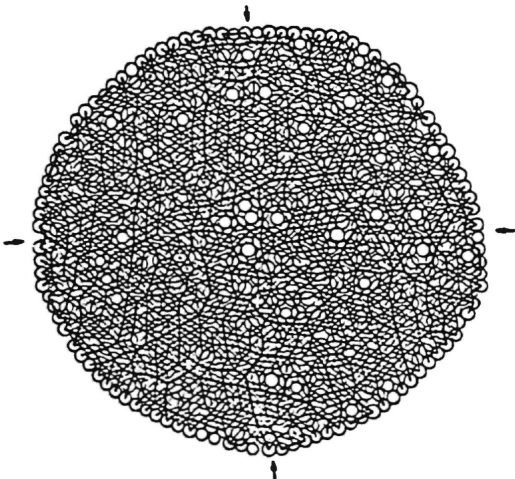
Figure 2. Compacted assembly of circular discs.
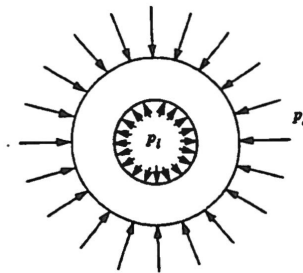
Figure 3. Boundary conditions around
an opening in granular media.

medium, without having to prejudice the results by stipulating possibly unrealistic behavioral law.

Opening in cohesionless media

The possibility of a stable opening in cohesionless media can be questioned if the problem is posed in terms of simplistic continuum mechanics models, such as the ideal Mohr-Coulomb elasto-plastic model. In order to explain this, consider a boundary value problem of determining stresses around an opening in cohesionless material, Figure 3. Can this opening exist if the pressure in the opening , p_i , is reduced to zero?

To solve this problem it is necessary to find a stress distribution that satisfies the equation of equilibrium:

$$\frac{\delta \sigma_r}{\delta r} + \frac{\sigma_r - \sigma_\theta}{r} = 0 \tag{1}$$

where σ_θ is the circumferential stress and σ_r is the radial stress. Radial stress far away from the opening is assumed to be prescribed by $\sigma_r = P_r$. Since the objective is to find a solution to assess the possibility of having a stable opening in cohesionless material, the first attempt is to assume

281

that the system can be in an elastic state without violating the yield condition. With the pressure at infinity, p_r, and the internal pressure at $r=r_o$ taken as zero, the solution for stresses, assuming elastic material behavior, is as follows:

$$\sigma_r = P_r\left(1 - \left(\frac{r_o}{r}\right)^2\right) \quad ; \quad \sigma_\theta = P_r\left(1 + \left(\frac{r_o}{r}\right)^2\right) \tag{2}$$

For this state of stress to be admissible, it should not violate the Mohr-Coulomb yield condition. The mobilized friction angle with the above stresses can be computed as follows:

$$\sin \phi = \frac{\sigma_\theta - \sigma_r}{\sigma_r + \sigma_\theta} = \left(\frac{r_o}{r}\right)^2 \tag{3}$$

With the mobilized friction angle as high as above, the elastic state can exist for only when ratio of radii (r_o/r) is less than 2. When $r/r_o = 1.14$, $\sin\phi = 0.5$ and the mobilized friction angle of $\phi = 30°$ can be sustained by any sand. The conclusion, therefore, is that with the linear elastic model no stable unsupported opening is possible in a cohesionless granular material. This conclusion from a conventional and rather simplistic model is not really true. Only, numerical simulations of discrete particulate assemblies can clearly show that this is in fact incorrect.

Figure 4 illustrates a numerical simulation of an opening in a granular assembly. The opening is produced by equilibrating an assembly of particles under hydrostatic stress and removing several particles to create a plane representation of a borehole. Figure 4 (b) and (c) show the distribution of contact forces and disc trajectories after the removal of particles in the circular area near the center of the assembly. Figure 4 (d) shows the stress distributions determined from a discrete simulation and compares it with the elastic solution presented above along with Kirsch solutions. The force field prior to opening creation was carried uniformly by all grains. After opening creation, forces are redistributed and transferred through adjacent grains around the opening. The stress and strain condition around the opening changes considerably, resulting in an induced stress or force condition. Contact forces are lower in the borehole wall than further in the medium. Displacements are concentrated on the borehole wall, involving an annular region of two layers of particles that dilate. In addition grain deformation vectors [Figure 4 (c)] are not symmetric, which reflects inhomogeneity on the micro-scale. On the surface of the opening, a small group of grains tend to separate from their neighbors and move as a unit inward [Figure 4 (a)]. The process of separation of the grains at their contacts implies that load carrying ability near the borehole is reduced. It can be seen that the build-up of radial stress is slower and the circumferential stress is much smaller compared to the elastic solution near the borehole wall. The state of stress is elastic and corresponds to the mobilized friction angle of 25 degrees at most. The system went through some plastic deformation [see Figure 4(c)] and adjusted itself in such a way that the number of contacts in the vicinity of the opening is reduced. As a result of this loss of interparticle contacts, the elastic modulus is reduced and stresses readjust. This behavior can be identified as arching. The contact force redistribution showing an arching effect is illustrated in Figure 4 (b).

The key element in the arching behavior is related to a lock-up in an elastic state after significant plastic deformation. It is very unlikely that this type of behavior can be described in continuum terms and no known constitutive modelling scheme can bring the system into an elastic state after plastic deformation. For this to happen in a continuum scheme, unloading is necessary. Here the system effectively screened the opening from high stresses by forming a strong shell of particles located at about two to four particle diameters from the opening. The position of this shell coincides with the point of peak circumferential stress in Figure 4 (d).

Opening in bonded particulate media

In this section, a detailed analysis of microscopic processes around an opening in a particulate
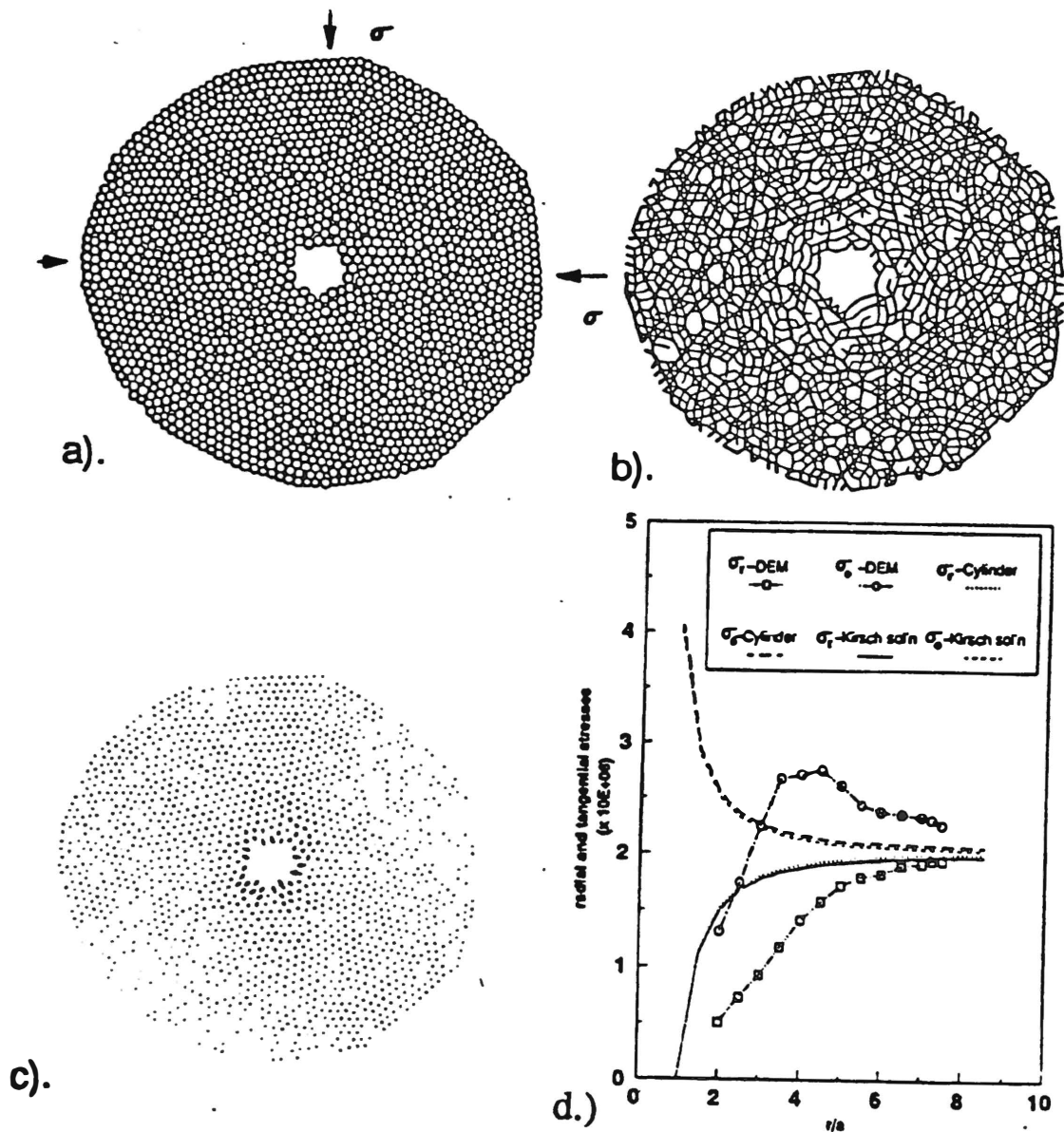
Figure 4. Stresses around an opening in an hydrostatic stress

media comprise of particles with a fixed system of indestructible contacts (with infinite cohesion at particle contacts) is presented. In this case, the contacts do not break or reform during the deformation process, the unbalance forces redistribute by elastic contact deformation only. Numerical simulation of a borehole in a bonded particulate system shows that despite the

simplicity of such systems, their behavior is complex at the grain scale level.

To simulate the borehole, a constant stress is maintained on boundary discs of the compacted assembly containing a hole, and cycles are iterated until static equilibrium conditions are satisfied. Stresses are calculated by averaging contact force vectors in radial and tangential directions over an area. In this case, an annular ring of varying thickness around the opening was used to represent the area (Figure 5), which provides a sufficiently large number of contacts to calculate the average stress. Stresses are calculated by the following equation:

$$\sigma_{rt} = \frac{1}{V}\sum_{c \in V} f_r^c l_t^c \qquad r,t = 1,2 \qquad (4)$$
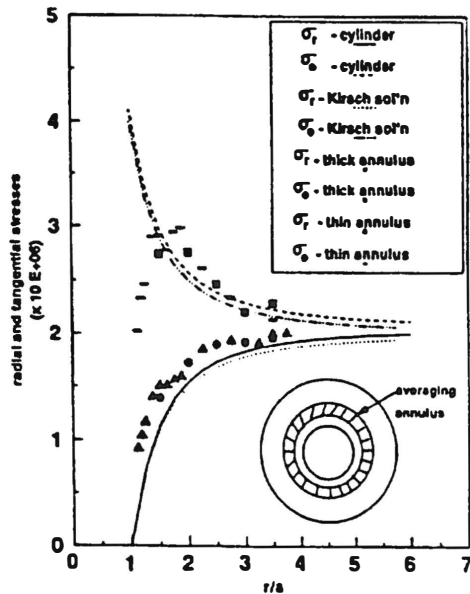
Figure 5. Comparison of DEM results with the elastic Kirsch solutions

Here, f_r^c and l_t^c represent scalar components of contact forces in the radial and tangential directions and the contact vector associated with each assembly contact. V corresponds to the area of the annular ring considered, and c∈V denotes summation over all contacts in the annular ng. The above equation is a direct consequence of equations of static equilibrium for all discs.

Figure 5 shows results from DEM along with analytical solutions for stresses around a circular opening. Analytical solutions are presented both for Lame's equations for a thick cylinder and Kirsch solutions for hydrostatic loading around an opening. Away from the borehole wall, DEM results compare well with analytical solutions. However, close to the borehole wall stresses are reduced, compared to elastic solutions. As the particles are bonded, all the contacts are preserved, which eliminates the possibility of particle rearrangement. The reduction in stress close to the borehole wall is attributed to a reduction in modulus, which is caused by micro-structural anisotropy that is created during redistribution of the contact forces around the opening (in a way, an arching effect). The evolution of microstructural anisotropy in the bonded assembly is therefore the cause of the shift in peak tangential stress away from the borehole wall.

Borehole simulation with fluid flow

The injection and production tests in a borehole a e carried out to study the effect of outward and inward flow on the deformation process, as well as the effect of outward flow in an opening on fracture initiation pressures and their o ientations. Pressure or flow boundary condition is applied on the inside and on the outside of the model. The assembly is subjected to a prescribed boundary stress, that is, a force applied to each of the boundary particles. The details of the simulations are presented elsewhere (Thallak et al.,1992). Figure 6 shows an example problem where in a hydraulic fracturing is simulated by incremental increase of injection pressure or outflow from the borehole, maintaining constant total stress and pore pressure at the boundary, until the contact force between two particles becomes zero. When this occurs, the two adjacent pores are coalesced, and this corresponds to fracture initiation. Repeated iterations with slowly increasing pressures result in a progressive coalescence of pores and a propagating fracture is created.

Figure 6. Borehole simulation in hydrostatic stress field with outward flow: a) Disc assembly; b) Contact force distribution (thickness of line indicates the magnitude of contact force); c) Disc displacement vectors

CONCLUSIONS

The discrete particle method adequately simulates deformation mechanisms in particulate media in a more realistic way than any continuum based model developed so far. The power of DEM in identifying mechanisms is evident from the simulations and DEM methods have potential to emulate the realistic behavior of granular geomaterials in complex conditions. Although these particulate mechanics simulations of borehole are not a design tool at the present time, they do provide more insight into the load-transfer mechanisms, and this insight will guide other numerical approaches.

ACKNOWLEDGEMENTS

REFERENCES

Bathurst,R.J., 1985. A study of stress and anisotropy in idealized granular assemblies, Ph.D Dissertation, Queen's University, Kingston, Canada.

Campbell,C.S., and Brennen,C.E., 1983. Computer simulation of shear flows of granular material, Mechanics of Granular Materials: New Models and Constitutive Relations, Jenkins and Satake (eds), pp. 313-326.

Cundall,P.A., and Strack,O.D.L. 1979. The distinct element method as a tool for research in granular media PART II, Report to NSF, Dept. of Civ. & Min. Engineering, Univ. of Minnesota, USA.

Hakuno,M., and Tarumi,Y., 1988. A granular assembly simulation for the seismic liquefaction of sand, Structural Eng. / Earthquake Eng., Japan Society of Civil Engineers, Vol. 5, No.2, pp. 333s-342s.

Harper,T.R., and Last,N.C., 1989. Interpretation by numerical modelling of changes of fracture system hydraulic conductivity induced by fluid injection, Geotechnique, 39, No.1, pp. 1-11.

Hawkins,G.W. 1983. Simulations of granular flow, Mechanics of Granular Materials: New Models and Constitutive Relations, Jenkins & Satake (eds), pp. 305-312.

Hockney,R.W., and Eastwood,J.W. 1981. Computer simulation using particles, McGraw-Hill Int'l Book Co., New York.

Lorig,L.J., and Brady,B.H.G. 1984. A hybrid computational scheme for excavation in support design in jointed rock media, Design and Performance of Underground Excavations IRSM/BGS, Cambridge, England, pp. 105-112.

Ng Tang-Tat, 1989. Numerical simulation of granular soil under monotonic and cyclic loading: A particulate mechanics approach, Ph.D. Dissertation, Rensselaer Polytechnic Institute, Troy, New York.

Rothenburg,L., and Bathurst,R.J. 1989. Analytical study of induced anisotropy in idealized granular materials, Geotechnique, 39, No.4, pp. 601-614.

Strack,O.D.L., and Cundall,P.A. 1978. The distinct element method as a tool for research in granular media PART I, Report to NSF concerning Grant Eng.76-20711, Dept. of Civ. & Min. Engineering, Univ. of Minnesota, USA.

Thallak,S.G., 1991. Numerical simulation of hydraulic fracturing in granular media, Ph.D Thesis, University of Waterloo, Waterloo,Ontario, Canada.

Thallak,S.G., Rothenburg,L.R., and Dusseault,M.B., 1991. Analysis of borehole stability using discrete element models, Proc. of 7th International Congress on Rock Mechanics, Aachen, Germany, pp. 813-818.

Thallak,S.G., Holder,J., and Gray,K.E., 1992. Physical mechanisms of solids production, DRM-125, Solids Production Research Program, CESE, Univ. of Texas at Austin, Texas.

Thornton,C. and Barnes,D.J. 1986. Computer simulated deformation of compact granular assemblies, Acta Mechanica, 64, pp. 45-61.

Ting,J.M., and Corkum,B.T. 1988. Strength behavior of granular materials using discrete numerical modelling, 6th International Conference on Numerical Methods in Geomechanics, Innsbruck, Austria.

Application of the inverse method for in situ stresses determination with USBM cell.

A. Misbahi, J.F. Shao, J.P. Henry
Mechanics Laboratory of Lille - URA 1441 CNRS
EUDIL - University of Lille I
59 655 - Villeneuve d'Ascq Cédex. FRANCE

ABSTRACT

The knowledge of in situ stresses is one of the primordial data. In order to determine in situ stresses in the anisotropic medium like a schistos rock, a probability approach using the inverse problems theory and the overcoring technic (**USBM cell**) was developed.The direct problem consisting to modelling the overcoring tests is solved by the Displacements Discontinuity method (**DISDEPLAN's code**).The connexion between the inverse problems theory and DISDEPLAN's code is then etablished (**SINVERS's code**).The validation of this code is realized by the simple compression tests on the cubic samples of schistos rock (40*40*40 cm). The sensibility study of the results to the material parameters shows there importance in the determination of in situ stresses.The SINVERS'code is then used in an experimental gallery which depth is about 430 m , we obtained :
- The vertical stress (10.5 - 11 MPa) is closely related to the ground weight.
- The horizontal stresses are equal respectively to 15.2 MPa perpendicularly at the plane of schistosity and to 12.4 MPa parrallel at the plane of schistosity.

RESUME

La connaissance des contraintes naturelles du site est l'une des données primordiales. Dans l'objectif de déterminer ces contraintes in situ dans les milieux très anisotropes comme le schiste,une approche probabiliste utilisant la théorie des problèmes inverses et la technique de surcarottage (**cellule USBM**)est développée.Le problème direct qui consiste à modéliser les essais de surcarottage est résolu par méthode des Discontinuités de Déplacement (code DISDEPLAN) .La connexion entre la théorie des problèmes inverses et DISDEPLAN est alors établie(code SINVERS).La validation de ce code est réalisée par des essais de compression simple sur des cubes de schiste(40*40*40cm).L'étude de sensibilité des résultats aux modules du matériau montre leur importance dans la détermination des contraintes in situ.Le code SINVERS est en suite utilisé dans une galerie expérimentale à environ 430m de profondeur,on obtient:
- La contrainte verticale (10,5-11MPa) est proche du poids des terrains,
- Les contraites horizontales sont égales respectivement à 15,2 MPa perpendiculairement au plan de schistosité et à 12,4 MPa parallèlement au plan de schistosité.

I - Introduction

The in situ stresses determination very often comes to inverse the values that are in complex relations, more or less, with in-situ stresses. Theorically and in the case of USBM cell, for exemple, Bonnechere [1] showed the entire determination of the tightener required the use of Three drillings of different orientations. He also added that it was enough to take six values of independant displacement in order to determine a problem perfectly.

This deterministic approach poses some problems nawely those linked to the solution stability in its relation, for exemple, with experimental errors and quality values of rock modulus.

However, we can increase the measurements number in order to minimize the experimental errors. There arises then the inverse problem of subordinate data. A simple method, of a deterministic type, consists in resolving the system by injecting successively a set data and in optimizing the obtained results through the least squares. Unfortunately, this method does not consider the positive aspect of subordinate data and experimental dispersions.

We propose in this work a general inversion of data in the parameters field. We will use the techniques of inversion applied in diagraphes (Tarantola [7], Shao and all [6]).

In the first part, we will present the calculation method and we will validate it by tests in laboratory. In the second part, we will apply the method to in-situ tests in mine.

II - Presentation of the calculation method

II.1 The Displacement discontinuity method (plane elasticity anisotropic)

The calculation method of stresses is essentially composed of a numeric calculation method of Displacements around a drilling in plane elasticity and of the inverse method. The numeric method used here is the Displacement Discontinuity method coined initially by Crouch [2] for elastic mediums and adjusted to studies in fissured mediums. It uses a normal or a tangential discontinuous displacement in the length of a fissure. This numeric border technique was extended by Morel [5] to anisotropic mediums using an approach with a complex field [4]. The determination of linear coefficients enables us to calculate the stresses and the displacements in the contour and in the studied field.

In order to resolve elastic and anisotropic problems an application program was found : it called DISDEPAN.

II.2 Application of the inverse problem theory to stresses measurements

II.2.1 Definition of the problem

According to the principes of the USBM cell, the calculation of radial displacements are function of stresses, materials behaviour and geometry problem constitutes a direct problem that can be described by the following relation :

(2.1) $\qquad D = F(P, C)$

In this F, the functional, represents the relation between the displacements D and the in-situ stresses that

288

are the problem parameters. They can be designated by the vector P. The vector C representes a set of constants of the problem such as the law of the rock behaviour and the dimension of the USBM cell measurement.

The determination of the in-situ stresses consists in getting P due to the measurements in-situ of radial displacements designated as Dm. This leads to defining an inverse problem as follows :

(2.2) $P = F^{-1} (D_m, C)$

The explicit resolution of this inverse problem is generally impossible. It is necessary to use an optimization process. The problem consists then in determining the vector P as follows :

(2.3) $D_c = F(P, C)$ and $|\cdot D_m - D_c| \le \varepsilon$

Or, D_c is the vector of radial displacements calculated by DISDEPAN and ε is the sill of tolerance.

II.2.2   Statistic approach

We will use a statistic approach in order to resolve the inverse problem by the optimization process.

The displacements measurement in-situ on the USBM cell are carried out with a certain degree of uncertainty. We consider then the experimental values used in the relation (2.2) like the average values and we can associate to the latter a vector of standard deviation. Therefore, the vector of the calculated displacements are considered as an uncertain variable. We put forward a hypothesis that the uncertain variable checks Gauss' distribution. We define as a consequence, the density function of probability by :

(2.4) $f_1 (P) = P_1 = \text{constant } \exp (- 1/2 \,[^t (D_c - D_m) \; C_d^{-1} (D_m - D_c)])$

In this relation C_d is the covariance matrix calculated by standard variations. As D_c is the function of P, the problem is therefore to look for P in such a way that D_c gives the maximum of P_1. This leads then to minimize the quantity of S_d :

(2.5) $S_d = + (D_c - D_m) \; C_d^{-1} (D_c - D_m)$

The resolution of the minimizing problem gives some times many possible solutions as it is undicated by figure 1. As the in-situ stresses vary in a margin of values phsically accepted, it is necessary to eliminate the solutions that are purely mathematical. This leads us to define a physical field of parameters based on the knowledge of the values of these parameters. For exempler, the normal in-situ stresses in depth, are generally in compression.

For this prupose, we use as the reference values of the parameters the average of the physical field of the parameters and we associate this average to the standard types. Using again Gauss' distribution, we get the density function of the following probability

(2.6) $f_2 (P) = P_2 = \text{constant } \exp (- 1/2 \,[^t (P - P_o) \; C_d^{-1} (P - P_o)])$
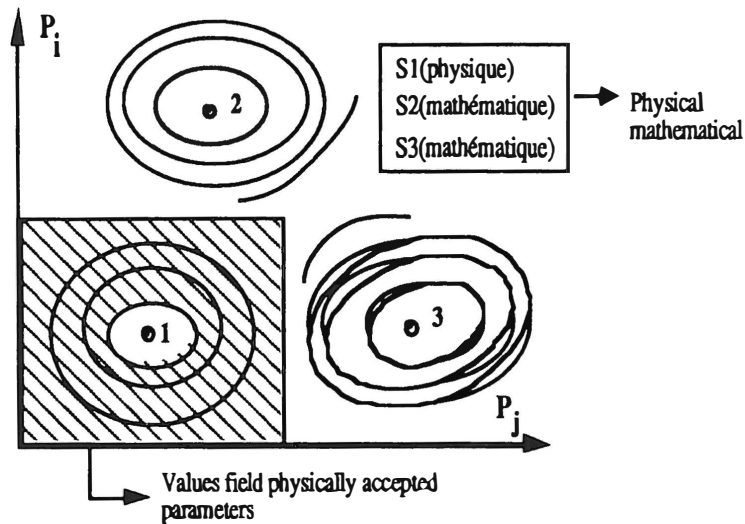
Figure 1 : Physical parameters field

In this relation C_d is the covariances matrix calculated by standard types.

The resolution of the inverse problem (2.2) consists then is finding the vector P in the physical field that satisfies the condition (2.3). This corresponds to defining the intersection P_1 and P_2, so a globale function density of probability

(2.7) $\qquad f(P) = P_1 \, P_2 = \text{constante} \cdot \exp(-S)$

with : $\qquad S = 1/2 \, [{}^t (D_c - D_m) \, C_d^{-1} (D_c - D_m) + {}^t (P - P_o) \, C_p^{-1} (P - P_o)]$

The resolution of the inverse problem is transformed into minimizing $f(P)$ and Therefore into minimizing the quantity S. The vector of the parameters to be determined is the one that minimizes S.

II.2.3   The resolution method

There exists different resolution methods of the minimization problem, (Fletcher [3], Tarantola [7]. For our work, we consider that Gauss Newton's method is the most powerful and the most used in the problems in which the function $D_c(P)$ is derivative and this is the case. For this reason we adapted this method in our study.

II.2.4   General structure of SINVERS program

The calculation programme by the inverse method is composed two main modulus, the first modulus that concerns the optimization part. Second, the direct resolution problem by the Displacements Discontinuity method. The general structure of the programme may be summed up by figure 2.

$$P_{k+1} = P_k - \left(\frac{\partial^2 S}{\partial p^2}\right)^{-1}_{P_k} \left(\frac{\partial S}{\partial p}\right)_{P_k}$$
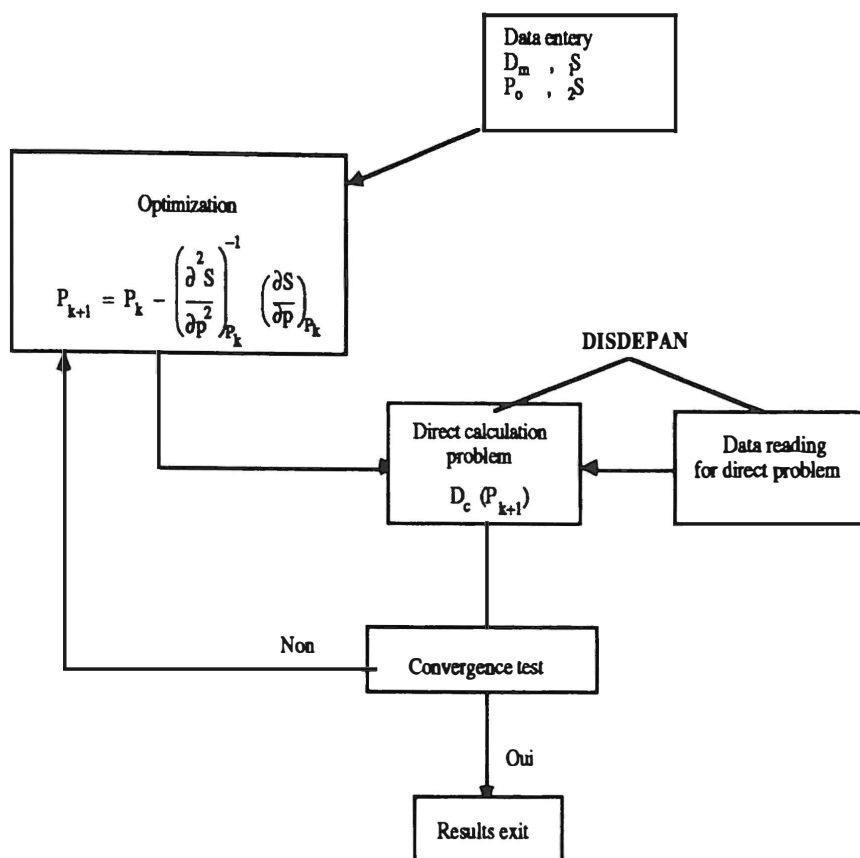
Figure 2 : Organisation figure of SINVERS logiciel

III. The validation of the method from tests in laboratory

After having established the method, it is important to validate it on perfectly defined data. On the one hand, we will give a brief account of the results obtained from the direct method. On the other hand, we will use the results given by the cell in order to find for the stresses perfectly known.

III.1   Simple compression tests on schist cube with the USBM cell
III1.1   Description of simple compression tests on schist cube with the USBM cell

The cube schist (40 cm x 40 cm x 40 cm) was pierced by a hole of 4 cm of diameter in its center. The USBM cell was installed inside it.

The compromise between the available tests means and the avoiding of exceeding the conditions limits have incited us to use a cube of 40 cm of edge. To avoid fissuring the block, the simple compression loading was carried out moderately and perpendicularly to the schistosity plan.

III.1.2   Tests measurement and studying

The caracterization of the cube deformation field was carried out by extensometry gauges (of 20 mm of lenght). The gauges enabled us to determine the Young's modulus E_1 and the Poisson's coefficient

v_{12} of great level following four tests (see tables 1 and 2).

	Gauge 1	Gauge 2	Average 1 + 2
Test 1	29 000	48 000	39 000
Test 2	30 000	49 000	39 500
Test 3	35 000	40 000	37 500
Test 4	32 000	49 000	40 500

	v_{12}
Test 1	0.30
Test 2	0.35
Test 3	0.39
Test 4	0.29

Tableau 1 : Modulus value E_1 during different tests   **Tableau 2 :** Poisson's coefficient values v_{12}
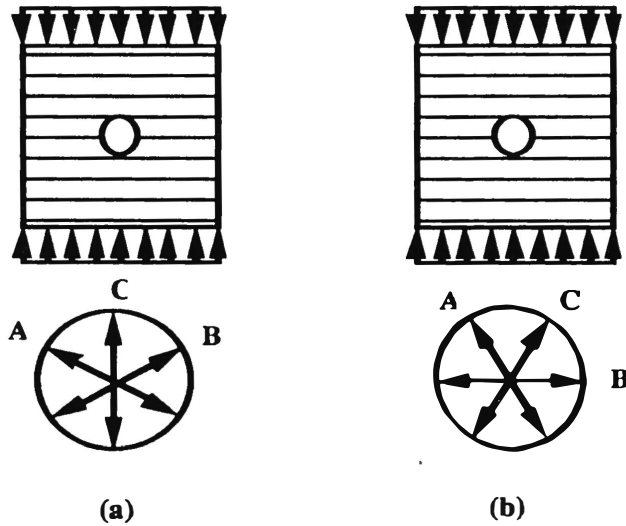
Figure 3 : USBM cell arrangement - (a) : tests 1 and 3 ; (b) : tests 2 and 4

The radial displacements (U_r) inside a drilling were measured by the USBM cell following four tests of simple compression. We used two sets of measurement a and b (see figure 3). The applied stresses on the cube did not exced 10 MPa.

* set (a) :   is composed of two tests measurements U_r (tests 1 and 3) following the orientations (30°, 90°, 150°) (figure 3a).
* set (b) :   is composed of two tests measurements U_r (tests 2 and 4) following the orientations (0°, 60°, 120°) (figure 3b).

III.2   Direct problem modelization by DISDEPAN

The schist cube is modelling in plan problem by a square plate 2a (a = 20 cm) pierced in its center by a circular hole of 4 cm of diameter. If we take the reper (0 / X, Y) of the figure 4, we will notice that the load is applied on the sides y = + a, y = - a.

The problem to be modelling directly by DISDEPAN is the following (figure 4).
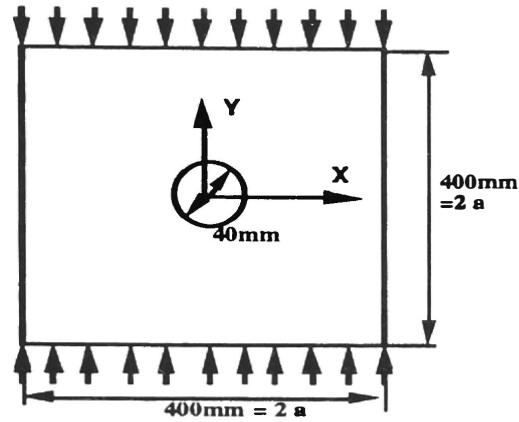
Figure 4 : Definition of simple compression test on schist cube

III.3   Application of the inverse method (SINVERS USE)
III.3.1   Results

The present results take into account the two sets of experimental measurement (set 1 = test 1 + test 2, set 2 = test 3 + test 4). We shouled point out that they are superabondant in the deterministic approach.

We added to there two sets another one designated as set n° 3. The latter considers all the measurements (set 3 = set 1 + set 2). It is worthy of noting that in this case, we have two convergence values by an orientation, consequently, we can deduct an average value and a first approach of the standard deviation.

The different obtained results by SINVERS are presented in tables 3 and 4, the elastic characteristics values of material are $E_1 = 35\ 000$ MPa, $E_2 = 107\ 000$ MPa, $v_{12} = 0,3$, $G_{12} = 10\ 000$ MPa. The initial stress value injected in the calculation is 5 MPa.

However, it is important to note the precision of the proposed method. The iterations number is weak, that is to say, that the calculation time is very weak.

The table 4 presentes set 3 for which the calculation starting is made at $\sigma = 3$ MPa instead of $\sigma = 5$ MPa. This was carried out bearing in mind two things. First, to check if we find the same inverse value and second to determine the additional iterations number if we inject an initial value away from the optimal value.

	Série n°1	Série n°2	Série n°3
Parameters number to be determined	1	1	1
Parameter to be determined	σ(MPa)	σ(MPa)	(MPa)
Exact value	5	5	5
Value by SINVERS	4,93	5,8	5,42
Iterations number	12	9	8
Error purcentage	1,4 %	16 %	8 %

	Série n° 3	
Parameters number to be determined	1	1
Parameter to be determined	σ(MPa)	σ(MPa)
Exact value	5	5
Starting value	5	3
Inverse value	5,42	5,45
Iterations number	8	12

Table 3 : Stresses values obtained by SINVERS

Table 4 : Influence of starting value

293

III.3.2 The influence study of elastic coefficient on optimal value

The initial elastic values are $E_1 = 35\ 000$ MPa, $E_2 = 107\ 000$ MPa, $v_{12} = 0,3$ et $G_{12} = 10\ 000$ MPa (tables 5, 6, 7 et 8)

E_1 (MPa)	30 000	35 000	40 000	45 000
σ (MPa) exacte	5	5	5	5
σ (MPa) inversed	4,62	4,93	5,95	6,5

v_{12}	0,2	0,3	0,4
σ (MPa) exacte	5	5	5
σ (MPa) inversed	4,44	4,93	5,41

Table 5 : Influence study E_1 on the stress value by SINVERS

Table 6 : Influence study v_{12} on the stress value by SINVERS

E_2	90 000	100 000	107 000	115 000	130 000
σ (MPa) exacte	5	5	5	5	5
σ (MPa) inversed	5,61	5,28	4,93	4,91	4,90

G_{12} (MPa)	4 000	6 000	8 000	10 000	12 000
σ (MPa) exacte	5	5	5	5	5
σ (MPa) inversed	4,50	4,68	4,79	4,93	4,94

Table 7 : Influence study E_2 on the stress value by the SINVERS

Table 8 : Influence study G_{12} on the stress value by SINVERS

IV. APPLICATION TO IN SITU STRESSES DETERMINATION IN A MINE
IV.1 The site

The test site, of a depth of about 430 m in schist, has the following geometrical arrangements (figure 5) :
* Schistosity is lightly sloping in relation to the vertical
* A main sub-horizontal gallery was carried out with a first perpendicularly part to the schistosity and a second parallel to the schistosity level
* Three horizontal drillings were perforated (figure 5)
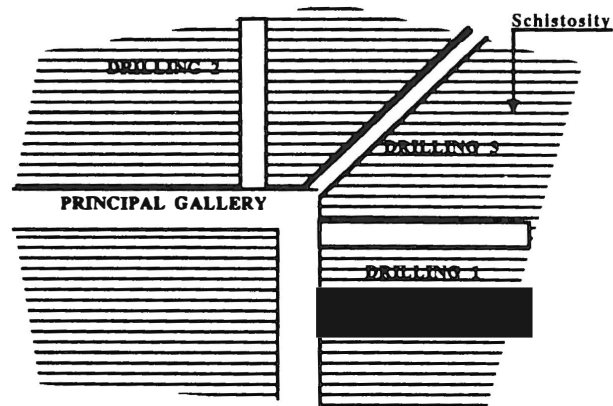
Figure 5 : Definition of the test site

IV.2   STRESSES DETERMINATION

The DISDEPAN logiciel was used for planes problems, so the modelization of drilling 1 (figure 6.a) and drilling 2 (figure 7.a). The given signals by the USBM cell (figures 6.b, 7.b) allowed us to dispatch the SINVERS logiciel in order to determined the stresses σ_v, σ_H for the drilling 1 and the stresses σ_v, σ_h for the drilling 2.
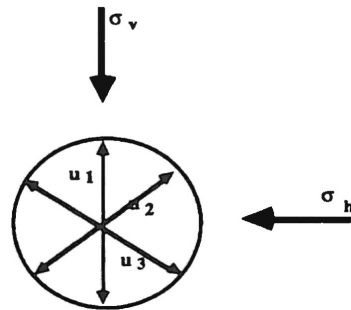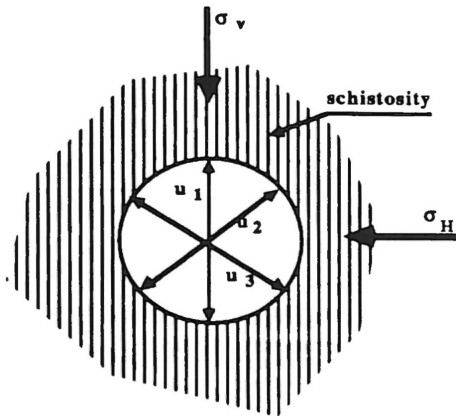
Figure 6.a : Drilling 1 with USBM cell position   **Figure 7.a** : Drilling 2 the USBM cell position
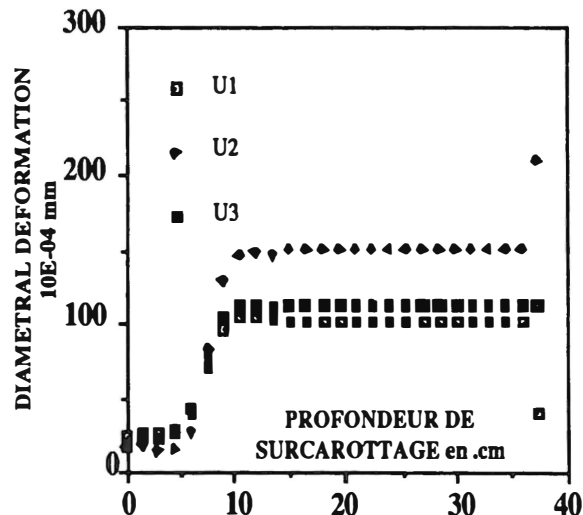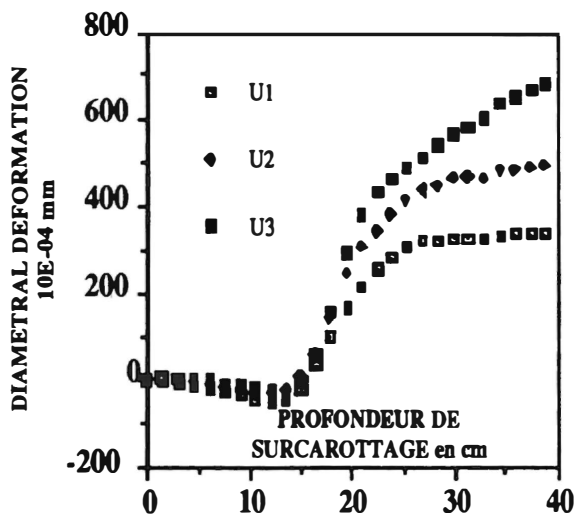
Figure 6.b : Deformation measurements to the   **Figure 7.b** : Deformation measurements to the
USBM information to overcoring   USBM information to overcoring

However, we have to determine $\sigma_v, \sigma_H, \sigma_h$. If σ_v supposed equal to the soil weight and if the forwarded different hypothesis were not too inexact, we have to find the identical values for σ_v and these have to be quite equal to the soil weight.

The use of SINVERS with radial displacements values give (figure 8) :

* drilling 1   : σ_v = 10,5 MPa   , σ_H = 15,2 MPa

* drilling 2   : σ_v = 11 MPa   , σ_h = 12,4 MPa
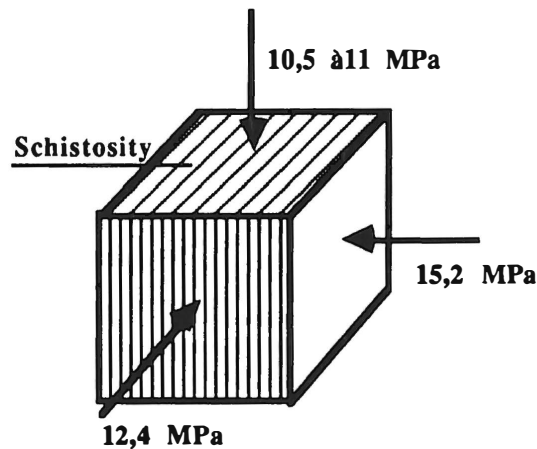
Figure 8 : In-situ stresses values obtained by the inverse method used on the studied site

V. CONCLUSION

The inverse problem method which we applied to the determination of the in-situ stresses showed its performences with very short calculation time. To resolve the direct problem we used the displacement discontinuity method extend in anisotropic meduims, this method applied now only to resolve plan problems.

This approach of the determination of in-situ stresses in the case of anisotropic meduims has two important advantages :

* It shows that it is necessary to desoriente the cell from one test to another, to increase the vector D_m and as a consequence to increase the results reliability.

* It allows to study in a short time the sensibility of the results to the modulus values that are, in anisotropic meduims, difficult to be determined on site.

BIBLIOGRAPHY

[1] **Bonnechere F.** (1971) - "Contribution à la détermination de l'état de contraintes des massifs rocheux" - Thèse de Docteur ès Sciences, Université de Liège

[2] **Crouch** - "Solution of plane elasticity problems by the displacement discontinuity method" - Int. J. Num. Meth. In Eng., Vol., p. 301-343

[3] **Fletcher R.** (1980) - Pratical methods of optimization" - John Wiley and Sons, 1980

[4] **Lekhnitski S.G.** (1963) - "Theory of elasticity of an anisotropic elastic body" - Hoden Day Inc.

[5] **Morel E.** (1987) - "Contribution à l'étude de la propagation des discontinuités dans les roches anisotropes. Mise au point d'une technique de calcul utilisant l'intégrale de Cauchy et étude expérimentale d'un schiste ardoisier" - Thèse de Doctorat USTL

[6] **Shao J.F., Dahou A., Henry J.P.** - "Application de la théorie des problèmes inverses à l'estimation des paramètres des modèles rhéologiques" - Revue Française de Géotechnique (à paraître 1991)

[7] **Tarantola A.** (1987) - "Inverse problem Theory" - Elsevier

PROPAGATION OF RANDOM ERRORS IN FINITE ELEMENT ANALYSES

A. Szostak-Chrzanowski
Department of Surveying Engineering, University of New Brunswick

A. Chrzanowski
Department of Surveying Engineering, University of New Brunswick

S.L. Kuang
Superconducting Super Collider Laboratory, Dallas, Texas

ABSTRACT

The accuracy of finite element analyses depends mainly on: (1) discretization error (2) computer round-off errors, and (3) Biases (systematic errors) and uncertainties (random errors) of the mechanical properties of the material and of the input observation data (loads and/or displacements). The first two effects and the influence of systematic errors have already been extensively investigated and discussed in the literature by many authors. The influence of random errors has lacked a rigorous treatment. The authors have perfomed modelling of random errors of the material properties and of the observed input data and developed a methodology for the determination of the variance-covariance matrix of the quantities derived from a finite element analysis. The theory of variance-covariance propagation has been applied in the study. A practical example is given.

RÉSUMÉ

La précision des calculs exécutés par la méthode des éléments finis dépend principalement sur: (1) les erreurs discréminatoires (2) les erreurs d'arrondissement, et (3) des biais (erreurs systématiques) et les incertitudes (erreurs aléatoires) des propriétés mécaniques du matériau et de l'entrée des données (charges et déformations). Les deux premiers effets et l'influence des erreurs systématiques ont été longuement discutés dans diverses littératures. Par contre, les erreurs aléatoires ne sont pas traitées d'une manière aussi rigoureuse. Les auteurs ont donc modelisé les erreurs aléatoires associées aux propriétés du matériau et à l'entrée des observations, et ont developpé une méthode pour déterminer la matrice de variance-covariance à partir des résultats générés par la méthode des éléments finis. La théorie de propagation d'erreur a été appliquée. Un exemple pratique est aussi inclus.

1. INTRODUCTION

The accuracy of finite element method (FEM) analyses depends mainly on: (1) discretization error (2) computer round-off errors, (3) matrix ill-conditioning, and (4) errors in the physical parameters of the material and input boundary conditions (observed loads and/or deformation). These effects never allow for an exact solution to be obtained. Therefore, users of the finite element method must always be aware of the accuracy limitations and should always perfom a quantitative analysis of the errors of the FEM results before using them for any further analysis and/or interpretation.

The influence of the first three factors has been extensively investigated and discussed in the literature by many authors (e.g., Zienkiewicz and Taylor, 1989). The influence of errors in the physical parameters of the material and errors in the boundary conditions, though generally recognized, particularly in rock and soil mechanics, as the main sources of errors in FEM analyses, have lacked a rigorous treatment. These errors may be classified into two groups, (a) systematic biases from the true values and (b) random uncertainties. The influence of a systematic bias, for example a difference between the in-situ and laboratory values of Young modulus, E, can be introduced into the error analysis in a *trial and error* mode by performing the FEM analysis separately for each value of E and checking whether the difference in the output results is significant. Propagation of random errors, however, is much more complex and requires a rigorous propagation of variances and covariances of the parameters which are treated as random variables. This approach is particularly important in any rock mechanics problems where mechanical properties of the same type of rock may be significantly changing from one location to another due to inhomogenities and discontinuities in the rock material. In this case, even if in-situ determination of the properties is performed, it can be done only at a few discrete points while in other places the values may differ randomly within a certain, statistically determined, confidence (±) interval.

This paper summarizes a methodology developed by the authors for the propagation of random errors in the process of finite element analyses and determination of the variance-covariance matix of the quantities derived from an analysis. Due to limitations in the length of the paper, the given methodology refers only to the determination of variances and covariances of displacements at nodal points obtained from a linear-elastic FEM analysis assuming that the random errors of the physical parameters of the material, acting forces, and displacement boundary conditions are known. A brief review of the basic concepts and definitions of error propagation are given first, followed by the summary of the developed methodology and an exmple of FEM calculations of surface and underground displacements produced by a tunnel excavation.

2. THEORY OF PROPAGATION OF RANDOM ERRORS

2.1. Basic Terms and Definitions

Results of any measurements (treated as random variables) or quantities derived from random variables are meaningless unless they are accompanied by information on their accuracy. Terms such as variance, covariance, standard deviation, confidence level, and probability, are commonly used in accuracy analysis. They are briefly defined (after Chrzanowski, 1993) below. More details can be found in any basic textbook on the theory of errors and statistical analysis (e.g., Mikhail, 1976).

The *variance* (usually denoted by σ^2) of a random variable is a statistical measure of the dispersion and reliability of the value. It is also called mean square error. The variances of observations can be determined either through repetitive test measurements, or through evaluation of all component sources of errors (pre-analysis).

The *covariance* (denoted, e.g., as σ_{ab}) of two observations, a and b, which are affected by the same source of errors or two quantities derived from the same random variables is a measure of statistical dependence (correlation) of the two values. If two observation values are uncorrelated, their covariance equals zero.

The *standard deviation* (denoted by σ) of an observation is the positive square root of the corresponding variance. It is also called standard error or root mean square (rms) error. The standard deviation of a random variable, if determined from a large (approaching infinity) sample of observations, represents a probability (confidence level) of 68% that the difference between its observed and true values is within the interval $+\sigma$ to $-\sigma$. To increase the confidence level to 95% or 99%, the standard deviation must be multiplied by 1.96 or 2.58, respectively. Usually, the 95% confidence level is selected as a tolerance for the maximum expected difference between the calculated and observed quantities. The *variance-covariance matrix* is an ensemble of variances and covariances of the individual values. The matrix, denoted by $\mathbf{C}$, is square and symmetrical with variances on the main diagonal and covariances between i-th and j-th values at the intersections of the ith and j^{th} rows and columns.

2.2. Propagation of Variances and Covariances

If a set of n unknowns u_i (vector $\mathbf{u}$) is computed from a set of k known variables z_i (vector $\mathbf{z}$) that have known variances and covariances (matrix $\mathbf{C_z}$), then according to the general formula, known as the propagation of variance-covariance matrices, we can calculate the variance-covariance matrix $\mathbf{C_u}$ of the unknowns from

$$\mathbf{C_u} = \mathbf{A}\,\mathbf{C_z}\,\mathbf{A^T} \tag{1}$$

where $\mathbf{A}$ is the design matrix containing partial derivatives of the functions $u_i = u_i(z_1, z_2, \ldots, z_k)$, where $i = 1, 2, \ldots, n$ at the approximate points of variables.

If only one unknown, say u_1, is a function of several known variables, say z_1, z_2, and z_3, then the above general law of variance-covariance propagation leads to the formula of error propagation,

$$\sigma_{u_1}^2 = \left(\frac{\partial u_1}{\partial z_1}\right)^2 \sigma_{z_1}^2 + \left(\frac{\partial u_1}{\partial z_2}\right)^2 \sigma_{z_2}^2 + \left(\frac{\partial u_1}{\partial z_3}\right)^2 \sigma_{z_3}^2$$

$$+ 2\frac{\partial u_1}{\partial z_1}\frac{\partial u_1}{\partial z_2}\,\sigma_{z_1 z_2} + 2\frac{\partial u_1}{\partial z_1}\frac{\partial u_1}{\partial z_3}\,\sigma_{z_1 z_3} + 2\frac{\partial u_1}{\partial z_2}\frac{\partial u_1}{\partial z_3}\,\sigma_{z_2 z_3} \tag{2}$$

where the partial derivatives are calculated for approximate values of z_1, z_2, and z_3.

3. PROPAGATION OF RANDOM ERRORS IN FEM DISPLACEMENT ANALYSIS

3.1. Basic Definitions and Formulations in FEM

Using the well known principles of the finite element displacement approach, the global equilibrium equation for the investigated object may be written as:

$$K\delta = r - f^b - f^{\sigma 0} - f^{\varepsilon 0} \tag{3}$$

where $\delta = (u_1\ v_1\ u_2\ v_2 \ldots\ldots\ldots\ldots u_n\ v_n)^T$ is the vector of nodal displacements (in a two dimensional analysis, K is the global stiffness matrix of the material, f^b is the global loading vector of body forces, $f^{\sigma 0}$ is the global loading vector from initial stresses, $f^{\varepsilon 0}$ is the global loading vector from initial strains, and r is the vector of external forces concentrated at nodal points. The global matrices and vectors are calculated through a superimposition of local (at each element or at each node of the FEM mesh) matrices K_e and vectors f_e^b, $f_e^{\sigma 0}$, and $f_e^{\varepsilon 0}$. The transformations may be expressed as:

$$K = \sum_{e=1}^{ne} T_e^T K_e T_e \tag{4}$$

$$f^b = \sum_{e=1}^{ne} T_e^T f_e^b \tag{5}$$

$$f^{\varepsilon 0} = \sum_{e=1}^{ne} T_e^T f_e^{\varepsilon 0} \tag{6}$$

$$f^{\sigma 0} = \sum_{e=1}^{ne} T_e^T f_e^{\sigma 0} \tag{7}$$

The local stiffness matrix and local loading vectors are calculated from:

$$K_e = \iint B_e^T D B_e\, t\, dxdy \tag{8}$$

$$f_e^b = - \iint N_e^T b t\, dxdy \tag{9}$$

300

$$f_e^{\varepsilon 0} = - \iint B_e^T D \varepsilon_0^e \, t \, dxdy \tag{10}$$

$$f_e^{\sigma 0} = \iint B_e^T \sigma_0^e \, t \, dxdy \tag{11}$$

where B_e is the matrix relating strains in the element to its nodal displacements, N_e is the shape function, D is the constitutive matrix of the material which, in case of the linear elastic analysis, contains the elasticity parameters E and v, t is the unit thickness of the elements (two-dimensioanl analysis), $b = (b_x \, b_y)^T$ is the vector of body force, ε_0 is the vector of initial strains, and σ_0 is thevector of initial stresses.

Since the stiffness matrix K is singular, boundary conditions must be applied in order to solve equation (3) for the displacements. Assume that the displacement boundary conditions are given by

$$H^T \delta = d \tag{12}$$

where d is a nd by 1 vector of known displacements. Then, the solution of equation (3) is given by

$$\delta = (K + sHH^T)^{-1}(sHd + r - f^b - f^{\sigma 0} - f^{\varepsilon 0}) \tag{13}$$

where s is a scale factor which should be chosen to be sufficiently large according to the computer capability.

3.2. Propagation of Variances and Covariances in FEM

If one treats the variables E, v, σ_0, ε_0, r, and body forces b in each element as random variables with a known variance covariance matrix C_z, then, using the general rule (equ.1) of the error propagation, one can calculate the variance-covariance matrix C_δ of the nodal displacements from:

$$C_\delta = AC_z A^T \tag{14}$$

where

$$A = \left(\frac{\partial \delta}{\partial E} \quad \frac{\partial \delta}{\partial v} \quad \frac{\partial \delta}{\partial \varepsilon_{01}^1} \quad \frac{\partial \delta}{\partial \varepsilon_{02}^1} \quad \frac{\partial \delta}{\partial \varepsilon_{03}^1} \quad \cdots \quad \frac{\partial \delta}{\partial \varepsilon_{01}^{ne}} \quad \frac{\partial \delta}{\partial \varepsilon_{02}^{ne}} \quad \frac{\partial \delta}{\partial \varepsilon_{03}^{ne}} \quad \frac{\partial \delta}{\partial \sigma_{01}^1} \quad \frac{\partial \delta}{\partial \sigma_{02}^1} \quad \frac{\partial \delta}{\partial \sigma_{03}^1} \quad \cdots \right.$$

$$\left. \frac{\partial \delta}{\partial \sigma_{01}^{ne}} \quad \frac{\partial \delta}{\partial \sigma_{02}^{ne}} \quad \frac{\partial \delta}{\partial \sigma_{03}^{ne}} \quad \frac{\partial \delta}{\partial b_x} \quad \frac{\partial \delta}{\partial b_y} \quad \frac{\partial \delta}{\partial r_{1x}} \quad \frac{\partial \delta}{\partial r_{1y}} \quad \cdots \quad \frac{\partial \delta}{\partial r_{nx}} \quad \frac{\partial \delta}{\partial r_{ny}} \quad \frac{\partial \delta}{\partial d_1} \quad \cdots \quad \frac{\partial \delta}{\partial d_{nd}} \right)$$

(15)

with

$$\frac{\partial \delta}{\partial \sigma_{0i}^e} = - (K + sHH^T)^{-1} (T_e^T \iint B_e^T \frac{\partial \sigma_0^e}{\partial \sigma_{0i}^e} t \, dxdy) \quad (i=1, ..., 3; e=1, ..., ne)$$

$$\frac{\partial \delta}{\partial b_x} = (K + s\, H\, H^T)^{-1} (\sum_{e=1}^{ne} T_e^T \iint N_e^T \binom{1}{0} t \, dxdy)$$

$$\frac{\partial \delta}{\partial b_y} = (K + s\, H\, H^T)^{-1} (\sum_{e=1}^{ne} T_e^T \iint N_e^T \binom{0}{1} t \, dxdy)$$

$$\frac{\partial \delta}{\partial E} = - (K + sHH^T)^{-1} \left\{ \sum_{e=1}^{ne} T_e^T \left(\iint B_e^T \frac{\partial D}{\partial E} B_e \, dxdy \right) T_e \right\} t \, \delta$$

$$\frac{\partial \delta}{\partial v} = - (K + sHH^T)^{-1} \left\{ \sum_{e=1}^{ne} T_e^T \left(\iint B_e^T \frac{\partial D}{\partial v} B_e \, dxdy \right) T_e \right\} t \, \delta$$

$$\frac{\partial \delta}{\partial \varepsilon_{0i}^e} = (K + s\, H\, H^T)^{-1} (T_e^T \iint B_e^T D \frac{\partial \varepsilon_0^e}{\partial \varepsilon_{0i}^e} t \, dxdy) \quad (i=1, ..., 3; e=1, ..., ne)$$

$$\frac{\partial \delta}{\partial r_{ix}} = (K + s\, H\, H^T)^{-1} \left(\frac{\partial r}{\partial r_{ix}} \right) \qquad (i=1, ..., n)$$

$$\frac{\partial \delta}{\partial r_{iy}} = (K + s \, H H^T)^{-1} \left(\frac{\partial r}{\partial r_{iy}} \right) \qquad (i=1, ..., n)$$

$$\frac{\partial \delta}{\partial d_i} = (K + s H H^T)^{-1} \left[s \, H \frac{\partial d}{\partial d_i} \right] \qquad (i=1, ..., nd)$$

In case of a plane strain two-dimensional analysis

$$\frac{\partial D}{\partial E} = \frac{1}{(1+v)(1-2v)} \begin{pmatrix} 1-v & v & 0 \\ v & 1-v & 0 \\ 0 & 0 & \frac{1-2v}{2} \end{pmatrix}$$

$$\frac{\partial D}{\partial v} = \frac{E(1+4v)}{[(1+v)(1-2v)]^2} \begin{pmatrix} 1-v & v & 0 \\ v & 1-v & 0 \\ 0 & 0 & \frac{1-2v}{2} \end{pmatrix} + \frac{E}{(1+v)(1-2v)} \begin{pmatrix} -1 & 1 & 0 \\ 1 & -1 & 0 \\ 0 & 0 & -1 \end{pmatrix}$$

$\partial d / \partial d_i$, $\partial \varepsilon_0^\varepsilon / \partial \varepsilon_{0i}$, and $\partial \sigma_0^\varepsilon / \partial \sigma_{0i}$ are vectors of zeros except for identity at the i-th position; $\partial r / \partial r_{ix}$ is a vector of zeros exept for identity at the (2*i-1)-th position; and finally, $\partial r / \partial r_{iy}$ is a vector of zeros exept for identity at the (2*i)-th position.

More details on the developed methodology are given in (Szostak-Chrzanowski et al., 1992).

4. EXAMPLE

To demonstrate the developed methodology, a simple example is given which deals with the analysis of rock deformations produced by excavating a circular tunnel of a 6 m diameter. The linear elastic analysis has been perfomed using software FEMMA (Szostak-Chrzanowski, 19...) with four -nodal elements. The FEM mesh and boundary conditions are shown in Fig. 1. An enlargement of the tunnel section is shown in Fig.2. For a simplicity of the example, only one type of rock material has been considered throuout the cross-section and only the weight of the rock, distributed as body forces acting in each element, has been taken as the acting load. The following physical parameters of the rock have been taken for the calculation of the expected displacements:

Young modulus: $E = 1$ GPa

Poisson ratio: $v = 0.300$

Unit weight: $\gamma = 19$ KN/m^3

It was assumed that the standard deviation of each of the above given parameters amounts to 20% of the given values, i.e.,

$\sigma_E = 0.2\ E$

$\sigma_v = 0.2\ v$

$\sigma_\gamma = 0.2\ \gamma$

Due to the symmetry of the problem, only half of the opening has been analyzed. The predicted (calculated from FEM analysis) displacements at several selected points on the surface and in the tunnel and their standard deviations, obtained from the described propagation of the random errors, are listed in Table 1. The results indicate that, in the given conditions, the calculated from FEM horizontal displacements of points 2 to 4 are statistically insignificant because their errors at the 95% confidence level (i.e., 1.96 σ) are larger than the values of the displacements. All the vertical displacements, however, are significant.

In order to verify the calculations, a reversed problem has been solved by taking the value of E as an unknown parameter which is supposed to be determined in-situ from observed vertical displacements at the points 1 to 5 as listed in table 1. It was assumed that the vertical displacement of each point had been obtained from repeated geodetic levelling with standard deviations of 0.5 mm. Table 2 lists the obtained values of E and their standard deviations as obtained from individual vertical displacements. The results show that the weakest determination of E would be obtained if the measurements of the vertical displacements would be limited only to pint 3. If the value of E would be estimated from vertical displacements of all 5 points simultaneously, then

$E = 999.7$ MPa and

$\sigma_E = 41.3$ MPa.

One can see that the calculated mean value of E is, as expected, very close to the original input value. This verifies the correctness of the computation procedures.

Table 1: The predicted displacements and their corresponding standard deviations

Point	dx (mm)	σ_{dx}(mm)	dz(mm)	σ_{dz}(mm)
p1	0.00	0.00	3.13	1.01
p2	0.67	0.48	1.43	0.46
p3	0.73	0.57	-0.44	0.14
p4	0.52	0.39	-2.78	0.90
p5	0.00	0.00	-3.87	1.26
p6	0.00	0.00	0.00	0.01
p7	0.15	0.04	-0.06	0.03
p8	0.25	0.08	-0.60	0.19
p9	0.10	0.04	-0.77	0.29
p10	0.00	0.00	-0.79	0.30

Table 2: Young modulus E and its accuracy (σ_E) calculated from the measured vertical displacements

Point	dz(mm)	σ_{dz}(mm)	E(MPa)	σ_E(MPa)
p1	3.13	0.50	999.6	79.7
p2	1.43	0.50	999.7	127.4
p3	-0.44	0.50	999.4	568.4
p4	-2.78	0.50	999.8	64.6
p5	-3.87	0.50	999.8	89.9
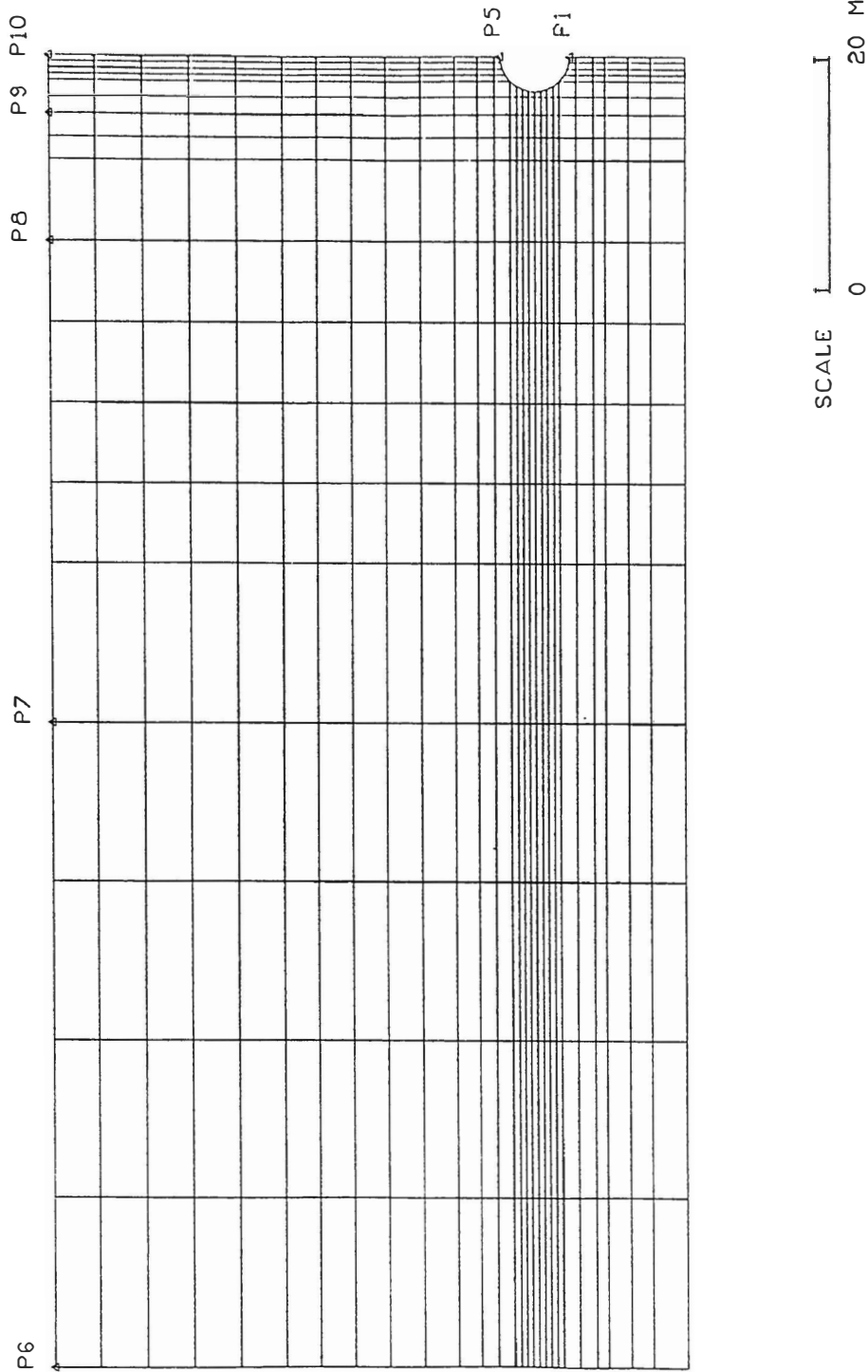
Fig.1. FEM mesh for the rock deformation analysis due to a tunnelling excavation
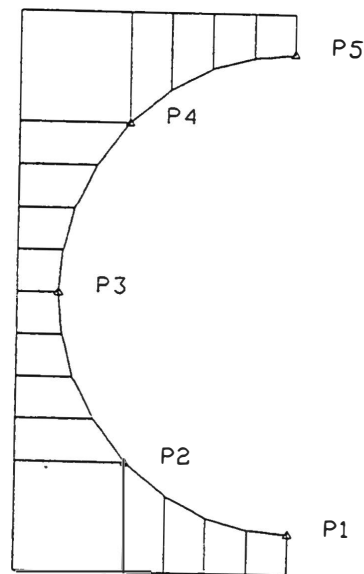
Fig.2. FEM mesh around the tunnel

5. REFERENCES

Chrzanowski, A. (1993): "Modern Surveying Techniques for Mining and Civil Engineering" in "Comprehensive Rock Engineering" vol.3 (ed. J.A.Hudson), Pergamon Press, (in press)

Mikhail, E.M. (1976):"Observations and Least Squares"IEP- A Dun-Donnelley Publisher, New York.

Szostak-Chrzanowski, A., and A. Chrzanowski (1991): "Use of Software FEMMA in 2-D and 3-D Modelling of Ground Subsidence", Proceedings of the 2-nd Canadian Conference on Computer Applications in the Mineral Industry (ed. R.Poulin et al.), CIM, Vancouver, B.C., 15-18 September, pp.689 - 700.

Szostak-Chrzanowski, A., A. Chrzanowski, and S.L.Kuang (1992): "Error Modelling and Quality Analysis for Finite Elelement Method", Internal Report, Dept. of Surveying Eng., Univ. of New Brunswick

Zienkiewicz, O.C. and R.L. Taylor (1989): "The Finite Element Method", 4-th edition, McGraw Hill, London,Toronto.

Modélisation et conception d'un bâti de chargement à l'aide de la méthode des éléments finis

A.-P. Bois, M. Lizotte, J.-C. Michel, G. Ballivy
Laboratoire de mécanique des roches, Département de génie civil, Université de Sherbrooke,
Sherbrooke, Canada

K. Saleh
Institut de recherche en électricité du Québec (IREQ), Montréal, Canada

RÉSUMÉ

Le développement de tout instrument passe nécessairement par la simulation de son
fonctionnement en laboratoire. Cette opération peut être délicate à réaliser de par les deux
principales contraintes qui lui sont associées, à savoir: être proche de la réalité in situ et
minimiser les coûts engagés.
Le Laboratoire de mécanique des roches de l'Université de Sherbrooke a développé une
cellule de suivi des variations de déformation, cellule trouvant son application dans les
milieux rocheux ou en béton. Le but de cette communication est de présenter les différentes
étapes de la modélisation numérique d'un bâti de chargement conçu pour en simuler le fonc-
tionnement . Sa précision en tant que bâti simulant la réalité in situ ainsi que la minimisation
des coûts impliqués sont discutés. Le code de calcul employé est CÉSAR-LCPC (France).

ABSTRACT

Laboratory simulation of an instrument's operation is an essential phase. It is, however, a
delicate balance of replicating in situ conditions as closely as possible while minimizing
related costs.
The Rock Mechanics Laboratory of the Université de Sherbrooke has developed a cell for
monitoring strain variations that can be used in both rock and concrete. This paper presents
the various stages in the numerical modelling of a loading frame designed to simulate in situ
conditions. The system's precision in replicating conditions and cost minimizing are
discussed. The CÉSAR code from LCPC (France) has been used.

1. INTRODUCTION

La mécanique des roches est une science théorique et expérimentale. Elle nécessite la conception, la fabrication et la calibration d'outils appropriés mis en pratique au laboratoire ou sur le chantier. Cependant, avant de pouvoir mettre toute sa confiance sur de tels instruments, il est nécessaire de tester leur précision, leur fiabilité et leurs dérives; ceci se fait généralement à l'aide d'un bâti de simulation.

L'auscultation des milieux rocheux ou en béton est un des domaines de recherche du Laboratoire de mécanique des roches et de géologie appliquée de l'Université de Sherbrooke; un des principaux outils utilisés est le Cylindre instrumenté de l'Université de Sherbrooke (C.I.U.S.) qui a pour but le suivi des variations de déformation et de contrainte dans le temps et à long terme (Ballivy et coll. 1990).

Il s'agit d'une inclusion cylindrique de béton instrumentée d'extensomètres à corde vibrante. Le béton est choisi suivant les propriétés du milieu encaissant, l'objectif étant d'avoir une inclusion aussi homogène que possible avec celui-ci. Les extensomètres à corde vibrante ont été sélectionnés en raison de leur grande longévité et stabilité dans le temps. Ils mesurent les déformations ainsi que les températures. Dans le cas d'une cellule tridimensionnelle, six sont nécessaires et leur orientation est donnée dans la figure 1.
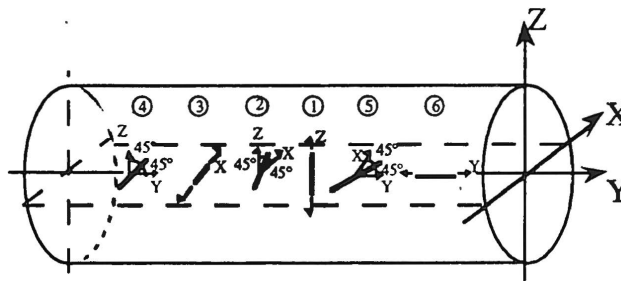
Figure 1 - Orientation des extensomètres

La longueur du C.I.U.S. est de 535 mm et son diamètre de 140 mm. Le volume de l'inclusion est donc important, ce qui assure d'une bonne représentativité des mesures, surtout dans le cas des barrages en béton, où les granulats peuvent être très gros (jusqu'à 200 mm de diamètre équivalent).

La fabrication consiste en l'installation des extensomètres dans un moule approprié, et coulage du béton du C.I.U.S.; les extensomètres ayant été calibrés auparavant. Une fois le démoulage effectué, le cylindre subit un mûrissement d'au moins 28 jours en atmosphère hygroscopique saturée. La calibration s'en suit à l'aide d'une cellule de confinement biaxial de type Hoek.

L'installation du C.I.U.S. (fig. 2) se fait dans un trou de forage de 152 mm de diamètre (6 pouces); il est scellé par un coulis à base de ciment contenant un agent expansif pour limiter les effets du retrait et un réducteur d'eau pour obtenir un module élastique relativement élevé. Environ deux mois sont requis pour que le C.I.U.S. devienne stable et remplisse ses fonctions, à savoir: le suivi des variations de déformation et de contrainte dans le temps.
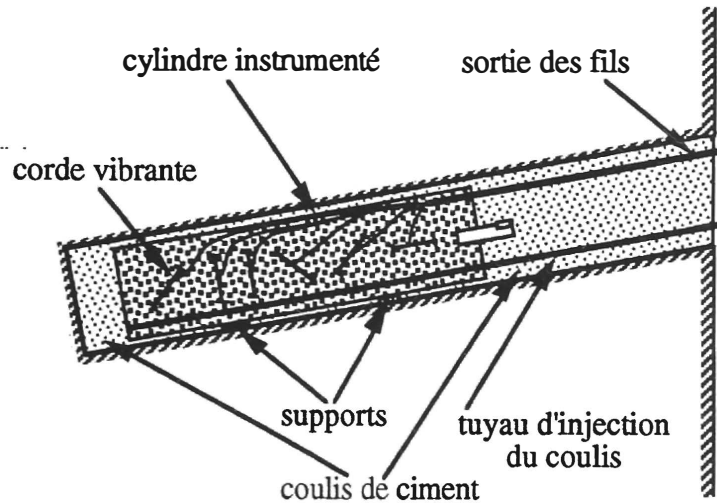
Figure 2 - Installation du C.I.U.S.

À ce jour, quatre barrages, un pilier de mine, un tunnel du Laboratoire souterrain d'ÉACL, une butée du Biodôme de Montréal et un pont ont été instrumentés, ce qui représente un total de 39 C.I.U.S.

Ainsi, c'est dans le but d'améliorer nos connaissances sur cette technique, d'évaluer le comportement de différents extensomètres, de coulis d'injection de compositions différentes qu'il a été décidé de construire un bâti de simulation en vraie grandeur.

2. OBJECTIFS DE LA SIMULATION

Les contraintes associées à la conception d'un tel bâti sont de plusieurs ordres:

- contraintes géométriques: diamètre du trou égal à 152 mm, longueur du trou au moins égale à 525 mm;

- contraintes mécaniques: le bâti devant simuler un milieu encaissant dont les propriétés élastiques peuvent être très élevées, il est fabriqué à l'aide de béton à haute performance ($E \geq 50$ GPa, $C_0 \geq 100$ MPa). Ainsi, le comportement d'un C.I.U.S. dans un milieu très rigide peut être simulé en utilisant un C.I.U.S. de module faible, et celui d'un C.I.U.S. de même rigidité que le milieu dans lequel il est installé par un C.I.U.S. de fort module. Les propriétés extrêmes des différents milieux telles que modélisées sont données dans le tableau I.

Tableau I - Propriétés des milieux présents

	Module de Young (GPa)	Coefficient de Poisson
Milieu encaissant	70	0,1
Coulis d'injection	20	0,2
Béton du C.I.U.S.	30	0,2

- contraintes structurelles: le bâti doit pouvoir transmettre une pression uniforme de 8MPa tout en demeurant sécuritaire;

- contraintes pratiques: le bâti doit être réutilisable afin de pouvoir tester plusieurs combinaisons d'extensomètres, de coulis, de béton. Il doit être simple à l'emploi;

- contraintes financières: il est nécessaire de minimiser les coûts impliqués dans le bâti afin d'investir dans les tests qui nécessitent pour la plupart l'achat d'extensomètres. Ceci est particulièrement vrai lorsque l'on considère le prix des bâtis vendus sur le marché.

Le modèle choisi est illustré à la figure 3. Il s'agit d'un cube central de béton contenant l'inclusion, entouré de deux autres cubes dont le but est de parfaire l'homogénéisation du transfert de charge. L'ensemble repose sur une grande plaque d'acier et est recouvert d'une petite plaque d'acier, d'un vérin plat et d'une plaque d'acier de mêmes dimensions que la première. Les deux grandes plaques sont reliées par plusieurs tiges d'acier et la charge est appliquée à l'aide du vérin. Le dimensionnement des divers éléments s'est fait à l'aide du code CÉSAR-LCPC, code utilisant la méthode des éléments finis.

Tiges d'acier (Ø7,5 × 300)

Plaque d'acier (120 × 120 × 6,35)

Superposition d'une plaque d'acier (60 × 60 × 2,54) et d'un vérin plat entouré de ses deux galettes métalliques

Cube tampon (60 × 60 × 60)

Trou de forage (Ø 15)

Cube central (60 × 60 × 60)

Cube tampon (60 × 60 × 60)

Plaque d'acier (120 × 120 × 6,35)

Support en béton armé (100 × 100)
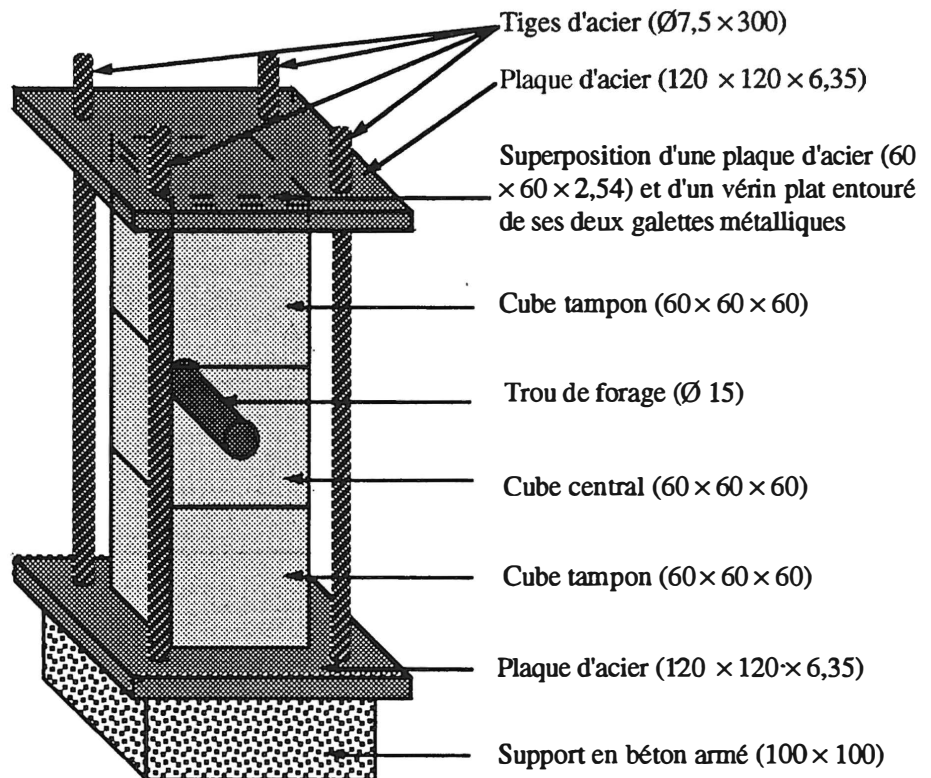
Figure 3 - Bâti de chargement (dimansions en cm)

3. DIMENSIONNEMENT DE LA FACE DU CUBE PERPENDICULAIRE AU C.I.U.S.

3.1 Modèle théorique de Spathis et Truong

Le problème d'une inclusion en milieu infini a fait l'objet d'une étude de Spathis et Truong (1989). Ils ont utilisé les équations de Savin (1961) et ont fourni l'expression analytique des contraintes exercées dans une inclusion pour un problème comportant trois milieux différents sous l'effet d'un champ biaxial. Ces analyses ont été faites en élasticité plane.

Afin de tester la fiabilité des maillages, une première simulation, consistant en un chargement uniaxial σ_y (Fig. 4), a été réalisée et a été comparée avec la solution exacte. L'analyse a porté sur l'évaluation de l'erreur relative $(\sigma_{César} - \sigma_\infty)/\sigma_\infty$ où $\sigma_{César}$ et σ_∞ sont fournis par le code numérique et les équations de Spathis et Truong. Pour des raisons de symétrie, la modélisation n'a considéré qu'un quadrant du plan (Fig. 4) et correspond à un carré de 1,50 m de côté, soit 10 fois le diamètre de l'inclusion. Cette géométrie modélise donc le milieu infini et a fourni les informations nécessaires à l'évaluation de l'erreur commise par le code de calcul. Le modèle comporte 923 noeuds et 1750 éléments de type triangle à trois noeuds.
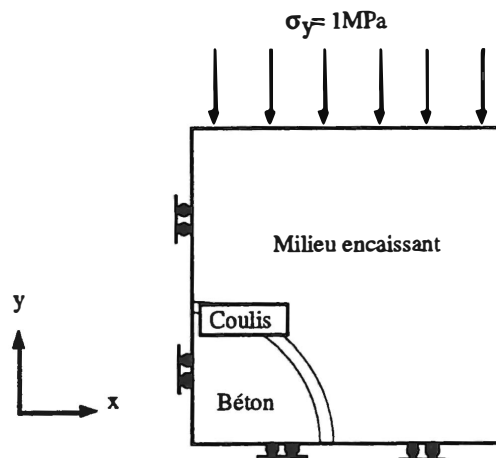
Figure 4 - Modélisation du cube central.

Compte tenu du champ de contrainte créé par ce chargement, deux coefficients ont été analysés, à savoir $C_x = S_x/\sigma_y$ et $C_y = S_y/\sigma_y$ où S_x et S_y sont les contraintes normales selon les directions Ox et Oy. La figure 5 représente ces valeurs telles que calculées par CÉSAR - LCPC ainsi que la solution de Spathis et Truong selon les axes de symétrie horizontal et vertical: on y constate la bonne précision des calculs. C_x a une valeur quasiment nulle dans l'inclusion (10^{-4}) et C_y de l'ordre de 0,7. Les autres directions donnent des résultats identiques. Ainsi, pour un cube de 1,50 m de côté, l'erreur est limitée à 1%.

3.2 Recherche de la 1re dimension du parallélépipède

La taille de cube de roche choisi doit correspondre au meilleur compromis entre des impératifs de maniabilité en laboratoire et des motifs financiers d'une part, et un majorant de l'erreur commise sur les mesures de contrainte à l'intérieur du cylindre d'autre part.

312

Plusieurs modélisations ont été réalisées en faisant varier la longueur du côté de la face. Et l'analyse des résultats montre qu'une 1re dimension du parallélépipède égale à 60 cm est nécessaire pour limiter l'erreur à 5% (Fig. 6).
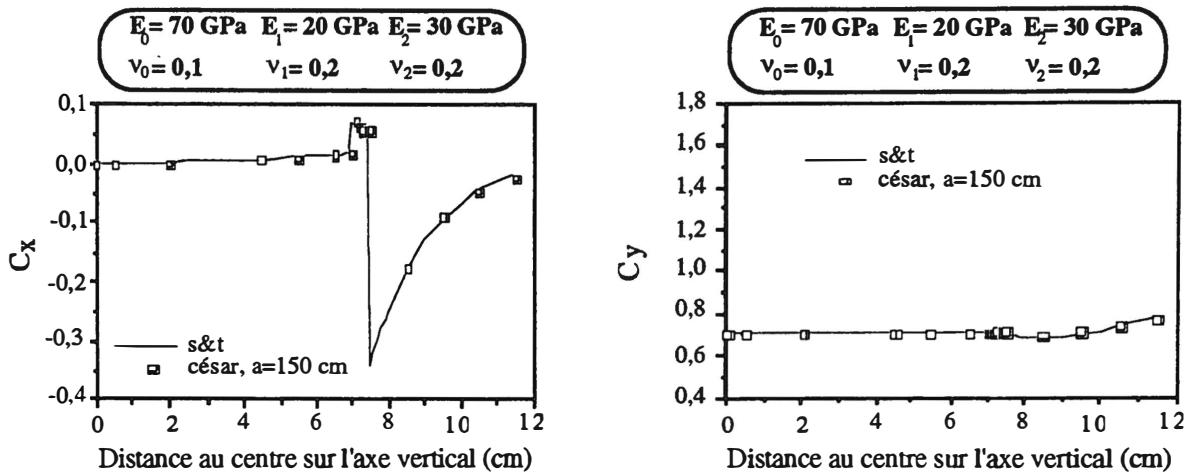
Figure 5: Variations de C_x et C_y sur l'axe vertical
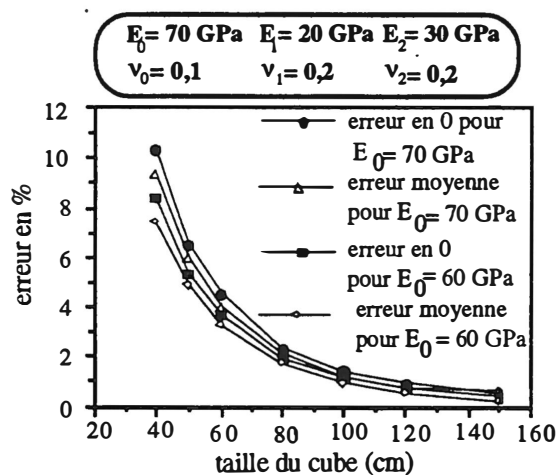
Figure 6 - Erreur au centre (O) et erreur moyenne pour différentes tailles de cube
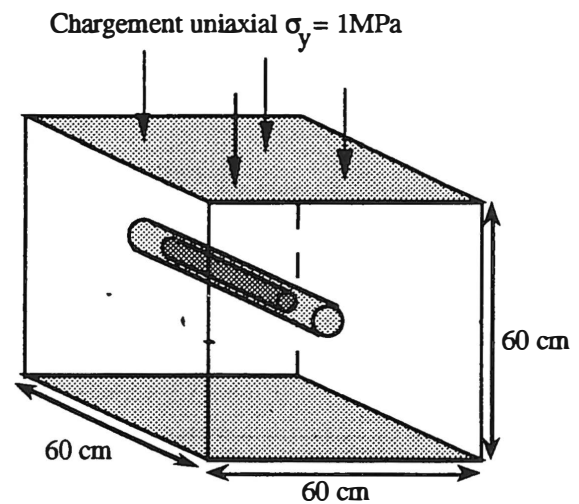
Figure 7 - Chargement uniaxial du cube

4. DIMENSIONNEMENT DE LA TROISIÈME DIMENSION DU CUBE CENTRAL

Etant donnée la longueur du cylindre (525 mm), une modélisation a été entreprise avec un cube de 60 cm (60> 52,5) (Fig. 7) Le maillage ne représente qu'un quart du cube et comprend 2360 éléments prismatiques à base triangulaire à 6 noeuds et 1617 noeuds. Les conditions limites sont du même type que celles du modèle en deux dimensions.

Soumis à un chargement uniaxial suivant la direction Oy (Fig. 7), ce modèle montre une concentration C_{yy} rigoureusement stable sur l'axe z sur plus de 55 cm comme le confirment les courbes d'isovaleurs de C_{yy} dans les plans de symétrie horizontal et vertical (Fig. 8 et 9). Ainsi, la stricte uniformité de C_{yy} valide les calculs précédents en déformation plane où était tenue pour acquise une bonne restitution des contraintes.
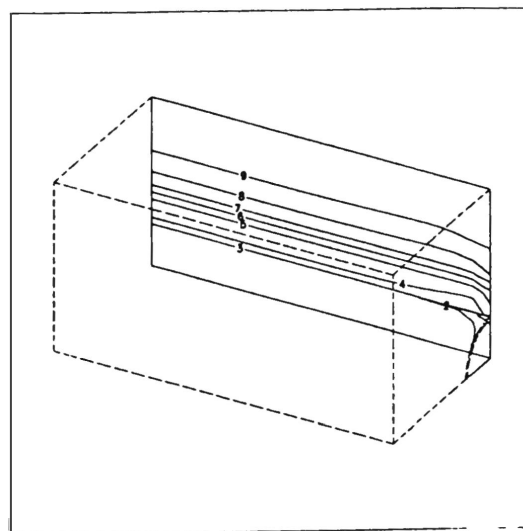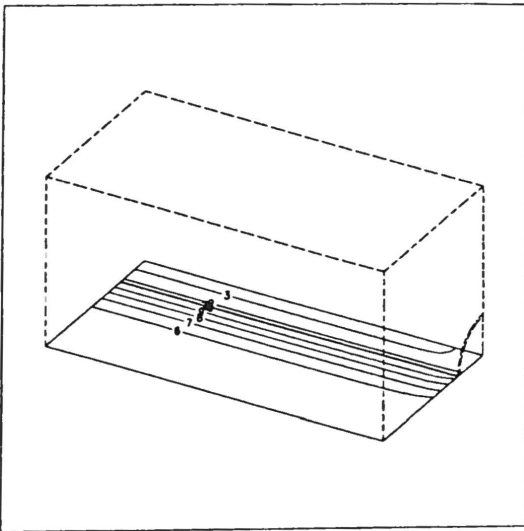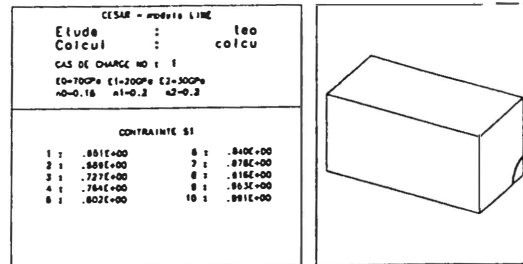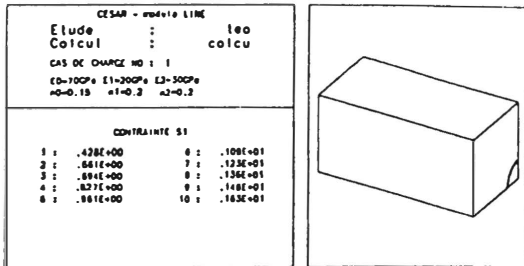
Figure 8 - Courbes d'isovaleur de Czz sur
le plan de symétrie horizontal

Figure 9 - Courbes d'isovaleur de Czz sur
le plan de symétrie vertical

5. MONTAGE EN LABORATOIRE

L'expérience et la théorie montrent qu'il est quasiment impossible d'obtenir un champ uniforme lorsqu'un cube de béton est chargé axialement à l'aide de plaques métalliques (Al-Chalabi 1974, Bonnechère 1967). Ceci provient du fait que les plaques, n'ayant pas tendance à se dilater horizontalement autant que le béton, confinent le cube par friction. Le champ de contrainte à l'intérieur de l'échantillon devient polyaxial. En fait, le seul cas où ce problème n'apparait pas est lorsque le rapport v/E des plaques est égal à celui du béton.

Ainsi, il a été décidé, pour remédier à ce problème, d'entourer le cube central par deux autres cubes de mêmes dimensions. Une autre technique, plus délicate toutefois, aurait été d'utiliser des inserts de téflon (Peng 1971).

314

Afin d'obtenir les 8 MPa de pression sur le bâti, un vérin plat de type Freyssinet de 60 cm de diamètre a été sélectionné. Sa capacité interne étant de 14,5 MPa, il peut exercer une pression de 10 MPa sur le bâti.

La rigidité du bâti a été obtenue à l'aide de quatre tiges en acier de 75 mm de diamètre, ce qui représente une capacité maximale de 4 * 4310 kN , soit un facteur de sécurité de 6.

Les dernières pièces à dimensionner ont été les deux plaques d'acier. La longueur de leur côté a été choisi à 120 cm pour des raisons pratiques. Deux modélisations aux éléments finis (éléments prismatiques à base triangulaire) ont été faites: la première modélisant une moitié des cubes sans le trou de forage avec la plaque de dessous (Fig. 10) (1068 noeuds et 1470 éléments); la seconde modélisant la plaque de dessus avec la pression du vérin plat (Fig. 11) (890 noeuds et 1204 éléments). Ces deux modélisations ont permis de vérifier l'homogénéité du champ de contrainte à l'intérieur du cube central ainsi que de déterminer l'épaisseur de ces deux plaques. Pour des plaques de 6,35 cm d'épaisseur, les résultats sont donnés dans le tableau II.

Tableau II - Résultats de la modélisation des plaques pour 8 MPA sur le bâti

Plaque	E(GPa)	ν	Tension maximale (MPa)	Flèche maximale (mm)
inférieure	220	0,28	184	.8
supérieure	220	0,28	360	3,6

Le suivi de la pression dans le bâti se fait soit à l'aide de la mesure de la pression dans le vérin plat, soit à l'aide des lectures d'extensomètres à corde vibrante collées sur chacune des tiges d'acier (deux jauges par tige), soit par l'intermédiaire de quatre cellules de charge installées entre la plaque supérieure et le boulons de chacunes des tiges.

Enfin, le remplacement des C.I.U.S. se fait à l'aide d'un carottier de 152 mm de diamètre extérieur et de 66 cm de longueur. Une photo du bâti est présentée sur la figure 12.

6. CONCLUSION

La conception et la fabrication d'un bâti ayant pour but la simulation des instruments de mesure en conditions réelles est une nécessité. Il a été présenté, ci-dessus, la technique qui a été utilisée au Laboratoire de mécanique des roches de l'Université de Sherbrooke. La méthode utilisée pour la conception a l'avantage d'être simple tout en modélisant au plus près les futures opérations en laboratoire. Quant au bâti, il a été conçu pour être proche des conditions en chantier tout en minimisant les coûts; le matériel employé est ainsi facile à se procurer et demande peu de rectifications (tiges et plaques d'acier, vérin plat, cubes de béton). Il peut être construit dans un atelier conventionnel de mécanique et sa précision se situe aux alentours de 10%.

Le procédé de conception utilisé pour dimensionner le bâti n'est pas propre au cas présenté. Il peut être appliqué à n'importe quelle autre simulation en laboratoire. De plus, un tel montage peut être utilisé pour la simulation d'autres instruments (cellules de mesure, comportement d'ancrage sous charge uniaxiale, ...).
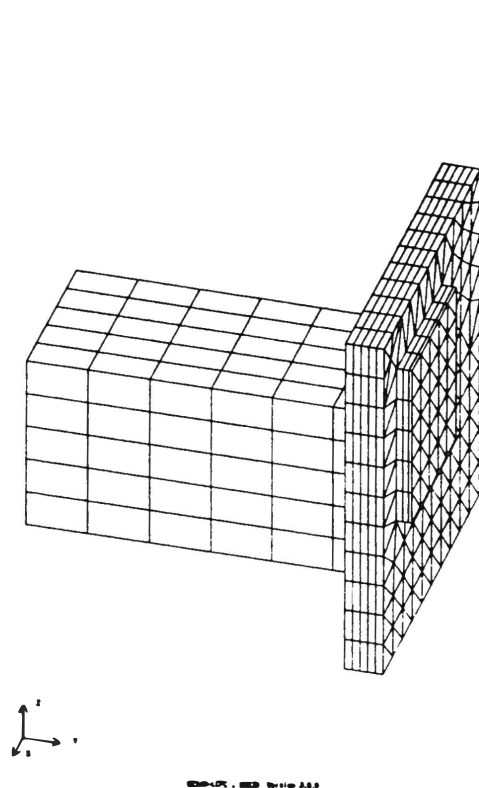
Figure 10 - Maillage pour dimensionner
la plaque inférieure
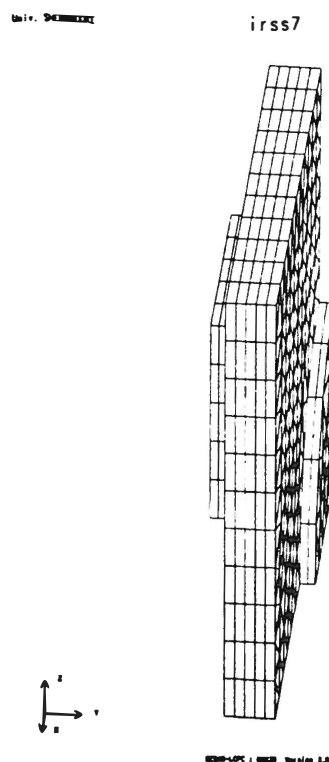
Figure 11 - Maillage pour dimensionner
la plaque supérieure

7. REMERCIEMENTS

7. RÉFÉRENCES

AL-CHALABI, M., HUANG, C.L. (1974) *Stress distribution within circular cylinders in
compression.*, Int. J. Rock Mech. Min. Sci & Geomech. Abstr., **11**, p.45-56.
BALLIVY, G., BENMOKRANE, B., POULIN, R., SALEH, K. (1990) *Une nouvelle
technique d'inclusion pour la mesure à long terme des déformations dans des barrages en
béton*, Revue Canadienne de Génie Civil, 17-6.
BONNECHÈRE, F. (1967) *A comparative study of in-situ rock stress measurement
techniques*, M.S. Thesis, University of Minnesota.

PENG, S.D. (1971) *Stresses within elastic circular cylindres loaded uniaxially and triaxially,*
Int. J. Rock Mech. Min. Sci & Geomech. Abstr., **8**, p.399-432.
SAVIN, G. (1961) *Stress concentration around holes*, Pergamon, New York.
SPATHIS, A.T.,TRUONG, D. (1987) *Analysis of a biaxial elastic inclusion stressmeter,*
Int. J. Rock Mech. Sci & Geomech. Abstr., **24**, n° 1, p. 31-39.
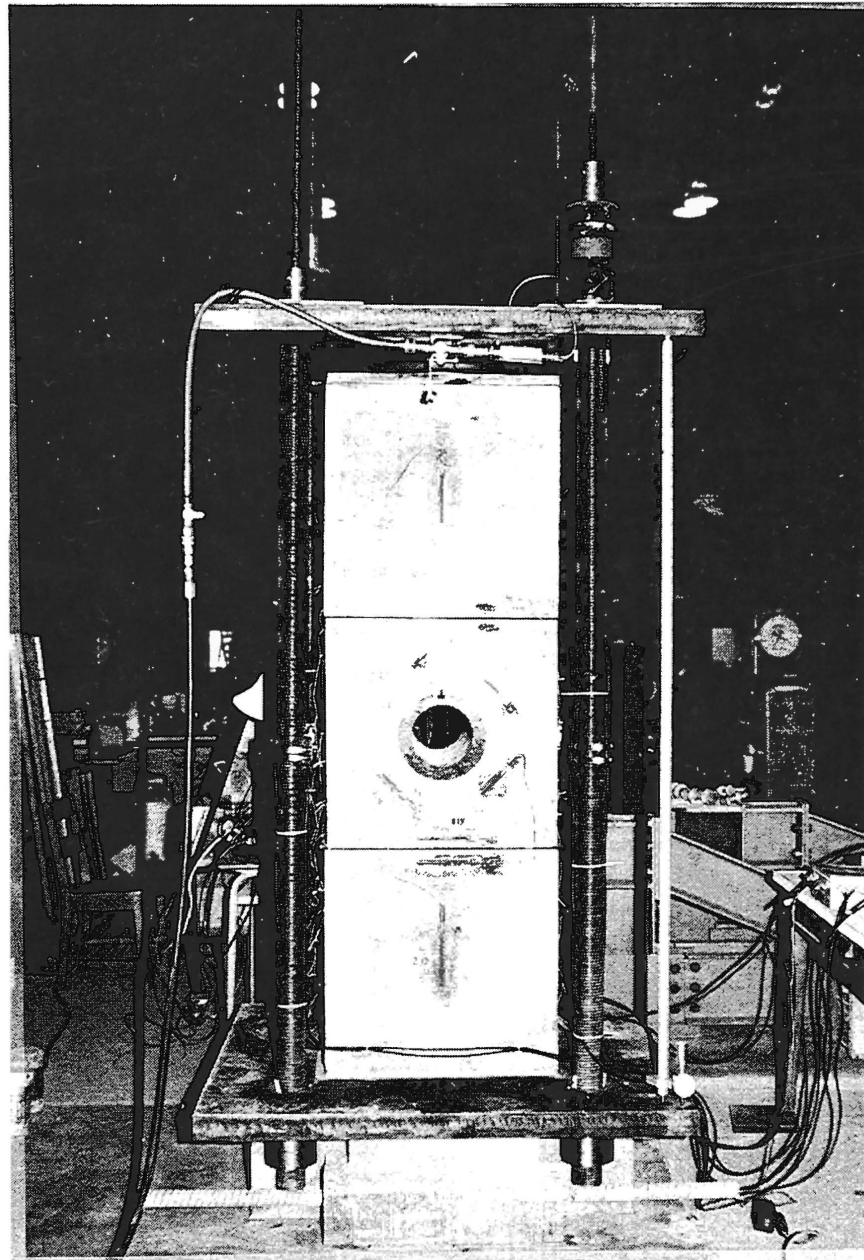
Figure 12 - Bâti de chargement

Study of Transient Flow in Hard Fractured Rocks with a Discrete Fracture Network Model

Souheil Ezzedine[1], Ghislain de Marsily[2]

[1]*CIG/LHM, Ecole des Mines de Paris, 35 Rue St Honoré, 77305 Fontainebleau Cedex.*

[2]*LGA, Université Pierre et Marie Curie, 4-5 Place Jussieu, 75252 Paris Cedex 05.*

ABSTRACT

A model was developed for transient flow in a fractured medium on the basis of a three-dimensional discrete fracture model. The fracture network is reduced to a system of one- dimensional connexions where the flow is governed by Darcy's law. The model is based on the solution, by Laplace transform, of the diffusion equation in one dimension for all the connexions, assumed to be cylindrical. The continuity of heads and flow at each node makes it possible to express the transformed heads at the nodes as a system of linear equations. In order to solve this system of equations it is necessary to numerically invert the Laplace transform of the heads, which was done with the methods by Talbot and Stehfest. The model was tested on simple geometries and promises well for use on real cases.

RÉSUMÉ

Un modèle d'écoulement transitoire dans un milieu fracturé modélisé au moyen d'un modèle à fracture discrète tridimensionnel a été mis au point. Le réseau de fracture est ramené à un système de liens monodimensionnels où l'écoulement est régit selon la loi de Darcy. Ce modèle basé sur la résolution de l'équation de diffusivité en une dimension, dans tous les liens supposés cylindriques, par la méthode de la transformée de Laplace. La continuité des charges et des flux en chaque nœud permet de mettre sous forme d'un un système d'équations linéaires les charges transformées aux nœuds. La résolution du système établit nécessite une inversion numérique de la transformée de Laplace des charges, ceci a été fait par les méthodes de Talbot et de Stehfest. Le modèle a été testé sur des géométries simples et laisse présager de bons résultats dans son application à des cas réels.

INTRODUCTION

This study lies within the framework of forced flow in fractured rocks and concerns, in particular, the research into heat extraction from deep, hot, dry rocks. Because of the geometric scale on which the observations were made and the phenomena occur, it was not possible to use an equivalent porous medium approach, and a discontinuous representation was therefore chosen. Moreover, data of observed characteristics in the fractured medium (borings, outcrops, etc.) are, overall, very scarce, making it seem preferable to consider each family of fractures in the network as random.

Thus, the geometrical model assumes that the fractures are finite and can be assimilated to simple elements, such as discs or polygones whose geometric properties, distribution in space, direction and extension can be sampled on the basis of probability distributions, deduced from structural observations on the site (Dershowitz et al., 1988; Long et al., 1983). It is assumed that the stationary hypothesis is satisfied and these magnitudes are not taken to be regionalized variables.

GEOMETRIC MODEL

In this approach, based on the model by Cacas et al. (1990) and Ezzedine (1991), the fractures are treated as discs. The density and extensions are difficult to determine independently. There are relations between these magnitudes that can be used to test the connectivity of the medium (Charlaix et al., 1984). The hydaulic model is a bond model. The flow is not two-dimensional in the fracture plane but occurs in channels linking the centers of the connected discs. The walls are impervious. An additional parameter called "hydraulic thickness" is attributed to each disc in the model.

Characteristics of the fracture families

In natural networks, fractures can usually be divided into families of directions. For a realization lots are drawn sequentially, for one family of directions at a time. The families are then placed on top of each other to create the final network (Figure 1).
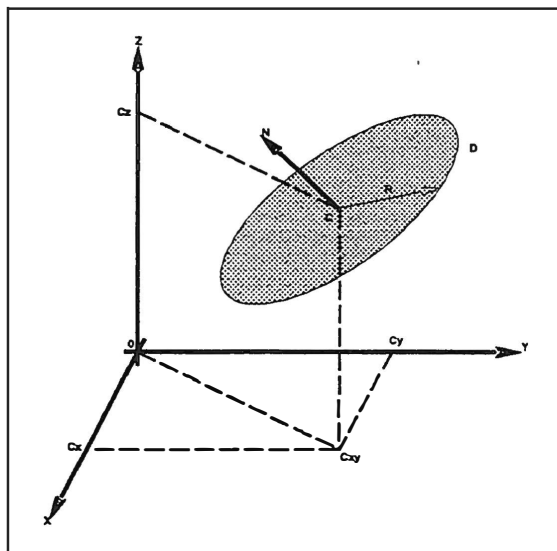
Figure 1: Characteristics of a network.

For a given family, the draw is made as follows:

Number of fractures. A Poisson process is used to obtain the number of discs belonging to family i in the simulated volume $V(m^3)$ as a function of the volumetric density $\lambda_i (number\ of\ discs/m^3)$. The following expression gives the probability of having an N_i number of centers in the volume V.

$$p(N_i = k) = e^{-\lambda_i V} \frac{(\lambda_i V)^k}{k\,!}$$

Location of the disc centers. The centers of the discs are independently distributed. The drawing of the Cartesian coordinates of the centers is done in a domain called the "generation domain". If this bloc is the group of points satisfying $x_1 \le x \le x_2$; $y_1 \le y \le y_2$ et $z_1 \le z \le z_2$, the x, y and z coordinates of the centers are drawn according to a uniform law in the intervals $[x_1, x_2]$, $[y_1, y_2]$ and $[z_1, z_2]$.

Direction. The direction of a fracture is defined by its normal unit vector $\overrightarrow{N}$. The families of directions in a network consists of fractures with similar directions. Their normal vectors form an approximately cone-shaped segment, the axis of which is the "pole" of the family. The probability density of Fisher's law is expressed as follows:

$$f_\kappa(\alpha) = C(\kappa)\, e^{\kappa \cos \alpha}\, \sin \alpha \quad \text{with} \quad C(\kappa) = \frac{\kappa}{4\pi \sinh(\kappa)}$$

where f represents the probability density of the angle α formed with the pole of the family (the pole is here the mean normal vector of the family); α is the angle between the fracture pole and the pole of the family; κ is the parameter of the law. For $\kappa \to \infty$ the distribution is very concentrated around the mean direction. For $\kappa \to 0$, this distribution is closer to the uniform law.

Radius. The radius is the parameter describing the extension of the fracture. Several statistical laws are available:

Law	Density f(x)	Mean E(X)	Variance V(X)
Log-normal	$\dfrac{1}{\sigma\, x \sqrt{2\pi}} \exp\left[-\dfrac{1}{2}\left(\dfrac{\ln(x) - \mu}{\sigma}\right)^2\right]$	$\exp\left[\mu + \tfrac{1}{2}\sigma^2\right]$	$\exp[2\mu + \sigma^2]\; \exp[\sigma^2 - 1]$
Exponential	$\lambda e^{-\lambda\, x}$	$\dfrac{1}{\lambda}$	$\dfrac{1}{\lambda^2}$
Gamma	$e^{-\lambda x}\dfrac{(\lambda x)^{k-1}}{(k-1)\,!}$	$\dfrac{k}{\lambda}$	$\dfrac{k}{\lambda^2}$

CONNECTIVITY

The analysis of the connectivity and the search for continuous paths within such fracture networks use algorithms shared with the theory of graphs which have already been used by, for example Robinson (1984). It is, in fact, easy to ascertain whether two fractures are interconnected or not but, in a network of fractures, it becomes very costly (in computer time) to examine all the fracture couples. Therefore, the flow region is cut up into a certain number of blocs. A given disc intersects one or several of these elementary volumes. Two discs will not cut across each other unless both of them together cross at least one of the blocs. It is therefore necessary to test a possible intersection of two discs only if they are geographically fairly close to each other. This method makes it possible to limit the number of tests. Then, the number of fracture couples is reduced from $\frac{1}{2}N \times (N-1)$ to $\frac{1}{2}\frac{N^2 h^3 k^2}{R^3}$ if the flow region is divided into cubes of volume h^3 and a fracture crosses k cubes (Robinson suggests $\frac{1}{2}\frac{N^2 h^2 k^2}{R^2}$ in two-dimensional cases). Thus, the number of tests is reduced by $\frac{h^3 k^2}{R^3}$ provided that h is chosen as small as possible and k is of the order of 2 or 3 for one fracture.

Furthermore, the group of fractures that are not included in the flow are taken out of the system by means of a "from one to the next" procedure (Cuthil-McKee, 1969). In this procedure, one looks for the fractures connected at the limits (fractures of level 0), then for those that intersect them (fractures of level 1)... The fractures not affected by this procedure and the discs connected to only one other disc are eliminated from the system.

320

CHANNELLING

The "channelling hypothesis" is taken into account in the model by defining a permeability, said to be "integrated", into which the effective flow area is introduced. This permeability is defined later.

FLOW IN THE FRACTURE NETWORK, INTEGRATED PERMEABILITY

Once the interconnected geometry of the formation has been constructed, one defines the links connecting the centers of the two fractures that pass through the middle of the intersection segment. Thus, the geometry is reduced to a group of one-dimensional elements placed end to end in a three-dimensional domain (Figure 2).
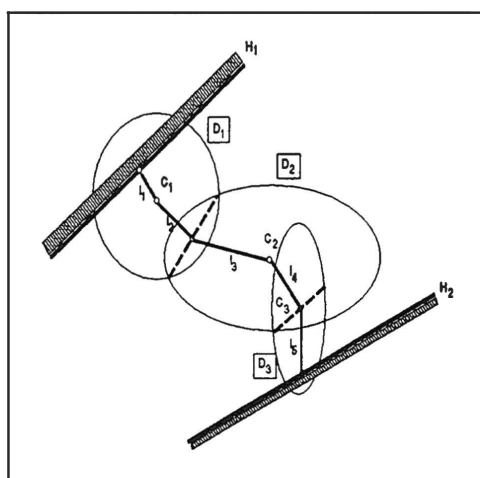
Figure 2: A simple hydraulic system.

Between two secant fractures, water circulates in a tube linking their centers and passing through the intersection segment. Assuming a fixed, straight, hollow cylinder of l length, large compared to the diameter $2R$, the volumetric flow in the tube is proportional to the fall of the pressure and to the fourth magnitude of the radius (Snow, 1969).

$$Q = \frac{\pi}{8\mu}R^4 \nabla h \tag{1}$$

where μ is the kinematic viscosity and ∇h the hydraulic gradient between the ends of the tube. The "integrated hydraulic conductivity" of a connexion is defined as the ratio between the flow rate and the head gradient:

$$k = \frac{Q}{\nabla h} = \frac{\pi}{8\mu}R^4 \tag{2}$$

Such as it is defined here, the integrated hydraulic conductivity is the product of the "real" hydraulic conductivity (expressed in m/s) multiplied by the cross-section of the flow, which is difficult to measure by hydrogeological tests.

In this model, each disc is characterized by an integrated hydraulic conductivity which is determined by a drawing of lots for the aperture (radius) according to a log-normal law. Then expression (2) is used. Take a connexion linking together two discs whose integrated conductivities are k_1 and k_2, the integrated conductivity of the connexion is then fixed at the following value:

$$k_{12} = \frac{(l_1 + l_2)k_1 k_2}{(l_2 k_1 + l_1 k_2)} \tag{3}$$

where l_1 and l_2 are the length of the two segments forming the complete connexion. This magnitude represents the mean resistance which prevents the water from circulating between two secant fractures. It integrates the whole flow geometry at the scale of the fracture: roughness of the walls, real tortuosity and length of the flow lines, channelling, etc.

TRANSIENT FLOW IN A FRACTURE NETWORK

Flow hypotheses and equations

Consider a branch of a flow network (Fig. 3) limited by two nodes i, j, of length L_{ij} where the flow is governed by Darcy's law. This flow is characterized by a spatial variation of the conductivity $k_{ij}(x)$ and a specific storage $S_{ij}(x)$ where x is the distance between the observed section and the node i, measured along the branch.
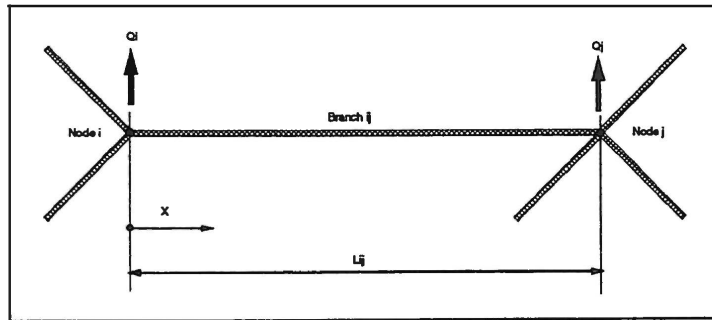
Figure 3: Flow network.

The conventions used here are: 1) $k_{ii} = 0$; 2) if two nodes are not connected, $k_{ij} = 0$; 3) in general, the nodes have no capacity.

Let $s_{ij}(x, t)$ be the drawdown in the ij branch, at distance x from node i, at time t (Fig. 3). Using Darcy's law and the continuity equation, we can write:

$$S_{ij}(x)\frac{\partial s_{ij}}{\partial t} = \frac{\partial}{\partial x}\left(k_{ij}(x)\frac{\partial s_{ij}}{\partial x}\right) \tag{4}$$

The drawdowns are measured in relation to an initial state of equilibrium. Subsequently, all the drawdowns are equal to zero at $t = 0$:

$$s_{ij}(x, 0) = 0 \tag{5}$$

and

$$s_{ij}(0, t) = s_i(t) \tag{6}$$

$$s_{ij}(L_{ij}, t) = s_j(t) \tag{7}$$

Because of the Darcy equation, the flow toward node i in branch ij is written:

$$q_{ij}(t) = -k_{ij}(0)\frac{\partial s_{ij}}{\partial x}(0, t) \tag{8}$$

and similarly

$$q_{ji}(t) = k_{ij}(L_{ij})\frac{\partial s_{ij}}{\partial x}(L_{ij}, t) \tag{9}$$

322

Assuming that the nodes have no capacity, the mass balance equation at each node i is:

$$\sum_{j \neq i} q_{ij}(t) = Q_i(t) \tag{10}$$

Solution of the equations for a network with homogeneous branches.
In the case where each branch of the homogeneous network is characterized by a constant conductivity k_{ij} and a constant diffusivity $D_{ij} = k_{ij}/S_{ij}$, equation (4) is simplified to:

$$\frac{\partial s_{ij}}{\partial t} = D_{ij} \frac{\partial^2 s_{ij}}{\partial x^2} \tag{11}$$

Applying the Laplace transform to equation (11) and introducing the boundary conditions expressed by (5) and (7) we have:

$$\bar{s}_{ij}(x,p) = \bar{s}_i(p)\cosh(\lambda_{ij}x) + [\bar{s}_j(p) - \bar{s}_i(p)\cosh(\lambda_{ij}L_{ij})]\frac{\sinh(\lambda_{ij}x)}{\sinh(\lambda_{ij}L_{ij})} \tag{12}$$

where

$$\lambda_{ij}^2 = \frac{p}{D_{ij}} \tag{13}$$

By using (12) in the Laplace transform of (8) in order to obtain $\bar{q}_{ij}$ which is substituted in the Laplace transform of (10), we obtain a system of linear equations for the drawdowns at the transformed nodes:

$$\sum_j a_{ij}\bar{s}_j(p) = \bar{Q}_i(p) \tag{14}$$

where

$$a_{ij} = -k_{ij}\lambda_{ij}\operatorname{csch}(\lambda_{ij}L_{ij}) \qquad i \neq j \tag{15}$$

$$a_{ii} = \sum_{k \neq i} k_{ik}\lambda_{ik}\coth(\lambda_{ik}L_{ik}) = -\sum_{k \neq i} a_{ik}\cosh(\lambda_{ik}L_{ik}) \tag{16}$$

It is assumed that the matrix $[a_{ij}]$ cannot be inverted and that $[b_{ij}]$ is its inverted form, then the formal solution of (14) is:

$$\bar{s}_m(p) = \sum_k b_{mk}\bar{Q}_k(p) \tag{17}$$

which is the solution for the drawdowns at the nodes. The drawdown at each point of the branch is given by (12).
Numerical methods for inverting the Laplace transform
We used two methods to invert the linear system of Laplace transforms for the drawdowns at the nodes in order that one may serve to validate the other. The two methods are those of Stehfest (1970) and Talbot (1978). Stehfest's method does not only have the advantage of being easy to adapt and of programming in a real mode but it also uses the values of the function to inverse directly, without any transformation. As opposed to this, Talbot's method demands a few prior transformations and its adaptation needs programming in a complex mode. Both methods lead to the solution of systems of linear equations in $\mathbb{R}$ and $\mathbb{C}$, which are written $Ax = b$, where A is a sparse symmetric matrix with x the vector of the transformed unknown heads and b the right-hand vector defining the hydrogeologic boundary conditions of the formation. The coefficients of A, x and b are either real or complex.

Solution of the linear equation systems

Because the matrix is so sparse, it is tempting to use an iterative solver (e.g. Gauß-Seidel, Jaccobi or SOR). However, the matrix is very ill-conditioned because it is only just diagonally dominant, and these methods all converge extremely slowly, so we used a semi-iterative solver, the pre-conditioned conjugate algorithm. Conjugate gradient-type methods used in combination with preconditioning are among the most effective iterative procedures for solving large, sparse, nonsingular systems of linear equations (Freund, 1992).

EXAMPLES AND CONCLUSIONS

o One-dimensional

A succession of 19 connected fractures has been used to represent a pipe. These fractures are regular and have the same radius and aperture, 5 m and $2 \times 210^{-3} m$ respectively. This pipe, $0 \le x \le l$ with a zero initial drawdown, is subject to a maintained head of 100 m at $x = 0$ and 0 m at $x = l$ (Fig. 4). A 10 h transient flow has been simulated (Fig. 5) and it is shown a good convergence to the steady state flow. This test was calculated with the two numerical methods for inverting the Laplace Transform discussed herein and yields two indistinct curves.
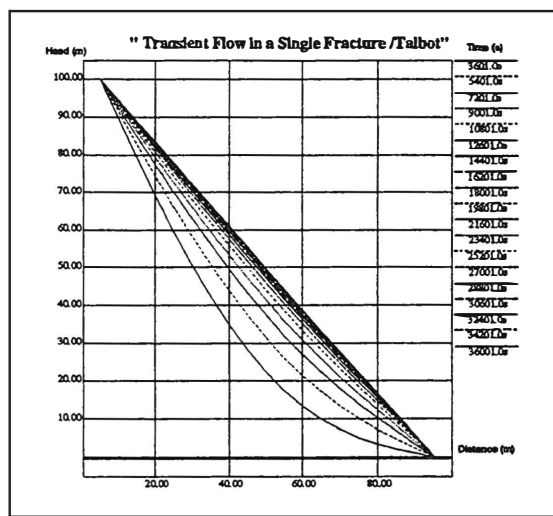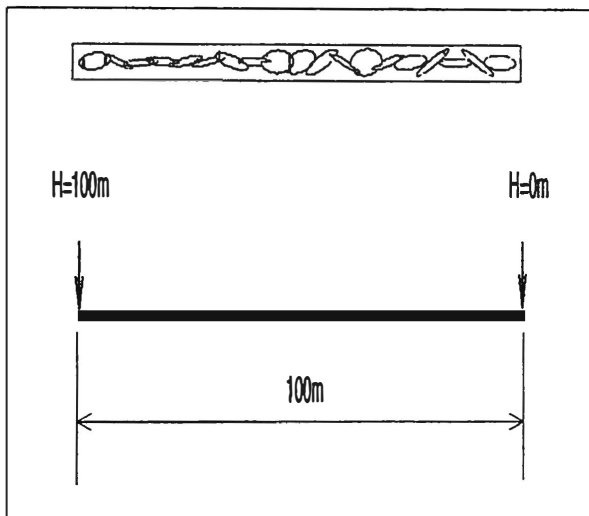
Figure 4: One-dimensional flow network.   Figure 5: Transient flow through a pipe.

o Two-dimensional

Two tests related to a two-dimensional approach have been performed to verify the model. The first one represents a transient fluid flow trough a circular plate composed by a set of connected fractures to give a circular network. The plate is subject to maintained head and no flow conditions at the boundary, as shown in Figure 6. Three scenarios have been simulated :

* Flow through a symmetrical geometry with an homogeneous permeability. Head distribution is presented at four times (Fig. 8: 1a,b,c,d, 4);

* Flow through a symmetrical geometry with and heterogeneous permeability at four times (Fig. 8: 2a,b,c,d). The permeability was independently distributed according to Log-normal law (Fig. 8: 3);

* Flow through a non-symmetrical geometry and homogeneous permeability at two times (Fig. 6, 8: 5a,b) to show the impact of the asymmetric geometry compared to the 1st scenario.

The second test represents a transient fluid flow trough a square plate composed by a set of connected fractures to give a square network flow. The plate is subject to a maintained head and no flow conditions as shown in Figure 7. As in the 1st test, three scenarios have been simulated :

* Flow through a asymmetrical geometry and homogeneous permeability at four times (Fig. 7, 9: 1a,b,c,d);

* Flow through a symmetrical geometry and homogeneous permeability at four times (Fig. 9: 2a,b,c,d, 4).

* Flow through a symmetrical geometry and heterogeneous permeability at two times (Fig. 9, 5a,b). The permeability was independently distributed according to Log-normal law (Fig. 9: 3);

All tests show a good concordance with some analytical solutions for steady and transient flow in non-homogeneous and anisotropic rock joints (Amadei et al., 1992).
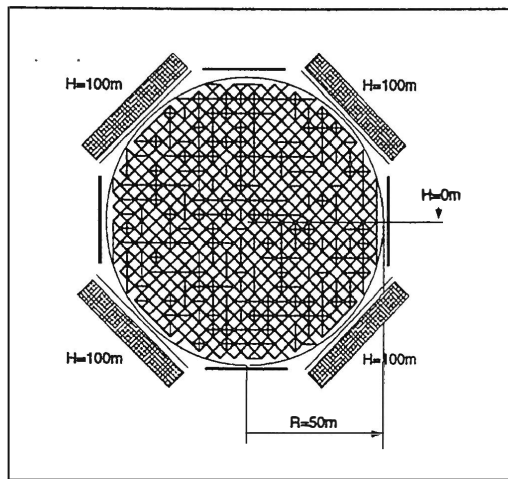
Figure 6: Circular flow network.
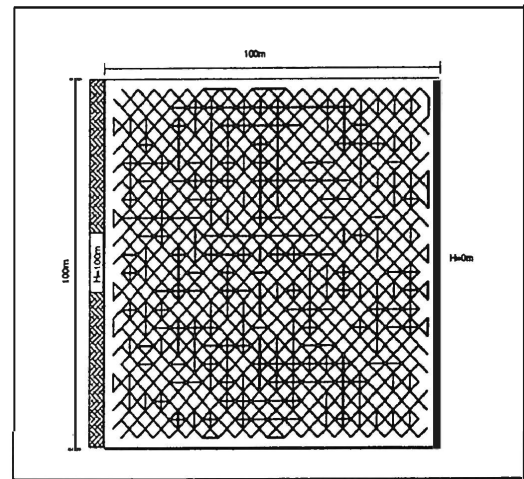
Figure 7: Square flow network.

REFERENCES

o Amadei B., Illangasekare T., Analytical solution for steady and transient flow in non-homogeneous and anisotropic rock joints. Int. J. Rock Mech. Min. Sci. & Geomech. Abstr. vol. 29, No. 6, pp. 561-572, 1992.

o Cacas M.C., E. Ledoux, G. de Marsily, B. Tillie, A. Barbreau, E. Durand, B. Feuga, P. Peaudecerf, Modelling fracture flow with a discrete fracture network: calibration and validation. 1. The flow model. Water Resources Research, vol.26, no.3, 479-489, 1990.

o Charlaix E., E. Guyon, N. Rivier, A criterion for percolation threshold in a random array of plates. Solid State Communications, vol.50, no.11, 999-1002, 1984.

o Cuthil E., McKee J, Reducing the Bandwidth of Sparse Symmetric Matrices. Proc. 24th Nat. Conf. Assoc. Comput. Mach. ACM Publ. P-69, New York, 1969.

o Dershowitz W.S. and H.H. Einstein, Characterizing Rock Joint Geometry with joint system models. Rock Mechanics and Rock Engineering 21, 21-51, 1988.

o Ezzedine S., Projet Européen d'extraction de la chaleur des roches profondes. Conception et utilisation du modèle FRACAS. EMP, CIG - LHM/RD/91/23, 1991.

o Freund R.W., Conjugate Gradient-Type Methods for Linear Systems With Complex Symmetric Co-efficient Matrices. Siam J. Sci. Stat. Comput. Vol. 13, No 1, pp. 425-448, January 1992.

o Long J.C.S., Investigation of equivalent porous medium permeability in networks of discontinuous fractures. Ph. D. thesis, LBL, Univ. of California, pp. 277, 1983.

o Robinson P.C., Connectivity, Flow and Transport in Network Models of Fractured Media. PhD, Oxford Univ. 1984.

o Snow D.T., Anisotropic Permeability of Fractured Media. Water Resour. Res., vol 5, no 6, pp. 1273-1289, 1969.

o Stehfest H., Algorithm 368, Numerical Inversion of Laplace Transform. ACM, Vol 13, No 1, 1970.

o Talbot A., The accurate numerical inversion of Laplace transforms. J. Int. Math. Appl., 23, 97-120, 1979.
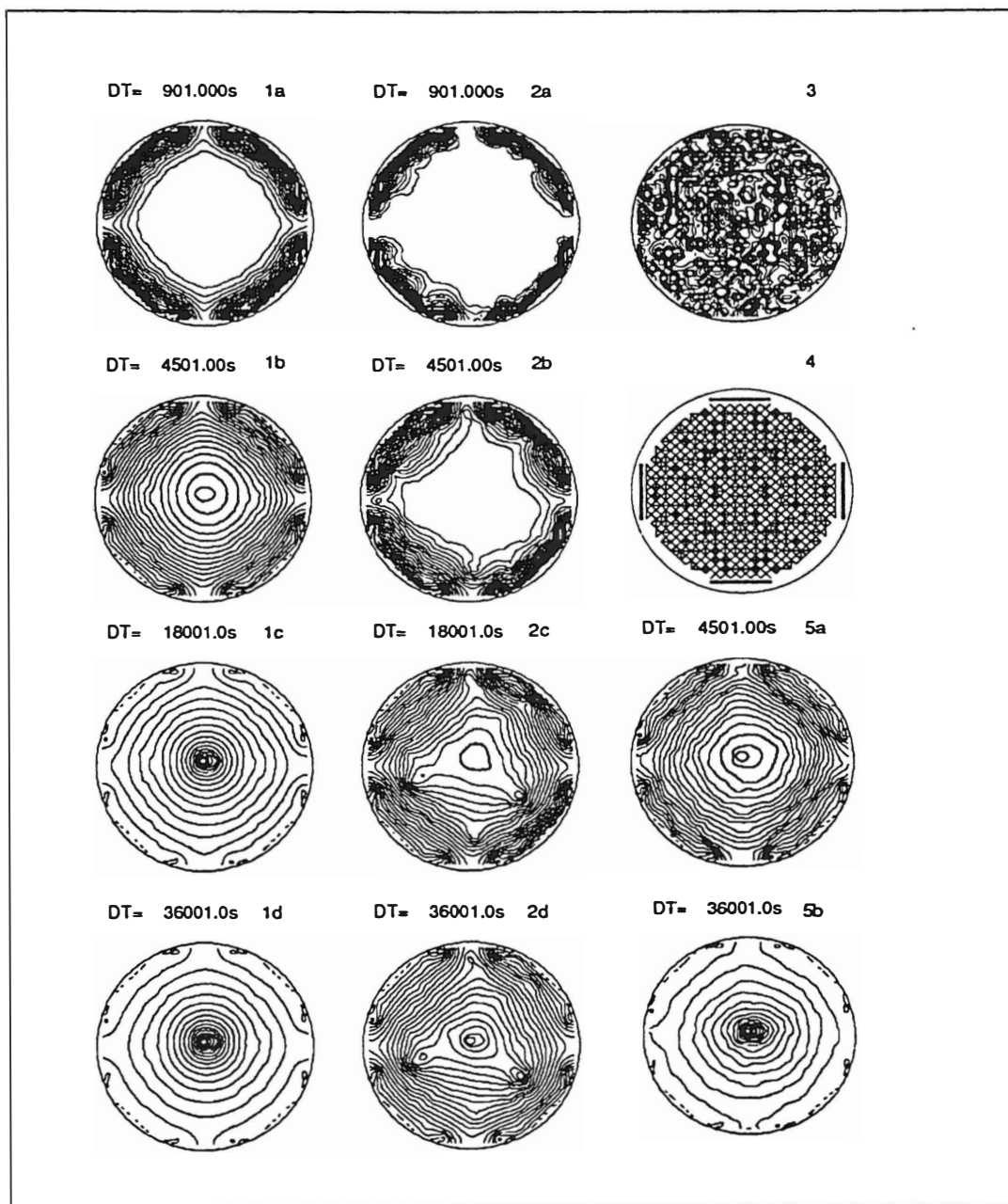
Figure 8: 1a,b,c,d: symmetric geometry, homogeneous permeability; 2a,b,c,d: symmetric geometry, heterogeneous permeability; 3: random distribution of the permeability, 4: flow network; 5a,b: asymmetric geometry effect with homogeneous permeability.
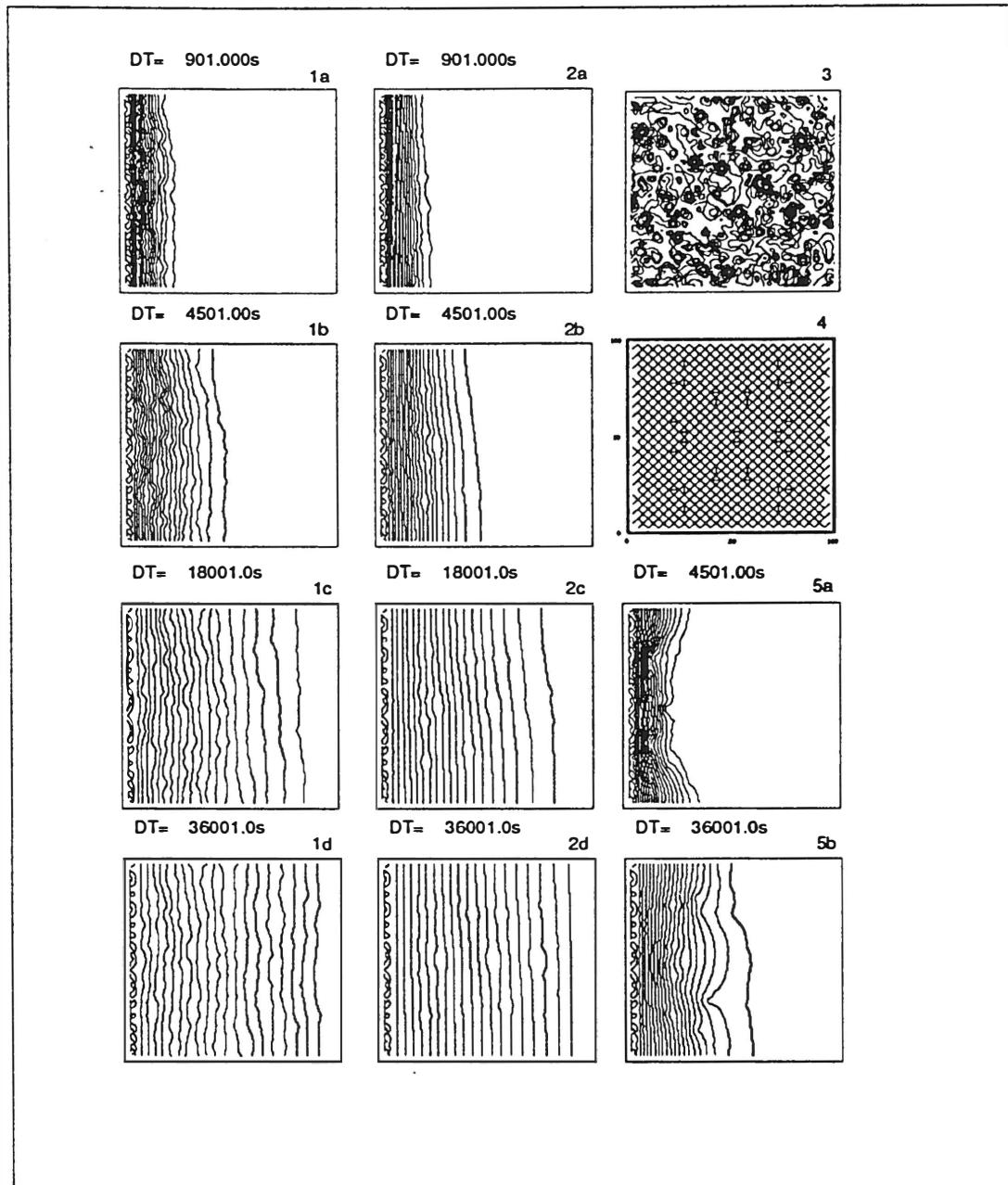
Figure 9: 1a,b,c,d: asymmetric geometry, homogeneous permeability; 2a,b,c,d: symmetric geometry, homogeneous permeability; 3: random distribution of the permeability, 4: flow network; 5a,b: symmetric geometry effect with heterogeneous permeability.